Yuman Fong · Pier Cristoforo Giulianotti
Jason Lewis · Bas Groot Koerkamp · Thomas Reiner
Editors

Imaging and Visualization in the Modern Operating Room

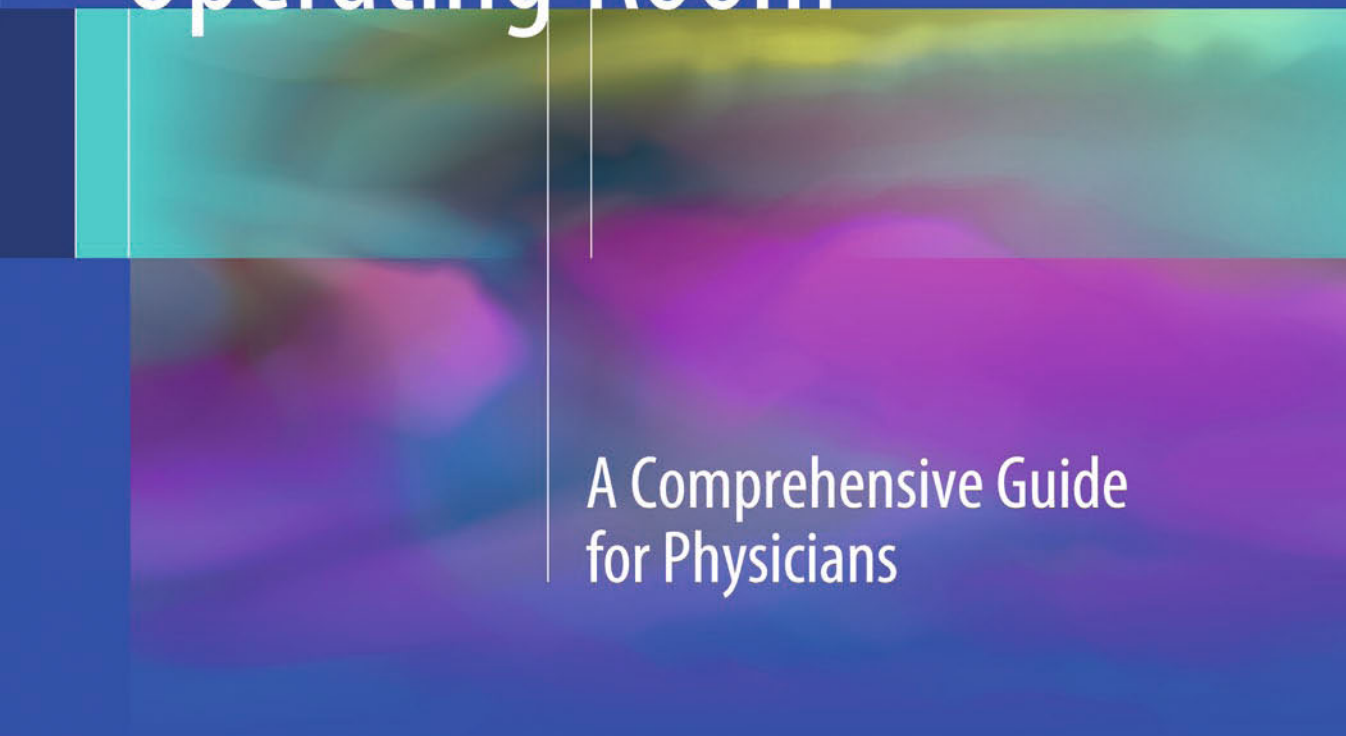

A Comprehensive Guide for Physicians

Springer

Imaging and Visualization in the Modern Operating Room

Yuman Fong
Pier Cristoforo Giulianotti
Jason Lewis
Bas Groot Koerkamp
Thomas Reiner
Editors

Imaging and Visualization in the Modern Operating Room

A Comprehensive Guide for Physicians

Springer

Editors
Yuman Fong
Department of Surgery
City of Hope National Medical Center
Duarte
California
USA

Pier Cristoforo Giulianotti
General & Robotic Surgery
University of Illinois at Chicago
Division of Minimally Invasive
Chicago
Illinois
USA

Jason Lewis
Department of Radiology
Memorial Sloan-Kettering Cancer
Center
New York
New York
USA

Bas Groot Koerkamp
Department of Surgery
Erasmus University Medical Center
Rotterdam
The Netherlands

Thomas Reiner
Department of Radiology
Memorial Sloan-Kettering Cancer
Center
New York
New York
USA

ISBN 978-1-4939-2325-0 ISBN 978-1-4939-2326-7 (eBook)
DOI 10.1007/978-1-4939-2326-7

Library of Congress Control Number: 2015930823

Springer New York Heidelberg Dordrecht London

Printed on acid-free paper

Springer is part of Springer Science+Business Media (www.springer.com)

Preface

White Light and Beyond

The evolution of advanced procedure rooms in the last two decades has been remarkable. The advanced technology operating room (OR), the image-guided interventional radiology (IR) suites, and the hybrid rooms with duo capability are springing up not only in academic centers, but also in disease-specific clinical sites, and high-volume private-practice sites. As simultaneous multi-team procedures for complex disease, minimally invasive surgery, and multi-imaging guidance continue to proliferate, the need for complex lighting solutions grows.

Along with advanced procedure technology, non-white light imaging has also matured to become a usable and useful modality in the modern procedure/operating room. Optical imaging using near-infrared or fluorescent imaging now allows real-time biologic imaging exploiting cellular biology to enhance contrast between normal tissues and pathology. Biologic optical imaging now also highlights locations of essential structures such as nerves and vessels to avoid procedure-related injury. These contrast and biologic labeling agents hold the promise of precisely guiding resection of cancers, drainage of infections, and relief of luminal obstruction of anatomic conduits while avoiding damage of nearby essential structures.

This book aims to summarize the birth and current status of this exciting applied field. Our work is divided into two sections. We first start with a "basis of practice" section discussing the most important advances, the potential of various novel imaging modalities, and the current status. The book then presents a "current clinical practice" section summarizing the current status of approved and near-approval modalities.

The authorship of this work includes many of the luminary and most innovative investigators in this field. We thank them for their contributions and this most wonderful collaboration. This work is intended for anyone working in a modern interventional or operating room. In particular, we are targeting those who may be asked to evaluate new technology for hospitals and clinics or may be asked to help design and implement the next generation of operating/intervention/hybrid rooms.

The quick progress of procedural imaging and visualization in the last years is due not only to scientists, engineers, and clinicians, but also due to patients who have enrolled in the necessary trials. We therefore thank the patients who have contributed to the advances, and whose diseases are the targets that push us to create new solutions.

Gratitude also goes to our postdocs, research fellows, and colleagues who helped us gather data, refine our hypothesis, and design the next tools, and our editor at Springer Daniel Dominguez. Finally, we thank our families and particularly our spouses Nicole, Mikel, Paola, Salome, and Virginia for the patience and support they have given us to do our daily investigative and clinical work, and then to complete a work such as this.

Yuman Fong, Duarte
Jason Lewis, New York
Pier Cristoforo Giulianotti, Chicago
Bas Groot Koerkamp, Rotterdam
Thomas Reiner, New York

Contents

Contributors

P. Beatriz Beatriz Garcia-Allende Institute for Biological and Medical Imaging, Technical University of Munich, Munich, Germany

John Benson Ultrasound Business Unit, Siemens AG Healthcare, Issaquah, WA, USA

Jeffrey Berman Jeffrey Berman Architect, New York, NY, USA

Vivek Bindal Department of Surgery, Sir Ganga Ram Hospital, New Delhi, India

Michelle S. Bradbury Department of Radiology, Memorial Sloan-Kettering Cancer Center, New York, NY, USA

Cesar M. Castro Center for Systems Biology, Harvard Medical School, Massachusetts General Hospital and Harvard University, Boston, MA, USA

Kai Cheng Department of Radiology, Stanford University, Stanford, CA, USA

Zhen Cheng Department of Radiology, Molecular Imaging Program at Stanford, Canary Center at Stanford for Cancer Early Detection, Stanford, CA, USA

Aileen L. Co Department of Chemical and Biological Engineering, University of Maine, Orono, ME, USA

François Cornelis Department of Radiology, Memorial Sloan-Kettering Cancer Center, New York, NY, USA

Farhad Daghighian IntraMedical Imaging LLC, Hawthorne, CA, USA

Despoina Daskalaki Department of Surgery, University of Illinois Hospital and Health Sciences System, Chicago, IL, USA

Christoph Dickmann Healthcare Sector, Siemens AG Healthcare, Forchheim, Bavaria, Germany

Brian J. Dunkin Department of Surgery, Houston Methodist Hospital, Houston, TX, USA

Caroline Flowers Department of Surgery, Houston Methodist Hospital, Houston, TX, USA

Yuman Fong Department of Surgery, City of Hope National Medical Center, Duarte, CA, USA

Robert L. Galloway Department of Biomedical Engineering, Neurosurgery, Surgery, Vanderbilt University School of Engineering, Vanderbilt University School of Medicine, Nashville, TN, USA

David A. Geller University of Pittsburgh Medical Center, Pittsburgh, PA, USA

Pier Cristoforo Giulianotti Department of Surgery, University of Illinois Hospital and Health Sciences System, Chicago, IL, USA

Segundo Jaime González H. Lee Moffitt Cancer Center, Tampa, USA

Jeremy L. Grant Department of Chemical and Biological Engineering, University of Maine, Orono, ME, USA

Jan Grimm Molecular Pharmacology and Chemistry and Department of Radiology, Memorial Sloan-Kettering Cancer Center, New York, NY, USA

Nora M. Hansen 1Prentice Woman's Hospital, Northwestern Memorial Hospital, Chicago, IL, USA

Harry W. Herr Department of Urology, Memorial Sloan-Kettering Cancer Center, New York, NY, USA

Hyungsoon Im Center for Systems Biology, Harvard Medical School, Massachusetts General Hospital and Harvard University, Boston, MA, USA

Takeaki Ishizawa Department of Gastroenterological Surgery, Cancer Institute Hospital, Japanese Foundation for Cancer Research, Tokyo, Japan

Norihiro Kokudo Hepato-Biliary-Pancreatic Surgery Division, Department of Surgery, Graduate School of Medicine, University of Tokyo, Tokyo, Japan

Hakho Lee Center for Systems Biology, Harvard Medical School, Massachusetts General Hospital and Harvard University, Boston, MA, USA

Sungon Lee Division of Electrical Engineering, Hanyang University, Ansan, Republic of Korea

Robert Brian Leiter Architectural Lighting Design, Hillmann Dibernardo Leiter Castelli, New York, NY, USA

Arthur G. Lerner Medical Tech Consultants, Palm City, FL, USA

Jason S. Lewis Department of Radiology, Memorial Sloan Kettering Cancer Center, New York, NY, USA

Michael D. Mason Department of Chemical and Biological Engineering, University of Maine, Orono, ME, USA

Philip Mewes Healthcare Sector, Siemens AG Healthcare, Forchheim, Bavaria, Germany

Andreas Meyer Healthcare Sector, Siemens AG Healthcare, Forchheim, Bavaria, Germany

Michael I. Miga Biomedical Engineering, Neurosurgery, Radiology, Vanderbilt University School of Engineering, Vanderbilt University School of Medicine, Nashville, TN, USA

Peter Mountney Healthcare Sector, Siemens AG Healthcare, Forchheim, Bavaria, Germany

Stéphane Andre Nicolau R&D, IRCAD of Strasbourg, Strasbourg, France

Georg Nollert Healthcare Sector, Siemens AG Healthcare, Forchheim, Bavaria, Germany

Vasilis Ntziachristos Institute for Biological and Medical Imaging, Technical University of Munich, Munich, Germany

Kristin Patton Department of Surgery, University of Illinois Hospital and Health Sciences System, Chicago, IL, USA

Mohan Pauliah Department of Radiology, Memorial Sloan-Kettering Cancer Center, New York, NY, USA

Thomas Reiner Department of Radiology, Memorial Sloan Kettering Cancer Center, New York, NY, USA

Michael A. Scherer Analogic Corporation, Peabody, MA, USA

Ina Schwabenland Healthcare Sector, Siemens AG Healthcare, Forchheim, Bavaria, Germany

Mikhail Silk Department of Radiology, Memorial Sloan-Kettering Cancer Center, New York, NY, USA

A. M. Sitarski Department of Chemical and Biological Engineering, University of Maine, Orono, ME, USA

Luc Soler R&D, IRCAD of Strasbourg, Strasbourg, France

Stephen Solomon Department of Radiology, Memorial Sloan-Kettering Cancer Center, New York, NY, USA

Jonathan Sorger Intuitive Surgical Incorporated, Sunnyvale, CA, USA

Vivian Strong Surgery Department, Memorial Sloan-Kettering Cancer Center, New York, NY, USA

Dirk Sunderbrink Healthcare Sector, Siemens AG Healthcare, Forchheim, Bavaria, Germany

V. Suzanne Klimberg Winthrop P. Rockefeller Cancer Institute, Little Rock, AR, USA

Chris Tihansky Mauna Kea Technologies, Doylestown, PA, USA

Evan K. Tummel Department of Surgery, University of Arkansas for Medical Sciences, Little Rock, AR, USA

Claudio Vinegoni Center for Systems Biology, Massachusetts General Hospital, Harvard University, Boston, MA, USA

Markus Weingarten Healthcare Sector, Siemens AG Healthcare, Forchheim, Bavaria, Germany

Ralph Weissleder Center for Systems Biology, Harvard Medical School, Massachusetts General Hospital and Harvard University, Boston, MA, USA

Ralph Weissleder Center for Systems Biology, Massachusetts General Hospital, Harvard University, Boston, MA, USA

Eric B. Whitacre The Breast Cancer Center of Southern Arizona, Tucson, AZ, USA

Ulrich Wiesner Materials Science and Engineering, Cornell University, Ithaca, NY, USA

Li Zhang Healthcare Sector, Siemens AG Healthcare, Forchheim, Bavaria, Germany

Yachao Zhang Department of Radiology, Memorial Sloan Kettering Cancer Center, New York, NY, USA

Part I
Basis of Practice

Lighting in the Operating Room: Current Technologies and Considerations

1

Jeffrey Berman, Robert Brian Leiter and Yuman Fong

Lighting is a critical design element in the construction of functional and efficient operating rooms (ORs). Before the invention of electric lights, the challenge was to adequately light the surgical field and the work area to allow doctors, nurses, and support staff to see what they are doing. Procedures could only be done when there was sufficient daylight. For the last 50 years, during the time of open surgery and electric lights, the challenge was to provide even lighting without shadows that was consistent and color corrected in order to enhance the ability of surgical staff to see and focus in the surgical site. With the advent of robotic minimally invasive, image-guided laparoscopic procedures and other enhanced visualization and guidance systems, PACS and electronic medical records, the demands and needs for different qualities, types and intensities of light as well as variations of brightness and focus in the different zones around the room have become primary functional and design challenges and concerns.

Y. Fong (✉)
Department of Surgery, City of Hope National Medical Center, 1500 E. Duarte Road, Duarte, CA 91010, USA
e-mail: yfong@coh.org

J. Berman
Jeffrey Berman Architect, New York, NY, USA

R. B. Leiter
Architectural Lighting Design, Hillmann Dibernardo Leiter Castelli, New York, NY, USA

Lighting systems today must provide flexibility in terms of intensity in the level and movement of light in the space, so that the system can adapt to the different requirements of open surgery, minimally invasive surgery, or image-guided procedures (Fig. 1.1) [1].

The need for different lighting in different zones within the OR to support the specialized functions during the procedure, and the complexity of the integrated OR control systems have added an additional level of complexity beyond what was seen even in the recent past. The commercialization of new light sources, specifically light-emitting diodes (LEDs), has raised a series of interesting life cycle, maintenance and complex design and selection issues that must be considered in order to provide consistency of lighting and color balance from room to room and from specialty area to specialty area, and adequate and proper color rendering of tissues, organs, and patients during the procedure.

These advancements create opportunities and add complexity to the design and integration of these rooms. The typical modern OR operates in several different modes in the course of the day. If we look at simple open surgical cases, we have the set-up mode, the patient prep modes, surgical procedure mode, patient transfer mode, cleanup mode, and the time when the room is closed in between cases and overnight. At each time, lighting issues are different.

ORs require an even and consistent shadow-free general lighting as well as the correct number of focused articulated surgical lights. The

Y. Fong et al. (eds.), *Imaging and Visualization in The Modern Operating Room,*
DOI 10.1007/978-1-4939-2326-7_1, © Springer Science+Business Media New York 2015

Fig. 1.1 3T magnetic resonance imaging (MRI) image-guided interventional OR. Diagnostic and interventional systems are integrated into standard OR environments with common controls and information displays. LED installation matches fluorescent lighting in adjacent ORs

number of lights depends on the complexity of procedure being performed. For the traditional open operation, there is usually little movement of the work area. The location of the work site, the instruments and, for the most part, all of the effort is focused on supporting the surgeon working at a single site. In more complex cases, we must be able to support multiple surgeons working simultaneously in closely spaced or distant parts of the body. This complicates the number of light sources, the types of lights, the locations of those lights, and the control requirements.

Work Zones

There are 2–6 work zones in a functioning OR. Each needs to be supported and given the proper light levels and type of light [2]. When designing the lighting, we must be aware of the multiple and very different work functions that are occurring simultaneously within the room that need to be supported. Each type of procedure has different lighting requirements based on the visualization guidance system and instruments that are being used. This is further complicated by the fact that often these procedures are performed in combination or composite, either simultaneously or immediately sequentially. The lighting either has to support multiple needs in very closely spaced parts of the room or needs to switch very rapidly as we move from mode to mode in procedures (Figs. 1.2, 1.3, and 1.4).

In concert with the actual procedure are a large assortment of support functions, ranging from charting that is often done on computer or some combination of computer and paper, and administration of anesthesia and assorted medications. The organization and arrangement of instruments, both sterile and used, which are either being arranged and set out to come into the field or being repackaged and catalogued or inventoried to leave the room to be reprocessed. The constant flow of supplies and other materials to the room need to be picked up, visualized, scanned, catalogued, opened, set out and repacked and returned at the end of the case. There are treatment, planning, and research into both the medical records and diagnostic information, such as PACS and other image guidance data sets that need to be visualized on video screens both in the field and at a desk. Then, there are general administrative scheduling and other planning functions that are mapped on computers around the room or accessed from time to time by a computer.

This wide variety of functions and activities presents a unique challenge both in its dynamic and changing nature and in the different requirements each one represents in terms of lighting for proper working functional support. In many cases, these different needs can be met by creating different zones and work areas with task lighting either mounted on the equipment or mounted on the ceiling. In either case, the important thing to provide is local controls that are convenient to the individual uses that can be accessed without disturbing other lighting within the room or other people working. This is done with a combination of programmable lighting controls that are accessed from the computers in the room as well as a series of conveniently located wall switches and control panels. These are all part of an integrated lighting system that controls all of lighting in the room.

The complexity of the modern OR and the difficulty in dealing with the large number of zones

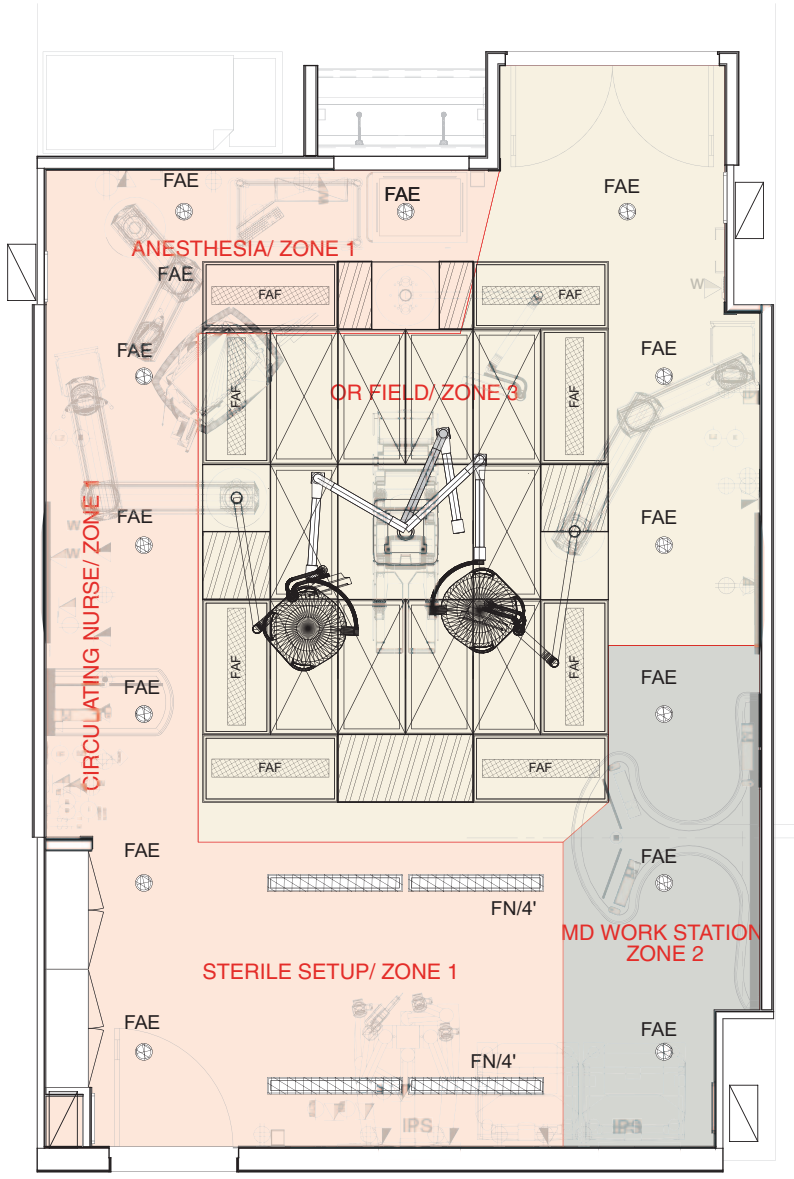

Fig. 1.2 Work zone diagram. MD desk, anesthesia, and circulating nurse and OR field are separately controlled and specifically designed for separate needs during cases. Represents a minimal number of functional zones to support simple cases. This is a recent OR design produced as a universal design to support multiple specialties and modes of work: open/laparoscopic, robotic, and some multiple surgeries and composite procedures

is mitigated by the computer programmable controls of the lighting systems that allow us to program optimized scenes coordinating lighting schemes in each of the zones. For each operation or function, an optimized and orchestrated lighting scene can be planned and set up, and stored that allows immediate use. This allows an optimal lighting scheme to be recalled for immediate use. Such programmed scenes allow general staff and individuals not familiar with the operation of the lighting system to alter the environment for their needs without extensive training

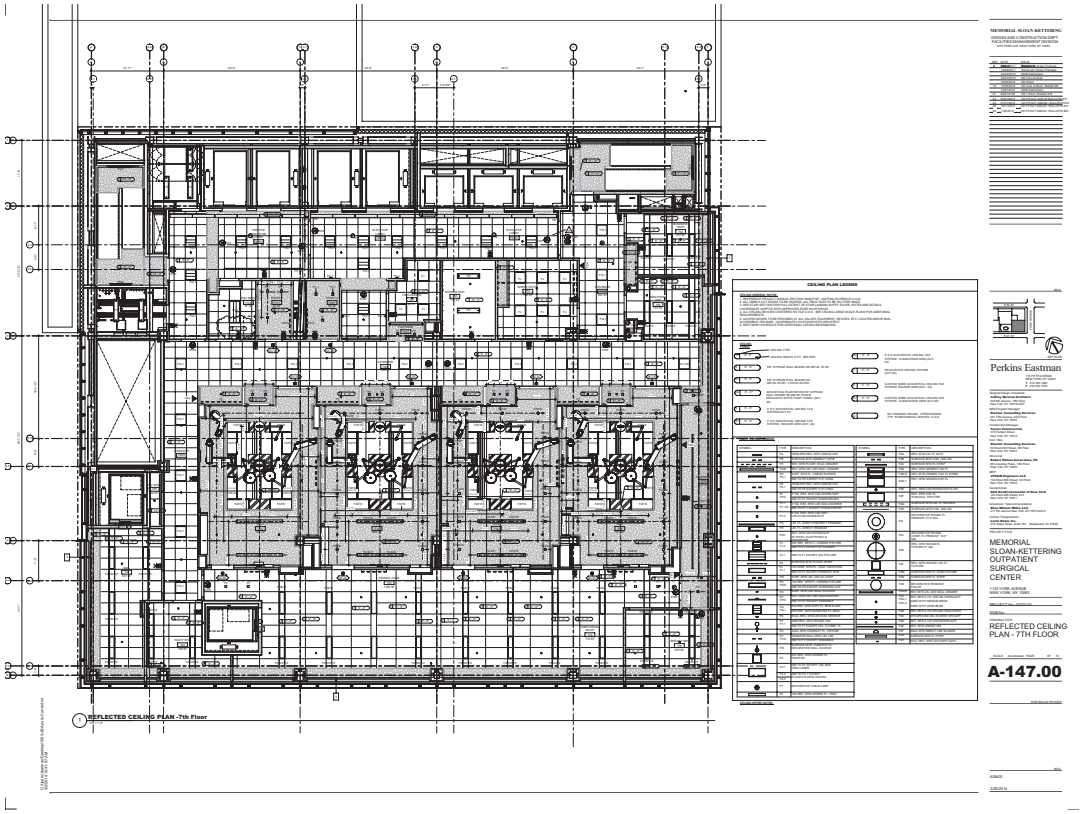

Fig. 1.3 A more complex control scheme is overlaid to provide more control and zones to allow for finer adjustment and better lighting relationships to changing or more complex needs in larger cases. The figure shows complex lighting system incorporating six working zones with individual functions and controls

Fig. 1.4 MIS general OR. ORs at specific hospitals are designed to a common standard. Equipment is always integrated within the standard work environments, and interfaces remain consistent throughout the ORs. This photograph illustrates lighting requirements, including ceiling lights, spot LED lights, and green light for dimmed environments. Diffusers in the center of the room for laminar airflow are also seen

or assistance to operate the lights that support such functions such as cleaning and maintenance of the room with simple and familiar wall switch controls.

Sterile Installations, Seals, and Suspensions

In order to create and maintain clean and sterile work areas, it is key that all fixtures remain contaminant free by virtue of being sealed for infection control, protecting against any contaminants from either the plenum or room side. Materials must stand up to cleaning protocols using chemical cleaners without breaking down. Likewise, these fixtures and their suspensions need to be gasketed and sealed properly in the

integration into the ceiling system. Fixtures must be reviewed for gasketing, antimicrobial finishes, smooth surfaces (including lenses) and stainless steel fasteners. Housings should be completely hole free and seams welded. Antimicrobial coatings on painted surfaces help to maintain a sterile surface, particularly in hard to reach or clean surfaces in the fixtures.

ORs require special fixtures and special ceiling systems that differ in their dimensions and construction from normal systems and light fixtures. Code [2] calls for a sealed monolithic ceiling. In order to install modular light fixtures, we need to either use a drywall system where the fixtures are taped and spackled into the system or a clean room gasketed system that has silicone seals built into the grid. Because surgical suites will be positively pressurized to minimize intrusion of contaminants, the fixtures should be engineered to provide a leakproof barrier between the flange and the ceiling, eliminating the transfer of contaminants between the interior and the plenum. The grid has a different dimension than a standard ceiling system and so the light fixtures need to be modified to fit.

Electromagnetic Interference Reduction

Within surgical suites it is critical to mitigate the potential of interference between radio frequency interference, also known as electromagnetic interference (EMI), emissions from the light fixtures and power distribution systems that cause complications and interference with the surgical equipment, which is sensitive to such interference. AC-powered light fixtures are known to generate EMI, particularly with the inclusion of dimming into the system of the OR. LED light fixtures have advantage over fluorescent in this regard, as the DC-based systems produce less EMI; but any light fixtures must reduce the EMI through additional integrating shielding systems within the luminaires which can be located both in the fixture housings and the lenses themselves.

Heat Dissipation and Ventilation

Production of light from electricity is not 100% efficient; a significant percentage of the energy put into the system comes out as light, but there is also portion that is dissipated as heat. This heat needs to be managed explicitly because it will be projected either into the room or into the ceiling plenum. In either case, heat dissipated into the room (radiant) will have a negative impact on the comfort of the patient and staff in the room. To maintain comfort of gowned, scrubbed, and masked surgical staff, lower temperatures are required. These lower temperatures will create issues maintaining the comfort and stasis of the patient. Heat dissipated into the ceiling plenum must be controlled and managed to maintain reasonable temperatures in the fixtures and prevent early aging of lamps and failure of ballasts or drivers in the fixtures.

Energy usage expended for lighting is a small component of total energy use when compared to HVAC and ventilation energy load requirements. While care must be taken in selecting light sources and fixtures, the generally accepted modern lighting sources—fluorescent, compact fluorescent and LED—are all sufficiently efficient both in terms of watts per lumen produced and fixture efficiency so that in general we can provide lighting where and as needed throughout the room. The provision of some redundant fixtures and zones to allow flexibility in room set up and function is an appropriate expenditure and design goal.

Dimming, Light Levels, and Green Light

Surgeons require excellent image quality and visibility of monitors during procedures, requiring an environment with high contrast, low glare and no incidence of screen washout. Many existing ORs have no dimming capacity. In this scenario, where there is a limited choice of level of light, lights around the room are often turned off to facilitate the viewing of the monitors (sonogram monitor, PACS monitor, laparoscopic or robotic

display). However, there are many additional tasks occurring within the OR, between the support team and the anesthesiologists who require light. Additionally, the staff encounters hazards while moving about a dark room, from tripping hazards to collision hazard with overhead projections. In response, a practice of bathing the room with dim green light was developed to accomplish the same goal without having the room grow dark or providing dimming. The internal surgical site was unaffected because it was still illuminated by the white light of the procedure lights or scopes, and visibility of the monitors was believed to be unaffected or even enhanced. Use of green light is further driven by issues associated with dimming of the fixtures around the OR. Fluorescents in downlights are limited in how far down they can dim, and they produce more EMI when they are dimmed, making it harder to mitigate light in the room.

Advances in the development of LED downlights and control systems now allow for great brightness control and dimming flexibility. This allows the surrounding OR environment to be lit to low levels, without washout or incident glare on the OR monitors. Given this development, there is debate as to the current usefulness of green lighting. Some studies have shown that visual acuity as related to seeing detail can improve in a monochromatic light, favoring the yellow/green bandwidth over white light. Yet other studies have shown that monochromatic light is not preferable, indicating that physiological mechanisms come into play. In the end, effects of wavelength appear to be negligible, so the success of green light in surgical suites may have more to do achieving the result of reduction in brightness in rooms that do not have proper dimming and brightness control capacity than in the quality of the green light as a source. With advances in the control of the lighting with LED fixtures in the broader OR space, green light no longer serves the original intended purpose (Fig. 1.5).

The use of green lighting is no longer a default position and, while its use is not fundamentally flawed, the development of more sophisticated means for controlling the OR environment

Fig. 1.5 The computer model shows ceiling lights and equipment, OR with data from lighting model to evaluate layouts and sight lines, contrast, and hotspots

make this approach unnecessary. This idea was generated in the late 1990s when laparoscopic surgery and equipment was being retrofitted into existing ORs with very basic lighting and very limited controls. At the time dimming was not feasible for fluorescent fixtures and general incandescent lights were not dimmed because it was more important to maintain consistent and uniform lighting throughout the OR. The need was to light instruments, open work areas and the floor for walking, cleaning, and other functions. With the adoption of laparoscopic procedures which at the time used television sets with curved face cathode ray tubes, it became critically important to dim the lighting in the room sufficiently so that there was no glare on the screen. This meant turning off all the fluorescent lights and finding a way to lower the brightness of the downlights to a level necessary to provide light in the room for walking and handling of instruments without replacing all the light fixtures, rewiring, and rebuilding the entire room. It was found that the application of colored gels to the fixture's lens of sufficient density was a quick fix that could be implemented by either house staff or a surgeon with a little bit of tape and a ladder.

Modern lighting fixtures and light sources can now be controlled and dimmed to 1 or 2% without flicker, buzz, eye strain, or other issues that compromise the work area, including color

shift and lamp-life problems. The ability to light the OR to low levels with color-controlled white light source as opposed to a colored light is a clear functional improvement. Many of the issues related to surgical procedures require the visualization and evaluation of tissues, organs, blood flow, and other differences that are directly related to color. Working under monochromatic lights creates problems of visualization of perception that we no longer need to adjust to in an effort to maximize the visibility of the monitors.

In the surgical environment consisting of many rooms with varying procedures and operations occurring simultaneously, it is a significant advantage to have absolute lighting uniformity and color balance consistency from room to room to allow flexibility in scheduling and consistency in the working environment which will enhance both staff comfort and patient safety.

Consistency Within Rooms Versus Room-to-Room

It is now common for there to be many different types of procedures and equipment used on a typical OR platform. With this diversity comes a variance in ages of rooms and equipment and a shifting of specialty staff required to operate certain special equipment such as robots or image guidance systems. As the staff moves between rooms, it is important to provide a consistent environment so that they are not required to think about which room they are working in or what is special or different about each room. This uniformity and consistency is important in reducing errors and limiting eye strain and fatigue caused by a necessity to overthink normal operations and simple processes when complicated by environmental factors that vary from location to location.

Color characteristics of the lighting are critical to maintaining consistency in the appearance of the rooms and in viewing the objects and individuals with the rooms. Color characteristics include color temperature and the color rendering index (CRI) of the light source. Color temperature is a measure of the relative warmness or coolness of the light, measured in degrees Kelvin (K). CRI is a measure of how well a light source reveals the color of an object relative to a reference source. The most common color temperature for a hospital OR is 3500 K. The CRI of the sources should be as high as possible, but typically sources used in the OR will be nominally 85 CRI. Care in considering color consistency insures that objects moved from place to place within a room or from room to room should not change its appearance due to lighting. Achieving this consistency requires purchasing and selecting the fixtures that have identical color, temperatures, and color-rendering indices regardless of the light source.

Fixture performance is defined by the fixture's photometry. Photometrics is the testing of a light fixture's performance, where the light output is registered in a lab test and then published, indicating fixture distribution of light and efficiency of output. In using the photometry when designing a space, one is able to predict light distribution in the room, resulting in light levels from fixture layouts, and characteristics of the fixtures such as fixture glare. Photometric data are in a chart or graph format described as an Illuminating Engineering Society (IES) file. These files are used in lighting-calculation programs, developing computer models that demonstrate the achievement of the light levels, measured in foot-candles (FC), for the fixtures planned for the ceiling. Light levels for any space are typically designed to fall within the parameters defined by the Illuminating Engineering Society of North America, or IES. Within the surgical suite, the IES requires achieving nominally 100 FC for cleanup/setup, 200 FC generally over task area throughout the room, and 300 FC specifically at the table [3].

Depending on the procedure, the actual site of the surgery may require, up to 2500 FC provided not by the room lighting, but rather by specific surgical articulated procedure lights. These illumination targets are general, so multilevel switching at a minimum, and preferably, dimming fixtures, need to be utilized. In minimally invasive image-guided procedures, the light levels need to be dramatically reduced but

still allow for moving about the room, charting, and work of the anesthesiologist. While there are no specific criteria for these tasks from the IES, reading recommendations tend to be in the 30 FC range, so lights of a controlled brightness and distribution dedicated to the area of the anesthesiologist should be employed to facilitate functions such as reading labels.

Fixture selection and its related photometry are critical is assessing the success of the lighting design, reviewing the effectiveness of the lighting, anticipating visual comfort and disabling glare. Control of fixture brightness through physical source cutoff or brightness-controlling lenses is critical in assessing where the light source can actually be seen by the eye, either directly or peripherally, which compromises the vision of a person working in the space. Both horizontal distribution and vertical distribution need to be considered so that the light is not only even across the space horizontally, but also even vertically, both within the space and along the perimeter, avoiding scallops on walls caused by fixtures being placed too close to surfaces, and should be used to properly space fixtures, walls, and other objects in the field close to the fixture.

Producing an even contrast and controlled brightness are significant design issues which must be considered in selecting fixtures, placing and distributing the fixtures and then programming the control systems to set the lighting levels in the work areas. When performing highly detailed work in a surgical area including surgery selection and arrangement of instruments and inspection of instruments, shadows are a significant impediment to efficient work. Similar fixtures must be evenly distributed and set so that important work areas are lit from two or more angles to fill-in and eliminate the production of shadows from a single light source caused by an object between the working plane and a single light source.

In surgical environments, the highly detailed work, visual focus, and concentration necessary are physically demanding. These stresses and difficulties can be amplified by differences in light levels, glare or contrast from point to point within a single room. Small differences in lighting from point to point can be a distraction or require extra time and energy to allow ones eyes to adjust to changes in lighting or working distances. These differences need to be minimized and controlled. Designers must understand that room arrangements for different cases or teams will vary, sometimes slightly and sometimes substantially. The lighting must either consistently cover the working field in the room or be sufficiently adjustable or controllable to respond to these changes and support the procedures as they evolve (Fig. 1.6).

Video Recording and Observation

Video is now used universally throughout all ORs. The primary uses of video are for recording cases, for observation both locally and remotely, and as information sources for image guidance and reference. Video recording of open cases is generally best done through cameras above the surgical field, such as from light mounted cameras. These cameras now work at HD resolutions and are built into the heads of the surgical lights. They work well because in the cluttered overhead area above the surgical field there is little space for a camera and the clear view paths into the surgical field are generally blocked by heads and hands. In the organization of the case, the path from the light to the actual site of the surgery is always left clear so that the light can be focused on the work area. Though you can find better cameras, you generally do not get a better view than that provided by the light mounted camera.

Room observation and overview are generally provided by wall-mounted cameras. We must be careful to assure that their views to the areas of interest in the room are not blocked by booms and arms of booms and that the lighting does not shine into the cameras and produce glare or distortion. The ubiquitous use of video displays throughout the OR now requires thought in selecting and locating light sources so they do not produce glare on screens in locations where physicians are working and that areas are not overly lit so as to washout the detail on the screens.

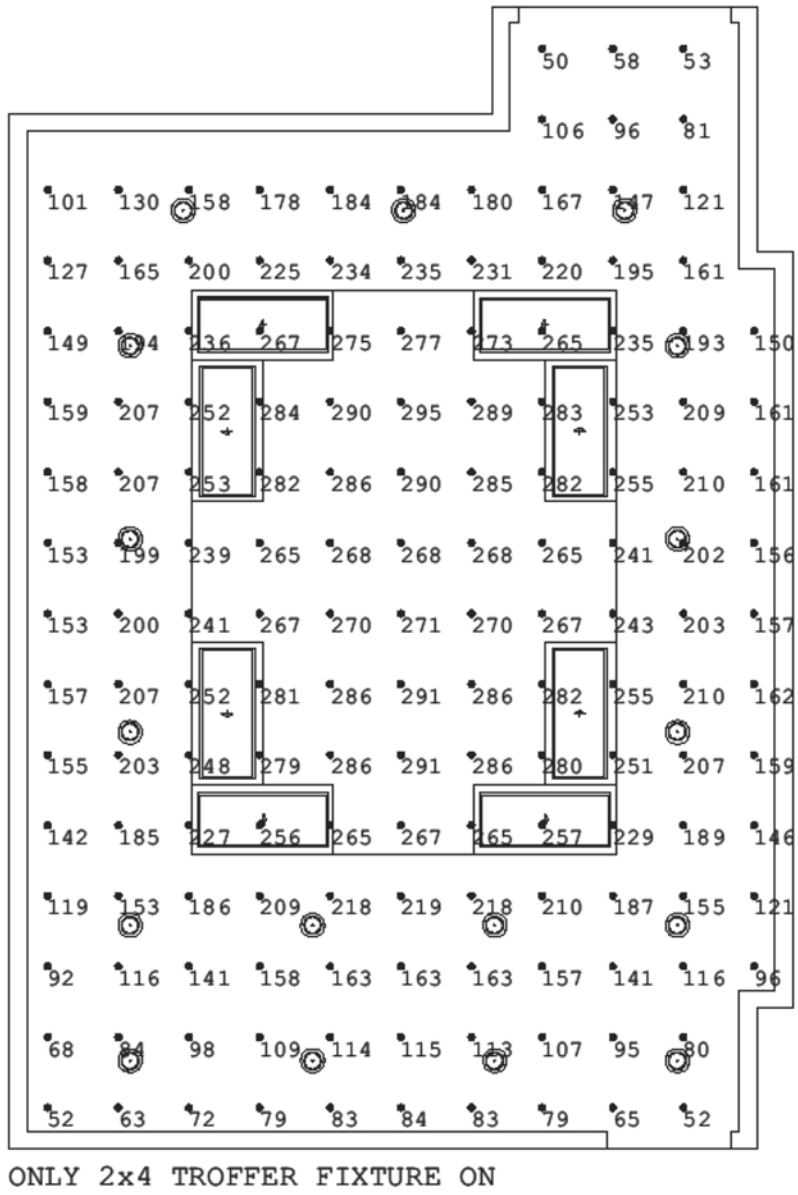

Fig. 1.6 Lumen microplots of light levels at working plane 36″ AFF for OR field lights only. We can see a fall off to the edges of the room, but there is enough light to work

Light

Sources have advanced and evolved extensively over the past several years: LED, incandescent, fluorescent light sources are all considered viable and useful light sources for commercial and specialized uses such as ORs. Each of these sources has various good and bad properties and is better for some functions than others. In the past few years, we have seen LEDs become very popular commercially and used extensively in certain applications. Their application in downlights and spotlighting points in an OR would be an excellent application. This takes advantage of the LED's compact size, making it more controllable and allowing for higher efficiencies in fixtures.

Also, LEDs are easily dimmable down to 1% and lower with reduced EMI. For general lighting there are still some limitations and compromises that may make fluorescent lighting a better choice than LED. This should be reviewed as technology develops.

Warmer color temperatures in white light LEDs are achieved principally by the use of phosphors, either directly on the board or in a module that functions as a mixing chamber. In linear fixtures, it is only available with the use of phosphors directly on the chips themselves, which makes the source much more vulnerable to color shift from fixture to fixture and over its rated life. As the chips age the colors shift slightly and maintaining a consistent color is difficult. While fluorescents drop to 85–90% of the original rated lumen output over their rated life, LEDs drop to nominally 70% over their rated life, so light intensity needs to be checked and may require that the LED boards be replaced significantly before the rated life of the fixtures. LED applications do not have a replacement or upgrade path other than to replace the circuit board or chip. Changing an individual circuit board will likely create problems of color consistency and color matching in rooms where single fixtures are repaired or replaced. Therefore, in using LEDs it must be anticipated that there will be a group replacement when significant board failure or lumen depreciation dictates such. The cost factor at that point will be significant to replace all of the boards.

Fluorescent tubes have a shorter lamp life than the LED fixtures, rate at 36,000 versus 50,000 h for the LEDs. Also, while LEDs fade over the rated lamp life, they will have far fewer premature failures. The rating of the fluorescents at 36,000 h is the point where half the lamps are out. However, fluorescents are more consistent in terms of color, temperature and spot relamping is rarely a problem in terms of perceived color, temperature shift or color rendering. Also fluorescents hold their lumen output much better over their rated life than the LEDs. The multiphosphorous tubes can be tuned to produce a wide range of color and temperatures and remain very accurate over their usable life although their usable life is shorter than that of an LED Chip. The issue of light loss depreciation due to aging of the lamps as well as physical deterioration of the materials in the fixture is less of an issue where the fluorescent bulbs are easily replaced and the fixture surfaces cleaned as part of the relamping. While the LEDs continue to improve with each generation of boards (which, at this point, are released annually), for the reasons stated previously we still recommend the use of T5 or T8 high output fluorescent fixtures for use in troffers and, due to efficiency increases in the design of LED downlights and spotlights, recommend the use of these light sources for this type of fixture. Proper selection specification of the light sources and the fixtures will result in an evenly and consistently lit OR that is easily maintained and meets the requirements for design contrast, even lighting and consistency we discussed above (Figs. 1.7 and 1.8).

Service access to maintain sterility in the modern OR is mandated by regulatory code: ceilings must be monolithic and while some flexibility for access and accommodations are made to install 2 × modular fluorescent fixtures, for all practical purposes fixtures once installed are fixed in place and can only be accessed from the front face or lens. This makes selection of these fixtures a critical maintenance decision. Each fixture must be reviewed for access, service, cleaning, lamping, and maintenance. This work should all be accomplished from below the ceiling without removal of the fixture housing, which should be completely sealed to control dust entry from the ceiling plenum. The service should include access to the power connections in the junction box, replacement of all the internal parts, including ballast or driver lamps, and all control circuitry, and the face of the fixture should be sealed to prevent anything in the fixture, from dust to a broken lamp, from falling out and into the sterile zones. The correct lens frame and reflector selection will control the light distribution, bright spots and reflections.

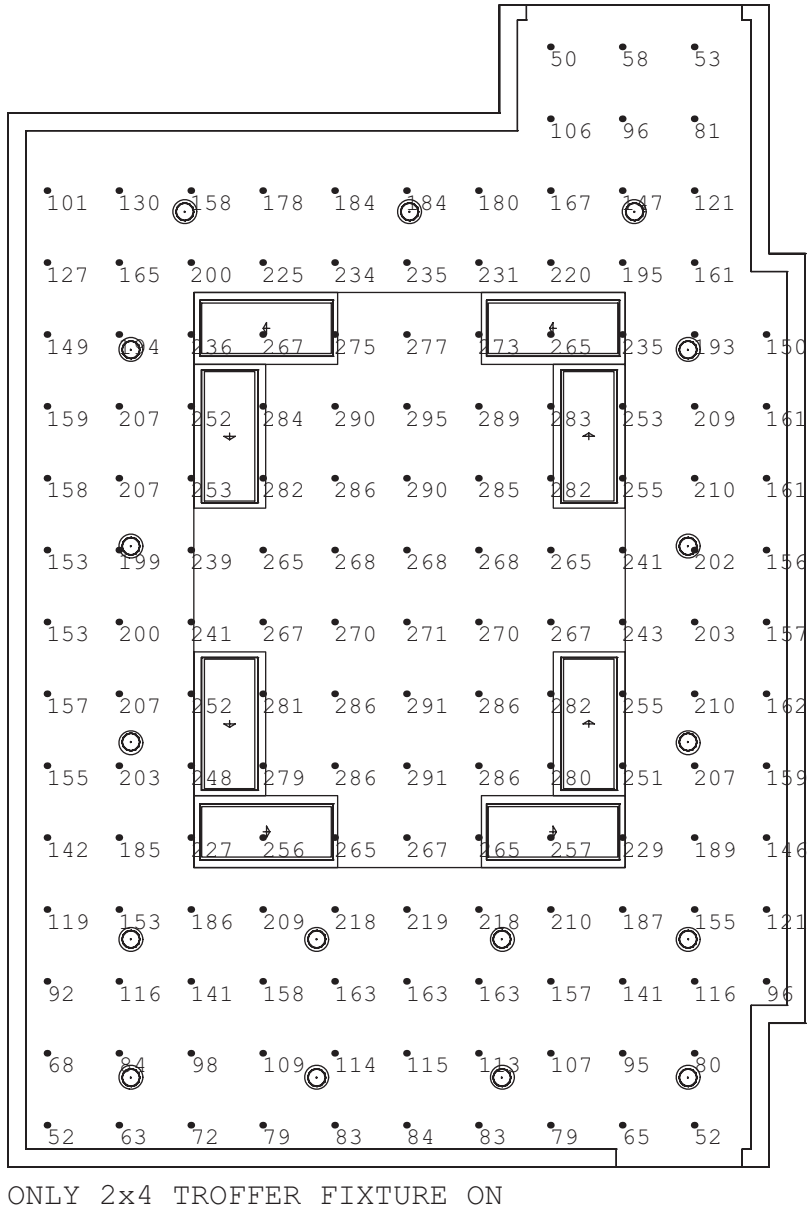

Fig. 1.7 Lighting to produce even illumination in work areas. *Numbers* indicate dim-lighting fixtures to adjust for video screen viewing and provide even light distribution around the perimeter

Controls

Controls for lighting systems in ORs can range from simple wall switches and single point on-off devices to complex computer controlled systems integrated with the OR computers, imaging systems, and other equipment in the OR. As the systems become more complex and integrated devices that appear and function as basic wall switches remain but evolve in operation to become interfaces and controllers for the computer systems that actually operate the lighting, touchscreens, and other visual interface devices, they are often incorporated to provide ease-of-use for a complicated system. The control systems also incorporate several complicated

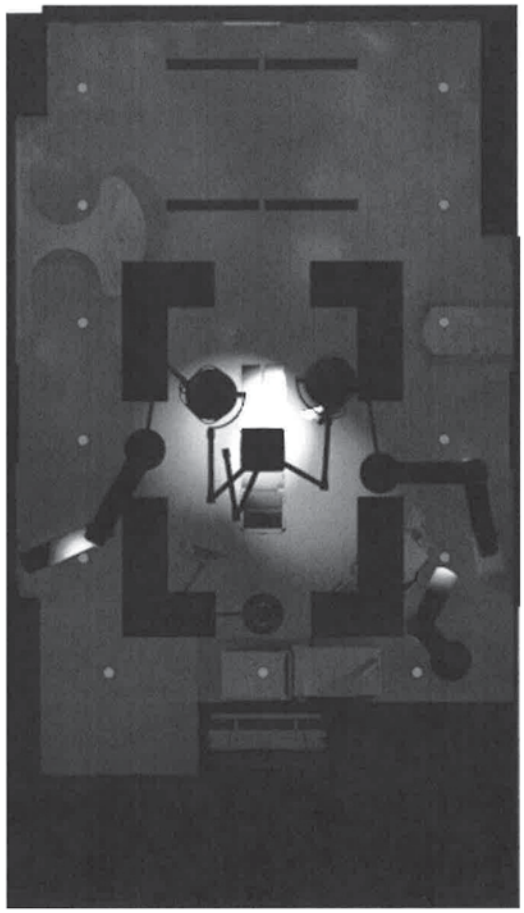

Fig. 1.8 Light patterns and intensity during an MIS or robotic case with room lights dimmed, task lights at desks and anesthesia area, and lit walkway around the field

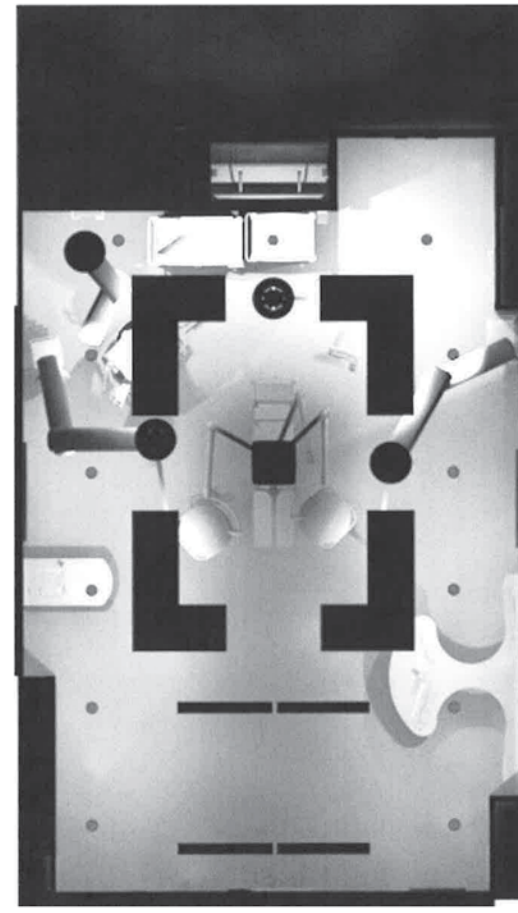

Fig. 1.9 Lighting at full brightness for open surgery, room set-up, cleaning, patient transfer or prep. The image illustrates consistency from edge to edge and lack of shadows

control schemes and paradigms. These include networked digital communication as well as separate low-voltage control circuits that provide control information to the fixtures, and are independent of the wiring, providing power and voltage, and operate the light sources. The control systems on the fixtures must be selected to be compatible and work together. Different control schemes generally cannot be interconnected. Control points need to be distributed and located so that staff can correct the lighting and make the adjustments they need without traveling around the room or asking other staff for assistance. Systems integration is sometimes a simple wall panel that is mounted in the room and is sometimes a panel or mounted set of devices that communicates to the fixtures through separate wiring.

The number of channels provided in the control system will determine the points of control available to the staff and the number of differently lit or controlled zones that are available. This needs to be clearly thought out in design because the wired systems are not easily rezoned or expanded after installation. The programmable systems vary in their adaptability depending on the system, where and how the programming is done and how the individual sources zones and fixtures are identified and addressed (Fig. 1.9).

Summary

With many different sources and more complex fixtures, photometrics and construction of light fixtures, the complexity inherent in designing and building the lighting system for a modern operating suite, whether general purpose, specific use, or hybrid has become significantly more technically complex than it was even a few years ago. The multiple work zones and differing needs of the specialized staff and functions in the modern OR further complicate selection of fixtures and the design of lighting control systems. The coordination of the ballasts and drivers with the integrated OR control systems and the programmed scene lighting controllers requires familiarity and experience in assembling and coordinating the components of these systems to enable them to work together and, despite a great complexity, appear simple and intuitive to the staff using them everyday.

With all of the options available for lighting the OR, the surgeon needs to be particularly knowledgeable of the technology and engaged in the design and use. During the planning process, communicating the planned uses to the architect so that adequate numbers of lights, as well as optimized and flexible placement of lights must be accomplished. During deployment, programming the orchestrated scenes during walk-through sessions and simulations will allow greater efficiency in use. Finally, positioning the OR table, as well as the articulated lights and displays for optimized performance requires knowledge, planning, and attention from the surgeon.

References

1. Berman J, Fong Y. The interventional operating room environment. In: Dupuy D, Fong Y, McMullen W, editors. Interventional oncology. Philadelphia: Springer; 2014.
2. Facilities Guideline Institute. Guidelines for design and construction of healthcare facilities. Dallas: FGI; 2014.
3. IESNA Lighting Handbook. Reference and application. Healthcare illuminance recommendations, for lighting functions, areas and uses in an OR. 10th edn. New York: IES; 2011.

Optical Image-Guidance to Bridge the Gap Between Preoperative Planning and Postoperative Control

2

P. Beatriz Garcia-Allende and Vasilis Ntziachristos

Many minimally invasive imaging modalities including ultrasonography, magnetic resonance imaging (MRI), x-ray computed tomography and positron emission tomography (PET) have become standard clinical practice for tumor detection, staging, and treatment evaluation. If surgery is necessary, clinical decision making in the operating room still relies, however, on the visual appearance and palpation of the tumor. Undoubtedly, tissue discolorations and tactile characterization encode valuable information about the underlying pathologies, but obvious contrast typically represents progressed disease. The surgical outcome is, therefore, compromised by the difficulties in cancer spread identification and in the accurate delineation of the tumor margins, which frequently leads to positive resection margins that critically compromise the prognosis of patients. This gap between the wide contribution of radiological imaging during preoperative and postoperative stages and the actual surgery, where the surgeon has to rely on his visual and tactile senses is explained by the challenges associated with the translation of these imaging technologies to the operating room being mainly their cost, size, the use of ionizing radiation and the need to enclose the patient to provide a tomographic image [1].

V. Ntziachristos (✉) · P. Beatriz Garcia-Allende
Institute for Biological and Medical Imaging,
Technical University of Munich, Trogestr 9,
Munich 81675, Germany
e-mail: v.ntziachristos@tum.de

Optical imaging appears as a promising modality for bridging this gap in modern operating rooms, since it relates directly to the surgeon's vision and offers highly attractive advantages for wide dissemination in the operating room over existing radiological techniques, including high flexibility in contrast mechanisms and ease of adaption to intraoperative practice. Herein, an overview of the optical imaging mechanisms considered for surgical guidance is presented, and their physical fundamentals are briefly explained. Imaging strategies are grouped according to the origin of the optical contrast, which could be inherent to the biological tissue or exogenously enhanced by the administration of nonspecific and tumor-selective markers. More importantly, their capabilities to reveal accurate information about various surgical markers are discussed, together with potential shortcomings that surgeons need to be aware of.

Intrinsic Optical Contrast in Tissue

Biological tissues are heterogeneous in constitution and morphology. As a result of this spatial heterogeneity, light undergoes multiple absorption and scattering events during propagation in biological tissues [2]. The main tissue compounds that absorb light radiation, broadly known as tissue *chromophores*, are water, hemoglobin, lipids, cytochrome *c* oxidase, melanin, and myoglobin. Each chromophore has its own unique absorption

Y. Fong et al. (eds.), *Imaging and Visualization in The Modern Operating Room,*
DOI 10.1007/978-1-4939-2326-7_2,

spectrum. Water absorption is relatively low in the visible range and up to 900 nm, where it starts increasing with a maximum around 970 nm, while hemoglobin, in its oxygenated and deoxygenated forms, is the predominant absorber in spectral ranges of minimal water absorption. The absorption spectra of oxyhemoglobin (HbO_2) and deoxyhemoglobin (Hb) differ notably in the visible and NIR spectral ranges, which explains the differences in the color appearance from arterial blood, which is bright red by comparison with the dark reddish or purplish appearance of venous blood. The diagnostic ability of optical measurements first arises from these spectral fingerprints of the tissue chromophores. Thereby, variations in the molecular composition of the tissue such as increased blood concentration due to sustained angiogenesis or decreased saturation caused by hypermetabolism translates into absorption contrast. Capturing precise spectral information at a larger number of narrower wavebands than the most commonly used three red, green, and blue bands enhance the sensitivity to subtle variations in the tissue molecular composition. Scattering events result from refractive index mismatches at the boundaries between two media or structures, such as those variations of the refractive index between extracellular fluid and cell membranes [3]. Very briefly, epithelial malignancy is characterized by an increase in the overall epithelial cell density with an increased nuclear and nucleolar size. Hence, scattering measures also encoded diagnostically relevant information, particularly about pathophysiologic and morphologic changes. Optical coherence tomography (OCT) [4], frequently seen as the optical equivalent to ultrasound imaging, exploits backscattered light attributed to tissue scattering for the generation of high resolution images of the tissue.

An additional illustration of a native tissue-interaction that can serve diagnostic purposes is tissue *autofluorescence*, or the irradiation from endogenous tissue fluorophores following the absorption of light typically in the UV or VIS regions of the spectrum. These are mainly nicotinamide adenine dinucleotide (NADH), collagen, elastin and lipopigments [5]. Dysplastic and malignant tissues have been shown to have increased red/green fluorescence ratio, as well as an increase in NAD(P)H fluorescence [6].

The survey about clinical demonstrations of optical guidance that follows covers only large field of view methods, which are exceptionally attractive for surgery. High-resolution approaches such us fiber spectroscopy, OCT or confocal imaging are, however, obviated. These methods hold great promise for *virtual* or *optical biopsy*, for example, but they are not particularly suitable for the screening of large surfaces, and still require the guidance of macroscopic imaging methods. It is also worth highlighting that the studies mentioned herein are far from being an exhaustive list of the capabilities of intrinsic optical contrast for surgical guidance. They merely illustrate progress towards clinical translation. Recent reviews give a more extended synopsis of the countless preclinical evidences [7].

Intrinsic optical contrast for interventional guidance has been mostly exploited in oxygenation level monitoring. In a pilot clinical study on 37 patients, Liu et al. [8] have assessed the renal oxygenation profiles to explore the functional advantages for artery-only (AO) versus artery and vein (AV) occlusion during partial nephrectomy (PN). To this aim, a conventional clinical laparoscope is combined with a digital light processing-hyperspectral imaging technique to record the reflectance images from the tissue surface at high spectral resolution. The interpretation of these images using customized spectral interpretation algorithms provided color-coded maps of the tissue surface oxygenation. Although in this particular trial no significant advantage of AO to mitigate ischemia/reperfusion injury was confirmed, it is a remarkable evidence of the capabilities of optical imaging not only to improve interventional outcome but also to aid in the modernization of surgical practices. Yet, it should be noted that, independently of the spectral resolution of the imaging system, the establishment of the oxygen saturation maps and the determination of the tissue composition is still challenged by the problem of accounting for the influence of the spectrally dependant tissue scattering, which, as mentioned earlier, jointly with chromophore absorption modulates the measured reflectance. In light of this, i.e., in order to quantify both absorption and scattering variations across the surgical site and to independently explore their

diagnostic relevance, alternative solutions have been considered [9, 10]. Wilke et al. [9] clinically evaluated the performance of an optical spectral imaging system for intraoperative assessment of breast tumor margins in a comprehensive study involving 54 patients. The participants were undergoing primary breast conserving therapy for an invasive or noninvasive breast malignancy, and the surgeries were performed by surgical oncologists according to their standard practice. Once the surgeons completed their review of the margins, excised specimens were placed in the imaging box of the system for optical assessment of the breast tumor margins (sensitivity 79%, specificity: 66.7%). The latter was accomplished computing the parameters related to light scattering and the total hemoglobin and β-carotene concentrations. Separation of the intermingled effects of absorption and scattering is feasible via the employment of a multichannel fiber-optic imaging probe. Each individual channel consists of an illumination fiber surrounded by four collection fibers. Thereby, spatially resolved measurements of the reflectance are carried out and, from these, it is plausible to separately resolve absorption and scattering influences. More recently, Nguyen et al. [10] have further advanced towards this direction (Fig. 2.1a). Establishment of two-dimensional maps of optical properties with remote camera measurements was in this case attained through a newly reported imaging approach, namely *modulated imaging* [11]. In order to prevent contact with the tissue under interrogation and still be capable of independently estimating absorption and scattering coefficients, spatial patterns of multiple frequencies are projected onto the tissue surface. The fundamental advancement by comparison to fiber-probe systems is the possibility to image directly the surgical cavity and not only excised specimens, since the sterile field is not compromised, and measurements are not affected by the pressure applied by the probe's tip. A fundamental drawback of these latest developments is still the imaging time because of the projection of the different spatial patterns. The surgical oncology community, therefore, still awaits an optimized optical technique that can provide relevant information about surgical markers by purely exploiting absorption and scattering variations in tissue.

In spite of the growing number of publications reporting on the feasibility of the differences in

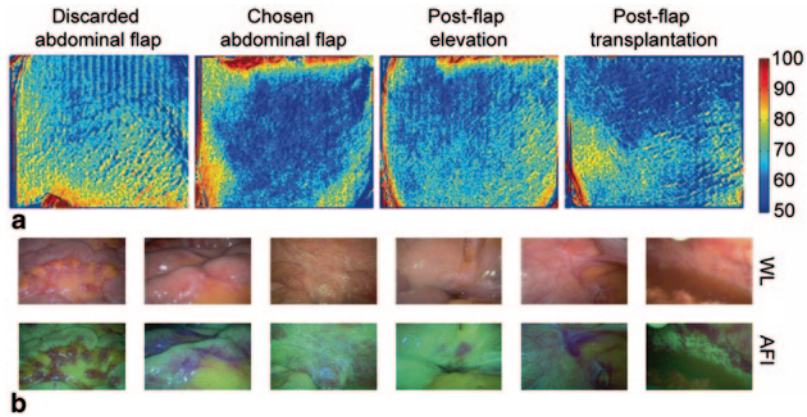

Fig. 2.1 Representative images from Nguyen et al. [10] and Von Breitenbuch et al. [13]that showcase the intraoperative exploitation of intrinsic optical contrast in tissue. **a** Intraoperative assessment of oxygenation of perforator flaps during reconstructive surgery using spatial frequency domain imaging (*SFDI*). Columns from *left* to *right* include abdominal skin flaps after preparation (*discarded and chosen*), skin flap after elevation, and skin flap after attachment (*transplantation*) of a participant in the first in human pilot study of SFDI oxygenation imaging system (Adapted from Ref. [10]), **b** Intraoperative white-light (*WL*) and autofluorescence images (*AFI*) demonstrating that the addition of AFI to WL may be promising in the detection of neoplastic peritoneal foci in laparoscopic surgery of peritoneal carcinomatosis. (Adapted from Ref. [13])

the overall autofluorescence emission to aid in tissue discrimination and demarcation [6], autofluorescence-based contrast has been scarcely considered for guidance in open surgery [12], being the majority of examples found in laparoscopy in peritoneal carcinomatosis [13] (Fig. 2.1b) and endometriosis [14]. The reliability of the autofluorescence signal is impaired by benign changes that are also associated with changes in autofluorescence, and temporal variations of the autofluorescence signal that are not related to disease progression, but purely to bleaching of the endogenous fluorophores or to metabolic changes. These effects consequently compromise the specificity of the autofluorescence signal. Likewise, subtle autofluorescence variations can be easily masked by deviations in the crosstalk conditions or by the influence that other spatially variant optical properties of the tissue, i.e., absorption and scattering, have on them. In light of this, clinical adoption of autofluorescence imaging is limited to surveillance endoscopy [15], and only as part of a multimodal imaging scheme [16], since no conclusive outcomes regarding its potential to be used as a stand-alone diagnostic modality have been reached so far.

Intraoperative Imaging Using Exogenous Contrast

Given the incapacity of imaging strategies based on intrinsic tissue–light interaction mechanisms to fulfill clinical needs, the application of extrinsic contrast agents has been considered even since the late 1940s [17] and, since then, it has experienced an explosive growth. Almost exclusively all clinical studies, like the examples included in Fig. 2.2, use not ligand-targeted contrast agents that together with their proven ability to image vascularity, accumulate passively in tumors due to the enhanced permeability and retention effect (EPR) of tumor vasculature [18]. The clinically approved organic fluorophore *fluorescein*, with absorption and emission maxima in the visible range, has been widely used in glioma surgery [19, 20], thoratoscopy [21], and gynecological diseases [22]. Another agent that has also been extensively employed for contrast enhancement in brain surgery is 5-aminolevulinic acid (5-ALA). Oral administration of ALA induces the visualization of the red fluorescence of protoporphyrin IX (PpIX) and this modality has become standard-of-care for resection of high-grade glioma in Germany based on outcomes from a randomized multicenter Phase III trial comparing progression-free survival in patients undergoing either fluorescence-guided resection or conventional resection under white light visualization [23, 24]. In addition, intraoperative imaging employing ALA for enhanced tumor visualization has been demonstrated in other settings, particularly in parathyroidectomy [25], gastric [26] and colorectal cancer [27], spinal tumor [28], while extensive literature also discusses on its effectiveness in improving visualization of resection margins in bladder cancer [29, 30]. For this specific cancer type, even metaanalysis comparing the results of numerous prospective trials has been reported concluding an overall additional detection rate of 20% [29]. Fewer studies have explored the use of *methylene blue* [31, 32], which fluoresces at longer wavelengths. Shifting to NIR fluorophores favors penetration since tissue attenuation (absorption and scattering) is minimized with respect to the visible spectrum, and enhances target-to-background ratio, because autofluorescence of endogenous tissue fluorophores is also reduced. An additional advantage is that fluorescence measurements are carried out at a nonoverlapping band with the surgeon's vision. In light of this, the number of studies reporting on the use of the clinically approved *indocyanine green* (ICG) with an excitation peak around 800 nm in the operating room are countless. From its initial use as blood flow marker [33], it has become the most exploited contrast agent for intraoperative imaging with applications to be found in the vast majority of medical specialties. Many studies have first demonstrated its promise to improve current standard-of-care for sentinel lymph node mapping in breast [34, 35], head-and-neck [36], lung [37], and vulvar [38] cancers, and melanoma [39], among others. Although it is possible to combine sentinel lymph node navigation using NIR-guided ICG with

current standard-of-care based on blue dyes and/or radioisotopes [40], its most significant benefit over conventional methods is that exposure to ionizing radiation is prevented. In addition, it outperforms radioactive approaches in terms of the cost and the spatial and temporal resolutions [41] and visible blue dyes in terms of the depth [42]. Potential of NIR fluorescence-guided sentinel node navigation sooner sparked interest in other surgical applications. Robot-assisted and laparoscopic surgery particularly benefit from the contrast enhancement between the tumor and normal surrounding caused by the variations in ICG uptake and the corresponding changes in the fluorescence intensity. This is due to the fact that during these procedures the surgeon needs to rely only on his eyes and has no aid from his tactile sense. In response to this, numerous studies can be found in cholecystectomies [43], renal and rectal surgeries [44, 45], and hepatectomies [46].

Clinical utility of fluorescence-guidance in the operating room is mainly determined by the specificity of the contrast agent, which ICG and the other fluorescent dyes mentioned earlier lack. On the contrary, targeted NIR fluorescent agents that yield molecularly specific detection of cancer cells would provide a red-flag detection strategy that allows tumor imaging with optimal sensitivity and specificity, increased accuracy and reproducibility in surgical procedures could be afforded, and operator variability minimized. As a result, the development of optical agents with molecular specificity has recently experienced dramatic attention [47], and in animals fluorescent agents have been successfully used to target colonic dysplasia [48], glucose-related pathologies [49], and cardiovascular syndromes [50], among other multiple conditions. Unfortunately, scarce evolvement from these small animal applications to clinical indications has been observed to date, and disease-specific agents have barely impacted patient care compared to not ligand-targeted contrast agents, in spite of their potentiality to image cancer at a molecular level [1]. Van Dam et al. [51] demonstrated the first in-human use of intraoperative tumor-specific fluorescence imaging for real-time surgical visualization of tumor tissue in patients undergoing exploratory laparatomies for suspected ovarian cancer. Folate conjugated to fluorescein isothiocyanate (folate-FITC), an agent that allows targeting of folate receptor-α (FRα), was injected intravenously into patients that were earlier diagnosed with ovarian cancer and scheduled for surgery. Folic acid-based targeting strategies have been previously followed in SPECT/CT and PET imaging and exploit the absence or inaccessibility of the folate receptor on the normal cells. The imaging implementation consisted of a camera system that can detect and unmix fluorescence in real-time and makes use of different cameras operating in parallel to simultaneously acquire color and fluorescence data through a common objective [52]. This system meets the required criteria for the clinical intraoperative use of an imaging technology, since it provides high-spatial resolution, video-rate capability, portability, no radiation exposure, and is easily adapted to the operating room. Figure 2.3 demonstrates that cancer lesion visualization greatly improves under targeted fluorescence guidance. Quantitatively, five times as many lesions were identified by comparison with the naked human eye. Great clinical relevance is therefore expected from targeted fluorescence guidance regarding the enhancement of surgical procedure outcome, but standardization of medicine across hospitals and countries is also expected to improve, since specificity and reproducibility are enhanced relative to the current approach, dependent on the surgeon's experience.

Following the example of this study, and also using fluorescent labels in the visible range, several clinical trials are currently approved and recruiting patients to further investigate the potential of targeted fluorescence guidance in clinical indications that seek tumor visualization in ovarian (ClinicalTrials.gov number, NCT02000778), lung (ClinicalTrials.gov number, NCT01778920), and renal (ClinicalTrials.gov number, NCT01778933) cancers. Currently, there are only two clinical trials approved and recruiting patients that employ targeted contrast agents with NIR labeling (ClinicalTrials.gov numbers, NCT01508572 and NCT01987375). The first study seeks at determining the uptake, (semi-)quantification and localization of

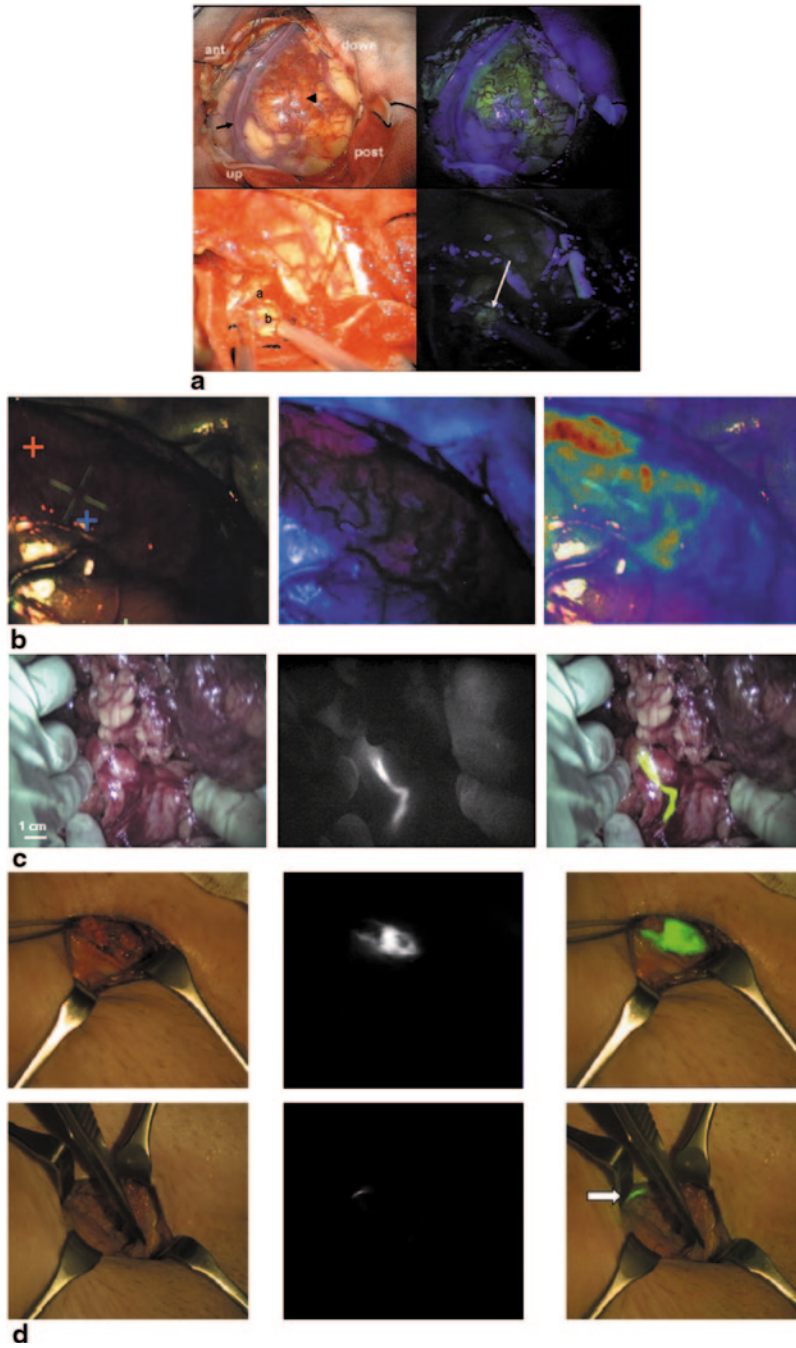

Fig. 2.2 Examples of intraoperative fluorescence imaging using externally administered non-targeted contrast agents: **a** Fluorescein-guided surgery for grade IV gliomas. Color (*left column*) and fluorescence (*right column*) images of the vertex (*up*) and the frontal lobe anterior to the tumor (*ant*) of a patient in the left lateral position participating in the study. Tumor area is delineated as a *yellowish* zone, surrounded by normal *blue* parenchyma in the fluorescence images, and tumor removal was continued until no fluorescent area was visualized. (Reproduced from Ref. [20]). **b** Color, fluorescence, and color with overlaid fluorescence images during fluorescence-guided human glioblastoma multiforme (*GBM*) surgery using oral 5-ALA-induced PpIX. (Adapted from Ref. [24]). **c** Color, fluorescence, and color with overlaid fluorescence images for ureter identification during lower abdominal surgery using methylene *blue*. (Adapted from Ref. [32]). **d** Intraoperative NIR fluorescence imaging for sentinel lymph node detection in vulvar cancer using indocyanine green (*ICG*). Color (*left*), fluorescence (*middle*), and color image with superimposed fluorescence (*right*) of a sentinel lymph node before excision (*top row*) and the

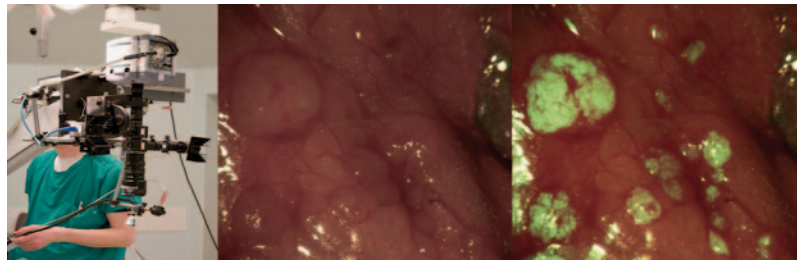

Fig. 2.3 From *left* to *right*: color and fluorescence imaging system placed above a patient prepared for surgery, color image from an ovarian cancer patient and color image with superimposed fluorescence (*green*). (Photos from van Dam et al. [51])

the vascular endothelial growth factor (VEGF) [53] targeting fluorescent tracer bevacizumab-IRDye800CW in breast cancer tissue, surrounding healthy tissue, tumor margins, and lymph nodes, while the second consists of a phase 1 dose-escalation study to determine the safety of epidermal growth factor receptor (EGFR) targeting fluorescent tracer, cetuximab-IRDye800CW, used in subjects with head and neck squamous cell carcinoma. This gap between the extensive contribution of targeted fluorescence imaging in small animal applications and the inexistence of numerous clinical trials studying its potential in patient care is justified by the challenges associated with the clinical translation of the contrast agents engineered to be disease-specific [47]. Toxicity and stability studies are required prior to obtaining human use approvals. Regardless, success in preclinical animal studies may not assure the performance of the agents, since they do not necessarily predict an accurate human efficacy. The above-mentioned clinical trials that use targeted agents with NIR labeling confronted the difficulties in the clinical translation by utilizing optical agents based on clinically approved drugs and a clinically applicable NIR fluorophore, like IRDye 800CW, a strategy to minimize the translational risk that has also been suggested by others [54]. These agents are commonly administered at a microdosing concentration, which is defined either as the administration of 100 µg of a small-molecule ligand or 1 % of the pharmacological dose determined on animal data to yield a pharmacological effect, whichever is less [47]. As a result, tight requirements for the sensitivity of the specific optical acquisition technology are imposed.

An alternative strategy to alleviate the risk in the clinical translation of selective contrast agents is the use of spray administration, which is expected to decrease toxicity concerns over systemic administration, as proposed by Mitsunaga et al. [55]. It involves the topical application of an activatable fluorescent probe that only becomes fluorescent after cleavage of its glutamyltranspeptidase-specific sequence, a cell-surface enzyme of glutathione metabolism that is highly expressed in various types of human cancer [56]. This would avoid waiting for hours or days prior to effective visualization as required for intravenous injection of a targeted probe. The design of this probe to be activatable also avoids tissue washing, which is required when fluorescently labeled probes are topically applied because otherwise the entire sprayed area would become fluorescent. Consequently, it perfectly fits within surgical procedures with minimum impact on the workflow. Toxicity concerns would probably be decreased due to the spray administration. Conversely, this requires a careful evaluation of the rate of agent diffusion within tissue, the ability to visualize disease extent as a function of tissue

cavity after excision (*bottom row*) with faint remaining fluorescence coming from a lymph vessel. (Reproduced from Ref. [38])

depth, field of view and the homogeneity of agent delivery in different areas. For an extended in-depth overview of these novel fluorescent agents for cancer molecular imaging, currently at a preclinical stage, see for example the primer compiled by James and Gambhir [56].

Interventional Use Beyond Surgical Oncology

The clinical studies described herein mainly highlight the potential of optical imaging modalities in surgical oncology, and their fundamental advantage over conventional technique of fresh frozen sectioning to image both the tissue remaining in the surgical cavity, as well as the excised tissue to verify clean margins. In addition, their capability to monitor tissue oxygen saturation and for sentinel node navigation has also been briefly mentioned. Other interventional uses that are worth noting are the visualization of vasculature anatomy during reconstructive surgeries [57], as well as highlighting of nerves [58] and vital organs [59], whose damage could lead to severe complications and function losses.

Fluorescence Imaging in the Operating Room

Earlier sections evidence that targeted imaging with near-infrared fluorescence is the most promising optical contrast mechanism to revolutionize the future outcome of surgical procedures. In short, it meets the three fundamental criteria for a medical technology: there is unmet real clinical need for it regarding the accurate estimation of the extent of disease and the identification of small foci of tumor, the technology solves the problem, and it does not impede normal clinical workflow in the operating room. The surgeons, however, should approach the variations in the fluorescence signals with uncertainty, since the captured fluorescence images are not only dependent on the agent concentration of the imaged tissue. The fluorescence signal is in a complex way affected by variations in the intrinsic optical properties of the tissue, the fluorochrome's depth, and illumination inhomogeneities as a result of the "photographic" or "video" imaging methods. In addition, fluorescence information is diffusive in nature and lacks of anatomical marks because it originates within tissue, what complicates orientation for the surgeon. In current acquisition systems, the latter is normally faced by concurrent acquisition of color and fluorescence videos, being the areas of elevated fluorescence signal superimposed onto the color image for facilitating guidance [60, 61]. Still, the surgeon needs to look away from the surgical cavity and to the monitor displaying these pseudo-diagnosis images/videos, but recently more innovative goggle-based proposals have shown up [62]. Even a more novel alternative would be the projection of the molecular information directly onto the surgical cavity [67]. Compensating the influence of the absorption and scattering in tissue and the depth of the fluorescence activity to quantify the absolute fluorophore concentration is not such a straight forward issue as improving the easiness of guidance. Some correction techniques that utilize multi-spectral information have proven their capacity for absorption correction [52] but an overall solution to this challenge and capable to report the underlying agent concentration is still pending.

Another typical measurement condition in the operating room that is commonly obviated by state-of-the-art imaging systems is the ambient light, and surgical lamps for example need to be dramatically dimmed or fully turned off to carry out fluorescence acquisitions. Latest developments aim at implementing ambient light removal alternatives [63, 64] to allow fluorescence guided surgery under normal room lighting conditions, which further minimizes its already minimal impediment in normal surgical workflow.

An equally important unmet aspect of optical imaging with respect to other medical imaging modalities, like ultrasound or CT, is the reduced number of attempts to standardize its performance metrics and limits [65, 66]. In particular, the different devices used in the clinical studies refereed throughout this chapter use different excitations, filtering, and have a wide range of sensitivities for fluorescence imaging. Consensus documents equivalent to those from CT and

ultrasound detailing guidelines to report on their effectiveness and sensitivity would facilitate data standardization across studies and jointly its clinical translation.

Future Outlook

Overall, the authors herein believe that novel optical imaging holds great potential to extend the current surgeon's vision at the molecular level in modern operating suites. Particularly, targeted near-infrared fluorescence guidance is really well posed to change surgery from a visual interrogation practice to biomarker-based detection. This technology is geared to reduce incomplete cancer surgeries manifested as positive tumor margins on the excised specimen and improve clinical decision making during operations, finding additional small foci of tumor and aiding visualization in difficult to operate surgical cavities. Intrinsic optical contrast and clinically approved non-targeted agents avoids the intricate translation path of disease-specific fluorescent tracers but also the provided contrast enhancement is limited. Undoubtedly, and similarly to nuclear imaging, the identification of potent biomarkers is crucial for the success of targeted fluorescence guidance and should be based on careful evaluation of unmet medical needs. Progress in addressing translation hurdles has also intensified recently, a sign perhaps that conventional visual inspection may find helpful allies in the modern operating suites.

References

1. Garcia-Allende PB, Glatz J, Koch M, Ntziachristos V. Enriching the interventional vision of cancer with fluorescence and optoacoustic imaging. J Nucl Med. 2013;54:644–67.
2. Patterson M, Wilson B, Wyman D. The propagation of optical radiation in tissue I. Models of radiation transport and their application. Lasers Med Sci. 1991;6:155–68.
3. Joel M, Tuan VD. Optical properties of tissue. In: Tuan VD, editor. Biomedical photonics handbook. Boca Raton: CRC Press; 2003. p. 1–76.
4. Robles FE, Wilson C, Grant G, Wax A. Molecular imaging true-colour spectroscopic optical coherence tomography. Nat Photonics. 2011;5:744–7.
5. Tuan VD, Brian MC. Fluorescence spectroscopy for biomedical diagnostics. In: Tuan VD, editor. Biomedical photonics handbook. Boca Raton: CRC Press; 2003. p. 1–51.
6. Lee P, van den Berg RM, Lam S, Gazdar AF, Grunberg K, McWilliams A, et al. Color fluorescence ratio for detection of bronchial dysplasia carcinoma in situ. Clin Cancer Res. 2009;15:4700–5.
7. Lu G, Fei B. Medical hyperspectral imaging: a review. J Biomed Opt. 2014;19:010901.
8. Liu ZW, Faddegon S, Olweny EO, Best SL, Jackson N, Raj GV, et al. Renal oxygenation during partial nephrectomy: a comparison between artery-only occlusion versus artery and vein occlusion. J Endourol. 2013;27:470–4.
9. Wilke LG, Brown JQ, Bydlon TM, Kennedy SA, Richards LM, Junker MK, et al. Rapid noninvasive optical imaging of tissue composition in breast tumor margins. Am J Surg. 2009;198:566–74.
10. Nguyen JT, Lin SJ, Tobias AM, Gioux S, Mazhar A, Cuccia DJ, et al. A novel pilot study using spatial frequency domain imaging to assess oxygenation of perforator flaps during reconstructive breast surgery. Ann Plast Surg. 2013;71:308–15.
11. Cuccia DJ, Bevilacqua F, Durkin AJ, Ayers FR, Tromberg BJ. Quantitation and mapping of tissue optical properties using modulated imaging. J Biomed Opt. 2009;14:024012.
12. Poh CF, Zhang L, Anderson DW, Durham JS, Williams PM, Priddy RW, et al. Fluorescence visualization detection of field alterations in tumor margins of oral cancer patients. Clin Cancer Res. 2006;12:6716–22.
13. Von Breitenbuch P, Jeiter T, Schreml S, Glockzin G, Agha A, Piso P, et al. Autofluorescent imaging in patients with peritoneal carcinomatosis. Surg Innov. 2014;21:187–93.
14. Buchweitz O, Staebler A, Tio J, Kiesel L. Detection of peritoneal endometriotic lesions by autofluorescence laparoscopy. Am J Obstet Gynecol. 2006;195:949–54.
15. Jacobson MC, deVere White R, Demos SG. In vivo testing of a prototype system providing simultaneous white light and near infrared autofluorescence image acquisition for the detection of bladder cancer. J Biomed Opt. 2013;17:036011.
16. Song LMWK, Banerjee S, Desilets D, Diehl DL, Farraye FA, Kaul V, et al. Autofluorescence imaging. Gastrointest Endosc. 2011;73:647–50.
17. Moore GE, Peyton WT, French LA, Walker WW. The clinical use of fluorescein in neurosurgery; the localization of brain tumors. J Neurosurg. 1948;5:392–8.
18. Matsumura Y, Maeda H. A new concept for macromolecular therapeutics in cancer chemotherapy: mechanisms of tumoritropic accumulation of proteins and the antitumor agent smancs. Cancer Res. 1986;46:6387–92.

19. Koc K, Anik I, Cabuk B, Ceylan S. Fluorescein sodium-guided surgery in glioblastoma multiforme: a prospective evaluation. Br J Neurosurg. 2008;22:99–103.
20. Acerbi F, Broggi M, Eoli M, Anghileri E, Cuppini L, Pollo B, et al. Fluorescein-guided surgery for grade IV gliomas with a dedicated filter on the surgical microscope: preliminary results in 12 cases. Acta Neurochir (Wien). 2013;155:1277–86.
21. Noppen M, Dekeukeleire T, Hanon S, Stratakos G, Amjadi K, Madsen P, et al. Fluorescein-enhanced autofluorescence thoracoscopy in patients with primary spontaneous pneumothorax and normal subjects. Am J Respir Crit Care Med. 2006;174:26–30.
22. Misas JE, Cold JC, Hall FW. Vulvar Paget disease: fluorescein-aided visualization of margins. Obstet Gynecol. 1991;77:156–9.
23. Stummer W, Pichlmeier U, Meinel T, Wiestler OD, Zanella F, Reulen HJ. Fluorescence-guided surgery with 5-aminolevulinic acid for resection of malignant glioma: a randomised controlled multicentre phase III trial. Lancet Oncol. 2006;7:392–401.
24. Valdes PA, Leblond F, Jacobs VL, Wilson BC, Paulsen KD, Roberts DW. Quantitative, spectrally-resolved intraoperative fluorescence imaging. Sci Rep. 2012;2:798.
25. Prosst RL, Weiss J, Hupp L, Willeke F, Post S. Fluorescence-guided minimally invasive parathyroidectomy: clinical experience with a novel intraoperative detection technique for parathyroid glands. World J Surg. 2010;34:2217–22.
26. Kishi K, Fujiwara Y, Yano M, Inoue M, Miyashiro I, Motoori M, et al. Staging laparoscopy using ALA-mediated photodynamic diagnosis improves the detection of peritoneal metastases in advanced gastric cancer. J Surg Oncol. 2012;106:294–8.
27. Harada K, Harada Y, Beika M, Koizumi N, Inoue K, Murayama Y, et al. Detection of lymph node metastases in human colorectal cancer by using 5-aminolevulinic acid-induced protoporphyrin IX fluorescence with spectral unmixing. Int J Mol Sci. 2013;14:23140–52.
28. Eicker SO, Floeth FW, Kamp M, Steiger HJ, Hänggi D. The impact of fluorescence guidance on spinal intradural tumour surgery. Eur Spine J. 2013;22:1394–401.
29. Evelyne CCC, de la Rosette JJMCH, de Reijke TM. Emerging optical techniques in advanced cystoscopy for bladder cancer diagnosis: a review of the current literature. Indian J Urol. 2011;27:245–51.
30. Garfield SS, Gavaghan MB, Armstrong SO, Jones JS. The cost-effectiveness of blue light cystoscopy in bladder cancer detection: United States projections based on clinical data showing 4.5 years of follow up after a single hexaminolevulinate hydrochloride instillation. Can J Urol. 2013;20:6682–9.
31. Winer JH, Choi HS, Gibbs-Strauss SL, Ashitate Y, Colson YL, Frangioni JV. Intraoperative localization of insulinoma and normal pancreas using invisible near-infrared fluorescent light. Ann Surg Oncol. 2010;17:1094–100.
32. Verbeek FP, van der Vorst JR, Schaafsma BE, Swijnenburg RJ, Gaarenstroom KN, Elzevier HW, et al. Intraoperative near infrared fluorescence guided identification of the ureters using low dose methylene blue: a first in human experience. J Urol. 2013;190:574–9.
33. Miller DE, Gleason WL, McIntosch HD. A comparison of the cardiac output determination by the direct Fick method and the dye-dilution method using indocyanine green dye and a cuvette densitometer. J Lab Clin Med. 1962;59:345–50.
34. Sevick-Muraca EM, Sharma R, Rasmussen JC, Marshall MV, Wendt JA, Pham HQ, et al. Imaging of lymph flow in breast cancer patients after microdose administration of a near-infrared fluorophore: feasibility study. Radiology. 2008;246:734–41.
35. Verbeek FP, Troyan SL, Mieog JSD, Liefers GJ, Moffitt LA, Rosenberg M, et al. Near-infrared fluorescence sentinel lymph node mapping in breast cancer: a multicenter experience. Breast Cancer Res Treat. 2014;143:333–42.
36. van der Vorst JR, Schaafsma BE, Verbeek FP, Keereweer S, Jansen JC, van der Velden LA, et al. Near-infrared fluorescence sentinel lymph node mapping of the oral cavity in head and neck cancer patients. Oral Oncol. 2013;49:15–9.
37. Yamashita S, Tokuishi K, Miyawaki M, Anami K, Moroga T, Takeno S, et al. Sentinel node navigation surgery by thoracoscopic fluorescence imaging system and molecular examination in non-small cell lung cancer. Ann Surg Oncol. 2012;19:728–33.
38. Crane LMA, Themelis G, Arts HJG, Buddingh KT, Brouwers AH, Ntziachristos V, et al. Intraoperative near-infrared fluorescence imaging for sentinel lymph node detection in vulvar cancer: first clinical results. Gynecol Oncol. 2011;120:291–5.
39. Gilmore DM, Khullar OV, Gioux S, Stockdale A, Frangioni JV, Colson YL, et al. Effective low-dose escalation of indocyanine green for near-infrared fluorescent sentinel lymph node mapping in melanoma. Ann Surg Oncol. 2013;20:2357–63.
40. van den Berg NS, Brouwer OR, Klop WM, Karakullukcu B, Zuur CL, Tan IB, et al. Concomitant radio- and fluorescence-guided sentinel node biopsy in squamous cell carcinoma of the oral cavity using ICG-(99m)Tc-nanocolloid. Eur J Nucl Med Mol Imaging. 2012;39:1128–36.
41. van der Vorst JR, Schaafsma BE, Verbeek FP, Hutteman M, Mieog JS, Lowik CW, et al. Randomized comparison of near-infrared fluorescence imaging using indocyanine green and 99(m) technetium with or without patent blue for the sentinel lymph node procedure in breast cancer patients. Ann Surg Oncol. 2012;19:4104–11.
42. Jung SY, Kim SK, Kim SW, Kwon Y, Lee ES, Kang HS, et al. Comparison of sentinel lymph node biopsy guided by the multimodal method of indocyanine green fluorescence, radioisotope, and blue dye versus the radioisotope method in breast cancer: a randomized controlled trial. Ann Surg Oncol. 2014;21:1254–9.

43. Tagaya N, Shimoda M, Kato M, Nakagawa A, Abe A, Iwasaki Y, et al. Intraoperative exploration of biliary anatomy using fluorescence imaging of indocyanine green in experimental and clinical cholecystectomies. J Hepatobiliary Pancreat Sci. 2010;17:595–600.
44. Tobis S, Knopf JK, Silvers C, Messing E, Yao J, Rashid H, et al. Robot-assisted and laparoscopic partial nephrectomy with near infrared fluorescence imaging. J Endourol. 2012;26:797–802.
45. Jafari MD, Lee KH, Halabi WJ, Mills SD, Carmichael JC, Stamos MJ, et al. The use of indocyanine green fluorescence to assess anastomotic perfusion during robotic assisted laparoscopic rectal surgery. Surg Endosc. 2013;27:3003–8.
46. Kudo H, Ishizawa T, Tani K, Harada N, Ichida A, Shimizu A, et al. Visualization of subcapsular hepatic malignancy by indocyanine-green fluorescence imaging during laparoscopic hepatectomy. Surg Endosc. 2014;28:2504–8.
47. Scheuer W, van Dam GM, Dobosz M, Schwaiger M, Ntziachristos V. Drug-based optical agents: infiltrating clinics at lower risk. Sci Transl Med. 2012;4:134ps11.
48. Liu Z, Miller SJ, Joshi BP, Wang TD. In vivo targeting of colonic dysplasia on fluorescence endoscopy with near-infrared octapeptide. Gut. 2012;62:395–403.
49. Guo J, Du C. Shan L, Zhu H, Xue B, Quian Z, Achilefu S, et al. Comparison of near-infrared fluorescent deoxyglucose probes with different dyes for tumor diagnosis in vivo. Contrast Media Mol Imaging. 2012;7:289–301.
50. McCarthy JR, Patel P, Botnaru I, Haghayeghi P, Weissleder R, Jaffer FA. Multimodal nanoagents for the detection of intravascular thrombi. Bioconjug Chem. 2009;20:1251–5.
51. Van Dam G, Themelis G, Crane LM, Harlaar NJ, Pleijhuis RG, Kelder W, et al. Intraoperative tumor-specific fluorescent imaging in ovarian cancer by folate receptor-α targeting. Nat Med. 2011;17:1315–9.
52. Themelis G, Yoo JS, Soh KS, Schulz R, Ntziachristos V. Real-time intraoperative fluorescence imaging system using light-absorption correction. J Biomed Opt. 2009;14:064012.
53. Kroemer G, Pouyssegur J. Tumor cell metabolism: cancer's Achilles' heel. Cancer Cell. 2008;13:472–82.
54. Marshall MV, Draney D, Sevick-Muraca EM, Olive DM. Single-dose intravenous toxicity study of IR-Dye800CW in Sprague-Dawley rats. Mol Imaging Biol. 2010;12:583–94.
55. Mitsunaga M, Kosaka N, Choyke PL, Young MR, Dextras CR, Saud SM, et al. Fluorescence endoscopic detection of murine colitis-associated colon cancer by topically applied enzymatically rapid-activatable probe. Gut. 2013;62:1179–86.
56. James M, Gambhir SS. A molecular imaging primer: modalities, imaging agents, and applications. Physiol Rev. 2012;92:897–965.
57. Lee BT, Hutteman M, Gioux S, Stockdale A, Lin SJ, Ngo LH, et al. The FLARE intraoperative near-infrared fluorescence imaging system: a first-in-human clinical trial in perforator flap breast reconstruction. Plast Reconstr Surg. 2010;126:1472–81.
58. Gibbs-Strauss SL, Nasr KA, Fish KM, Khullar O, Ashitate Y, Siclovan TM, et al. Nerve-highlighting fluorescent contrast agents for image-guided surgery. Mol Imaging. 2011;10:91–101.
59. Verbeek FP, van der Vorst JR, Schaafsma BE, Swijnenburg RJ, Gaarenstroom KN, Elzevier HW, et al. Intraoperative near infrared fluorescence guided identification of the ureters using low dose methylene blue: a first in human experience. J Urol. 2013;190:574–9.
60. Troyan SL, Kianzad V, Gibbs-Strauss SL, Gioux S, Matsui A, Oketokoun R, et al. The FLARE intraoperative near-infrared fluorescence imaging system: a first-in-human clinical trial in breast cancer sentinel lymph node mapping. Ann Surg Oncol. 2009;16:2943–52.
61. Glatz J, Varga J, Garcia-Allende PB, Koch M, Greten F, Ntziachristos V. Concurrent video-rate color and near-infrared fluorescence laparoscopy. J Biomed Opt. 2013;18:101302.
62. Liu Y, Bauer AQ, Akers WJ, Sudlow G, Liang K, Shen D, et al. Hands-free, wireless goggles for near-infrared fluorescence and real-time image-guided surgery. Surgery. 2011;149:689–98.
63. Sexton K, Davis SC, McClatchy D III, Valdes PA, Kanick SC, Paulsen KD, et al. Pulsed-light imaging for fluorescence guided surgery under normal room lighting. Opt Lett. 2013;38:3249–52.
64. Banghe Z, Rasmussen JC, Sevick-Muraca E. Non-invasive fluorescence imaging under ambient light conditions using a modulated ICCD and laser diode. Biomed Opt Express. 2014;5:562–72.
65. Marshall MV, Rasmussen JC, Tan IC, Aldrich MB, Adams KE, Wang X, et al. Near-infrared fluorescence imaging in humans with indocyanine green: a review and update. Open Surg Oncol J. 2010;2:12–25.
66. Thurber GM, Figueiredo JL, Weissleder R. Detection limits of intraoperative near infrared imaging for tumor resection. J Surg Oncol. 2010;102:758–64.
67. P. Sarder, K. Gullicksrud, S. Mondal, et al; Dynamic optical projection of acquired luminiscence for aiding oncologic surgery; J. Biomed. Opt. 18, 120501 (2013).

Fluorescent Probes

3

Kai Cheng and Zhen Cheng

Fluorescent Probes in Medical Imaging

Intraoperative optical imaging in the surgical theatre exploiting fluorescence, especially near-infrared (NIR, 650–950 nm) fluorescence, holds great promises for largely improving medical surgery outcomes, significantly shortening operation time, and potentially reducing overall health-care costs [1–3]. As a primary treatment modality for most solid tumors, surgery provides significant improvements in overall survivals. Many well-established molecular imaging techniques, such as positron emission tomography (PET), magnetic resonance imaging (MRI), computerized tomography (CT), and ultrasound, have been proven to have meaningful impacts on the care of cancer patients by providing preoperative imaging and improving diagnostic accuracy [4]. Similarly, optical imaging has been successfully used in tumor identification, image-guided resection and therapy, monitor of therapeutic outcomes, and detection of sentinel lymph nodes in both preclinical and clinical studies, because of its high sensitivity, short scanning time, relatively high throughput, and great clinical relevance. In particular, accurately evaluating and lineating tumor positive margins based on the intraoperative optical imaging instead of traditional palpation and visual inspection during the surgery can lead to a dramatic improvement in completeness of tumor resections, especially when primary or metastatic tumors are adjacent to or surrounded within important physiological structures such as nerves, blood vessels, ureters, and bile ducts. Furthermore, by using current fluorescence imaging facilities without changing the appearance of the surgical field, it is easy for physicians or surgeons to reduce the learning curve in order to translate their surgical skills between open and minimally invasive image-guided surgery.

The fluorescent agents have played an important role in the optical image-guided surgery and therapy. Different from the conventional visual distinction of the boundaries of each tissue types with white-light reflectance, the fluorescent imaging allows the surgeons to visualize the fluorescence signal from specific tissues or organs, differentiate malignant from normal tissues, and highlight anatomy or disease states with exceptional sensitivity and accuracy. Although there might be some endogenous fluorescence contrasts associated with tumors or abnormalities, it is hard to find robust spectroscopic differences between malignants and normal tissues, due to autofluorescence, Raman scattering, and infrared reflectivity [3]. In fact, the development of NIR fluorophores and fluorescent nanoprobes as exogenous fluorescence contrast agents over the past decade was dramatically facilitating

Z. Cheng (✉)
Department of Radiology, Molecular Imaging Program at Stanford, Canary Center at Stanford for Cancer Early Detection, 1201 Welch Road, Lucas Center, P095, Stanford, CA 94305-5484, USA
e-mail: zcheng@stanford.edu

K. Cheng
Department of Radiology, Stanford University, Stanford, CA, USA

Y. Fong et al. (eds.), *Imaging and Visualization in The Modern Operating Room,*
DOI 10.1007/978-1-4939-2326-7_3, © Springer Science+Business Media New York 2015

the translation of intraoperative optical imaging from a proof-of-concept stage to clinical routine. A few NIR imaging probes have already received approval from the Food and Drug Administration (FDA) and/or European Medicines Agency (EMA) or other comparable authorities. For example, previously as a visible dye in surgery, methylene blue has been introduced into clinical practice for many years and has recently been used as a NIR fluorophore in fluorescence clinical studies. Another contrast agent, indocyanine green (ICG), has been approved for sentinel lymph node mapping, tumor resection, and determination of cardiac output and hepatic function. During the past decade, there has been significant progress in the development of optimized and targeted NIR fluorophores for *in vivo* intraoperative molecular imaging as an image-guided surgical tool in preclinical research and clinical trials. Since fluorescence imaging is relevant for tissues close to the surface of skin, or tissues accessible by endoscopy and intraoperative visualization, it is a vital for fluorophores to have minimal interferential absorption and refraction, low biological autofluorescence, and high tissue penetration. In the past few years, significant efforts on the development of novel fluorophores in NIR window with high signal to background ratio (SBR), relatively deep tissue penetration, and targeting capability have successfully wielded the full power of the image-guided surgery and greatly facilitated the clinical translation of intraoperative fluorescent imaging. In this chapter, we outline the desired chemical, physical, and biological properties necessary for NIR fluorophores, including wavelength, brightness, and photostability. Because most of NIR fluorophores, as exogenous contrast agents, need to be administered intravenously, intraparenchymally, or intraluminally, it is critical to explore their biocompatibility, pharmacokinetics, targeting and activation in order to improve *in vivo* applications.

Recently, there have been vast literatures on the development of NIR fluorophores for *in vivo* molecular imaging. In general, NIR fluorophores can be categorized into two major groups: small-molecule fluorophores and nanoparticle-based probes. The former ones have the advantages of relatively low molecular weight, fast hepatic and urinal excretion, unique spectral determination, favorable *in vivo* characteristics, superior selectivity and specificity, and intrinsic accessibility to desired sites. Concerning their extensive use in *in vivo* applications, it is time- and cost-efficient in terms of synthesis, modification, and regulatory approval of small molecule NIR fluorophores. On the other hand, the majority of the recent developments in NIR fluorophore design focus on nanoparticle-based probes because the integration of nanotechnology with molecular biology and medicine could offer to dramatically improve detection sensitivity and specificity in the fluorescence molecular imaging. Compared to the conventional NIR organic dyes, the nanoparticle-based fluorophores with defined size, shape, and composition exhibit unique, superior chemical and physical properties, such as high quantum yield, size-dependent excitation/emission, large Stokes shift, excellent photostability, long circulation/favorable pharmacokinetics, high detection sensitivity and specificity, and capability to multiplexing. A variety of novel fluorescent nanomaterials such as dye-loaded organic/inorganic nanoparticles, inorganic semiconductor quantum dots (QDs), organic conjugated polymer particles, metal nanocluster, carbon nanotubes, and up-conversion nanoparticles have received immense attention for their superior NIR luminescence properties and high signal to background ratio. Upon optimization of size, shape, and surface modification, the functional nanofluorophores can either passively accumulate in tumors through the enhanced permeability and retention (EPR) effect or actively target the tumors by the specific binding with tumor-associated biomarkers such as overexpressed receptors, tumor extracellular matrix and enzymes [5]. Targeted NIR nanoprobes can be divided into several subgroups based on the type of targeting moieties such as small molecules, peptides, aptamer, proteins, and antibody. Accordingly, there are numerous approaches utilized to improve the targeting or activation of NIR probes, including pH activation, enzyme cleavage, and self-illumination.

In this chapter, we mainly focus on the design and development of NIR fluorescent probes for molecular imaging and image-guided surgery.

More specifically, we discuss the key issues relevant to optimization of NIR fluorescent agents for intraoperative optical imaging, and summary the development of various NIR fluorophores based on the compositions and functions, and evaluate their potentials for advanced applications in medical imaging.

Requirements for Fluorophores in Medical Imaging

Wavelengths of Excitation and Emission

The NIR region (650–950 nm) offers an optimal window for fluorescence imaging with minimal interferential absorption and refraction, low biological autofluorescence and high tissue penetration (Fig. 3.1) [6]. Due to the strong absorption of biological chromophores, such as oxyhemoglobin, deoxyhemoglobin, myoglobin, and cytochromes, the tissue penetration depth of visible light below 600 nm is limited to the micrometer range. Although NIR light, like visible light, can be attenuated by reflection, refraction, and scattering at the tissue surface or through the tissue, the absorption coefficient of tissue in NIR region is at a minimum. Other biological components such as water and lipids are optically transparent from the visible to the NIR but strongly absorb light in the infrared [7]. Furthermore, the tissue autofluorescence from endogenous chro-

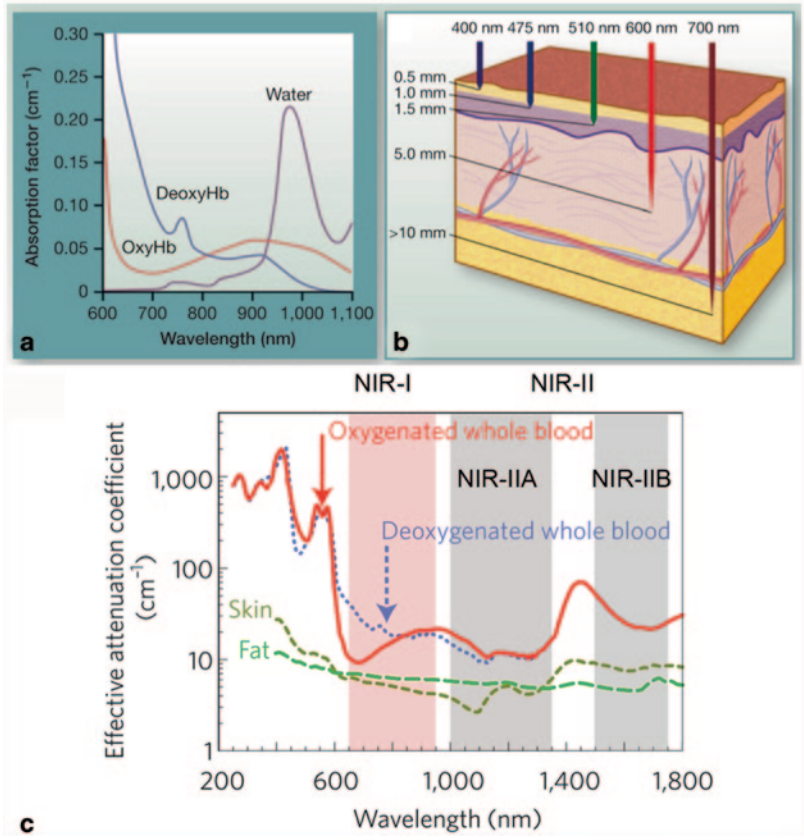

Fig. 3.1 Absorption and tissue penetration of light and optical windows in biological tissues. **a** Water and oxy- and deoxyhemoglobin plotted ranging from visible to NIR wavelength. **b** Tissue penetration of light (reprinted with permission from [2]; copyright 2014, AACR Publications). **c** Optical windows in biological tissues. Plots of effective attenuation coefficient (on a log scale) versus wavelength show that absorption and scattering from oxygenated blood, deoxygenated blood, skin and fatty tissue is lowest in either the first or second near-infrared window (*NIR-I:* the first near-infrared window, *NIR-II:* the second near-infrared window) (reprinted with permission from [7]; copyright 2009, Macmillan Publishers)

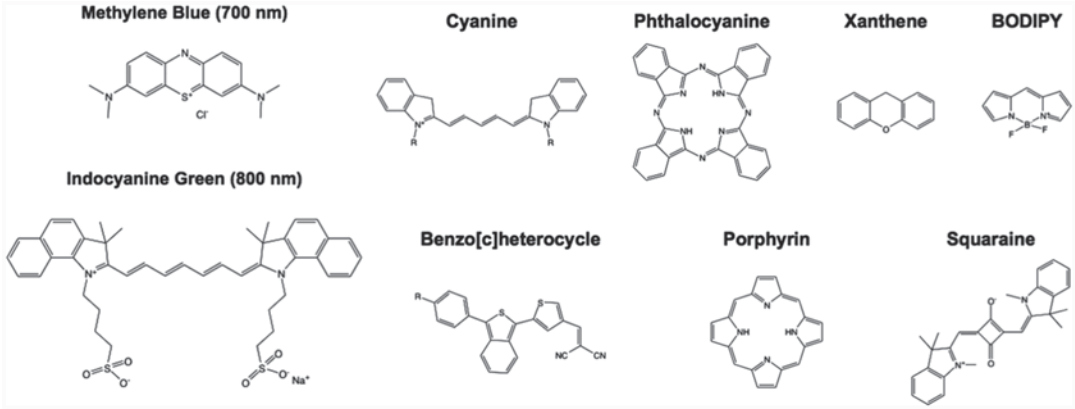

Fig. 3.2. Chemical structures of NIR fluorophores. Methylene blue (700 NIR fluorophore), indocyanine green (800 nm fluorophore). Chemical base structure of known classes of NIR fluorophores including cyanine, phthalocyanine, xanthene, borondipyrromethane (*BODIPY*), benzo[c]heterocycle, porphyrin, and squaraine (squarylium). The physical and optical properties of each of the base structures can be tuned through the addition of functional groups. (Reprinted with permission from [16]; copyright 2012, AME Publishing Company)

mophores including structural proteins (collagen and elastin), amino acids, enzymes, porphyrins, and other biological fluorophores generally has visible emission but do not strongly interfere with NIR emitters. Therefore, optimal fluorophores with far-red or NIR excitation and emission wavelengths could enable maximum tissue penetration depth from a few millimeters to even half centimeters [2]. As discussed previously, methylene blue and ICG act as 700 and 800 nm fluorophores for NIR fluorescence clinical studies (Fig. 3.2 and Table 3.1), and their tissue absorption and autofluorescence are minimal so that they have maximal tissue penetration depth. The difference in energy or wavelength between excitation and emission is called the Stokes shift, which is fundamental to the sensitivity of fluorescence imaging because the large Stokes shift allows emission photons to be isolated from excitation photons to obtain high signal-to-noise ratio. Many common organic dyes based on known classes of NIR fluorophores such as cyanine, BODIPY, AlexaFluor, etc. are widely used but have the disadvantage of short Stokes shift (less than 50 nm). An emerging new class of NIR organic compounds containing the conjugated polyene, polymethine, and donor-acceptor chromophores have been extensively explored for potential applications in fluorescence imaging because of their unique properties such as tunable energy gaps, facile synthesis, large Stokes shifts and acceptable quantum yields [8]. During the past decade, the quantum dots as light-emitting nanocrystals, have been a major focus of fluorescence imaging and medical applications, due to their unique chemical and optical properties including size-tunable light emission and large Stokes shift (more than 100 nm), which could guarantee the fluorescence imaging acquisition with high signal-to-noise ratio [9, 10]. Many other organic dyes, metal cluster, silicon nanoparticles, and conjugated polymer dots have been recently developed to take advantage of their long Stokes shifts and tunable wavelengths for sensitive *in vivo* fluorescent imaging [11].

Very recently, fluorescence imaging in the second near-infrared window (NIR-II, 1000–1700 nm, Fig. 3.1c) instead of the visible and traditional NIR windows have been attracting considerable attention as an alternative optical tool for medical imaging because of its superior spatial resolution, largely reduced photon scattering, deep tissue penetration, and negligible tissue autofluorescence [7]. There are only several fluorophores available for NIR-II fluorescence imaging, such as single-walled carbon nanotube (SWNT), silver sulfide quantum dots, etc., and they exhibit exceptional potentials in microvascu-

W Summary of chemical and physical properties of NIR fluorescent probes

Fluorescent probes	Emission peak (excitation) (nm)	MW (g/mol) or size (nm)	Molar extinction coefficient (M^{-1} cm^{-1})	Quantum yield Φ (%)	Area of application
Small molecule NIR dyes (*clinically approved*)					
Methylene blue	700	319.85	71,200	52	FDA and EMA approved for injection, indicated for drug-induced methaemoglobinaemia. An intraluminal gastrointestinal tract contrast agent
ICG	822 (807)	774.96	121,000	9	FDA and EMA approved for injection, indicated for determining cardiac output, hepatic function, and liver blood flow and for ophthalmic angiography. Monitor fluid-filled structures as a vascular, renal or excretory pathway contrast agent
5-ALA and its ester	635 (405) PpIX	–	–	–	FDA approved as a topical solution. EMA approved as an orally administrated drug. 5-ALA is metabolized by glioblastoma into protoporphyrin IX (PpIX)
Small molecule NIR dyes (*commercial sources*)					
CyDye Cy5.5	694 (675)	~700	190,000	23	Preclinical evaluation
CyDye Cy7	767 (743)	~800	200,000	28	Preclinical evaluation
IRDye 800CW	800 (770)	~1100	240,000	3.4	Preclinical evaluation
Alexa fluor 680	714 (684)	~1000	175,000	36	Preclinical evaluation
Alexa Fluor 750	782 (753)	~1300	290,000	12	Preclinical evaluation
Small molecule NIR-II dye					
IR-1061	1100 (808)	749.13	–	1.7	Preclinical evaluation, Second NIR window fluorescent imaging
Quantum dots (*QDs*) *core/shell*					
InAs	800–1240	2–6	–	2.5	*In vitro* cell labeling
InAs/ZnS or CdSe	700–1400	4–16	–	20–90	*In vitro* cell labeling and *in vivo* tumor targeting
InAs/InP/ZnSe	800	16	–	19	*in vivo* tumor targeting
CdTe	670–800	3–13	–	~10	*In vitro* cell labeling
CdTe/CdSe	700–850	5–11	–	10 to ~60	*in vivo* tumor targeting and sentinel lymph node mapping
CuInP	630–1100	4	–	20	*in vivo* tumor targeting
QD 705	705	15–20	–	10 to ~20	*In vitro* cell labeling and *in vivo* tumor targeting
QD 800	800	15–20	–	10–20	*In vitro* cell labeling and *in vivo* tumor targeting
Ag_2S	900–1300	5–12	–	10–30	*In vitro* cell labeling
PbS	700–1600	5–12	–	10–30	*In vitro* cell labeling
PbSe	1200–1500	7–12	–	10–30	*In vitro* cell labeling

Table 3.1 (continued)

Fluorescent probes	Emission peak (excitation) (nm)	MW (g/mol) or size (nm)	Molar extinction coefficient (M^{-1} cm^{-1})	Quantum yield Φ (%)	Area of application
Metal clusters					
Gold cluster (Au-NC-BSA)	640	0.8	–	6	*In vitro* cell labeling and *in vivo* tumor targeting
Au-NC-ferritine	665	1	–	8.2	*In vitro* cell labeling and *in vivo* targeting
Au-Cu alloy cluster	900–1060	2–3	–	10–29	*In vitro* cell labeling
Single wall carbon nanotubes (*SWCN*)					
SWCN	1000–1700	1 ~ 2 × 100 ~ 200	–	1 to ~2	*In vitro* cell labeling and *in vivo* targeting
Polymer dots (*PDots*)					
PFBT + PF-DBT5	630–650	30 ~ 50	10,000,000	1 to ~20	*In vitro* cell labeling
NIR fluorescent protein					
iRFP	713 (690)	–	85,000	5.9	*In vitro* cell labeling and *in vivo* targeting
IFP1.4	707 (684)	–	54,700	7.7	*In vitro* cell labeling and *in vivo* targeting
eqFP670	670 (605)	–	70,000	6	*In vitro* cell labeling and *in vivo* targeting

FDA Food and Drug Administration, *EMA* European Medicines Agency

lar imaging and hemodynamic measurement with improved spatial resolution over X-ray computer tomography (CT) and broader dynamic range of blood flowmetry than ultrasound [12–14]. Along with recent progress in the development of new NIR-II fluorescence probes, it is expected that the NIR-II window offers a tremendous new opportunity for *in vivo* fluorescence imaging of living subjects with excellent sensitivity and exceptional resolution [7].

Brightness

The brightness of the NIR fluorescence probes, defined as fluorescence output per fluorophore, is one of the most important considerations to get deep tissue images with high signal-to-noise ratio. As an inherent property of the fluorophore, the brightness is proportional to the product of the extinction coefficient (at the relevant excitation wavelength) and the fluorescence quantum yield (measure of the total photon emission over the entire fluorescence spectral profile) [15]. Normally, the extinction coefficient among organic dye and autofluorescent protein fluorophores are in the range from 5000 to 200,000 M^{-1} cm^{-1}. For example, the extinction coefficient of ICG and methylene blue equal to 121,000 and 71,200 M^{-1} cm^{-1}, respectively [16]. The quantum yield is defined as the ratio of the number of photons emitted to the number of photon absorbed. Typical small NIR organic molecule fluorophores usually have quantum yields between 10 and 20% in the *in vivo* environment [6]. The extinction coefficients of NIR quantum dots are relatively high (more than 2000,000 $M^{-1}cm^{-1}$) but their quantum yields vary from 10 to 80% and mostly in the range of 10 to ~30% (Table 3.1) [9, 10]. Thus, the NIR quantum dots are usually extremely bright in the physiological condition.

Stability

The photostability is of paramount importance for NIR fluorophores as fluorescence contrast agents during the surgical procedure because of continuous illumination of surgical field of view. Under high-intensity illumination conditions,

most of small molecule fluorophores, including fluorescein, BODIPY, and cyanine derivatives, often undergo irreversible destruction or photobleaching, which limits their fluorescence detectability and compromises sensitivity, particularly for long-term imaging and tracing experiment [6, 17]. Some fluorophores with rhodamine derivatives have been proven to improve the photostability [6]. Significant improvements of the photostability have been found for semiconductor polymer dots [18]. Most of the colloidal semiconductor inorganic quantum dots exhibit excellent photostability. The photostability of fluorophores can be characterized by the photobleaching quantum yield, defined as percentage of the number of photobleached molecules divided by the total number of photons absorbed over a given time interval. The photobleaching quantum yields of fluorescent organic dyes are typically in the range of 10^{-4}–10^{-6}. Due to improved photostability, semiconductor quantum dots exhibit photobleaching quantum yields in the range of 10^{-7}–10^{-10} [18].

Pharmacokinetics

Comprehensive insights on understanding the biodistribution, pharmacokinetics, and clearance of various NIR fluorescent probes are of critical importance towards designing fluorescent probes suitable for intraoperative fluorescence imaging so as to realize their preclinical evaluation and further facilitate the corresponding clinical translation. Control of the probe *in vivo* behaviors involves many variables such as blood half-life, clearance mechanism, and tissue extravasation. Significant efforts are recently underway to investigate and optimize these parameters for preferred *in vivo* behaviors to improve imaging efficacy. Many studies have already confirmed that optimal visualization could be achieved by maximizing the signal-to-background ratio, according to types of contrast agents (small molecule dyes or nanoparticle-based probes), routes of administrations (intravenous or topical), target strategies (passive or active) and imaging goals (tumor imaging or lymph node mapping).

The utility of NIR fluorescence imaging is dependent on the *in vivo* behaviors of fluorescence probes. Typically, NIR fluorescence probes within the first few seconds after intravenous administration could highlight the arterial system and then the venous system. The hepatic and renal clearance along with tissue distribution and target binding of fluorescence probes will occur over the next minutes to hours [3]. It is now clear that the physical size, surface charge, and coating materials of fluorescent probes have profound effects on their *in vivo* behaviors. Normally, small molecule dyes have short blood half-lives (on the order of minutes). According to the chemical and physical properties of systemically administered small molecule NIR dyes, there are two routes of clearance from the living subjects: renal (urine) and hepatic (bile to feces) clearances. For examples, methylene blue is predominantly cleared by the kidneys. By taking this advantage of fast renal clearance, methylene blue could be used to intraoperatively identify the ureters using NIR fluorescence imaging. In contrast, ICG is cleared by the liver and excreted into the bile ducts [3]. Accordingly, intraoperative NIR fluorescence cholangiographies using ICG as fluorescence probes have been studied [3]. Since some NIR fluorophores, especially cyanine dyes, are too lipophilic to dissolve in aqueous solution, it is necessary to formulate them to enable circulation in the bloodstream by conjugation or addition of solubilizing groups (such as sulfonic acid or polyethylene glycol chains) to their base structures. Such a modification not only dramatically improves biocompatibility but significantly changes their pharmacokinetics and clearance, resulting in relatively long circulation and desired renal clearance. Like small molecule dyes, nanoparticle-based NIR fluorescent probes have ability to reach the targeted tissues through blood circulation after administered intravenously. However, many NIR nanoprobes are rapidly cleared from the bloodstream by mononuclear phagocytes system (MPS), and then largely accumulated in the liver and spleen, due to their great accessibility. In fact, their particle size, surface charge, shape, and surface coating are major features responsible for *in vivo* behavior

of fluorescence nanoprobes in living subjects. Firstly, there is a size threshold (hydrodynamic size less than 7 nm) below which the nanoprobes are likely to be cleared by the renal system. The renal clearance is preferred clinically because it is significantly faster than hepatic clearance so that administrated nanoprobes have less chances to be sequestered in the body for an extensive time. For relatively large particles (more than 20 nm), however, they typically accumulate in the liver and spleen and could be to some extent cleared hepatically. Similar to the size effect, the surface charge and charge distribution of NIR fluorescence nanoprobes have a significant impact on their *in vivo* behaviors. Normally, the NIR fluorescence probes with neutral, distributed net charge could show minimal nonspecific binding to normal organs and tissues [5]. Finally, the surface coating of NIR nanoprobes also plays an important role in biodistribution, extravasation, and elimination. After coated with a passivation layer such as silica shells, hydrophilic polymers (polyethylene glycol), or dendrimers, NIR nanoprobes show improved solubility and exhibit the ability to escape from the immune recognition via reducing direct exposure to the plasma proteins, eventually resulting in prolonged circulation time and enhanced specific accumulation in malignant. For fluorescent probes to be effectively delivered to the desired sites, many biological barriers in the living subjects have to be passed, including walls of blood vessels, extracellular matrix tissues surrounding the target cells, and the cellular basement membrane. Generally, the fluorescent probes with molecular weight of roughly larger than 40 kDa can passively accumulate in tumor through EPR effect, due to leaky tumor vasculature [16]. On the basis of available tumor-specific targets, the fluorescent probes with targeting moieties could actively bind the tumors with minimal nonspecific uptake in normal tissues or organs, leading to improved signal-to-background ratio. Indeed, according to the pathways of clearance, pharmacokinetics, targeting ability of fluorescence probes, it is necessary to optimize and determine the necessary dose and timing, extensive dosing for contrast administration and imaging prior to the surgical procedure.

Toxicity

Both biocompatibility and toxicity are important considerations for NIR fluorescence probes aimed at preclinical evaluation and clinical translation. Although the conjugation and/or surface modification of NIR fluorescence probes could improve their biocompatibility, their potential toxicity still could result from probes themselves or their constituent components released during degradation *in vivo* [5]. Given that fluorescent techniques rely on the concentration of probes and method of administration, the *in vivo* toxicity effects of NIR fluorescence probes are species-specific and dose- or concentration-dependent. Considering the sensitivity of fluorescent imaging technique, the NIR fluorescence probes with regular brightness and reasonable dose after normal systemic administration usually do not cause detectable acute toxic effect. So far, there are many paradigms and metrics for toxicity study evolving to bypass animal testing and preclinical evaluation. It is very critical to improve our understanding of toxicities associated with NIR fluorescent probes for their translation to the clinic.

Classification of NIR Fluorophores in Medical Imaging

Small-Molecule NIR Fluorophores

Many small molecule organic dyes with defined core structures including cyanines, borondipyrromethane (BODIPY), phthalocyanines, benzo[c]heterocycles, porphyrin, squaraine, and xanthenes (Fig. 3.2. and Table 3.1) have been extensively studied as NIR fluorophores for fluorescence imaging [16]. Their desired physical and optical properties could be tuned through the conjugation of functional groups to each basic core structure. As the most common class of NIR fluorophores, the cyanine structure could be modified with varied length polymethine chains and dual nitrogen-containing aromatic heterocycles with variable substitutions in order to tune the excitation and emission wavelengths. According to the basic core with pentamethine

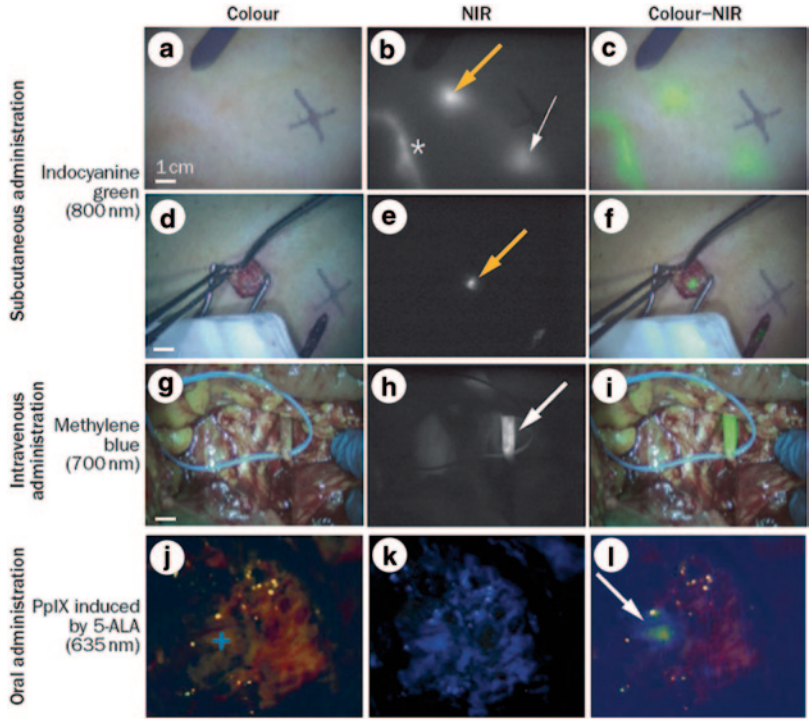

Fig. 3.3 Intraoperative near-infrared (*NIR*) fluorescence imaging using small *NIR* fluorescence probes with three different administration methods. **a–f** Sentinel lymph nodes (SLN) mapping using ICG after subcutaneous administration in a patient with cutaneous melanoma. **a** and **d** White light optical images. **b** and **e** *NIR* fluorescence images (arrows indicate SLN). **c** and **f** Merge images. **d–f** Identification of an SLN (*arrow* in panel **e**) using 800 nm *NIR* fluorescence imaging 15 min after local injection of ICG around the tumor. **g–i** Intraoperative *NIR* fluorescence imaging of the ureter (*arrow* in panel **h**) during lower abdominal surgery in a patient with ovarian carcinoma 45 min after intravenous administration of methylene blue. **g** Visible optical image. **h** *NIR* fluorescence image. **i** Merge image. **j–l** Fluorescence imaging in brain surgery during resection of a glioblastoma multiforme using oral 5-ALA-induced protoporphyrin IX (PpIX). **j** White light image. **k** Visible fluorescence image. **l** Overlay image (fluorescent tumour signal marked by arrow). (Reprinted with permission from [3]; copyright 2013, Macmillan Publishers Limited)

derivatives, the cyanine structure with longer polymethine chains such as heptamethine derivatives could cause bathochromatic shifts in both excitation and emission wavelengths. One of the most famous examples is ICG, which fluoresces at 800 nm (Table 3.1). ICG and fluorescein sodium are the only fluorescent probes so far approved for imaging guided intraoperative dissection [19]. However, there are many limitations of the use of the latter one because its excitation and emission wavelengths are in the range of visible light. In contrast, as a NIR fluorophore, ICG has capability of imaging deep or buried tissues such as tumors, blood vessels and nerves, and currently has become available clinically for sentinel lymph node (SLN) mapping, tumor resection, graft, and vascular patencyin cardiac. Significant efforts have recently been made to visualize lymphatic channels transcutaneously using ICG as fluorescent contrast agent, potentially improving localization of SLN, and minimizing the necessary incision for surgery (Fig. 3.3a). As the other approved dyes, methylene blue after intravenously administrated has been proven to be predominantly cleared by renal system, and can be thus used to identify the ureters intraoperatively using NIR fluorescence imaging (Fig. 3.3g–i). Preclinical identification of insulinomas and visualization of fibrous tumors in clinic using methylene blue as a NIR fluorescent agent have been recently reported. Another agent, 5-aminolevulinic acid (5-ALA) as the major substrate for protopor-

phyrin synthesis, has been used clinically for imaging guided tumor detection and therapy. After oral or topical administration, 5-ALA induces the synthesis and accumulation of fluorescent protoporphyrin IX (PpIX, part of emission spectrum centered at 700 nm) in malignant gliomas and meningiomas (Fig. 3.3j–l) [3]. So far 5-ALA-induced PpIX has been successfully studied for intraoperative identification and resection of various brain tumors. Similar to the base structure of naturally occurring PpIX, both phthalocyanine- and porphyin- based molecules are two dimensional 18π-electron aromatic cyclic structures. Their chemical and optical properties such as absorption, emission, and photostability can be controlled by incorporation of various metal ions and conjugation of a variety of substituents at the periphery and axial positions. In the same manner, after conjugated with sulfonate moieties, squaraine fluorophores with a central four-membered (square) ring and resonance stabilized zwitterionic structures not only have improved stability and solubility but also have strong extinction coefficient and show enhanced NIR excitation and emission. As the other class of promising NIR fluorescence agents for *in vivo* study, the BODIPY and its derivatives have improved photostability, increased quantum yield, large extinction coefficient and optimized NIR optical properties, which can grant them intraoperative access to fluorescent guided surgery. Most commercially available NIR fluorophores are based on the cyanine chemical structure with specific modifications by different manufacturer. CyDyes are the most well-known NIR fluorophores, such as the 700 nm fluorophore Cy5.5 and the 800 nm fluorophore Cy7. To date, IRdye 800CW is the most widespread use in the *in vivo* preclinical evaluation. A serial of Alexa fluor dyes such as Alexa fluor 680 or 750 have great promise in the *in vivo* study because of their improved stability and brightness. In short, many efforts have been recently made on the design and development of various NIR dyes and their derivatives to obtain improved chemical photostability, enhanced fluorescence intensity, and prolonged the fluorescent life for fluorescent imaging. Although most of NIR dyes have limited targeting capabilities, they can be conjugated with various biomakers or protein for specific *in vivo* targeting because they are often available commercially or experimentally as N-hydroxysuccinimide (NHS) esters, isothiocyanates or maleimide derivatives which can be readily conjugated to ligands, peptides or proteins via free amine or thiol groups [5].

Fluorophores with a unique donor-acceptor or push-pull type design have NIR fluorescent properties and show promise for *in vivo* imaging applications [8]. The electron donor (high-lying HOMO) and the electron acceptor (low-lying LUMO) units can be linked by a conjugated π spacer, resulting in a D-π-A-π-D type of chromophores. By changing the donor, acceptor, and π spacer, their absorption and emission can be tuned within both NIR-I and NIR-II windows (600–1600 nm). Based on these base structures, a new series of low energy gap chromophores have been recently designed and characterized, and well-reviewed [8]. After appropriate substituent modification, they further show great potential in biological applications.

NIR-Dye-Loaded Nanoprobes

NIR-dye-loaded nanoprobes are organic or inorganic matrix-based nanomaterials either incorporated, encapsulated or attached with/by organic or metallorganic NIR dye molecules [20]. The matrix materials are typically transparent to both visible and NIR light, including inorganic scaffolds or matrixes (silica NPs and calcium phosphate NPs (CPNPs)) [21], or organic nanocarriers (liposomes, polymersomes, micelles, and dendrimers) [6, 22, 23]. Compared with bare NIR dyes, there are many unique features of NIRF-dye-loaded nanoprobes highly desirable for *in vivo* imaging [22]. Firstly, chemically inert matrixes can protect the incorporated fluorescent molecules from a harsh physiological environment, thereby enhancing their stability and improving biocompatibility. Secondly, the imaging contrast or signal-to-noise ratio could be dramatically improved because high payload of the NIR dyes can be delivered to the sites of interest. Thirdly, the matrixes or nanocarriers as

versatile and general platforms could be available for subsequent biomodification with numerous targeting moieties such as peptides, proteins, and antibodies. Lastly, different from bare dye, NIR-dye-loaded NPs show improved biodistribution, favorable pharmacokinetics, and desired clearance pathway, making themselves suitable for intraoperative fluorescence imaging.

Due to the planar nature of the chemical structures, the solubility of many NIR fluorescent dyes in their native forms such as porphyrin and squaraine is relatively poor in the physiological condition. Various platforms including liposomes and polymersomes have been developed as nanocarriers for *in vivo* optical imaging. They not only dramatically enhance signal-to-background ratio and improve imaging sensitivity by carrying thousands of copies of NIR fluorophores, but also actively target specific receptors overexpressed by tumors [22]. Recently, a new class of phototransducing liposomes named as porphysomes were reported by Zheng and coworkers [24]. Their self-assembled porphyrin bilayers provide tunable optical properties in the NIR region (Fig. 3.4). Combined with unique structure-dependent fluorescence self-quenching, activated porphysomes enable molecular imaging of tumors with low-background fluorescence.

Although there are a small number of commercially available organic molecules with fluorescence in the NIR-II window, they are usually highly hydrophobic, water-insoluble cyanine or thiopyrilium dyes such as IR-26, IR-1048, IR-1051, and IR-1061 [25]. Dai and coworkers recently reported the synthesis and application of the first biocompatible NIR-II agent by embedding organic dye IR-1061 within a poly(acrylic acid) matrix coated with PEGylated phospholipids (DSPE-mPEG). The resulting IR-PEG NPs as a NIR-II contrast agent provided facile, clear delineations of different inner organs of the mouse, or even blood vessels with excellent spatial resolution and deep tissue penetration because of their largely reduced light scattering and tissue autofluorescence in the NIR-II window (Fig. 3.5).

Inorganic Semiconductor Quantum Dots

The quantum dots (QDs), as a special class of nanometer-sized inorganic fluorescent semiconductor crystals, have recently attracted much attention for fluorescence imaging because they have unique chemical and optical properties, such as size-tunable photoluminescent emission, continuous and broad absorption spectra, narrow and symmetric emissions spectra, and high photostability. As a direct result of quantum confinement effect, QDs exhibit unique size- and composition-dependent optical and electrical features over the corresponding properties of conventional organic fluorophores [4]. QDs have high quantum yields (usually 20 to ~60%) and large extinction coefficients (~600,000 M^{-1} cm^{-1}, roughly an order of magnitude higher than Rhodamine 6G), thus leading to much brighter (approximately 10 to ~20 times) fluorescence than organic dyes [9]. Furthermore, QDs are highly photostable under continuous illumination over certain periods of time. Typically, QDs have a long excited-state lifetime (30–100 ns, compare to less than 5 ns for organic dyes at room temperature), which is desirable for the time-gated imaging of tissues *in vivo* to significantly improve the signal-to-background ratio by eliminating shorter lived emission signals from tissue autofluorescence [26]. Since the bandwidth at half-maximum of QD emission bands is typically as narrow as 20 nm and the spectral overlap could be reduced to a large extent, QDs hold great multiplexing capability for molecular imaging. So far there are vast literatures on QDs and some semiconductor crystals for *in vivo* imaging, which will be reviewed in another chapter of this book.

Recently emerged as promising fluorescent probes, NIR QDs are a major focus of *in vivo* molecular imaging and image-guided therapy because of deep tissue penetration and minimal tissue autofluorescence. Many NIR-emitting QDs, including cadmium (Cd) and noncadmium based QDs, have been recently developed to overcome the limitations of organic NIR dyes or dye-loaded NPs and meet the requirements of *in vivo* biological imaging applications [27–32]. As

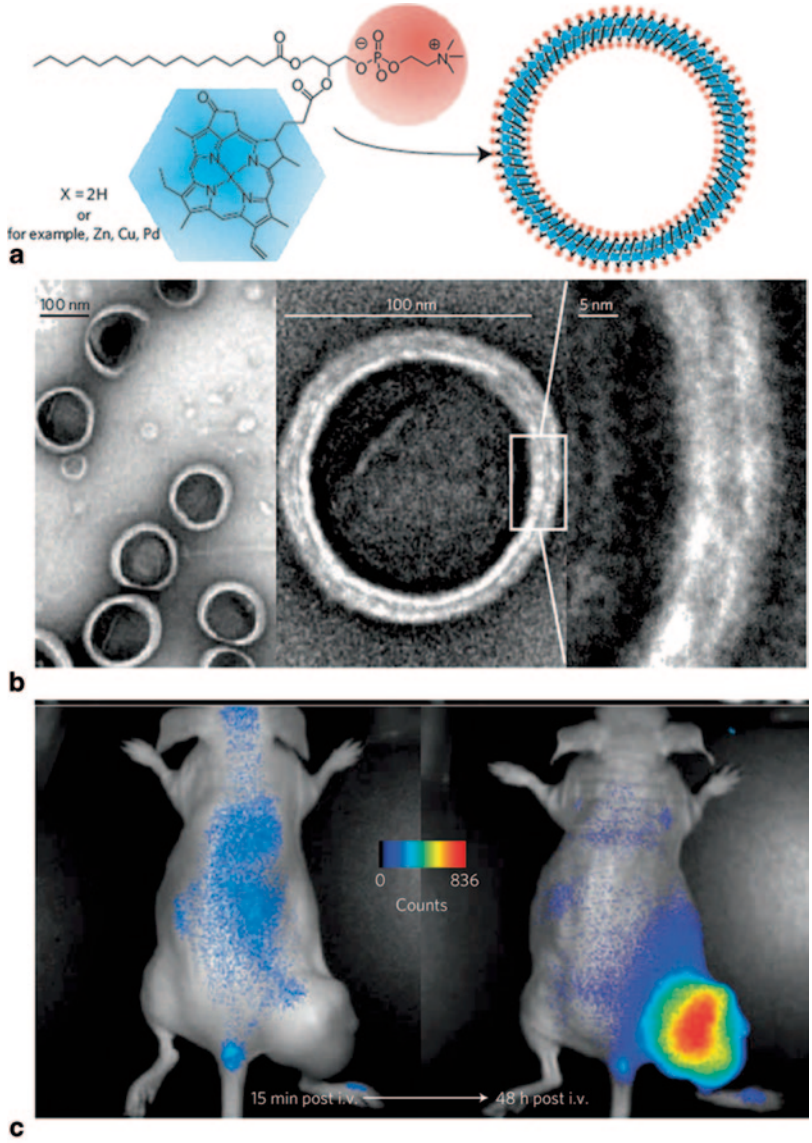

Fig. 3.4 Porphysomes are optically active nanovesicles formed from porphyrin bilayers for use as active NIR nanoprobes. **a** Schematic representation of a pyropheophorbide-lipid porphhysome. The phospholipid head group (*red*) and porphyrin (*blue*) are highlighted in the subunit (*left*) and assembled nanovesible (*right*). **b** Electron micrographs of negatively stained porphysomes. **c** Fluorescence activation after intravenous injection of porphysomes (7.5 pmol) in a KB xenograft-bearing mouse. (Reprinted with permission from [24]; copyright 2011, Nature Publishing Group)

one of representative III-V type QDs, InAs (indium arsenide) and its core/shell structures have attracted considerable attention in fluorescence imaging because they show very promising optical properties in both NIR-I and NIR-II windows (Table 3.1) [9]. The biological use of IV–VI semiconductor QDs (such as lead chalcogenide, PbX, X = S, Se, Te) is primarily limited by their potential toxicity, even though their absorption and emission could be easily tuned from the far red to NIR spectral range because of strong quantum confinement. The II–VI type QDs (such as

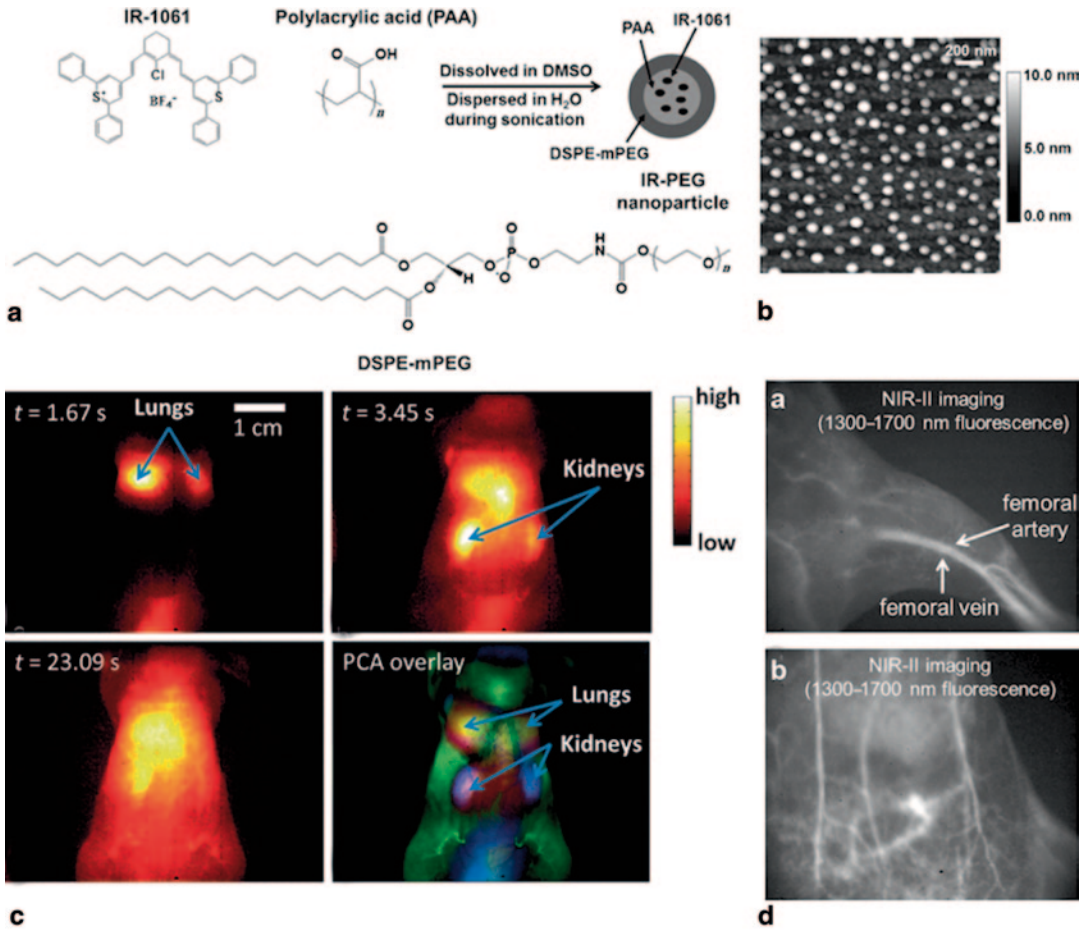

Fig. 3.5 **a** Synthesis of biocompatible IR-PEG nanoparticles with fluorescence emission more than 1000 nm. IR-1061 molecules are embedded in a poly(acrylic acid) matrix coated with PEGylated phospholipids (DSPE-mPEG). **b** AFM image of IR-PEG NPs on silicon substrate. **c** *In vivo* near-infrared (NIR)-II imaging at various times of a nude mouse with intravenously injected IR-PEG NPs. The principal component analysis (*PCA*) overlaid imaging allows the delineation of different inner organs. **d** *In vivo NIR* imaging of the hindlimb and abdomen of nude mice with IR-PEG NPs circulating in the blood streams after intravenous injection. (Reprinted with permission from [25]; copyright 2013, Wiley-VCH Verlag GmbH & Co)

cadmium chalcogenide, CdX, X = Se, Te) as NIR fluorescence probes are a major focus of optical imaging. Their chemical and optical properties have been extensively studied and successfully optimized for *in vivo* fluorescence imaging. The colloidal core/shell structures have been developed to control the basic optical properties of the QDs and improve their *in vivo* performance. Based on the core and shell constituents, there are two types of band gap structures (type-I and type-II) for heterostructure QDs. In the type-I core/shell QDs, the electrons and holes generated in the core are confined inside because the band gap of the shell is larger than that of the core, resulting in a more narrow band gap than that of original core material. Of particular interest are type-II NIR QDs (such as CdTe/CdSe), which have a staggered bang gap because the valence and conduction bands in the core are lower (or higher) than in the shell [9]. Such a spatial separations of carriers could cause smaller band gap compared to that of either core or shell material, which permits access to higher wavelengths in the NIR region.

Fluorescent Nanocrystals

The metal or alloy nanoclusters (such as gold nanoclusters (Au-NC)) have recently attracted much attention as a new class of fluorophores for optical imaging largely due to their ultrasmall sizes and unique optical properties [33, 34]. Unlike bulky metals or other nanomaterials, metal nanoclusters only consist of a small number of atoms. Their sizes are usually smaller than 2 nm and can approach the Fermi wavelength of electrons, resulting in molecule-like behavior including discrete energy levels and size-dependent fluorescence [5, 35]. Up to now, significant efforts have been devoted to the improvement of quantum yield, photostability, and biocompatibility of NIR gold nanoclusters [36]. Their size-dependent emission wavelengths could be tuned into the NIR window by optimizing the cluster size [36]. As efficient surfactants, scaffolds, or templates, various ligands or large molecules including small thiol-containing molecules, dendrimers, polymers, or proteins are used not only to make gold nanoclusters soluble and stable in aqueous solution, but also to dramatically improve their quantum yields. By using bovine serum albumin (BSA) as a scaffold, Ying and coworkers reported a simple, one-pot synthesis route for preparation of gold clusters with strong red luminescence intensity, large Stoke shift, excellent photostability and biocompatibility. It is believed that gold clusters combined with specific properties of the constituents in versatile protein templates would have great potential in targeting molecular imaging [35]. Nie and coworkers reported that a pair of gold nanoclusters assembled with Apoferritin showed a red-shift and tunable emission with enhanced intensity. Furthermore, the conjugates of gold clusters and Apoferritin showed organ-specific targeting ability and could be used for *in vivo* kidney targeting and biomedical imaging [37]. Recently, bimetallic gold-copper alloy clusters have been reported and displayed unique photoluminescent properties in NIR window, which could be tuned by changing the alloy composition [38].

Upconversion Nanophosphors

According to the excitation mechanism, NIR probes are categorized into two major groups: downconversion and upconversion (UCN) fluorophores. Most traditional fluorescent probes belong to downconversion fluorophores, meaning that the probes emit long-wavelength light when they are excited by short-wavelength light. In contrast, upconversion fluorophores convert low energy light into high energy fluorescence by the anti-Stokes emission mechanism. Generally, the basic composition of UCNs consists of inorganic fluorescent matrices (such as fluorides, (e.g., LaF_3, YF_3, and $NaYF_4$), oxides (e.g., Y_2O_3) and phosphates (e.g., $LaPO_4$)) and two trivalent lanthanide ions (such as Tm^{3+}, Er^{3+}, and Yb^{3+}) embedded inside matrices [39]. Autofluorescence-free illumination imaging in mice using UCN was impressively demonstrated by many research groups [40–44]. UCNs have recently shown the ability to image tissues or tumors at a deep depth because UCNs can absorb and produce light in the NIR window with minimal autofluorescence background [39].

Single-Walled Carbon Nanotubes

Single-walled carbon nanotubes (SWNTs) are viewed as a tubular graphene sheet identified by the vector connecting two points that meet upon rolling. For biomedical application, the rolled single tubes are approximately on the order of a couple of nanometer in diameter and several 100 nm in length. Due to their high aspect ratio, intrinsic NIR fluorescence, and relative ease of surface modification and bioconjugation, SWNTs are attractive molecular imaging agent candidates and ideal for *in vivo* imaging of real-world medical issues. Dai and co-workers developed a strategy to prepare biocompatible fluorescent SWNTs with emission in the NIR-II window by pre-treating SWNTs with sodium cholate before PEGylation. The biocompatible SWNTs as NIR-II fluorescent agents are applied to microvascular imaging and hemodynamic measurement in an *in vivo* animal model of lower limb ischemia, with

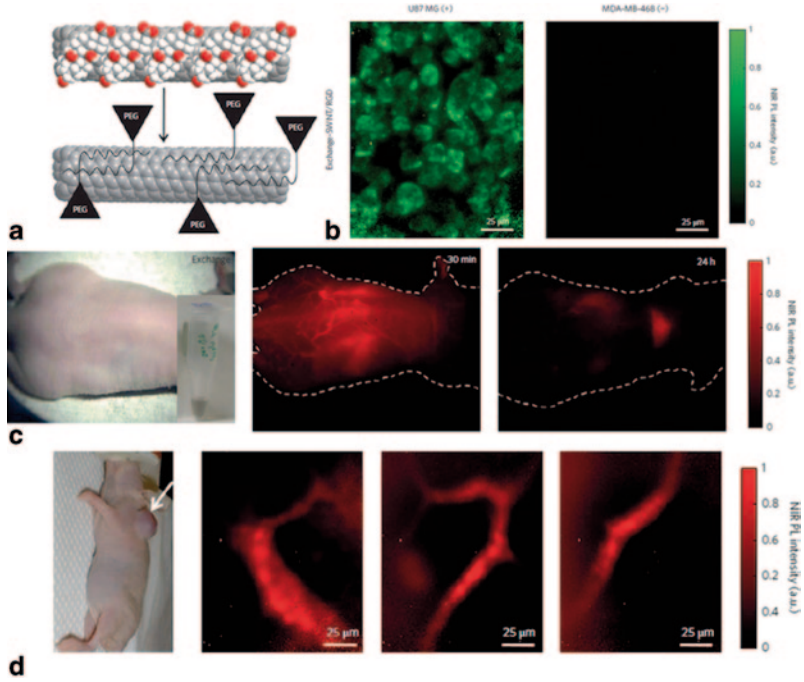

Fig. 3.6 **a** Schematic of the exchange process of SWNTs. **b** In vitro NIR photoluminescence images of human malignant glioma cells (U87 MG) treated with exchange-SWNT/RGD conjugates. **c** *In vivo* NIR photoluminescence images of nude mice treated with exchange-SWNTs. **d** Intravital NIR photoluminescence imaging of tumor vessels of LS174T tumor-bearing mouse. (Reprinted with permission from [40]; copyright 2009, Nature Publishing Group)

improved spatial resolution over X-ray computer tomography (CT) and broader dynamic range of blood flowmetry than ultrasound (Fig. 3.6) [40]. Their recent work further demonstrated many fascinating advantages of fluorescence imaging in the NIR-II windows, considering its flexibility and compatibility with other imaging modalities, which is currently opening up new imaging possibilities in preclinical and clinical use [14].

Semiconducting Polymer Dots

Semiconducing polymers, primarily consisting of π-conjugated backbones, have recently attracted much attention in fluorescence imaging and biosensing because of their outstanding characteristics as fluorescent probes such as high fluorescence brightness, fast emission rate, high quantum yields, excellent photostability, and nonblinking [18]. Important examples of fluorescent semiconducting polymers include poly (phenylene vinylene), fluorene-based copolymer and related derivatives [41–45]. In order to obtain far-red or NIR emitting probes, many strategies have been developed to tune their absorption and emission spectra, including backbone or side chain modification, chemical introduction of narrow-band-gap moieties in backbones, and physical blending of conjugated polymers with NIR fluorescent acceptors [18]. In spite of the great potential of conjugated polymers in biological application, few of them so far have been successfully used for *in vivo* fluorescent imaging because of their poor water-solubility and short excitation wavelength maximum in a visible blue region. Significant efforts have been made to improve the biocompatibility and solubility of conjugated polymers via encapsulation with other biocompatible matrices or coprecipitation with amphiphilic polymers [46]. Due to the densely packed structure and high-volume fraction of

fluorephore polymer, engineered semiconducting polymers show extraordinary light-gathering capability and efficient intraparticle energy transfer, making it possible for enhancing fluorescence brightness, tuning the emission color, and improving the photostability [41].

Fluorescent Proteins

Genetically encoded fluorescent proteins, capable of NIR fluorescing when exposed to a certain excitation light, have been extensively studied for *in vivo* imaging [5, 47]. Due to high effective brightness, intracellular stability, and photostability, NIR fluorescent proteins can be used as reliable *in vivo* reporters for whole-body imaging. A phytochrome-derived NIR fluorescent protein (iRFP) recently developed by Verkhusha and co-workers allows deep imaging in the living subjects [48]. Compared with far-red GFP-like proteins, iRFP provides a substantially higher signal-to-background ratio in living subjects due to its infrared-shifted emission spectra. Furthermore, iRFP is stable, noncytotoxic and sensitive, making its applications as easy as the traditional GFP-like fluorescent protein reporters. Chudakov and coworkers also reported a class of NIR dimeric fluorescent proteins (eqFP650 and eqFP670) with relatively high red-shifted emission maximum and high photostability, making it feasible as a targeting specific fluorescent protein probe to increase the sensitivity and capabilities of deep-tissue imaging techniques.

Advanced Applications of Fluorescent Probes in Medical Imaging

Targeted Fluorescent Probes

One of the major concerns for *in vivo* administration of NIR fluorescence probes is efficient delivery and specific targeting and/or activation of the probes in the tissue of interest [11]. Through the specific interactions between the targeting moieties of the probes and receptors on specific cell membranes or extracellular matrix enzymes, the NIR fluorescence probes can efficiently recognize the intended molecular target and selectively accumulate on the malignancy sites, thereby rendering dramatic improvements in signal-to-background ratio over nontargeted probes. There are numerous specific molecular targeting groups including small molecules, peptides, engineered protein fragments, Affibody, antibodies, and nanoparticles (Table 3.2). Due to different chemical and physical properties, each type of fluorescent probes possesses different pharmacokinetic and binding properties. Accordingly, targeted NIR fluorescent probes are categorized into several subgroups based on the type of targeting moieties or functionalities used. Very recently, Cheng and co-workers explored the feasibility of Cy5 labeled dipicolyamine-Zinc (Cy5-DPA-Zn) probes for cartilage degeneration imaging *ex* vivo and *in vivo*. Cy5-DPA-Zn selectively binds to the anionic glycosaminoglycans (GAGs) and can differentiate cartilage degeneration based on the content of GAGs in the surgically induced osteoarthritis model [49]. Small molecules show a great impact on molecular imaging because their small sizes (less than 500 Da) and ease of control over properties allow them to access and image a large range of molecular targets. The major drawbacks of small molecule probes are fast excretion and poor specificity. It is almost infeasible to conjugate a fluorophore to a small molecule without changing its pharmacokinetics and targeting properties. When nanoparticle-based fluoresecent probes are conjugated with small targeting molecules, their selectivity and specificity can be improved to some extent due to relatively long circulation of nanoparticle substrates.

Compared with the small-molecule probes, peptides show superior selectivity and specificity, and chemical flexibility in terms of the modifications that they can tolerate without changing binding affinity and pharmacokinetics. Although peptides generally have a lower affinity than antibodies, they are more stable and less likely to cause immunogenic effects. There are many specific examples of peptide-based fluorescent probes for *in vivo* optical imaging of specific targets (Table 3.2), including integrins, matrix

Table 3.2 Summary of targeted and activatable NIR fluorescent probes

Fluorescent probes	Biological target(s)	Application(s)	Used preclinically and/or clinically?	References
Small-molecule				
Folate	Folate receptor	Cancer	Preclinical	Weissleder et al. [60]
Zn(DPA)-Cy5	Anionic glycosaminoglycans	Osteoarthritis	Preclinical	Cheng et al. [49]
Peptide				
c(RGDyK)-Cy5.5	$\alpha_v\beta_3$ integrin	Cancer	Preclinical	Cheng et al. [61]
MMP-2 peptide substrate with quenched NIR fluorophores	MMP-2	Cancer	Preclinical	Bremer et al. [62]
Activatable cell-penetrating peptides (ACCPs)	MMP-2 and -9	Cancer	Preclinical	Jiang et al. [63]
AB50-Cy5.5	Caspase 3 and 7	Apoptosis/cancer	Preclinical	Edginton et al. [64]
FAPα-Cy5.5	Fibroblast activation protein-alpha	Cancer	Preclinical	Cheng et al. [51]
Engineered protein (*antibody, affibody*)				
Cy7-CC49	Tumor-associated glycoprotein (TAG)-72	Cancer	Preclinical	Zou et al. [65]
ICG-Herceptin	HER2	Cancer	Preclinical	Ogawa et al. [66]
Herceptin-RhodG	HER2	Cancer (intraoperative visualization of metastases)	Preclinical/clinical	Koyama et al. [67]
Alexa 680-$Z_{EGFR:1907}$	EGFR	Cancer	Preclinical	Cheng et al. [68]
Cy5.5-$Z_{EGFR:1907}$	EGFR	Cancer	Preclinical	Cheng et al. [69]
Anti-CEA-Diabody-RLucB	CEA	Cancer	Preclinical	Venisnik et al. [70]
Nanoparticle				
Cy5.5-SPIO-chlorotoxin NPs	MMP-2	Cancer	Preclinical	Veiseh et al. [71]
HER2-QDs	HER2	Cancer	Preclinical	Tada et al. [72]
RGD-QDs	$\alpha_v\beta_3$ integrin	Cancer	Preclinical	Cai et al. [73]
RGD_2-QDs710	$\alpha_v\beta_3$ integrin	Cancer	Preclinical	Cheng et al. [10]
Affibody Z_{HER2}-QDs	HER2	Cancer	Preclinical	Cheng et al., 2011[28]
Folate-UCNP	Folate receptors	Cancer	Preclinical	Huang et al. [74]
Cy5.5-FANPs	MMP-2	Cancer	Preclinical	Chen et al. [75]

metalloproteinases, caspases, et al. As one of the most famous target peptide examples, the cyclic arginine-glycine-aspartic acid (cRGD) peptide has been widely studied as a targeting agent for tumor angiogenesis imaging because it specifically binds to $\alpha_v\beta_3$ integrin which is highly expressed on both tumor vasculature and tumor cells. *In vivo*-targeted imaging of tumor vasculature was recently achieved using RGD-conjugated NIR QDs. Due to relatively low toxicity, noncadmium NIR QDs (InAs/InP/ZnSe core/shell/shell NPs) (emissions at 800 nm) after conjugation with RGD peptides can selectively target $\alpha_v\beta_3$ integrin-positive tumor vasculature [30]. In an SKOV-3 mouse ear tumor model using intravital microscopy imaging, it was found that QD-RGDs cannot easily extravasate but mainly target the tumor neovasculature as aggregates rather than individual nanoprobes [31].

As a promising type of engineered small protein, Affibody molecules are generally small in size (58-aminoacid residues, ~7 kDa) and their

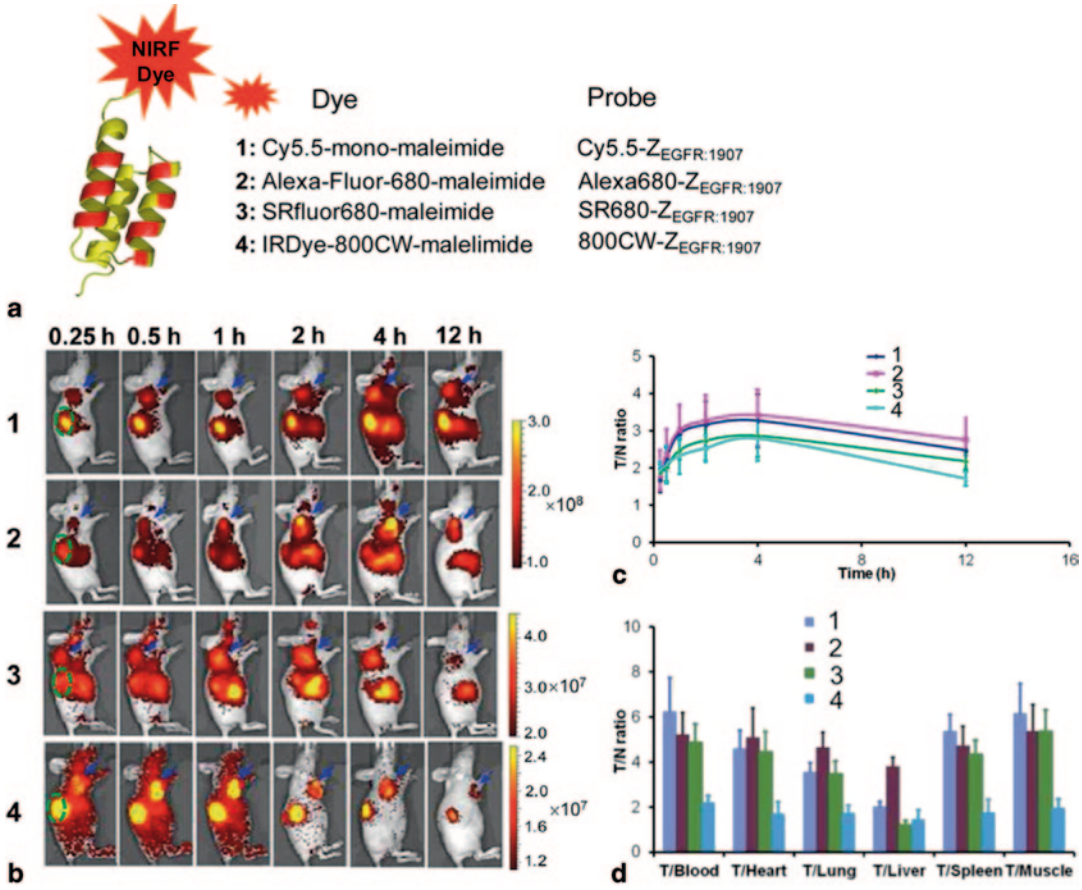

Fig. 3.7 **a** Schematic structure of anti-EGFR Affibody protein-based NIR fluorescent probes. *1:* Cy5.5-$Z_{EGFR:1907}$, *2:* Alexa680- $Z_{EGFR:1907}$, *3:* SR680- $Z_{EGFR:1907}$, *4:* 800CW- $Z_{EGFR:1907}$. **b** In vivo fluorescence imaging of subcutaneous A431 tumor-bearing nude mice at 0.25, 0.5, 1, 2, 4, and 12 h after injection of 0.5 nmol of *1:* Cy5.5-$Z_{EGFR:1907}$, *2:* Alexa680- $Z_{EGFR:1907}$, *3:* SR680- $Z_{EGFR:1907}$, *4:* 800CW- $Z_{EGFR:1907}$. *Blue arrows* indicate the tumors and *green ovals* indicate the location of kidneys. **c** Region of interest (ROI) analysis of tumor-to normal tissue ratios of the four probes in mice at different time points. **d** Fluorescent intensity ratios of tumor-to-normal tissues based on the ROI analysis. (Reprinted with permission from [68]; copyright 2012, ACS Publication)

three-helix bundle structure simulates the binding sites of the monoclonal antibody with considerable affinity. All of their superior features such as chemistry versatility, high stability, and high affinity and specificity with many molecular targets, make them excellent platforms for *in vivo* molecular imaging. Different from antibodies, Affibody has relatively shorter *in vivo* biological half-life and less immunogenic effects, thereby resulting in fast clearance from blood and rapid accumulation at their target site. Cheng and coworkers prepared and evaluated a monomeric and dimeric version of HER-2 Affibody molecule in SKOV3 tumor-bearing mouse model. Monomeric one outperformed the dimeric form with its high and rapid uptake into HER2 overexpressed tumors [4]. By conjugating a similar version of Affibody for epidermal growth factor receptor (anti EGFR Affibody, $Z_{EGFR:1907}$) with four different commercial NIR dyes: Cy5.5, Alexa680, SR680, and 800CW, they further demonstrated that it is very critical to choose appropriate NIR dyes to label Affibody molecules without dramatically altering their targeting affinity and pharmocokinetics (Fig. 3.7). Cy5.5-$Z_{EGFR:1907}$ and Alex680-$Z_{EGFR:1907}$ showed higher tumor-to-

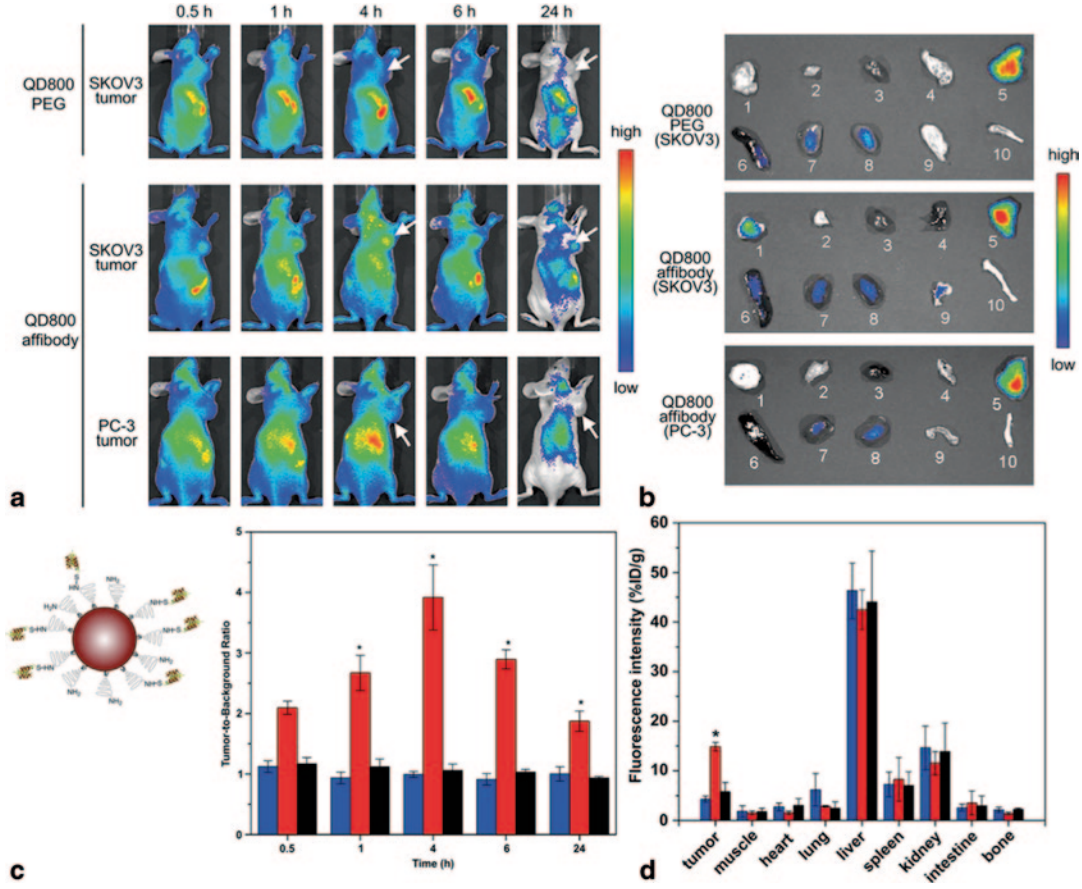

Fig. 3.8 Affibody-based quantum dots (*QDs*) for HER2-expressing cell and tumor imaging. **a** *In vivo* NIR fluorescence imaging of tumor-bearing mice (*white arrows*) injected with QD800-PEG or QD800-Affibody at 0.5, 1, 4, 6, and 24 h. **b** Tumor-to-background ration of mice injected with QD800-PEG (*blue:* SKOV3 tumor) or QD800-Affibody (*red:* SKOV3 tumor; *black:* PC-3 tumor). **c** *Ex vivo* NIR fluorescence imaging after 4 h p.i. of QD900-PEG or QD800-Affibody. *1:* tumor, *2:* muscle, *3:* heart, *4:* lung, *5:* liver, *6:* spleen, *7:* kidney (left), *8:* kidney (right), *9:* intestine, *10:* bone. **d** ROI analysis of major organs in ex vivo fluorescence imaging after 4 h p.i. QD900-PEG or QD800-Affibody. (Reprinted with permission from [28]; copyright 2011, Elsevier)

normal tissue ratio and faster tumor accumulation than the other two dyes. Recently, a HER2 Affibody was conjugated to AlexaFluor680 and used to image HER2-positive tumors in mice xenograft model to monitor their response to treatment with heat shock protein 90 inhibitor [50]. Furthermore, Cheng and coworkers reported *in vivo* targeted imaging of tumor HER2 receptors using anti-HER Affibody conjugated noncadmium NIR QDs (InAs/InP/ZnSe core/shell/shell), which exhibited specific tumor targeting ability and excellent tumor contrast (Fig. 3.8) [28]. The in vitro and *in vivo* studies revealed that HER-Affibody-QDs were highly specific to target and image HER2-overexpressing cells and tumors.

There is a recent explosion in development of peptide- or Affibody-based molecular imaging agents. With on-going efforts to enhance their targeting ability and endow capability of multiplexing imaging or more functions, targeted NIR fluorescent probes are expected to play major and important roles for *in vivo* optical imaging for preclinical evaluation and clinical trial.

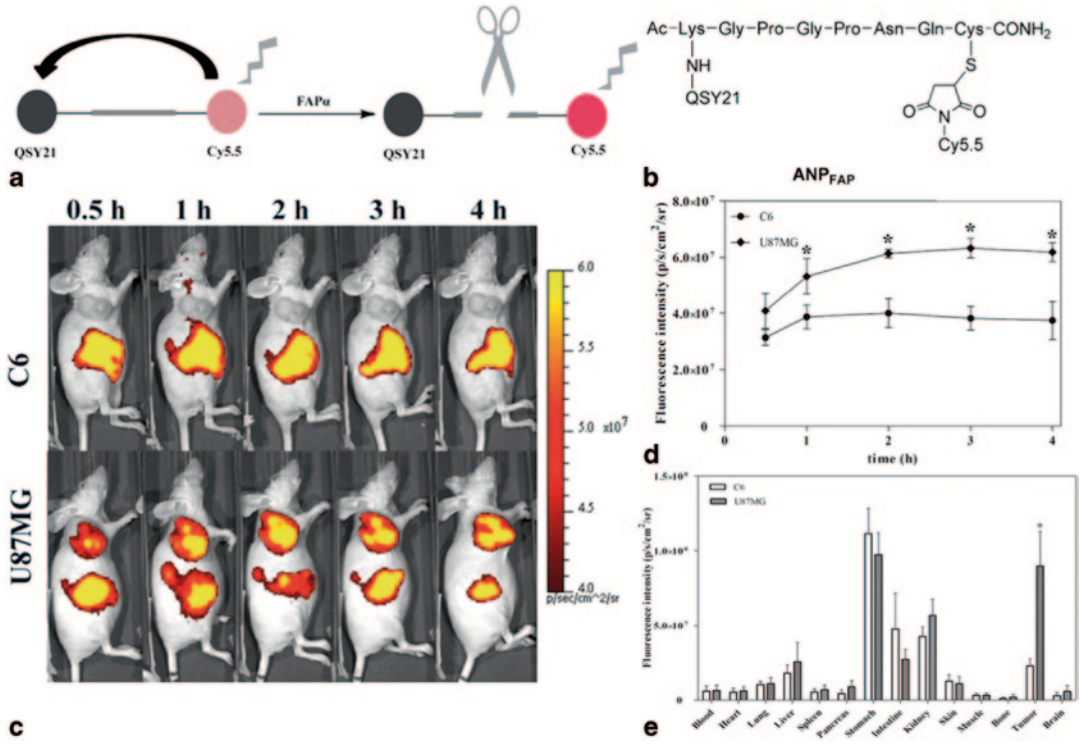

Fig. 3.9 **a** A schematic of activatable NIR fluorescent probes for *in vivo* imaging of fibroblast activation protein-α (*FAP α*). **b** Molecular structure of activatable NIR fluorescent probes (ANP_{FAP}). **c** *In vivo* fluorescent imaging of subcutaneous C6 and U87MG tumor-bearing mice at 0.5, 1, 2, 3, and 4 h post tail vein injection of ANP_{FAP} (1 nmol). **d** Fluorescence ROI analysis of tumor and muscle in mice bearing C6 and U87MG tumor from 0.5 to 4 h p.i. **e** Ex vivo imaging quantification of tumor and normal tissue of C6 and U87MG mice after mice were sacrificed at 4 h postinjection. (Reprinted with permission from [51]; copyright 2012, ACS Publication)

Activatable Fluorescent Probes

Literally, activatable fluorescent probes can amplify output signals by switching the probe from a silent state to active state when they undergo a chemical or biological reaction (e.g., enzymatic cleavage or oxidation) upon interaction with their intended target or in response to an environmental change in a real time (e.g., pH or temperature). Significant improvement in signal-to-noise ratio and specificity for *in vivo* optical imaging has been achieved with activatable fluorescent probes. Design plays a key role in the success of activatable probes for fluorescent molecular imaging, and largely relies on fluorescent components, quenching mechanism, and specific tumor-related enzymes (such as cathepsin, matrix metalloproteinases-2/-9 (MMP-2 or MMP-9)). Recently, fibroblast activation protein-alpha (FAPα) as a tumor-associated surface glycoprotein has been used as a promising target for designing activatable fluorescent probes [51]. A NIR dye Cy5.5 and corresponding quencher dye (QSY21) are linked together to form activatable probes by a short peptide sequence (KGPGPNQC) as a substrate sequence specific for FAPα (Fig. 3.9). Due to efficient fluorescence resonance energy transfer (FRET) between fluorophore and quencher dye, a dramatic transition between silent and active state can be achieved after the cleavage of the peptide by FAPα, resulting in relatively high contrast on the NIR fluorescence images. The specificity of such activatable probes has been confirmed on U87MG tumor models with high FAPα expression.

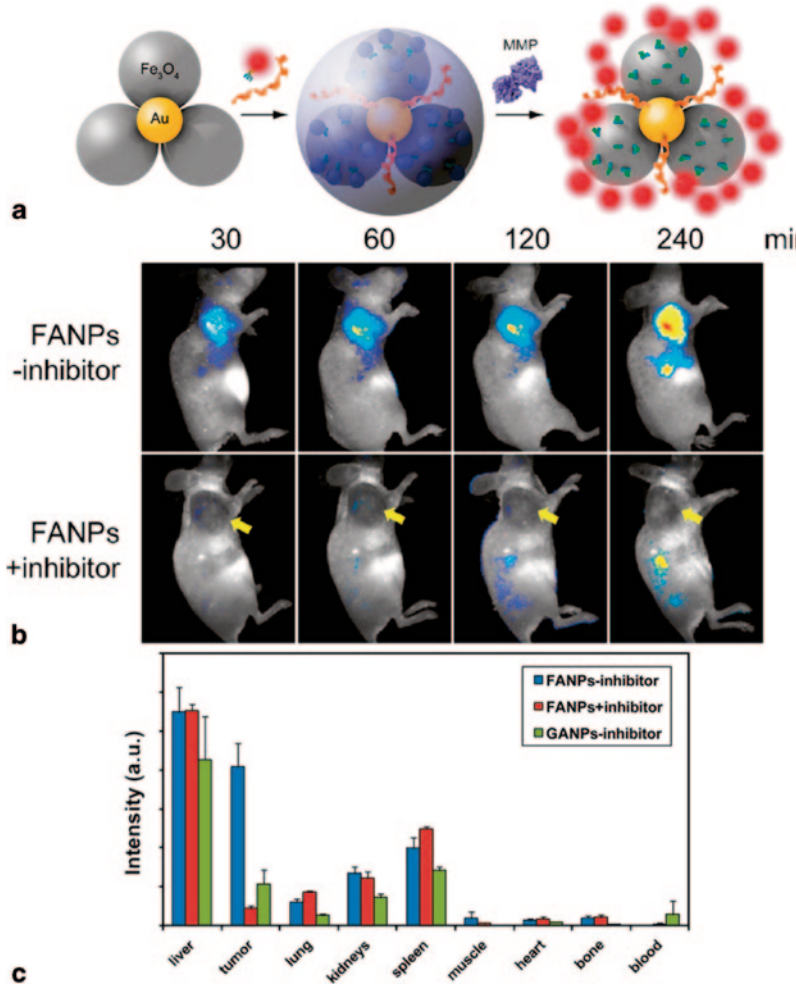

Fig. 3.10 **a** Schematic illustration of the formation and working mechanism of activatable NIR probes (FANPs). **b** *In vivo* NIRF imaging after the injection of *FANPs,* with and without the preinjection of MMP inhibitor. In a control group, gold NPs at the same Cy5.5 dose were injected. **c** Ex vivo quantization of tumor and major organs after the forth h of *in vivo* imaging. (Reprinted with permission from [57]; copyright 2011, American Chemical Society)

Due to efficient surface energy transfer properties of various semiconducting or metal NPs such as gold or iron oxide NPs, [52–55] they can absorb energy emitted from adjacent fluorophores upon excitation, causing strong fluorescence quenching over distances as long as 10 nm [56]. The selectivity and specificity of such activatable nanoparticle-based probes are attributed to the corresponding properties of cleavable sequences used for coupling of fluorophores and NPs [52]. In a recent report, flower-like Au-Fe_3O_4 NPs have been developed to conjugate different functional moieties together without any interference (Fig. 3.10) [57]. The MMP-cleavable peptide was selectively immobilized on the iron oxide surface while leaving gold surface exclusively for water-soluble coating. The precise control of surface properties is essential in rendering the activatable probes with excellent specificity and selectivity.

It is a challenge to detect a wide range of tumors in cancer diagnostics. By exploiting changes in the tumor microenvironments, Gao and co-workers recently developed a polymeric, micelle-based nanoprobe that is ultra-pH-sensitive

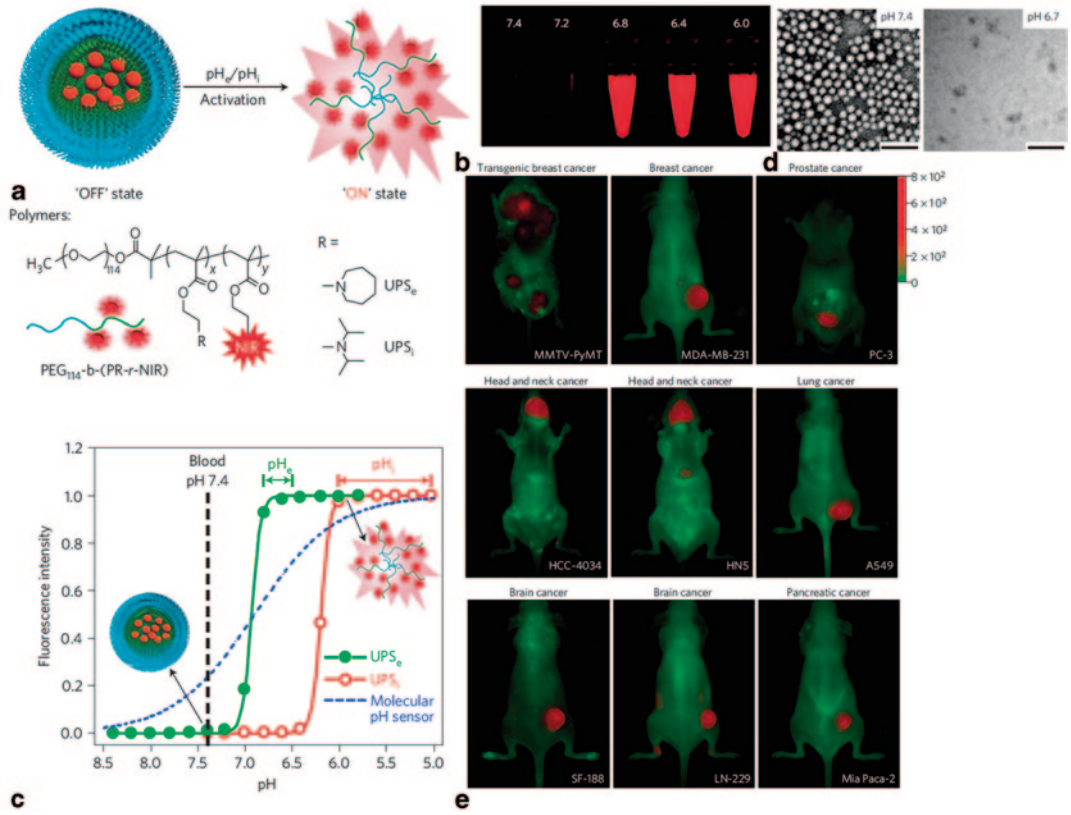

Fig. 3.11 **a** Structural composition of two types of nanoprobe, UPS_e, and UPS_i, with pH transitions at 6.9 and 6.2, respectively. Cy5.5 is used as the near-infrared fluorophore in most of the animal studies. **b** Normalized fluorescence intensity as a function of pH for UPS_e and UPS_i nanoprobes. At high pH, both probes stay silent. At pH below their transitions (6.9 or 6.2), the nanoprobes can be activated as a result of micelle dissociation. **c** Fluorescent images of UPS_e-Cy5.5 nanoprobe solution in different pH buffers. **d** Transmission electron micrographs of UPS_e nanoprobes at pH 7.4 and 6.7. **e** iUPS nanoprobes target both acidic pH_e and tumor vasculature with broad tumor specificity. iUPS nanoprobes show broad tumor imaging specific and efficacy in ten different tumor models of different cancer types (breast, prostate, head and neck, lung, brain, and pancreatic cancers) and organ sites. (Reprinted with permission from [58]; copyright 2014, Nature Publishing Group)

with a sharp and tunable response to pH change, which enables ultrasensitive tumor-specific imaging in many types of cancers regardless of their genotypes and phenotypes [58, 59]. The tertiary amines have been introduced as ionizable hydrophobic blocks for the pH-sensitive core. The hydrophobic NIR dyes were subsequently incorporated into the core. As a result of assembled dyes in close proximity with each other in the center of particles, the nanoprobes are highly quenched and exhibit very little fluorescence at physiological pH. A slight drop in pH in the tumor site can cause protonation of amine groups, resulting in dissociation of micelle as a consequence of electrostatic repulsion. The nanoprobes become dramatically activated in response to the low extracellular pH or neovascular uptake in tumors. Such a transition is fast and sharp, and tumor-to-blood fluorescence ratio is extremely high with more than 300-fold increase in fluorescence in the desired site. The generality of the nanoprobes has been validated in a variety of cancer models including transgenic, orthotopic, and subcutaneous models) (Fig. 3.11). Those impressive results suggest that the pH-activatable nanoprobe as a robust and universal fluorescent agent is very

promising for the early detection of primary tumors and metastases [58].

Conclusion

NIR flurorescent image-guided surgery holds great promise to improve surgical outcomes for patients. Numerous novel NIR fluorescent probes have recently been developed and evaluated, and some of them have shown great potential as contrast agents for molecular optical imaging with excellent specificity and sensitivity. Although several NIR fluorescent probes have been approved for clinical use, most of them are still at the early stage of clinical translation. Many issues are overwhelming and need to be overcome for successful clinical translation of NIR fluorescent probes. There are some requirements or features for NIR fluorophores in order to make image-guided surgery a reality for patients and surgeons, such as photostability, penetration, and brightness. The major challenges for clinic use of NIR fluorescent probes are their pharmacokinetics and toxicity. Nontoxic, biodegradable, and biocompatible materials are thus highly recommended for preparing the NIR probes. Despite their potential toxicity being under the investigation, nanoparticle-based probes show great promises in molecular optical imaging for cancer diagnosis and treatment monitoring. The uses of receptor-specific or activatable NIR fluorescent probes have great advantages for tumor delineation and intraoperative surgical guidance for full tumor resection in an accurate and proficient manner.

References

1. Nguyen QT, Tsien RY. Fluorescence-guided surgery with live molecular navigation—a new cutting edge. Nat Rev Cancer. 2013;13(9):653–62.
2. Keereweer S, et al. Optical image-guided cancer surgery: challenges and limitations. Clin Cancer Res. 2013;19(14):3745–54.
3. Vahrmeijer AL, et al. Image-guided cancer surgery using near-infrared fluorescence. Nat Rev Clin Oncol. 2013;10(9):507–18.
4. James ML, Gambhir SS. A molecular imaging primer: modalities, imaging agents, and applications. Physiol Rev. 2012;92(2):897–965.
5. Cheng K, Cheng Z. Near infrared receptor-targeted nanoprobes for early diagnosis of cancers. Curr Med Chem. 2012;19(28):4767–85.
6. Kobayashi H, et al. New strategies for fluorescent probe design in medical diagnostic imaging. Chem Rev. 2010;110(5):2620–40.
7. Smith AM, Mancini MC, Nie S. Bioimaging: second window for in vivo imaging. Nat Nanotechnol, 2009;4(11):710–1.
8. Qian G, Wang ZY. Near-infrared organic compounds and emerging applications. Chem Asian J. 2010;5(5):1006–29.
9. Ma Q, Su X. Near-infrared quantum dots: synthesis, functionalization and analytical applications. Analyst. 2010;135(8):1867–77.
10. Gao J, Chen X, Cheng Z. Near-infrared quantum dots as optical probes for tumor imaging. Curr Top Med Chem. 2010;10(12):1147–57.
11. Hilderbrand SA, Weissleder R. Near-infrared fluorescence: application to in vivo molecular imaging. Curr Opin Chem Biol. 2010;14(1):71–9.
12. Welsher K, et al. A route to brightly fluorescent carbon nanotubes for near-infrared imaging in mice. Nat Nanotechnol. 2009;4(11):773–80.
13. Hong G, et al. In vivo fluorescence imaging with Ag2S quantum dots in the second near-infrared region. Angew Chem Int Ed Engl. 2012;51(39):9818–21.
14. Hong G, et al. Multifunctional in vivo vascular imaging using near-infrared II fluorescence. Nat Med. 2012;18(12):1841–6.
15. Lakowicz J. Principles of fluorescence spectroscopy. London: Academic; 2010.
16. Gibbs SL. Near infrared fluorescence for image-guided surgery. Quant Imaging Med Surg. 2012;2(3):177–87.
17. Guo Z, et al. Recent progress in the development of near-infrared fluorescent probes for bioimaging applications. Chem Soc Rev. 2014;43(1):16–29.
18. Wu C, Chiu DT. Highly fluorescent semiconducting polymer dots for biology and medicine. Angew Chem Int Ed Engl. 2013;52(11):3086–109.
19. Su X, et al. Image-guided resection of malignant gliomas using fluorescent nanoparticles. Wiley Interdiscip Rev Nanomed Nanobiotechnol. 2013;5(3):219–32.
20. Gao JH, Chen XY, Cheng Z. Near-infrared quantum dots as optical probes for tumor imaging. Curr Top Med Chem. 2010;10:1147–57.
21. Cho EC, et al. Inorganic nanoparticle-based contrast agents for molecular imaging. Trends Mol Med. 2010;16(12):561–73.
22. He X, Wang K, Cheng Z. In vivo near-infrared fluorescence imaging of cancer with nanoparticle-based probes. Wiley Interdiscip Rev Nanomed Nanobiotechnol. 2010;2(4):349–66.
23. Kobayashi H, et al. Rational chemical design of the next generation of molecular imaging probes based

on physics and biology: mixing modalities, colors and signals. Chem Soc Rev. 2011;40(9):4626–48.
24. Lovell JF, et al. Porphysome nanovesicles generated by porphyrin bilayers for use as multimodal biophotonic contrast agents. Nat Mater. 2011;10(4):324–32.
25. Tao Z, et al. Biological imaging using nanoparticles of small organic molecules with fluorescence emission at wavelengths longer than 1000 nm. Angew Chem Int Ed Engl. 2013;52(49):13002–6.
26. Gu L, et al. In vivo time-gated fluorescence imaging with biodegradable luminescent porous silicon nanoparticles. Nat Commun. 2013;4:2326.
27. Michalet X, et al. Quantum dots for live cells, in vivo imaging, and diagnostics. Science. 2005;307(5709):538–44.
28. Gao J, et al. Affibody-based nanoprobes for HER2-expressing cell and tumor imaging. Biomaterials. 2011;32(8):2141–8.
29. Smith BR, et al. Dynamic visualization of RGD-quantum dot binding to tumor neovasculature and extravasation in multiple living mouse models using intravital microscopy. Small. 2010;6(20):2222–9.
30. Gao J, et al. In vivo tumor-targeted fluorescence imaging using near-infrared non-cadmium quantum dots. Bioconjug Chem. 2010;21(4):604–9.
31. Smith BR, et al. Real-time intravital imaging of RGD—quantum dot binding to luminal endothelium in mouse tumor neovasculature. Nano Lett. 2008;8(9):2599–606.
32. Schipper ML, et al. Particle size, surface coating, and PEGylation influence the biodistribution of quantum dots in living mice. Small. 2009;5(1):126–34.
33. Xie JP, Zheng YG, Ying JY. Protein-directed synthesis of highly fluorescent gold nanoclusters. J Am Chem Soc. 2009;131(3):888.
34. Shi XG, et al. Dendrimer-entrapped gold nanoparticles as a platform for cancer-cell targeting and imaging. Small. 2007;3(7):1245–52.
35. Zhang L, Wang E. Metal nanoclusters: new fluorescent probes for sensors and bioimaging. Nano Today. 2014;9(1):132–57.
36. Zheng J, Zhang CW, Dickson RM. Highly fluorescent, water-soluble, size-tunable gold quantum dots. Phys Rev Lett. 2004;93(7):077402.
37. Sun C, et al. Controlling assembly of paired gold clusters within apoferritin nanoreactor for in vivo kidney targeting and biomedical imaging. J Am Chem Soc. 2011;133(22):8617–24.
38. Andolina CM, et al. Photoluminescent gold-copper nanoparticle alloys with composition-tunable near-infrared emission. J Am Chem Soc. 2013;135(14):5266–9.
39. Chatterjee DK, Gnanasammandhan MK, Zhang Y. Small upconverting fluorescent nanoparticles for biomedical applications. Small. 2010;6(24):2781–95.
40. Welsher K, et al. A route to brightly fluorescent carbon nanotubes for near-infrared imaging in mice. Nat Nanotechnol. 2009;4(11):773–80.
41. Li K, Liu B. Polymer-encapsulated organic nanoparticles for fluorescence and photoacoustic imaging. Chem Soc Rev. 2014;43(18):6570–97.
42. Liu J, et al. Bright far-red/near-infrared fluorescent conjugated polymer nanoparticles for targeted imaging of HER2-positive cancer cells. Polymer Chem. 2013;4(16):4326.
43. Liu J, Geng J, Liu B. A bright far-red and near-infrared fluorescent conjugated polyelectrolyte with quantum yield reaching 25%. Chem Commun (Camb). 2013;49(15):1491–3.
44. Jeong K, et al. Conjugated polymer/photochromophore binary nanococktails: bistable photoswitching of near-infrared fluorescence for in vivo imaging. Adv Mater. 2013;25(39):5574–80.
45. Ahmed E, et al. Fluorescent multiblock pi-conjugated polymer nanoparticles for in vivo tumor targeting. Adv Mater. 2013;25(32):4504–10.
46. Ding D, et al. Bright far-red/near-infrared conjugated polymer nanoparticles for in vivo bioimaging. Small. 2013;9(18):3093–102.
47. Lecoq J, Schnitzer MJ. An infrared fluorescent protein for deeper imaging. Nat Biotechnol. 2011;29(8):715–6.
48. Filonov GS, et al. Bright and stable near-infrared fluorescent protein for in vivo imaging. Nat Biotechnol. 2011;29(8):757–61.
49. Hu X, et al. Optical imaging of articular cartilage degeneration using near-infrared dipicolylamine probes. Biomaterials. 2014;35(26):7511–21.
50. van de Ven SM, et al. Optical imaging with her2-targeted affibody molecules can monitor hsp90 treatment response in a breast cancer xenograft mouse model. Clin Cancer Res. 2012;18(4):1073–81.
51. Li J, et al. Activatable near-infrared fluorescent probe for in vivo imaging of fibroblast activation protein-alpha. Bioconjug Chem. 2012;23(8):1704–11.
52. Lee S, et al. A near-infrared-fluorescence-quenched gold-nanoparticle imaging probe for in vivo drug screening and protease activity determination. Angew Chem Int Ed Engl. 2008;120(15):2846–9.
53. Dubertret B, Calame M, Libchaber AJ. Single-mismatch detection using gold-quenched fluorescent oligonucleotides. Nat Biotechnol. 2001;19(4):365–70.
54. Cha EJ, et al. Development of MRI/NIRF 'activatable' multimodal imaging probe based on iron oxide nanoparticles. J Control Release. 2011;155(2):152–8.
55. Oh E, et al. Inhibition assay of biomolecules based on fluorescence resonance energy transfer (FRET) between quantum dots and gold nanoparticles. J Am Chem Soc. 2005;127(10):3270–1.
56. Kircher MF, Weissleder R, Josephson L. A dual fluorochrome probe for imaging proteases. Bioconjug Chem. 2004;15(2):242–8.
57. Xie J, et al., Manipulating the power of an additional phase: a flower-like Au-Fe3O4 optical nanosensor for imaging protease expressions in vivo. ACS Nano. 2011;5(4):3043–51.
58. Wang Y, et al. A nanoparticle-based strategy for the imaging of a broad range of tumours by nonlinear amplification of microenvironment signals. Nat Mater. 2014;13(2):204–12.

59. Ling D, Hackett MJ, Hyeon T. Cancer imaging: lighting up tumours. Nat Mater. 2014;13(2):122–4.
60. Tung C-H, et al. A receptor-targeted near-infrared fluorescence probe for in vivo tumor imaging. Chembiochem. 2002;3(8):784–6.
61. Chen X, Conti PS, Moats RA. In vivo near-infrared fluorescence imaging of integrin αvβ3 in brain tumor xenografts. Can Res. 2004;64(21):8009–14.
62. Bremer C, Tung CH, Weissleder R. In vivo molecular target assessment of matrix metalloproteinase inhibition. Nat Med. 2001;7(6):743–8.
63. Jiang T, et al. Tumor imaging by means of proteolytic activation of cell-penetrating peptides. Proc Natl Acad Sci U S A. 2004;101(51):17867–72.
64. Edgington LE, et al. Noninvasive optical imaging of apoptosis by caspase-targeted activity-based probes. Nat Med. 2009;15(8):967–73.
65. Zou P, et al. Near-infrared fluorescence labeled anti-TAG-72 monoclonal antibodies for tumor imaging in colorectal cancer xenograft mice. Mol Pharm. 2009;6(2):428–40.
66. Ogawa M, et al. In vivo molecular imaging of cancer with a quenching near-infrared fluorescent probe using conjugates of monoclonal antibodies and indocyanine green. Cancer Res. 2009;69(4):1268–72.
67. Koyama Y, et al. Spectral fluorescence molecular imaging of lung metastases targeting HER2/neu. Clin Cancer Res. 2007;13(10):2936–45.
68. Qi S, et al. Evaluation of four affibody-based near-infrared fluorescent probes for optical imaging of epidermal growth factor receptor positive tumors. Bioconjug Chem. 2012;23(6):1149–56.
69. Miao Z, et al. Cy5.5-labeled affibody molecule for near-infrared fluorescent optical imaging of epidermal growth factor receptor positive tumors. J Biomed Opt. 2010;15(3):036007.
70. Venisnik KM, et al. Bifunctional antibody-Renilla luciferase fusion protein for in vivo optical detection of tumors. Protein Eng Des Sel. 2006;19(10):453–60.
71. Veiseh O, et al. Optical and MRI multifunctional nanoprobe for targeting gliomas. Nano Lett. 2005;5(6):1003–8.
72. Tada H, et al. In vivo real-time tracking of single quantum dots conjugated with monoclonal anti-HER2 antibody in tumors of mice. Cancer Res. 2007;67(3):1138–44.
73. Cai W, et al. Peptide-labeled near-infrared quantum dots for imaging tumor vasculature in living subjects. Nano Lett. 2006;6(4):669–76.
74. Hu H, et al. Multimodal-luminescence core-shell nanocomposites for targeted imaging of tumor cells. Chemistry. 2009;15(14):3577–84.
75. Xie J, et al. Manipulating the power of an additional phase: a flower-like Au–Fe3O4 optical nanosensor for imaging protease expressions in vivo. ACS Nano. 2011;5(4):3043–51.

Detectors for Intraoperative Molecular Imaging: From Probes to Scanners

4

Farhad Daghighian and Yuman Fong

Radioguided surgery until recently involved injecting noncancer-specific agents such as technetium-99m nanocolloid to track lymph trafficking using low-energy gamma probes. The development of cancer-specific agents such as 18F-FDG for preoperative imaging, which tracks to hypermetabolic cancer cells or radiolabeled antibodies directed at cancer antigens now allows the possibility of cancer-specific radioguided surgery. Tracking radiolabeled antibodies or metabolites requires much more sophisticated intraoperative instrumentation. The most common radioactive tracer used for positron emission tomography (PET) is Flouro-deoxyglucose (FDG). The radioactive isotope in FDG is F-18 that emits a positron. Positrons quickly decay to gamma rays. Therefore, a piece of tissue that contains positron-emitting radio-pharmaceutical emits two types of radiation, positrons, and gamma rays. Two types of intraoperative hand-held detectors have been developed. One type for direct detection of positrons, and one type for detection of high energy gamma rays. These hand-held detectors may assist surgeons in locating cancerous tissues. In this chapter, we will present the current state of intraoperative radioguidance, including risks, instrumentation, and future prospects.

F. Daghighian (✉)
IntraMedical Imaging LLC, 12569 Crenshaw Boulevard, Hawthorne, CA 90250, USA
e-mail: fd@intra-medical.com

Y. Fong
Department of Surgery, City of Hope National Medical Center, Duarte, CA, USA

Radiation Dose Received by the Surgeon, Anesthetist, and OR Staff

No discussion of radiation detection in an interventional setting can begin without a discussion of risk to the OR or interventional suite personnel. Because, all patients injected with high energy gamma or beta emitters are by definition radioactive, understanding the risks to personnel and optimizing the workflow to minimize risk is important.

Povoski et al. [1] measured deep-dose equivalent in ten such surgical cases and found that the surgeon received the highest radiation exposure of 9 ± 2 microSv/mCi of FDG injected. Heckathorne et al. [2] did similar measurements and conclude that for a 2-h procedure beginning 1 h after administration of 10 mCi of FDG, the exposure would be 5.8 mR to the primary personnel (surgeon) and 2.2 mR to the secondary personnel (nurses), or the effective dose equivalents would be 58 and 22 microSv, respectively. The standard injected dose of F-18 FDG is 10 mCi (or 370 MBq). The occupational radiation exposure to all intraoperative and perioperative personnel involved in radio-guided surgical procedures utilizing 18F-fluorodeoxyglucose (18F-FDG) have been measured and found to be relatively small.

For every isotope and tracer used, studies will need to be conducted to ensure safety.

Y. Fong et al. (eds.), *Imaging and Visualization in The Modern Operating Room,*
DOI 10.1007/978-1-4939-2326-7_4, © Springer Science+Business Media New York 2015

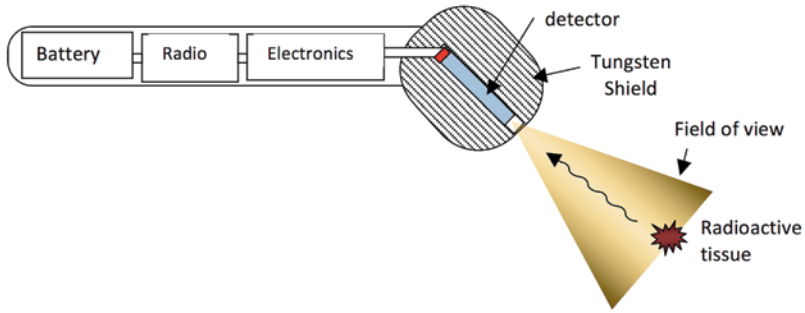

Fig. 4.1 Schematic of a high-energy gamma probe

Probes for Detection of High Energy Gamma Rays

An optimal detector probe for gamma rays emitted from the annihilation of positron is called a *high-energy gamma probe*. These gamma rays have energy of 511 keV that requires at least a 20 mm deep high-density detector material (e.g., LYSO crystal), encased in a collimator made of tungsten with at least 15 mm wall thickness. (Fig. 4.1) The need for such a large collimator is the biggest challenge in designing such probes, particularly as cancer surgery has become more commonly delivered through laparoscopy.

A high-energy gamma probe is shown in Fig. 4.2. Its sensitivity at 1 cm distance was determined to be 125 cps/microCi of F-18. A typical tumor weighting 0.5 g has a diameter of 1 cm and contains 0.5 microCi of FDG 1 h after injection. Therefore, the probe will record 62 cps when placed within 1 cm distance from such a tumor. This count rate is adequate to distinguish the tumor over a background that has 40% less radioactive concentration.

To probe, a small (0.5 cm diameter) source of F-18 was placed at different distances and count rates were measured. The angular resolution of the probe was determined by placing this source of 5 cm away from the probes tip at different angular positions and yield a full width at half maximum of 52°. The spatial resolution of this probe was found at three different distances from the tip of the probe. The results of these measurements are presented in Fig. 4.3.

Fig. 4.2 A commercially available high energy gamma probe, the PET-Probe®. (Courtesy of IntraMedical Imaging LLC, Hawthorne, CA)

A laparoscopic high-energy gamma probe is also available from IntraMedical Imaging. This probe has an outer diameter of 15 mm, therefore, the detector is narrower, and the wall shielding is thinner than those of the hand-held high-energy probe, resulting in lower sensitivity and compromised spatial resolution (Fig. 4.4). Its clinical use in detection of colorectal cancer and lung cancer has proved to be difficult due to inadequate collimation and large size.

Clinical Trials of High Energy Gamma Probes

Essner et al. [3] conducted a phase II diagnostic trial evaluating the performance and detection sensitivity of a high-energy gamma probe capable of processing 511 keV photons of ^{18}F-labeled pharmaceuticals. The study included patients who underwent a comprehensive diagnostic work-up for a known or suspected malignancy. A total of forty patients (14 women, 26 men, ages 18–78 year) were studied. All patients underwent a diagnostic whole body FDG-PET scan and CT and/or MR imaging of the suspected regions. Indication for surgery, surgical strategy, and study eligi-

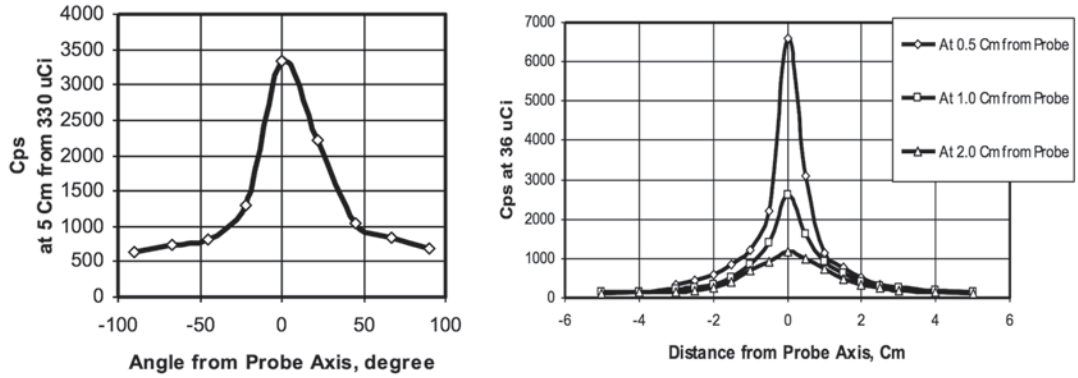

Fig. 4.3 Spatial and angular resolution of the high energy gamma probe

bility were determined based on the preoperative imaging findings. Patients who had presumed resectable recurrent/metastatic disease demonstrating one or more hot foci of uptake on their PET imaging were enrolled for the study. The patients received a second injection of 7–10 mCi dose of FDG within 1–4 h of surgery, and underwent surgical exploration using the high-energy gamma probe (PET-Probe®, IntraMedical Imaging LLC, Hawthorne, CA).

At surgery, the PET-Probe® was used to determine absolute counts/sec at the known tumor site(s) demonstrated by whole body PET and adjacent normal tissue (at least 4 cm away from tumor-bearing sites). Tumor-to-background ratio (TBR) obtained in the surgical field was called the "in-situ TBR". An in-situ TBR of 1.5:1 or greater was considered a +itive probe detection criterion. If the surgical specimen included an adjacent normal tissue, a +t-resection TBR was also calculated on the back table. This TBR was called the "ex-vivo TBR" in a subset of patients.

Indication for surgery was exploration for recurrent or metastatic disease in 32 (80%) patients (melanoma: 26, colon ca: 4, breast ca: 1, thyroid ca: 1). Five (14%) patients (lymphoma:1, Colon ca:1, seminoma:1, breast cancer of unknown primary:1, sarcoidosis:1) underwent high-energy gamma probe-guided diagnostic exploratory surgery prompted by a +itive FDG-PET scan which revealed an abnormal focal uptake during a comprehensive work-up without any prior cancer diagnosis. Three lymphoma patients underwent excisional biopsy with probe localization for re-grading/restaging of their disease.

Anatomic locations of the lesions were neck and supraclavicular ($n=7$), axilla ($n=5$), groin and deep iliac ($n=4$), trunk and extremity soft tissue ($n=3$), abdominal and retroperitoneal ($n=19$), and lungs ($n=2$). Absolute count rates (counts per second) at 4 h over index lesions ranged from 131 to 156 (mean: 136.8). Absolute count rates at 4 h over brain (measurements over temporal region), heart (over left precordium), liver (over right upper outer quadrant), soft tissue (over thigh) were 218–243 (mean: 221), 52–72 (mean: 61), 53–69 (mean: 57), and 24–53 (mean: 56), respectively.

The in-situ TBR ranged from 1.4 to 2.5 (mean: 1.9). The ex-vivo TBR ranged from 1.5 to 3.3 (mean: 2.1). In situ TBR for melanoma, colon cancer, lymphoma, and breast cancer lesions were 1.5–2.5 (mean: 1.8), 1.5–2.2 (mean: 1.9),

Fig. 4.4 Laparoscopic high-energy gamma probe. (Courtesy of IntraMedical Imaging LLC)

1.7–2.4 (mean: 2.1), and 2.1–2.2 (mean: 2.1), respectively.

PET-Probe® detected all FDG-PET-imaged lesions. Smallest detectable lesion was 0.5 cm. PET-probe was instrumental in localization of lesions that were not immediately apparent at the surgical exploration in 14 patients. In four cases, the probe localized a lesion in a previously explored field (neck: 1, axilla: 2, abdomen: 1). in eight cases, the probe localized a non-palpable lesion (neck: 2, axilla: 1, lung: 2, soft tissue: 3). In two cases, the probe identified an additional lesion that was not seen on the preoperative imaging study (both retroperitoneal).

All the lesions identified on preoperative PET scans were also detected by the PET-Probe®. PET-probe® disclosed a deep peri-portal nodal disease site which was not found on visual and manual exploration. The patient was having a second reexploration for metastatic colorectal cancer. Two axillary, and two cervical second explorations for recurrent nodal disease were successfully completed using the PET-Probe®.

Two lung and three soft tissue lesions in five patients with melanoma were located using PET-probe®. PET-probe® facilitated diagnostic lymphadenectomy in two patients by setting a line of sight through a small skin incision.

Kim et al. [4] conducted a prospective, controlled study on 12 patients with thyroid cancer, to evaluate the feasibility of an intraoperative high-energy gamma probe, the PET-probe® with respect to precise tumor localization, verification of complete resection, and a decrease in unnecessary reoperations and complications. Inclusion criteria were thyroid cancer requiring a total thyroidectomy with a modified radical neck dissection (MRND) and recurrent thyroid cancer after thyroid surgery. The types of procedures included total thyroidectomy with MRND, selective neck dissection (SND), and excision of recurrent thyroid masses. Operative exploration was carried out between 2 and 6 h after injection of 18F-FDG. The surgeon calculated the target-to-background ratio (T/B ratio) by checking the 10-s accumulated count using the PET probe. SNDs, mass excisions, total thyroidectomy with MRND, and MRND were performed on seven, four, and one patient, respectively. All tumors were localized by the high-energy gamma probe precisely in real time. In seven patients, high-energy gamma probe detected lesions not observed on preoperative PET scans. In one patient, the high-energy gamma probe detected a cancerous lymph node that was not identified in preoperative ultrasonography. The mean T/B ratio of thyroid carcinoma was 1.51 ± 0.53 (range, 1.17–4.03) and the postoperative serum thyroglobulin off thyroid hormone was < 2.0 ng/ml. Radioguided surgery using an intraoperative PET probe in thyroid cancer appears to be a useful method for real-time tumor localization, verification of complete excision, and minimization of the possibility of residual cancer. Therefore, an intraoperative high-energy gamma probe in thyroid cancer may decrease unnecessary reoperations and complications due to persistent disease.

Current Status

Clinical applications of high-energy probe-guided surgery include restaging for previously treated lymphoma patients, localization and resection of metastatic FDG avid nodules especially in previously operated or radiated fields and biopsy of PET findings difficult to localize. The ability of a high-energy gamma probe to identify a lesion depends on a number of factors: the FDG avidity of the tumor, timing of surgical exploration in reference to injection of FDG, anatomic location of the lesion, its relative proximity to main sites of physiologic uptake, and technical properties of the probe. Locating a lesion masked under scar tissue is probably the strongest indication for PET-probe-guided exploration.

Overall these clinical trials demonstrated limited success for the high-energy gamma probe. This is due to a number of shortcomings of the current probe designs. Thus, it is still difficult to rely on the current probes if (1) the tumor to

background was less than 1.5, (2) the tumor was smaller than 0.5 cm, (3) the tumor was more than 5 cm deep inside the normal tissue, and (4) the tumor was located near an organ with high radioactive concentration (such as brain).

Positron-Sensitive Probes (Beta Probes)

Many radioisotopes in addition to gamma rays emit electrons or positrons (beta rays). Gamma rays travel several centimeters in tissue. Therefore, a detector sensitive to gamma rays will be susceptible to spurious gamma rays emitted by distant organs and background tissue. This background radiation could mis-locate small lesions. Beta rays travel just a few millimeters, and a beta detector has the advantage of sensing only the local radioactive concentration.

One limitation of gamma probes in surgery is their inability to distinguish between the signal and the background radioactivity which obscures small tumors with low tumor/background uptake ratios. The beta probe was invented to circumvent this limitation in traditional gamma probe technology. Since beta rays have short depth of penetration in tissue (~ mm), a beta sensitive probe is not affected by the background radiation.

The beta probe is ideal for the detection of minute tumor remnants, which, due to the short penetration range of beta rays in tissue, are not obscured by the radioactivity accumulated in normal tissues. In an experiment utilizing prostate cancer cells and antibody labeled with I-131, the beta probe was capable of detecting 0.06 g of tumor in presence of 2 mCi of background (Fig. 4.5). The first intraoperative beta probe was built by Daghighian et. al. [5] This beta-sensitive probe utilizes a plastic scintillator which is relatively insensitive to gamma radiation although a small amount is always detected. These spurious gamma rays may become significant when background radioactivity is high. A reference gamma ray detector was placed near the beta detector in order to subtract the background gamma rays from the beta detector [5, 6]. Figure 4.6 shows a laparoscopic version of a positron-sensitive probe with 5 mm diameter.

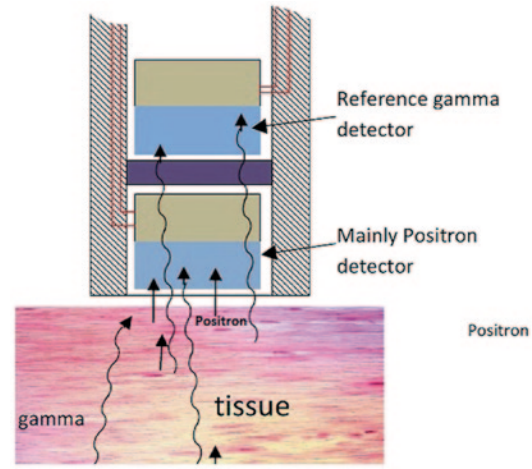

Fig. 4.5 Beta or positron probe. Positrons emitted more than a few millimeters under the beta probe are stopped in the tissue. The gamma rays from the background may generate some counts in the front detector. To subtract this count rate, another "reference" detector is added that count the gamma rays only

Fig. 4.6 Laparoscopic positron or beta probe. (Courtesy of IntraMedical Imaging LLC)

Clinical Trials of Positron-Sensitive Probes

Breast Cancer In 14 patients with breast cancer, 10 mCi of F-18 FDG was injected iv 1–4 h before surgery. The Beta Probe was used to scan the resected tumor. The profile of the count rates for three of the cases are shown here, demonstrating that the beta counts correlate with the cancer. (Fig. 4.7)

Intra-Abdominal Cancers Strong et. al. [7] conducted a pilot study for beta probe applications in abdominal cancers, using monoclonal antibodies labeled with a positron emitting isotope of iodine; I-124. These were humanized monoclonal antibodies for colorectal cancer (Hu-A33)

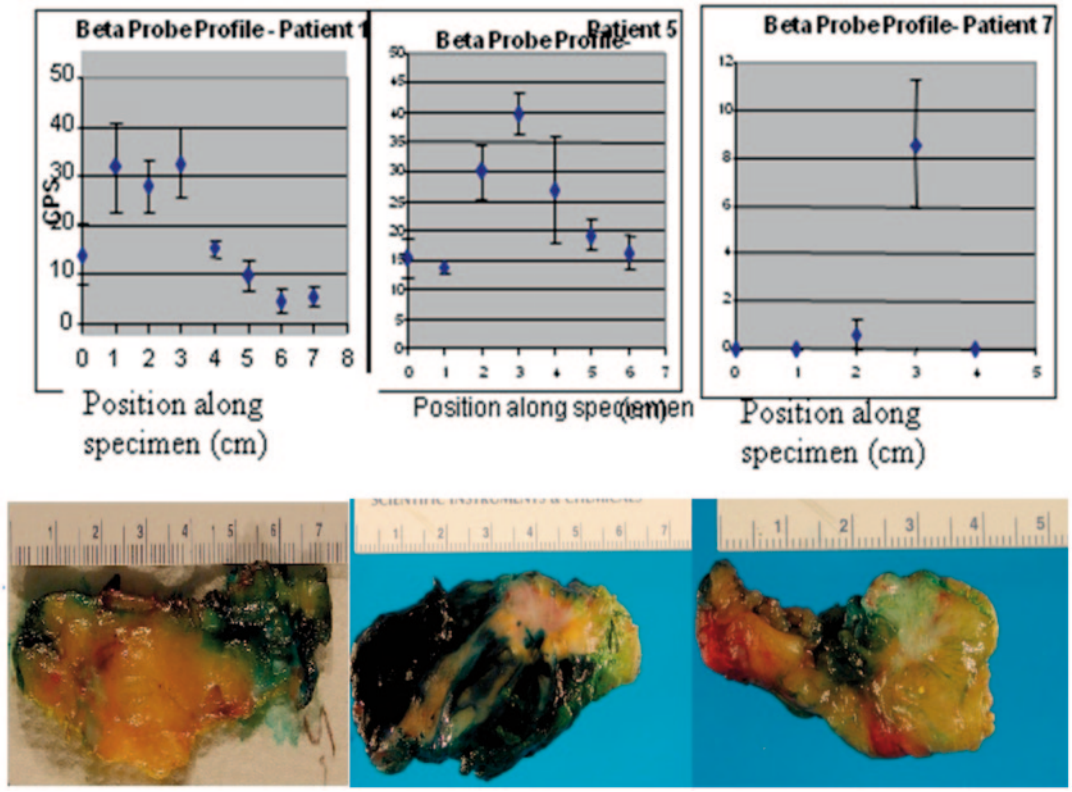

Fig. 4.7 Excised breast tumor samples were scanned with a positron probe. Note that count rate increased when the probe was placed on top of the tumor

and renal tumors (cG250). Both types of probes, the high-energy gamma probe as well as the positron-sensitive probe were used intra-operatively, on regions of intensity shown on pre-operative PET images and other regions suspicious for cancer. After the surgery these probes were used *ex vivo* on tissue samples positive for tumor by H + E staining and autoradiography. Beta and gamma emissions were correlated. Metastatic colorectal cancer ($n=4$) and renal cell carcinoma ($n=2$) patients were evaluated. Count rates of the gamma probe on the cancerous tissue ranged from 80 to 532 cps *in vivo*, and 72–278 cps *ex vivo*. For the beta probe these were 31–82 cps *in vivo* and 34–95 cps *ex vivo*. Beta emission showed a stronger correlation than gamma rays with tissue radioactivity. Figure 4.8 shows the excised liver specimen with tumor deposits of one of the patients with colorectal cancer. Not only was the large deposit (long arrow) detected by intraoperative probes, the small tumor deposit (short arrow) which was not seen by external FDG-PET or A33 mAb-PET was detected by both the high energy gamma probe and the beta probe *in vivo*. These results suggest that the proposed laparoscopic beta probe will find occult tumors. This study also suggests that beta emission detection may offer superior real-time localization of tumor on or near the surface.

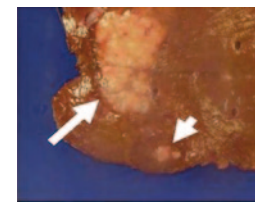

Fig. 4.8 Excised liver specimen with tumor deposits, even the smaller tumor was detected by PET probe and beta probe *in vivo*

Melanoma In one patient with melanoma that was injected with F-18 FDG, the bulk of the tumor was removed and the beta probe scanned the resected margins. In one area on the base of skull, the beta probe registered high activity compared with the normal tissue. Pathology demonstrated microscopic positive margins that would have otherwise been missed by the surgeon [8] (Table 4.1).

Current Status

The positron probe was successful in finding small superficial tumor deposits in these limited clinical trials. Reliable screening of an area larger than 20 × 20 mm would require more than 5 min time, and it is difficult to ensure that the entire surface was scanned.

Positron Camera

Several minutes are required to scan the resected tumor cavity with a 5 mm diameter positron probe. In order to address this issue a beta camera was developed, that is equivalent to having several beta probes touching the surface of the surgical field simultaneously (area of 20 × 20 mm). One such camera is built by coupling a thin sheet of plastic scintillator to an array of solid-state photomultipliers (Fig. 4.9). Solid state photomultipliers (SSPM) detect the light produced in the scintillator by incident positron with very high gain of $\sim 10^6$, quantum efficiency > 70 %, high stability and low dark current (Fig. 4.10).

The sensitivity of the beta camera to positrons of F-18 was determined by placing a 5 × 5 mm piece of filter paper soaked in F-18 solution, on top of the beta camera (Fig. 4.11a–d). The sensitivity is 36 cps/kBq, or 12,320 cps/microCi with linearity over four orders of magnitude. A typical 1 mg tumor would have 1 nCi of radioactivity, generating 120 counts in 10 s exposure to this positron camera.

Spatial Resolution was obtained by taking a profile through the image and measuring the FWHM along both axes of the array correcting for the size of the source (in this case the FWHM of the image measured at the center) for the collimated source is 1.5 mm.

Effect of Background Radiation on Lesion Detection

Two types of background count rates can affect the lesion detection: Distant organs with high uptake, and uptake in the surrounding normal tissue.

To work out the issues with interfering gamma rays from distant background uptake, studies were performed to examine annihilation photon background from the source. In order to make a source for this experiment a piece of 1 × 1 mm filter paper was soaked in ^{18}F FDG. This source was placed 3 mm above the beta camera. Images were acquired (for 1 min), once with a 3 mm thick piece of plastic between the source and the camera, so only gamma rays reached the camera, and once without it so both positron and gamma rays can reach the camera. The "gamma-only" case generated only 2 % of the count rate of the "positron + gamma" case. Experiments were conducted using unscattered photons (511 keV) (Fig. 4.12) or scattered photons (Fig. 4.13). In both experiments, a syringe was filled with 1 mCi of FDG and a 0.5 mm collimated Tl-204 beta source (7 microCi) centered on the beta camera's plastic scintillator provided the beta images. In this case, the syringe was inserted into a hole in acrylic block, 5 cm from one side, 12.5 cm from orthogonal side. Side of this block was placed next to the beta camera. The image acquisition was repeated for various distances of the syringe to the camera (Fig. 4.13). The background gamma rays from organs containing 1 mCi, even as close as 5 cm, has little effect on detectability of the 0.5 mm collimated beta ray source (Tl-204; 7 microCi).

Uptake in surrounding normal tissue was then studied using a 1 mm^2 circle painted with F-18 solution (approximately 1 nCi/mm^2). Its image was acquired for 30 s and is shown in Fig. 4.14a–d. In subsequent experiments, beta emitting uptake in normal tissue surrounding the lesion was mim-

Table 4.1 Summary of clinical trials of the high-energy gamma probe

Ref		Sensitivity	Summary
[3]	(40 patients total, 32 patients with known tumors—supraclavicular, axilla, groin and deep iliac, trunk, abdominal and retroperitoneal, and lung)	In vitro: 1440 cps/uCi (at 0 cm from source) 255 cps/uCi (at 1 cm from source) In situ: mean T/B 1.9:1 Ex vivo: mean T/B 2.1:1	7-10 mCi FDG administered to 40 patients 1–4 h before surgery. 32 patients had known tumors sites and eight patients underwent surgery for diagnostic exploration. PET probe detected all known lesions. The probe localized additional lesions in 15 patients that were not immediately apparent by surgical exploration. The smallest detectable lesion was 0.5 cm
[4]	(12 patients with thyroid cancer requiring a total thyroidectomy)	T/B = 1.51 (mean) 1.17–4.03 (full range)	FDG 2–6 h before surgery. All tumors were localized by the probe. In seven patients, lesions that were not observed on preoperative PET scan were detected by the probe. In one patient, the probe identified additional lymph nodes that were not identified on preoperative ultrasonography
[9]	(8 patients, metastatic colon cancer or melanoma)	T/B varied from 1.16:1 to 4.67:1 for melanoma (13 tumors) T/B varied from 1.19:1 to 7.92:1 for colon cancer (four tumors)	7–10 mCi of FDG administered ≤3 h before surgery. The probe identified lesions with a 50 % reduction in maximum counts at a distance of 1.7 cm from the source. 17 tumors identified by probe in eight patients. The smallest tumor resected had a count ratio of 2.9:1, suggesting the probe is able to identify subcentimeter tumors
[10]	24 patients, 18 therapeutic surgery, 6 pt diagnostic explorer	In vivo T/B ≥ 1.5:1	All lesions identified on a preoperative FDG-PET scan were detected by the probe. Probe was able to localize lesions that were nonpalpable and non-obvious at surgical exploration in eight patients. The smallest detectable lesion was 0.8 cm
[11]	(Nine patients, 12 total lesions. Five patients had lesions in previously operated and/or radiated fields)		Patients were injection with 10–12 mCi of FDG 3–4 h before surgery. The PET probe easily localized all targeted lesions, even in cases where the region was heavily scarred from previously operations
[7]	2 pt. colorectal, 2 pt. kidney ca. I–124 Mab both ɣ and β probes)	ɣ measured: 48–306 cps T/B > 2 for all tumors, for both probes	Patients underwent pre-operative PET scans. The ɣ and β probes used during surgery detected emissions from all tumors. While the absolute counts measured by the two probes were different, they exhibited a strong positive correlation. While the ɣ probe has a higher sensitivity, the β probe may offer superior specificity for real-time localization of small tumor deposits

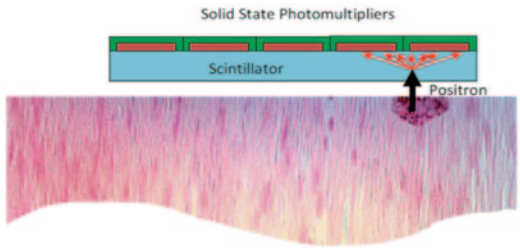

Fig. 4.9 Positron or beta camera with an area of 20 × 20 mm. The positrons from the tumor get absorbed in the plastic scintillator and emit light that in turn get detected by the 5 × 5 array of solid state photomultipliers

icked by filter paper (17 × 17 mm) painted with less radioactive concentrations. Different background contrasts of 4–1, 2–1, and 1.3–1 were achieved. In each case, the background paper was placed on top of the "lesion" and beta camera images were acquired for 30 s duration. Figure 4.14 shows that we can distinguish a 1 nCi lesion in a background of 0.5 nCi (2–1 ratio of lesion to background). The effects of background gamma rays were studied and found to be relatively negligible. The limit of lesion detectability was established: distinguishing a 2–1 ratio of lesion to background, where the lesion had approximately 1 nCi of F-18 activity.

Testing of the Positron Camera Ex vivo

This positron camera was tested under an [12] IRB-approved protocol at John Wayne Cancer Institute. Patients were injected with 10 mCi of FDG 1 h prior to the surgery. Breast tumors were removed and placed on top of the beta camera. Figure 4.15 shows such a specimen that was painted by pathologist. The image is acquired for 10 s showing the 5 mm diameter tumor.

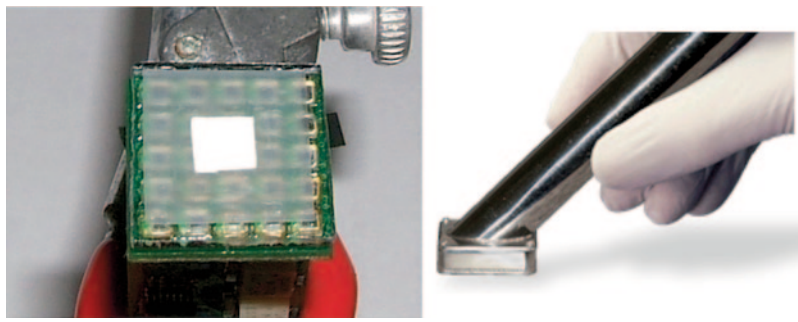

Fig 4.10 **a** Filter paper soaked with F-18 solution, and enclosed by a layer of Scotch tape placed on top of the plastic scintillator of the positron camera. **b** The intramedical's positron camera (MARGINator™)

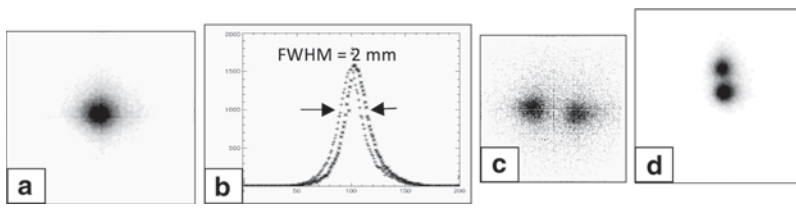

Fig. 4.11 **a** Image of one F-18 collimated source for 1 minute (1.25 mm diameter), **b** line profile through image (FWHM ~ 2 mm), **c** two F-18 collimated sources, each ~ 1.25 mm diameter, *7* mm apart and; **d** 3 mm apart

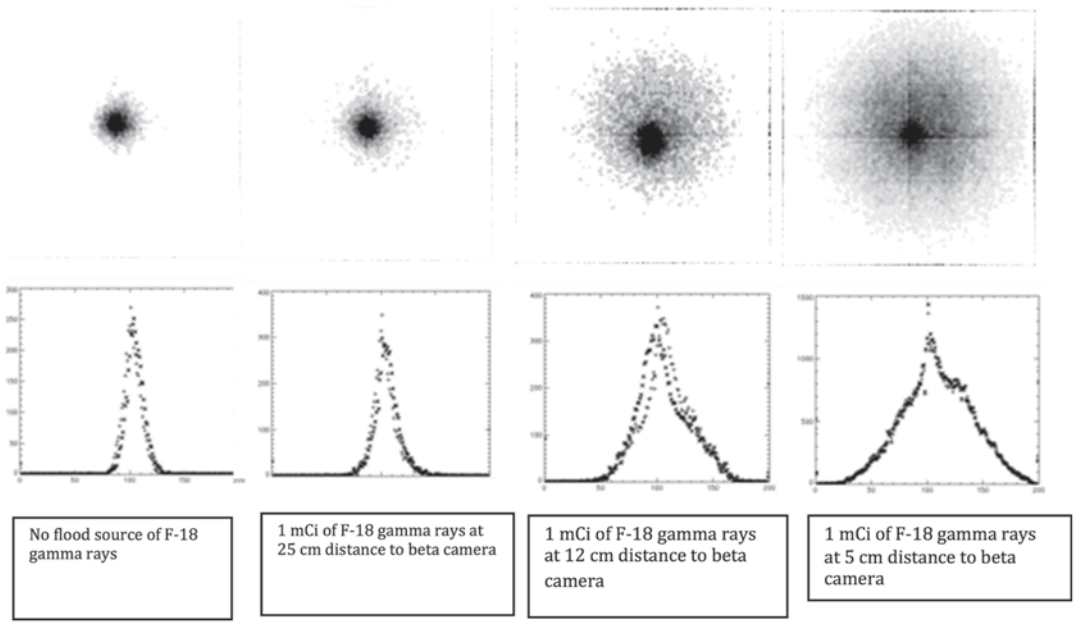

Fig. 4.12 Effect of background gamma rays on the beta camera

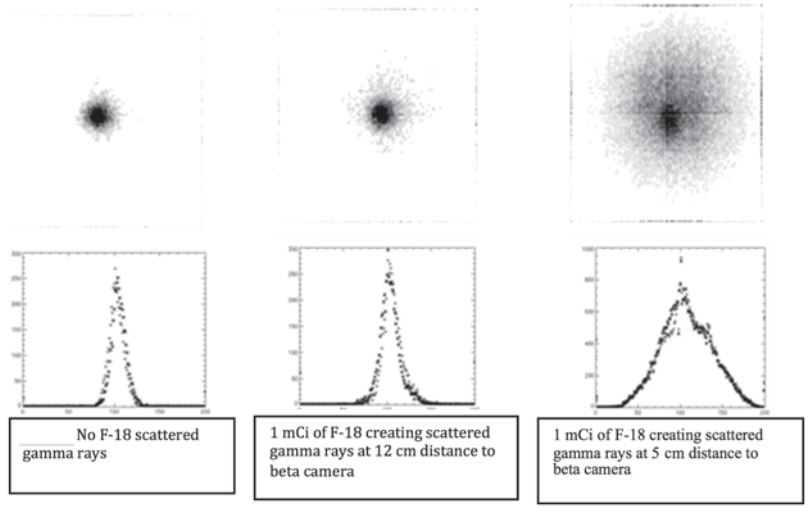

Fig. 4.13 Effect of scattered gamma rays on lesion detection

Intraoperative PET Scanner

The current standard of surgery is to compare preoperative images with intraoperative findings as seen by the naked eye. Conventional PET scanners or CT scans only provide a two-dimensional "roadmap" for the surgeon, who then must navigate the patient in a three-dimensional space in the operating room. Accurate intraoperative tumor localization is critical in a variety of procedures, such as reoperative thyroid or breast lumpectomies, re-operative intra-abdominal surgery, and initial pancreatic surgery for neuro-endocrine tumors. For this purpose, some academic centers have PET/CT in their operating rooms. The theoretical advantages of intraoperative PET

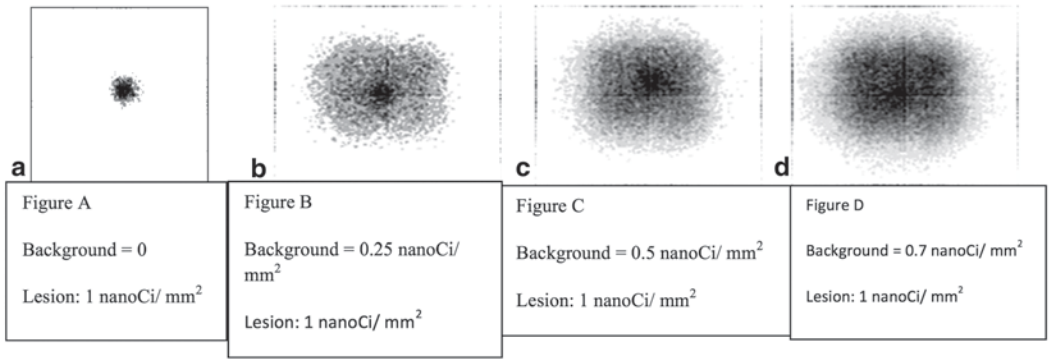

Fig. 4.14 Effect of beta rays in the background surrounding a lesion

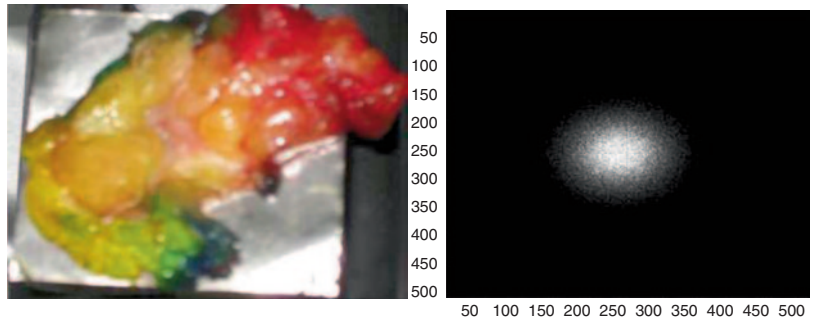

Fig. 4.15 *Left* Lumpectomy sample containing a breast tumor at its center, *right* the image of obtained from this sample with the beta camera showing the central tumor

are many. An intraoperative PET scanner may help localize a metabolically active site, and provide *real-time*, *three-dimensional images* of this metabolically active site, to guide tumor resection or ablation. The use of a standard diagnostic PET/CT in such a capacity however, has turned out to be both expensive and cumbersome. This is the reason that development has started for a portable PET.

The C-Arm and intraoperative ultrasound brought the power of x-ray and ultrasound imaging into the operating room. These diagnostic tools made many surgical procedures possible and simplified others. Since surgery is a hands-oriented technique, it is also important to convey the tumor's location to the surgeon in an *intuitive* manner. Adapting PET for application in the operating room will enable the generation of real-time functional images. Surgical PET-guidance techniques, being developed in the most advanced surgical research centers in conjunction with other image guidance technologies, will be more improved and widely accessible with the development of an intra-operative PET scanner. True real time intra-operative imaging using PET has not been possible due to the geometric and size constraints of typical clinical PET detectors.

Intraoperative PET Scanning

Prescient Imaging LLC is currently developing a portable whole-body PET scanner. This PET scanner has a 360° detector coverage with an axial field of view of 22 cm. The detectors are assembled into three sets, one set is planar, and the other two are circular arcs of 90°. These two arcs are joined together with a hinge allowing the outer arc to open. This PET scanner has wheels and is more compact than a conventional PET

Fig. 4.16 Prototype of intraoperative portable PET scanner. (Courtesy of Prescient Imaging LLC, Hawthorne, CA)

scanner. The unique configuration of detectors is such that the planar detector assembly moves under the patient and forms complete detector coverage around the patient. Attenuation correction will be performed using "rotating rod" method (Fig. 4.16).

In addition to locating lesions more accurately and quickly, the application of real-time PET during surgery will present unique opportunities for applying image-guided *intuitive* surgical navigation tools.

This enables intra-operative localization of hypermetabolic activity seen on a previously performed (usually several days before) pre-operative PET/CT, and verification of its removal within a few minutes in OR. Other intra-operative devices, such as PET probes, beta detectors embedded in needle biopsies, and beta cameras, will work in conjunction with this PET scanner to provide a complete suite of molecular imaging guidance tools.

Such technology would be invaluable for a spectrum of different tumors, such as colorectal, breast, pancreas and gastric cancer as well as for resection or evaluation of sarcomas, where the surgeons eyes cannot always see the microscopic tumor edge, or lymphoma, where finding and sampling the most metabolically active site of disease among many spots is critical to the treatment of the patient, for example, determining if a patient is given chemotherapy alone or a stem-cell transplant (a life-threatening treatment that has a 30% chance of curing the patient and a 30% chance of dying from complications of the transplant).

For such malignancies as gastric cancer and pancreatic cancer, an intraoperative PET scanner may provide better resolution of tumor nodules that are under 1 cm in size. This could allow for improved detection of peritoneal disease, liver metastases, and lymph nodes that may have cancer. This would also allow biopsy of such sites to alter intra-operative resection. For pancreatic cancer, discovery of involved lymph nodes may stop the operation. For gastric cancer, identifying a lymph node with cancer may alter the extent of lymphadenectomy and thus limit the morbidity of an operation. Other possible applications include the ability to detect peritoneal disease in other tumor types, such as ovarian cancer, to aid in de-bulking of the tumor.

References

1. Povoski SP, Sarikaya I, White WC, Marsh SG, Hall NC, Hinkle GH, et al. Comprehensive evaluation of occupational radiation exposure to intraoperative and perioperative personnel from 18F-FDG radioguided surgical procedures. Eur J Nucl Med Mol Imaging. 2008;35(11):2026–34. PubMed PMID: 18618106.
2. Heckathorne E, Dimock C, Dahlbom M. Radiation dose to surgical staff from positron-emitter-based localization and radiosurgery of tumors. Health Phys. 2008;95(2):220–6. PubMed PMID: 18617803.
3. Gulec SA, Dahgighian F, Essner R (2006) PET Probe: Evaluation of technical performance and clinical utility of a handheld high-energy gamma probe in oncologic surgery. Ann Surg Oncol. Pages: 1–8
4. Kim WW, Kim JS, Hur SM, Kim SH, Lee SK, Choi JH, et al. Radioguided surgery using an intraoperative PET probe for tumor localization and verification of complete resection in differentiated thyroid cancer: a pilot study. Surgery. 2011;149(3):416–24. PubMed PMID: 20965536.
5. Daghighian F, Mazziotta JC, Hoffman EJ, Shenderov P, Eshaghian B, Siegel S, et al. Intraoperative beta probe: a device for detecting tissue labeled with positron or electron emitting isotopes during surgery. Med Phys. 1994;21(1):153–7. PubMed PMID: 8164582.

6. Raylman RR. Performance of a dual, solid-state intraoperative probe system with 18F, 99mTc, and (111) In. J Nucl Med. 2001;42(2):352–60. PubMed PMID: 11216536.
7. Strong VE, Humm J, Russo P, Jungbluth A, Wong WD, Daghighian F, et al. A novel method to localize antibody-targeted cancer deposits intraoperatively using handheld PET beta and gamma probes. Surg Endosc. 2008;22(2):386–91. PubMed PMID: 18027053.
8. Essner R, Daghighian F, Giuliano AE. Advances in FDG PET probes in surgical oncology. Cancer J. 2002;8(2):100–8. PubMed PMID: 11999944.
9. Essner R, Hsueh EC, Haigh PI, Glass EC, Huynh Y, Daghighian F. Application of an [18F] Fluorodeoxyglucose-Sensitive Probe for the Intraoperative Detection of Malignancy. J Surg Res. 2001;96(1):120–6.
10. Gulec SA, Hoenie E, Hostetter R, Schwartzentruber D. PET probe-guided surgery: applications and clinical protocol. World J Surg Oncol. 2007;5:65.
11. Molina MA, Goodwin WJ, Moffat FL, Serafini AN, Sfakianakis GN, Avisar E. Intra-operative use of PET probe for localization of FDG avid lesions. Cancer Imaging. 2009;9:59–62.
12. Heckathorne E, Ph.D. Thesis, University of California Los Angeles, 2009.

Isotopes and Procedural Imaging

5

Yachao Zhang, Thomas Reiner and Jason S. Lewis

Introduction

In the twentieth century, intraoperative imaging technologies, or procedural imaging, have evolved from a niche application to be a valuable and powerful tool in visualizing biological and biochemical processes. Radioactive isotopes, which are mostly used for radiological applications, formed the foundation for procedural imaging. In contrast to diagnostic imaging, procedural imaging allows real-time guidance for physicians at the time of surgery, directly influencing the outcome of a surgical intervention [1]. The majority of applications for isotope-guided intraoperative imaging focuses on tumor and lymph node detection. The concept of radioguided surgery (RGS) was pioneered in the 1940s at Harvard Medical School, where Selverstone et al. used radioactive ^{32}P to detect brain tumors [2]. In the 1950s, Harris et al. [3]. reported using ^{131}I and a handheld gamma probe during thyroidectomy to localize residual, overlooked parts of thyroid tissue, marking the birth of RGS The technique rapidly developed to now an established discipline within the practice of surgery and revolutionized the surgical management of many malignancies [1].

RGS has found a plethora of different applications and evolved into a number of subdisciplines. The commonly known types of intraoperative procedures are named based on the application and the molecules, to which the radiotracers are linked: radioimmunoguided surgeries (RIGS), radioguided sentinel lymph node biopsy (RGSLNB), and radioguided occult lesion localization (ROLL). RIGS first found its application in colon cancer [4, 5]. The approach used a monoclonal antibody (mAB), linking to the radiotracer, to identify intra-abdominal spread of the malignant growth [4, 5]. Advances in medicinal chemistry and radiochemical development have achieved multiple methodologies to covalently link these biologically active and highly selective biomolecules to a radiotracer, allowing the potential identification of a variety of tissues of interest. ROLL refers to the identification of tumor from surrounding normal tissue. It conveniently applies to locating tumors in solid organs such as the lungs and soft tissue such as the breast. It can feature different kinds of targeting vectors, ranging from large biomolecules over peptides to small molecules. Neuroendocrine tumors, for example, can be identified by a somatostatin receptor-targeting peptide, which has been covalently linked to a radiotracer [6, 7]. While the application is still being explored in many oncologic surgeries, it has a well-established protocol in localizing breast lesions [8]. During the progression of malignant growth, many types of cancer spread via the lymphatic system. The identification of tumor cells in a sentinel lymph node can have important prognostic values [9, 10]. It may contribute significantly to guiding subsequent surgical management plans [9, 11]. RGSLNB made it possible for sampling the lymph node of interest without an open incision. Additionally, radioguided lymph node

J. S. Lewis (✉) · Y. Zhang · T. Reiner
Department of Radiology, Memorial Sloan Kettering Cancer Center, New York, NY 10065, USA
e-mail: lewisj2@mskcc.org

Y. Fong et al. (eds.), *Imaging and Visualization in The Modern Operating Room,*
DOI 10.1007/978-1-4939-2326-7_5, © Springer Science+Business Media New York 2015

dissection helps surgeons during surgery to accurately identify such draining lymph nodes in real time. The technique cultivated the practice of tumor staging by sentinel lymph node. While molecular biology and immunology continue to make progress, more techniques and applications for isotope-assisted procedural imaging are being developed. Not only are the more traditional surgical interventions benefitting from isotope-guided procedures, interventional radiology, a rapidly growing technique in modern medicine, is also utilizing radioactive isotopes for various procedures, i.e., vascular mapping and visualization of the intra-arterial delivery of radioembolization agents [12–16]. For patients, the advent of radioguided surgical procedures and interventions means more individualized treatment and less adverse effects. As we continue to make discoveries in molecular targeting of malignant growths and other tissue of interests, procedural guidance and imaging are becoming a standard of care in the operating room. Especially so in the field of oncology, the advancement in molecular imaging techniques will provide an integration of disease staging, prognosis, and delivery of therapy in real time [17]. In this chapter, the impacts, milestones, and possible outlooks of image-guided procedures with radioactive isotopes are reviewed.

Radioactive Isotopes

Starting from preclinical investigations, the development of an imaging probe requires a multidisciplinary team. It takes combined efforts from biologists, immunologists, chemists, physicists, and physicians. Generally, biologists and immunologists identify and validate molecular targets, chemists design and optimize targeted radiolabeled entities, physicists coordinate the design of detection systems to interrogate the underlying biology, and clinicians validate novel technologies in human trials. The isotopes used in procedural imaging applications need to have certain desirable characteristics. Factors to be considered for an effective radionuclide-imaging probe include efficiency (sensitivity), energy resolution, spatial selectivity, spatial resolution, and contrast [18]. Also of importance is the half-life of an isotope, which needs to be suited to the pharmacokinetics of the targeting agents, to which the radionuclide is linked. For intraoperative applications, the main detection systems are handheld gamma and beta probes. Gamma probes detect gamma or x-rays, and are the most popularly used detection system during procedural imaging. Radionuclides that emit gamma rays can be detected even in deep tissue, as gamma rays have the ability of traveling long distances in tissue without significant absorption or scattering. While this can be an advantage in some cases, the limited absorption of gamma radiation in organic tissue can result in elevated background signals [1, 18]. Beta probes detect negatron or positron radiation, both of which have relatively short ranges in tissue and therefore cause less background noise. The limited tissue penetration of these particles however makes them best suited for the surface detection of lesions. Figure 5.1 shows three representative kinds of handheld detector probes for RGS [18]. The handheld collimator depicted in panel A is used for the detection of low-to-medium energy x- and γ-rays. The detector in panel B is used for the detection of high-energy annihilation gamma rays of positron emitters, which could be an end product of ^{18}F-FDG decay. This probe is thicker at the tip; it has increased shielding and collimation to reduce the high amount of background signal emitted from underlying or surrounding tissue. The shielding of this collimator is designed to reduce the field of view, and by doing so to improve detector contrast and spatial resolution. However, sensitivity is reduced as a compromise. In contrast, the handheld probe in panel C is designed to detect beta emissions (both positrons and negatrons). This type of radiation is highly absorbed in living tissue, and thus generates less background radiation than low and high x- and γ-radiation. The tip is very thin as minimal collimation and shielding is required. As stated earlier, this type of radiation also results in less tissue penetration and more challenges in detecting malignant growths buried deeper below the tissue surface.

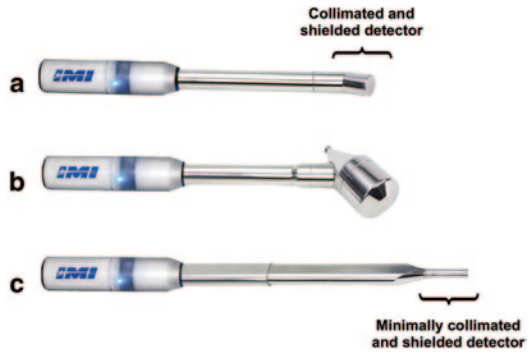

Fig. 5.1 Comparative thickness of the collimation and shielding among different intraoperative gamma and beta probes. **a** The handheld collimator is used for the detection of low-to-medium energy x- and γ-rays. **b** The detector is used for the detection of high-energy annihilation gamma rays of positron emitters. This probe is thicker at the tip compared to (**a**); it has increased shielding and collimation to reduce the high amount of background signal from underlying or surrounding tissue, which is typical for this type of radiation. **c** This detector is designed for beta emissions counting (both positrons and negatrons). This type of radiation generates less background radiation than low and high x- and γ-radiation. The tip is very thin as minimal collimation and shielding is required. (Adapted from [18]. Courtesy of IntraMedical Imaging, Los Angeles, CA, with permission)

The radioactive isotopes that have been utilized most frequently in RGS are the technetium isotope (^{99m}Tc), the fluorine isotope (^{18}F), the iodine isotopes (^{123}I, ^{125}I, ^{131}I) and the indium isotope (^{111}In).

^{99m}Tc has a physical half-life of 6.04 h and a principle gamma photon emission energy of 140 keV with absent beta particle emissions and is widely available at a low cost [1, 19]. ^{99m}Tc can be generated in portable ^{99}Mo/^{99m}Tc generators, which makes the isotope's availability independent from sophisticated infrastructure, cyclotron-sites, and nuclear reactors. These features make ^{99m}Tc ideal for intraoperative RGS. The list of radiopharmaceuticals used with ^{99m}Tc labeling for imaging modalities is extensive. Their main application lies in radioguided sentinel lymph node mapping. The commonly used agents are ^{99m}Tc sulfur colloid, ^{99m}Tc colloidal human serum albumin, and ^{99m}Tc antimony trisulfide colloid [20–22].

Fluorine (^{18}F): the fluorine isotope ^{18}F emits positrons, which annihilate with electrons close to the site of origin, resulting in gamma rays of high energy of 511 keV. This feature allows dual detection with both gamma and beta (positron) detectors. The most established agent for ^{18}F-assisted procedural imaging is ^{18}F-FDG for the detection of tumors that have elevated metabolic activity [23].

Iodine ($^{123/131}$I): The iodine isotope and beta particle emitter ^{125}I has a half-life of 60 days and low emission energy of 35 keV. The properties render it a suitable candidate for conjugation with mABs. It is also used either alone or in combination with ^{99m}Tc for ROLL in breast lesions [24]. Decay of the iodine isotope ^{131}I results in both beta particle emission as well as gamma emission [19]. Its intraoperative use is centered on the detection of residual tumor tissue post thyroidectomy [25, 26]. The isotope ^{123}I has a short half-life of 13.2 h, which makes it unsuitable for conjugation with long-circulating biomolecules like antibodies or nanoparticles [19, 25, 26]. However, it has a low emission energy, which makes it safe to administer in large doses and can be conjugated to small molecules with shorter circulation times. It has been used in RGS when conjugated with MIBG in the past [1].

Indium (^{111}I): The Indium-isotope ^{111}In has a half-life of 2.8 days and was explored with many mABs [26]. It does, however, accumulate in the reticuloendothelial system (i.e., liver, spleen, and bone marrow), which may increase background signal in the abdominal cavity and thus limits its use during surgery [1].

Beta particles are emissions of negatrons or their antiparticles, positrons. Both types of particles have a relatively short range in tissue, and therefore it is ideal for detecting superficial lesions [27]. Typically, the average emission range is at 2.8 mm and it penetrates a maximum of 10 mm [18, 28]. Several positron emission radiotracers, such as ^{18}F, ^{124}I, ^{131}I, and ^{32}P, are known to be used in the development of intraoperative beta probes.^{32}P is a pure high-energy negatron emitter. While it is not commonly used any more, it was in the focus of research during the initial development of intraoperative beta probes and

successfully used in brain tumor detection [29]. Many of the beta emitting radiotracers like ^{18}F and ^{131}I are not exclusively beta emitters, as positrons annihilate with electrons in the body and result in gamma energy. Similarly, radiotracers like ^{124}I have complex decay schemes and can include both gamma and beta emissions [30]. The more recent gamma emission-based detector systems took the high amount of scattering into account, and developed dual detector systems that pick up surrounding gamma emissions in tissue and mathematically subtract the signal from the tissue of interest to improve contrast [27, 31–33]. However, this does increase the read-out time, as measurements will take longer. While beta positive probes have shorter tissue penetration compared to gamma probes, they still produce gamma emission and therefore increased radiation exposure as a "side effect," an aspect that raises concern for both the patient on the table as well as the operating team of healthcare professionals. This concern is thought to be significantly less with beta (negatron) emitters [34]. While the background and radiation exposure to healthy tissue is typically lower, the known limitation of shorter range of penetration may limit their application. For procedures that require deeper penetration such as identification of sentinel lymph nodes, gamma-emitting nuclides are still superior. As detector systems reach higher sophistication, gamma and beta probes might ultimately complement each other to allow improved sensitivity and resolution in detection and wide intraoperative applications. This will potentially open new doors for dual gamma/beta emitters and complex decay scheme emitters that were initially thought to be unfavorable in intraoperative applications [30].

Radioguided Procedures

Figure 5.2 shows the evolution of imaging in RGS. In general, there are two major categories of applications; lymph node mapping and tumor detection using a handheld detector. Sometimes in lymph node mapping, the radiotracer is used in conjunction with the isosulfan "blue dye" to improve surgical outcome [35–39]. In more recent years, as interventional and minimally invasive procedures escalated, radioguided procedures also expanded to aid in mapping of vessels and intravascular delivery of therapy [13, 16]. An example of the early clinical application of RGS is the organometallic Technetium complex ^{99m}Tc-sestamibi. Historically, the ^{99m}Tc-sestamibi scan was the standard diagnostic tool for preoperative imaging of parathyroid lesions. When its value for RGS was discovered, the same tracer dose used during preoperative imaging was then used during surgery to accurately localize parathyroid adenomas [40]. The radioactive agent ^{99m}Tc-sestamibi is of high value for the detection of parathyroid adenomas, because parathyroid glands that are physiologically or abnormally active will become radioactive after the injection of radiotracer, while those that are dormant do not [40]. A normally enlarged parathyroid gland, a hyperplastic parathyroid gland or a true adenoma therefore would have different degrees of radioactive uptake. This difference can be used to distinguish the different types of lesions in real-time during surgery based on the detected in vivo and ex vivo level of radioactivity against the background [40]. More successful examples of RGS are listed in Table 5.1.

Radioguided Lymph Node Mapping and Sentinel Lymph Node Biopsy (RGSLNB) This technique was initially described in the 1950s, when Gold colloid was experimented on for the evaluation of lymph nodes in the breast [41]. The natural physiology of lymphatic vessels is to pick up and transport small particles and drain to the local lymph nodes [42]. RGSLNB relies on this mechanism to transport radiotracers (which have to be injected close to malignant lesions) to the draining lymph nodes. This allows their identification using a handheld gamma probe. After initially being used in breast and cutaneous melanoma, RGSLNB gained wide acceptance and is now being used in gastrointestinal (GI) cancer [43], head and neck cancer [36, 44], thyroid cancer [44], gynecologic malignancies [37, 38, 45], urologic malignancies [46, 47], lung cancer [48], and soft tissue malignancies [49].

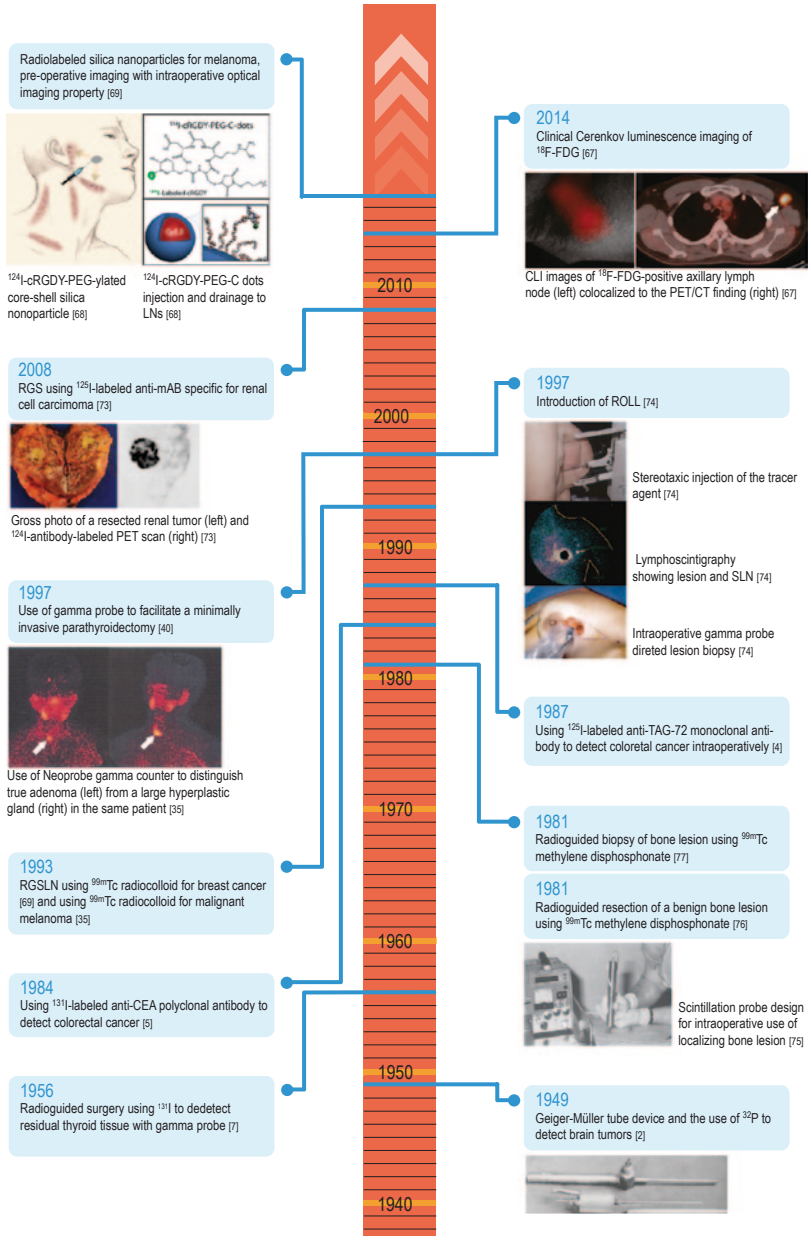

Fig. 5.2 Timeline of radioguided surgical techniques. The diagram displays some of the milestones of radioguided procedures from its birth in the 1940s to the current time

Radioimmunoguided Surgery (RIGS) Radioguided procedures other than lymph node mapping usually involve the targeting of biological properties of tissues of interest to improve specificity of detection. Radiotracers are usually linked to small molecules such as mABs, peptides, or other metabolites to facilitate their accumulation in tissues of interest. In the 1970s, the radiolabeled mAB (B72.3), which targets the carcinoembryonic antigen (CEA) was first described and tested on a colon cancer patient at the Ohio State University Comprehensive Cancer Center [4, 5, 50]. Since their initial introduction, RIGS had been tested in other GI malignancies

Table 5.1 Clinical applications of radioguided procedures

Radioguided surgery (RGS) application	Clinical applications
Radioguided sentinel lymph node biopsy (RGSLNB)	Breast cancer [41]
	Cutaneous malignancies (i.e., melanoma) [42]
	Gastrointestinal (GI) cancer [43]
	Head and neck cancer including thyroid cancer [36, 44]
	Gynecologic malignancies [37, 38, 45]
	Urologic malignancies [46, 47]
	Lung cancer [48]
	Sarcoma [49]
Radioimmunoguided surgery (RIGS)	Breast cancer [50]
	GI: colorectal [4, 50, 51], gastric [52], pancreatic cancer [53]
	Ovarian cancer [54]
	Urologic: prostate cancer [55], renal cell carcinoma [56]
	Lung cancer [57]
Radioguided occult lesion localization (ROLL)	Breast [58, 59]
	Lung nodules [61]
	Splenosis [62]
Radioguided interventional procedures	Hepatic angiographic study prior to radioembolization [12]
	Cardiology [14, 15]
	Monitoring of radioembolization dosimetry [16]

[51, 52, 53], and other types of cancer including breast cancer [51], ovarian cancer [54], prostate cancer [55], renal cell carcinoma [56], and lung cancer [57].

Radioguided Occult Lesion Localization (ROLL) The use of radiotracers in breast surgery is one of the most studied techniques. Traditionally, prior to lumpectomy, lesions were identified in the operating room by locating a metal wire, placed by radiologists immediately before the procedure. With the possibility of injecting a molecularly targeted radiolabeled vector days prior to surgery, surgeons now have more freedom for surgical planning. A randomized prospective evaluation concluded in 2008 that ROLL is at least as effective as the traditional wire-guided lumpectomy for non-palpable breast lesions [58]. A more recent systemic review, published in 2011, demonstrated the superiority of this technique for lowering the number of positive surgical margins, directly resulting in lower numbers of reoperations [59]. Having revolutionized the lumpectomy procedure, ROLL soon found applications in other fields of surgeries. In 2000, ROLL was utilized to support thoracic surgery [60–62]. A review concluded that radioguided surgical localization is superior to the other available approaches such as intraoperative ultrasound, hook-wire, spiral-wire or fluoroscopy in pinpointing subcentimeter nodules during video-assisted thoracoscopic surgeries; it demonstrated higher sensitivity, required less operator dependence, and lowered risk of complications and procedure failures [58]. Additionally, ROLL has also been reported to be an excellent tool for locating foci of during abdominal surgery for its capability in identifying small intra-abdominal lesions [61].

Radioguided Interventional Procedures With the development of minimally invasive procedures, radiotracers find new applications in endoscopic and interventional techniques. Recently, Dickfeld and colleagues studied the use of ^{123}I-MIBG as an imaging probe for the sympathetic nervous system of cardiac tissue to provide insights for guiding ablation procedures in patients with cardiomyopathy and ventricular arrhythmias (VT). Based on their study of monitoring patients with ^{123}I-MIBG imaging pre- and post-pacemaker-implantation, they concluded

that ^{123}I-MIBG can accurately identify the site of VT and thus guide VT ablation procedures. The imaging approach can also have a potential role for predicting sustained VT after pacemaker implantation and determining the right patient populations that may benefit from receiving a pacemaker implant [15]. In vascular interventional procedures, radioisotope guided mapping of vascularity is often performed prior to delivery of radiation microspheres and to provide quality assurance for interventional radiologists, allowing for safer delivery of radiation doses [12].

Cherenkov-Guided Surgery (CGS) The physics behind radionuclide decay itself allows the application of coupled imaging modalities, specifically Cherenkov radiation. This type of light emission was discovered in the1930s. Imaging of this physical phenomenon is based on the decay energy of a positron-emitting radionuclide to result in the generation of photons, detectable in the visible light range. Cherenkov radiation first found its application in optical imaging in a report published by Robertson et al. [63], and has since been recognized as an important new modality in molecular imaging. It offers the advantage of using already approved radiotracers in PET imaging [64]. It has therefore significant potential in intraoperative radionuclide-guided surgical applications. Preclinical studies have demonstrated the utility of Cherenkov luminescence (CL) imaging using radiolabeled FDGs or other targeting molecules such as mABs or peptides for potential intraoperative guidance in sentinel lymph node dissection [65, 66]. The clinical result from patients undergoing diagnostic ^{18}F-FDG scans for nodal disease validated the translational potential of this technique [67]. Liu and colleagues also proposed its feasibility in endoscopic or laparoscopic procedures [66].

Nanoparticle-Guided Surgery While there is tremendous success in radioguided procedures, the implementation of the technique is yet to be standardized in most disciplines. One of the current unmet clinical needs is the clear and high-resolution delineation of tumor margins with radiolabeled tracers. Consequently, researchers are directing attention towards the development of other molecular imaging techniques, including optical imaging, which could be used in combination with RGS to form a hybrid bimodal imaging technology capable of high depth penetration in concert with high-resolution imaging. One clinically ongoing example of combining the two imaging modalities is the use of nanoparticles. Bradbury and colleagues presented a recent design of multimodal silica nanoparticles (^{124}I-cRGDY-PEG-C dots). The modified fluorescent core–shell silica nanoparticles were attached to a small number of peptide ligands, which were labeled with ^{124}I, and coated with short, particle-bound, polyethylene glycol chains (PEGs). The nanoparticles therefore allowed isotope-guided imaging and at the same time fluorescent imaging [68]. A bimodal probe like this could represent an improvement for some of the current isotope-guided procedural imaging techniques, combining the merits of both high-penetration isotope imaging as well as high-resolution optical imaging in one single entity. This particle is currently undergoing a clinical trial, and its potential as a probe for standard of care is being evaluated.

Conclusion

Over the years, the roles of radiologists have transitioned significantly from being the sole interpreters of imaging data. As biomedical imaging technologies evolved to allow real time procedural guidance, radiologists now commonly perform biopsies under imaging guidance. The field of interventional radiology pioneered imaging-guided minimally invasive procedures, and many conditions that used to require surgery can now be treated by interventional radiologists. These procedures are often associated with less invasive interventions and therefore fewer side effects. As research and technology in imaging continue to advance, the field of radiology continues to blend and bridge into other medical specialties, opening the doors for a truly ef-

ficient integration in medicine. Imaging-guided procedures have virtually brought radiology into the operating room. As molecular imaging techniques pioneered, the future of radiology lies in visualizing disease processes in real-time to the cellular level, bridging imaging to pathology. Real time intraoperative pathological analysis will be made possible in the operating room. We envision that molecular imaging techniques will result in highly integrated tools for the health care system, allowing efficient real time preoperative, intraoperative, and postoperative diagnoses, interventions, and follow up. Radiologists and pathologists might work alongside with surgeons in the operating room to perform an integrated high-precision surgery. Ultimately, this integrated medicine system will foster the success in personalized medicine.

References

1. Povoski SP, et al. A comprehensive overview of radioguided surgery using gamma detection probe technology. World J Surg Oncol. 2009;7:11.
2. Selverstone B, Sweet WH, Robinson CV. The clinical use of radioactive phosphorus in the surgery of brain tumors. Ann Surg. 1949;130(4):643–51.
3. Harris CC, Bigelow RR, Francis JE, Kelly GG, Bell PR. A Csi(Ti)-crystal surgical scintillation probe. Nucleonics. 1956;14:102–8.
4. Sickle-Santanello BJ, et al. Radioimmunoguided surgery using the monoclonal antibody B72.3 in colorectal tumors. Dis Colon Rectum. 1987;30(10):761–4.
5. Aitken DR, et al. A gamma-detecting probe for radioimmune detection of CEA-producing tumors. Successful experimental use and clinical case report. Dis Colon Rectum. 1984;27(5):279–82.
6. Adams S, Baum RP. Intraoperative use of gamma-detecting probes to localize neuroendocrine tumors. Q J Nucl Med. 2000;44(1):59–67.
7. Adams S, et al. Radioisotope-guided surgery in patients with pheochromocytoma and recurrent medullary thyroid carcinoma: a comparison of preoperative and intraoperative tumor localization with histopathologic findings. Cancer. 2001;92(2):263–70.
8. Postma EL, et al. Efficacy of radioguided occult lesion localisation (ROLL) versus wire-guided localisation (WGL) in breast conserving surgery for non-palpable breast cancer: a randomised controlled multicentre trial. Breast Cancer Res Treat. 2012;136(2):469–78.
9. Morton DL, et al. Final trial report of sentinel-node biopsy versus nodal observation in melanoma. N Engl J Med. 2014;370(7):599–609.
10. de Boer M, et al. Micrometastases or isolated tumor cells and the outcome of breast cancer. N Engl J Med. 2009;361(7):653–63.
11. Gipponi M, et al. Sentinel lymph node as a new marker for therapeutic planning in breast cancer patients. J Surg Oncol. 2004;85(3):102–11.
12. Dezarn WA. Quality assurance issues for therapeutic application of radioactive microspheres. Int J Radiat Oncol Biol Phys. 2008;71(1 Suppl):S147–51.
13. Ayala S, et al. Radioguided surgery in Meckel's diverticulum. Rev Esp Med Nucl Imagen Mol. 2014;33(4):231–3.
14. Dickfeld T, Kocher C. The role of integrated PET-CT scar maps for guiding ventricular tachycardia ablations. Curr Cardiol Rep. 2008;10(2):149–57.
15. Klein T, et al. The potential role of iodine-123 metaiodobenzylguanidine imaging for identifying sustained ventricular tachycardia in patients with cardiomyopathy. Curr Cardiol Rep. 2013;15(5):359.
16. Lam MG, et al. Prognostic utility of 90Y radioembolization dosimetry based on fusion 99mTc-macroaggregated albumin-99mTc-sulfur colloid SPECT. J Nucl Med. 2013;54(12):2055–61.
17. Gates VL, Salem R, Lewandowski RJ. Positron emission tomography/CT after yttrium-90 radioembolization: current and future applications. J Vasc Interv Radiol. 2013;24(8):1153–5.
18. Heller S, Zanzonico P. Nuclear probes and intraoperative gamma cameras. Semin Nucl Med. 2011;41(3):166–81.
19. Evaluated Nuclear Reaction Database. NEA Data Bank Nuclear Data Services. 2014. http://www.oecd-nea.org/janisweb/search/endf.
20. Breitz HB, et al. Clinical experience with Tc-99m nofetumomab merpentan (verluma) radioimmunoscintigraphy. Clin Nucl Med. 1997;22(9):615–20.
21. Lechner P, et al. Probe-guided surgery for colorectal cancer. Recent Results Cancer Res. 2000;157:273–80.
22. Hladik P, et al. Immunoscintigraphy and intraoperative radioimmunodetection in the treatment of colorectal carcinoma. Colorectal Dis. 2001;3(6):380–6.
23. Yun M. Imaging of gastric cancer metabolism using 18F-FDG PET/CT. J Gastric Cancer. 2014;14(1):1–6.
24. Jakub JW, et al. Current status of radioactive seed for localization of non palpable breast lesions. Am J Surg. 2010;199(4):522–8.
25. Sergides IG, Austin RC, Winslet MC. Radioimmunodetection: technical problems and methods of improvement. Eur J Surg Oncol. 1999;25(5):529–39.
26. Hinkle GH, Laven DL. Radionucleotides. In: Martin EW, editor. Radioimmunoguided surgery (RIGS) in the detection and treatment of colorectal cancer. Austin: Landes Company; 1994. pp. 29–39.
27. Daghighian F, et al. Intraoperative beta probe: a device for detecting tissue labeled with positron or electron emitting isotopes during surgery. Med Phys. 1994;21(1):153–7.

28. Hoffman E, Tornai M, Janecek M, Patt B, Iwanczyk J. Intraoperative probes and imaging probes. In: Aarsvold J, Wernick M, editor. Emission tomography: the fundamentals of PET and SPECT. California: Academic; 2004. p. 336.
29. Reinhardt H, Stula D, Gratzl O. Topographic studies with 32P tumor marker during operations of brain tumors. Eur Surg Res. 1985;17(6):333–40.
30. Braghirolli AM, et al. Production of iodine-124 and its applications in nuclear medicine. Appl Radiat Isot. 2014;90:138–48.
31. Piert M, Carey J, Clinthorne N. Probe-guided localization of cancer deposits using [18F]fluorodeoxyglucose. Q J Nucl Med Mol Imag. 2008;52(1):37–49.
32. Singh B, et al. A hand-held beta imaging probe for FDG. Ann Nucl Med. 2013;27(3):203–8.
33. Gonzalez SJ, et al. An analysis of the utility of handheld PET probes for the intraoperative localization of malignant tissue. J Gastrointest Surg. 2011;15(2):358–66.
34. Camillocci ES, et al. A novel radioguided surgery technique exploiting beta(−) decays. Sci Rep. 2014;4:4401.
35. Norman J. Recent trends becoming standard of care yielding smaller, more successful operations at a lower cost. Otolaryngol Clin North Am. 2004;37(4):683–8, vii.
36. Vigili MG, et al. Lymphoscintigraphy and radioguided sentinel node biopsy in oral cavity squamous cell carcinoma: same day protocol. Eur Arch Otorhinolaryngol. 2007;264(2):163–7.
37. Sideri M, et al. Detection of sentinel nodes by lymphoscintigraphy and gamma probe guided surgery in vulvar neoplasia. Tumori. 2000;86(4):359–63.
38. Barranger E, et al. Laparoscopic sentinel lymph node procedure using a combination of patent blue and radioisotope in women with cervical carcinoma. Cancer. 2003;97(12):3003–9.
39. Morton DL, et al. Validation of the accuracy of intraoperative lymphatic mapping and sentinel lymphadenectomy for early-stage melanoma: a multicenter trial. Multicenter selective lymphadenectomy trial group. Ann Surg. 1999;230(4):453–63. Discussion 463–5.
40. Norman J, Chheda H. Minimally invasive parathyroidectomy facilitated by intraoperative nuclear mapping. Surgery. 1997;122(6):998–1003. Discussion 1003–4.
41. Leborgne FE, et al. Study of the lymphatic systems of the mammary gland with radiogold 198. Bol Soc Cir Urug. 1956;27(1):109–29.
42. Obenaus E, et al. Radiopharmaceuticals for radioguided surgery. In: Mariani G, Giuliano AE, Strauss HW, editors. Radioguided surgery: a comprehensive team approach. New York: Springer; 2008. pp. 3–11.
43. Kitagawa Y, et al. Laparoscopic detection of sentinel lymph nodes in gastrointestinal cancer: a novel and minimally invasive approach. Ann Surg Oncol. 2001;8(9 Suppl):86S–9S.
44. Guelfucci B, et al. Papillary thyroid and squamous cell carcinoma in the same radioguided sentinel lymph node. Clin Nucl Med. 2004;29(4):268–9.
45. Raspagliesi F, et al. Hysteroscopic injection of tracers in sentinel node detection of endometrial cancer: a feasibility study. Am J Obstet Gynecol. 2004;191(2):435–9.
46. Hadway P, et al. Evaluation of dynamic lymphoscintigraphy and sentinel lymph-node biopsy for detecting occult metastases in patients with penile squamous cell carcinoma. BJU Int. 2007;100(3):561–5.
47. Beri A, Janetschek G. Technology insight: radioguided sentinel lymph node dissection in the staging of prostate cancer. Nat Clin Pract Urol. 2006;3(11):602–10.
48. Nwogu C, et al. Radioguided detection of lymph node metastasis in non-small cell lung cancer. Ann Thorac Surg. 2006;82(5):1815–20. Discussion 1820.
49. Bitencourt AG, et al. New applications of radioguided surgery in oncology. Clinics (Sao Paulo). 2009;64(5):397–402.
50. Martin EW Jr, et al. Radioimmunoguided surgery: intraoperative use of monoclonal antibody 17-1A in colorectal cancer. Hybridoma. 1986;5(Suppl 1):S97–108.
51. Bertoglio S, et al. Role of tumor-associated antigen expression in radioimmunoguided surgery for colorectal and breast cancer. Semin Surg Oncol. 1998;15(4):249–53.
52. Lucisano E, Bertoglio S. Role of radioimmunoguided surgery using iodine-125-labeled B72.3 monoclonal antibody in gastric cancer surgery. Semin Surg Oncol. 1998;15(4):212–4.
53. LaValle GJ, et al. Assessment of disseminated pancreatic cancer: a comparison of traditional exploratory laparotomy and radioimmunoguided surgery. Surgery. 1997;122(5):867–71. Discussion 871–3.
54. Bell J, et al. Intraoperative radioimmunodetection of ovarian cancer using monoclonal antibody B72.3 and a portable gamma-detecting probe. Obstet Gynecol. 1990;76(4):607–11.
55. Anderson RS, et al. Radioimmunoguided surgery using indium-111 capromab pendetide (PROSTASCINT) to diagnose supraclavicular metastasis from prostate cancer. Urology. 2000;56(4):669.
56. Avital S, et al. Localization of monoclonal antibody CC49 in colonic metastasis from renal cell carcinoma. Eur J Surg Oncol. 1998;24(2):149–51.
57. Grazia M, et al. Radioimmunoguided surgery and intraoperative lung cancer staging. Semin Surg Oncol. 1998;15(4):215–9.
58. Medina-Franco H, et al. Radioguided occult lesion localization (ROLL) versus wire-guided lumpectomy for non-palpable breast lesions: a randomized prospective evaluation. J Surg Oncol. 2008;97(2):108–11.
59. Lovrics PJ, et al. Systematic review of radioguided surgery for non-palpable breast cancer. Eur J Surg Oncol. 2011;37(5):388–97.

60. Chella A, et al. A pilot study of the role of TC-99 radionuclide in localization of pulmonary nodular lesions for thoracoscopic resection. Eur J Cardiothorac Surg. 2000;18(1):17–21.
61. Zaman M, et al. In patients undergoing video-assisted thoracoscopic surgery excision, what is the best way to locate a subcentimetre solitary pulmonary nodule in order to achieve successful excision? Interact Cardiovasc Thorac Surg. 2012;15(2):266–72.
62. Mari Hualde A, et al. Utility of radioguided surgery in splenosis. Rev Esp Med Nucl Imagen Mol. 2014;33(3):180–2.
63. Robertson R, et al. Optical imaging of Cerenkov light generation from positron-emitting radiotracers. Phys Med Biol. 2009;54(16):N355–65.
64. Thorek D, et al. Cerenkov imaging—a new modality for molecular imaging. Am J Nucl Med Mol Imaging. 2012;2(2):163–73.
65. Holland JP, et al. Intraoperative imaging of positron emission tomographic radiotracers using Cerenkov luminescence emissions. Mol Imaging. 2011;10(3):177–86, 1–3.
66. Liu H, et al. Intraoperative imaging of tumors using Cerenkov luminescence endoscopy: a feasibility experimental study. J Nucl Med. 2012;53(10):1579–84.
67. Thorek DL, Riedl CC, Grimm J. Clinical Cerenkov luminescence imaging of (18)F-FDG. J Nucl Med. 2014;55(1):95–8.
68. Bradbury MS, et al. Clinically-translated silica nanoparticles as dual-modality cancer-targeted probes for image-guided surgery and interventions. Integr Biol (Camb). 2013;5(1):74–86.
69. Krag DN, et al. Surgical resection and radiolocalization of the sentinel lymph node in breast cancer using a gamma probe. Surg Oncol. 1993;2(6):335–9. Discussion 340.
70. Harcke HT. Bone scintigraphy in children: benign tumors. Ann Radiol (Paris). 1983;26(8):670–4.
71. Ghelman B, Thompson FM, Arnold WD. Intraoperative radioactive localization of an osteoid-osteoma. Case report. J Bone Joint Surg Am. 1981;63(5):826–7.
72. Harvey WC, Lancaster JL. Technical and clinical characteristics of a surgical biopsy probe. J Nucl Med. 1981;22(2):184–6.
73. Alex JC, et al. Gamma-probe-guided lymph node localization in malignant melanoma. Surg Oncol. 1993;2(5):303–8.
74. Barros A, et al. Radioguided localisation of non-palpable breast lesions and simultaneous sentinel lymph node mapping. Eur J Nucl Med Mol Imaging. 2002;29(12):1561–5.
75. Strong VE, et al. A novel method to localize antibody-targeted cancer deposits intraoperatively using handheld PET beta and gamma probes. Surg Endosc. 2008;22(2):386–91.

Radiologically Imageable Nanoparticles

6

Aileen L. Co, A. M. Sitarski, Jeremy L. Grant and Michael D. Mason

Introduction

The past decade has witnessed explosive growth in the number and scope of potential applications of nanomaterials. In large part, the excitement around these systems arises from the apparent tunability and adaptability of the relevant physical and chemical properties. Unlike most conventional chemical entities, nanomaterials can often be made more complex, incorporating additional properties without loss of the original features. For example, wavelength-specific light scattering nanoparticles can be made less toxic by modifying their surface without significantly affecting their optical properties. This ability to tailor nanomaterials for improved contrast and reduced patient risk and discomfort has great potential, yet few candidate nanomaterials have made their way into the clinical setting. This will surely change over the next decade as an evolving health care system demands better and more cost-effective technologies. Here we focus on describing existing and emergent nanotechnologies engineered specifically to produce improvements in diagnostic contrast imaging, while at the same time addressing deficiencies found in existing chemical contrast agents.

M. D. Mason (✉)
Department of Chemical and Biological Engineering, University of Maine, 209 Jenness Hall, Orono, ME 04469, USA
e-mail: mmason@umche.maine.edu

A. L. Co · A. M. Sitarski
Department of Chemical and Biological Engineering, University of Maine, 5737 Jenness Hall Rm 208, Orono, ME 04469, USA
e-mail: aileenco@umche.maine.edu

A. M. Sitarski
e-mail: anna.sitarski@maine.edu

J. L. Grant
Department of Chemical and Biological Engineering, University of Maine, 5737 Jenness Hall Rm. 208C, Orono, ME 04469, USA
e-mail: jeremy.grant@umit.maine.edu

X-ray/CT Scan

X-rays are employed in two of the most widely used noninvasive medical imaging and diagnostic tools. The first and the one developed the earliest, projection radiography (standard X-ray image), provides a 2D image of a bodily region of interest which is obtained by transmitting X-ray photons through the body to an undeveloped film (film-screen radiography) or a sensor array (digital radiography). In this method, the image contrast is controlled by variation of the photon energy and the duration of the exposure. To date, projection radiography remains the primary imaging and diagnostic tool for a host of medical conditions due to rapid image acquisition, widespread availability, and extremely low cost relative to other radiological imaging techniques [1]. More recently, with the development of advanced computing techniques, an imaging method called computed tomography or com-

Y. Fong et al. (eds.), *Imaging and Visualization in The Modern Operating Room,*
DOI 10.1007/978-1-4939-2326-7_6,

puterized axial tomography (CT or CAT) was developed to expand the existing capabilities of projection radiography. In this technique, a series of planar X-ray transmission images (slices) is obtained from multiple angles around a central axis of rotation and passed to a computer, which employs geometry-processing algorithms to reconstruct a virtual 3D representation of a bodily region of interest [2].

Transmission images produced by X-rays are dependent on the degree to which the X-rays lose intensity, or attenuate, as they pass through a medium. Generally, signal attenuation depends largely on scattering and photoelectric absorption properties of a given material, which can be directly correlated to the atomic numbers and relative abundance of elements present [3].

The attenuation phenomenon is described by the Beer–Lambert law, which states that the transmitted intensity, I, is determined by $I = I_0 e^{-\alpha x}$, where I_0 is the initial beam intensity, α is the linear attenuation coefficient of the material, and x is the beam path length. For clinical CT scans, the radiodensity is typically described using the Hounsfield scale:

$$\mathrm{HU} = 1000 * \frac{\mu_m 0 \mu_{water}}{\mu_{water}}$$

where μ_m is the linear attenuation coefficient of the medium and μ_{water} is the linear attenuation coefficient of distilled water at standard temperature and pressure. The benefit of this linear transformation (also called the CT number) for biological systems is that it defines water and air as 0 and −1000 Hounsfield units (HU), respectively. Soft tissues generally range from −500 HU for the lungs to 60 HU for liver, and bone ranges from 700 to 3000 HU, depending on density (Table 6.1). This means that bone is easily distinguished from soft tissue; however, it is difficult to distinguish most soft tissue types from each other since they fall into a close range of values [4]. This problem can be rectified to some degree by varying the beam intensity or exposure times, but these solutions increase the potentially harmful effects of ionizing radiation. As a result, circulating chemical contrast agents are introduced to provide the required image enhancement necessary for tissue differentiation by increasing the signal-to-noise ratio. Design of contrast agents involves selection of materials with high atomic numbers, low toxicity, and high circulation time. A comparison of mass attenuation coefficients for a range of elements is shown in Fig. 6.1.

Table 6.1 Common biological CT numbers [5]

Tissue	CT number (HU)
Bone	+1000
Liver	40–60
White matter	−20 to −30
Gray matter	−37 to −45
Blood	40
Muscle	10–40
Kidney	30
CSF	15
Water	0
Fat	−50 to −100
Air	−1000

CSF cerebrospinal fluid

Currently barium sulfate and iodine-based molecules are the two most widely used contrast agents for X-ray image enhancement. Barium sulfate has been used extensively in gastrointestinal (GI) imaging, having many desirable qualities as a GI contrast agent such as remaining almost completely inert within the GI tract, smooth coating of mucosal surfaces, and resistance to dilution [7]. For all other applications, commercially available iodine-based

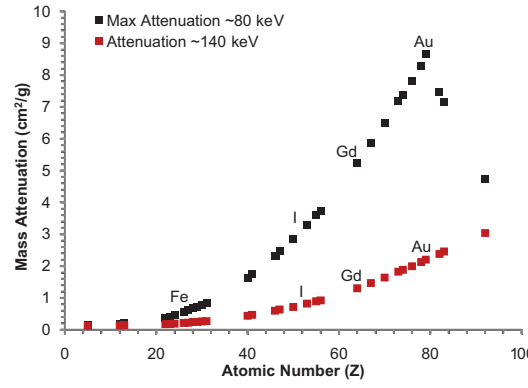

Fig. 6.1 Comparison of mass attenuation coefficients versus atomic number for a range of relevant elements [6]

preparations are the industry standard for clinical CT contrast agents. Over several decades of use, these contrast agents have undergone successive improvements to address the pitfalls associated with iodinated small molecules. Still there exists a demonstrated need for further development of CT contrast agents. For example, although advances have been made in both ionic and nonionic forms of iodinated small molecules prepared for clinical use which reduce the overall toxicity of these agents, problems of nonspecific biodistribution, rapid renal clearance, and nephropathy still exist [8].

To address the shortcomings of standard iodine-based preparations, a number of nanoparticle constructs are currently being investigated for use as CT contrast agents with targeted distribution, longer circulation times, and reduced toxicity while maintaining or even surpassing the level of image enhancement achieved by iodine-based contrast agents. One such approach involves incorporating the contrast-generating material into micellular, polymeric, or liposomal shells. Although these so-called "soft" nanoparticles require careful design for stability and durability to resist premature rupture in biological media, they can be engineered for high contrast, passive or active targeting, and extremely long circulation times [9]. For example, polymeric poly(iohexol) nanoparticles with high iodine payload cores have been shown to have a 36-fold increase in CT contrast 4 h postinjection and greatly increased circulation time (15.9 h vs 3.8 h) when compared to standard iodine-based iohexol [10].

In addition to continued research on improved iodinated contrast media, solid-core metal nanoparticles are being investigated as potential alternatives for their unique biological, physical, and chemical properties. Given that elements with high atomic numbers generally exhibit greater X-ray attenuation, and therefore better CT contrast (approximately proportional to Z^3), nanomaterials containing metals such as ytterbium, tantalum, tungsten, gold, and bismuth ($Z = 70$, 73, 74, 79, and 83, respectively) are implicated as replacements for iodine ($Z = 53$) as a standard contrast agent. Additionally, surfaces of these nanomaterials may offer strong binding affinity for thiol, disulfide, and amine groups, allowing for surface conjugation with biomolecules such as proteins and antibodies for bioconjugation and biomodification [11].

Perhaps the most widely researched metal nanoparticle for CT imaging, despite the relatively high cost, are gold nanoparticles that can be synthesized in a variety of shapes and sizes. This material system offers excellent intrinsic biocompatibility and surface modification options, and has been investigated for active in vivo targeting of cancer-specific biomarkers and passive targeting of tumor tissue by the enhanced permeation and retention (EPR) effect [12–14]. On the other end of the expense spectrum, ytterbium and bismuth-based nanoparticles are being investigated as low-cost contrast solutions that show great promise for CT applications, however further toxicity studies are required to fully assess the safety profiles of these nanoparticles [15–17]. Similarly, although tantalum oxide nanoparticles have been traditionally used as X-ray contrast material for tracheobronchial and GI imaging, sufficient studies of the biological effects of these nanoparticles have yet to be performed [18]. Tungsten oxide nanorods have recently been investigated as a CT contrast agent in conjunction with near-infrared photothermal therapy [19]. Given the recent advances and promising early results of nanoparticles as X-ray contrast agents, it seems likely that nanoparticles of some form will find future use in clinical CT imaging.

As with virtually all nanoparticles designed for biological application, a surface coating is required to eliminate problems associated with agglomeration and to increase biocompatibility. More complex coatings can also be employed to impart multifunctionality such as theranostic (meaning *therapeutic* and *diagnostic*) or multimodal imaging applications [4]. Examples of nanoparticles that have been investigated for X-ray imaging (and CT scan) are presented in Table 6.2 where the core material and surface coatings are listed.

Table 6.2 Potential nanoparticles-based contrast agents for X-ray/CT scan imaging

Nanoparticle	Composition/type	Attributes/constraints	Ref.
Gold	Multiple coatings/PEG, DEN, HDL	Low toxicity, high biocompatibility, easily size-tuned and surface modified/expensive	[12–14]
Ytterbium	Yb_2O_3:Er, PEG-silane-$BaYbF_5$, $NaYbF_4$	Contrast efficiency higher than all currently researched nanoparticles, promising for multicolor spectral imaging/toxicity research required	[15]
Tantalum	Ta_2O_5/metal oxide	High biocompatibility, chemically inert/research is required for health effects	[18]
Tungsten	PEG-$WO_{2.9}$/metal oxide nanorods	Good water dispersibility and colloidal stability/toxicity research required	[19]
Bismuth	Bi_2S_3/PEG-thiol or PVP coated	Low cost, long circulation time/research required to determine roles of agglomeration and degradation on toxicity	[16, 17]
Iodine	mPEG-PLA-poly(iohexol)/polymeric "soft" nanoparticle	Negligible toxicity if shell remains intact, much higher iodine payload, good stability, higher biological retention/challenging production	[10]

PEG polyethylene glycol, *DEN* dendrimeric polymer, *HDL* high-density lipoprotein, *PVP* polyvinylpyrrolidone, *PLA* polylactic acid

MRI

Unlike X-rays and CT scans where ionizing radiation is used, magnetic resonance imaging (MRI) uses nuclear magnetic resonance (NMR) to noninvasively image in vivo physiological structures. This powerful instrument is frequently used to image the brain and central nervous system, cardiac function, and detect tumors [20].

Images acquired by MRI are a result of the temporal response of the nuclear spin orientation of protons in the body in response to applied magnetic fields. When the protons in the body are exposed to an external magnetic field (B_0) from the MRI, the proton nuclei spins align with respect to the direction of B_0. A second RF magnetic field can be used to rapidly reorient these spins relative to B_0. When the RF is removed, there is a gradual realignment of nuclear spins in the direction of B_0. Based on this principle, there are two relaxation processes that can be measured, T_1 and T_2, in the *longitudinal* and *transverse* direction, respectively [20]. T_1 or *spin–lattice relaxation* relies on the time it takes a proton to return to its equilibrium state, showing a signal increase over repetition time. T_2 imaging or *spin–spin relaxation* is dependent on the time that is required for two protons to spin out of phase with respect to each other, where signal intensities decrease over time [21]. (Fig. 6.2)

Despite MRI does have its advantages over X-ray and CT scan, its inherent low sensitivity hinders the quality of the subtle changes in the tissues. To overcome this issue, a contrast agent is used prior to imaging to enhance the visualization of the tissues in the living organism [22]. Contrast agents used for T_1 and T_2 imaging have special attributes to which they are able to enhance the differentiation of the tissues.

T_1 or *positive contrast agents* result in increased signal intensities in their immediate vicinity. Prototypical T_1 contrast agents are paramagnetic and have accessible unpaired electrons. Gadolinium (Gd^{3+}), for example, has seven unpaired electrons that dramatically reduce its T_1 and is therefore widely used as a contrast agent for MRI [20]. However, the Gd-based contrast agents must be used at high doses to improve signal and, consequently, the potential of toxic side effects such as nephrogenic systemic fibrosis (NSF) is increased. Given these limitations, patients with kidney disorders are unable to tolerate these contrast agents, and thus alternatives are currently being investigated [22, 23]. Chelates such as gadolinium (III) diethlyene triaminepentaacetate (Gd-DTPA, Magnevist®) are popular contrast agents used in clinical practice showing some reduction in toxicity.

Nanoparticles of gadolinium and manganese (Mn) are also being researched for use as potential

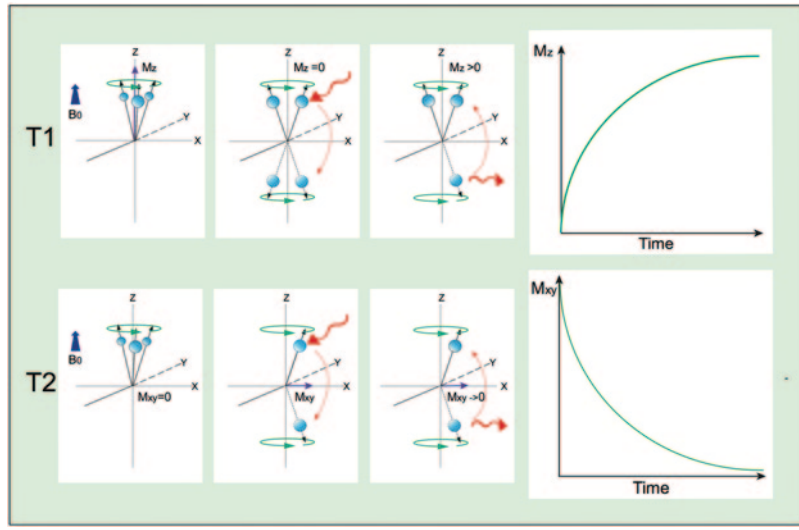

Fig. 6.2 A cartoon depiction of the net magnetization of the protons in response to applied magnetic fields over time

T_1 contrast agents. Inorganic nanoparticles containing gadolinium in comparison to chelates have several advantages such as ease of synthesis, functionalization, and larger relaxivites. Mn-based nanoparticles have also shown potential as a contrast agent with five unpaired electrons and long relaxation times, however, more work needs to be done due to the difficulties in their synthesis and design for clinical applications [24].

T_2 or *negative contrast agents* reduce signal intensities by decreasing the relaxation time (T_2) of protons in water in their vicinity. Superparamagnetic nanoparticles are commonly investigated for use as T_2 contrast agents due to their relatively large transverse relaxivities (r_2). Among the most common are superparamagnetic iron oxide (SPIO) nanoparticles, which, in addition to large relaxivities, exhibit exceptional size tunability, production control, and inherently low toxicity [4]. Iron oxide-based contrast agents that have been researched and used clinically are shown in Table 6.3.

Generally, iron oxide nanoparticles, due to their strong magnetic properties, tend to agglomerate in most systems. To eliminate this potential problem, surface coatings composed of various materials such as dextran, TaO_x, silica, polymers (i.e., PEG), or fatty acids such as dimercaptosuccinic acid (DMSA) are used [21, 29]. These coatings primarily make use of steric or electro-

Table 6.3 Iron oxide nanoparticles used as MRI contrast agents

Contrast agent	Chemical composition	Description	Ref.
GastroMARK® AMI-121	SPIO core + silicone shell	Bowel imaging. Oral administration [a]AMAG/Mallinckrodt Inc.	[25]
Feridex IV® AMI-25	SPIO core + dextran shell	Liver lesion imaging through Intravenous injection. Predominantly used as a T_2 contrast agent DISCONTINUED in the market in November 2008 [a]AMAG/Berlex Laboratories	[26]
Resovist® SHU-555A	SPIO core + carboxydextran shell	Liver lesion imaging, mainly T2. Bolus fashion injection. Approved for European Market DISCONTINUED for clinical use in 2009, replaced by Gd based Primovist aHealthcare/schering AG	[27, 28]

SPIO superparamagnetic iron oxide
[a] Supplier/distributor of the contrast agent

Table 6.4 Potential nanoparticles-based contrast agents for MRI

Nanoparticle	Composition/Types	Attributes/constraints	Ref.
Feraheme®	Ferumoxytol	FDA approved for iron replacement therapy, under investigation for detection of CNS inflammation, brain neoplasm and cerebral metises from lung or brain cancer/In Phase 1 clinical trial	[30, 31]
Iron oxide $Fe_3O_4/\gamma\text{-}Fe_2O_3$	SPIOs core + DMSA shell	Dispersible in water for in vivo testing/found to show the best contrast (tumor: muscle) 12 h after injection in a mouse model	[20, 32]
	SPIOs core + SiO_2-PEG shell	Stable, easy to synthesize, easily immobilizes other nanoparticles to impart multifunctional capabilities. Fast labeling and clearance by I.V. in comparison to intraperitoneal injection. Under research for surface modification	[33]

CNS central nervous system, *SPIO* superparamagnetic iron oxide, *PEG* polyethylene glycol

static stabilization with the goal of minimally perturbing the interaction of water with the nanoparticle surface, yielding the largest possible effect on T_2. (Table 6.4)

PET

Positron emission tomography (PET) is a well-established clinical imaging modality that uses tracers radiolabeled with positron-emitting radioisotopes for noninvasive in vivo imaging of tissue-level biochemical changes in disease and in response to treatment [34]. Images are formed by tagging biological carrier molecules in the body with an isotope that has the ability to produce two γ-rays by emitting a positron from its nucleus. When the positron collides with a nearby electron both are annihilated and two 511 keV γ-rays are emitted at ~180° with respect to each other [34]. By correlating the detection time of the two γ-rays, the point of origin can be determined [35, 36]. In this way, 3D images are constructed from regions of radioisotope accumulation throughout the body. Commonly used radioisotopes are ^{11}C, ^{13}N, ^{15}O, and ^{18}F, but ^{14}O, ^{64}Cu, ^{62}Cu, ^{124}I, ^{76}Br, ^{82}Rb, and ^{68}Ga are also used depending on the application [35]. Some of the existing PET radioisotopes have short lives so production and use can be expensive [36].

Nanoparticles have recently gained interest for use in PET imaging primarily due to their potential for surface modification, functionalization, and bioconjugation using molecules containing radioisotopes [37]. To date, radiolabeled nanoparticles for PET have been used in both preclinical and clinical studies [38]. One such contrast agent, Cornell Dots, are porous silica nanoparticles embedded with radioactive iodine. This system was approved by the Food and Drug Administration (FDA) for clinical trials in 2011 [39].

Multimodal Imaging

Using nanoparticles rather than conventional imaging agents is becoming more widespread due to the potential for early detection and staging of disease as well as therapeutics in a single application [38]. Multimodal imaging techniques seek to combine different imaging modalities (X-ray, PET, and MRI) into one diagnostic tool [39]. Combinations of these techniques can offer more accurate and reliable detection of disease and disease progression at multiple spatial scales, while tracking effectiveness of treatments on the metabolic and cellular levels [40]. In addition, to spatially correlating information of different types, multimodal imaging may lessen the negative immune response frequently observed following the repeated administration of an imaging probe to a patient [39]. Specific to these combined techniques, more complex nanoparticle constructs are mandated. There is, however, some discussion ongoing on the sensitivity of these nanoparticles since some imaging modalities require higher concentrations of nanoparticles than oth-

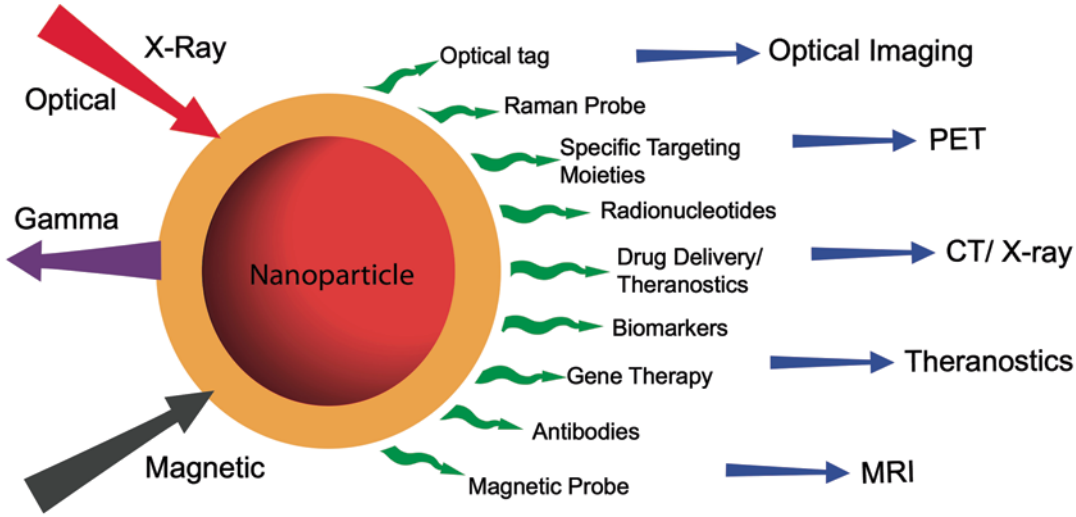

Fig. 6.3 Multimodal nanoparticle applications

ers for an adequately resolved image [38]. Researchers working on this problem are attempting to determine the ideal concentration threshold for multimodal imaging agents. (Fig. 6.3)

Specific examples of new contrasting agents are being designed for use in imaging schemes such as PET/fluorescence, single-photon emission computed tomography (SPECT)/fluorescence, PET/MRI, SPECT/MRI, PET/MRI/optical imaging, and SPECT/MRI/optical [41]. MRI and PET dual modal nanoparticles are a major area of study. MRI has good spatial resolution and excellent contrast between different soft tissues in the body. This gives good anatomical information but inadequate resolution to detect physiological changes such as those in molecular and cellular activity or to delineate small lesions. PET, on the other hand, provides quantitative physiological information with high sensitivity. However, the anatomical localization of the signal is not conferred in PET, necessitating the correlation of the radioactivity distribution with an anatomical image derived from MRI or CT [41]. As a modality, PET is of high interest because of its high sensitivity and limitless tissue penetration [42]. A dual mode nanoparticle for MRI/PET may have higher combined sensitivity and accuracy. A promising dual-mode nanoparticle under investigation is ^{89}Zr-ferumoxytol for improvement of preoperative planning for nodal resection and tumor staging [43]. The most common dual modal nanoparticles used for MRI/PET are SPIOs that are labeled with chelates of ^{64}Cu [39].

Gold nanoparticles combined with SPIOs are increasingly being investigated for combined CT and MRI techniques [4]. Suspensions containing gold, or constructs based on gold nanoparticles, are used in many emergent multimodal schemes. For example, CT and optical imaging are possible using unmodified gold nanoparticles, whereas near infrared fluorescence (NIRF) and PET imaging use gold nanoparticles modified with fluorophore or a fluorinated or iodinated molecule, respectively, to visualize tumors [4].

Recently, trimodal imaging nanoparticles for PET/optical/MRI were generated that combined radiometal chelates such as ^{64}Cu-DOTA (1,4,7,10-Tetraazacyclododecane-1,4,7,10-tetraacetic acid) to dual MRI/optical probes [38]. Another trimodal gold nanoparticle of interest is for imaging of brain tumors. This system is modified for simultaneous use in MRI, photoacoustic, and Raman imaging. Researchers apply this system to a mouse model and subsequently were

Table 6.5 Potential nanoparticles-based contrast agents for PET/multimodal imaging

Nanoparticle	Composition/type	Attributes/constraints	Ref.
Cornell Dots *PET/fluorescence*	Silica embedded with fluorophores or radioactive iodine	Deemed safe/still need radioactive iodine	[47]
^{89}Zr-ferumoxytol *PET/MRI*	^{89}Zr radiolabeled SPIOs	Safe, enhancement of soft tissue/ longer scan times	[43]
^{64}Cu-DOTA/matrix metalloproteinase *PET/optical/MRI*	Radiometal chelate	Image enhancements/still need radionuclide, only preclinical use	[38]
^{111}In-DOTA/Rituximab (anti-CD20) *SPECT/optical/MRI*	Carbon nanotubes	Image enhancements/still need radionuclide, only preclinical use	[48]
SPIOs/Au *CT/MRI*	Au nanoparticle + SPIOs	Image enhancement/stability, only preclinical use	[39]
SPIOS/TaO_x *CT/MRI*	SPIOs core + tantalum (V) oxide shell	Biocompatible, prolonged circulation time, only preclinical use	[21, 29]

able to guide tumor resection using photoacoustic and Raman imaging. In a separate application, this system made it possible to perform photoacoustic imaging to delineate malignant tissue in situ and obtain high-resolution intraoperative Raman images during the resection [40]. Trimodality of this type has also been achieved using iron oxide nanoparticles that are functionalized for use in PET/NIRF/MRI [4].

In addition to diagnostic imaging, some multimodal nanoparticles are engineered for therapeutic uses. These so-called "theranostics" are intended to provide, in a single application, enhanced imaging and improved therapeutic effectiveness (i.e., drug delivery) [44], as an avenue towards more personalized medical treatment [45]. These nanoparticle systems also allow physicians to make real-time decisions to improve surgical success and postsurgical assessment to ensure clearance of the disease or tumor [46]. Early detection and staging of cancer and cardiovascular disease are of special interest since patient prognosis and treatment side effects may be reduced if diagnosed accurately and early [45]. Despite the recent surge in multimodal nanoparticle imaging research, these imaging agents are not yet widely approved for clinical use [39]. (Table 6.5)

Conclusion

Nanotechnologies are now being implemented at the preclinical level in a host of medical imaging and disease staging applications. Many of these new material systems have great promise, demonstrating improved imaging fidelity, decreased patient discomfort, and the potential for cross-platform applications. Here we have presented a subset of those nanomaterials that have shown specific utility at the preclinical or clinical level, and have illustrated their structural and functional differences. While this important class of materials has steadily evolved, even the most recent advancements are not without some limitations. For example, future nanomaterials will need to exhibit better disease specificity, improved long-term stability, and dramatically reduced toxicity. Ultimately, these challenges relate to interactions between the nanoparticle surface and the host surrounds. As such, we should expect to see increasingly complex nanomaterials in the future.

References

1. Chen LC, Huang JL, Wang CR, Yeh KW, Lin SJ. Use of standard radiography to diagnose paranasal sinus disease of asthmatic children in Taiwan: Comparison with computed tomography. Asian Pac J Allergy Immunol. 1999;17(2):69–76.
2. Hounsfield GN. Computerized transverse axial scanning (tomography).1. description of system. Br J

Radiol. 1973;46(552):1016–22.
3. Jackson DF, Hawkes DJ. X-ray attenuation coefficients of elements and mixtures. Phys Rep-Rev Sec Phys Lett. 1981;70(3):169–233.
4. Chantler CT, Olsen K, Dragoset RA, Chang J, Kishore AR, Kotochigova SA, Zucker DS. X-ray form factor, attenuation, and scattering table. Gaithersburg: National Institute of Standards and Technology; 2005.
5. Nicholas Joseph Jr RT. Quality assurance and the helical (Spiral) scanner. CE Esssentials; 2004–2010. http://www.ceessentials.net/article33.html. Accessed 7 April 2014.
6. Ott DJ, Gelfand DW. Gastrointestinal contrast agents—indications, uses, and risks. JAMA. 1983;249(17):2380–4.
7. Lusic H, Grinstaff MW. X-ray-computed tomography contrast agents. Chem Rev. 2013;113(3):1641–66.
8. Cormode DP, Naha PC, Fayad ZA. Nanoparticle contrast agents for computed tomography: a focus on micelles. Contrast Media Mol Imaging. 2014;9(1):37–52.
9. Yin Q, Yap FY, Yin LC, Ma L, Zhou Q, Dobrucki LW, et al. Poly(iohexol) nanoparticles as contrast agents for in vivo X-ray computed tomography imaging. J Am Chem Soc. 2013;135(37):13620–3.
10. Shilo M, Reuveni T, Motiei M, Popovtzer R. Nanoparticles as computed tomography contrast agents: current status and future perspectives. Nanomedicine. 2012;7(2):257–69.
11. Xi D, Dong S, Meng X, Lu Q, Meng L, Ye J. Gold nanoparticles as computerized tomography (CT) contrast agents. Rsc Adv. 2012;2(33):12515–24.
12. Reuveni T, Motiei M, Romman Z, Popovtzer A, Popovtzer R. Targeted gold nanoparticles enable molecular CT imaging of cancer: an in vivo study. Int J Nanomed. 2011;6:2859–64.
13. Chien CC, Chen HH, Lai SF, Wu KC, Cai XQ, Hwu YK, et al. Gold nanoparticles as high-resolution X-ray imaging contrast agents for the analysis of tumor-related micro-vasculature. J Nanobiotechnol. 2012;10:10. doi:10.1186/1477-3155-10-10.
14. Liu YL, Liu JH, Ai KL, Yuan QH, Lu LH. Recent advances in ytterbium-based contrast agents for in vivo X-ray computed tomography imaging: promises and prospects. Contrast Media Mol Imaging. 2014;9(1):26–36.
15. Kinsella JM, Jimenez RE, Karmali PP, Rush AM, Kotamraju VR, Gianneschi NC, et al. X-Ray Computed tomography imaging of breast cancer by using targeted peptide-labeled bismuth sulfide nanoparticles. Angew Chem-Int Edit. 2011;50(51):12308–11.
16. Rabin O, Perez JM, Grimm J, Wojtkiewicz G, Weissleder R. An X-ray computed tomography imaging agent based on long-circulating bismuth sulphide nanoparticles. Nat Mater. 2006;5(2):118–22.
17. Bonitatibus PJ, Torres AS, Goddard GD, FitzGerald PF, Kulkarni AM. Synthesis, characterization, and computed tomography imaging of a tantalum oxide nanoparticle imaging agent. Chem Commun. 2010;46(47):8956–8.
18. Zhou Z, Kong B, Yu C, Shi X, Wang M, Liu W, et al. Tungsten oxide nanorods: an efficient nanoplatform for tumor CT imaging and photothermal therapy. Sci Rep. 2014;4:3653. doi:10.1038/srep03653.
19. Na HB, Song IC, Hyeon T. Inorganic nanoparticles for MRI contrast agents. Adv Mater. 2009; 21(21):2133–48.
20. Gallo J, Long NJ, Aboagye EO. Magnetic nanoparticles as contrast agents in the diagnosis and treatment of cancer. Chem Soc Rev. 2013;42(19):7816–33. (Epub 21 Jun 2013.)
21. Nohyun Lee TH. Designed synthesis of uniformly sized iron oxide nanoparticles for efficient magnetic resonance imaging contrast agents. Chem Soc Rev. 2011;41(7):2575–89.
22. Pierre VC, Allen MJ, Caravan P. Contrast agents for MRI: 30+ years and where are we going? J Biol Inorg Chem. 2014;19:127–31.
23. Zhu D, Ma L, Liu D, Wang Z. Nanoparticle-based systems for T1-weighted magnetic resonance imaging contrast agents. Int J Mol Sci. 2013;14(5):10591–607.
24. Josephson L. Magnetic nanoparticles for MR imaging. In: Ferrari M, Lee AP, Lee LJ, editors. BioMEMS and biomedical nanotechnology. USA: Springer; 2006. p. 227–37.
25. Pablico-Lansigans MH, Situ SF, Samia AC. Magnetic particle imaging: advancements and perspective for real-time monitoring and image-guided therapy. Nanoscale. 2013;5(10):4040–55.
26. Wang Y-XJ. Superparamagnetic iron oxide based MRI contrast agents: current status of clinical application. Quant Imaging in Med Surg. 2011;1(1):35–40.
27. Magnetic Resonance TIP—MRI database: resovist softways. http://www.mr-tip.com/serv1.php?type=db1&dbs=Resovist. Accessed 28 July 2014.
28. Sun Sheng-Nan WC, Zhu Zan-Zan, et al. Magnetic iron oxide nanoparticles: synthesis and surface coating techniques for biomedical applications. Chin Phys B. 2014;23(3):037503.
29. Tassa C, Shaw SY, Weissleder R. Dextran-coated iron oxide nanoparticles: a versatile platform for targeted molecular imaging, molecular diagnostics and therapy. Acc Chem Res. 2001;44(10):842–52. (Epub June 10, 2011.)
30. Peter L. Choyke YM. Ferumoxytol enhanced MRI for the detection of lymph node involvement in prostate cancer national cancer institute at the national institutes of health; 2014 [updated March 16, 2014; cited 2014]. http://www.cancer.gov/clinicaltrials/search/view?cdrid=695775&protocolsearchid=6587666&version=healthprofessional. Accessed 8 April 2014.
31. Guoqiu Wu, Xiaodong W, Gang Deng, Linyuan Wu, Shenghong Ju, Gaojun Teng, Yuyu Yao, Xiyong Wang, Naifeng Liu. Novel peptide targeting integrin V3-rich tumor cells by magnetic resonance imaging. J Magentic Reson Imaging. 2011;34(2):395–402.
32. Ling D, Hyeon T. Chemical design of biocompatible iron oxide nanoparticles for medical applications. Small. 2013;9(9–10):1450–66. (Epub December 12, 2012.)
33. Alauddin MM. Positron emission tomography (PET)

imaging with 18F-based radiotracers. Am J Nucl Med Mol Imaging. 2012;2(1):55–76.
34. Gambhir SS. Molecular imaging of cancer with positron emission tomography. Nat Rev Cancer. 2002;2:683–93.
35. Brindle K. New approaches for imaging tumour responses to treatment. Nat Rev Cancer. 2008;8:94–107.
36. Welch MJ, Hawker CJ, Wooley KL. The advantages of nanoparticles for PET. J Nucl Med. 2009;50:1743–6.
37. Lee S, Kang SW, Ryu JH, Na JH, Lee DE, Han SJ, Kang CM, Choe YS, Lee KC, Leary JF, Choi K, Lee KH, Kim K. Tumor-homing glycol chitosan-based optical/PET dual imaging nanoprobe for cancer diagnosis. Bioconjug Chem. 2014;25:601–10.
38. Bao G, Mitragotri S, Tong S. Multifunctional nanoparticles for drug delivery and molecular imaging. Annu Rev Biomed Eng. 2013;15:253–82.
39. Hussain T, Nguyen QT. Molecular imaging for cancer diagnosis and surgery. Adv Drug Deliv Rev. 2013;66:90–100.
40. Xing Y, Zhao J, Conti PS, Chen K. Radiolabeled nanoparticles for multimodal tumor imaging. Theranostics. 2014;4(3):290–306. (Epub January 24, 2014.)
41. Liu Y, Welch MJ. Nanoparticles labeled with positron emitting nuclides: advantages, methods, and applications. Bioconjug Chem. 2012;23:671–82.
42. ThorekDL, Ulmert D, Diop NF, Lupu ME, Doran MG, Huang R, Abou DS, Larson SM, Grimm J. Non-invasive mapping of deep-tissue lymph nodes in live animals using a multimodal PET/MRI nanoparticle. Nat Commun. 2014;5:1–9.
43. Wang D, Lin B, Ai H. Theranostic nanoparticles for cancer and cardiovascular applications. Pharma Res. 2014;31: 31(6): 1–17.
44. Lu ZR. Theranostics: fusion of therapeutics and diagnostics. Pharm Res. 2014; 31(6):1355–3.
45. Chen G, Qiu H, Prasad PN, Chen X. Upconversion nanoparticles: design, nanochemistry, and applications in theranostics. Chem Rev. 2014;114:5161–214.
46. Benezra M, Penate-Medina O, Zanzonico PB, Schaer D, Ow H, Burns A, DeStanchina E, Longo V, Herz E, Iyer S, Wolchok J, Larson SM, Wiesner U, Bradbury MS. Multimodal silica nanoparticles are effective cancer-targeted probes in a model of human melanoma. J Clin Invest. 2011;121(7):2768–80.
47. Enrique Morales-Avila GF-F, Ocampo-Garcia BE, Ramirez FM. Radiolabeled nanoparticles for molecular imaging. In: Schaller PB, editor. Molecular imaging: InTech; 2012.

Flat-Panel CT and the Future of OR Imaging and Navigation

7

Ina Schwabenland, Dirk Sunderbrink, Georg Nollert, Christoph Dickmann, Markus Weingarten, Andreas Meyer, John Benson, Philip Mewes, Peter Mountney, Li Zhang, Stéphane Andre Nicolau, Luc Soler and Chris Tihansky

Introduction

Evolving interventional and surgical procedures demand the design of a new working environment allowing interdisciplinary teams to collaborate. The novel concept was first introduced in 1990 when the first hybrid operating room (OR) was installed for endovascular procedures at the Monaco Cardio-Thoracic Center. Cardiac and vascular surgeons first developed endovascular workflows to treat aneurysms and degenerated heart valves. However, the overall trend in surgery toward minimally invasive surgery and the dedicated technology developments started to expand in almost all surgical disciplines.

At present, interdisciplinary workflows and surgical requirements from hygiene to patient positioning define the designs of the theaters. The set-up of such a room allows both interventional and open surgical procedures, as well as "one-stop" procedures for optimal patient care. "One-stop" surgery implies complete multidisciplinary treatment of a patient in one session, i.e., marking of lung nodule with a hook wire and its minimally invasive resection through video-assisted thoracoscopic surgery (VATS).

I. Schwabenland (✉) · D. Sunderbrink · G. Nollert · C. Dickmann · M. Weingarten · A. Meyer · P. Mewes
Healthcare Sector, Siemens AG Healthcare, SiemensStr. 1, Forchheim 91301, Bavaria, Germany
e-mail: ina.schwabenland@siemens.com

D. Sunderbrink
e-mail: dirk.sunderbrink@siemens.com

G. Nollert
e-mail: Georg.nollert@siemens.com

C. Dickmann
e-mail: christoph.dickmann@siemens.com

M. Weingarten
e-mail: markus.weingarten@siemens.com

A. Meyer
e-mail: andreas.am.meyer@siemens.com

P. Mewes
e-mail: philip.mewes@siemens.com

J. Benson
Ultrasound Business Unit, Siemens AG Healthcare, Issaquah, WA, USA
e-mail: jwbenson@msn.com

P. Mountney
Healthcare Sector, Siemens AG Healthcare, 23–38 Hythe Bridge Street, Oxford, UK

L. Zhang
Siemens AG Healthcare, Princeton, NJ, USA

CT RTC ICV, Siemens Corporation, Corporate Technology, 755 College Road East, Princeton, NJ, USA
e-mail: lizhang@siemens.com

S. Andre Nicolau
R&D, IRCAD of Strasbourg, 1, place de l'hôpital, Strasbourg, France
e-mail: stephane.nicolau@ircad.fr

L. Soler
R&D, IRCAD-IHU of Strasbourg, 1, place de l'hôpital, Strasbourg, France
e-mail: luc.soler@ircad.fr

C. Tihansky
Maunakea Technologies, 18 West State St, Suite 208, Doylestown, PA 18901, USA
e-mail: tchris@maunakeatech.com

Y. Fong et al. (eds.), *Imaging and Visualization in The Modern Operating Room,*
DOI 10.1007/978-1-4939-2326-7_7,

New technologies are being developed to improve user interface, data connectivity and display, image fusion of different imaging modalities, and three-dimensional (3D) representation of anatomy in real time, to name but a few. In the future, operating theaters will connect a wide variety of key surgical systems such as robotics, X-ray, navigation, ultrasound, and endoscopy. Therefore, it is important for the design of a hybrid OR not only to consider current needs and systems, but also to accommodate rapidly developing therapies and future needs.

Fig. 7.1 Hybrid operating room at the University of Ulm, Germany, showing the complex setup of components in a surgical environment. (Courtesy Siemens AG)

Imaging Techniques and Systems in Hybrid Operating Theaters

Room Planning The hybrid OR requires a thoroughly planned environment that considers the space needed for imaging equipment and the integration of different OR components into one comprehensive functional system. All disciplines should be involved in the development of the new operating theatre from the very start of the planning phase. A multifunctional room requires a more refined design and functional working concept than conventional ORs. A room size of 70 m^2/750 ft^2 or larger is recommended with an additional technical and control room of 10 m^2/33 ft^2. Depending on whether the theatre is being reconstructed in an existing setup or if a new building is being built, the planning and implementation of a hybrid OR usually demand 12–18 months.

Related medical technical equipment. The plan of a hybrid OR requires a detailed analysis of the technical equipment and the workflows in the OR. Large displays or monitors integrating the different imaging signals need to be positioned at both sides of the patient to allow adequate visualization. The positioning of the large imaging modality (CT, MR, angio, etc.) plays a crucial role when defining the workflows and considering the different disciplines that will use the room (Fig. 7.1). State-of-the-art floor-mounted fixed C-arm systems allow the most flexible set-up and access to the patient while keeping the highest hygienic standards [1]. The placement of a laminar air flow field above the operating field depends on the hygienic requirements of the hospital and different surgical procedures. Choosing appropriate anesthesia equipment, gas outlets and OR lamps, storage of surgical equipment, and the right table are important topics to consider from an interdisciplinary perspective.

Tables The selection of the table depends on the primary use of the system. Interventional tables with floating tabletops, tilt, and cradle compete with fully integrated flexible OR tables (Fig. 7.2a, b). Identifying the right table involves

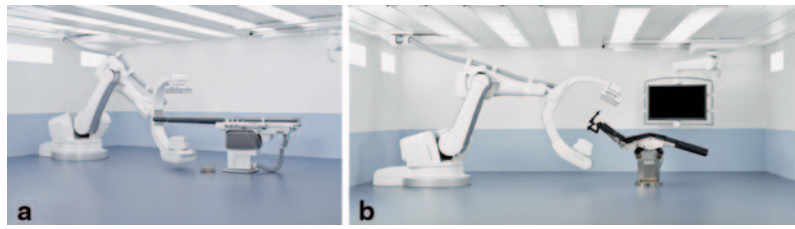

Fig. 7.2 **a** Interventional free-floating tables offer a free-floating tabletop. (Courtesy Siemens AG)**. b** Operating tables allow sophisticated surgical positioning. (Courtesy Siemens AG)

Table 7.1 The installation of a hybrid operating room offers advantages for the patient and the hospital, as well as integration of future technologies. Advantages of a hybrid operating room

Patients	Hospital
Optimized and confident treatment	Teamwork of multiple disciplines
Individualized care	Use and development of innovative workflows
Faster mobilization	Optimization of procedures
Care of multimorbid and high-risk patients	Expansion of medical services
Shorter hospital stay	Cost effectiveness

compromise between interventional and surgical requirements [2, 3].

Surgeons, particularly orthopedic, general, and neurosurgeons, usually expect a table with a segmented tabletop for flexible patient positioning. As a compromise, floatable angiography tables specifically made for surgery with vertical and lateral tilt may be considered [4]. However, the highest utilization flexibility can only be achieved if an OR system table is installed.

Important additional aspects should be considered when planning the table, among them position in the room, radiolucency (carbon fiber tabletop), compatibility, and integration of imaging devices with the operating table, e.g., robots. Further aspects include table load, patient coverage (length) adjustable table height, and horizontal mobility (floating) including vertical and lateral tilt. It is important to also have proper accessories available, such as rails for mounting special surgical equipment (retractors, camera holder) (Table 7.1).

Choosing the Angiographic System

Choosing the imaging system for a hybrid OR depends on the intended utilization of the room. Expert consensus rates the performance of mobile C-arms in hybrid ORs as insufficient and recommends fixed floor-mounted systems for hygienic reasons [2, 5]. In fact, some hospitals do not allow systems situated directly above the surgical field (i.e., ceiling-mounted systems), because of the potential of contaminated dust particles falling into the surgical situs. Since any ceiling-mounted system includes moving parts above the surgical field and impairs laminar airflow, ceiling-mounted systems may be considered incompatible with the highest hygienic standards needed, such as in orthopedic surgery. In addition, ceiling-mounted systems require substantial ceiling space and reduce the options to install surgical lights or booms while increasing the chances of collisions.

In a crowded environment like the OR, bulky biplane systems add to the complexity. Biplane systems are currently subject to selected procedures like neurosurgery or pediatric cardiology [2, 6]. Monoplane systems are recommended for most rooms. The robot-supported surgical C-arm (multiaxis system controlled by the surgeon) permits full flexibility and access for precise and quick patient care, including imaging and parking positions [5].

A detector size of 30 × 40 cm (12″ × 16″) allows coverage of a large organ or, for example, visualizing the entire pelvis with both iliac arteries in only one image. On the other hand, a small detector of 20 × 20 cm (8″ × 8″) or midsize detector of 30 × 30 cm (12″ × 12″) finds application in cardiac interventions.

Tube and Detector Technology In typical X-ray tubes, electrons emitted at the cathode are accelerated in a vacuum by high voltage (30–150 kV) toward a rotating tungsten anode. Heat is produced when the electrons hit the anode and are decelerated. Approximately 1 % of the energy is converted into X-rays. The X-ray beam is normally emitted perpendicular to the anode. Filters modify the beam so that the X-ray spectrum used for image generation is selected, while collimators ensure that only the field of view is irradiated. Power, sharpness and radiation dose are underlying factors in different tube architecture determining optimal image quality. Optimally the cathode is capable of handling a large

electrical power flux as well as being constructed as a single electron emitter spot; this allows very short, powerful pulses and concentrates energy on a small focus, improving temporal resolution. Flat emitters offer better defined electron emission and therefore a smaller focal spot at a given power compared to 3D filaments. The anode should have a high capacity to absorb heat and to cool. A minimum heat unit capacity of 1 million heat units is recommended to avoid overheating. Modern tubes provide surplus well above this requirement.

Flat-panel X-ray detectors are based on similar principles as image sensors used in digital photography and video. X-rays hit a scintillator layer of gadolinium oxysulfide or cesium iodide and are converted into light. Directly attached to the scintillator layer is an amorphous silicon-on glass detector array that converts the light into electrical signals. The signals from the photodiodes are amplified and encoded to produce an accurate and sensitive digital representation of the X-ray image. The signals from each pixel are transferred to the image processor for postprocessing and optimization of image quality. New detector materials like crystalline silicone, intelligent signal amplification, and fast image data transfer allow an improved signal-to-noise ratio and improved image quality at very low dose levels.

Imaging Techniques

Two-Dimensional Imaging

Fluoroscopy Conventionally, fluoroscopy provides real-time, high-resolution, low-contrast images in two dimensions through the use of an image intensifier or a flat panel detector. Fluoroscopy is—a main imaging modality used in ORs, most frequently used in orthopedic and trauma surgery. For spine and pelvis surgery, intra-articular fractures, and in obese patients, fluorescence imaging requires higher power output to depict fine anatomic structures and details. The required image quality can be achieved only by employing high powered fixed angiography systems with fixed and dedicated generators. In modern fluoroscopy systems, image intensifiers have been replaced with digital flat panel detectors providing fully digitized, high-contrast, high-resolution images without distortion. These high-quality images are a prerequisite for 3D reconstruction by cone-beam CT (e.g., syngo DynaCT, Siemens Healthcare, Germany).

Digital Subtraction Angiography Over the past three decades, digital subtraction angiography (DSA) has become a well-established 2D imaging technique for the visualization of blood vessels in the human body. A sequence of 2D digital X-ray projection images is acquired to investigate the anatomy and flow dynamics of an injected contrast agent through vessels of interest. Background structures are largely removed by subtracting an image acquired prior to injection (the mask image) from the live images (the contrast images). In the resulting subtracted images, background structures are completely removed if these structures are stationary. Various motion correction algorithms are applied to reduce artifacts.

DSA is clinically used for diagnostic and therapeutic applications of more or less stationary vessel visualization throughout the entire body. During complex interventional procedures, DSA is often combined with road mapping. In this mode, a DSA sequence is performed and the frame with maximum vessel opacification is identified, which becomes the road map mask. The road map mask is subtracted from subsequent live fluoroscopic images to produce real-time subtracted fluoroscopic images overlaid on a static image of the vasculature. Road mapping is useful for manipulation and placement of devices in complex vascular procedures. Road mapping may also be combined with a feature called image fade, which allows the user to manually adjust the brightness of the static vessel roadmap overlay.

Viewing of 2D Digital X-ray Images

After having selected individual images or scenes from an overview of the imaging study, basic image manipulations and processing options can be done:

- *Windowing:* changing contrast and brightness.
- *Zoom/pan:* magnifying and centering into structures of interest in an image.
- *Filtering:* an image or enhancing edges to clearer see delineation of structures.
- *Inverting:* the greyscale image or changing the image colors (e.g., from greyscale to a yellow-red coloring color table).
- *Calibration and measurements:* 2D images contain geometric information that allow for measuring in the projection plane (straight/curved distance, angle, area, perimeter, diameter). Measurements on projection images may not be precise if the structure to be measured is projected oblique and thus shortened (forshortening); precise measuring requires a perpendicular view onto the structure.
- *Pixel values* representing the tissue characteristics (absorption) can be read out for regions of interest.
- Contrast-enhanced scenes allow for summarizing images and thereby can visualize maximum *opacification* of contrasted vessels.

Three-Dimensional Imaging (3D)

3D Imaging: Cone-Beam CT (CBCT) Three-dimensional (3D) C-arm computed tomography is a new and innovative imaging technique that uses series of two-dimensional (2D) X-ray projections acquired with a flat-panel detector C-arm angiography system to generate CT-like images [7]. The C-arm sweeps around the patient acquiring projections that serve as input for 3D cone-beam reconstructions. Typically, a C-arm CT device requires at least 200° (minimum angular scan range of 180°, plus the fan angle of the X-ray tube) for artifact-free reconstruction. For typical C-arm CT devices, this results in an angular scan range requirement of at least 200°. The resulting volume data set can be displayed either as cross-sectional images or as 3D data sets using different volume rendering techniques [7].

The spatial resolution provided by CBCT can be in the submillimeter range. With dedicated protocols and 1 × 1 binning, resolutions of 0.1 mm are possible. The acquired volume can reach up to 35 cm × 25 cm with specialized protocols.

Fig. 7.3 The flexibility of the system, sterility preservation, and autonomous use by the surgeon offer quick and precise treatment here at a laparoscopic liver case at the University of Heidelberg. (Courtesy Siemens AG)

CT-like soft-tissue image quality can be achieved in the hybrid OR with a contrast resolution of up to 3–5 HU (compared to 1 HU in conventional CT) depending on the acquisition protocol (see Fig. 7.3). Beyond their use for transarterial catheter procedures, these 3D data sets are also valuable for guidance and optimization of nonvascular percutaneous, musculoskeletal or laparoscopic treatments. The image quality for the visualization of lymph nodes is comparable to CT and a laparoscopic diagnostic nodule resection was facilitated by intraoperative CBCT imaging [8].

Intraoperative 3D Imaging Integrating acquisitions of 3D images in the OR into routine clinical workflows requires a thoroughly planned setup. Since the position of the equipment and staff varies with the type of intervention, the flexibility of the imaging system is important to adapt to the specific surgical situation. The integration of the imaging system with a surgical table allows imaging in sophisticated surgical positions without repositioning for acquisition. While the room and surgical equipment have specific requirements for MRI compatibility and do impair access to the patient when using CT in the OR, the angiography system offers the most

flexibility and has shown advantages in patient treatment [9] without sacrificing image quality [10].

Sterility of the surgical field must be ensured during the 3D acquisition. Covering the patient with an additional sterile sheet and taping the sheet around the table ensures sterility and minimizes the infection risk for the patient. During 3D acquisitions, the C-arm rotates around the patient in 3–20 s depending on the imaging protocol and the machine. The operator controls the acquisition from a sterile-draped control panel at the table or on a trolley.

Visualization of 3D X-ray or Angiographic Images

3D visualization adds valuable information to 2D projection images when it comes to understanding complex anatomy or pathology like fractured vertebrae or ruptured cerebral aneurysms. The structures are contained in a volume that can be inspected freely by generating cross-sections (double oblique), rotating or clipping, so that the spatial relationships of structures become clear and foreshortening effects seen in 2D are overcome. While 2D images consist of pixels in a plane, the 3D volume consists of voxels, i.e., small volumes as minimal unit of image information. The 3D images can be divided into a volume of interest (VOI) in which a section of the acquired volume may be specifically reconstructed, e.g., to increase the spatial resolution of this VOI. During image processing, cross-sections of the volume are generated in axial (feet to head), saggital (left to right) and coronal (anterior to posterior) orthogonal orientations and allow scrolling through individual slices. Additional cross-sections can also be placed freely to oblique (e.g., for cranio-maxillary or facial), radial (e.g., for brain) or curved (e.g., for spine, aorta) orientations that cut through the structures of interest in more informative ways.

- *Multiplanar reconstruction (MPR)* of an imaging volume generates cross-sections with slice thickness in the submillimeter (thin) or millimeter (thick) range.
- *Maximum intensity projection (MIP)* displays the maximum voxel values from a cross section's voxel column over its slice thickness. This increases the image contrast which is useful for viewing vessels or dense structures.
- *Minimum intensity projection (MinIP)* displays the minimum voxel values over a cross section's slice thickness, e.g., enhancing air or soft-tissue voxels.
- *Slabs* are subvolumes that allow concentrating on a part of the volume, showing its boundaries as planes.

Volume rendering techniques (VRT) present 2D views onto a volume which voxels are colored and opaque to differentiate the anatomical structures and where shading and light casting provides the 3D impression. Visualization presets that define coloring, lighting, contrast, and opacity for structures with certain voxel values (e.g., Hounsfield Units, HU) can be applied to enhance certain structures and generate different VRT impressions, e.g., soft tissue in abdominal regions, bones in cerebral volumes, calcifications in vessels.

Clip planes can be placed in any orientation and be moved from one side of a volume to the other side. This allows looking inside the volume in a 2D way as potentially distracting structures in front of the observer were removed so that, e.g., irrelevant contrasted vessels in front are not visible any more.

Surface rendering visualizes different organs whose boundaries have been detected and are displayed in an enhanced way, which helps inspecting outer surfaces of bones or inner surfaces of hollow structures like bowels or bronchi.

Segmentation of organs or structures, i.e., its isolation from the surrounding structures in the volume, can be performed automatically by a system if it incorporates knowledge about organ shapes or characteristics. Segmentation may also be done interactively by setting seed points (region growing), drawing contours (stroke-based segmentation) or cropping out the structure of interest (punching). Hollow or tube-like segmented objects may contain a *center line* for exact length measuring and may be viewed in a fly-*through* mode showing the inside of the structure, e.g., to better detect intraluminal tumors or stenoses.

If there are multiple segmented structures in a volume, it may be possible to view them individually or select which ones should be displayed at the same time. For instance, when planning endoleak closure, the neighboring vertebrae may be segmented and hidden while one looks for the nurturing vessel but may be displayed again when determining at which level of the spine the endoleak is located.

During review of a volume, the visualization can be manipulated analogously to 2D images, e.g., by windowing, zooming, panning, and rotating. In addition, 3D volumes allow changing the transparency or opacity of the whole volume or (segmented) parts so the different structures can be faded in or out and made more or less prominent.

Measurements in 3D volumes can be done in different ways, but the operator needs to consider certain preconditions or limitations. Exact measurements can be done in two-dimensional (2D) cross-sections of minimal slice thickness or on centerlines: The observer can be sure that the measurement is done precisely in the structure that he sees. The thicker the slice, the more surrounding tissue is contained so that the projection shown in the cross-section may average out small structures or may show foreshortening. Additionally, the monitor shows only a 2D impression of the 3D volume the operator cannot reliably assume that the measuring graphics are placed at the correct depth of the volume. Thus, when measuring in VRT visualization, the operator needs to check by rotating or zooming/panning that the measurement graphics are correctly placed onto or into the structure to be measured.

Two or more volumes can be fused and viewed at the same time in order to match morphology and function (e.g., PET-CT), to view morphology and current blood flow (e.g., CT-CBCT) or to compare structures before and after surgery or intervention (e.g., CT-CT). The individual volumes first need to be registered to each other so that the structures match as perfectly as possible. If the volumes have different voxel geometries or locations, the system needs to interpolate voxels which may lead to slight inaccuracies (resampling, nonrigid registration).

In order to distinguish individual structures or its boundaries between the different fused volumes, it is necessary to dynamically blend or change the transparency between the volumes to see the one or the other volume more prominent.

Volumes enable the surgeon to create precise guiding structures that can make the procedure safer, faster or spare radiation dose or contrast media. The surgeon can:

- Choose the best access path for punctures or placing trocars, including laser guidance for percutaneous access, e.g., for spine surgery or thoracic endoscopy
- Mark structures to be cannulated and followed like ostia of branching vessels
- Define points or landing zones for placing implants in bones or vessels
- Identify anatomical regions for resection, e.g., a liver's vessel-tree segment
- Define structures to display in perpendicular X-ray projection in order to exactly place an implant like a transcatheter aortic valve implant

3D renderings or guiding structures can be overlaid onto live images, mainly on live fluoroscopy. This eases the surgeon advancing the instruments or placing devices at the right location by matching the instrument and the planning overlay. It is optimal if rotations of the C-arm (i.e., no radiation applied yet) also move the overlay structures so that C-arm projection and displayed orientation of the guiding structures are matching.

Manually adjusting or automatically reregistering the overlay to the live imaging is needed to correct patient or organ movement. This requires optimal projections and structures that can be detected and tracked. Motion compensation or tracking improves guidance when the surgical field moves, e.g., due to the lungs inflating or the heart beating. This is helpful if it is not possible to avoid or stop motion during image acquisition or surgical work, e.g., holding breath or increasing cardiac rate cannot be used.

The correctness of the overlay depends on many factors, including C-arm mechanics and angulations, patient and organ movement, and surgical manipulations. The surgeon needs to take these factors into account when using over-

lay for guidance and can detect overlay inaccuracy that go beyond 2 mm.

Imaging from more than one intraoperative imaging modality can be fused. This is especially true for X-ray and ultrasound so that dynamic, radio-opaque and soft-tissue structures can be visualized side-by-side or coregistered and overlaid. A prominent example is mitral valve repair where X-ray provides guidance for catheters and wires, whereas the dynamic ultrasound images allow for deploying the prosthesis. Integration of multiple intraoperative modalities are rapidly evolving.

Radiation Dose

The effective dose in angiography depends on several factors, primarily on organ ration sensitivity and beam angle. For instance, bone marrow cells are far more radiation sensitive than liver [11]. The angle of the beams cause angiography to be less "homogeneous" than CT, which must be considered when estimating the irradiation damage. Effective dose provides a suitable comparison with natural background radiation, which is on average about 2.4 mSv/year. Typically, during a cardiac diagnostic intervention with 15 X-ray pulses per second (p/s), the effective dose per minute is 0.6 mSv [12]. In the past, higher image quality often required higher doses, but advanced tube and detector technologies and real-time digital image processing allow safe diagnostic imaging and real-time image guidance with significantly less radiation dose to the patient and the team in the hybrid OR [13].

The operator can reduce the radiation exposure by adapting:

1. Footswitch on-time: Footswitch on-time controls how long the body is exposed to X-ray beams or how long the body is irradiated (less time means less radiation).
2. Frame rate: High frame rates are used to visualize fast motion without stroboscopic effects, but radiation exposure is directly proportional to the frame rate. Therefore, the frame rate should be kept as low as possible. Modern angiographic systems can adjust the frame rate downward in various steps, from 60 pulses per second (p/s) used in pediatric cardiology to 0.5 p/s in some systems for slowly moving objects. The reduction from 30 to 7.5 p/s results in decreasing the radiation dose by 75%.
3. Source-image distance (SID): According to the quadratic law and a requested constant dose at the detector, a greater distance between the source and the image increases the skin dose. Raising SID from 105 cm (=SID 1) to 120 cm (=SID 2) increases skin dose by approximately 30% if C-arm angles, table position, patient, and requested dose at the detector do not change.
4. Collimation: Reducing the area of the beam by collimating the beam to the clinically relevant structures saves dose because less radiation is emitted.

Modern angiographic systems provide additional inherent features to reduce dose, such as:

1. Variable copper filters reduce the skin dose by filtering out the low-energy photons that are absorbed in the body and do not contribute to the image. Some systems adjust the filter thickness automatically according to the absorption of the patient entrance dose along the X-ray beam through the patient.
2. Using the last image hold as a reference, the system displays the effect of changing collimation or targeting the region of interest without additional radiation.
3. The systems automatically calculate system parameters like tube voltage and beam filtration to optimize X-ray quality and detector entrance dose.

More and more countries and authorities require reporting of patient exposure to radiation. To meet current and future regulations, modern angiographic systems allow effective reporting of dose exposure, enabling enhanced in-house dose reporting and analysis.

Radiation Safety for the Staff

The team in the hybrid OR should be familiar with local radiation protection procedures. Depending on country regulations, designated radiation protection supervisors enforce radiation safety, check dose meters, and analyze radiation documentation. The most important source of radiation for the OR team is scattered radiation

that originates from the primary radiation beam by interacting with patient tissue. Scattered radiation is particularly high close to the patient and depends on patient size and C-arm angulations. Radiation protection is most efficient by applying the inverse-square law, which states that the amount of radiation reaching a surface is inversely proportional to the square of the distance between the source and the surface.

Wearing radiation protection like lead aprons reduces radiation exposure to the body to a small fraction. LE thyroid shields and lead glasses should be worn by team members as appropriate. Additionally, adjustable lead glass shields and lower body radiation protection may be necessary to reduce personnel radiation exposure. Dosimetry systems are available that display the actual radiation received on-line for immediate (real-time) feedback. These systems (Unfors Raysave, Sweden) provide every team member on-line feedback on current exposure.

Advanced Visualization

User Interface and the Integration in the OR

Gabe Newell, the CEO of Valve, stated in 2012 that touch technology will only be a bridging technology for 10 years, although it will replace the keyboard and mouse interaction that had been standard for almost 25 years [14]. Taking this statement seriously, the challenge is: "What will be the next standard user interface for private use as well as in the ORs?"

In the last several years, perhaps the most influential idea was free-hand gesture control. The Kinect hardware introduced by Microsoft in 2010 laid the groundwork for Kinect-based research projects and products in different environments, including the OR. The advantage of a touchless, sterile control of the system sounds appealing [15]. However, usability in the OR still needs to be proven. Robustness of recognition and ergonomic issues are limitations. "Gorilla arm" is the metaphorical term for the fatigue felt after longer interaction using free-hand gestures [16]. Overall, gesture control will become a user interface of the future in the OR, but limit the amount of gestures and shorten the time of interaction.

But if the hands-free user interface is not the interaction style of the future, then what is? Joysticks and hardware keys are still present in the OR due to the disadvantages of mice. Attempts were made to bring the mouse into the OR (e.g., by putting it inside sterile covers or providing a sterile, disposable mouse), but the mouse requires space with which to interact, since the mouse pad basically represents the display space on a smaller scale. There is no direct interaction with digital objects compared to the introduction of multitouch displays. In multitouch displays surgeons are able to rotate or zoom objects without having to click buttons and perform artificial mouse movements. But similar to gestures, touch will not become the standard user interface in the OR because touch adds to the user interfaces by virtue of its intuitiveness. Although the "intuitive" buzzword is often bandied about carelessly, intuitive essentially means fitting the expectations (mental models) of the users. Intuitiveness is a subjective impression a user has when a user interface or system behaves in the expected way. That is the reason for the real-world metaphors in the digital world. Skeuomorphism means that digital content or tools are derived from things in the real world [17]. Mimicking real things can help to improve intuitiveness. Since smartphones and tablet sales are overtaking the sales of desktop computers, the distribution of multitouch interfaces is on the rise. This will also happen in the OR, but due to advantages (e.g., directness of object manipulation) and disadvantages (e.g., exposure to bodily fluids, sterile covers), the touch interface will only augment other user interfaces.

Another such interface will be eye tracking. One signals the receiver that words are directed to him or her through eye contact. Speaking to someone without focusing on this person causes confusion. The upcoming user interfaces will track our eyes to identify our current interest, our focus of attention. With this technology, content can be highlighted if the user is interested

in it. This comes in handy whenever the amount of information cannot be shown on one screen. Another example could be that the target of our interaction with the digital world will be selected by a look instead of an explicit selection. Again this will not be the sole user interface in the OR since eye tracking (including blinking) has its limits too [18].

Besides gestures, touch, and vision, speech control has always been expected to develop for user interfaces. Communication with other human beings through speech is a primary mode of interaction, so why should not this communication also work with a machine? Command-based speech control solutions have been in use for years, and in the past some functions on angiography systems were controllable through speech, but the systems had limitations. Besides the nonnatural way of communicating via fixed commands, users raised concerns like missing robustness of the speech recognition or ambiguity of the receiver in a room with multiple persons. New speech-based user interfaces like Siri took away the artificiality and provided a natural language interaction, but ambiguity and robustness in an OR are still concerns.

In sum, many user interfaces mimic real-world and human interaction. Therefore, the future will be combinations of user interfaces that are chosen depending on the tasks that need completing. Sensors will enable digital devices to see, hear, and feel. We will also provide them with actuators to speak and push back (e.g., force feedback). The goal will be to make the machines in the future OR as close to a helpful team member as possible. To achieve this vision, the machines will need to become more intelligent and anticipate the next likely work step, like a good assistant would do. But while trying to get closer to the abilities of human beings, technology has already helped to increase surgical accuracy (with robots) and overcome our visual limits (through microscopy). Digital technology will provide additional senses or memory, enriching reality with additional information.

Image Fusion of 3D Information on 2D Fluoroscopy

3D imaging is the prerequisite for more advanced visualization and workflows for navigation and guidance [19]. Advanced intraoperative overlay or fusion imaging may be used with the same effect as external navigations systems, thereby avoiding additional systems being prepared, used or placed in the OR (Fig. 7.4). Preoperative radiologic images can be registered to the intraoperative cone-beam CT images. Intraoperative 3D imaging provides images that are acquired in the actual surgical position and can be updated and easily accessed at all times. However, information retrievable from MRI or other preoperative modalities is indispensable. Therefore, the fusion of preoperative and intraoperative images gives the surgeon additional information in the OR. The fusion of these two volumes can be overlaid consecutively onto live fluoroscopy. This 3D/3D fusion and overlay in live fluoroscopy helps the surgeon to guide his or her instruments, visualize the target organ(s), and avoid crucial anatomy such as vessels. By changing the angulation of

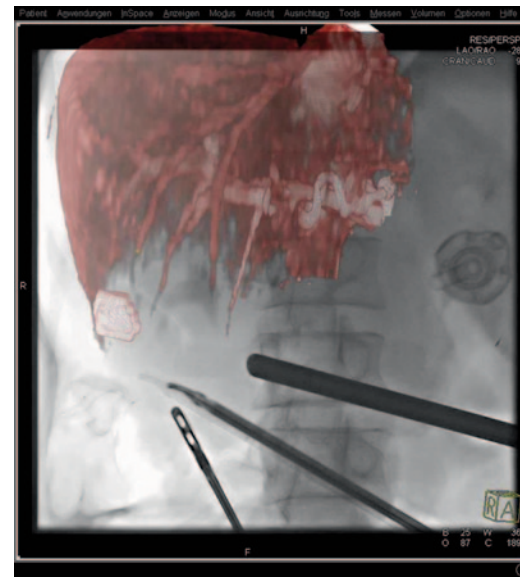

Fig. 7.4 Intraoperative fusion of preoperative imaging, in this case MRI, with CBCT and overlay onto live fluoroscopy adds more information and facilitates instrument guidance. (Courtesy Siemens AG)

the C-arm, the volumes automatically adapt so the surgeon is able to safely guide instruments. An algorithm to adapt the registration even for patients with pneumoperitoneum in laparoscopic surgery has been developed [20, 21].

Navigation and Guidance Intraoperative 3D imaging can also be used in conjunction with navigations systems that perform tracking of instruments or external markers. Navigation is a proven technology in surgical disciplines with rigid structures like orthopedic surgery, craniomaxillo-facial (CMF) surgery, and neurosurgery [22, 23]. The majority of surgical navigation systems are based on optical tracking technology. Beyond that there is a growing field of systems that support electromagnetic tracking. Electromagnetic tracking eliminates the line of sight problem. Furthermore the position sensor can be integrated into the device tip, which enables the use of electromagnetic tracking in flexible instruments. These two benefits will drive future developments based on electromagnetic tracking.

Navigations systems need to be integrated into the intraoperative imaging modality in order to provide a streamlined workflow. This integration includes image transfer and smooth registration techniques (Fig. 7.5). There are two main factors that influence the accuracy of surgical navigation. The first one is the accuracy of the registration of the 3D volume to the navigation system. Intraoperative imaging modalities offer the advantage of an automated registration process that minimizes the errors of human interaction. Highly reproducible trajectories of a fixed C-arm system (e.g., Artis zeego) support this process through table integration, hence knowing its location in relation to the table, and through a larger field of view and a high dynamic range.

The second main factor for high precision is the correctness of the 3D data used for navigation. There are many conceivable reasons that may change the morphology of the imaging data if they are not acquired intraoperatively. Examples include changes in spine morphology through patient positioning or brain shift during a craniotomy.

Fig. 7.5 The integration of an external navigation system to an intraoperative imaging system adds accuracy, increases safety, and helps the surgeon. (Courtesy Siemens AG)

Intraoperative 3D imaging will help to overcome these challenges by updating the images for navigation purposes with current high-quality 3D scans. These updates can also be done by applying a nonrigid deformation to the preoperative images, which is based on an intraoperative scan.

3D rotational angiography may also use certain acquisition protocols to capture temporal information of contrast dye flow so that the dynamics of blood flow can be viewed in a 3D volume, i.e., 4D DSA. This may help to compare blood flow dynamics before and after surgery.

Image Fusion of 3D Information with Laparoscopy

The laparoscopic approach becomes more and more important to make procedures less invasive and safer for the patient. While ports in minimally

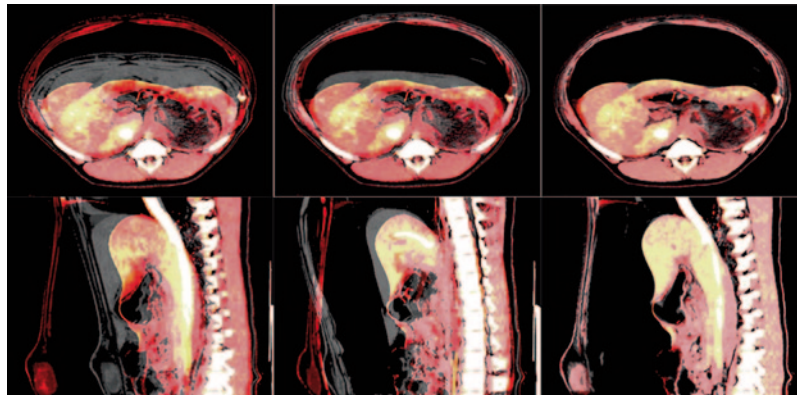

Fig. 7.6 Volumetric image slices before (*gray*) and after (*red*) pneumoperitoneum showing the three steps of registration: initial position, model-based registration, and diffeomorphic nonrigid refinement (pig animal study). (Courtesy Institut de Chirurgie Guidée par l'Image, Strasbourg, France)

invasive surgery decrease, laparoscopic systems develop high-resolution visualization techniques. However, laparoscopic imaging is restricted to visualizing the surface of the organs but not the structures below, e.g., vessels or pathologic structures. Radiologic and functional pre or intraoperative 2D and 3D imaging can make an important contribution to extend the available visualization when registered to the laparoscopic imaging device. This "augmented reality" has the potential to facilitate the localization of important anatomy and decrease tissue trauma and procedure time [24–26].

The anatomical shape and position of an organ changes as soon as surgery starts. The preoperative plan does not match the actual situation in a pneumoperitoneum. Therefore further registration steps are necessary in order to deploy preoperative models during laparoscopic surgery. First, a preoperative CT dataset is registered to an intraoperative 3D C-Arm dataset after CO2 gas insufflation. The anatomical variations between both dataset are represented using a biomechanical model (Fig. 7.6). This model triggers a two-stage intensity-based registration algorithm that achieved accuracy below 2 mm for a CT only dataset. Second, an algorithm has been developed to register between two anatomical surfaces, a surface of an organ segmented from an intraoperative or preoperative 3D volume and the same surface reconstructed from stereo-endoscopic images. The registration method is triggered by a priori knowledge of the organ-specific anatomy and is implemented nonrigidly (see Fig. 7.7).

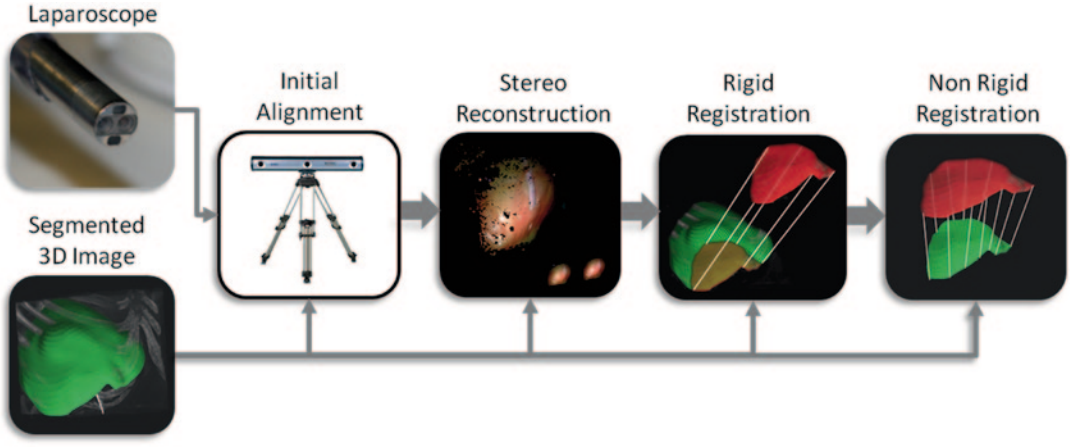

Fig. 7.7 Registration workflow of 3D volumetric data to the laparoscopic video stream. (Courtesy)

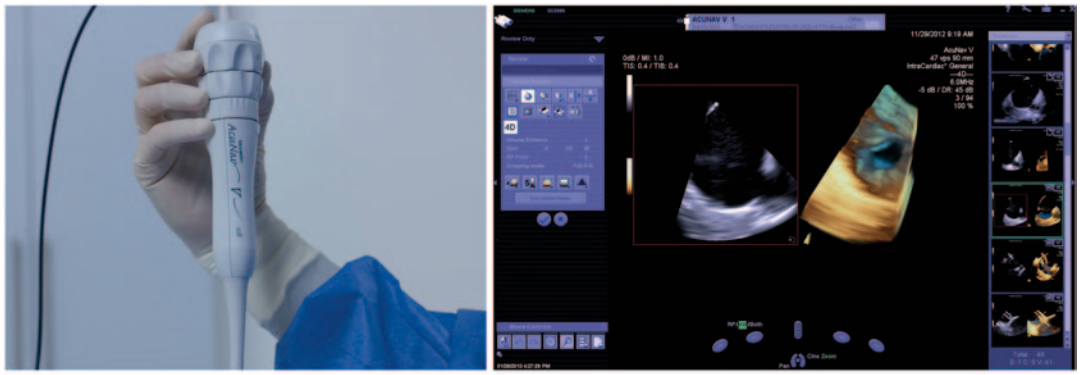

Fig. 7.8 **a** and **b** Catheter-based transducers provide 3D images and **b** visualize color flow. (Courtesy Siemens AG)

Based on phantom experiments, an accuracy of less than 1 mm was achieved using a point-to-surface error metric. While the first registration step establishes a preoperative to intraoperative image-to-image relation, the second registration step has the potential to detect and compensation in real-time for anatomical changes occurring while the procedure takes place.

Integration of Ultrasound

The development of new specialized transducers has increased the use of ultrasound as traditional "open" surgeries have steadily been replaced by minimally invasive procedures that can improve surgical outcomes and shorten recovery times [27].

Smaller hand-held transducers designed for intraoperative use as well as endoscopic, laparoscopic, and catheter-based transducers allow greater access for today's advanced ultrasound imaging capabilities. Laparoscopic ultrasound (LUS) has become more commonly used in abdominal and pelvic surgical procedures, as new laparoscopic transducer technology has improved image quality and has become less cumbersome to use within a 10 mm laparoscopic port. LUS has been used successfully in the surgical staging of gastric cancer, where the rationale for LUS is to decrease the rate of negative laparotomies in patients thought to have resectable disease by preoperative imaging [28].

Catheter-based transducers have provided an effective means to visualize transseptal catheterization for percutaneous catheter mapping and either left atrium or left ventricle ablation procedures, or transcatheter defect closure [29]. A new volumetric version advances the ability to visualize anatomy in multiple planes or in a 3D surface-rendered view for more precise localization (Fig. 7.8).

A significant new advance in reducing the clutter of wires and cables within the operating theater is the introduction of wireless transducer technology for ultrasound systems. Using ultra-wideband radio technology, the transducers are able to send images at a high sustainable data rate back to the ultrasound system with high spatial and temporal resolution (Fig. 7.9).

Fig. 7.9 ACUSON FreestyleTM with wireless transducers. (Courtesy Siemens AG)

The primary advantage of wireless transducer technology is in infection control. With wired ultrasound transducers, the transducer cables move in and out of the sterile field. Without cables, the surgeon can focus on the procedure with more flexibility. The small size of the system reduces clutter in the OR and the availability of different specialized transducers allows a wider range of applications in focused surgical procedures.

Recently, 3D transesophageal echocardiography (TEE) has been introduced. This technology has advanced minimally invasive cardiac surgery such as transcatheter aortic valve replacement (TAVR) and percutaneous mitral valve repair (PMVR) with the MitraClip procedure. In the future, 3D quantitative modeling of the valve and valve function will aid in percutaneous heart valve treatment planning, therapy selection and delivery (Fig. 7.10).

The capability to view and fuse preoperative CT and MRI images as well as intraoperative CBCT images with real-time ultrasound guidance has simultaneously made difficult surgical and interventional procedures easier and more feasible. Ultrasound fusion also has the advantage that postoperative follow-up examinations can be performed more cost effectively and without radiation or restrictions from surgical implants. Automatic registration of ultrasound images with other images reduces preparation and setup time in focused guided procedures (Figs. 7.11 and 7.12).

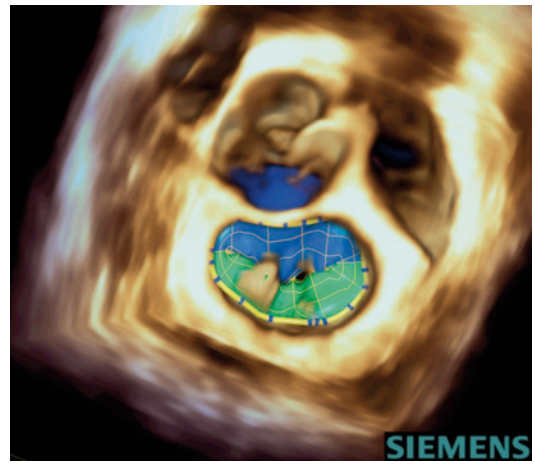

Fig. 7.10 3D TEE-based valve modeling and visualization. (Courtesy Siemens AG)

Advances in ultrasound transducers, ultrasound system miniaturization, ultrawideband wireless technology and new image processing and visualization techniques will continue to make ultrasound an increasingly valuable imaging tool for a wide range of surgical interventions in the future.

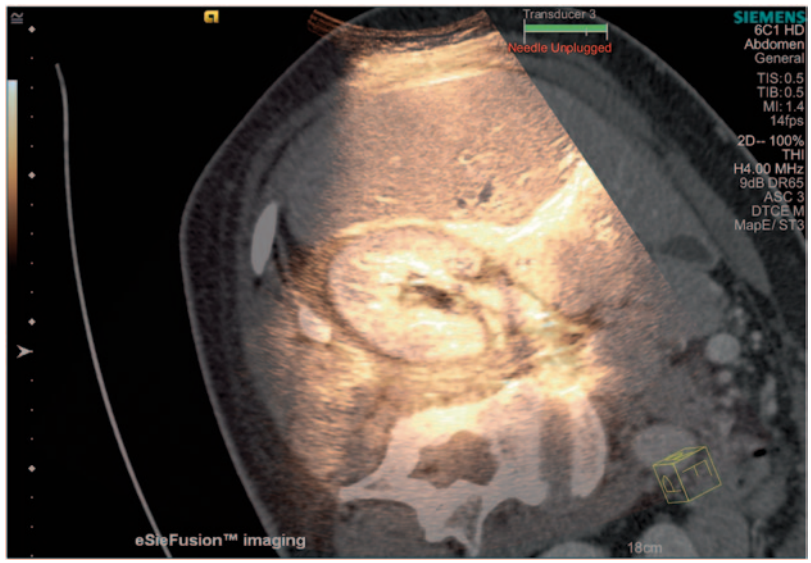

Fig. 7.11 Image fusion between CBCT and ultrasound demonstrating a liver and kidney. (Courtesy Siemens AG)

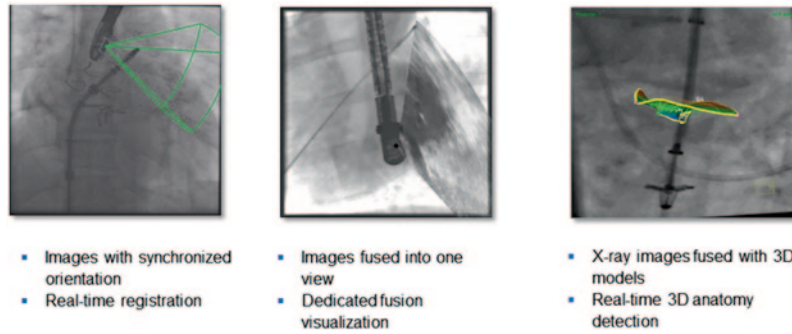

Fig. 7.12 Future direction of ultrasound and fluoroscopy fusion in percutaneous valve repair procedures. (Courtesy Siemens AG)

Confocal Laser Endomicroscopy

Imaging technology plays a vital role in the modern OR with the use of CT, MR, rotational angiography, ultrasound, PET, SPECT, and macroscopic optical fluorescence imaging. One imaging modality that interventionalists and surgeons will find essential in the future, is confocal laser endomicroscopy (CLE). This technology (Cellvizio®) creates an optical biopsy by providing physicians with in vivo microscopic images videos of tissue instantaneously and in a minimally invasive manner (Fig. 7.13).

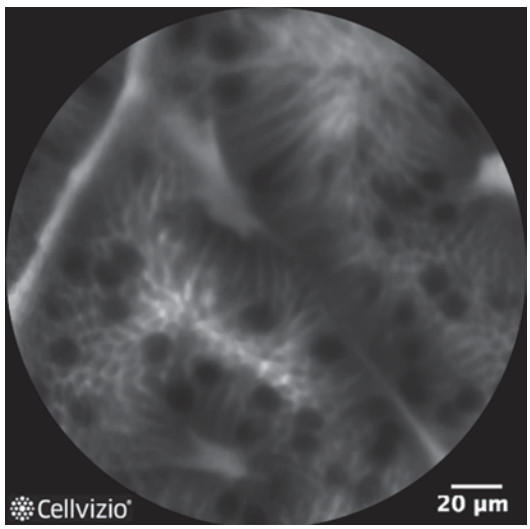

Fig. 7.13 Confocal laser endomicroscopic image of intestinal metaplasia of the esophagus. (Courtesy Mauna Kea Technologies, SA)

CLE is increasingly becoming commonplace in various flexible endoscopy procedures, including upper and lower GI procedures [30], bronchoscopy [31] and the upper and lower urinary tracts [32]. There has also been an emergence of CLE through 19G needles (Fig. 7.14) to access organs such as the pancreas and lymph nodes via the GI tract [33]. An abundance of peer-reviewed publications support CLE's accuracy, easy learning curve, and clinical value across numerous indications.

Like macroscopic optical fluorescence imaging, CLE utilizes fluorescence to visualize tissue microstructure and perfusion including dynamic blood flow, thereby identifying areas suspicious for cancer or other inflammatory conditions; however, in CLE's case, one micron resolution is possible thus providing cellular images on a scale familiar to pathologists. CLE has also been miniaturized sufficiently into highly flexible fiber bundles, or probes, that carry low-powered laser light to illuminate and image the tissue of interest. Currently, these probes range from 0.85 to 2.5 mm in diameter. Today, CLE probes are introduced inside the body via the working channel of almost all flexible endoscopes; however, in the future, they can be optimized for use in numerous surgical applications and delivered through a laparoscope or trocar, via a needle for percutaneous approaches, through the working port of a surgical robotic instrument or even hand-held where appropriate.

With additional hardware and software integration, CLE could become an integral part of a

Fig. 7.14 The confocal laser endomicroscopy probe in a 19-gauge needle. (Courtesy Mauna Kea Technologies, SA)

multimodal imaging approach whereby preoperative and intraoperative imaging could allow for precise tissue mapping and targeting at the microscopic level, thus offering real-time pathologic analysis. This could reduce the need for frozen sections or could significantly improve cytological yields. In addition, it may be possible to correlate the precise location of optical biopsies from one procedure to another.

The advent of the optical biopsy suggests that the interventionalist or surgeon who is acquiring the image and the pathologist who might interpret it will both have a role to play. The interventionalist or surgeon will benefit from the use of sophisticated image-recognition algorithms and embedded databases of known pathologies that will allow them to run a real-time query for images that are similar to the intraoperative image at hand. This ability will aid in the diagnosis and provide valuable guidance and peace of mind. In the case of the pathologist, more precise intraoperative tissue targeting will allow for a more efficient workflow with fewer nonproductive samples. Remote porting of an image will also allow the pathologist to do their evaluations in real-time on their tablet or smartphone while being compliant with a hospital's electronical medical record (EMR) protocol.

Next on the horizon is the ability to add fluorescently labeled molecular markers to the imaging spectrum. These markers could be engineered to bind to a specific cellular pathology and provide real-time, highly sensitive, and specific optical biopsies. This dynamic step will be useful to the physician, and beneficial to the patient while offering potential savings to a healthcare system.

Summary

Technologies and workflows in hybrid ORs are rapidly evolving. The concept of a multidisciplinary approach around an imaging system opens new possibilities in image-guided surgery. Integrated surgical tables, medical technical equipment as well as user interfaces and angiography system design have been modified to address the requirements of an operating theater and will continue to do so. The improved ergonomics as well as new devices create higher acceptance of the imaging technology and will develop into a new environment that support hygienic aspects and flexible usage. What is currently making the hybrid OR a standard of care for cardiovascular surgery will expand into other areas of minimally invasive surgery. In future iterations, dedicated applications will be developed to simplify workflows and to adapt the currently complex user interface made for interventional experts to one more simple and intuitive for the casual user of the system. The future promises true integration of the different and currently isolated systems in the OR including angiography, ultrasound, endoscopy, fusion imaging, information technology (IT) and image integration, a common user interface, navigation, and robotics.

References

1. http://www.ihf-fih.org/content/download/1933/18009/file/Lueder%20F. Clausdorff.pdf.
2. Bonatti J, Vassiliades T, Nifong W, Jakob H, Erbel R, Fosse E, Werkkala K, Sutlic Z, Bartel T, Friedrich G, Kiaii B. How to build a cath-lab operating room. Heart Surg Forum. 2007;10:E344–8 (Accessed 14 April 2014).
3. Nollert G, Wich S. Planning a cardiovascular hybrid OR—the technical point of view. Heart Surg Forum. 2008;12:E125–30.
4. Ten Cate G, Fosse E, Hol PK, Samset E, Bock RW, McKinsey JF, Pearce BJ, Lothert M. Integrating surgery and radiology in one suite: a multicenter study. J Vasc Surg. 2004;40:494–9.
5. http://www.intechopen.com/books/special-topics-in-cardiac-surgery/the-hybrid-operating-room. Accessed 14 April 2014.
6. Tomaszewski R. Planning a better operating room suite: design and implementation strategies for success. Perioper Nursing Clin. 2008;3:43–54.
7. Kalender W, Kyriakou Y. Flat-detector computed tomography (FD-CT). Eur Radiol. 2007;17:2767–79.
8. Strobel N, Meissner O, Boese J, Brunner T, Heigl B, Hoheisel M, Lauritsch G, Nagel M, Pfister M, Rührnschopf EP. Medical radiology, 3D imaging with flat-detector C-arm systems. In: Reiser MF, Takahashi M, Modic M, Becker CR, editors. Multislice CT. Heidelberg: Springer; 2009. p. 33–51.
9. Biasi L, Ali T, Ratnam LA, Morgan R, Loftus I, Thompson M. Intra-operative DynaCT improves technical success of endovascular repair of abdominal aortic aneurysms. J Vasc Surg. 2009;49:288–95.
10. Nozaki T, Iida H, Morii A, Fujiuchi Y, Komiya A, Fuse H. Efficacy of laparoendoscopic single-site biopsy for diagnosis of retroperitoneal tumor of unknown origin. Urol Int. 2013;90(1):95–100.
11. ICRP. The 2007 Recommendations of the International Commission on Radiological Protection. ICRP Publication. Ann. ICRP. 2007;103(37):2–4.
12. Cusma JT, Bell MR, Wondrow MA, Taubel JP, Holmes DR. Real-time measurement of radiation exposure to patients during diagnostic coronary angiography and percutaneous interventional procedures. J Am Coll Cardiol. 1999;33:427–35.
13. Balter S, Hopewell JW, Miller DL, Wagner LK, Zelefsky MJ. Fluoroscopically guided interventional procedures: a review of radiation effects on patients' skin and hair. Radiology. 2010;254:326–41.
14. http://venturebeat.com/2012/07/25/valves-gabe-newell-talks/.
15. Ruppert GC, Reis LO, Amorim PH, de Moraes TF, da Silva JV. Touchless gesture user interface for interactive image visualization in urological surgery. World J Urol. 2012;30(5):687–91.
16. http://techland.time.com/2012/12/10/touchscreens-and-the-myth-of-windows-8-gorilla-arm/.
17. http://en.wikipedia.org/wiki/Skeuomorph. Accessed 14 April 2014.
18. Atkins MS, Tien G, Khan RS, Meneghetti A, Zheng B. What do surgeons see: capturing and synchronizing eye gaze for surgery applications. Surg Innov. 2013;20(3):241–8. http://techland.time.com/2012/12/10/touchscreens-and-the-myth-of-windows-8-gorilla-arm/.
19. Kenngott HG, Wagner M, Gondan M, Nickel F, Nolden M, Fetzer A, Weitz J, Fischer L, Speidel S, Meinzer HP, Böckler D, Büchler MW, Müller-Stich BP. Real-time image guidance in laparoscopic liver surgery: first clinical experience with a guidance system based on intraoperative CT imaging. Surg Endosc. 2014;28(3):933–40. doi: 10.1007/s00464-013-3249-0. Epub 2013 Nov 1.
20. Oktay O, Zhang L, Mansi T, Mountney P, Mewes P, Nicolau S, Soler L, Chefd'hotel C. Biomechanically driven registration of pre- to intra-operative 3D images for laparoscopic surgery. Med Image Comput Comput Assist Interv. 2013;16(PT2):1–9.
21. Figueroa Garcia I, Peyrat J-M, Hamarneh G, Abugharbieh R. Biomechanical kidney model for predicting tumor displacement in the presence of external pressure load. ISBI 2014.
22. Gelalis ID, Paschos NK, Pakos EE, Politis AN, Amatoutoglou CM, Karageorgos AC, Ploumis A, Xenakis TA. Accuracy of pedicle screw placement: a systematic review of prospective in vivo studies comparing free hand, fluoroscopy guidance and navigations techniques. Eur Spine J. 2012;21(2):247–55.
23. Luther N, Iorgulescu JB, Geanette C, Gebhard H, Saleh T, Tsiouris AJ, Haertl R. Comparison of navigated versus non-navigated pedicle screw placement in 260 patients and 1434 screws; screw accuracy, screw size and the complexity of surgery. J Spinal Disord Tech. 2013 Nov 6. [Epub ahead of print].
24. Hughes-Hallett A, Mayer EK, Marcus HJ, Cundy TP, Pratt PJ, Darzi AW, Vale JA. Augmented reality partial nephrectomy: examining the current status and future perspectives. Urology. 2014;83(2):266–73.
25. Stoyanov D, Scarzanella MV, Pratt P, Yang G-Z. Real-time stereo reconstruction in robotically assisted minimally invasive surgery, in Medical Image Computing and Computer-Assisted Intervention MICCAI 2010. (Jiang T, Navab N, Pluim JPW, Viergever MA, editor.), no. 6361 in Lecture Notes in Computer Science, pp. 275–82, Springer, Berlin, Heidelberg, Jan 2010.
26. Teber D, Guven S, Simpfendrfer T, Baumhauer M, Gven EO, Yencilek F, Gzen S, Rassweiler J. Augmented reality: a new tool to improve surgical accuracy during laparoscopic partial nephrectomy? Preliminary in vitro and in vivo results. Eur Urol. 2009;56(2):332–8.
27. Sadik K, Kell M, Gorey T. Minimally invasive parathyroidectomy using surgical sonography. Int J Med Sci. 2011;8(4):283–6.

28. Guidelines for the Use of Laparoscopic Ultrasound. Society of American Gastrointestinal and Endoscopic Surgeons. http://www.sagecms.org.
29. Ren J, Marchlinski F, Callans D, Herrmann H. Clinical use of AcuNav diagnostic ultrasound catheter imaging during left heart radiofrequency ablation and transcatheter closure procedures. J Am Soc Echocardiogr. 2002;15(10 Pt 2):1301–8.
30. Sharma P. et al. Real-time increased detection of neoplastic tissue in Barrett's esophagus with probe-based confocal laser endomicroscopy: final results of a multi-center prospective international randomized controlled trial. GIE, 2011.
31. Thiberville L, et al. Human in-vivo fluorescence microimaging of the alveolar ducts and sacs during bronchoscopy. Eur Respir J. 2009;33(5):974–85.
32. Liu J, et al. Dynamic real-time microscopy of the urinary tract using confocal laser endomicroscopy. Urology. 2011;78(1):225–31.
33. Konda VJA, et al. A pilot study of in vivo identification of pancreatic cystic neoplasms with needle-based confocal laser endomicroscoscopy under endosonographic guidance. Endoscopy. 2013;45(12):1006–13.

Further Reading

Sikkink CJ, Reijnen MM, Zeebregts CJ. The creation of the optimal dedicated endovascular suite. Eur J Vasc Endovasc Surg. 2008;35:198–204.

Tsagakis K, Konorza T, Dohle DS, Kottenberg E, Buck T, Thielmann M, Erbel R, Jakob H. Hybrid operating room concept for combined diagnostics, intervention and surgery in acute type A dissection. Eur J Cardiothorac Surg. 2013;43:397–404.

Kpodonu J. Hybrid cardiovascular suite: the operating room of the future. J Card Surg. 2010;25:704–9.

Brozzi NA, Roselli EE. Endovascular therapy for thoracic aortic aneurysms: state of the art in 2012. Curr Treat Options Cardiovasc Med. 2012;14:149–63.

Reed AB. Advances in the endovascular management of acute injury. Perspect Vasc Surg Endovasc Ther. 2011;23:58–63.

Cerenkov Luminescence Imaging

8

Jan Grimm

Introduction

Cerenkov light is generated when charged particles (either positrons, electrons, or alpha particles) travel through a dielectric medium faster than the (phase) velocity of light in that medium (Fig. 8.1a). This light is polarized and has a continuous spectrum, peaking in the ultraviolet (UV) and blue area of the spectrum (Fig. 8.1b). It is most commonly observed as the blue glow in the water coolant of nuclear reactors and their cooling basins and was probably first noted by Madame Curie in her autobiography [1]. This *Cerenkov effect* was first scientifically described in 1934 [2], when Pavel Alekseyevich Cerenkov was a researcher at the Lebedev Institute of Physics in Moscow, one of the leading research institutes in Physics in the former USSR. Cerenkov was a postgraduate student in Sergei Ivanovich Vavilov's laboratory, where his project was to study the luminescence of uranyl salt solutions under irradiation by an underlying radium source. Vavilov was a renowned expert on luminescence phenomena. However, Cerenkov soon found out that even simple solvents like water experienced a weak blue glow of light under irradiation [3]. In his chapter in the same edition of the journal, Vavilov, Cerenkov's mentor, reasoned that the blue glow was caused by electrons generated by the highly energetic gamma-rays from the radium [4]. The theoretic background of the Cerenkov effect was established in 1937 by Ilya Frank and Igor Tamm [5]. The equation named after both physicist allows calculating the number of Cerenkov photons produced along the particle's path over a specified region of the light spectrum. Subsequently, all three physicists shared the Nobel Prize for Physics in 1958.

Physical Background

Charged particles traveling faster than the speed of light in a medium transfer their kinetic energy through interactions with the surrounding material, in biological tissues mostly with water. The randomly oriented water molecules will align with the passing charged particle. If this particle is traveling faster than the speed of light in that medium, the water molecules relax by releasing the transferred energy in the form of luminescence [2].

However, how can a particle travel faster than the speed of light? We all learned that according to Einstein's theory of relativity nothing can travel faster than the speed of light! The speed of light in a medium depends on its refractive index. In a medium with a refractive index of x the speed of light 1/x-times the speed of light in vacuum. Therefore, in water—which has a refractive

J. Grimm (✉)
Molecular Pharmacology and Chemistry and Department of Radiology, Memorial Sloan-Kettering Cancer Center, New York, 1275 York Avenue NY 10021, USA
e-mail: grimmj@mskcc.org

Y. Fong et al. (eds.), *Imaging and Visualization in The Modern Operating Room,*
DOI 10.1007/978-1-4939-2326-7_8, © Springer Science+Business Media New York 2015

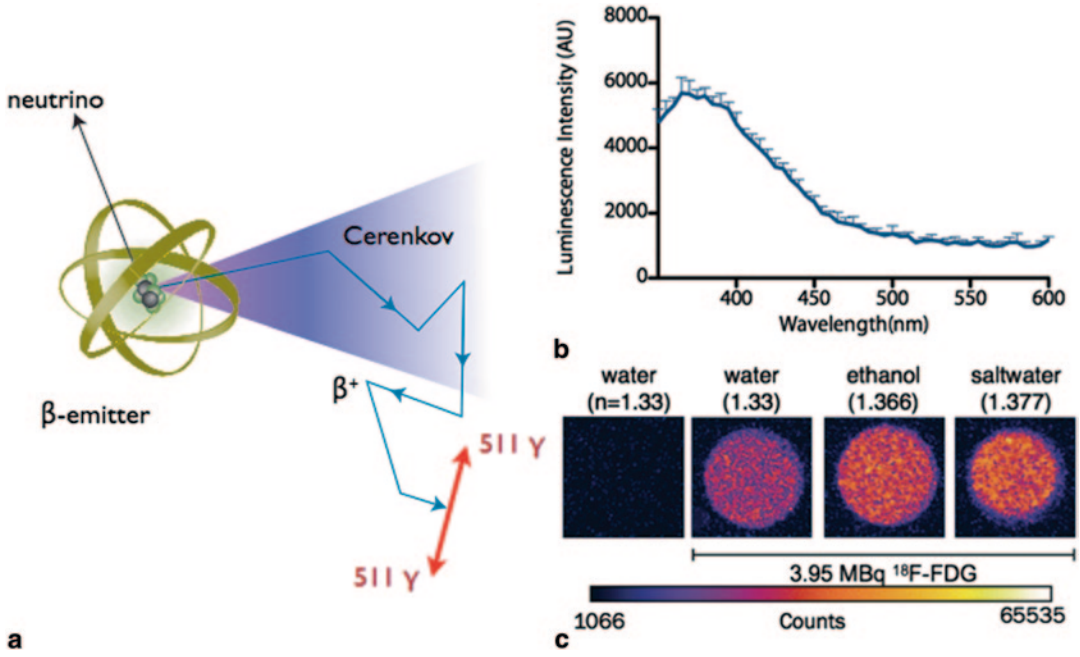

Fig. 8.1 Cerenkov light and characteristics. **a** Cerenkov radiation (CR) is produced by a charged particle traveling through a dialectric medium faster than the speed of light (in that medium). **b** Relaxation of the molecules in the medium, polarized by the passage of the charged particle, produces visible light weighted towards the higher energy of the spectrum (UV/*blue*) and dropping towards the *red* part of the spectrum. The profile of the CR is centered at the *blue*, as shown with ^{68}Ga (18.5 MBq) in 0.1 M HCl diluted in water, using a Molecular Diagnostics M5 spectrophotometer. **c** Equal activity concentration of ^{18}F samples (3.952 MBq in 20 µL) were diluted in 2 mL of water (H_2O, refractive index: $n = 1.3359$), ethanol (C2H5OH, $n = 1.366$), saltwater (H_2O and saturating NaCl, $n = 1.377$) along with a control sample of water without ^{18}F-FDG. Higher Cerenkov luminescence (CL) intensity is seen in medium with higher refractive index. (**b** and **c** with permission from [37])

index of 1.33—the speed of light is only ~3/4 of its value in vacuum. In water, the threshold for the production of Cerenkov kinetic energy for an electron is 0.263 MeV and in tissue, where the refractive index is slightly higher, this threshold is therefore also slightly lower, ca. 0.21–0.24 MeV [6]. The vast majority of positron-emitting radiotracers for positron emission tomography (PET) has kinetic energies significantly higher than the threshold in tissue and are therefore suitable Cerenkov luminescence (CL) producers [7, 8]. This also implies that a medium with a higher refractive index provides more Cerenkov light (Fig. 8.1c).

The higher the kinetic energy of a particle is, the further it travels and the higher the intensity of the emitted CL; its spectral characteristics though does not change. For typical PET studies in mice, 100 µCi of ^{18}F-labelled radiotracers would produce a total of ca. 9×10^6 photons/s. A similar activity of the therapeutic radiotracer ^{90}Y would generate approximately 250×10^6 photons/s [6]. Since its electrons are more energetic, they also travel further until they loose enough energy to drop under the kinetic threshold, therefore the footprint of the light is ca. six-times larger, which results in a decreased resolution [6]. Isotopes that generate higher energetic particles have a stronger CL intensity but this comes at the cost of a decreasing resolution (Fig. 8.2).

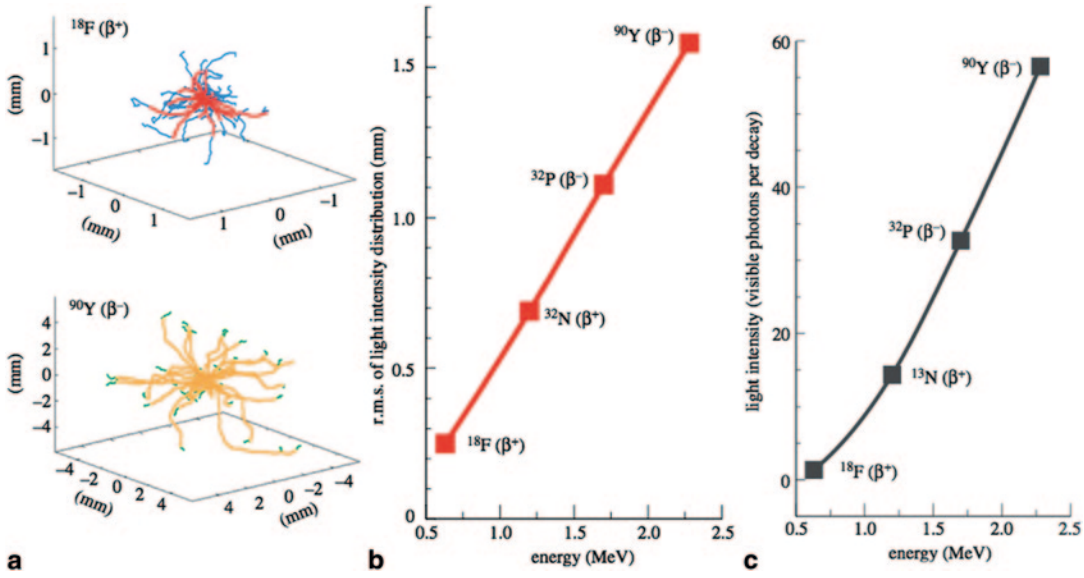

Fig. 8.2 **a** Monte Carlo simulation of several β-particle tracks emanating from a point source of ^{18}F (*top*) and ^{90}Y (*bottom*) in water. Note the different spatial scales for clarity. The change in color in the tracks indicates the location at which the energy of the β-particle drops below the Cerenkov kinetic threshold. **b** Simulation results showing the predicted spatial distribution (root mean spare (r. m. s.) spread) in Cerenkov light production as a function of the β-particle endpoint energy. **c** Simulation results showing the predicted photon yield per decay in water (in the wavelength range 400–800 nm) as a function of the particles endpoint kinetic energy for four clinical radionuclides. (With permission from [6])

Preclinical Applications

Cerenkov light has been utilized for a long time in physics, e.g., to gauge the fuel status in a nuclear reactor or to detect cosmic particles either through generation of CL in large sub terrain water basins or even in the atmosphere itself. Its transition into biological sciences began with a brief report in Nature, describing 1971 the measurement of ^{32}P for radiotherapy in the eye, generating CL in the vitreous body [9], following descriptions of flashes seen by astronauts of the Apollo 11, 12 and 13 missions travelling to and from the moon, caused by cosmic particles passing through the vitreous humor of the eye [10]. However, only as recently as 2009 Robertson et al. described the dedicated optical imaging of ^{18}F-FDG in a tumor-bearing mouse, attributing the signal to Cerenkov light originating from the ^{18}F-FDG's positrons. Since then, Cerenkov luminescence imaging (CLI) has quickly emerged as a valuable preclinical molecular imaging modality, and many new applications of CLI in preclinical research described the utilization of Cerenkov with different radiotracers [7, 8, 11]. Several groups have shown that CLI is a powerful tool in cancer research, for example to monitor tumor therapy [12, 13], to image gene expression [14−16] or to monitor radiotherapy with radiolabeled peptides [17]. Especially in the context of radiotherapy CLI is particularly interesting as it is able to image the otherwise un-imageable isotopes with electron or even alpha particle emission [7, 8], which are particularly suited for CLI due to the high kinetic energy of the particles [6]. However, the mass of alpha particles would require too much kinetic energy to reach the kinetic threshold, which makes them unsuitable for CLI in biomedical applications. Observed CL from, e.g., ^{225}Ac is probably derived from short-lived, beta-emitting daughter nuclides [8].

Cerenkov Luminescence for Intraoperative Imaging

Visual inspection and manual palpation are the main means to identify tumors during surgery. Imaging methods to improve visualization of tumor deposits during surgery is expected to lead to a more efficient tumor surgery with improved outcome and postsurgical management. Current technologies for image-guided cancer surgery use mainly optical imaging, which has been considered for intraoperative approaches since the original use of fluorescein in 1947 [18] but still remains mostly experimental. Camera systems are continuously being improved and explored in the clinic, mostly with either fluorescein or indiocyanine green [19, 20]. The costly regulatory requirements to approve fluorescent agents though resulted in a lack of clinically approved optical agents and therefore in a slow clinical translation of optical modalities. Only recently has a first preliminary clinical study with a targeted fluorescent agent been published [21]. On the other hand, nuclear medicine has long enjoyed a wide variety of clinically used tracers. Intraoperative use of radiotracers is done frequently in oncological surgery today using hand-held detectors to identify tumors, both with radiolabeled antibodies [22] or with ^{18}F-FDG [23]. Radiotracers have also been used for interventional procedures with PET, guiding the radiologist to the metabolically active part of the lesion instead of a necrotic area [24, 25]. In fact, intraoperative use of radiotracers is the gold standard for sentinel node detection, using ^{99m}Tc-preparations and hand-held detectors [26, 27]. However, these hand-held probes only produce an audible signal. Portable gamma cameras require an iodine seed pointer for exact localization [28, 29] and are not well suitable for imaging the 511 keV photons emitted by PET tracers [30]. CLI provides the opportunity to utilize existing clinical radiotracers with optical imaging methods for intraoperative optical imaging, merging nuclear and optical imaging. CLI combines the benefits of optical imaging (low cost instrumentation, high spatiotemporal resolution) with advantages of PET tracers (widespread availability of clinically used targeted agents).

Subsequently, first animal studies were performed to explore CLI in intraoperative imaging. We demonstrated the use of CLI from ^{89}Zr-herceptin in open surgery to visualize a subcutaneously implanted HER2/neu-positive tumor [31]. The tumor could be delineated clearly and differentiated from it HER2/neu-negative counterpart (Fig. 8.3). After exposing the tumor through skin incision and retraction its CL signal increased ~10%. This increased radiance is due to decreased attenuation and scattering by removal of the skin. After removal of the tumor no optical signal was detected from the tumor bed in the mouse as the CL translocated with the excised tumor mass (placed in the upper left corner). After closing the postoperative CLI showed again no significant signal from the tumor bed. The entire procedure, including surgical resection and acquisition of all images, was completed in 40 min. Another study demonstrated the utilization of CLI to aid in the resection of sentinel lymph nodes [32]. After intradermal injection of ^{18}F-FDG the sacral node can be seen after removal of the skin (i.e., in an intraoperative setting), before any further surgical exposure through the overlying musculature (Fig. 8.4). The resected node demonstrates CL and therefore confirms the lymphatic nature of the tissue.

The group in Stanford University demonstrated the possibility of CL endoscopy [33, 34] for minimally invasive surgical resection, using a prototype system. This system couples an optical fiber bundle to a highly sensitive intensified charge-coupled device (CCD) camera. This system, with a resolution of 1.2 mm, was able to differentiate a minimum of approximately 45 kBq (1.21 μCi) of ^{18}F-FDG in a phantom from the noise background with a 5 min acquisition time [33]. In a proof-of-concept study, it was then used to visualize uptake of ^{18}F-FDG in a C6 glioma xenograft and to track tumor excision (Fig. 8.5). Just recently, a group in China reported on the first human endoscopic Cerenkov luminescence imaging system [50]

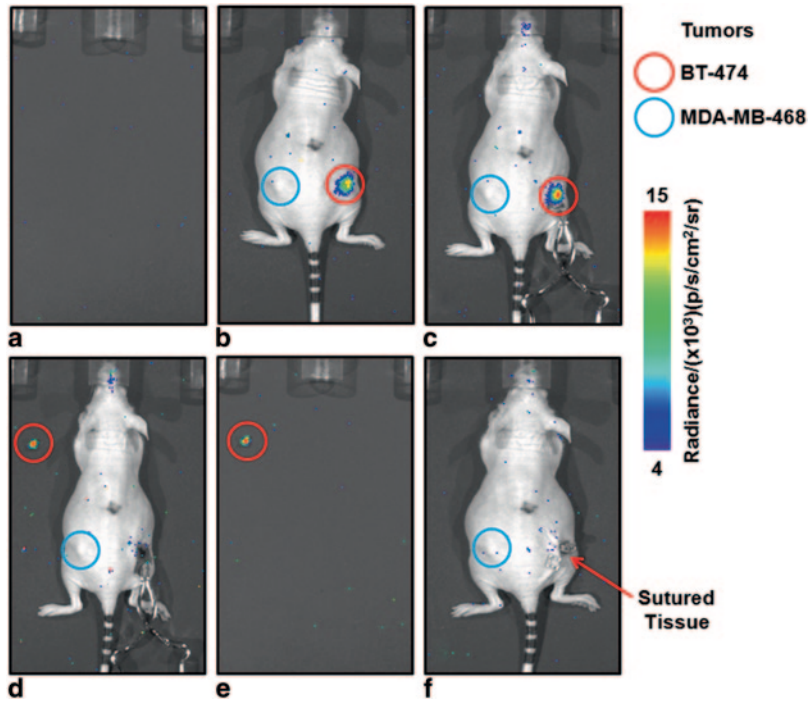

Fig. 8.3 Intraoperative CLI for surgical resection of the BT-474 (HER2/neu positive) tumor at 144 h postadministration of ^{89}Zr-DFO-trastuzumab. **a** Background CLI of the scanner stage recorded immediately prior to commencing surgery. **b** Preoperative CLI prior to surgical incision. **c** Intraoperative CLI of the exposed tumor immediately prior to resection. Note the increased intensity of the CLI signal owing to reduced attenuation and scattering from removal of the skin. **d** Resected tumor (put in the *upper left corner*) and exposed surgical site showing the complete removal of CL. **e** CLI of the excised BT-474 tumor alone. **f** Postoperative CLI after closing the incision site with sutures. All CLIs are shown at the same radiance scale for direct quantitative comparison. (With permission from [31])

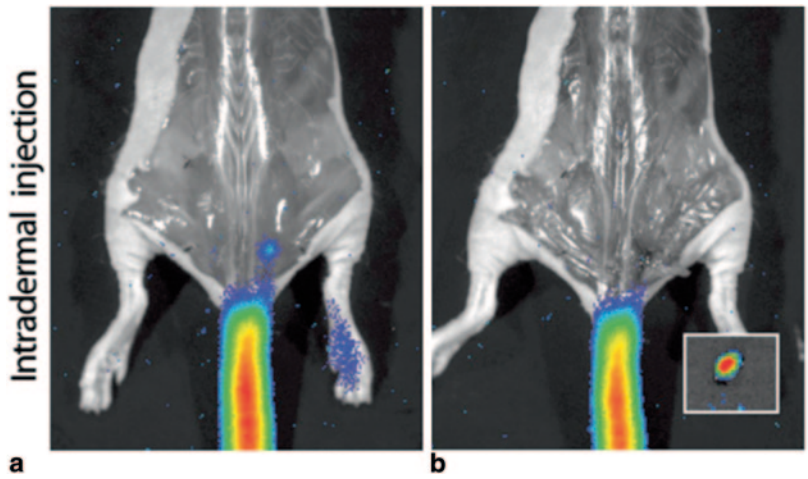

Fig. 8.4 Cerenkov-guided surgical resection of sentinel lymph node, 10 min after intradermal injection of ^{18}F-FDG into the tail with surgical resection. **a** Lateral-tail intradermal injection yields greater uptake in one sacral node, seen with just skin removed but still overlying musculature. **b** CLI guides resection of node, excised specimen magnified in inset. (With permission from [32])

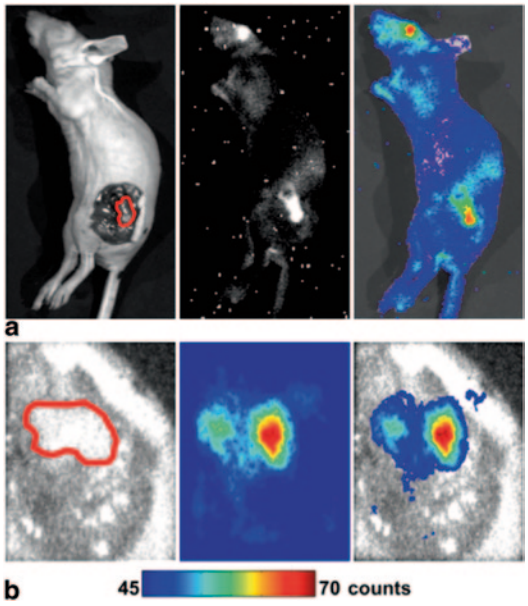

Fig. 8.5 A mouse bearing a C6 glioma xenograft after tail-vein administration of 37 MBq (1 mCi) of ^{18}F-FDG. **a** CLI with commercially available optical IVIS system and **b** CLI with prototype fiber-system. Tumor tissues are outlined by *red* lines. Ambient-light images are on *left*, luminescent images are in *middle*, and fused images are on *right*. (With permission from [33])

Advantages of Cerenkov Imaging for Intraoperative Imaging

CLI combines the benefits of optical imaging (low cost instrumentation, high spatiotemporal resolution) with advantages of radiotracers (proven safety, widespread availability of clinically used targeted agents). It provides the opportunity to utilize approved radiotracers for optical imaging, circumventing the requirement for lengthy approval processes required for fluorescent imaging agents. Radiotracers for intraoperative *optical* imaging will likely not require additional FDA approval and are therefore rapidly available for intraoperative usage if a new promising target and binding moiety become available. Unlike fluorescent imaging, the positron decay of the radiotracer allows for true multimodality imaging with PET and optical imaging (Fig. 8.6). This opens the way for a one-shop approach with a presurgical PET scan, followed by the actual CLI-guided surgery and also a postsurgical follow up scan, all with the same clinical approved radiotracer (Fig. 8.7).

An important issue for intraoperative imaging is the detection of lesions that are localized too deep to be visualized with fluorescence optical imaging. If radiotracers are used for intraoperative detection a hand-held detector can always be used to guide the surgeon to deeper tumor deposits, to complement CLI of superficial tumors (Fig. 8.8a). To provide this opportunity with fluorescent agents requires chemical modifications such as attaching a radiotracer to the fluorochrome. However, this invariably changes the properties of the agent: its size, charge, and therefore biodistribution will be different with implications for the approval for clinical use [35].

Since a positron emitter can be always detected and quantified with PET imaging a unique internal quantitative standard is available. Based on the uptake determined with PET (from the standard uptake value) and the Frank-Tamm equation the amount of CLI generated by the radiotracer can be calculated and compared with the actual measurement. The result can be used to correct, e.g., for the tissue absorption of the light or to calculate activation of the probe (see below) [36]. Fluorochromes do not provide such an inherent internal standard for absolute quantification.

Standard fluorescence imaging requires excitation through an external excitation source, either a LED, Laser, or high-intensity lamp with a filter to provide the correct excitation wavelength. Since the intensity of the excitation light can be strong the resulting fluorescent signal is high as well, allowing for live imaging under ambient lighting. At the same time, the incident light though causes autofluorescence and can be backscattered into the camera (Fig. 8.8b), both degrading the quality of the fluorescent signal and requiring additional filtering or postprocessing to correct for this image degradation [21, 36]. This is not the case for CL, where no excitation light is required and the Cerenkov light can actually be used to excite fluorochromes for advanced Cerenkov imaging (see below), which increases the signal-to-noise ratio [36] albeit at a much lower signal intensity.

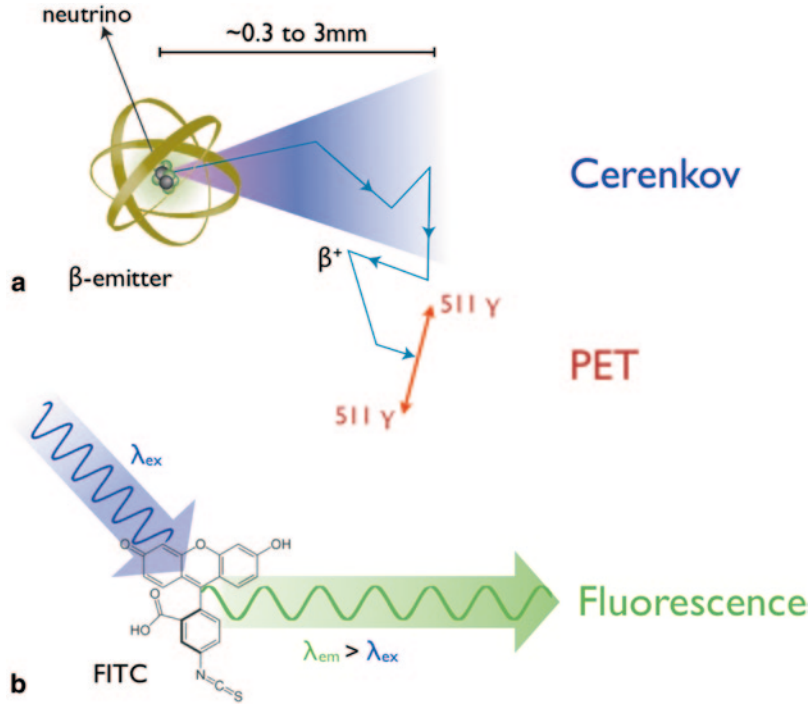

Fig. 8.6 **a** Cerenkov imaging allows for both optical Cerenkov imaging as well as quantitative PET imaging. The radioactivity provides the opportunity for an internal standard, for additional imaging and for additional intraoperative detection of the radiotracer through the decay signal of either detecting the β-particle or the annihilation photons. **b** Fluorescence requires an external excitation light (λ_{ex}), which induces the fluorescence emission (λ_{em}), shifted to a longer wavelength. Unlike for radiotracers, no additional quantitative signal can be detected

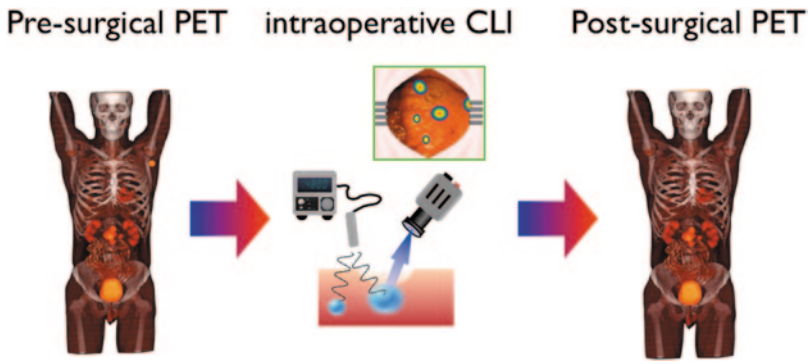

Fig. 8.7 One-stop approach using intraoperative imaging with radiotracers and CLI. Presurgical PET imaging, intraoperative imaging and postsurgical PET monitoring can be done with the same radiotracer, which allows also for detection of deeper lesions using hand-held probes. This cannot be achieved with fluorescence imaging without modification of the imaging probe

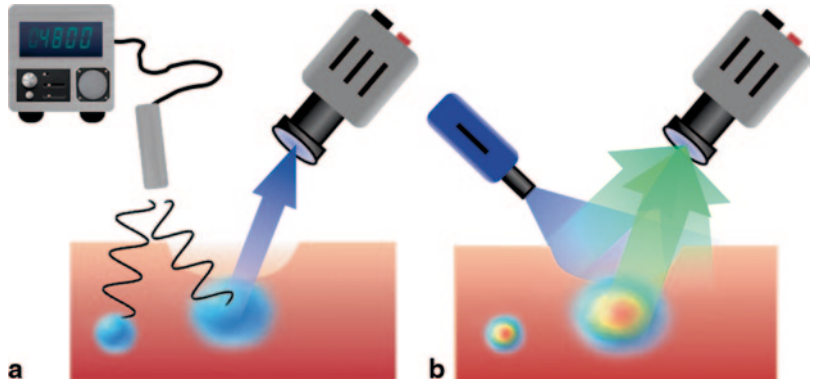

Fig. 8.8 **a** Intraoperative imaging with CLI allows not only for optical CLI but also for additional detection of deeper lesions with hand-held probes or gamma cameras. **b** Fluorescence imaging requires excitation through an external excitation source. The strong intensity of the excitation allows for live imaging under ambient lighting. At the same time the incident light though causes autofluorescence and can be backscattered into the camera, both degrading the quality of the fluorescent signal and requiring additional filtering or post-processing to correct for this image degradation, which is certainly achieved with modern systems. Deeper lesions can be overlooked as they are not reached by the excitation light

Another benefit of intraoperative CLI, be it either minimal invasive or for open surgery with direct visualization, is that it provides at the tissue surface higher spatial resolution than even the better nuclear imaging modalities (here small-animal PET imaging) (Fig. 8.9). The signal is detected with a CCD chip, which provides a much higher resolution than any nuclear imaging systems [33, 36].

Challenges of Intraoperative CLI

Mitchell et al. calculated with the Frank-Tamm equation the number of optical (400–800 nm) photons produced for a number of different medical isotopes [6]. At the low end ^{18}F generated on average 1.4 photons per individual decay while ^{90}Y at the high-end generated 57 photons/decay. This means that the amount of Cerenkov light is very low, in the order of at least ten-times less than for bioluminescence imaging. Therefore, longer imaging times (several minutes) and highly sensitive cameras with high aperture lenses are required. Luckily, these are already available and probably constitute the most widely used imaging devices: scanner for bioluminescence imaging. These devices have a highly sensitive and usually cooled camera for highest sensitivity and lowest noise and are mounted for preclinical imaging on a black box to shield all interfering ambient light [37]. Any ambient light will be stronger than the CL, threatening to overpower the weak CL signal, so great care must be taken to exclude as much ambient light as possible. For example, the ambient light in an operating room will be at least one billion time brighter than the CL in the surgical field (Table 8.1). This includes also removing otherwise inconspicuous items from the field of view that can interfere with the signal by luminescence (in our experience, e.g., white 96-well plates transferred from the lab to a Cerenkov imager can destroy the signal with luminescence of the plate detected by the sensitive cameras). Furthermore, Cerenkov light is predominantly in the UV to blue range with its spectrum continuously decreasing towards the red side of the spectrum. Therefore, it is far away from the near-infrared window for optimal in vivo optical imaging [38]. However, the Cerenkov light-exiting tissue is mostly in the penetrating and less absorbed part of the Cerenkov spectrum further to the red [39].

To exclude ambient light, Cerenkov endoscopy is a possible good solution since ambient light is naturally excluded. However, since CL has very low-signal intensity, care must be taken

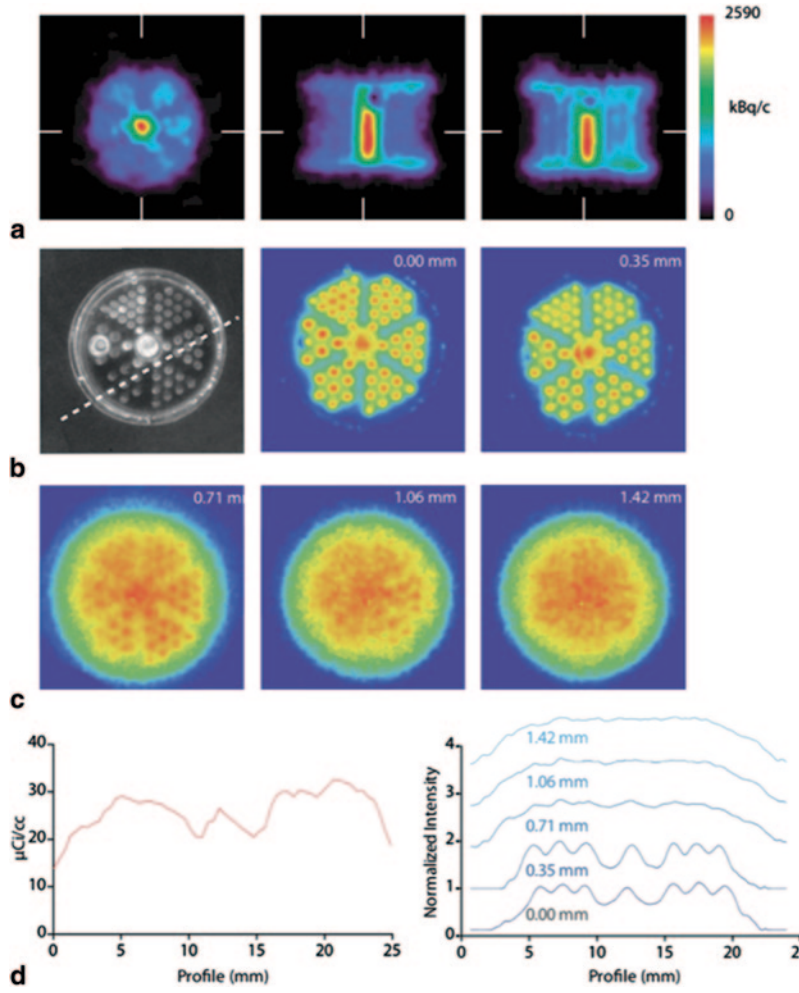

Fig. 8.9 PET and Cerenkov surface resolution on a Jaczeck phantom. **a** PET image of ^{68}Ga (240 μCi; 8.88 MBq). The diameter of the rods in the phantom is 1.0–1.5 mm, in 0.1 mm increments. Small-animal PET possesses a greater resolving power than that of clinical systems but is unable to resolve the individual rods. **b** White light and CLI of the phantom, under increasing depths of a tissue scattering and absorbing mimic. The phantom rods are clearly distinguishable at the surface but details are getting lost with increasing depth over 1 mm. **c** Line profile across the phantom (*dashed line* on photograph) of the PET (*left*) and CLI (*right*) acquisitions. The plots reveal that the surface resolution of Cerenkov radiation can sufficiently distinguish millimeter-width sites of uptake, which cannot be clearly resolved by PET. (With permission from [36])

Table 8.1 Cerenkov intensity compared to other light sources, given in power, illuminance, irradiance and the subsequent reduction of ambient light required. (Courtesy of Lightpoint Medical Ltd)

	Power W/cm^2	Illuminance lux	Irradiance p/s/cm^2	Required reduction
Bright sunlight	1.00E-01	100,000	2.8E+17	3.E+13
Overcast	4.00E-02	40,000	1.1E+17	1.E+13
Operating theatre—bright	5.00E-04	500	1.4E+15	1.E+11
Operating theatre—dim	5.00E-06	5	1.4E+13	1.E+09
0.5 mW green LED over 1 m^2	2.50E-08	0.17	6.9E+10	7.E+06
Cerenkov	3.60E-15	3.60E−09	1.0E+04	1.E+00

to collect as many CL photons as possible. Therefore, wide aperture lenses are best (numerical aperture of 0.5 or even higher) but unfortunately typical apertures of endoscopes are much lower (0.2 or even lower) with significant loss of signal over the length of the scope, therefore being less than optimal for CL [34]. In their study, Liu et al. concluded that if their endoscopic system would be used for tumors of the oropharynx 2.1 GBq (54 mCi) of ^{18}F-FDG would have to be injected into a 70-kg patient to achieve enough activity to visualize a 300-mg tumor within 5 min acquisition time [33]. Scintillation in the fibers from incident annihilation photons of 511 keV can additionally cause undesired background signal. Increased sensitivity may be achieved by using fibers optimized for CL.

Besides the very low signal and the less-than-optimal spectrum of Cerenkov light, another concern often voiced is one of the exposures to radioactivity for both patient and personnel. However, the radiation doses that would typically be used for intraoperative Cerenkov imaging are considered a trivial risk according to international standards [40]. Based on dosimetry results from intraoperative use of ^{18}F-FDG [41], the exposure to the surgeon from a 1-h CLI procedure is estimated to be 5–10 microSv, comparable to 1/10th the dose of a transatlantic flight. Lymphoscintigraphy for intraoperative detection of sentinel lymph nodes with ^{99m}Tc-sulfacolloid is standard of care, e.g., in uterine cancer [42], melanoma [43] or breast cancer [27]. ^{18}F-FDG has been used to identify primary tumors during surgery, both with radiolabeled antibodies [22] or with ^{18}F-FDG [23]. In recent ^{18}F-FDG PET/CT-guided biopsies, the operator dose was not significantly different from typical doses from fluoroscopically guided surgical procedures [24, 25], used all over the world and not discussed as a significant risk. In a study at our institution [41], intraoperative injection of 15–20 mCi ^{18}F-FDG resulted in doses between 0.4 and 1.6% of the annual whole-body occupational dose limit (50 mSv). For the patient, it would be the dose of one additional PET scan without the CT part, so even less than one diagnostic study. Therefore, the radioactive exposure from studies that would use CLI for intraoperative guidance are not prohibitive.

Clinical Cerenkov Imaging

Given the above-mentioned challenges, the possibility of clinical translation of Cerenkov imaging seemed poor. However, we demonstrated the first clinical Cerenkov images from several patients receiving standard dosages of ^{18}F-FDG for routine clinical PET/CT imaging [44]. In this study, we demonstrated a significant difference ($p=0.02$) between the Cerenkov emissions from PET-positive lymph nodes and the contralateral normal side (Fig. 8.10). CL was detected in lymph

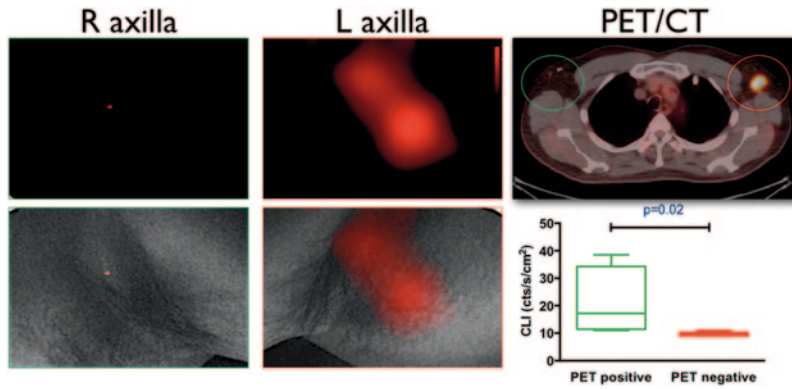

Fig. 8.10 Representative CL and PET/CT images of ^{18}F-FDG–positive *left* axillary lymph node in a lymphoma patient. Negative CLI of *right* axilla without ^{18}F-FDG–positive lymph node. No significant CL emission from ^{18}F-FDG decay is seen on the *right*. Both CLI overlaid with white-light photograph in the *lower row*. The CL signal colocalized with positive PET/CT findings. (With permission from [44])

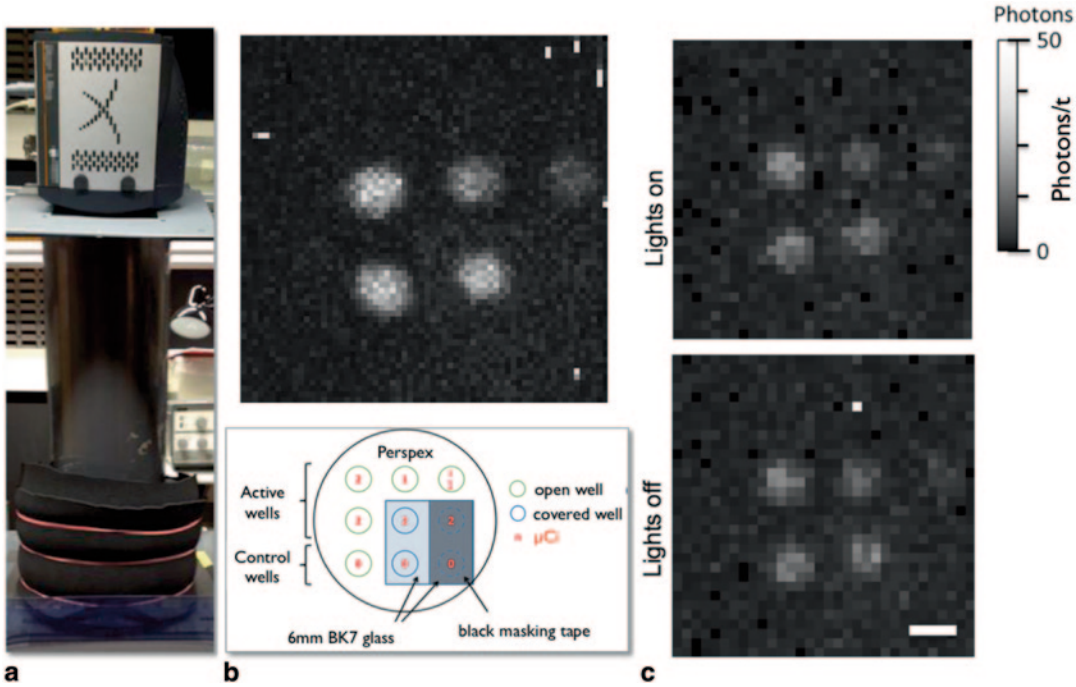

Fig. 8.11 CLI at ambient lighting with Lightpoint's prototype system. **a** Setup with emCCD camera and optical drape, excluding the room light. **b** Acquisition of as little as 0.8 μCi/ml in a phantom with 0.73 mm resolution in 50 s. **c** With higher binning acquisition in 5 s is possible; with or without room lights on (Courtesy of Lightpoint Medical Ltd.)

nodes from patients with lymphoma or nodal metastases with local activity as low as 0.05 MBq/mL (0.03–0.3 MBq/mL; median, 0.05 MBq), equivalent to 0.01 % injected dose of ^{18}F-FDG localizing to lymph nodes 1.6 ± 0.5 cm under the skin. In another study, Cerenkov imaging was reported from one patient undergoing ^{131}I therapy for Graves disease [45]. These two studies demonstrate the feasibility of clinical CLI.

Critical barriers had to be overcome for the clinical translation of CLI: (1) achieving sufficient sensitivity and (2) blocking ambient light from the field of view. This was achieved in the two clinical studies by using dark and windowless rooms with additional shielding of the patients [44, 45]. However, achieving this in an operating room constitutes yet another challenge. A first step towards its realization is a novel CLI fiberscope under development by the start-up company Lightpoint Medical Inc. (Cardinal Point UK; in the USA: Lightpoint Medical, LLC in Cambridge, MA). The Lightpoint CLI system is a lens mounted on a flexible, coherent fiber bundle optimized for CL that relays the signal to an ultrasensitive emCCD camera. The device will combine the maneuverability of a small hand-held device with the signal performance of an ultrasensitive camera. It addresses the technical challenges currently faced by CLI through an emCCD optimized for CL and it excludes ambient light in the operating room with a specialized optical drape. The system is designed to perform simultaneous white light and CL imaging through time-multiplexing, which allows for continuous monitoring of the surgical field and motion correction. Lightpoint has a technical proof-of-concept prototype for the system, demonstrating CLI under ambient light (Fig. 8.11). Importantly, the challenges faced are of a technical nature that will be easier to address with progressing technology while no new imaging agents have to be created. Just recently, a first endoscopic Cerenkov study in humans has been reported [50].

Advanced CLI

CLI can also be utilized as the internal excitation source for fluorochromes, effectively now merging fluorescence and Cerenkov imaging. This has been achieved with quantum dots [46, 47] and fluorochromes [36]. For example, Liu et al. used in an example of multiplexing three different types of quantum dots (QD) mixed with [^{131}I]-NaI and recorded with different filters three separate emission peaks in phantoms and mice, corresponding to the characteristic emissions of these QDs [47]. Expanding this concept, targeted and activatable fluorescent probes excited by CL were created for an approach we termed *Secondary Cerenkov-induced Fluorescence Imaging* (SCIFI) [36] SCIFI allowed to utilize targeted quantum dots in conjunction with ^{18}F-FDG as excitation source to image two molecular information, metabolic activity through ^{18}F-FDG and integrin expression through the targeted QDs, excited by the ^{18}F-FDG. As the first radioactive-decay-based activatable imaging agents gold nanoparticles (AuNP) were conjugated to a fluorescein (FAM) with a peptide linker cleavable by metallopeptidase-2 (MMP-2), which is expressed in more aggressive tumors. The FAM fluorescence was quenched by the AuNp in the native state of the agent. Once the linking peptide was cleaved by MMP-2, the FAM was released and its fluorescence, excited by ^{18}F-FDG's Cerenkov emission was recovered, thus indicating MMP-2 activity (Fig. 8.12). Recently, we described the quenching of CL by iron oxide nanoparticles or vital blue dyes as additional mechanism for modulating a Cerenkov signal [48]. These strategies can lead to further interesting applications of CL for intraoperative imaging, especially since the

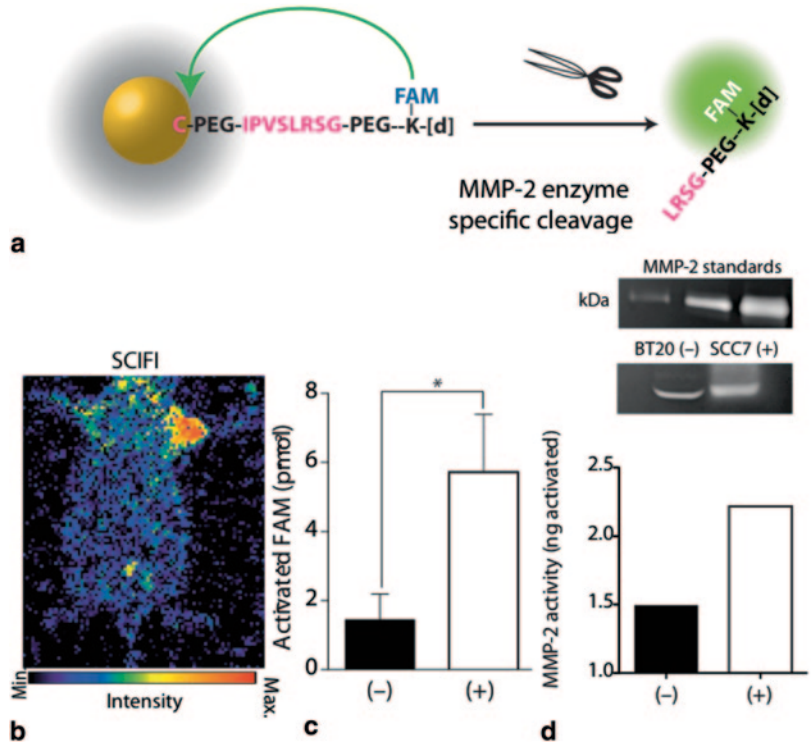

Fig. 8.12 Advanced Cerenkov imaging sensing MMP-2 activity. **a** Scheme of the system: FAM is coupled with a gold nanoparticle via a MMP-2 cleavable linker; close to the nanoparticle the FAM does not fluoresce. **b** SCIFI image showing MMP signal from the MMP expressing tumor on the *right* shoulder but not from the MMP-negative tumor in the *left* shoulder. **c** SCIFI quantification of activated probe and **d** Zymography from the tumors correspond very well. (With permission from [49])

clinically approved fluorescein is due to its excitation wavelength in the blue range ideally suited for SCIFI. It is therefore foreseeable to combine intraoperative CLI with fluorescence imaging and harvest the combined power of CL, fluorescence and nuclear imaging.

Conclusion

Overall the future for CL is bright even though its signal intensity is rather dim. It merges nuclear and optical imaging and allows utilizing the wide variety of approved radiotracers for optical imaging. Challenges to CLI such as low-signal intensity and the blue signal have already been overcome in clinical imaging, and further technical developments will lead this technology from the verge of clinical applications to a new modality for intraoperative imaging, mostly in oncology and probably complimentary to the existing fluorescent techniques.

Acknowledgements: This work and JG was partially supported by funding from the NIH NIBIB and NCI (NIH R01EB014944 and R01CA183953)

References

1. L'Annunziata MF. Radioactivity: introduction and history. 1st edn. Oxford: Elsevier; 2007.
2. Cerenkov PA. Visible emission of clean liquids by action of gamma-radiation. C R Dokl Akad Nauk SSSR. 1934;2:451–4.
3. Bolotovskii BM. Vavilov-Cherenkov radiation: its discovery and application. Phys Uspekhi. 2009;52(11):1099–110.
4. Vavilov SI. On the possible causes of blue gamma-glow in liquids. C R Dokl Akad Nauk SSSR. 1934;2(8):457.
5. Frank I, Tamm I. Coherent visible radiation of fast electrons passing through matter. Compt Rend Dokl Akad Mauk SSSR. 1937;14:109–14.
6. Mitchell GS, Gill RK, Boucher DL, Li C, Cherry SR. In vivo Cerenkov luminescence imaging: a new tool for molecular imaging. Philos Trans A Math Phys Eng Sci. 2011;369(1955):4605–19.
7. Liu H, Ren G, Miao Z, et al. Molecular optical imaging with radioactive probes. PLoS One. 2010;5(3):e9470.
8. Ruggiero A, Holland JP, Lewis JS, Grimm J. Cerenkov luminescence imaging of medical isotopes. J Nucl Med. 2010;51(7):1123–30.
9. Burch WM. Cerenkov light from 32 P as an aid to diagnosis of eye tumours. Nature. 1971;234(5328):358.
10. Fazio GG, Jelley JV, Charman WN. Generation of Cherenkov light flashes by cosmic radiation within the eyes of the Apollo astronauts. Nature. 1970;228(5268):260–4.
11. Boschi F, Calderan L, D'Ambrosio D, et al. In vivo 18F-FDG tumour uptake measurements in small animals using Cerenkov radiation. Eur J Nucl Med Mol Imaging. 2011;(38):120–7
12. Robertson R, Germanos MS, Manfredi MG, Smith PG, Silva MD. Multimodal imaging with (18)F-FDG PET and Cerenkov luminescence imaging after MLN4924 treatment in a human lymphoma xenograft model. J Nucl Med. 2011;52(11):1764–9.
13. Xu Y, Chang E, Liu H, Jiang H, Gambhir SS, Cheng Z. Proof-of-concept study of monitoring cancer drug therapy with Cerenkov luminescence imaging. J Nucl Med. 2012;53(2):312–7.
14. Jeong SY, Hwang MH, Kim JE, et al. Combined Cerenkov luminescence and nuclear imaging of radioiodine in the thyroid gland and thyroid cancer cells expressing sodium iodide symporter: initial feasibility study. Endocr J. 2011;58(7):575–83.
15. Wolfs E, Holvoet B, Gijsbers R, et al. Optimization of multimodal imaging of mesenchymal stem cells using the human sodium iodide symporter for PET and Cerenkov luminescence imaging. PLoS One. 2014;9(4):e94833.
16. Yang W, Qin W, Hu Z, et al. Comparison of Cerenkov luminescence imaging (CLI) and gamma camera imaging for visualization of let-7 expression in lung adenocarcinoma A549 Cells. Nucl Med Biol. 2012;39(7):948–53.
17. Zhang J, Hu H, Liang S, et al. Targeted radiotherapy with tumor vascular homing trimeric GEBP11 peptide evaluated by multimodality imaging for gastric cancer. J Control Release. 2013;172(1):322–9.
18. Moore GE. Fluorescein as an agent in the differentiation of normal and malignant tissues. Science. 1947;106(2745):130–1.
19. De Grand AM, Frangioni JV. An operational near-infrared fluorescence imaging system prototype for large animal surgery. Technol Cancer Res Treat. 2003;2(6):553–62.
20. Themelis G, Yoo JS, Soh KS, Schulz R, Ntziachristos V. Real-time intraoperative fluorescence imaging system using light-absorption correction. J Biomed Optics. 2009;14(6):064012.
21. van Dam GM, Themelis G, Crane LM, et al. Intraoperative tumor-specific fluorescence imaging in ovarian cancer by folate receptor-alpha targeting: first in-human results. Nat Med. 2011;17(10):1315–9.
22. Povoski SP, Hall NC, Murrey DA Jr, et al. Multimodal imaging and detection strategy with 124 I-labeled chimeric monoclonal antibody cG250 for accurate localization and confirmation of extent of

disease during laparoscopic and open surgical resection of clear cell renal cell carcinoma. Surg Innov. 2013;20(1):59–69.
23. Povoski SP, Hall NC, Martin EW Jr, Walker MJ. Multimodality approach of perioperative 18F-FDG PET/CT imaging, intraoperative 18F-FDG handheld gamma probe detection, and intraoperative ultrasound for tumor localization and verification of resection of all sites of hypermetabolic activity in a case of occult recurrent metastatic melanoma. World J Surg Oncol. 2008;6:1.
24. Ryan ER, Sofocleous CT, Schoder H, et al. Split-dose technique for FDG PET/CT-guided percutaneous ablation: a method to facilitate lesion targeting and to provide immediate assessment of treatment effectiveness. Radiology. 2013;268(1):288–95.
25. Ryan ER, Thornton R, Sofocleous CT, et al. PET/CT-guided interventions: personnel radiation dose. Cardiovasc Intervent Radiol. 2013;36(4):1063–7.
26. Mariani G, Erba P, Villa G, et al. Lymphoscintigraphic and intraoperative detection of the sentinel lymph node in breast cancer patients: the nuclear medicine perspective. J Surg Oncol. 2004;85(3):112–22.
27. Tokin CA, Cope FO, Metz WL, et al. The efficacy of Tilmanocept in sentinel lymph mode mapping and identification in breast cancer patients: a comparative review and meta-analysis of the (9)(9)mTc-labeled nanocolloid human serum albumin standard of care. Clin Exp Metastasis. 2012;29(7):681–6.
28. Vermeeren L, Valdes Olmos RA, Meinhardt W, Horenblas S. Intraoperative imaging for sentinel node identification in prostate carcinoma: its use in combination with other techniques. J Nucl Med. 2011;52(5):741–4.
29. Dengel LT, More MJ, Judy PG, et al. Intraoperative imaging guidance for sentinel node biopsy in melanoma using a mobile gamma camera. Ann Surg. 2011;253(4):774–8.
30. Heller S, Zanzonico P. Nuclear probes and intraoperative gamma cameras. Semin Nucl Med. 2011;41(3):166–81.
31. Holland JP, Normand G, Ruggiero A, Lewis JS, Grimm J. Intraoperative imaging of positron emission tomographic radiotracers using Cerenkov luminescence emissions. Mol Imaging. 2011;10(3):177–86.
32. Thorek DL, Abou DS, Beattie BJ, et al. Positron lymphography: multimodal, high-resolution, dynamic mapping and resection of lymph nodes after intradermal injection of 18F-FDG. J Nucl Med. 2012;53(9):1438–45.
33. Liu H, Carpenter CM, Jiang H, et al. Intraoperative imaging of tumors using Cerenkov luminescence endoscopy: a feasibility experimental study. J Nucl Med. 2012;53(10):1579–84.
34. Kothapalli SR, Liu H, Liao JC, Cheng Z, Gambhir SS. Endoscopic imaging of Cerenkov luminescence. Biomed Opt Express. 2012;3(6):1215–25.
35. Grimm J, Scheinberg DA. Will nanotechnology influence targeted cancer therapy? Semin Radiat Oncol. 2011;21(2):80–7.
36. Thorek DL, Ogirala A, Beattie BJ, Grimm J. Quantitative imaging of disease signatures through radioactive decay signal conversion. Nat Med. 2013;19(10):1345–50.
37. Thorek D, Robertson R, Bacchus WA, et al. Cerenkov imaging—a new modality for molecular imaging. Am J Nucl Med Mol Imaging. 2012;2(2):163–73.
38. Weissleder R, Ntziachristos V. Shedding light onto live molecular targets. Nat Med. 2003;9(1):123–8.
39. Spinelli AE, D'Ambrosio D, Calderan L, Marengo M, Sbarbati A, Boschi F. Cerenkov radiation allows in vivo optical imaging of positron emitting radiotracers. Phys Med Biol. 2010;55(2):483–95.
40. ICRP. Radiological protection in biomedical research. A report of committee 3 adopted by the international commission on radiological protection. Ann ICRP. 1991;22(3):1–28, v–xxiv.
41. Gollub MJ, Akhurst TJ, Williamson MJ, et al. Feasibility of ex vivo FDG PET of the colon. Radiology. 2009;252(1):232–9.
42. Abu-Rustum NR, Khoury-Collado F, Gemignani ML. Techniques of sentinel lymph node identification for early-stage cervical and uterine cancer. Gynecol Oncol. 2008;111(2 Suppl):S44–50.
43. Mariani G, Erba P, Manca G, et al. Radioguided sentinel lymph node biopsy in patients with malignant cutaneous melanoma: the nuclear medicine contribution. J Surg Oncol. 2004;85(3):141–51.
44. Thorek DL, Riedl CC, Grimm J. Clinical Cerenkov luminescence imaging of 18F-FDG. J Nucl Med. 2014;55(1):95–8.
45. Spinelli AE, Ferdeghini M, Cavedon C, et al. First human Cerenkography. J Biomed Opt. 2013;18(2):20502.
46. Dothager RS, Goiffon RJ, Jackson E, Harpstrite S, Piwnica-Worms D. Cerenkov radiation energy transfer (CRET) imaging: a novel method for optical imaging of PET isotopes in biological systems. PLoS One. 2010;5(10):e13300.
47. Liu H, Zhang X, Xing B, Han P, Gambhir SS, Cheng Z. Radiation-luminescence-excited quantum dots for in vivo multiplexed optical imaging. Small. 2010;6(10):1087–91.
48. Thorek DL, Das S, Grimm J. Molecular imaging using nanoparticle quenchers of Cerenkov luminescence. Small. 2014;10(18):3729–34.
49. Thorek DL, Ogirala A, Beatty MW, Grimm J. Quantitative imaging of disease signatures through radioactive decay signal conversion. Nat Med. 2013:19(10):1345–50
50. Hu H, Cao X, Kang F, Wang M, Lin Y, Liu M, Li S, Yao L, Liang J, Liang J, Nie Y, Chen X, Wang J, Wu K. Feasibility study of novel endoscopic Cerenkov luminescence imaging system in detecting and quantifying gastrointestinal disease: first human results. Eur Radiol. 2015;(in press). http://www.ncbi.nlm.nih.gov/m/pubmed/25577521/?i=1&from=cerenkov%20AND%20endoscopy.

Organ Deformation and Navigation

9

Robert L. Galloway and Michael I. Miga

Registration and Guidance

As image-guided surgery (IGS) expands beyond intracranial neurosurgery, it takes on additional challenges. Organs other than the brain lack the encompassing bone of the skull which allows them to move and deform as a result of operative pose, respiratory and cardiac motion, and tractions placed on the tissue during the interventional process. Additionally, the skull was easily accessible via a minor incision into the skin. That allowed for the implantation of rigid reference points, or fiducial markers, which allowed for easy registration of tomographic spaces and physical space [1–3]. In other organs that rigid platform was not available. So both additional ways of using image information to guide procedures and techniques to account for deformation had to be developed.

Image-guided procedures require a methodology of matching imaging data with physiological position and tool orientation. This requires either a registration or a calibration. The difference is in the application. In a calibration, a device is created which can reach any point within a tomographic scanner (computed tomography, CT; magnetic resonance imaging, MRI; positron emission tomography, PET; or single-photon emission computed tomography, SPECT). A phantom object containing easy-to-locate and well-described points is first volumetrically scanned and then located by the device. This allows the determination of the mathematical relationship between localizer position and orientation to locations within the scanner. Then, when a patient is scanned, the image information is used to find targets of interest in the images and thus scanner space [4]. The localization device is then used to reach the point in scanner space. If desired, a second scan can be performed to confirm the accuracy.

Using ultrasound as a guidance method can also be considered a calibration. Here, a tracking system is attached to an ultrasound system and the mathematical relationship between the tracked ultrasound and its image slice is determined by a phantom process [5, 6]. That allows the location of objects seen in the ultrasound to be determined in tracking system space. Then a tracked surgical instrument (also localized in tracking system space) can move to the location determined in the ultrasound (see Fig. 9.1).

The strength of a calibration technique is that it requires no processing of the images and the time between obtaining the scan and the interventional procedure is minimized [7]. However, the most important issue to be addressed in a tomographic calibration technique is that no motion or deformation has occurred between the acquisition and

R. L. Galloway (✉)
Department of Biomedical Engineering, Neurosurgery, Surgery, Vanderbilt University School of Engineering, Vanderbilt University School of Medicine, 2201 West End Avenue, Stevenson Center, Nashville TN 37235, USA
e-mail: bob.galloway@vanderbilt.edu

M. I. Miga
Biomedical Engineering, Neurosurgery, Radiology, Vanderbilt University School of Engineering, Vanderbilt University School of Medicine, 5824 Stevenson Center, Nashville, TN, USA
e-mail: Michael.i.miga@vanderbilt.edu

Y. Fong et al. (eds.), *Imaging and Visualization in The Modern Operating Room,*
DOI 10.1007/978-1-4939-2326-7_9, © Springer Science+Business Media New York 2015

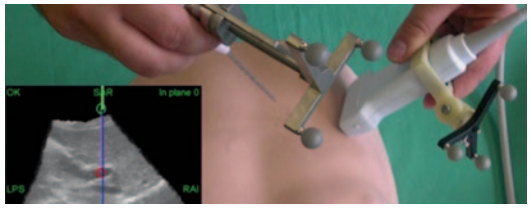

Fig. 9.1 The use of an ultrasound system to detect a surgical target and then guide a tool to that target

the intervention. Therefore, the patient cannot be moved, repositioned or, in some applications, has to have breathing controlled. In addition, multiple phantom runs need to be made to insure that the relationship between image information and scanner position is stable and reproducible. In an ultrasound technique, since the ultrasound image is generally a 2D slice, the tool often has to pass through unvisualized tissue before it reaches the target.

A *registration* takes homologous points or surfaces derived from the image space, and mathematically matches it to data located in physical space. This can be homologous anatomic points identified in image and physical spaces, external objects prospectively attached to the body prior to imaging or matching homologous shapes. Point-based registration is fast, well defined mathematically [8, 9] and can provide an absolute measure of accuracy [10]. It has become the standard technique in image-guided neurosurgery (IGNS). A number of researchers have attempted to bring point-based registration to organ-level therapies. This includes using identified points both as an initial estimate of a registration [11, 12] and as a stand-alone approach [13, 14].

Lange et al. [13] locate vessel bifurcations and vessel centerlines in preoperative tomographic angiograms (magnetic resonance angiography, MRA; or computed tomography angiography, CTA) and attempt to match those points to points found in power Doppler ultrasound images from a tracked ultrasonic probe. This is shown in Fig. 9.2.

Mauer et al. [15] demonstrated that adding shape information into a registration could improve the quality of that information. When that work was combined with the surface-based registrations of Pelizzari et al. [16] and the search mathematics of Besl and McKay [17] then it became possible to match spaces based on surface registrations. This was critical to moving image-guidance techniques from the brain to abdominal organs which lack the rigid skull in which points could be firmly attached.

Herline et al. [18] demonstrated that liver motion was essentially one dimensional by tracking points on the surface of the liver and resolving that motion into Eigen vectors. These data showed that liver motion was virtually one dimensional in the direction of diaphragm motion, and that the liver returned to locations throughout the respiratory cycle. This gave researchers confidence that a surface could be used to register image space to physical space. The image space data were segmented from preoperative tomograms (see Fig. 9.3).

With the belief that the liver motion could be controlled by respirator control of diaphragm motion, researchers developed organ-level surface registration. The first attempts used tracked localizers devices. In the liver that was an opti-

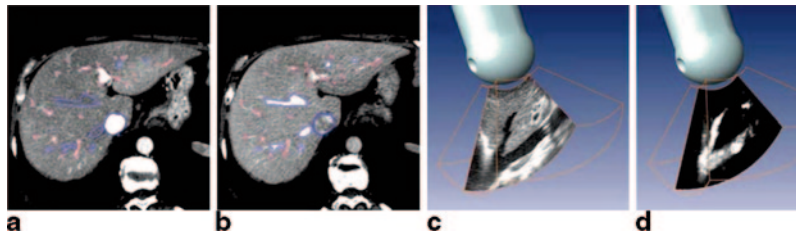

Fig. 9.2 A CTA is shown in (**a**) and (**b**). **a** Portal venous phase, and **b** late venous phase. **c** Shows a B-mode ultrasound of the liver, while **d** shows a power Doppler image of the same: lice. (From [14])

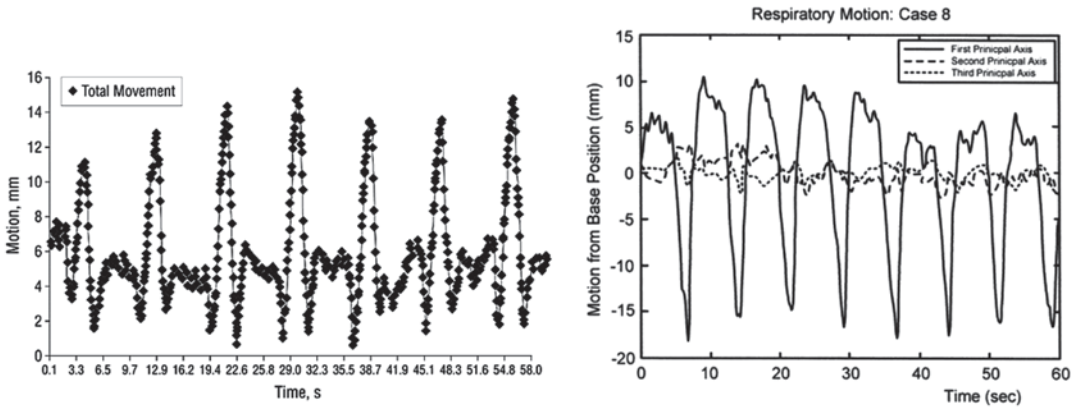

Fig. 9.3 Three-dimensional motion of the liver (*left*) resolved into Eigen vectors (*right*)

cally tracked probe dragged over the surface of the liver (see Fig. 9.4).

This same technique can be applied to a tracked daVinci robot [19–21]. Here the application is in kidney surgery.

As can be seen from Figs. 9.4 and 9.5, a handheld tracker is inefficient at obtaining dense, complete coverage of an organ surface. In addition, these are contact methods in which the surgeon has to drag a tool across the surface. Such a process is a difficult visual servoing task and can result in points from below the surface if the tracker digs in and from above the surface if the tracker loses contact with the surface. Such problems do not affect the usefulness of a contact-based surface registration—they just limit the ultimate accuracy. Figure 9.6 shows the process of adding image guidance to a partial nephrectomy using the daVinci robot. Figure 9.6a shows the standard daVinci endoscopic view, Fig. 9.6b shows an image-guided rendered view. The rendered view is updated at video frame rates [22].

Miga [23–25] pioneered the use of a laser range scanner (LRS) to quickly capture an even, densely sampled surface. Because it is contactless, that is, it uses a laser to locate the surface, there are no problems with acquiring surface points. In addition, it acquires 20,000–30,000 points in a 30-s acquisition. When the surface cloud is obtained, a color photograph is also obtained allowing for the texturing of the point cloud. This enables confirmation that the three-

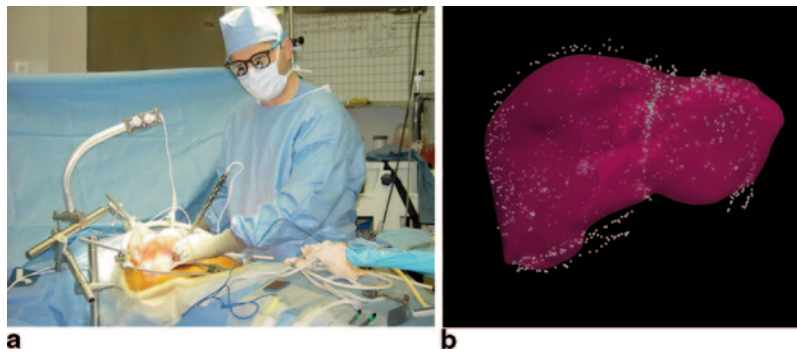

Fig. 9.4 One technique for capturing an intraoperative surface is to drag a tracked probe over the organ surface during surgery (**a**). This results in a sparse representation (*white dots* in **b**) which takes several minutes to obtain. (Fig. 9.b: Courtesy Dr. Logan Clements)

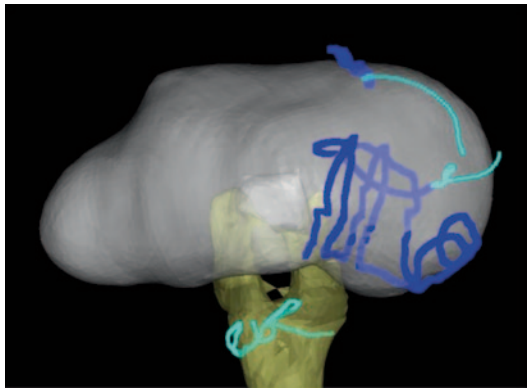

Fig. 9.5 The surface of a kidney outlined in surgery using the daVinci robot. The *dark blue lines* were used for the registration and the *cyan lines* were held out as a registration check. (Figure from [21])

dimensional points used for the surface registration arise from the organ in question and not from surrounding tissue. Figure 9.7 shows the tracked LRS from Pathfinder Therapeutics Inc. (Fig. 9.7a), the organ surface and textured laser range scan (Fig. 9.7b), and finally the surface fit of the textured surface in (Fig. 9.7c).

Surface registrations have a well-known difficulty in working with surfaces with high degrees of rotational symmetry. For example, a perfect surface fragment extracted from a billiard ball and registered back to that ball could fit anywhere on the ball. Similarly, organ surfaces tend to be round and for short spans show significant rotational symmetry. Therefore, surface registrations can "slide off" the correct answer and fit to a site that is incorrect but is a numerical local

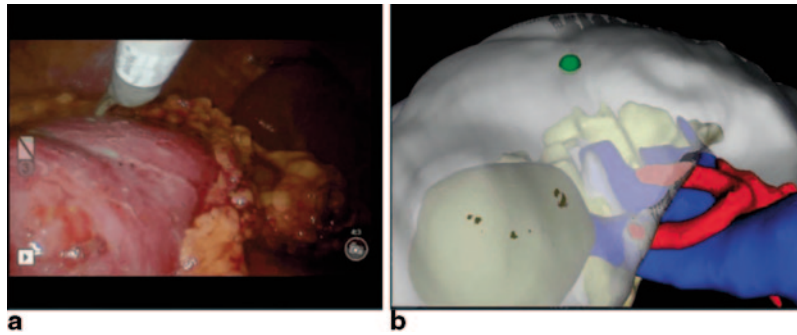

Fig. 9.6 Standard daVinci view (**a**). The initial surgical task is locating the tumor, the vascular system, and the collecting system to allow resection without intrusion into either system or the lesion capsule. **b** Shows a rendered, registered transparent image with the daVinci tool location updated at video frame rates

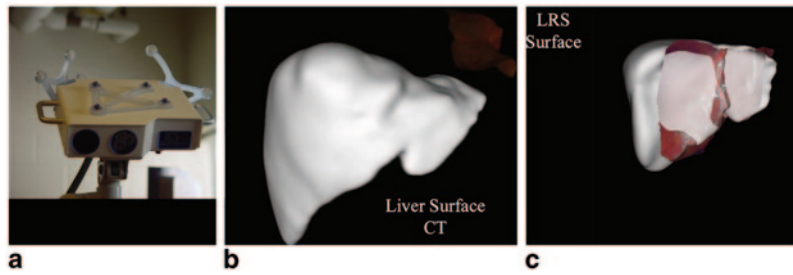

Fig. 9.7 The tracked LRS (**a**), the organ surface extracted from the preoperative imaging and the unregistered surface (**b**), and the registered surfaces (**c**)

minimum. One successful approach to that is the use of salient features. Here, the surfaces are captured as normal, but in addition the surgeon then uses either the tracked locator or the LRS data to mark specific features [26]. These features are then used to initially "direct" the surface registration during the first few iterations. Then, as the number of iterations climbs, the computational weight moves towards a pure surface registration. In liver surgery, the falciform ligament, the round ligament, and the inferior ridge are often outlined. This technique captures some information which is obvious to the surgeon but difficult to computationally capture. Figure 9.8 shows the registrations using point-based, conventional surface-based, and salient feature-based registrations.

While it is clear that organ-based registration is the most accurate and robust registration methodology for image-guided therapies in the abdomen, capturing a high-quality surface with a laser range scan requires an open procedure. In times where a minimally invasive approach is desired, the advantages of the LRS—high-point density, contactless acquisition, and textured surface—can be lost. Recent development [27–29] of a tracked laser conoscope allows the surface acquisition via a trochar. The tracked conoscope acts as a single vector range finder. By calibrating the conoscope and measuring its position and orientation, when the laser bounces off the surface, we can calculate the location of the point on the surface. If there is an endoscopic camera in a second trochar, a textured surface can be obtained as well (Fig. 9.9) [30].

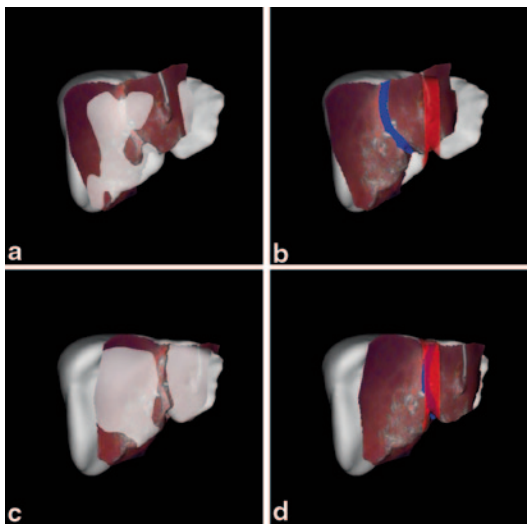

Fig. 9.8 Registrations using point-based, conventional surface-based, and salient feature-based registrations. A is ICP alone, b) shows the mismatch of the facliform ligament using ICP. C&D show the salient feature registration with the same check

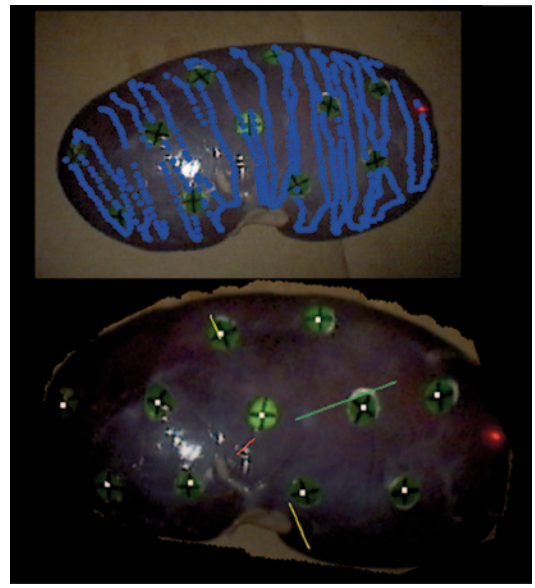

Fig. 9.9 Human kidney with conoscope surface acquisition. *Green markers* are fiducials for determining registration accuracy

Organ Deformation

From the earliest use of image-guided surgical techniques, the alignment of imaging data to the events occurring in intraoperative physical space has been a core characteristic. As the extent of imaging data grew, conventional guidance systems were developed and aligned the wealth of data acquired preoperatively to the physical patient within the operating room (OR) with that visualization achieved by displays. Although the initial assumption was of rigid-body alignment, clinically, surgeons were never under the illusion that this was the case. These assumptions were tolerated because the value of image-to-physical information was incontrovertible and that value

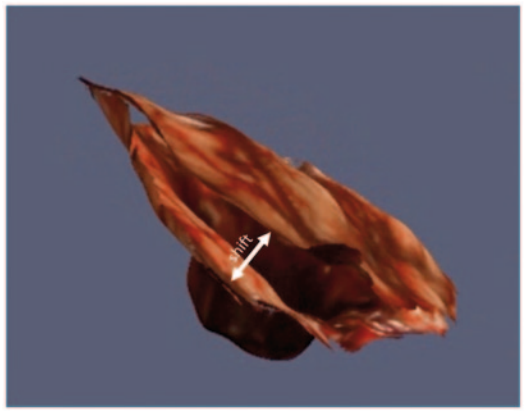

Fig. 9.10 Laser range scans of the brain's cortical surface before and after resection

continues today. Interestingly, as the first conventional frameless stereotactic systems were being realized for rigid-body-based image-guided brain surgery [31–33], surgeons were already adopting approaches almost simultaneously to account for nonrigid deformation-induced changes. For example, Kelly et al. inserted beads stereotactically at 5-mm increments within tumors to monitor shifts with lateral teleradiographs during laser resection [34]. Several years later, quantitative measurements of the discrepancy between conventional IGS displays and their soft-tissue intraoperative counterpart began to appear with Nauta reporting display-to-tissue misalignments on the order of 5 mm [35]. Subsequent investigations measuring intraoperative brain surface movements reported average surface deformations of 1 cm. Figure 9.10 illustrates two laser range scans of the cortical surface before and after surgical resection superposed in consistent physical space. A representative sagging and shifting of the cortical surface can easily be observed and is quite typical during image-guided brain tumor resection. From these initial observations, insightful relationships regarding the predisposition for brain movement in the direction of gravity have been reported [36, 37]. In addition, with the advent and use of intraoperative magnetic resonance (iMR) imaging systems, more detailed studies measuring both surface and subsurface shift have been performed [38, 39]. One of the first detailed studies documenting both surface and subsurface shift was reported by Nimsky et al. [39]. Using image-processing techniques and the shift scale proposed by Bucholz et al. [40] (low, 0–2.9 mm; moderate, 3.0–6.9; high, >7.0 mm), they classified surface and subsurface deformation on 64 patients undergoing various neurosurgical procedures. Their investigation revealed that "cortical shifts were high in 63% of cases, moderate in 14%, and low in 23%. Midline structures exhibited low shifts in 92% and moderate shifts in the remaining 8%; high shifts were not observed. There were low shifts of the deep tumor margin in 34% of cases, moderate shifts in 42%, and high shifts in 24%." Others have also shown similar iMR studies [38, 41] and within other brain surgery applications (e.g., deep brain stimulation [42], and convection-enhanced chemotherapy [43]). What is clear is that in one of the most confined soft-tissue domains within the human body, moderate-to-high soft-tissue shifts of the brain surface, and deep tumor margins was suggested to occur in approximately 75+% of cases. When one then considers the translation of image-guided techniques to other domains, this is a sobering reality. For example, in recent reports, soft-tissue deformation during liver resection has been documented with intraoperative computed tomography (iCT) and has demonstrated significant effects from deformation [44]. Contrary to the aforementioned studies of deformation in neurosurgical procedures, a majority of deformation in open liver surgery is imposed prior to resection and due to laparotomy, mobilization, and surgical presentation for resection. As such, methods of analyzing the organ shape change must be developed that would optimally use available minimally intrusive intraoperative data (e.g., laser range scans of the organ surface) which again, unfortunately, can only be acquired after the organ has deformed considerably. Going further, in a recent 12-patient interpatient liver registration study, intraoperative liver surfaces were acquired using laser range scan technology and rigidly registered to their segmented CT organ counterpart. Once achieved, the results were wholly registered to a common organ representation, i.e., "atlas" liver, and analyzed. Similar to [44], the results of the

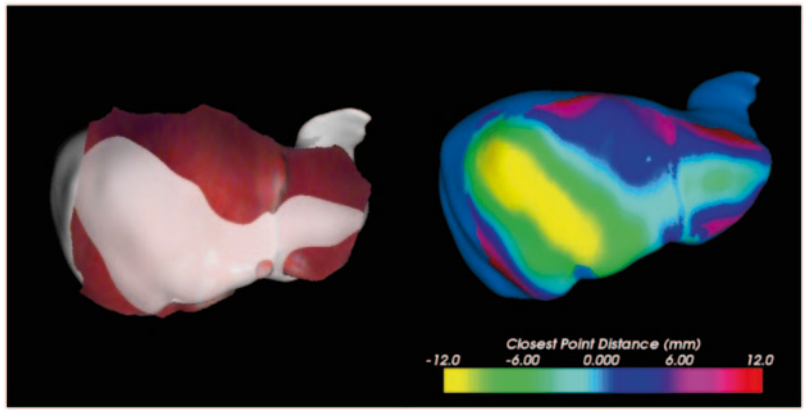

Fig. 9.11 Laser range scan overlaid on segmented CT-liver model (*left*); signed closest point distance which illustrates the shape change (*right*)

deformation measurement and analysis indicated the potential for soft-tissue deformation to compromise surgical guidance information and also suggested a similarity in imposed deformations among similar procedure types. Figure 9.11 is an example of a typical interoperative shape change and demonstrates quite clearly that guidance technologies for soft-tissue surgeries that rely on rigid-body alignment are compromised by deformation. However, it also supports that intraoperative deformations are to a degree systematic which may be very favorable for computational approaches.

As stated above, none of the conventional guidance platforms has a deformation correction approach embedded in the system, but rather commercial developers have elected to integrate their platforms with intraoperative imaging units to account for surgical changes. With respect to enhanced neuronavigation, intraoperative magnetic resonance (MR) has been the integration platform of choice. In a recent review paper by Shulz, Waldeck, and Mauer, 1400 papers concerned with IGNS over the past 25 years were reviewed with interestingly only 14 comparative trials concerning the effectiveness of IGNS being identified for inclusion. Despite the small number, many interesting results were reported across studies. In general, the use of *conventional* neuronavigation (i.e., rigid-body alignment IGNS) led to reduced residual tumor burden postoperatively, prolonged survival, reduced neurological deterioration, and negligible additional intraoperative timing (longer setups were experienced however) [45]. With the addition of iMR imaging, in general, more complete resections have been reported with no additional deficits. In approximately 30 % of cases, additional tumor resections resulted with no added neurological deterioration. While results did vary, iMR-enhanced neuronavigation also improved survival times over conventional neuronavigation. The only considerable intraoperative compromises were with respect to limiting patients to those without ferromagnetic implants and to the additional time of surgery (noted time increases as much as 50 % over conventional IGS). With respect to drawbacks of iMR technology outside the OR, the authors readily point out the expense, the encumbrance and upkeep, the special instrumentation needed, and the potential technical excess associated with such a costly high-tech tool. In addition, iMR investments previously made by medical centers are largely in their first generation, studies regarding updating, and maintenance of these suites has not yet been forthcoming. Nevertheless, an important finding across iMR studies, albeit sparse, is a growing agreement that taking into account soft-tissue anatomical changes intraoperatively does provide additional benefit over conventional IGS approaches.

An alternative to iMR technologies that is less expensive is intraoperative computed tomography (iCT). While iCT was explored in the 1980s

[46] and to a degree dismissed, better detectors, reductions in radiation, and more sophisticated reconstruction frameworks have led to renewed interest in the technology. Within the domain of surgical guidance, approaches using cone-beam CT (CBCT) technology have shown particular promise. In [47], CBCT was used in a series of 12 head and neck surgical cases. The impact of the technology was evaluated with respect to clinical workflow, image quality, and utility. The work demonstrated an effective surgical imaging tool with important roles in surgical guidance, specifically with respect to visualization of bony detail, guidance of bone ablation, and possibly anatomical reconstruction. While an important addition to the scope of intraoperative imaging tools, its lack of soft-tissue contrast, and radiation concerns do leave its role somewhat uncertain at this time. With that said, this technology may be a valuable source of intraoperative data in the future for updating.

Another alternative, intraoperative ultrasound (iUS) has shown promise in providing additional insight to the surgical field regarding soft-tissue deformation [48]. In another common soft-tissue resection surgery, breast-conserving lumpectomy, the need for clear margins is essential and reoperation rates and compromised margins are unacceptably high at this time. Several studies looking at the value of iUS imaging as purely an interventional imaging tool to assist tissue visualization have demonstrated benefit [49–52]. What is intriguing about this work is that these studies did not benefit from having advanced tracking and localization systems, and none had an ability to incorporate preoperative imaging data, yet clinical benefit was found. The results certainly encourage the use of low-cost nongantry-based, nonionizing intraoperative imaging data and demonstrate that surgical expertise can often accommodate technologies to improve outcomes despite not having the most extensive intraoperative guidance system that could possibly be imagined. Intraoperative imaging in all its forms is an important tool for assisting surgery; however, the inherent workflow and integration difficulties are significant and do open the possibilities that more cost-effective computational approaches may be needed to close the gap between workflow and accuracy design constraints [53–55]. Stereoscopic cameras and LRSs have been highly investigated sources of sparse data in the recent literature and have been used extensively to capture brain surface deformations [56–59], liver [26, 61, 62] and kidney organ surfaces [21, 62], as well as breast [63]. Some comparisons of the computer vision approaches have been made too [64]. With respect to modeling approaches to compensate for brain deformations, the growth in this literature has been considerable. For example, work from Dumpuri et al. has proposed using an atlas-based combinatorial approach driven by sparse-textured cortical surface point clouds [64]. Sun et al. uses similar point cloud data acquired from stereo-pair surgical microscope data within the context of a boundary force reconstruction approach [58]. DeLorenzo et al. used a variant on game theory to compensate for shift in epilepsy patients [65]. Lunn et al. proposed using stereo-pair data and ultrasound to drive their inverse approach [66]. Methodologically, all of these approaches are very similar inverse problem strategies, each having demonstrated reasonably similar prediction capabilities. In addition, there are now reports emerging on these preoperative and intraoperative pipelines that discuss the impact within surgical workflow [67]. Figure 9.12 is an example of one of these approaches for IGNS [64]. In this case, optically tracked laser range scans were acquired of the cortical surface before and after resection (Fig. 9.12a), measurements of shift were made, and used within the context of inverse problem framework (Fig. 9.12b). Once computed, the image volumes could be modified to reflect the deformation (Fig. 9.12c).

With respect to other soft-tissue organs, the results are more limited. With the context of image-guided liver surgery, the work by Lange et al. [13, 68, 69] is looking at a CT-to-US vessel-based nonrigid registration system for providing the link between image and physical space. While several cases have been conducted with good results, there are challenges to the approach that require the identification of as many bifurcations as possible with tracked ultrasound and then the determination of corresponding bifur-

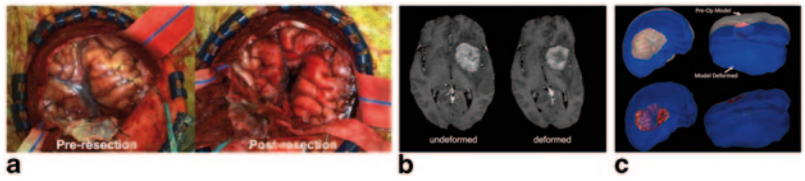

Fig. 9.12 **a** Pre- and post-resection images of the cortical surface, **b** *gray* pre-op brain model and *blue* model deformed, and **c** undeformed and deformed MR

cations within CT data. While the subsurface information would be valuable for nonrigid correction, there is a likelihood of misidentification in this highly vascularized organ, and the encumbrance may challenge adoption from a workflow perspective. Alternative approaches using liver surface data and finite element models within an inverse problem framework have also been proposed [70–72]. These are challenging approaches too because they rely on a general understanding of surgical presentation such that a proper representation of shape variability can be represented. In a recent study by Rucker et al. [73], this type of approach was studied within the context of understanding the effects of surface data extent, the inclusion of subsurface data, the trade-offs of using a nonlinear tissue model, robustness to rigid misalignments, and the feasibility in clinical datasets. The results suggest a robust approach and volumetric target registration errors compatible with the goals of image-guided liver surgery. Figure 9.13 is one example where the strategy by Rucker et al. was modified to include multiple control surfaces and demonstrates the degree of surface fit for the data shown in Fig. 9.11 that is possible.

While a straightforward solution is to integrate imaging and guidance into one device, the fully integrated solution still represents a resect-and-check approach. Its greatest advantage is the ability to modify a procedure based on data while the patient is still in the operating theatre. Furthermore, there is little question that preoperative data combined with intraoperative tissue characterization and localization data will continue to shape therapy. However, what is not apparent is if the translation of standard preoperative imaging equipment into the OR is the best approach in all instances. The environmental and interaction constraints are fundamentally different between the two and will influence adoption in the future. In addition, it is also important to recognize that more localized sensing methodologies to perform the same functions as larger gantry-based imaging units are on the horizon. For example, new approaches using fluorescence and reflectance spectroscopy are being pursued to help delineate high-glioma resections [74, 75]. These types of

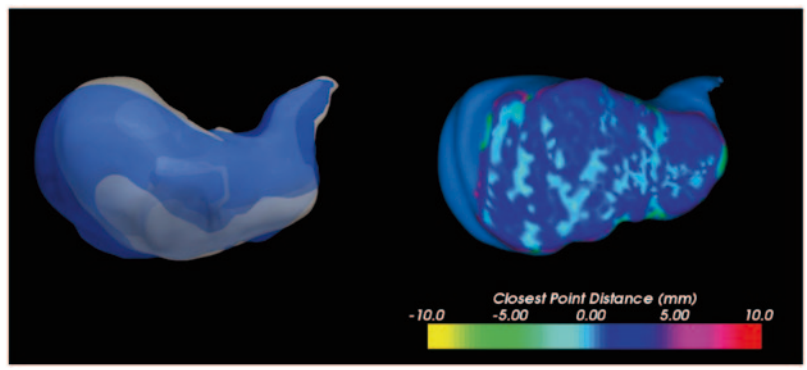

Fig. 9.13 Model deformed in *blue* with pre-op model in *gray* (*left*), and resulting signed closest point distance map after nonrigid deformation correction (*right*)

devices represent simple visual filters on surgical microscopes or small imaging probes and would be far more compatible with current operative workflow. While these methodologies are somewhat investigational at this time, it does provide some sense of the challenging nature for predicting what the best arrangement of instrumentation should be. What is presented in Figs. 9.2 and 9.4 is a means to nonrigidly register preoperative information to the intraoperative domain using cost-effective workflow-friendly, sparse-data driven, computational approaches. Combining a capability like this with a localized imaging device may be a very attractive approach allowing the surgeon to avoid critical surrounding structures by accounting for their changing positions intraoperatively while being able to provide a more precise resection based on inherent tissue characteristics. While ORs of the future will be ever evolving, it is clear that advanced instrumentation, imaging technologies, novel visualization platforms, and computation will be central to its realization.

References

1. Howard MA III, Dobbs MB, Simonson TM, LaVelle WE, Granner MA. A noninvasive, reattachable skull fiducial marker system. Technical note. J Neurosurg. 1995;83:372–6.
2. Ammirati M, Gross JD, Ammirati G, Dugan S. Comparison of registration accuracy of skin- and bone-implanted fiducials for frameless stereotaxis of the brain: a prospective study. Skull Base. 2002;12(3):125–30.
3. Maurer CR, Fitzpatrick JM, Wang MY, Galloway RL, Maciunas RJ, Allen GS. Registration of head volume images using implantable fiducial markers. IEEE TMI. 1997;16(4):447–62.
4. Jacob AL, Messmer P, Kaim A, Suhm N, Regazzoni P, Baumann B. A whole-body registration-free navigation system for image-guided surgery and interventional radiology. Invest Radiol. 2000;35(5):279–88.
5. Boctor EM, Iordachita I, Choti MA, Hager G, Fichtinger G. Bootstrapped ultrasound calibration. Stud Health Technol Inform. 2006;119:61–6.
6. Muratore DM, Galloway RL. Beam calibration without a phantom for creating a 3-D freehand ultrasound system. Ultrasound Med Biol. 2001;27(11):1557–66.
7. Brandenberger D, Birkfellner W, Baumann B, et al. Positioning accuracy in a registration-free CT-based navigation system. Phys Med Biol. 2007;52:7073–86.
8. Fitzpatrick JM, West JB, Maurer CR Jr. Predicting error in rigid-body point-based registration. IEEE Trans Med Imaging. 1998;17(5):694–702.
9. Wiles AD, Likholyot A, Frantz DD, Peters TM. A statistical model for point-based target registration error with anisotropic fiducial localizer error. IEEE TMI. 2008;27(3):378–90.
10. Fitzpatrick JM, West JB. The distribution of target registration error in rigid-body point-based registration. IEEE Trans Med Imaging. 2001;20(9):917–27.
11. Herline AJ, Herring JL, Stefansic JD, Chapman WC, Galloway RL Jr, Dawant BM. Surface registration for use in interactive, image-guided liver surgery. Comput Aided Surg. 2000;5(1):11–7.
12. Nolte LP, Zamorano LJ, Jiang Z, Wang Q, Langlotz F, Berlemann U. Image-guided insertion of transpedicular screws: a laboratory set-up. Spine. 1995;20:497–500.
13. Lange T, Papenberg N, Heldmann S, et al. 3D ultrasound-CT registration of the liver using combined landmark-intensity information. Int J Comput Assist Radiol Surg. 2009;4(1):79–88.
14. Porter BC, Rubens DJ, Strang JG, Smith J, et al. Three-dimensional registration and fusion of ultrasound and MRI using major vessels as fiducial markers. IEEE TMI. 2001;20(4):354–9.
15. Maurer CR, Maciunas RJ, Fitzpatrick JM. Registration of head CT images to physical space using a weighted combination of points and surfaces [image-guided surgery]. IEEE-TMI. 1998;17(5):753–61.
16. Pelizzari CA, Chen GTY, Spelbring DR, Weischelbaum RR, Chen CT. Accurate three-dimensional registration of CT, PET and/or MR images of the brain. JCAT. 1989;13(1):20–6.
17. Besl PJ, McKay ND. A method for registration of 3D shape. IEEE-Trans PAMI. 1992;14(2):239–57.
18. Herline AJ, Stefansic JD, Debelak JP, Hartmann SL, et al. Image-guided surgery preliminary feasibility studies of frameless stereotactic liver surgery. JAMA Surg. 1999;134(6):644–50.
19. Kwartowitz DM, Herrell SD, Galloway RL. Update: toward image-guided robotic surgery: determining the intrinsic accuracy of the daVinci-S robot. Int J Comput Assist Radiol Surg. 2007;1(5):301–4.
20. Herrell SD, Kwartowitz DM, Milhoua PM, Galloway RL. Towards image guided robotic surgery: system validation. J Urol. 2009;181(2):783–9. Discussion 789–90.
21. Ong RE, Glisson C, Altamar H, Viprakasit D, et al. Intraprocedural registration for image-guided kidney surgery. IEEE/ASME Trans Mechatron. 2010;15(6):847–52.
22. Herrell SD. The fantastic voyage: advances in robotic surgery. American Urological Society Meeting. Chicago Ill. 2011.
23. Cash DM, Sinha TK, Chapman WC, Terawaki H. et al. Incorporation of a laser range scanner into image-guided liver surgery: surface acquisition, registration, and tracking. Med Phys. 2003;30:1671–82.
24. Sinha TK, Miga MI, Cash DM, Weil RJ. Intraop-

erative cortical surface characterization using laser range scanning: preliminary results. Neurosurgery. 2006;59(4 Suppl. 2):368–76.
25. Pheiffer TS, Simpson AL, Lennon B, Thompson RC, Miga MI. Design and evaluation of an optically-tracked single-CCD laser range scanner. Med Phys. 2012;39(2):636–42.
26. Clements LW, Chapman WC, Dawant BM, Galloway RL, Miga MI. Robust surface registration using salient anatomical features for image-guided liver surgery: algorithm and validation. Med Phys. 2008;35(6):2528–40.
27. Lathrop RA, Hackworth DM, Webster RJ 3rd. Minimally invasive holographic surface scanning for soft-tissue image registration. IEEE Trans Biomed Eng. 2010;57(6):1497–506.
28. Burgner J, Simpson AL, Fitzpatrick JM, Lathrop RA, et al. A study on the theoretical and practical accuracy of conoscopic holography-based surface measurements: toward image registration in minimally invasive surgery. Med Robot Comput Assist Surg. 2013;9(2):190–203.
29. Simpson AL, Burgner J, Glisson CL, Herrell SD, et al. Comparison study of contact and non-contact intraoperative surface acquisition methods for surgical navigation. IEEE Trans Biomed Eng. 2013;60(4):1090–9.
30. Glisson CL, Ong R, Simpson AL, Clark P, et al. The use of virtual fiducials in image-guided kidney surgery. Proc SPIE Med Imaging. 2011:7964(2). doi:10.1117/12.877092.
31. Kwoh YS, Hou J, Jonckheere EA, Hayati S. A robot with improved absolute positioning accuracy for CT guided stereotactic brain surgery. IEEE Trans Biomed Eng. 1988;35:153–60.
32. Roberts DW, Strohbehn JW, Hatch JF, Murray W, Kettenberger H. A frameless stereotaxic integration of computerized tomographic imaging and the operating microscope. J Neurosurg. 1986;65:545–9.
33. Watanabe E, Watanabe T, Manaka S, Mayanagi Y, Takakura K. Three-dimensional digitizer (neuronavigator): new equipment for computed tomography-guided stereotaxic surgery. Surg Neurol. 1987;27:543–7.
34. Kelly PJ, Kall B, Goerss S, Earnest FI. Computer-assisted stereotaxic laser resection of intra-axial brain neoplasms. J Neurosurg. 1986;64:427–39.
35. Nauta HJ. Error assessment during "image guided" and "imaging interactive" stereotactic surgery. Comput Med Imaging Graph. 1994;18:279–87.
36. Roberts DW, Hartov A, Kennedy FE, Miga MI, Paulsen KD. Intraoperative brain shift and deformation: a quantitative analysis of cortical displacement in 28 cases. Neurosurgery. 1998;43:749–58.
37. Hill DLG, Mauer CR, Maciunas RJ, Barwise JA, Fitzpatric JM, Wang MY. Measurement of intraoperative brain surface deformation under a craniotomy. Neurosurgery. 1998;43:514–26.
38. Nabavi A, Black PM, Gering DT, Westin CF, et al. Serial intraoperative magnetic resonance imaging of brain shift. Neurosurgery. 2001;48:787–97.
39. Nimsky C, Ganslandt O, Cerny S, Hastreiter P, Greiner G, Fahlbusch R. Quantification of, visualization of, and compensation for brain shift using intraoperative magnetic resonance imaging. Neurosurgery. 2000;47:1070–9.
40. Bucholz RD, Yeh DD, Trobaugh J, McDurmont LL, et al. The correction of stereotactic inaccuracy caused by brain shift using an intraoperative ultrasound device. Cvrmed-Mrcas'97. 1997;1205:459–66.
41. Hartkens T, Hill DLG, Castellano-Smith AD, Hawkes DJ, et al. Measurement and analysis of brain deformation during neurosurgery. IEEE Trans Med Imaging. 2003;22:82–92.
42. Sillay KA, Kumbier LM, Ross C, Brady M, et al. Perioperative brain shift and deep brain stimulating electrode deformation analysis: implications for rigid and non-rigid devices. Ann Biomed Eng. 2013;41:293–304.
43. Hall WA. Convection-enhanced delivery: neurosurgical issues. Curr Drug Targets. 2009;10:126–30.
44. Heizmann O, Zidowitz S, Bourquain H, Potthast S, et al. Assessment of intraoperative liver deformation during hepatic resection: prospective clinical study. World J Surg. 2010;34:1887–93.
45. Schulz C, Waldeck S, Mauer UM. Intraoperative image guidance in neurosurgery: development, current indications, and future trends. Radiol Res Pract. 2012;197364.
46. Lunsford LD, Martinez AJ. Stereotactic exploration of the brain in the era of computed tomography. Surg Neurol. 1984;22:222–30.
47. King E, Daly MJ, Chan H, Bachar G, et al. Intraoperative cone-beam CT for head and neck surgery: Feasibility of clinical implementation using a prototype mobile C-arm. Head Neck. 2013;35:959–67.
48. Ohue S, Kumon Y, Nagato S, Kohno S, et al. Evaluation of intraoperative brain shift using an ultrasound-linked navigation system for brain tumor surgery. Neurol Med Chir. 2010;50:291–9.
49. Abbott JD, Huang Y, Liu D, Hickey R, Krause DS, Giordano FJ. Stromal cell-derived factor-1alpha plays a critical role in stem cell recruitment to the heart after myocardial infarction but is not sufficient to induce homing in the absence of injury. Circulation. 2004;110:3300–5.
50. Ahmed M, Douek M. Intra-operative ultrasound versus wire-guided localization in the surgical management of non-palpable breast cancers: systematic review and meta-analysis. Breast Cancer Res Treat. 2013;140:435–46.
51. Haid A, Knauer M, Dunzinger S, Jasarevic Z, Koeberle-Wuehrer R. Intra-operative sonography: a valuable aid during breast-conserving surgery for occult breast cancer. Ann Surg Oncol. 2007;14:3090–101.
52. Pan H, Wu N, Ding H, Ding Q, et al. Intraoperative ultrasound guidance is associated with clear lumpectomy margins for breast cancer: a systematic review and meta-analysis. Plos One. 2013;8(9):e74028.
53. Roberts DW, Miga MI, Hartov A, Eisner S, et al.

Intraoperatively updated neuroimaging using brain modeling and sparse data. Neurosurgery. 1999;45:1199–206.
54. Miga MI, Dumpuri P, Simpson AL, Weis JA, Jarnagin WR. The sparse data extrapolation problem: strategies for soft-tissue correction for image-guided liver surgery, presented at the medical imaging 2011: visualization, image-guided procedures, and modeling conference, Orlando, 2011.
55. Miga MI, Roberts DW, Hartov A, Eisner S, et al. Updated neuroimaging using intraoperative brain modeling and sparse data. Stereotact Funct Neurosurg. 1999;72:103–6.
56. Kumar AN, Pheiffer TS, Simpson AL, Thompson RC, Miga MI, Dawant BM. Phantom-based comparison of the accuracy of point clouds extracted from stereo cameras and laser range scanner, presented at the medical imaging 2013: image-guided procedures, robotic interventions, and modeling, Orlando, 2013.
57. Skrinjar O, Nabavi A, Duncan JS. A Stereo-guided biomechanical model for volumetric deformation analysis, IEEE Workshop on Mathematical Methods in Biomedical Image Analysis, 2001.
58. Sun H, Lunn KE, Farid H, Wu Z, et al. Stereopsis-guided brain shift compensation. IEEE Trans Med Imaging. 2005;24:1039–52.
59. Paul P, Morandi X, Jannin PA. Surface registration method for quantification of intraoperative brain deformations in image-guided neurosurgery. IEEE Trans Inf Technol Biomed. 2009;13:976–83.
60. Cash DM, Sinha TK, Chapman WC, Galloway RL, Miga MI. Fast, accurate surface acquisition using a laser range scanner for image-guided liver surgery, medical imaging 2002: visualization, display, and image-guided procedures: Proc. of the SPIE 2002, 4681, 100–110.
61. Clements LW, Dumpuri P, Chapman WC, Dawant BM, Galloway RL, Miga MI. Organ surface deformation measurement and analysis in open hepatic surgery: method and preliminary results from 12 clinical cases. IEEE Trans Biomed Eng. 2011;58(8):2280–9.
62. Altamar HO, Ong RE, Glisson CL, Viprakasit DP, et al. Kidney deformation and intraprocedural registration: a study of elements of image-guided kidney surgery. J Endourol. 2011;25:511–7.
63. Conley RH, Meszoely I, Pheiffer TS, Weis JA, Yankeelov TE, Miga MI. Image to physical space registration of supine MRI for image guided breast surgery, presented at the SPIE medical imaging 2014: image-guided procedures, robotic interventions, and modeling conference, San Diego.
64. Dumpuri P, Thompson RC, Sinha TK, Miga MI. Automated brain shift correction using a pre-computed deformation atlas. Proc SPIE Med Imaging. 2006;614.1–8.
65. DeLorenzo C, Papademetris X, Staib LH, Vives KP, Spencer DD, Duncan JS. Image-guided intraoperative cortical deformation recovery using game theory: application to neocortical epilepsy surgery. IEEE Trans Med Imaging. 2010;29:322–38.
66. Lunn KE, Paulsen KD, Liu FH, Kennedy FE, Hartov A, Roberts DW. Data-guided brain deformation modeling: evaluation of a 3-D adjoint inversion method in porcine studies. IEEE Trans Biomed Eng. 2006;53:1893–900.
67. Sun K, Pheiffer TS, Simpson AL, Weis JA, Thompson RC, Miga MI. Real-time computer assisted surgery for brain shift correction using biomechanical models. IEEE J Transl Eng Health Med. 2013 (Accepted).
68. Lange T, Wenckebach TH, Lamecker H, Seebass M, et al. Registration of portal and hepatic venous phase of MR/CT data for computer-assisted liver surgery planning. Comput Assist Radiol Surg. 2005;1281:768–72.
69. Lange T, Wenckebach TH, Lamecker H, Seebass M, et al. Registration of different phases of contrast-enhanced CT/MRI data for computer-assisted liver surgery planning: evaluation of state-of-the-art methods. Int J Med Robot Comput Assist Surg. 2005;1:6–20.
70. Cash DM, Miga MI, Sinha TK, Galloway RL, Chapman WC. Compensating for intraoperative soft-tissue deformations using incomplete surface data and finite elements. IEEE Trans Med Imaging. 2005;24:1479–91.
71. Clements LW, Dumpiri P, Chapman WC, Galloway RL Jr, Miga MI. Atlas-based method for model updating in image-guided liver surgery, in SPIE medical imaging 2007: visualization, image-guided procedures, and modeling, San Diego, 2007.
72. Dumpuri P, Clements LW, Dawant BM, Miga MI. Model-updated image-guided liver surgery: preliminary results using surface characterization. Prog Biophys Mol Biol. 2010;103:197–207.
73. Rucker DC, Wu YF, Clements LW, Ondrake JE, et al. A mechanics-based nonrigid registration method for liver surgery using sparse intraoperative data. IEEE Trans Med Imaging. 2014;33:147–58.
74. Acerbi F, Broggi M, Eoli M, Anghileri E, et al. Is fluorescein-guided technique able to help in resection of high-grade gliomas? Neurosurg Focus. 2014;36:E5.
75. Valdes PA, Kim A, Leblond F, Conde OM, et al. Combined fluorescence and reflectance spectroscopy for in vivo quantification of cancer biomarkers in low- and high-grade glioma surgery. J Biomed Optics. 2011;16:116007.

Clinical Milestones for Optical Imaging

10

Jonathan Sorger

My wife is a history teacher. George Santayana's observation that "those who cannot remember the past are condemned to repeat it," rings true in the field of optical imaging in the operating room. Much can be learned from historic difficulties in bringing optical imaging modalities successfully into the clinical workflow of the surgical suite. Few of the critical milestones in this field will be realized unless creativity is used to demonstrate that the failure to successfully translate optical and other imaging modalities can be avoided in this nascent area.

One important benefit that optical imaging offers over other modalities such as ultrasound, photo acoustic imaging (see Chap. 2), magnetic resonance, X-ray and computed tomography is the potential for coregistration of the white-light and augmented image. If the photons required for imaging can be gathered from the same camera used to guide the surgery, nontrivial issues such as organ deformation are dealt with automatically. Optical imaging of endogenous contrast is extremely appealing as the burden to generate in vivo proof-of-principle is quite low. Food and Drug Administration (FDA)-approved devices for implementing various optical imaging techniques such as narrow-band imaging (NBI) and autofluorescence have been available to clinicians and researchers since 2006 [1]. That said, these techniques are, for the most part, considered to be in the clinical research phase as surgeons seek ways to derive clinical value. While methods utilizing endogenous tissue contrast such as NBI, Raman spectroscopy, and autofluorescence have been used to evaluate bladder [2], head and neck [3], gastrointestinal [4] tissues on an experimental basis, few studies have demonstrated clinical data justifying routine use in the surgical environment.

While NBI, discussed in Chap. 21, has shown promise in guiding biopsies for the diagnosis of Barrett's esophagus [5], evaluating bladder cancer [6], and the detection of early neoplasia of the gastrointestinal tract as shown in Fig. 10.1, other efforts cast doubt on the usefulness of the techniques when compared to white-light endoscopy [8]. Techniques such as Raman spectroscopy have been shown to discriminate between normal and malignant tissues however the signals generated are very weak (Fig. 10.2) and the measurement area is very small [9]. An optical technique must demonstrate clinical relevance with a decent signal to noise ratio achievable in near-real-time, in addition to easily fitting into the clinical workflow. Acquired data needs to be presented in an easy-to-understand format, preferably overlaid, or related to the white-light image visible to the surgeon. The combination of wide-field and microscopic imaging techniques is required for realistic implementation of such technologies into the clinical workflow of the operating the-

J. Sorger (✉)
Intuitive Surgical Incorporated, 1266 Kifer Road, Sunnyvale, CA 94086, USA
e-mail: jonathan.sorger@intusurg.com

Y. Fong et al. (eds.), *Imaging and Visualization in The Modern Operating Room,*
DOI 10.1007/978-1-4939-2326-7_10, © Springer Science+Business Media New York 2015

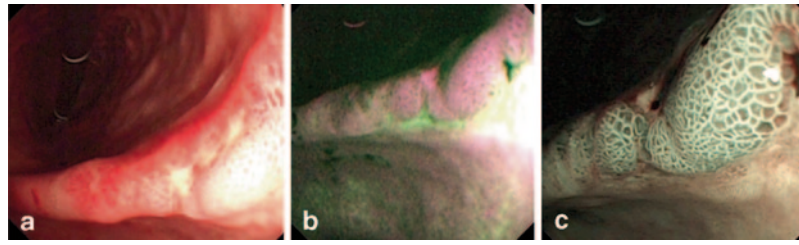

Fig. 10.1 **a** A gastric ulcer, as seen with white-light endoscopy, **b** autofluorescence imaging, and **c** narrow-band imaging, showing the irregular vascular patterns typical of early cancer. [7]

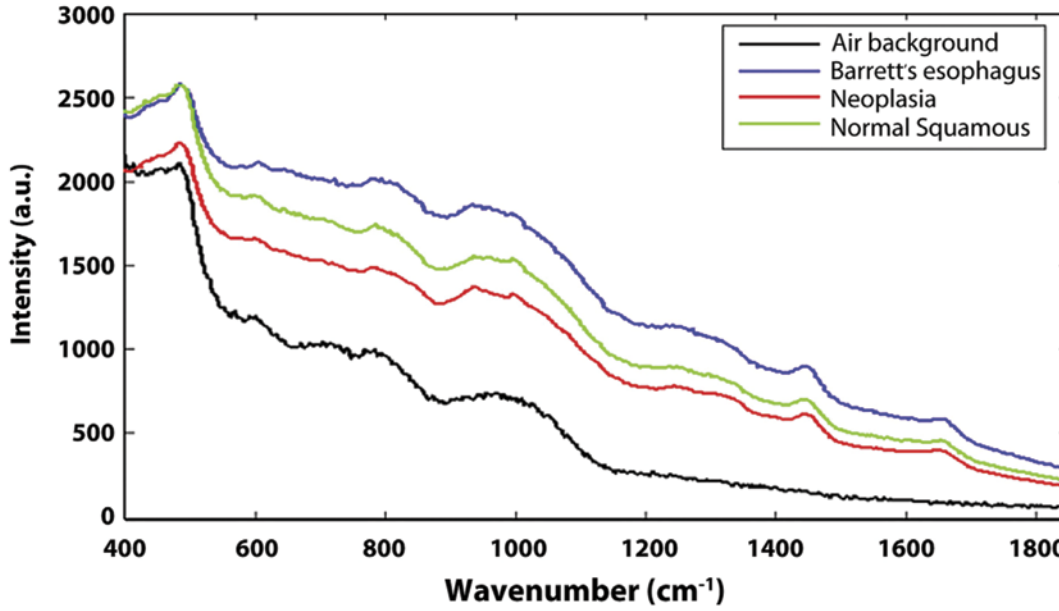

Fig. 10.2 Raman spectroscopic measurements of Barrett's esophagus, adenocarcinoma, and normal esophagus. Spectra have been offset for clarity. (From Almond et al. Endoscopic Raman spectroscopy enables objective diagnosis. Gastrointest Endosc. 2014;79:37–45)

ater, since the field of view in a typical surgery is often orders of magnitude larger than those offered by microscopic technologies, as demonstrated in Fig. 10.3.

Exogenous Contrast Agents

The administration of exogenous contrast agents involves a hurdle not encountered when using devices to generate endogenous contrast, namely the fact that such contrast agents are considered drugs and require the filing of an investigational new drug (IND) application with the FDA. The prospect of gaining the necessary resources for FDA approval for many of the imaging agents is a daunting proposition. Externally administered optical agents generally fall into three classes: Targeted, activatable, or passively accumulating. Examples of nontraditional ways to achieve clinical milestones for some of these optical imaging agents are discussed below.

Interest in the development of optical imaging agents for diagnostic and therapeutic use has increased dramatically in the past decade. Indeed, the ability to provide real-time visualization of critical structures and pathology during a surgical intervention has the potential to provide

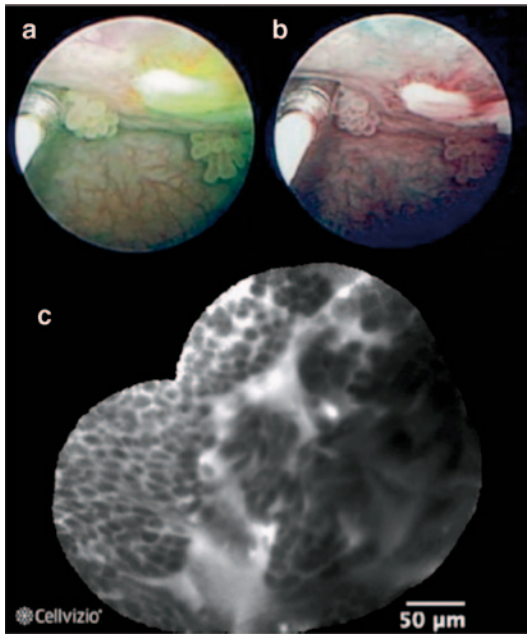

Fig. 10.3 Multimodal imaging using white-light endoscopy (**a**), narrow-band imaging (**b**), and confocal laser endomicroscopy (**c**) of a papillary tumor at the bladder dome. (Reprinted from Curr Urol Rep. 2014;15(5):406)

significant value to patients, surgeons, and the health care system as a whole. The availability of a variety of FDA-approved fluorescence imaging systems for use in the surgical setting is an important milestone that has added to the excitement and will allow easier clinical translation of agents discussed in Chap. 3 from the laboratory. Hamamatsu, Intuitive Surgical, Karl Storz, Leica, Novadaq, Olympus, and Zeiss all have FDA-approved systems available for fluorescence visualization during surgery. Over 1000 systems capable of imaging at a variety of wavelengths exist within operating rooms throughout the world in addition to a variety of experimental devices used in institutional review board cleared studies [10].

Given the availability of FDA and Institutional Review Board (IRB)-approved imaging devices available at a variety of institutions, a roadblock to translation has been lifted. That said, the only optical imaging agents used in significant volume are those that were approved pre-1976, as the translation of agents from the lab to the clinic is expensive. It is helpful for a brief review of optical imaging agents commonly used in the operating room.

The most widely used fluorescent imaging agent in the operating room is the water-soluble, tricarbocyanine dye indocyanine green (ICG), which was developed by Kodak corporation and first described by Fox at the Mayo Clinic in 1956 [11], and received FDA approval in 1959 [12]. It has been used extensively in evaluating hepatic and cardiac function [13], in addition to opthalmology [14] and perhaps most importantly was in use prior to the FDA Medical Device Amendments of 1976. With the introduction of the aforementioned intraoperative systems capable of imaging ICG, its use in the operating room has increased significantly in the past decade.

Recent milestones have been achieved through the use of FDA-approved optical imaging agents in novel procedures. Aside from the original indications for use, devices have recently been approved that use ICG as an adjunctive method for the evaluation of tissue perfusion [15], in addition to visualization of extrahepatic biliary duct structures during cholecystectomy [16]. Several groups have used the compound to identify lymph nodes during surgical procedures involving the head and neck [17], lungs, pelvis [18, 19], colon [20] and rectum [21], (Fig. 10.4), although the use of the compound for such indications has not been approved by the FDA. Sodium fluorescein is another fluorescent agent, first described by Alfred von Baeyer in 1871 [22] whose use exploded in the 1960s when angiography of the eye was first performed. While it is an FDA-approved tracer, the ideal use of fluorescein isothiocyanate (FITC) in open or minimally invasive surgery has not yet been determined. Methylene blue is known to fluoresce and has been used to image structures such as tumors and ureters (Fig. 10.5), although such use is considered to be off-label by US regulatory agencies, and agent toxicity is a potential concern [23]. 5-aminolevulinic acid (5-ALA), a precursor for an FDA-approved photodynamic therapy for skin cancer, has been in trials for use as a fluorescent tracer for over a decade to help delineate brain tumor margins as shown in Fig. 10.6. A similar compound, Hexaminolevulinate HCl was FDA

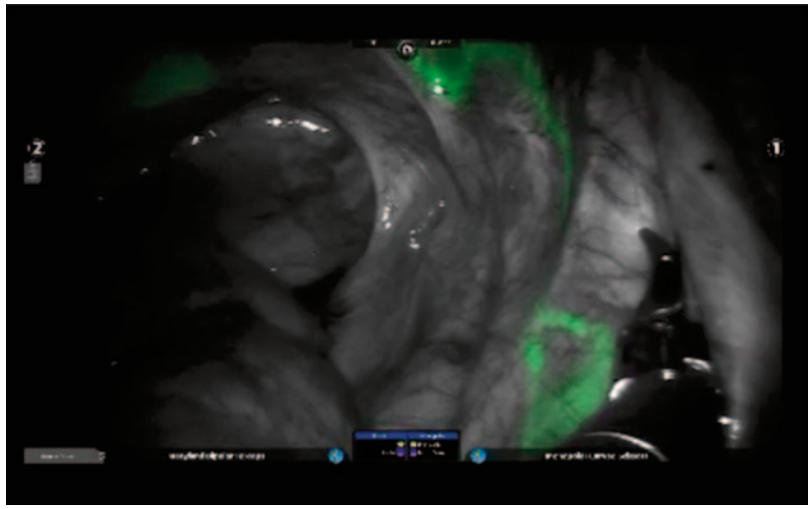

Fig. 10.4 Lymphatic mapping with NIR imaging of the right pelvis after injection of ICG into the uterine cervix. (From Rossi et al. Int J Gynecol Cancer. 2013;23(9):1704–11)

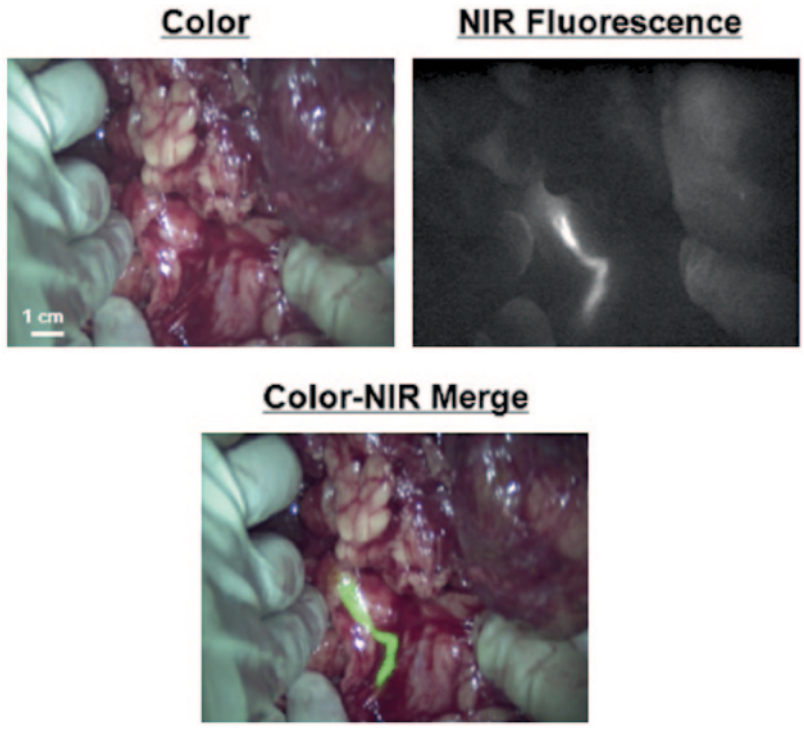

Fig. 10.5 A white-light, NIR fluorescence, and merged image of a ureter containing methylene blue during surgery. (From Verbeek et al. J Urol. 2013;190, 574–9)

approved in 2010 for the visualization of bladder cancer after 10 years of clinical study and is currently sold by Photocure (Oslo, Norway).

There is no shortage of interesting molecular targets for optical imaging, many of which are described in Chap. 3. A significant clinical

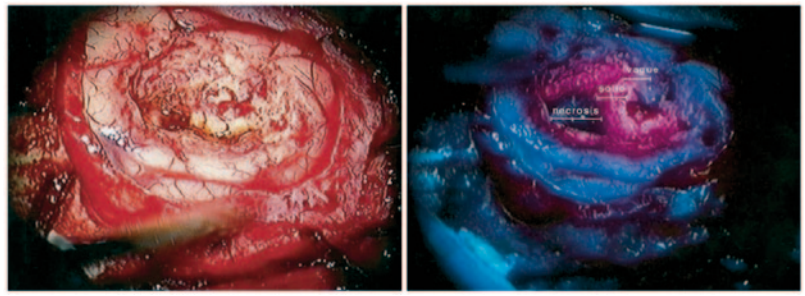

Fig. 10.6 Brain tumor cavity after administration of 5-ALA imaged with white light (*left*) and under fluorescence illumination (*right*). (From Stummer et al. J Neurosurg 2000;93:1003–13)

milestone that has been extremely difficult to achieve is the translation of promising agents to the clinic. An important reason for this is the fact that it costs approximately US $1M to perform the required preclinical testing and good manufacturing practice (GMP) production of compound for human administration. While the exploratory IND mechanism can be useful in reducing the costs of getting a Positron emission tomography (PET) tracer into humans under a phase 0 study, it is unlikely that optical imaging agents can be detected clinically at doses small enough to qualify for micro dosing (<100 μg). Traditional grant funding mechanisms have not historically scored applications for translating optical imaging agents highly, although some groups have had limited success via the Small Business Innovation Research (SBIR) route. The National Cancer Institute's Experimental Therapeutics program [24] (NExT) offers access to National Cancer Institute (NCI) resources and drug development expertise that can be extremely useful in helping researchers in academia, government, and industry generate preclinical data necessary for human use of investigational imaging agents. While not a grant program, these resources can be used to help bridge the IND-required pharm/tox studies, GMP synthesis, IND filing, or phase 0, 1, or 2 clinical evaluation. Three examples of optical imaging agents that have been the recipient of NExT resources include:

- ZW800–1, a novel cyanine near-infrared fluorophore from the laboratory of John Frangioni, for translation into human clinical studies [25]
- A conjugate of Imclone's Cetuximab and Licor's IRDye800 being tested in head and neck cancer by Eben Rosenthal [26]
- Lumicell's activatable nanoparticle whose fluorescence is quenched until in the presence of cancer-specific cathepsins [27]

Indeed, first human use is an incredibly important milestone in terms of demonstrating that the concept and mechanisms behind the agent demonstrates the same behavior in humans as in the petri dishes and preclinical models in which it was discovered/optimized. Examples of mechanisms used to translate optical imaging agents into the clinic are provided below.

Commercial Examples

There are a number of examples of efforts to commercialize optical imaging agents, although the 'exit strategy' typically desired by biotechnology/early stage pharmaceutical companies is not well defined. Much of the economics behind optical imaging agents is extrapolated from the world of PET, MRI, and ultrasound contrast media due to the significant history of such imaging compounds. Nobody likes to accept the numbers cited in Adrian Nunn's 2006 article [28] on imaging agent economics, however until a PET or optical agent is developed and gains FDA approval for less than the often-quoted US $100–200M, investors will be hesitant to place bets in this area.

Successful imaging agents are often failed or modified versions of therapeutics, where significant resources have been spent on some sort of therapeutic response. Indeed, the compound 2-deoxy-D-glucose, which did not demonstrate efficacy as a cancer drug was repurposed into a ^{14}C labeled version which was followed by the

fluorinated version, fludeoxyglucose (F18), that forms the basis for most PET scans performed today [29].

A modern example is that of EC17, an FITC conjugate compound developed by Endocyte (West Lafayette, IN) as an immunotherapy that targets antigenic molecules to cancer cells in order to help the immune system detect and reduce or eliminate cancerous tumors. As it is no longer present on the Endocyte pipeline webpage, the therapy presumably did not perform adequately to justify further investment. However, since it was developed for the clinical trials process under GMP, Endocyte provided some EC17 to the University of Groningen where van Dam administered the compound to ten patients undergoing surgical resection of ovarian tumors [30]. Although only 3/10 patients demonstrated tumor fluorescence, it was noted that since only 3/10 patients stained positive for folate receptor α, the sensitivity was 100%. This was a major milestone in the field of optical imaging, as it provided an in vivo example of real-time tumor assessment, something many in the field believe to be the 'holy grail' of molecular imaging (Fig. 10.7). EC17 was subsequently administered to 30 patients at the Mayo Clinic, after which its use was discontinued due to subpar image qual-

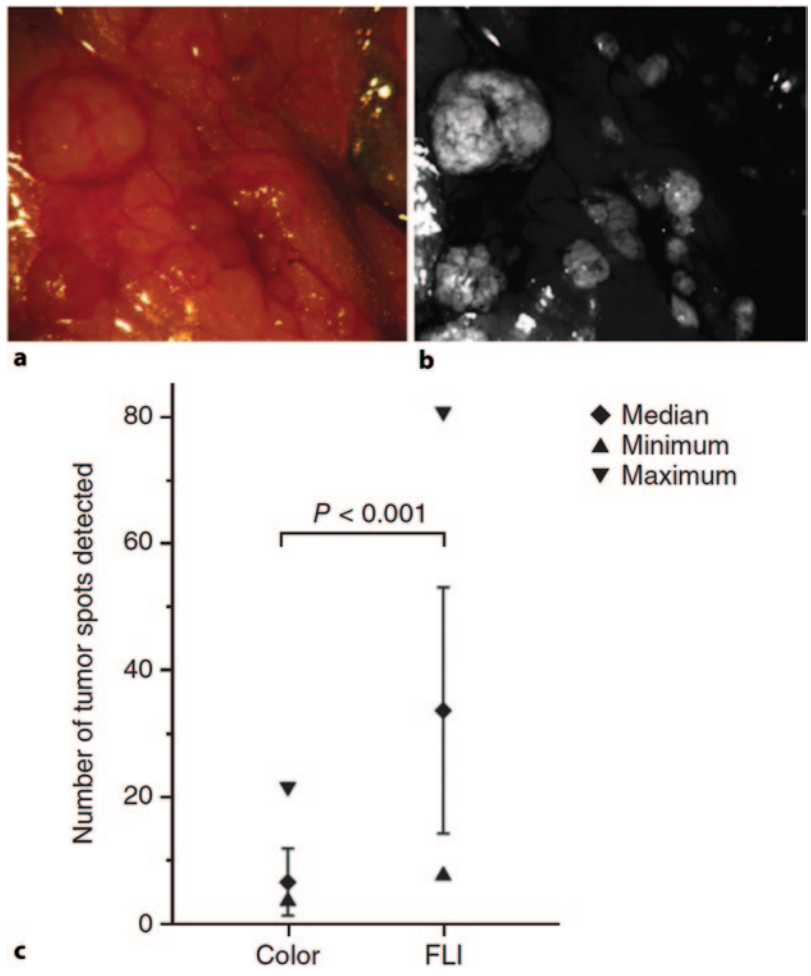

Fig. 10.7 Quantification of tumor deposits ex vivo. Color image (**a**) and the corresponding fluorescence (*FLI*) image (**b**). Scoring was made on three color images (median = 7) and their corresponding fluorescence images (median = 34). (Reprinted from [30])

ity [31]. Additional studies in lung, renal and breast cancer in addition to parathyroid disease took place at the University of Pennsylvania and Leiden University Medical Center, revealing the suboptimal performance of the FITC-based compound, namely depth penetration issues and problems with autofluorescence. EC17 continues to demonstrate its excellent safety profile, having been given to > 350 patients to-date. The technology has been licensed to OnTarget Laboratories (Northbrook, IL) as a fluorescent imaging agent. In order to overcome some of the shortcomings of the FITC-based agent, OnTarget has linked folate to a fluorophore in the near infrared range, and is currently in human trials.

Licor Biosciences (Lincoln, NE) has worked to facilitate the use of its IRDye800CW agent in clinical trials by manufacturing the ester form of the fluorophore under GMP and submitting drug master files for the compound with US and European regulatory agencies. A private company with products in the biotechnology equipment, reagent, and environmental analytics space, Licor has funded such efforts internally and has received many Small Business Innovation Research (SBIR) grants over the past two decades. The availability of the drug master files and GMP grade compound has enabled investigators to detect clinically available monoclonal antibodies such as Roche's bevacizumab and Imclone's cetuximab with fluorescence-capable cameras [32].

Akrotome Imaging (Cleveland, OH) was founded in 2008 with the goal of translating protease-binding, quenched, near-infrared probes that can be used in a variety of clinical applications, including optical imaging during cancer surgery (Fig. 10.8). The company was an SBIR recipient in 2011. While systemically or topically administered imaging agents must undergo toxicity testing required for pharmaceuticals, the application of Akrotome's imaging agents to excised tissue in order to verify a negative tissue margin lowers the economic burden for clinical testing. While Akrotome must still compare the efficacy of their agents against a clinical gold standard, it may be possible to get approval without a direct comparison to histopathology. It is interesting to note that Dune Medical (Caesarea, Israel) received FDA clearance of their MarginProbe radio frequency spectroscopy device by demonstrating a 6% ab-

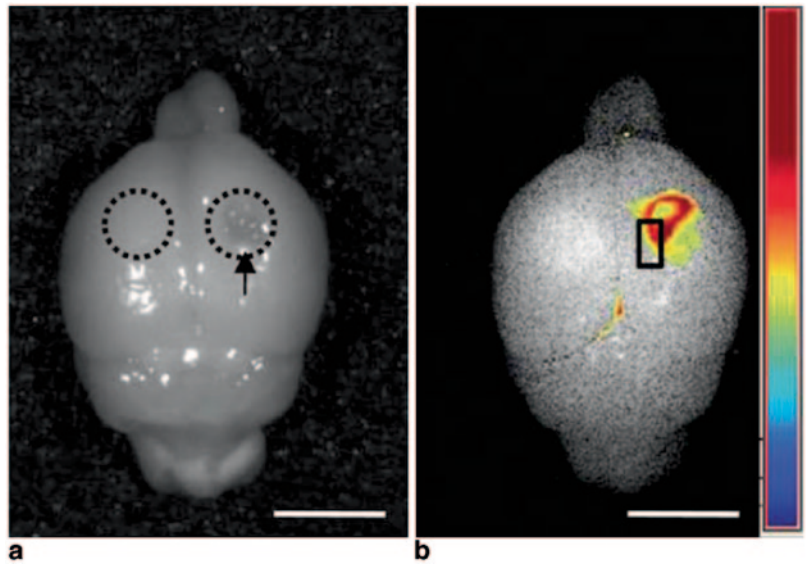

Fig. 10.8 A monochromatic image of a mouse brain **a** with a tumor growing near the dorsal surface (*arrow*). **b** The unmixed false colored map of pixel intensity representing the presence of topically applied quenched-activity-based imaging agent at 35 min post application. (From Cutter et al. Topical Application of Activity-Based Probes for Visualization of Brain Tumor Tissue. PLoS ONE 2012;7(3))

solute or 23 % relative reduction in re-excision procedure rates in breast-conserving surgery when compared to an arm without the use of the MarginProbe. Approval was granted despite the device producing false positive and negative readings as high as 66 and 25 %, respectively, in a randomized prospective multicenter trial involving nearly 600 patients [33].

Blaze Biosciences (Seattle, WA) was founded in 2010, based on the chlorotoxin work of Jim Olson [34]. TumorPaint, a modified chlorotoxin peptide tagged with ICG, has hit the first major milestone in optical imaging development, as it is currently undergoing human safety and dose-finding studies in skin cancer. Subsequent areas for the application of the technology may include brain, prostate, lung, breast, colorectal, head and neck cancers in addition to sarcomas. Blaze Biosciences recently raised a Series B financing round from its investors.

ImaginAb (Culver City, CA) re-engineers antibodies into smaller proteins whose pharmcokinetics differ from the larger antibodies from which they are derived. Founded in 2007 and the recipient of an SBIR award as well as a Series A financing round, ImaginAb is focused on the development of imaging agents in oncology and immunology, as stand-alone clinical tools to address unmet needs in pancreatic, prostate and ovarian cancer. Clinical trials for its two lead products commenced in 2013 and the lead program, a "minibody" against prostate-specific membrane antigen (PSMA) is currently in phase II studies as a ^{89}Zr-labeled PET tracer. Although the first agent is a PET tracer, significant potential exists for optical conjugates (Fig. 10.9) for intra-operative/surgical applications and the company is currently planning clinical studies of optical conjugates in the latter part of 2014 [35]. ImaginAb partners with pharmaceutical companies to develop imaging agents based on their biologic pipelines. This "partnership" model allows the rapid development of an imaging agent that binds to the same target as the parent antibody or antibody drug conjugate. This technology can be used for patient selection, indication scouting, and therapy management, streamlining clinical trials and aiding in regulatory approvals.

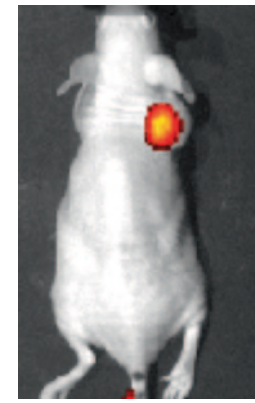

Fig. 10.9 Fluorescence image of a PSMA-expressing tumor tagged with a minibody conjugated to a near-infrared fluorophore. (Courtesy, ImaginAb)

As much of the economics in the optical imaging agent space is derived from the PET-imaging agent experience, it was significant when Siemens Healthcare exited the tracer development market in 2013, divesting its significant agent pipeline. Indeed, as Eli Lily (Indianapolis, IN) acquired the tau protein imaging compounds, and Threshold Pharmaceuticals (South San Francisco, CA) acquired the hypoxia imaging agent HX4 as a companion diagnostic to their hypoxia therapeutic TH-302, Siemens verified that the pharmaceutical company 10–15 year timelines and US $100–200M clinical trials processes were not compatible with the timelines of an established medical device company.

While first-in-human use is necessary to generate translational proof-of-concept data, an important clinical milestone related to agent development is the demonstration that an imaging agent can gain the reimbursement required to generate revenues to entice investors. This is no easy task. In order to argue for reimbursement, an agent must perform a task equivalent to, or better than the current gold standard measurement. Once again, looking at the development of imaging agents from other modalities can be instructive, namely PET-imaging agents for measuring tissue hypoxia. Many clinical studies argued for a comparison with Eppendorf needle electrodes, which had been used for decades to assess tissue oxygenation [36]. Unfortunately, it turned out

that Eppendorf electrodes have a difficult time distinguishing hypoxic from necrotic tissue [37]. In fact, Eppendorf electrodes are no longer sold or supported by any company. So what is a good gold standard? With optical imaging agents for oncologic tumor margin detection, one can imagine histopathology being a reasonable comparator.

The conflict between academic motivation and commercialization has also contributed to challenges in getting promising imaging tracers approved, as academics have traditionally been rewarded for publishing unique chemical compounds as opposed to cooperating with other groups to advance the clinical trials of such agents. If we once again look to hypoxia imaging as an educational example, one can see that no fewer than six hypoxia imaging markers were developed over the past 30 years: [18F]-EF5 [38], [18F]-FAZA [39], [18F]-FMISO [40], [18F]-HX4 [41], [18F]-FETNIM [42] and [64Cu]-ATSM [43]. None have gone through the entire clinical trials process and received FDA approval, despite hundreds of publications documenting their use. An 891 patient, 89 site, 16 country study of the hypoxia sensitizer tirapazamine failed to demonstrate a survival advantage over traditional chemotherapy for head and neck cancer [44], despite the knowledge that a hypoxia imaging agent had prognostic significance [45] for outcomes in patients demonstrating hypoxic tumors.

Today, there are no fewer than10 PSMA imaging agents that have been explored as fluorescent markers for prostate cells, or cancer [46–55]. Are we as a community heading in the right direction? Or will optical imaging go the route of hypoxia agents?

Examples of Recent Agent Approvals

Avid Radiopharmaceuticals' (Philadelphia, PA) Amyvid (florbetapir) was a long-overdue example of a novel medical imaging agent succeeding in gaining FDA approval. Capable of imaging beta-amyloid plaques in the brain, Amyvid is a rare imaging agent that has gained FDA approval prior to the availability of a therapeutic that can alter the course of the disease. Avid raised approximately US $70M prior to being acquired by Eli Lilly in 2010, and one can assume that the majority of these funds went towards funding florbetapir's approval. FDA approval was not granted until 2012, so it is likely that additional funds were required. An important milestone that remains to be achieved is the existence of an imaging agent of any kind whose reimbursement and revenue generation is sufficient to justify a return on investment by a corporate entity or other investors. It should be noted that 2 years after FDA approval and with over US $70M invested, florbetapir is not reimbursed for any indication.

Prostascinct (capromab pendetide, Jazz Pharmaceuticals, Dublin Ireland), is a SPECT imaging agent comprised of a monoclonal antibody linked to $Indium^{111}$ that specifically targets PSMA and was approved by the FDA in 1996. Ten years later, annual revenues stood at US $9.1M, approximately where they stood 1 year after approval, despite a potential market size of US $50M [56]. Similarly, Hexvix (hexaminolevulinate, Photocure, Oslo Norway), an optical imaging agent used in conjunction with blue light cystoscopy for the detection of bladder cancer had revenues of US $14M in 2013, 3 years after gaining FDA approval. In 2014, the Centers for Medicare & Medicaid Services is folding in the costs of Cysview into the procedure reimbursement code for cystoscopy, effectively not providing a separate reimbursement code for the imaging agent, reducing payment to the hospital for use of the drug.

Conclusion

Some believe that the only economically viable way to introduce an imaging agent to the market is to tie the agent to a therapeutic as a companion diagnostic. On the pharmaceutical side, Genentech (South San Francisco, CA) famously partnered with Dako (Glostrup, Denmark) for their fluorescence in situ hybridization test to indicate patient HER2 status in 1996 during their trials of Herceptin (trastuzumab). Herceptin received an

indication for patients "whose tumors overexpress the HER2 protein" and Genentech needed an approved test to stratify those patients for the approved indication. Dako's HercepTEST received simultaneous approval with Herceptin in 1998. Patients with wild-type K-ras mutation respond better to Erbitux (cetuximab) than those without. Roche's Tarceva (Erlotinib hydrochloride) is indicated to use in metastatic NSCLC patients who test positive for specific EGFR mutations, which can be tested for using clinically available EGFR mutation tests. The list will continue to grow in the coming years…. Some propose that companion imaging agents will be required to select therapy-responsive populations in the future, as might have been with Sanofi's tirapazamine.

Can we realize the benefits that optical imaging agents promise to deliver to surgical patients? Creativity and cooperation from members of the optical imaging community must be used to demonstrate that this modality can be a cost-effective solution for guiding patient therapy. Indeed, "history will teach us nothing…if we seek solace in the prisons of the distant past."

References

1. http://www.olympus-global.com/en/news/2006b/nr061226evisse.jsp. Accessed 7 April 2014.
2. Cheung G, et al. Recent advances in the diagnosis and treatment of bladder cancer. BMC Med. 2013;11:13.
3. Piazza C, et al. Narrow band imaging in endoscopic evaluation of the larynx. Curr Opin Otolaryngol Head Neck Surg. 2012;20(6):472–6.
4. Carnes J, et al. Optical molecular imaging in the gastrointestinal tract. Gastrointest Endosc Clin N Am. 2013;23(3):707–23.
5. Mannath J, et al. Narrow band imaging for characterization of high grade dysplasia and specialized intestinal metaplasia in Barrett's esophagus: a meta-analysis. Endoscopy. 2010;2(5):351–9.
6. Herr HW. Narrow-band imaging evaluation of bladder tumors. Curr Urol Rep. 2014;15(4):395. doi:10.1007/s11934-014-0395-4.
7. Singh R, et al. Comparison of high-resolution magnification narrow-band imaging and white-light endoscopy in the prediction of histology in Barrett's oesophagus. Scand J Gastroenterol. 2009;44(1):85–92.
8. Sharma P, et al. Standard endoscopy with random biopsies versus narrow band imaging targeted biopsies in Barrett's oesophagus: a prospective, international, randomized controlled trial. Gut. 2011;62(1):15–21.
9. Kallaway C, et al. Advances in the clinical application of Raman spectroscopy for cancer diagnostics. Photodiagn Photodyn Ther. 2013;10(3):207–19.
10. van den Berg NS, et al. Fluorescence guidance in urologic surgery. Curr Opin Urol. 2012;22(10):109–20.
11. Fox I, Brooker G, Heseltine D, Essex H, Wood E. New dyes for continuous recording of dilution curves in whole blood independent of variations in blood oxygen saturation. Am J Physiol. 1956;187:599.
12. http://www.accessdata.fda.gov/Scripts/cder/drugsatfda/index.cfmfuseaction=Search.Label_ApprovalHistory#apphist. Accessed 8 April 2014.
13. Schaafsma, et al. The clinical use of indocyanine green as a near-infrared fluorescent contrast agent for image-guided oncologic surgery. J Surg Oncol. 2011;104(3):323–32.
14. Flower R, Hochheimer B. Indocyanine green dye fluorescence and infrared absorption choroidal angiography performed simultaneously with fluorescein angiography. Johns Hopkins Med J. 1976;138:33–42.
15. http://www.accessdata.fda.gov/cdrh_docs/pdf9/K091515.pdf. Accessed 8 April 2014.
16. http://www.accessdata.fda.gov/cdrh_docs/pdf12/K124031.pdf. Accessed 8 April 2014.
17. Bredell MG. Sentinel lymph node mapping by indocyanin green fluorescence imaging in oropharyngeal cancer—preliminary experience. Head Neck Oncol. 2010;2:31.
18. Holloway RW, et al. Detection of sentinel **lymph nodes** in patients with endometrial cancer undergoing robotic-assisted staging: a comparison of colorimetric and fluorescence imaging. Gynecol Oncol. 2012;126(1):25–9.
19. Rossi EC, et al. Robotically assisted fluorescence-guided **lymph node** mapping with **ICG** for gynecologic malignancies: a feasibility study. Gynecol Oncol. 2012;124(1):78–82.
20. Hirche C, et al. Ultrastaging of colon cancer by sentinel node biopsy using fluorescence navigation with indocyanine green. Int J Colorectal Dis. 2012;27(3):319–24.
21. Noura S, et al. Feasibility of a lateral region sentinel **node** biopsy of lower rectal cancer guided by indocyanine green using a near-infrared camera system. Ann Surg Oncol. 2010;17(1):144–51.
22. von Baeyer A. Uber ein neue Klasse von Farbstoffen. Ber Deut Chem Ges. 1871;4:555.
23. Masannat YA, et al. DNA damaging effects of the dyes used in sentinel node biopsy: possible implications for clinical practice. J Surg Res. 2009;154(2):234–8.
24. http://next.cancer.gov. Accessed 21 March 2014
25. Hyun H, et al. cGMP-compatible preparative scale synthesis of near-infrared fluorophores. Contrast Media Mol Imaging. 2012;7(6):516–24.
26. http://www.cancer.gov/clinicaltrials/search/view?cdrid=754994&version=HealthProfessional&protocolsearchid=12556679. Accessed 28 March 2014.
27. http://clinicaltrials.gov/ct2/show/NCT01626066?term=Cathepsin+Activatable+Fluorescent+Probe&rank=1. Accessed 28 March 2014.

28. Nunn AD. The cost of developing imaging agents for routine clinical use. Invest Radiol. 2006;41(3):206–12.
29. Fowler JS, Wolf AP. 2-deoxy-2-[18F]fluoro-D-glucose for metabolic studies: current status. Int J Rad Appl Instrum A. 1986;37(8):663–8.
30. van Dam GM, et al. Intraoperative tumor-specific fluorescence imaging in ovarian cancer by folate receptor-α targeting: first in-human results. Nat Med. 2011;17(10):1315–9.
31. Personal Communication, Marty Low, OnTarget Laboratories. 11 March, 2014
32. http://clinicaltrials.gov/ct2/show/NCT01508572. Accessed 28 March 2014.
33. Schnabel F, et al. A randomized prospective study of lumpectomy margin assessment with use of MarginProbe in patients with nonpalpable breast malignancies. Ann Surg Oncol. 2014;21(5):1589–95.
34. Akcan M, et al. Chemical re-engineering of chlorotoxin improves bioconjugation properties for tumor imaging and targeted therapy. J Med Chem. 2011;54:782–7.
35. Personal communication Christian Behrenbruch, 31 March, 2014.
36. Vaupel P, et al. Oxygenation of human tumors: evaluation of tissue oxygen distribution in breast cancers by computerized O2 tension measurements. Cancer Res. 1991;51:3316–22.
37. Kelada OJ, Carlson DJ. Molecular imaging of tumor hypoxia with positron emission tomography. Radiat Res. 2014;181(4):335-49.
38. Ziemer LS, et al. Noninvasive imaging of tumor hypoxia in rats using the 2-nitroimidazole 18F-EF5. Eur J Nucl Med Mol Imaging. 2003;30(2):259–66.
39. Piert M, et al. Hypoxia-specific tumor imaging with 18F-fluoroazomycin arabinoside. J Nucl Med. 2005;46(1):106–13.
40. Jerabek PA, et al. Synthesis and biodistribution of 18F-labeled fluoronitroimidazoles: potential in vivo markers of hypoxic tissue. Int J Rad Appl Instrum A. 1986;37(7):599–605.
41. van Loon J, et al. PET imaging of hypoxia using [18F]HX4: a phase I trial. Eur J Nucl Med Mol Imaging. 2010;37(9):1663–8.
42. Chung JK, et al. The effect of tumor size on F-18-labeled fluorodeoxyglucose and fluoroerythronitroimidazole uptake in a murine sarcoma model. Ann Nucl Med. 1999;13(5):303–8.
43. Lewis JS, et al. Evaluation of 64Cu-ATSM in vitro and in vivo in a hypoxic tumor model. J Nucl Med. 1999;40(1):177–83.
44. Rischin D, et al. Tirapazamine, cisplatin, and radiation versus cisplatin and radiation for advanced squamous cell carcinoma of the head and neck: a phase III trial of the trans-Tasman radiation oncology group. J Clin Oncol. 2010;28(18):2989–95.
45. Rischin D, et al. Prognostic significance of [18F]-misonidazole positron emission tomography-detected tumor hypoxia in patients with advanced head and neck cancer randomly assigned to chemoradiation with or without tirapazamine: a substudy of trans-Tasman radiation oncology group study 98.02. J Clin Oncol. 2006;24(13):2098–104.
46. Chen Y. A low molecular weight **PSMA**-based fluorescent imaging agent for cancer. Biochem Biophys Res Commun. 2009;390(3):624–9.
47. Liu T, et al. A targeted low molecular weight near-infrared fluorescent probe for prostate cancer. Bioorg Med Chem Lett. 2010;20(23):7124–6.
48. Nakajima T, et al. Targeted, activatable, in vivo fluorescence imaging of prostate-specific membrane antigen (PSMA) positive tumors using the quenched humanized J591 antibody-indocyanine green (ICG) conjugate. Bioconjug Chem. 2011;22(8):1700–5.
49. Leung K. Quenched indocyanine green-anti-prostate-specific membrane antigen antibody J591. Molecular imaging and contrast Agent Database (MICAD) [Internet]. Bethesda (MD): National Center for Biotechnology Information (US); 2011 Dec 08.
50. Zhang F, et al. An anti-PSMA bivalent immunotoxin exhibits specificity and efficacy for prostate cancer imaging and therapy. Adv Health Mater. 2013;2(5):736–44.
51. Laydner H, et al. Robotic real-time near infrared targeted fluorescence imaging in a murine model of prostate cancer: a feasibility study. Urology. 2013;81(2):451–6.
52. Leung K. Cy7-(3S,7S)-26-Amino-5,13,20-trioxo-4,6,12,21-tetraazahexacosane-1,3,7,22-tetracarboxylic acid. Molecular Imaging and Contrast Agent Database (MICAD) [Internet]. Bethesda (MD): National Center for Biotechnology Information (US); 2012 Dec 27.
53. Kelderhouse LE, et al. Development of tumor-targeted near infrared probes for fluorescence guided surgery. Bioconjug Chem. 2013;24(6):1075–80.
54. Shen D, et al. Evaluation of phage display discovered peptides as ligands for prostate-specific membrane antigen (PSMA). PLoS One. 2013;8(7):e68339.
55. Lütje S, et al. Dual-modality image-guided surgery of prostate cancer with a radiolabeled fluorescent anti-PSMA monoclonal antibody. J Nucl Med. 2014;55(6):995–1001.
56. Cytogen Corporation Annual Report, 1998.

3D in the Minimally Invasive Surgery (MIS) Operating Room: Cameras and Displays in the Evolution of MIS

11

Brian J. Dunkin and Caroline Flowers

Introduction

Minimally invasive surgery (MIS) utilizes camera systems and video displays to allow for complex procedures to be performed through small access points. Most commonly, the term is applied to abdominal surgery, but it is also applicable to other areas such as neuro, vascular, and orthopedic surgery. This chapter focuses on MIS in the abdomen since most work in three-dimensional (3D) imaging in the operating room (OR) has been done in this area.

Historically, the field of minimally invasive surgery was limited in scope until the development of cameras that could be attached to a lens system for viewing. By projecting images from the camera on a video display, multiple operators could now see within the abdomen at the same time and thus participate in the procedure in a coordinated way, allowing for more complex operations to be performed. Looking into the abdomen with a camera/lens system is called laparoscopy, and the first complex operation done as part of the modern age of laparoscopy was removal of the gallbladder in 1988 [1]. Since that time, every abdominal surgery that had traditionally been done using an open approach has now been done laparoscopically. The technique has revolutionized surgery to the benefit of patients.

Learning laparoscopic surgery is particularly challenging because it requires performing complex procedures in a two-dimensional (2D) environment with long instruments that provide minimal haptic feedback, and work across a fulcrum—i.e., small points of entry across the abdominal wall. Limitations in the viewing area combined with loss of depth perception and less accurate tissue manipulation resulted in errors reflected in an increase in the incidence of bile duct injuries during the early days of laparoscopic cholecystectomy. This incidence has still not completely returned to the baseline seen during the open cholecystectomy era.

Laparoscopy also led to a technical revolution in imaging in surgery. Once the surgical field is captured electronically and displayed on a monitor, that image is now available for manipulation. This began with magnification and routing to multiple displays in the OR to improve team performance. It continues to advance in two major areas: (1) improvement of the quality of the visual image and (2) enhancement of the "reality" of the light image by using computer power to combine it with other data, such as radiologic imaging. Both areas of effort aim to improve the performance of the operative team.

One area of work focused on improving the quality of the operative visual image is the creation of 3D cameras and display systems. 3D technology holds the promise of restoring depth

B. J. Dunkin (✉) · C. Flowers
Department of Surgery, Houston Methodist Hospital, 6550 Fannin Street, SM1661A, Houston, TX, USA
e-mail: bjdunkin@tmhs.org

Y. Fong et al. (eds.), *Imaging and Visualization in The Modern Operating Room,*
DOI 10.1007/978-1-4939-2326-7_11, © Springer Science+Business Media New York 2015

perception to the operative team with the potential to improve accuracy and shorten the learning curve for MIS. It may be particularly useful when performing parts of a procedure that require a high degree of precision, such as the creation of an anastomosis or dissection of a critical structure. 3D light-based images may also be combined with other 3D imaging such as computer tomography (CT) or magnetic resonance imaging (MRI) to augment reality and improve operative performance. While 3D laparoscopic technology has been around for decades, only recently has it reached a level of quality that is leading to more common use in the modern OR. The move to lighter glasses, or no glasses, to view the 3D display and the achievement of high definition images with video recording capability have all been essential improvements.

This chapter reviews the topics of human sight, and the modern technology required to display operative images in 3D. It also provides descriptions of commercially available 3D platforms for the OR, reviews data regarding its performance, and discusses future developments in 3D including glassless displays and augmented reality.

How Humans Perceive Depth?

Human vision is amazingly complex, and multiple strategies are used by the human brain to understand the visual world. One of the most important visual elements when manipulating objects and navigating through the world is depth perception—the ability to perceive the relative distance of objects in one's visual field. Humans use 14 visual cues to perceive depth. Interestingly, only 3 of the 14 require binocular vision with two eyes (Table 11.1). This is why most surgeons are able to adapt to the 2D environment provided by a standard laparoscope. However, while monocular cues are effective at judging general distance between objects, they cannot accurately determine the difference in depth between them—a critical element in surgery. Binocular vision is required for that.

One of the strongest cues of depth is stereopsis, which relies on slightly different images of the same object being received by the left and right retinas due to their differing horizontal location (Fig. 11.1). These views are shifted relatively, and the magnitude of that shift creates the perception of three-dimensional locations [2]. Another cue for depth perception is vergence. As two eyes focus on an object, the angle of the pupil to the object is adjusted. This movement is controlled by the extra-ocular muscles and the activity of these muscles is perceived by the visual cortex and used to understand depth.

Accommodation is another activity used in human vision, but not required for depth perception. It is the adjustment of the optics of the eye to keep an object in focus on the retina as its distance from the eye varies. It is the process of adjusting the focal length of a lens. It is mentioned here because it is an important element in understanding why some people become nauseated or disoriented when viewing 3D displays.

Understanding 3D Technology

Viewing Glasses and Displays

While 3D image techniques have been around for nearly a century, advances in 3D video technology in both recording and viewing has made it a more common phenomenon in the last 30 years. To create the perception of a 3D image when using a camera, a visual phenomenon similar to binocular vision must be implemented, with the camera(s) capturing and projecting two views that are then transmitted to the corresponding eye separately (Fig. 11.2) [3]. Two technical approaches exist to achieve this: autostereoscopic systems and those utilizing viewing aids [2]. Autosteroscopic systems, also known as lenticular screens or holographic systems, do not require the use of glasses, relying instead on the position of the viewer's eyes in relation to the object. In the correct position, a 3D image is seen. A trivial example is the magic eye style pictures which use two overlapping 2D patterns to create 3D images. Austereoscopic technology is not used in surgical practice at present.

Systems with viewing aids can be divided into two categories: time parallel systems, where two camera views are displayed simultaneously, and

Table 11.1 Description of the 14 cues used by the human brain to understand object depth and position. Three require stereopsis

Name	Description	Mono- or binocular	Example
Motion parallax	Differences in relative movement of stationary objects from a moving frame	Monocular	When moving in a car, things by the side of the road are passed quickly, while things on the horizon appear stationary
Depth from motion	Differences in retinal projection of an object as it moves nearer or farther away	Monocular	Moving an object in front of an eye back and forth
Kinetic depth effect	Perceiving the 3D structural form of a moving object	Monocular	The way shadows cast by a 3D object change when the object is rotated, even if the object might appear in 2D
Perspective	Relative size of an object decreases the further away it is	Monocular	When driving, the road appears smaller in width further away, though the absolute width is constant
Relative size	If two objects appear to be similar in size, the	Monocular	
Familiar size	Knowledge of the size of an object at various distances gives information about its current distance	Monocular	Surgeons familiar with the size of a laparoscopic tool can judge its location in the body based on how small it appears on the camera
Aerial perspective	Objects further away have lower color saturation and luminance contrast	Monocular	Far-off objects appear hazy, harder to distinguish individual aspects compared to the same object when it is closer
Accommodation	When focusing on objects at different distances, inter-optical muscles stretch the eye lens and change its focal length. The movements of these muscles are sent to the visual cortex, which interprets the changes	Monocular	The adjustment time required when changing gaze from a near object to a far object
Occlusion	Judging objects' distance based off one object blocking parts of another—the object that appears to be in front must be closer	Monocular	In a solar eclipse, the moon blocks part of the sun—logically, then, the moon must be closer
Curvilinear perspective	Parallel lines appear curved at visual extremes	Monocular	Escher cityscapes
Texture gradient	The closer the object, the more fine the details that can be seen	Monocular	When looking at a finger close up, individual fingerprint shapes can be seen, but when it is moved back, the finger appears uniform in appearance
Lighting and shading	Light reflecting off surfaces and the shape and size of shadows	Monocular	One of the main ways depth is portrayed in drawings
Defocus blur	Since humans can only focus on a range of depths, things that are blurred must be outside of that field of view	Monocular	Used in video and photography for creating a perception of depth

Table 11.1 (continued)

Name	Description	Mono- or binocular	Example
Elevation	If the horizon is visible, objects closer to it are perceived to be farther away than objects far from it	Monocular	Viewing two ships on the water. If one appears at the horizon, then it is concluded to be farther away than one that is not
Stereopsis	Slightly different images of the same object being received by the left and right retinas due to the retinas' differing horizontal location	Binocular	
Vergence	When both eyes focus on the same object, the angle of the pupils change. This movement is controlled by extra-ocular muscles, which send signals to the visual cortex	Binocular	Eyes move toward each other when the object is nearer, and away from each other of the second object is further than the first
Shadow stereopsis	Objects with parallax disparity but with differing shadows are interpreted stereoscopically as a single image	Binocular	

time-multiplexed systems, which rapidly alternate projecting the video image between the right and left view with a time sequence so fast that the brain perceives the images as being projected simultaneously. Two methods of time parallel projection are used. The first uses two cameras and projects the image via individual displays to each eye. This requires a viewing console or head-mounted display and only allows those looking into the console or display to view in 3D. The second uses glasses to view a video monitor, which distinguish between images meant for the left and right eye. These glasses are described as "passive" because they do not communicate with the video display. The simplest of these are anaglyph glasses which use different colored lenses to filter out the images meant for the respective eyes (Fig. 11.3). Movie goers in the early days of 3D will remember these glasses. While inexpensive and able to operate with any image that has been created with these glasses in mind, they

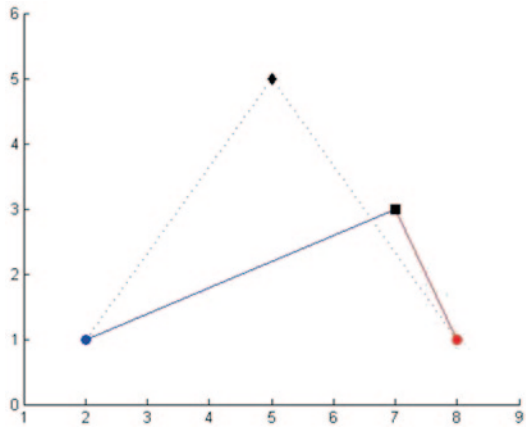

Fig. 11.1 Graphical example of stereopsis

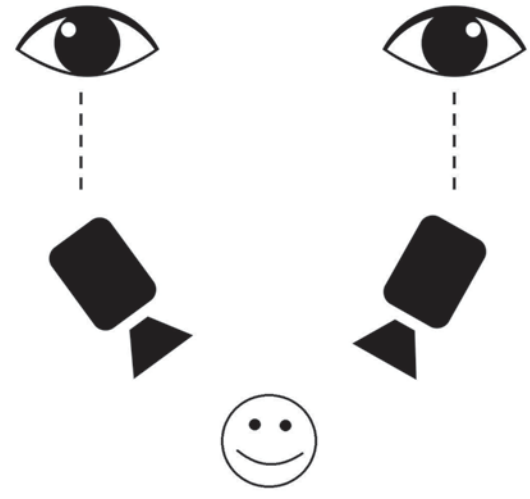

Fig. 11.2 Conceptual image of creating stereopsis with two cameras

Fig. 11.3 Anaglyph 3D glasses

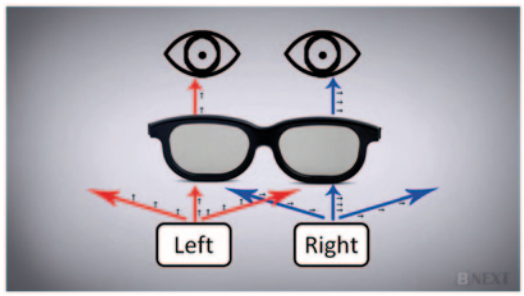

Fig. 11.4 Passive 3D glasses

do not provide an image quality adequate for surgery. However, a more advanced system based on the anaglyph technique has been developed, called super anaglyph. This system uses differing wavelengths of red, blue, and green to separate images in a more subtle way and has been used successfully in cinema. Another variety of passive glasses use polarized lenses to separate super-imposed projections. In this technique, the video monitor displays two images of the same object from different viewpoints. Each image is rendered with a specific polarity (i.e., vertical or horizontal, or circular). The lens of the glasses filters out the polarity of the image that is not intended for that eye (Fig. 11.4). The image quality is excellent with these glasses and they are light weight, durable, and relatively inexpensive. Linear polarized glasses require the user to maintain a level viewing angle while circular polarized glasses allow for the head to be tilted.

Time-multiplexed systems are often referred to as "active" glass systems and utilize alternating darkening of the lens while the corresponding eye's image is displayed on the monitor (Fig. 11.5). The image quality is excellent but the glasses are expensive, somewhat heavy and thus less comfortable to wear, less durable, and require battery power. They can also create a visible flicker that may be uncomfortable for the viewer. Active glasses communicate with the video monitor via an infrared or radiofrequency emitter to coordinate image projection with lens darkening (Table 11.2).

3D video monitors display an output in a variety of ways, including dual-stream (both video streams are combined into a single file without combining the streams themselves), line-by-line (the two streams are captured at different times and combined into a single image), and side-by-side (the video streams are displayed side-by-side). When displaying the video streams, half of the monitor must be devoted to each eye, which intuitively might seem to lead to lower resolution. However, with modern LCD display resolution, and the fact that each eye is still seeing as much information as it did with a standard display, 3D images can be rendered in high definition.

3D in Laparoscopy

When acquiring images for 3D display in laparoscopy, multiple options exist for obtaining the required binocular viewpoints. The most com-

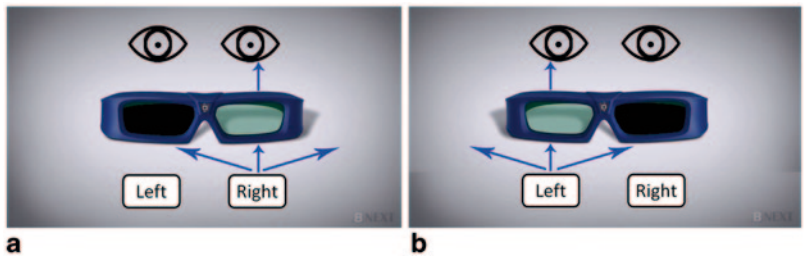

Fig. 11.5 **a** Active 3D glasses—left eye occluded. **b** Active 3D glasses—right eye occluded

Table 11.2 Viewing aids used for 3D

Type	Eye differentiation method	Monitor type	Advantages	Disadvantages
Active	Glasses darken each eye's lens in turn to correspond with the	Monitor must be synced with glasses	Full resolution	Expensive, must coordinate with monitor, uncomfortable
Polarized	Super-imposed images with different angles or handedness, with each eye corresponding to one of the two	Uses special silvered screen	Inexpensive	Lose half of the screen resolution
Anaglyph	The lens for one eye is one color (i.e., blue) while the lens for the other eye is a contrasting color (i.e., red)	Can work with any medium	Inexpensive and do not require special monitors	Low visual quality
Console	Presents two different videos to each eye	Built into the system	Do not lose resolution	Only person at console can see images

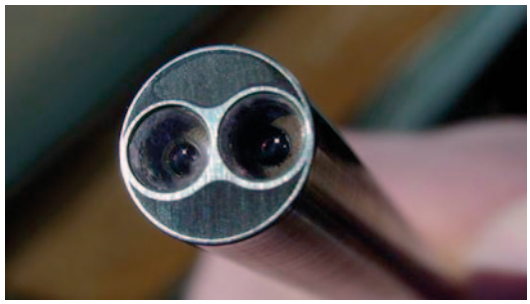

Fig. 11.6 Tip of bi-channeled laparoscope (Karl Storz Endoscopy, Tuttlingen, Germany)

mon solutions utilize either a bi-channeled or single-channeled laparoscope. Bi-channeled laparoscopes have two lens systems combined into one shaft (Fig. 11.6) and the image from each lens is projected into an individual camera for that lens (Fig. 11.7). Advantages of this system include tolerance of near-objects in the field, independent rotation in all directions, and handling identical to a traditional 2D laparoscope [3]. Disadvantages include extreme sensitivity to synchronization and a need for meticulous calibration; if the cameras are misaligned in any way, the program which generates the 3D image will give an inaccurate result.

To overcome these sensitivities some companies have begun producing single-channeled laparoscopes for 3D. One example is a lens occluding stereo endoscope which uses a moveable cover for part of the lens called an optical modulator. An image is captured with the optical modulator in one position (i.e., the "left" portion of the camera view is blocked) and then another image captured with optical modulator in a second position (i.e., the "right" portion of the camera view is blocked; Fig. 11.8). The result is a captured image from two vantage points that is the equivalent of a two-camera system without the concerns of misalignment. A similar device uses translation of the lens itself to achieve the same effect [4]. Another proposed method involves adding an object in front of the camera, such as a glass plate or a series of mirrors; after one image is taken, the center object rotates offering a different viewing angle and a second image is taken (Fig. 11.9). Both this option and the occluded lens system require the camera to remain stationary for at least as long as the two images are processing.

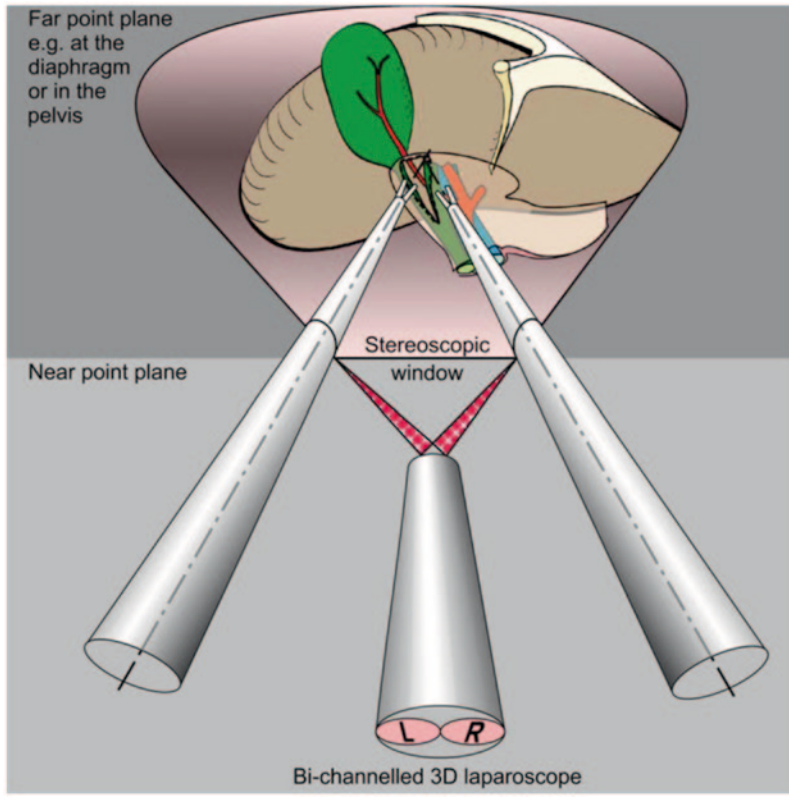

Fig. 11.7 Illustration of image captured with bi-channeled laparoscope

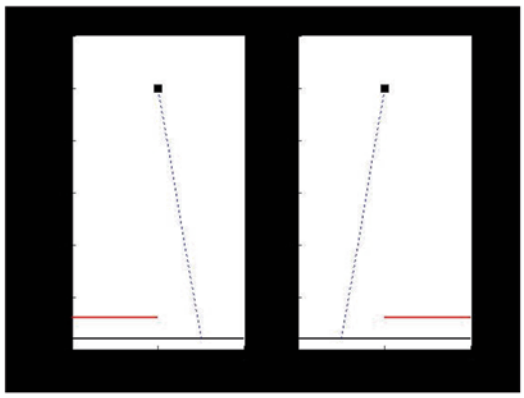

Fig. 11.8 Single-channel 3D laparoscopic camera system using an optical modulator. An image is captured with the optical modulator in one position (i.e., the "left" portion of the camera view is blocked) and then another image captured with optical modulator in a second position (i.e., the "right" portion of the camera view is blocked). The result is a captured image from two vantage points that is the equivalent of a two-camera system without the concerns of misalignment

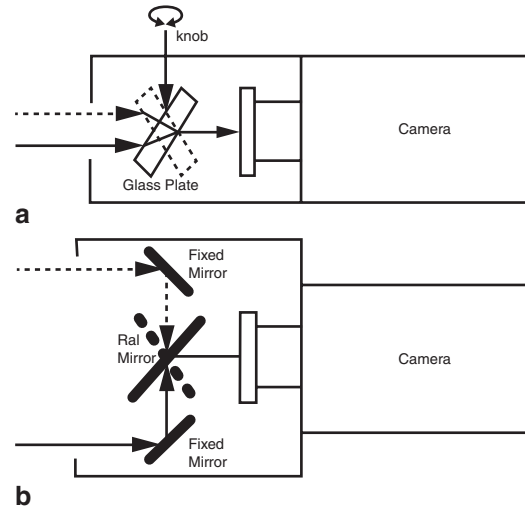

Fig. 11.9 Another method of creating stereopsis using an object in front of the camera, such as a glass plate or a series of mirrors; after one image is taken, the center object rotates offering a different viewing angle and a second image is taken

Commercially Available 3D Laparoscopic Systems

There are currently four companies that manufacture commercially available 3D laparoscopic systems for the OR: Intuitive Surgical (Sunnyvale, California, USA), Karl Storz Endoscopy (Tuttlingen, Germany), Olympus (Tokyo, Japan), and Viking Systems, Inc. (Westborough, Massachusetts, USA).

Intuitive Surgical manufactures the da Vinci Surgical System consisting of a surgeon console, a patient-side cart, Endowrist instruments, and a vision system (Fig. 11.10). The surgeon operates seated at the console while viewing a high definition, 3D image. When the surgeon's head engages the console, a video display for each eye is provided via a binocular laparoscope and dual camera system. The surgeon's fingers grasp the master controls below the display and the system translates the surgeon's hand, wrist, and finger movements into real-time movements of the Endowrist surgical instruments held by four robotic arms on the patient-side cart.

The Karl Storz 3D System consists of a binocular laparoscope with two image sensors installed distally (Fig. 11.11). Zero degree and 30° fields of view models are available. The images from the distal sensors are transmitted to the 3D camera control system, which allows for simultaneous 2D and 3D output and can save the video or still images in 2D form. Passive glasses and a 3D monitor are required to use the endoscope in its 3D capacity.

The Olympus ENDOEYE FLEX 3D videoscope is a deflectable-tip, binocular laparoscope with an 80° field of view and 100° of four-way deflection that can also alternate between 2D and 3D output (Fig. 11.12). The monitor uses circular polarizing glasses and the system can record in 3D. It can also provide multiple 3D outputs including dual-stream (where both video streams are combined into a single file), line-by-line (where the two streams are captured at different times and combined), and side-by-side (where the video streams are displayed side-by- side and processed using glasses).

The Viking 3DHD System model offers two 3D camera heads, each in 0 and 30° fields of view: a 3D single-channel version that allows the surgeon to rotate the laparoscope a complete 360° while the view of the surgical field remains upright, and a 3D dual-channel laparoscope that provides a binocular image as described in the other systems above. Images are displayed in

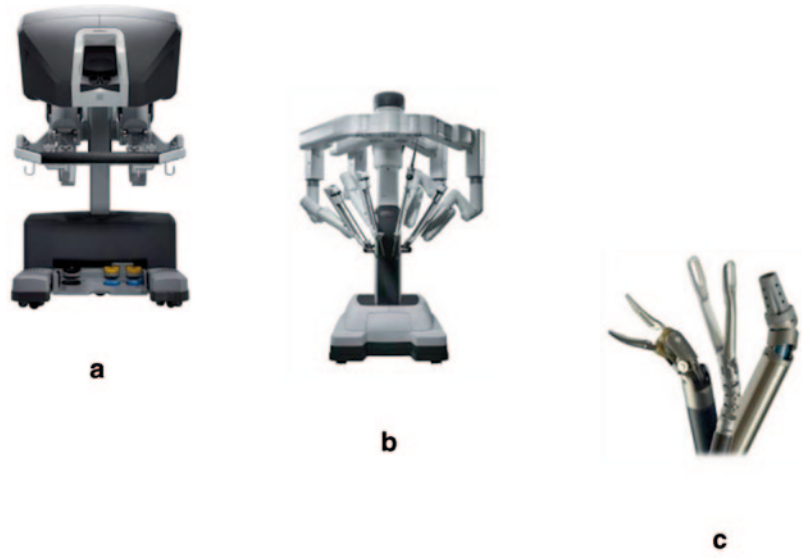

Fig. 11.10 The intuitive surgical da Vinci Surgical System: **a** surgeon console, **b** bedside cart, **c** Endowrist instruments

Fig. 11.11 The Karl Storz 3D system

Fig. 11.12 Olympus ENDOEYE FLEX 3D videoscope

high definition and the viewer wears circular polarized glasses (Fig. 11.13).

Limitations Encountered in 3D Viewing

Despite the technological advances in 3D viewing, the experience can still be uncomfortable for many. One of the main reasons for nausea, disorientation, and headaches encountered while viewing 3D images is a discrepancy between accommodation, a depth cue which extrapolates information from changes in the lens of the eye to achieve focus, and vergence, which extrapolates the same data from movement of both eyes (see Table 11.1). This relationship is one of the many

Fig. 11.13 Viking 3DHD system

redundancies found in the human sensory system. Problems arise, however, when those redundancies offer different "explanations" for what is being viewed and the brain cannot reconcile the two. Stereovision presents a discrepancy between accommodation and vergence. Accommodation is dependent on the *true distance* to the video display surface and does not change regardless of the content of the projection. Vergence is dependent upon the *apparent distance* of the object away from the video display surface (i.e., 3D images appear to "float" in front of the screen) (Fig. 11.14). As the brain attempts to reconcile these two sensory inputs, headaches, visual fatigue, and eyestrain can occur. One method of managing this discrepancy is to work in certain visual regions known as the "comfort zone," an experimentally determined relationship between focal and vergence distance where the eyes can compensate for the discrepancy without feeling side effects [5].

Even if one is not bothered by the common side effects described above, there are other challenges when trying to view in 3D. One in 30 people has complete stereo-blindness and is incapable of seeing in 3D while one in six has some level of stereoscopic impairment. Partial stereo-

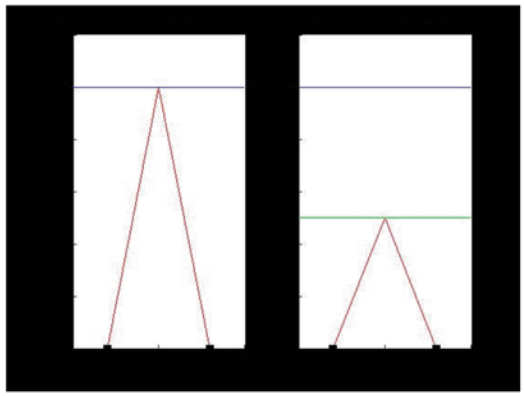

Fig. 11.14 In the first image, the distance for both vergence (*red*) and accommodation (*blue*) are identical. In the second image, the vergence distance is focused on the screens 3D object (represented by the *green line*), while the accommodation distance has not changed. The visual discomfort some feel when using 3D technology is attributed in part to this discrepancy

blindness is often the result of convergence issues such as strabismus, where the eyes are incapable of looking in the same direction, or significant differences in visual acuity (e.g., the vision in one eye is significantly worse than the other causing the "good" eye to become so strongly dominant that the brain does not use both eyes equally). Complete stereo-blindness is most often due to loss of vision in one eye or an inability to converge and/or focus on a point with both eyes [6].

Data

Many studies have been conducted to prove the worth of 3D systems in surgery. Most have been done in a simulation environment with subjects of varying clinical experience performing laparoscopic surgical tasks on inanimate objects. The results of these studies are variable depending on the generation of the technology tested and the experimental design. For instance, Tanagho et al. compared the performance of three laparoscopic surgical tasks by 33 individuals with varying laparoscopic experience in both 2D and 3D and found that 3D enhanced proficiency without producing eye strain or headaches [7]. In addition, participants preferred the 3D visualization. Alaraimi et al. tested novices on the same surgical tasks and found that 3D improved accuracy although it did not reduce overall performance times [8]. In contrast, Mistry et al. found improvement in medical student performance on only one of five of these tasks despite the fact that the majority of subjects believed their performance was aided by using the 3D system [9]. In addition, Currie et al. demonstrated that 3D visualization during robotically assisted mitral valve surgery could not overcome the loss of haptic feedback with both novice and expert surgeons applying significantly more force to the surrounding cardiac tissues compared to conventional open mitral valve annuloplasty [10].

Well-designed clinical studies supporting the use of 3D imaging in the OR are not available in the literature. However, a few small, single-center experiences support the modality. Bilgen et al. showed that using 3D during laparoscopic cholecystectomy significantly shortened procedure time [11]. Tabaee et al. report subjectively improved visualization during transphenoidal pituitary surgery with excellent surgical outcomes and no increase in operative time [12].

Because of the variability of results reported in the literature, some question the usefulness of 3D visualization in the OR. The balance of data, however, does seem to support two main advantages: (1) novice surgeons benefit more from 3D visualization than experts and (2) the utility of 3D depends on the inherent difficulty of the task [13]. Both findings are logical. Novice surgeons have little familiarity with laparoscopy and the additional visual information is useful for this group to judge depth. However, expert laparoscopic surgeons have learned to glean meaningful depth information from 2D images and don't require the stereo cues. Similarly, expert laparoscopists can perform complex tasks relying on nonstereo cues, while less experienced surgeons benefit from additional depth perception on these same advanced tasks. Some predict that as 3D technology evolves, it will become as common place as high definition 2D visualization is today. It was not long ago when high definition laparoscopic cameras and displays were considered a luxury in the OR. Now, they are considered essential for patient safety.

Future

3D technology will continue to advance with single camera systems, glassless (autostereoscopic) displays, and 3D on demand, for only those parts of the operation that require it (thus reducing fatigue). However, 3D imaging can be used for much more. One area of interest is to use the 3D image to obtain tissue surface geometry at the same time as the light visualization is used to guide the surgery. Computer algorithms then merge the surface geometry with the 3D light image to provide a real-time augmented reality that can be used to make organs appear transparent or correct for motion in beating heart surgery [14]. Just as the advent of laparoscopic surgery ushered in the digital age of operative visualization, 3D imaging has the potential to be merged with data acquired from other 3D reconstructed sources (CT, MRI, ultrasound) in order to provide more information to the surgery team at the point of care to make surgery more accurate and less invasive.

Summary

3D imaging in MIS has the potential to restore all 14 cues used by the brain to understand the position and depth of objects. This may be particularly critical for operations that require a high degree of accuracy. 3D technology has advanced significantly over the years with modern systems utilizing passive glasses and providing bright, high definition images. However, adoption into the OR continues to be slow due to cost, uncomfortable viewing by some, and lack of clinical data that proves utility. As the technology improves and is coupled to other methods of imaging (e.g., radiologic), 3D imaging has the potential to improve operative performance and augment visualization reality. When this occurs, it may become as essential in the OR as high definition laparoscopy is today.

References

1. Litynski GS. The American spirit awakens. In: Litynski GS, editor. Highlights in the history of laparoscopy. Frankfurt a. M.: Barbara Bernert; 1996. pp. 227–70.
2. Dabala L, Kellnhofer P, Ritschel T, et al. Manipulating refractive and reflective binocular disparity. Eurographics. 2014;33(2):53–62.
3. Destro F, Cantone N, Lima M. 3D laparoscopic monitors. Med Equip Insights. 2014;5:9–12.
4. Choi W, Sigal G, Rubtsov V, et al. A micro translating lens unit for stereo imaging through single-image endoscope. Micro electronic mechanical systems, 2012 IEEE 25th international conference, Paris. IEEE XPlore Digital Library. doi:http://dx.doi.org/10.1109/MEMSYS.2012.6170079.
5. Shibata T, Kim J, Hoffman DM, Banks MS. The zone of comfort: predicting visual discomfort with stereo displays. J Vision. 2011;11(8):1–29.
6. Mendiburu B. 3D movie making. Stereoscopic digital cinema from script to screen. Amsterdam: Elsevier; 2009.
7. Tanagho YS, Andriole GL, Paradis AG, et al. 2D versus 3D visualization: impact on laparoscopic proficiency using the fundamentals of laparoscopic surgery skill set. J Laparoendosc Adv Surg Tech A. 2012;22(9):865–70.
8. Alaraimi B, El Bakbak W, Sarker S, et al. A randomized prospective study comparing acquisition of laparoscopic skills in three-dimensional (3D) vs. two-dimensional (2D) laparoscopy. World J Surg. 2014;38(11):2746–52.
9. Mistry M, Roach VA, Wilson TD. Application of stereoscopic visualization on surgical skill acquisition in novices. J Surg Educ. 2013;70(5):563–70.
10. Currie ME, Trejos AL, Rayman R. Evaluating the effect of three-dimensional visualization on force application and performance time during robotics-assisted mitral valve repair. Innovations. 2013;8(3):199–205.
11. Bilgen K, Ustun M, Karakahya M, et al. Comparison of 3D imaging and 2D imaging for performance time of laparoscopic cholecystectomy. Surg Laparosc Endosc Percutan Tech. 2013;23(2):180–3.
12. Tabaee A, Anand VK, Brown SM, et al. Three-dimensional endoscopic pituitary surgery. Neurosurgery. 2009;64(Suppl. 2):288–93.
13. Held RT, Hui TT. A guide to stereoscopic 3D displays in medicine. Acad Radiol. 2011;18(8):1035–48.
14. Maier-Hein L, Mountney P, Bartoli A. Optical techniques for 3D surface reconstruction in computer-assisted laparoscopic surgery. Med Image Anal. 2013;17:974–96.

Nanotechnology Approaches for Intraprocedural Molecular Diagnostics

12

Cesar M. Castro, Hyungsoon Im, Hakho Lee and Ralph Weissleder

Overview of Devices for Protein Diagnostics

The clinical needs for a new generation of point-of-care (POC) devices include quantitative analysis of target molecules at low concentrations often below nM range [1–4]. With advances in nanotechnologies and microfluidics, significant progress has been made in integrating conventional assays into a miniaturized lab-on-a-chip [5–7]. For example, on-chip technologies have been developed for the gold standard methods of protein profiling such as mass spectrometry (MS) [8–11], enzyme-linked immunosorbent assay (ELISA) [12–15], Western blotting (WB) [16–19] and fluorescence detection [20, 21]. These on-chip assays reduce required sample volumes, shorten assay time and improve detection sensitivities compared to conventional assays with bench-top instruments. Many current methods, however, still often require time-consuming purification and labeling procedures. For low-concentration targets this often involves sample enrichment or signal amplification steps, leading to increased device complexity which is difficult to develop in on-chip devices at low cost [3, 22]. Also, the need for high-throughput multiplexing capabilities is a challenge for current POC devices.

Nanotechnology has also introduced highly innovative approaches for a new generation of POC devices [23–26]. The development of novel nanostructures and nanoparticles has been widely adapted across optical, electric, and magnetic sensing schemes among others. Novel metallic nanostructures and nanoparticles have been used for label-free surface plasmon resonance (SPR) sensing [27–30], in which specific molecular binding to the metallic sensing surface is detected through resonance shifts. Magnetic nanoparticles (MNPs) have led to advances in new magnetic biosensing devices based on giant magnetoresistance (GMR), Hall effect, nuclear magnetic resonance (NMR), and magnetic relaxation [31–34]. Fluorescent nanoparticles and quantum dots [35, 36] enable high signal contrast imaging even with low-cost optical components (e.g., low-power light source, affordable image sensors). Such development allow simple, affordable diagnostic assays with high throughput and sensitivity.

R. Weissleder (✉) · C. M. Castro · H. Im · H. Lee
Center for Systems Biology, Harvard Medical School, Massachusetts General Hospital and Harvard University, 185 Cambridge Street, Boston, MA 02114, USA
e-mail: rweissleder@mgh.harvard.edu

C. M. Castro
e-mail: Castro.Cesar@mgh.harvard.edu

H. Im
e-mail: im.hyungsoon@mgh.harvard.edu

H. Lee
e-mail: hlee@mgh.harvard.edu

Y. Fong et al. (eds.), *Imaging and Visualization in The Modern Operating Room,*
DOI 10.1007/978-1-4939-2326-7_12,

The success of clinical applications of POC diagnostic devices rest on the development of simple assays that can detect biomarkers from specimens with minimal sample processing and manipulation [4]. These devices need to be fully automated such that no technical or specialized training is required for operators. Microfluidics provide an automated sample isolation and enrichment from unprocessed specimens. Some highlights include microfluidic devices for capturing circulating tumor cells (CTCs) with downstream fluorescence or immunostaining imaging [37, 38], detecting HIV-associated antigen using immunoassays [1, 39] and isolating serum proteins directly from blood for barcode-typed immunoassays [40–42]. These lab-on-a-chip approaches based on the integration of nanotechnology and microfluidics, therefore, will bring fast, accurate, and sensitive diagnostic tests for POC applications.

Nano-Oncology Devices for POC Analyses

Similar to the motivations behind the above-mentioned platforms, the Weissleder group within the Center for Systems Biology at the Massachusetts General Hospital (Boston, MA) has had long-standing interests in creating and translating novel nanotechnology-based platforms for interrogating the spectrum of clinical specimens obtained during interventional procedures (Fig. 12.1**)**. Tailoring each platform described below to the unique clinical needs and constraints of the specimen type improves the reliability and practicality of the approach.

Micro Nuclear Magnetic Resonance

Nuclear magnetic resonance (NMR), the basis for clinically related imaging systems, offers promising inroads in nanotechnology-based biosensing strategies by allowing measurements in

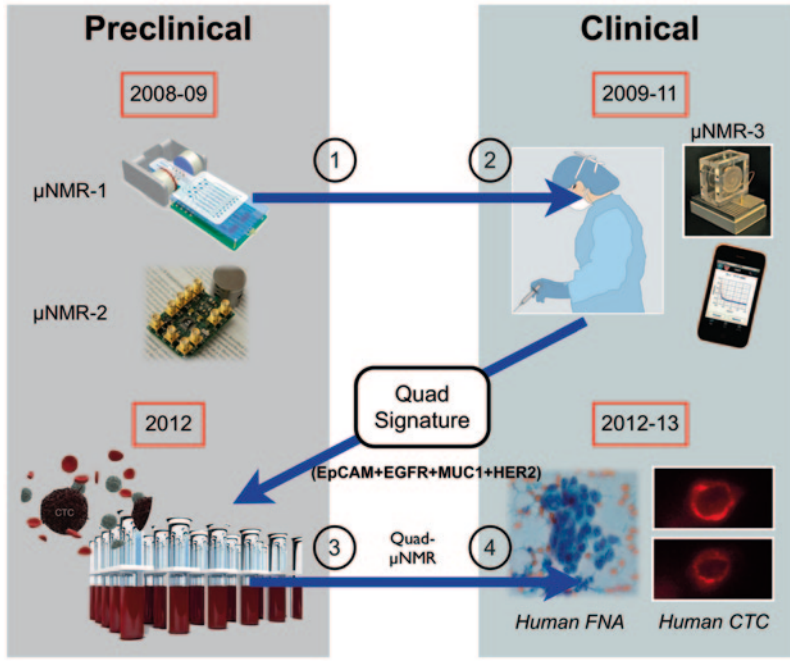

Fig. 12.1 Translational development of micro-nuclear magnetic resonance (μNMR) platform. The feedback between preclinical and clinical research accelerated the translation of the μNMR platform for sensitive protein detection in human diseases [48]

turbid samples. Through innovative microfabrication techniques and miniaturized components, the world's smallest NMR system to date was developed at the Center for Systems Biology (CSB) and coined micro-nuclear magnetic resonance (μNMR; Fig. 12.2a, b) [43]. This technology couples novel labeling chemistries and MNPs to sense specific molecular targets of interest within *minimally processed* samples in a multiplex, POC, and ex vivo fashion. The molecular specificity of μNMR is achieved through MNPs and antibody affinity ligands in one-step (direct conjugation), two-step (BOND), or multi-step assays (amplification; Fig. 12.2c) [44, 45]. Magnetic tagging results in a decrease in the bulk spin-spin relaxation time (T_2) or large amplifying increases in spin-spin relaxation rates ($R_2 = 1/T_2$) of water molecules. Cells tagged with MNPs display different relaxation times than their unbound counterparts. When benchmarked against flow cytometry and Western blot, the μNMR results showed an excellent linear correlation ($R^2 > 98\%$) [43, 46]. Importantly, μNMR can achieve these results using 100–10,000 fold less sample compared to flow cytometry and Western blot analyses, respectively. μNMR has driven various academically based cancer-investigative efforts while a commercial solution is now available for infection and hemostasis diagnostics, both highly relevant for intraoperative procedures (www.T2biosystems.com).

Human Fine-Needle Biopsies Recent published data supports the feasibility of μNMR testing across human specimens, notably fine-needle biopsies or aspirates (FNAs; Fig. 12.3) [47]. Using 70 patients with suspected solid epithelial malignancies, a single FNA pass proved sufficient for robust, multiplexed protein measurements of a dozen markers. Additionally, a four-protein panel (EpCAM, EGFR, Her2, MUC1), named "quad-marker," was found to have superior diagnostic performance compared to conventional pathology. Marked heterogeneity in protein expression was quantitated within and across patients. The time from sample procurement to readout averaged 1 h. A smartphone application mediated interactions between operator and the μNMR device (Fig. 12.2). Of further interest, marked protein degradation was identified after the first hour. This has profound implications for analyses of phosphorylation status, a dynamic process that could be underestimated if phosphoproteins degrade before testing. The rapid readouts achieved here align well with the timeline of common surgical oncology cases. The ability to promptly profile confirmed or suspicious masses during a surgical or interventional procedure using μNMR could enhance the breadth and depth of additional testing.

Circulating Tumor Cells (CTCs) Informed by the protein detection work in FNA described above and the high diagnostic performance of the quad-marker, we sought to tackle the extensive sensitivity challenges posed by querying CTCs [48] which inherently lack the enrichment benefits of directed biopsies. To examine the clinical performance of quad-μNMR, we pursued a pilot study using freshly collected peripheral blood from 15 patients with advanced ovarian cancer [49]. Quad-μNMR's broader dynamic range of CTC enumeration correlated well with a variety of clinical metrics. For example, average CTC counts were higher in more advanced cases such as stage IV, platinum resistant and progressive disease, and in patients not receiving active therapy for various reasons. Quad-μNMR also performed better than the EpCAM-based and FDA-approved CellSearch platform, by reporting a broader range of CTC counts. In addition to enumeration, quad-μNMR enabled comparisons of CTCs with matched distant metastases [50]. Notably, the platform led to the findings that highly aligned protein profiles between metastatic lesions and CTCs were less common than previously assumed. Concurrently profiling biopsies along with blood collected during the procedure could help identify scenarios where, if congruent, examining CTCs would serve as a proxy to the lesions [51]. Opportunities include serial blood sampling for CTCs as a means for minimally invasive monitoring of response or progression.

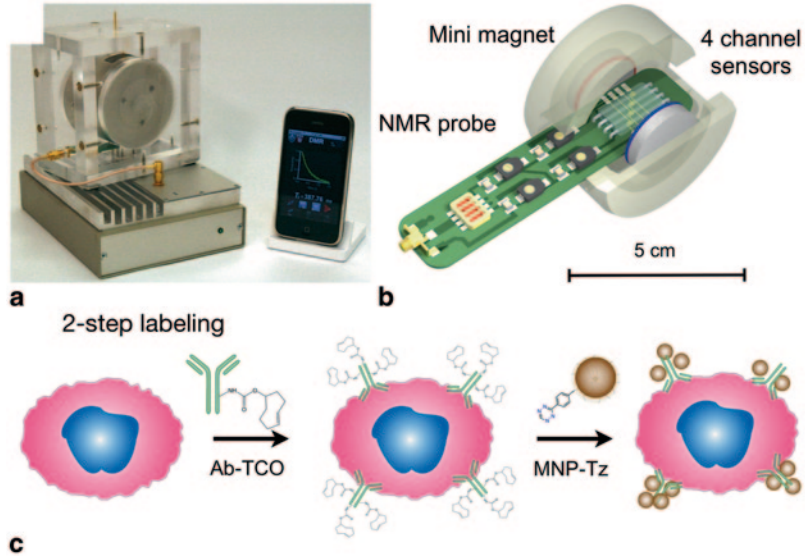

Fig. 12.2 µNMR platform for clinical applications. **a** The system features automatic system tuning and user-friendly interface (e.g., smartphone). **b** To improve the throughput, multiple detection coils can be integrated into a single NMR probe [47]. **c** A bioorthogonal labeling scheme, based on the click reaction between transcyclooctene (*TCO*) and tetrazine (*Tz*), has been developed. The method provides maximized MNP loading on target cells, thereby improving the overall detection sensitivity [44]

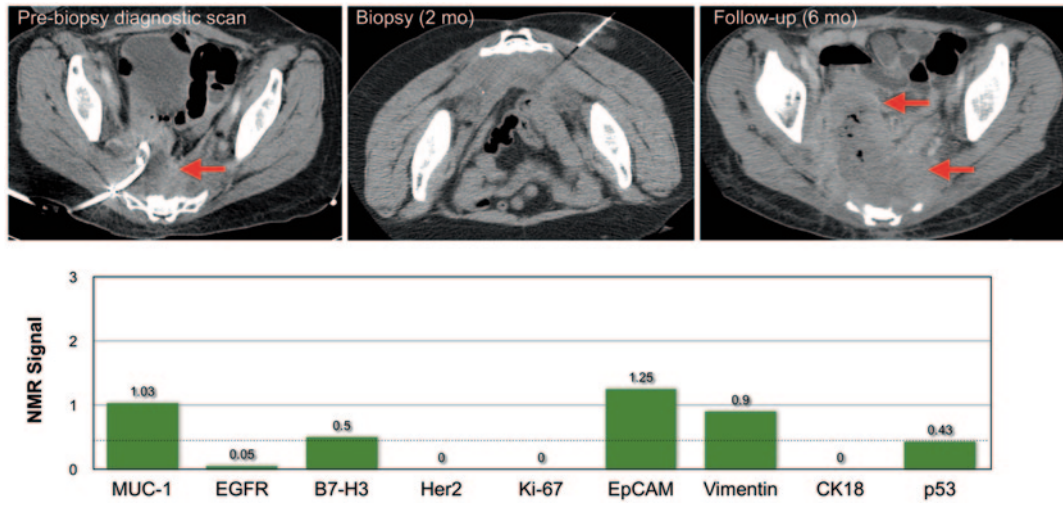

Fig. 12.3 A representative clinical case of µNMR application. A patient underwent computed tomography (CT)-guided biopsy for an enlarging (2.5 × 6.8 cm) presacral lesion. Both cytology and core biopsy reported the lesion as benign (inflammatory tissue). The µNMR analysis, however, unequivocally classified the lesion as malignant, which is based on the expression of the quad-marker combination (MUC-1 + EGFR + EpCAM + HER2). Repeated chest and abdomen CT after 2 months found a significant enlargement of the biopsied lesion, as well as new metastases [47]

Emergent Clinical Scenarios

Complications such as infection and bleeding resulting directly from tumor involvement or its therapies may challenge intra and postprocedural outcomes. As such, the prompt readouts afforded by μNMR have been leveraged by commercial entities (T2 Biosystems; www.t2biosystems.com) to address these issues. Disseminated infections incur significant morbidity and mortality and conventional diagnostics primarily rely on blood cultures that may take days. μNMR has been shown to detect low levels of bacterial and fungal pathogens (as low as 1 CFU/mL) and enabled prompt treatment before escalated growth. The platform has also been modified for comprehensive hemostasis profiling (e.g., platelet, coagulation, fibrinolysis) within 15 min and requires very small sample volumes (5–40 μL); this facilitates serial profiling during procedures if the clinical scenario warrants them.

μNMR leverages numerous advantages over existing detection technologies. They include:

- *Versatility*: μNMR methods can be used to measure virtually any type of target including whole cells, proteins, enzymes, nucleic acid sequences, and drugs.
- *No sample purification required*: μNMR uses magnetic fields for signal generation and detection (i.e., magnetic resonance). Because magnetic fields pass through biological samples regardless of their optical properties, assays can be performed in diverse media. Light-based assay methods, e.g., fluorescence, bioluminescence, absorption, or colorimetry are sensitive to materials in the sample that scatter light, absorb light, or fluoresce.
- *Sensitivity*: μNMR assays are of very high sensitivity (10^{-14} M) and enzymatic amplification is usually not required in contrast to polymerase chain reaction (PCR) or ELISA-based methods.
- *Multiplexed measurements*: μNMR's exquisitely sensitive technology is ideally suited for evaluating several CTC markers simultaneously, thus increasing the detection sensitivity.
- *Rapid clinical answers*: The technology can potentially be used at the POC. While not all assay types may require fast clinical answers, there are clearly scenarios where such information is desirable.
- *True quantitation*: NMR measurements are inherently quantitative. Parallel processing of control samples allows accurate measurements of cell number as well as biomarker densities.
- *Homogeneous assay format*: μNMR employs neither solid phase attachment nor separation of bound and free analytes. For example, there is no immobilization of the biomolecules (DNA, protein) onto glass slides, resulting in faster hybridization kinetics. These features make the technology particularly suitable for miniaturization and/or for microfluidic applications. The clinical application of our innovative customized tool would fulfill many (if not all) of the key requirements desired of biodiagnostic technologies, namely: assay sensitivity, selectivity, versatility, low cost, and portability. Minimal manufacturing costs from reusable NMR components (< $200) and the disposable microfluidic chip (<$1) also render μNMR technology a practical and scalable option.

Micro Hall Sensor Chip

In an effort to further simplify detection and to perform single cell analysis, we recently developed a miniaturized magnetometer chip, the micro-Hall detector (μHD) [52], that can rapidly and quantitatively screen individual cells in *unprocessed clinical specimens*. The system leverages the hall effect to detect the magnetic moments of cells in-flow, immunolabeled with MNPs (Fig. 12.4a**)**. Samples are injected into a microfluidic channel directly positioned above an array of miniaturized hall sensors. Paralleling standard motion detectors, as the sample flows through the channel, the magnetic field of each passing cell is rapidly measured by the underlying sensors. The larger number of tumor-specific proteins on malignant cells attract more MNPs; as a consequence, they generate larger signal spikes when these highly magnetic cells pass

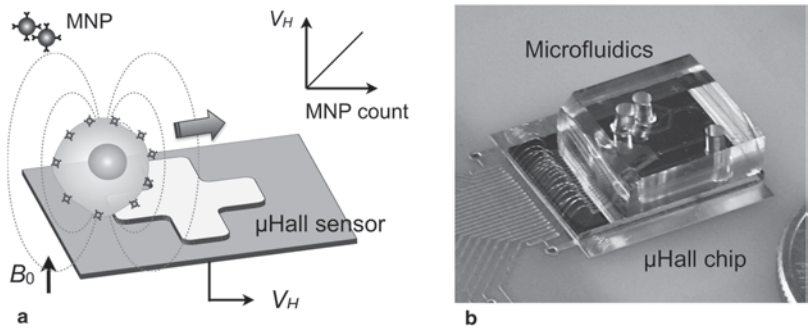

Fig. 12.4 Micro-Hall detector (μHD) for single-cell detection. **a** Each cell is labeled with target-specific MNPs, and its magnetic fields are detected by the μHall sensor. The measured Hall voltage (V_H) is linearly proportional to the MNP counts. B_0 external magnetic field. **b** A photo of a packaged μHD. The footprint of the sensor is ~1.5 × 2 cm^2 [52]

over the sensors. The entire assay is performed on a single microfluidic chip the size of a US quarter coin (Fig. 12.4b); this eliminates the need for expensive or bulky equipment, such as centrifuges that are not suited for procedure suites due to sterile field concerns, among others. Employing unprocessed samples reduces the likelihood of specimen loss and paves the way for rare cell detection across a range of biological substrates. The μHD also facilitates on-chip screening of multiple biomarkers on individual cells. Specifically, a panel of MNPs, distinguishable by their magnetization properties, can be used to target different cellular markers. The expression level of a target biomarker in a single cell is proportional to the measured quantity of each MNP type; the latter are distinguished through unique magnetization properties. The clinical use of the μHD has been explored through detection of rare CTCs in patients with advanced ovarian cancer and monitoring drug treatment efficacy in a murine tumor model.

Enumerating Rare Cells in Clinical Samples To explore the performance of the μHD for circulating rare cell detection in patient-derived specimens, we analyzed a cohort of advanced ovarian cancer patients for the presence of CTCs [52]. As a negative control, peripheral blood samples were obtained from healthy volunteers. Comparisons between the μHD using a quad marker panel with CellSearch, favored the former. CellSearch detected CTCs in only 5 of 20 ovarian cancer cases with a diagnostic accuracy of 25%. The μHD enumerated a higher number of CTCs across all patient samples and cell counts were notably elevated for patients with advanced disease who were no longer undergoing therapy or with aggressive histologic features (for example, poorly differentiated or carcinosarcoma). In contrast to CellSearch, the μHD successfully identified CTCs in 100% of patients with evidence of clinical progression as well as stage IV disease, whereas only 18% of cases were detected with CellSearch. In all, the diagnostic accuracy of μHD reached 94%. The platform itself is highly versatile and the protein markers of interest fully interchangeable. As such, the small sample requirements of the coin-sized chip lend themselves to employing parallel testing of a sample using multiple chips, each with their disease-specific panels. The ability to interrogate differential diagnoses (e.g., cancer subtypes versus infection) during a procedure, could accelerate the diagnostic workup and allow for therapeutic options to be deployed in a timely fashion.

ABCD Platform

Minimally invasive techniques such as core biopsies are increasingly employed to obtain serial measures of drug response during clinical trials. To assay for an ever increasing number of protein biomarkers it has become necessary to obtain more numerous core biospies, a practice not without significant risks. FNAs are an attractive alternative to multiple cutting core biopsies since the risk of bleeding and other complications is much lower. The challenge has been to obtain all the measurements of interest in these scanter samples where conventional immunocytology is not an option.

In response to such clinical needs, we designed an *A*ntibody *B*arcoding with photo *C*leavable *D*NA (ABCD) platform [53] to perform highly multiplexed protein measurements and system-wide profiling using small amounts of clinical sample material (~100 cells). We designed the method to preserve genetic material, not possible with traditional tools like multiplexed cytometry, and to enable up to single cell analyses (Fig. 12.5a**)**. Specifically, cells are tagged with antibodies of interest using short (~70-mer) DNA "barcodes"—with each antibody having a unique sequence—attached by a stable photocleavable linker (Fig. 12.5b). After antibody binding to the cells, UV light induces the photocleavable linker to release each unique DNA barcode, which can then be detected using conventional approaches. ABCD harnesses fluorescence hybridization technology traditionally used for multiplexed quantitation (16,384 barcodes) of femtomolar amounts of DNA and RNA (Fig. 12.5c**)**; however, this method had not been previously extended to measure proteins within cells or clinical samples.

The ABCD platform has demonstrated ease of use, reproducibility, and feasibility on FNA samples [53]. Importantly, proof-of-concept case studies showed that drug dosing potentially corresponds to cellular pharmacodynamics. Over a hundred key mechanistic markers were reliably tested on FNAs and even single cancer cells.

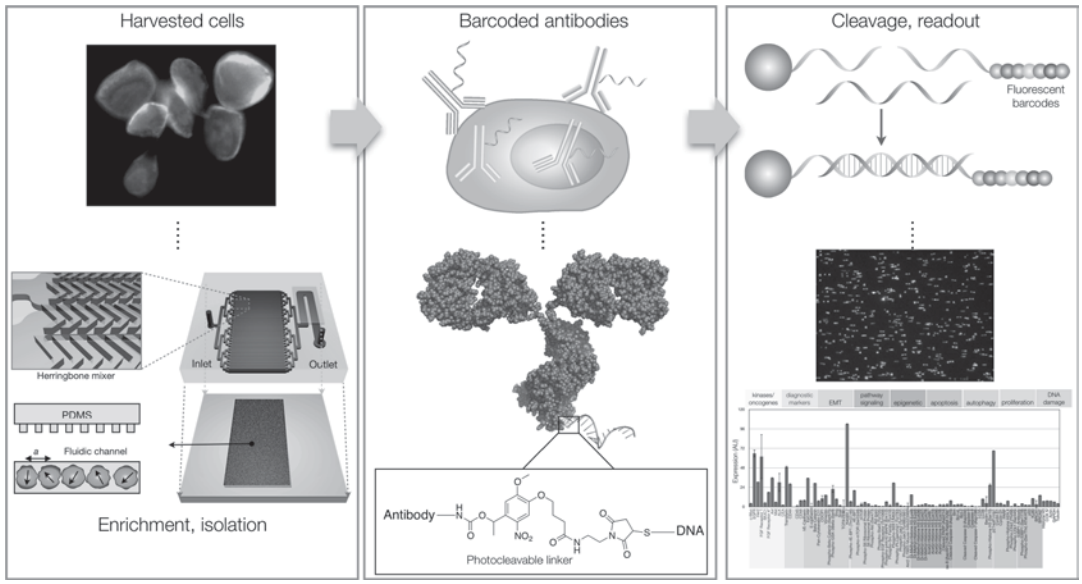

Fig. 12.5 *A*ntibody *B*arcoding with photo*C*leavable *D*NA (ABCD) platform. **a** Cells procured from fine-needle aspirates are enriched and isolated via magnetic separation using a microfluidic device with herringbone channels. **b** Cells of interest are incubated with a cocktail of DNA-conjugated antibodies containing photo cleavable linker. Upon UV exposure, DNA is released. **c** Released DNA barcodes are processed with a fluorescent DNA barcoding platform (NanoString); barcodes are hybridized and imaged with a charge-coupled device (CCD) camera. Quantified barcodes correlated with protein expression levels [53]

The ability to broadly profile protein markers expands the breadth and depth of tumor analyses. Single cell resolution enables deep level exploration of tumor heterogeneity, increasingly gaining traction as drivers of mixed response to cancer therapies. Another major advantage is that both genetic material and protein barcodes can be concurrently extracted from a single sample, thus paving the way for true integrated profiling (protein-DNA-RNA analyses). Oftentimes, cancer patients enrolled in targeted therapy trials have had their archival tumors analyzed for DNA aberrations. Yet, remote genomic changes at do not necessarily predict the activation state of the tumor at the time of enrollment. Integrative measurements could reconcile the mechanisms behind such discrepancies. Methods to further automate specimen processing and analyses are currently under development. Success here would increase the impact that clinical biopsies and, by extension, the providers who attain them have on personalized cancer care.

Surface Plasmon Resonance

We recently developed a transmission surface plasmon resonance (SPR) platform for label-free, high-throughput analyses [54]. The system is based on extraordinary optical transmission through periodic nano holes (Fig. 12.6a**)** rather than total internal reflection as used in commercial SPR systems. Plasmonic nanoholes offer an ideal sensing scheme, as its probing depth (<200 nm) can be readily matched to artificial beads (onto which biomarkers of interest are captured) or to similarly sized natural vesicles such as exosomes and other circulating microvesicles. Furthermore, the transmission optical setup allows system miniaturization (Fig. 12.6b**)** as well as the construction of highly-packed sensing arrays. Our platform utilizes arrays of periodic nanohole lattices patterned in a metal film. Each array is functionalized with affinity ligands for different exosomal protein markers. Upon target-specific exosome binding, the sensor reports spectral changes proportional to target marker expression levels.

A key application of the SPR technology lies in exosome analyses. Exosomes are membrane-bound phospholipid vesicles (50–200 nm in diameter) that are actively secreted by cancer cells into the peripheral circulation [55] and other biofluids. These vesicles carry cellular constituents of their originating cells, including extra and intracellular proteins, mRNA, DNA, and microRNA, and can thus serve as cellular surrogates [56]. Combined with their large abundance (e.g., $>10^9$ vesicles/mL blood) and ubiquitous presence in bodily fluids (e.g., blood, ascites, urine), exosomes could offer significant advantages for cancer detection. Namely, an exosomal assay can be robust and minimally invasive for repeated sampling; it affords relatively unbiased readouts of the whole tumor, less affected by the scarcity of the samples (e.g., CTCs) or intratumoral heterogeneity.

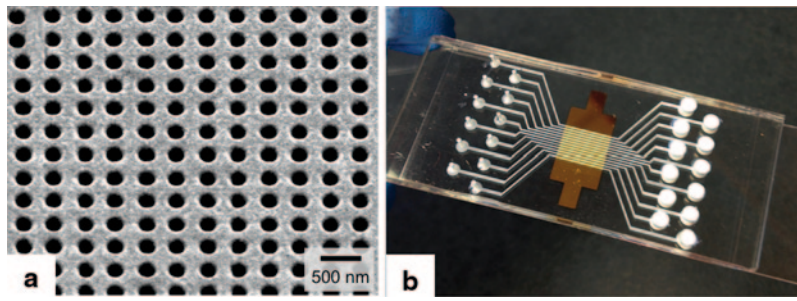

Fig. 12.6 Surface plasmon resonance (SPR) sensor. **a** An electron micrograph of the sensor. A periodic lattice of nanoholes was patterned in a gold film (200 nm thick) deposited on a glass substrate. **b** The SPR sensor chip was integrated with a multi-channel microfluidic cell for parallel analyses [54]

The SPR technology offered highly sensitive and label-free exosome analyses, and enabled fast molecular profiling of exosomes (<60 min) in native samples. This is consistent with the timeframes of moderate to involved clinical procedures. We demonstrated the platform's clinical potential using human ovarian cancer ascites. This intraabdominal fluid accumulation commonly occurs during disease progression (collected by paracenteses) or at the time of diagnosis (collected by paracenteses or during primary surgical resection). The former can provide the context for longitudinal analyses of ascites exosomes for treatment assessment while intraoperative analyses of peritoneal washings could help to properly stage patients.

Conclusion

The selected platforms described here showcase approaches towards the development of POC devices that will find utility in interventional and intraoperative cancer procedures. The challenges of further developing such technologies can be broadly based into (1) technological, (2) work-flow, and (3) regulatory challenges. From a technological perspective, each device should be accurate, simple, and fast without the need for extensive prepurification steps. While some of the technologies developed above still have considerable turn-around times (<1 h), we and others are developing faster approaches to sensing. There are clearly technological hurdles, but early results are promising. With respect to work-flow, new devices and approaches have to simplify, speed up, or circumvent superfluous interventions in order to be useful. Obviating the need for bacterial culture, bypassing lengthy immunohistology, or decreasing the need for repeat surgeries for cancer resection are examples where new technologies can have an impact. Finally, there are regulatory hurdles for approving new devices and appropriate reimbursements for a given test. It is hoped that new technology will ultimately save costs in eliminating obsolete practices rather than adding costs to diagnostic and therapeutic procedures.

Acknowledgments We would like to acknowledge Drs. Arezou Ghazani, Jered Haun, Adeeti Ullal, and David Issadore, as well as many others, for their invaluable contributions to the optimization of the abovementioned POC technologies and in assay development over the years.

Disclosures Ralph Weissleder is a founding member of T2 Biosystems.

References

1. Chin CD, et al. Microfluidics-based diagnostics of infectious diseases in the developing world. Nat Med. 2011;17:1015–9.
2. McNerney R, Daley P. Towards a point-of-care test for active tuberculosis: obstacles and opportunities. Nat Rev Microbiol. 2011;9:204–13.
3. Yager P, et al. Microfluidic diagnostic technologies for global public health. Nature. 2006;442:412–8.
4. Yager P, Domingo GJ, Gerdes J. Point-of-care diagnostics for global health. Annu Rev Biomed Eng. 2008;10:107–44.
5. Mark D, Haeberle S, Roth G, von Stetten F, Zengerle R. Microfluidic lab-on-a-chip platforms: requirements, characteristics and applications. Chem Soc Rev. 2010;39:1153–82.
6. Mouradian S. Lab-on-a-chip: applications in proteomics. Curr Opin Chem Biol. 2002;6:51–6.
7. Sackmann EK, Fulton AL, Beebe DJ. The present and future role of microfluidics in biomedical research. Nature. 2014;507:181–9.
8. Bindila L, Peter-Katalinić J. Chip-mass spectrometry for glycomic studies. Mass Spectrom Rev. 2009;28:223–53.
9. Lee J, Soper SA, Murray KK. Microfluidic chips for mass spectrometry-based proteomics. J Mass Spectrom. 2009;44:579–93.
10. Naik AK, Hanay MS, Hiebert WK, Feng XL, Roukes ML. Towards single-molecule nanomechanical mass spectrometry. Nat Nanotechnol. 2009;4:445–50.
11. Tubbs KA. Biosensor chip mass spectrometry: a chip-based proteomics approach. Electrophoresis. 2000;21:1155–63.
12. He H, et al. Design and testing of a microfluidic biochip for cytokine enzyme-linked immunosorbent assay. Biomicrofluidics. 2009;3:022401.
13. Sun S, Yang M, Kostov Y, Rasooly A. ELISA-LOC: lab-on-a-chip for enzyme-linked immunodetection. Lab Chip. 2010;10:2093–100.
14. Wang S, et al. Integration of cell phone imaging with microchip ELISA to detect ovarian cancer HE4 biomarker in urine at the point-of-care. Lab Chip. 2011;11:3411–8.
15. Zhu L, et al. An ELISA chip based on an EWOD microfluidic platform. J Adhes Sci Technol. 2012;26:2113–24.
16. Hughes AJ, Herr AE. Microfluidic western blotting. Proc Nat Acad Sci. 2012;109:21450–5.

17. Jin S, Anderson GJ, Kennedy RT. Western blotting using microchip electrophoresis interfaced to a protein capture membrane. Anal Chem. 2013;85:6073–9.
18. Pan W, Chen W, Jiang X. Microfluidic western blot. Anal Chem. 2010;82:3974–6.
19. Tia SQ, He M, Kim D, Herr AE. Multianalyte on-chip native Western blotting. Anal Chem. 2011;83:3581–8.
20. Rocheleau JV, Piston DW. Combining microfluidics and quantitative fluorescence microscopy to examine pancreatic islet molecular physiology. Methods Cell Biol. 2008;89:71–92.
21. Simpson RJ, Bernhard OK, Greening DW, Moritz RL. Proteomics-driven cancer biomarker discovery: looking to the future. Curr Opin Chem Biol. 2008;12:72–7.
22. Chin CD, Linder V, Sia SK. Commercialization of microfluidic point-of-care diagnostic devices. Lab Chip. 2012;12:2118–34.
23. Cheng MM-C, et al. Nanotechnologies for biomolecular detection and medical diagnostics. Curr Opin Chem Biol. 2006;10:11–9.
24. Erickson D, Mandal S, Yang AHJ, Cordovez B. Nanobiosensors: optofluidic, electrical and mechanical approaches to biomolecular detection at the nanoscale. Microfluid Nanofluid. 2008;4:33–52.
25. Jain KK. Nanodiagnostics: application of nanotechnology in molecular diagnostics. Expert Rev Mol Diagn. 2003;3:153–61.
26. Logothetidis S. Nanotechnology in medicine: the medicine of tomorrow and nanomedicine. Hippokratia. 2006;10:7–21.
27. Haes AJ, Van Duyne RP. A nanoscale optical biosensor: sensitivity and selectivity of an approach based on the localized surface plasmon resonance spectroscopy of triangular silver nanoparticles. J Am Chem Soc. 2002;124:10596–604.
28. Mayer KM, Hafner JH. Localized surface plasmon resonance sensors. Chem Rev. 2011;111:3828–57.
29. Willets KA, Van Duyne RP. Localized surface plasmon resonance spectroscopy and sensing. Annu Rev Phys Chem. 2007;58:267–97.
30. Wilson R. The use of gold nanoparticles in diagnostics and detection. Chem Soc Rev. 2008;37:2028–45.
31. Megens M, Prins M. Magnetic biochips: a new option for sensitive diagnostics. J Magn Magn Mater. 2005;293:702–8.
32. Gaster RS, et al. Quantification of protein interactions and solution transport using high-density GMR sensor arrays. Nat Nanotechnol. 2011;6:314–20.
33. Issadore D, et al. Ultrasensitive clinical enumeration of rare cells ex vivo using a micro-hall detector. Sci Transl Med. 2012;4:141ra92.
34. Min C, et al. Mechanism of magnetic relaxation switching sensing. ACS Nano. 2012;6:6821–8.
35. Klostranec JM, Chan WCW. Quantum dots in biological and biomedical research: recent progress and present challenges. Adv Mater. 2006;18:1953–64.
36. Michalet X, et al. Quantum dots for live cells, in vivo imaging, and diagnostics. Science. 2005;307:538–44.
37. Ozkumur E, et al. Inertial focusing for tumor antigen-dependent and -independent sorting of rare circulating tumor cells. Sci Transl Med. 2013;5:179ra47.
38. Stott SL, et al. Isolation and characterization of circulating tumor cells from patients with localized and metastatic prostate cancer. Sci Transl Med. 2010;2:25ra23.
39. Kotz KT, et al. Clinical microfluidics for neutrophil genomics and proteomics. Nat Med. 2010;16:1042–7.
40. Fan R, et al. Integrated barcode chips for rapid, multiplexed analysis of proteins in microliter quantities of blood. Nat Biotechnol. 2008;26:1373–8.
41. Jiang H, Weng X, Li D. Microfluidic whole-blood immunoassays. Microfluid Nanofluid. 2011;10:941–64.
42. Stern E, et al. Label-free biomarker detection from whole blood. Nat Nanotechnol. 2010;5:138–42.
43. Lee H, Sun E, Ham D, Weissleder R. Chip-NMR biosensor for detection and molecular analysis of cells. Nat Med. 2008;14:869–74.
44. Haun JB, Devaraj NK, Hilderbrand SA, Lee H, Weissleder R. Bioorthogonal chemistry amplifies nanoparticle binding and enhances the sensitivity of cell detection. Nat Nanotechnol. 2010;5:660–5.
45. Peterson VM, Castro CM, Lee H, Weissleder R. Orthogonal amplification of nanoparticles for improved diagnostic sensing. ACS Nano. 2012;6:3506–13.
46. Lee H, Weissleder R. Rapid detection and profiling of cancer cells in fine-needle aspirates. Proc Nat Acad Sci. 2009;106:12459–64.
47. Haun JB, et al. Micro-NMR for rapid molecular analysis of human tumor samples. Sci Transl Med. 2011;3:71ra16.
48. Castro CM, et al. Miniaturized nuclear magnetic resonance platform for detection and profiling of circulating tumor cells. Lab Chip. 2014;14:14–23.
49. Ghazani AA, Castro CM, Gorbatov R, Lee H, Weissleder R. Sensitive and direct detection of circulating tumor cells by multimarker μ-nuclear magnetic resonance. Neoplasia. 2012;14:388–95.
50. Ghazani A, et al. Comparison of select cancer biomarkers in human circulating and bulk tumor cells using magnetic nanoparticles and miniaturized micro-NMR system. Nanomedicine. 2013;9:1009–17.
51. Ghazani AA, et al. Molecular characterization of scant lung tumor cells using iron-oxide nanoparticles and micro-nuclear magnetic resonance. Nanomedicine. 2014;10:661–8.
52. Issadore D, et al. Ultrasensitive clinical enumeration of rare cells ex vivo using a μ-hall detector. Sci Transl Med. 2012;4:141ra92.
53. Ullal AV, et al. Cancer cell profiling by barcoding allows multiplexed protein analysis in fine-needle aspirates. Sci Transl Med. 2014;6:219ra9.
54. Im H, et al. Label-free detection and molecular profiling of exosomes with a nano-plasmonic sensor. Nat Biotechnol. 2014;32:490–5.
55. Shao H, et al. Protein typing of circulating microvesicles allows real-time monitoring of glioblastoma therapy. Nat Med. 2012;18:1835–40.
56. Kharaziha P, Ceder S, Li Q, Panaretakis T. Tumor cell-derived exosomes: a message in a bottle. Biochim Biophys Acta. 2012;1826:103–11.

13 Ultrasmall Fluorescent Silica Nanoparticles as Intraoperative Imaging Tools for Cancer Diagnosis and Treatment

Michelle S. Bradbury, Mohan Pauliah and Ulrich Wiesner

List of abbreviations

C dots.	Cornell dots
cRGDY.	Cyclic arginine–glycine–aspartic acid-tyrosine
CT.	Computerized tomography
EPR.	Enhanced permeability and retention (EPR)
FDA.	Food and Drug Administration
FDA-IND.	Food and Drug Administration-investigational new drug
^{18}F-FDG.	2-deoxy-2-[^{18}F] fluoro-D-glucose
HMB-45.	Human melanoma black
IND.	Investigational new drug
^{124}I.	Iodine-124
MIP.	Maximum intensity projection
MRI.	Magnetic resonance imaging
NIR.	Near infrared
PEG.	Poly(ethylene glycol)
PET.	Positron emission tomography
PET-CT.	Positron emission tomography—computerized tomography
RGB.	Red green blue
SLN.	Sentinel lymph node
SLNB.	Sentinel lymph node biopsy
^{99m}Tc.	Technetium-99m

M. S. Bradbury (✉) · M. Pauliah
Department of Radiology, Memorial Sloan-Kettering Cancer Center, 408 E 69th Street, RM Z-2001, New York, NY 10065, USA
e-mail: bradburm@mskcc.org

M. Pauliah
e-mail: pauliahm@mskcc.org

U. Wiesner
Materials Science and Engineering, Cornell University, 330 Bard Hall 14853, Ithaca, NY, USA
e-mail: ubw1@cornell.edu

Ultrasmall Fluorescent Silica Nanoparticles as Intraoperative Imaging Tools for Cancer Diagnosis and Treatment

Mapping biological processes that promote cancer at the cellular and molecular level requires highly sensitive and specific molecular or particle-based probes [1]. For instance, the use of optical or hybrid (e.g., optical-PET) particle-based probes to assay critical cancer targets may enhance our understanding and yield important insights into mechanisms governing cancer progression, metastatic potential, and invasion. To achieve these ends, design criteria need to be introduced which yield particles exhibiting superior physicochemical, photophysical, and biological properties, thereby enabling more precise and reproducible readouts of cancer cell activities, notably in their earliest stages. The coupling of such nanomaterials with real-time optical imaging devices, such as high-sensitivity handheld fluorescence camera systems, may enhance detection of micrometastases in regional lymph nodes within the surgical field using sentinel lymph node (SLN) mapping and biopsy (SLNB) techniques. In addition to potentially increasing the accuracy of lesion identification, the application of these tools may positively impact our

Y. Fong et al. (eds.), *Imaging and Visualization in The Modern Operating Room,*
DOI 10.1007/978-1-4939-2326-7_13, © Springer Science+Business Media New York 2015

ability to stage disease, determine prognosis, and improve clinical outcomes.

This chapter will discuss the use of a clinically approved ultrasmall (sub-10 nm) tumor-targeted fluorescent core-shell silica nanoparticles—termed Cornell dots (or C dots)—in conjunction with dual-modality positron emission tomography (PET) and optical imaging approaches for mapping metastatic lymph nodes in clinically-relevant melanoma models. To enhance metastatic nodal disease detection and tumor-to-background ratios, C dots have been adapted with cyclic arginine-glycine-aspartic acid-tyrosine (cRGDY) for targeting integrin receptors on tumor cell surfaces and activated tumor neovasculature. The use of a spontaneous melanoma miniswine model has yielded pre-operative PET findings of nodal disease following local administration of hybrid integrin-targeting C dots that can be readily translated into the intraoperative setting for direct optical visualization of the draining tumor lymphatics and fluorescent SLN/s with histologic correlation. Important considerations are the specificity of this platform relative to the standard-of-care radiotracer, ^{18}F-FDG, for potentially discriminating metastatic disease from metabolic processes (i.e., inflammation) in the setting of surgically-based therapies.

Introduction

In the past three decades, the incidence of malignant melanoma has gone up to threefold and, at present, in the USA, melanoma ranks as the fifth most common cancer in males and sixth most common in females [2]. Early diagnosis and treatment are essential to minimizing morbidity and mortality. Prognosis is largely determined by the thickness and ulceration of the primary lesion, although the presence of lymphatic metastases is a vital prognostic predictor [3]. Accurate identification of nodal metastases utilizing state-of-the-art molecular imaging tools has important implications for clinical outcomes. There are no currently accepted standard-of-care systemic treatment options available. Importantly, however, systemic treatment of melanoma is available in the clinical trial setting and is only offered to patients based on regional node risk stratification (i.e., SLN mapping). The definite treatment for primary cutaneous melanoma is wide local surgical excision with adjuvant radiation for specific indications.

SLN-mapping procedures are limited by a lack of intraoperative optical visualization tools, particularly fluorescence device technologies that result in the extremely sensitive detection of fluorophores (i.e., at least picomolar levels), essentially rivaling that of PET imaging. The utility of molecular imaging tools [4], when coupled with very bright dye-encapsulated intraoperative probes, such as C dots, is their combined ability to improve the accurate determination and staging of metastatic nodes during SLN biopsy procedures, as well as to enable discrimination of tumor burden within nodes on the basis of exquisitely high detection sensitivities. These advantages, in addition to being able to discriminate diseased nodes from adjacent critical structures (i.e., nerves), minimizes surgical risks, such as lymphedema, by enabling the selective harvesting of disease-bearing nodes. Patients with metastatic disease can thus be stratified to appropriate treatment arms in a more timely fashion, potentially yielding improved outcome measures.

Multimodal Molecular Imaging Tools for SLN Mapping: Current Clinical Practice

Conventional imaging techniques—such as magnetic resonance imaging (MRI) or PET—CT, are often used to assess or quantify tumor uptake kinetics. Although anatomic MRI is a routine diagnostic tool for characterizing tumors and monitoring tumor response, many imaging features lack biologic or molecular correlates. Signal changes and contrast enhancement reflect a combination of multiple superimposed physiologic processes and much of the molecular information encoded within these studies cannot be extracted and remains unknown. By integrating functional and real-time imaging technologies, increasingly more sensitive and specific readouts reflecting the biological status of tumors may be obtained. Imaging approaches that can identify

growth-regulating molecular events may determine new endpoints that can serve as accurate surrogates of receptor expression, biomarkers for early treatment response, as well as stimulate drug discovery efforts leading to the development of novel particle therapies.

For SLN-mapping procedures, although conventional methods are used preoperatively to identify abnormally enlarged and/or metabolically active nodes that are consistent with metastatic disease, these approaches are limited. For instance, although different tumor types demonstrate enhanced glucose metabolism and overexpression of glucose transporters (GLUTs) using the glucose mimetic, 2-deoxy-2-[^{18}F]fluoro-D-glucose (^{18}F-FDG), ^{18}F-FDG is not a specific or reliable agent, as nodal enlargement can be seen with other metabolically active processes and may, in fact, co-exist with the spread of cancerous cells. Even nodes less than 1.5 cm may harbor micrometastases, which may not be evident by traditional ^{18}F-FDG PET. In the case of technetium-99m-labeled sulfur colloid (^{99m}Tc-sulfur colloid), a standard-of-care tracer injected preoperatively about the primary tumor site, activity can be visualized within the tumor lymphatics/nodes on spatially coregistered CT-gamma camera images, but the larger size of the filtered colloid (i.e., 10–100 nm) may preclude visualization of the operative field due to its slow clearance. Intraoperatively, surgeons can typically localize the SLN by measuring radioactive emissions using a handheld gamma probe (Fig. 13.1). Another intraoperative adjunct for localizing SLNs is isosulfan (Lymphazurin 1%, US Surgical, North Haven, CT) or "blue dye," which allows visual identification of a "hot and blue" SLN following injection into the peritumoral region, but only if it is superficially located within the operative field of view.

The risk of injury to adjacent vital soft tissues (i.e., neurovascular structures) may occur and can subsequently alter normal function, such as speech and swallowing, as well as cosmetic appearance. Erman [5] reported that in approximately 10% of cases, there was a failure to identify any drainage pattern or to localize small nodes within the head and neck, an anatomically complex region. A major challenge in the intraoperative setting is the delineation difficult-to-

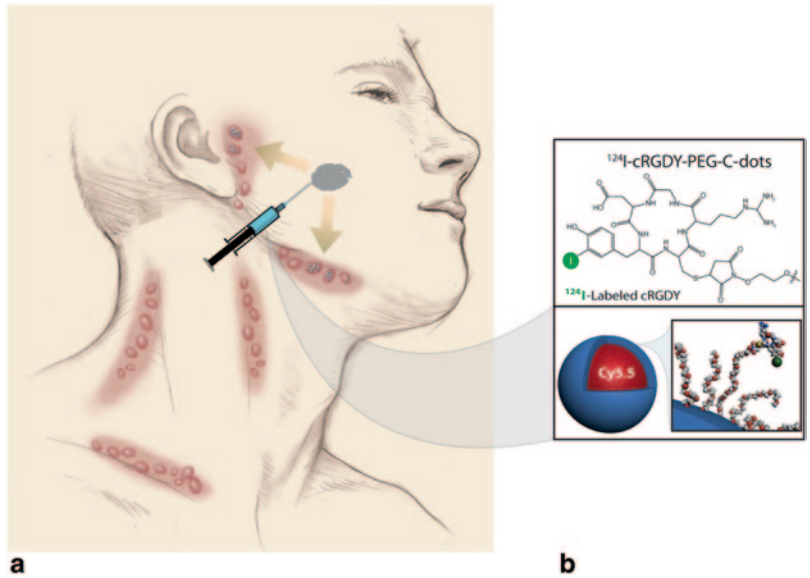

Fig. 13.1 Schematic of SLN mapping in the head and neck using ^{124}I-cRGDY-PEG-Cdots. **a** Injection of ^{124}I-cRGDY-PEG-C dots about an oral cavity lesion with drainage to preauricular and submandibular nodes. **b** ^{124}I-cRGDY-PEG-ylated core-shell silica nanoparticle with surface-bearing radiolabels and peptides and core-containing reactive dye molecules (*insets*)

detect nodes that are in anatomic proximity to tumor, precluding direct mapping of locoregional nodal distributions within an exposed nodal basin. These limitations have hampered melanoma staging, as well as the inability to transform sites of disease on pre-operative scans into three-dimensional (3D) locations within the exposed operative bed during surgical procedures.

Many articles have provided a detailed discussion on the newer-generation nontargeted activatable [6–8] and targeted organic fluorophores [9–11], gadolinium-labeled dendrimers [12–14] and other nanocarriers [15], and macromolecular agents [14, 16–21], including dual-modality particle imaging probes for use in image-guided procedures. One of these newer generation hybrid particle probes, C dots, an ultrasmall, cancer-targeted, fluorescent silica particle, exhibits unique physicochemical and photophysical properties, which can be exploited in a variety of surgically driven and/or minimally invasive/interventional settings. Coupling this with a real-time handheld fluorescence camera system has enabled the translation of this combined technology platform for visualizing the draining tumor lymphatics within the operative field.

Image-Guided Surgical Devices: The ArteMIS™ Handheld Fluorescence Camera System

About a decade ago, the FDA launched a Critical Path Initiative (http://www.fda.gov/ScienceResearch/SpecialTopics/CriticalPathInitiative/ucm076689.htm) to accelerate the development of technological advances leading to cost-effective, innovative medical products, including advanced imaging systems, which can improve data acquisition, feature extraction, and standardization in clinical practice. The opportunity to combine novel multimodal and multi-parametric image-driven metrics and informatics tools with these evolving systems in the future is expected to play a key role in ultimately improving outcome measures and clinical radiology practice, and will serve to accelerate device developments in the field of nanomedicine. An imaging modality that meets these objectives although in its early phases of clinical implementation—near-infrared (NIR) fluorescence optical imaging—has emerged as a robust, highly sensitive, and inexpensive technology that offers superior acquisition speeds and real time in vivo visualization and multiplexing capabilities for interrogating critical cancer targets and vital normal tissues during intraoperative procedures, without the risk of radiation exposure (Fig. 13.2).

Artemis™ Portable Fluorescence Image-Guided Camera System Technology

	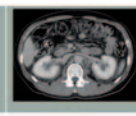	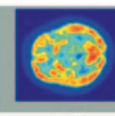	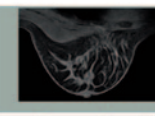	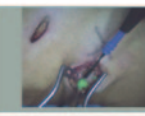
Device	***CT***	***PET***	***Conventional MRI***	***Artemis Portable Optical Camera***
Imaging speed	**Relatively fast**	**Slower than CT**	**Slower than CT**	**Video speed**
Radiation	**x-rays**	**Gamma Rays**	**radiowaves/ no radiation**	**None**
Depth	**100%**	**100%**	**100%**	**1 – 20 mm**
Resolution	**50μm**	**< 1 cm**	**50μm**	**50μm**
Device Cost	**$$**	**$$$**	**$$$**	**$**

Fig. 13.2 Real-time intraoperative fluorescence camera system technology: comparison with conventional imaging modalities. Device parameters for CT, PET, and MRI versus those used for the ArteMIS™ handheld fluorescence camera system

For intraoperative applications utilizing fluorescence camera systems to demonstrate real-time biological events in vivo in the presence of NIR dye-incorporated probes, the observed NIR signal emitted from cancerous or other biological tissues of interest needs to meet pre-established criteria for achieving superior contrast-to-noise ratios at the lowest detectable doses administered. These requirements, along with the achievement of increasing higher detection sensitivities (i.e., at least picomolar), will directly impact the ability of these combined systems to successfully interrogate biological structures at the cellular level, permitting differentiation of cancer-bearing nodes from adjacent normal tissues, as well as facilitating the detection of lower levels of tumor burden within and across nodal tissues.

One state-of-the-art intraoperative imaging device, the ArteMIS^{TM} handheld NIR fluorescence camera system (Quest Medical Imaging, Middenmeer, The Netherlands) (Fig. 13.3a), has been adapted for interrogating tissues close-up by utilizing either minimally invasive laparoscopic (Figs. 13.3b, c) or open lens configurations (Fig. 13.3c). A distinct advantage of this handheld system is that it can penetrate into anatomic locations that are difficult to navigate, such that assessments can be made within millimeters of the tissue surface. This multichannel, high-resolution camera system can also simultaneously detect and spectrally demix finely-tuned optical signals arising from different fluorescent channels after excitation of multiple NIR dye-containing probes. Optical fluorescence images are acquired in video mode (15 frames/s and higher) to enable real-time, higher sensitivity detection and/or monitoring of (1) flow within tumor lymphatic channels and nodes, (2) tumor margins, (3) residual sites of disease post resection, and/or (4) response during or after therapeutic intervention. The resulting four-panel display demonstrates both individual channels as well as channels showing composite images; the latter an overlay of color (red green blue; RGB) images and NIR fluorescent images (Fig. 13.3d).

Cancer-Targeted Ultrasmall Hybrid Silica Platform Technologies for Image-Directed Surgical Interventions

The successful preferential delivery to and accumulation of theranostic delivery vehicles at sites of cancerous spread is a necessary step toward maximizing the therapeutic index while reducing (or abrogating) dose-limiting toxicity. The design

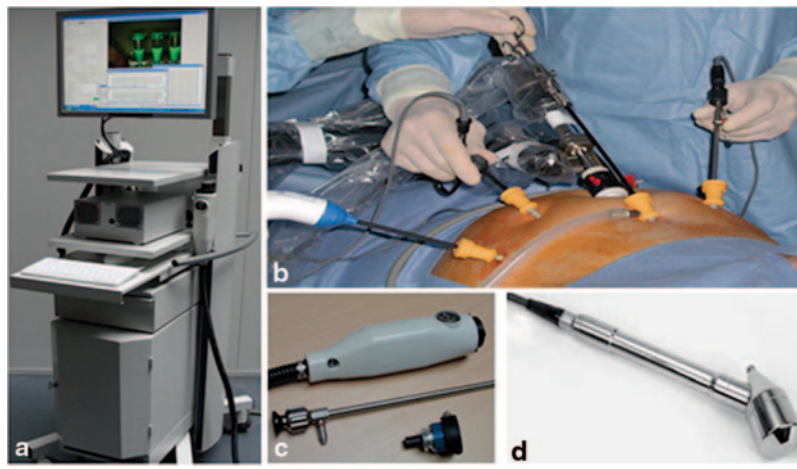

Fig. 13.3 Minimally invasive surgery utilizing a handheld fluorescence camera system. **a** ArteMIS^{TM} handheld fluorescence camera system for open and laparoscopic procedures. **b** Minimally invasive surgery using laparoscopic tools. **c** System components (*top to bottom*): camera, laparoscope, and ring light. **d** Handheld gamma probe for radiodetection. (Adapted from [38])

and surface chemistry of particle platforms, such as the one described herein, needs to be precisely tailored to achieve this end, as well as to ensure favorable pharmacokinetic and clearance kinetic profiles. Recent advances in imaging probe developments for nanomedicine and the hurdles associated with their subsequent clinical translation highlight this challenge. In addition to the foregoing considerations, additional critical properties of these probes need to be considered, including their size, charge, shape, stability, aggregability, toxicity, surface coat uniformity, and the type/number of particle surface components (i.e., targeting and/or contrast-producing ligands).

To advance a clinically translatable particle imaging platform, we developed an ultrasmall, dual-modality (optical-PET) silica nanoparticle platform for nanomedicine, termed (Cornell or C dots). C dots have core-containing reactive NIR dye molecules (i.e., Cy5) and bear surface radiolabels (i.e., iodine-124, ^{124}I) with extended half-lives (i.e., 4 days), as well as small integrin-targeting peptides (^{124}I-cRGDY-PEG-C dots) [22, 23]. This silica particle platform is the first inorganic particle of its class and kind to be FDA-IND approved for clinical use as either a PET-optical [24] or an optically driven probe. We are currently conducting a human SLN-mapping trial in melanoma patients in order to determine whether such a platform behaves as an ideal diagnostic agent—one which improves disease targeting while, at the same time, efficiently clearing the body. Prior preclinical studies utilizing this targeted particle tracer and PET-CT imaging in a well-established spontaneous melanoma miniswine model (Sinclair miniature swine, Sinclair Research Center) [25] revealed specific localization and accumulation of this probe in SLN metastases relative to the standard-of-care radiotracer, ^{18}F-FDG, and permitted differentiation of nodal tumor burden (see discussion below). More recently, a first-in-human clinical trial in metastatic melanoma patients [26] found the particle to be safe, in addition to demonstrating favorable pharmacokinetic, clearance, and dosimetric profiles.

The versatility of fluorescent C dots [23, 27] for intraoperative applications has been based on refinements of key design features, which include the following;

- Ultrasmall size with tunable radius (~4.0–~10 nm) with reproducible pharmacokinetic signatures defined by renal excretion.
- Encapsulation of a range of different NIR organic dyes (i.e., Cy5.5; emission maxima, ~694 nm) for enhanced photophysical features (i.e., photostability and brightness).
- Variety of cancer-directed targeting ligands to enhance preferential uptake, accumulation, and retention in integrin–expressing tumors, including melanoma [22].
- Neutral charge secondary to PEG-coated surfaces which, in turn, reduce nonspecific uptake by the reticuloendothelial system (RES) and facilitate renal clearance.
- Combination of several chemical entities to the particle surface to create a highly multifunctional delivery vehicle.
- *Target or clear concept:* Sub-10 nm C dots are an ideal diagnostic platform, as they either target disease or clear the body (i.e., whole body clearance half-times of ^{124}I-cRGDY-PEG-C dots range from 13 to 21 h in humans).

The hydrodynamic diameter of particles affects their circulation (or residence) half-times. For diagnostic studies, it is crucial for particles to exhibit relatively rapid whole body clearance, preferably via a renal route. Although target selectivity may increase with particle size [18], earlier studies have shown that for larger particle sizes (>10 nm), slower physiologic transport within cancer-infiltrated tissues may hinder a more uniform diffusion of particles throughout the interstitium. On the other hand, particle sizes less than about 3 nm (including dyes) are susceptible to extravasation and nonspecific tissue scattering [23, 28, 29]. Choi [30] suggested that size cutoffs of 10 nm or less are desirable for effective renal glomerular filtration, as prolonged exposure to administered particle loads may add to toxicity or adverse effects.

While longer particle probe circulation half-times are desirable to increase tissue penetration, the selectivity and preferential uptake of nanoparticle-based agents at the target site will primarily depend upon the enhanced permeability

and retention (EPR) effect [18, 31]; this effect is based on known heterogeneous alterations in the permeability of tumor neovasculature within and across tumors [32, 33]. Improved penetration and retention times have been observed by utilizing probes (i.e., peptides, antibodies and nanoparticles) targeting highly expressed critical cancer targets, such as cathepsins [18, 33, 34]. Cancer-directed probes exhibiting tumor-penetrating properties may enhance imaging detection sensitivity and specificity, and may allow delineation of tumor-infiltrated nodal tissue from normal tissue [35, 36] or other disease processes (inflammation, infection) that may similarly manifest with nodal enlargement.

The transport properties of particles across the vasculature and within the interstitium may be influenced by its net surface charge, which may be opsonized by serum proteins [23, 37]. By attaching PEG chains to the particle surface, the surface is rendered more chemically inert which, in turn, should enhance its diffusion and homogeneous distribution within the interstitial space of cancer-infiltrated tissues.

Newer-generation fluorescence probes (e.g., organic dyes, fluorescent proteins, dye-bound proteins/macromolecules, dye-containing nanoparticles) that emit in the NIR region of the light spectrum (650–900 nm) will exhibit decreased tissue attenuation and autofluorescence from nontarget tissues. In comparison with free NIR dyes, NIR dye-encapsulated particles exhibit significant increases in brightness (200–300%; Table 13.1) and prolonged photostability (two- to threefold increases) [23]; higher penetration depths of up to 2 cm have been observed empirically in biological tissues with the Artemis camera system.

Application of C Dots to Nanomedicine: SLN Mapping

The unique physicochemical and photophysical properties of C dots will enable a broad range of intraoperative applications to be pursued, and can be surface-functionalized to selectively evaluate different cancer types in the body. One such application, SLN mapping, has been extensively studied in both small (murine) [22] and larger animal (i.e., miniswine) models [38] harboring melanomatous lesions.

Real-Time Image-Guided SLN Mapping

Image-guided metastatic disease detection, staging, and the assessment of differential tumor burden in SLN/s have been evaluated in a melanoma miniswine model [25, 39, 40]. To screen for metastatic disease in miniswine, we performed dynamic high-resolution and whole body ^{18}F-FDG PET-CT scans following systemic injection of ^{18}F-FDG prior to local administration of ^{124}I-cRGDY-PEG-C dots about 48 h later. PET-avid nodes were confirmed intraoperatively within the exposed surgical bed by visual inspection and γ-counting using handheld PET devices prior to excision for histopathological correlation (Fig. 13.4). In most of the cases, baseline activity measurements, made over the primary tumor and SLN sites using the portable gamma probe, showed a 20-fold increase in activity within the SLN relative to background signal.

In a separate cohort of miniswine, we further investigated the draining of the tumor lymphatics and nodal metastases with real-time optical imaging using the ArteMIS^{TM} fluorescence camera system after a second subdermal injection of ^{124}I-cRGDY-PEG-C dots was performed near the

Table 13.1 Photophysical characterization of surface-functionalized C dots using fluorescence correlation analysis

–	Cy5 dye	PEG-C dots	cRGDY-PEG-C dots	cRADY-PEG-C dots[a]
Brightness/particle (kHz)	3.48	10.91	10.13	10.39
Concentration (mol/L)	5.37×10^{-4}	6.61×10^{-6}	8.80×10^{-6}	4.01×10^{-6}
Hydrodyn. radius (nm)	0.67 ± 0.008	3.53±0.04	3.40±0.04	3.25±0.04

[a] Control particle, C dot bearing a scrambled peptide, cRADY

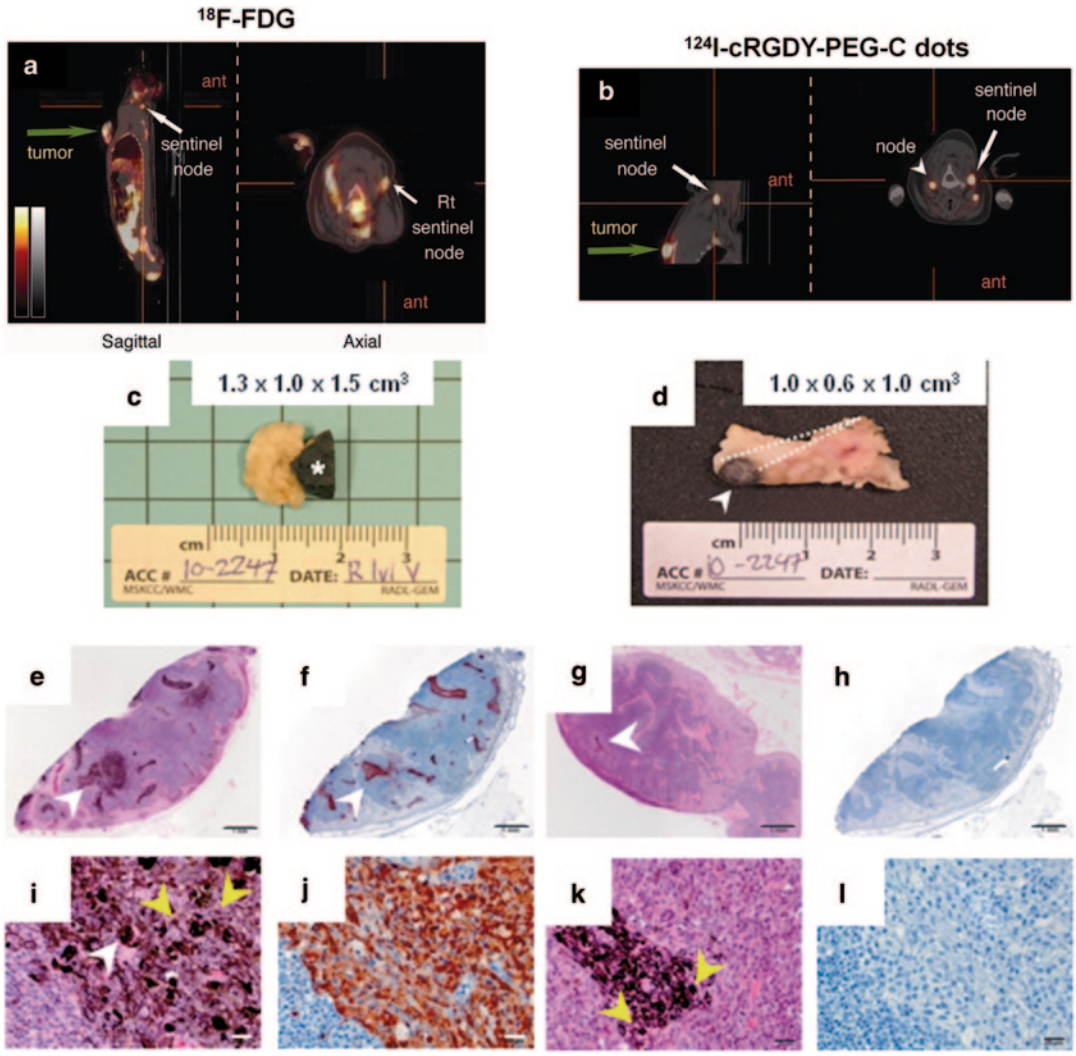

Fig. 13.4 Imaging of metastatic disease in a spontaneous melanoma miniswine model. **a** Whole-body ^{18}F-FDG PET-CT sagittal and axial views demonstrating primary tumor (*green arrow*) and single SLN (*white arrow*) posteriorly within the right (*Rt*) neck after intravenous injection (*ant* anterior). **b** High-resolution PET-CT scan reveals bilateral nodes 1 h after subdermal, four-quadrant, peritumoral injection of ^{124}I-cRGDY-PEG-C dots (*arrow* SLN, *arrowhead* left-sided node). **c**, **d** Gross images of the cut surfaces of the black-pigmented SLN (*asterisk*, **c**) and contralateral metastatic node (*arrowhead*, **d**) in the left posterior neck. **e** Low-power view of H&E-stained SLN demonstrating scattered melanomatous clusters (*white arrowhead*). **f** Corresponding high-power view of H&E-stained SLN, revealing melanoma cells (*yellow arrowheads*) and melanophages (*white arrowhead*). **g** Low-power image of a melanoma-specific marker, HMB-45 (*white arrowhead*), in representative SLN tissue. **h** High-power image of HMB-45-stained SLN tissue. **i** Low-power view of H&E-stained contralateral lymph node showing scattered melanomatous clusters (*white arrowhead*). **j** High-power image of contralateral node showing infiltration of melanomatous cells (*yellow arrowheads*). **k** Low-power image of representative normal porcine nodal tissue. **l** High-power image of representative normal porcine nodal tissue. Scale bars: 1 mm (**e**, **g**, **i**, **k**); 20 mm (**f**, **h**, **j**, **l**). (Adapted from [38])

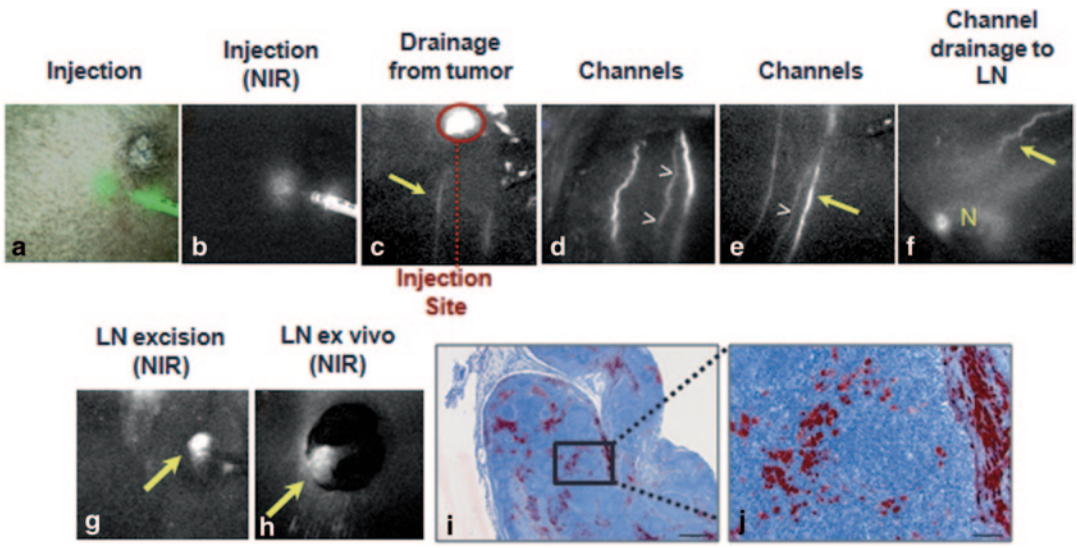

Fig. 13.5 Image-guided SLN mapping in a spontaneous melanoma miniswine model: real-time intraoperative optical imaging with correlative histology. Intraoperative SLN mapping was performed on the animal shown in Fig. 13.5. **a**–**h** Two-channel NIR optical imaging of the exposed nodal basin. Local injection of Cy5.5-incorporated particles displayed in dual-channel model **a** RGB color (*green*) and **b** NIR fluorescent channels (*white*). **c**–**f** Draining lymphatics distal to the site of injection. Fluorescence signal within the main draining proximal (**c**, **d**), mid (**e**), and distal (**f**) lymphatic channels (*yellow arrows*) extending toward the SLN (*N*'). Smaller-caliber channels are also shown (*arrowheads*). Images of the SLN acquired during (**g**) and after (**h**) excision displayed in the NIR channel. **i** Low-power view of HMB-45-stained (*red*) SLN confirms presence of metastases (*black box*, bar = 500 mm). **j** Higher magnification in **i** reveals clusters of HMB-45 + expressing melanoma cells (bar = 100 mm). (Adapted from [38])

tumor site with the skin intact. Two-channel NIR optical imaging of the exposed nodal basin after local injection of Cy5.5-incorporated C dots is displayed in the RGB color (green, Fig. 13.5a) and NIR fluorescent channels (white, Fig. 13.5b) flowing from the injection site (Fig. 13.5c) into the main proximal (Figs. 13.5c and d), mid (Fig. 13.5e) and distal (Fig. 13.5f) lymphatic branches toward the SLN (Fig. 13.5f). In addition, smaller caliber lymphatic channels are seen (Figs. 13.5d and e). Fluorescence signal seen within *in situ* (Fig. 13.5g) and *ex-vivo* (Fig. 13.5h) nodal specimens was confirmed by gamma emissions using the gamma probe, and was found to be consistent with melanoma, further confirmed by HMB45 expression on low-power (Fig. 13.5i) and high-power views (Fig. 13.5j).

^{124}I-cRGDY-PEG-C dots enabled superior detection sensitivity and discrimination between metastatic tumor infiltration and inflammatory processes in about one-third of the miniswine, relative to ^{18}F-FDG, the latter failing in many instances to accurately stage cancer spread. In about one-third of cases, ^{18}F-FDG identified sites of inflammation found to be additionally present in some of these animals, while the particle tracer did not, as confirmed by histopathologic analysis (Fig. 13.6). This result is best seen when comparing 3D integrated PET-CT ^{18}F-FDG images (Fig. 13.7a) and ^{124}I-cRGDY-PEG-C dot images (Figs. 13.7b, and c). PET-CT fused MIP images generated from dynamic PET imaging data reveals the bilateral metastatic neck nodes only after injection of the particle tracer. While ^{18}F-FDG shows clear absence of nodal metastases, diffusely increased activity is seen within metabolically active bony structures in these young animals, along with draining lymphatic channels. These findings suggest mechanistic differences at the cellular/subcellular levels related to the nature of these agents—one, a strictly metabolic probe (^{18}F-FDG), while the other is a nonmetabolic, integrin-targeting probe. These results highlight the potential utility of ^{124}I-cRGDY-PEG-C dots to selectively target, localize, and stage metastatic disease.

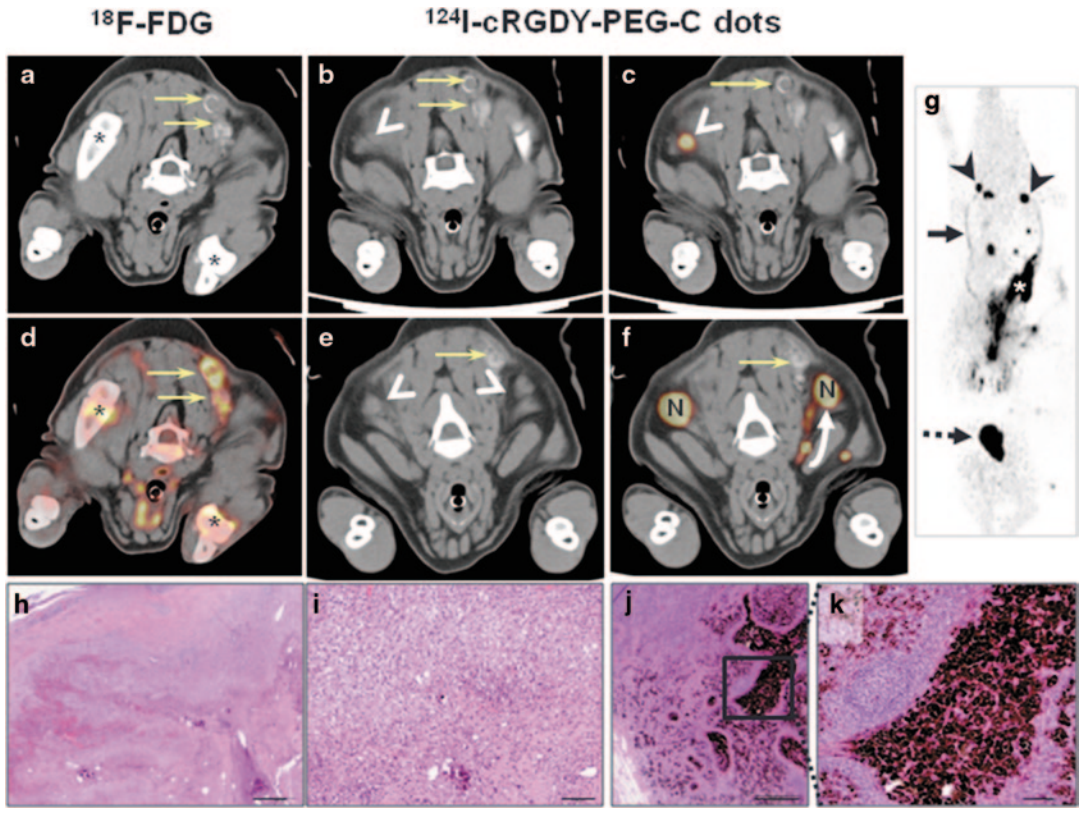

Fig. 13.6 Discrimination of inflammation from metastatic disease: comparison of ^{18}F-FDG and ^{124}I-cRGDY-PEG-C dot tracers. **a**–**d** Imaging of inflammatory changes using ^{18}F-FDG-PET with tissue correlation. **a** Axial CT scan of the ^{18}F-FDG PET study shows calcification within the left posterior neck (*yellow arrows*). **b** Fused axial ^{18}F-FDG PET-CT reveals hypermetabolic activity at this same site (*yellow arrows*). Increased PET signal is also seen in metabolically active osseous structures (*asterisks*). **c** Low- and **d** high-power views of H&E-stained calcified tissue demonstrate extensive infiltration of inflammatory cells. **e**–**k** Metastatic disease detection following injection of ^{124}I-cRGDY-PEG C dots about the tumor site. **e** Pre-injection axial CT scan of ^{124}I-cRGDY-PEG-C dots shows calcified soft tissues within the posterior neck (*yellow arrows*). **f** Coregistered PET-CT shows no evident activity corresponding to calcified areas (*arrow*), but demonstrates a PET-avid node on the *right* (*arrowhead*). **g** Axial CT at a more superior level shows nodes (*arrowheads*) bilaterally and a calcified focus (*yellow arrow*). **h** Fused PET-CT demonstrates PET-avid nodes (*N*) and lymphatic drainage (*curved arrow*). Calcification shows no activity (*arrow*). **i** Low- and **j** high-power views confirm the presence of nodal metastases. **k** Single frame from a three-dimensional (3D) PET image reconstruction shows multiple bilateral metastatic nodes (*arrowheads*) and lymphatic channels (*solid arrow*) draining injection site (*white asterisk*). Bladder activity is seen (*dashed arrow*) with no significant tracer accumulation in the liver (*black asterisk*). Bladder activity is seen with no significant tracer accumulation in the liver. Scale bars: 500 mm (**c**, **d**); 100 mm (**i**, **j**). (Adapted from [38])

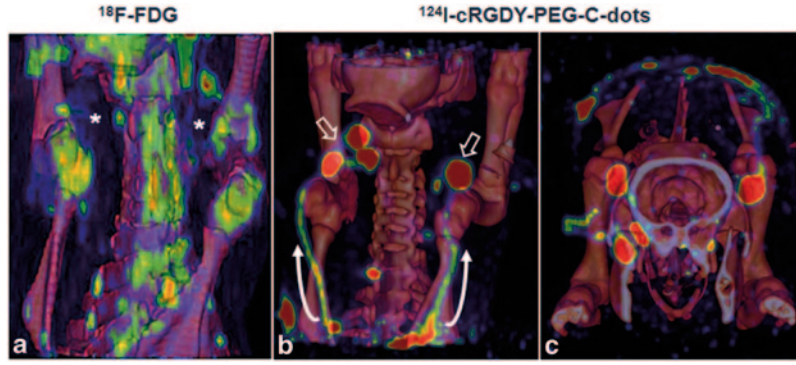

Fig. 13.7 3D integrated 18F-FDG and 124I-cRGDYPEG- C dot PET-CT. a–c 3D volume-rendered images were generated from CT and PET. (a) PET-CT fusion image (coronal view) shows no evident nodal metastases (asterisks). Increased activity within bony structures is identified. b, c High-resolution PET-CT fusion images showing coronal (b) and superior views (c) of bilateral metastatic nodes (open arrows) and lymphatic channels (curved arrows) within the neck following local injection of 124I-cRGDY-PEG-C dots.

Conclusions

Mapping the biological events leading to cancer at earlier stages may allow stratification of patients to appropriate treatment arms in a more timely fashion which can, in turn, potentially improve quality of life and patient survival. As lymph node metastases are a powerful predictor of outcome for melanoma, earlier detection of micrometastases in regional lymph nodes using real-time optical visualization tools may offer a distinct advantage over radioactivity-based identification of SLN/s, particularly in anatomically complex areas of the body. The ability to further probe critical cancer targets in a broader range of cancer types may elucidate important insights into the cellular and molecular processes that govern metastatic disease spread. The opportunity to combine these optical technologies with novel multimodal and multi-parametric image-driven metrics and informatics tools may play a key role in ultimately improving outcome measures and clinical radiology practice in the future.

References

1. Weissleder R. Imaging macrophages with nanoparticles. Nat Mater. 2014;13(2):13. Pubmed Central PMCID: 24452356.
2. ACS. Cancer Facts and Figs. 2012 Atlanta GA: 2012.
3. Balch CM, Soong SJ, Gershenwald JE, Thompson JF, Reintgen DS, Cascinelli N, et al. Prognostic factors analysis of 17,600 melanoma patients: validation of the American joint committee on cancer melanoma staging system. J Clin Oncol. 2001;19(16):3622–34. PubMed PMID: 11504744. Epub 2001/08/16. Eng.
4. Weissleder R. Molecular imaging in cancer. Science. 2006;312(5777):1168–71. PubMed PMID: 16728630. Epub 2006/05/27. Eng.
5. Erman AB, Collar RM, Griffith KA, Lowe L, Sabel MS, Bichakjian CK, et al. Sentinel lymph node biopsy is accurate and prognostic in head and neck melanoma. Cancer. 2012;118(4):1040–7. PubMed PMID: 21773971. Epub 2011/07/21. Eng.
6. Keereweer S, Mieog JS, Mol IM, Van Driel PB, Snoeks TJ, Baatenburg de Jong RJ, et al. Detection of oral squamous cell carcinoma and cervical lymph node metastasis using activatable near-infrared fluorescence agents. Arch Otolaryngol Head Neck Surg. 2011;137(6):609–15. PubMed PMID: 21690514. Epub 2011/06/22. Eng.
7. Mahmood U, Weissleder R. Near-infrared optical imaging of proteases in cancer. Mol Cancer Ther. 2003;2(5):489–96. PubMed PMID: 12748311. Epub 2003/05/16. Eng.
8. Wunderbaldinger P, Turetschek K, Bremer C. Near-infrared fluorescence imaging of lymph nodes using a new enzyme sensing activatable macromolecular optical probe. Eur Radiol. 2003;13(9):2206–11. PubMed PMID: 12802615. Epub 2003/06/13. Eng.
9. Gleysteen JP, Duncan RD, Magnuson JS, Skipper JB, Zinn K, Rosenthal EL. Fluorescently labeled cetuximab to evaluate head and neck cancer response to treatment. Cancer Biol Ther. 2007;6(8):1181–5. PubMed PMID: 17637562. Epub 2007/07/20. Eng.
10. Lee SB, Hassan M, Fisher R, Chertov O, Chernomordik V, Kramer-Marek G, et al. Affibody molecules for in vivo characterization of HER2-positive tumors by near-infrared imaging. Clin Cancer Res.

2008;14(12):3840–9. PubMed PMID: 18559604. Epub 2008/06/19. Eng.
11. Withrow KP, Newman JR, Skipper JB, Gleysteen JP, Magnuson JS, Zinn K, et al. Assessment of bevacizumab conjugated to Cy5.5 for detection of head and neck cancer xenografts. Technol Cancer Res Treat. 2008;7(1):61–6. PubMed PMID: 18198926. Epub 2008/01/18. Eng.
12. Koyama Y, Talanov VS, Bernardo M, Hama Y, Regino CA, Brechbiel MW, et al. A dendrimer-based nanosized contrast agent dual-labeled for magnetic resonance and optical fluorescence imaging to localize the sentinel lymph node in mice. J Magn Reson Imaging. 2007;25(4):866–71. PubMed PMID: 17345640. Epub 2007/03/09. Eng.
13. Kobayashi H, Kawamoto S, Bernardo M, Brechbiel MW, Knopp MV, Choyke PL. Delivery of gadolinium-labeled nanoparticles to the sentinel lymph node: comparison of the sentinel node visualization and estimations of intra-nodal gadolinium concentration by the magnetic resonance imaging. J Control Release. 2006;111(3):343–51. PubMed PMID: 16490277. Epub 2006/02/24. Eng.
14. Lucarelli RT, Ogawa M, Kosaka N, Turkbey B, Kobayashi H, Choyke PL. New approaches to lymphatic imaging. Lymphat Res Biol. 2009;7(4):205–14. PubMed PMID: 20143919. Pubmed Central PMCID: 2883526. Epub 2010/02/11. Eng.
15. Jain R, Dandekar P, Patravale V. Diagnostic nanocarriers for sentinel lymph node imaging. J Control Release. 2009;138(2):90–102. PubMed PMID: 19445982. Epub 2009/05/19. Eng.
16. Rasmussen JC, Tan IC, Marshall MV, Fife CE, Sevick-Muraca EM. Lymphatic imaging in humans with near-infrared fluorescence. Curr Opin Biotechnol. 2009;20(1):74–82. PubMed PMID: 19233639. Pubmed Central PMCID: 2692490. Epub 2009/02/24. Eng.
17. Povoski SP, Hall NC, Murrey DA Jr, Sharp DS, Hitchcock CL, Mojzisik CM, et al. Multimodal imaging and detection strategy with 124 I-labeled chimeric monoclonal antibody cG250 for accurate localization and confirmation of extent of disease during laparoscopic and open surgical resection of clear cell renal cell carcinoma. Surg Innov. 2013 Feb;20(1):59-69. PubMed PMID: 22455975. Pubmed Central PMCID: 3758170. Epub 2012/03/30 Eng.
18. Jain RK, Stylianopoulos T. Delivering nanomedicine to solid tumors. Nat Rev Clin Oncol. 2010;7(11):653–64. PubMed PMID: 20838415. Pubmed Central PMCID: 3065247. Epub 2010/09/15. Eng.
19. Keereweer S, Kerrebijn JD, van Driel PB, Xie B, Kaijzel EL, Snoeks TJ, et al. Optical image-guided surgery—where do we stand? Mol Imaging Biol. 2011;13(2):199–207. PubMed PMID: 20617389. Pubmed Central PMCID: 3051067. Epub 2010/07/10. Eng.
20. Schroeder A, Heller DA, Winslow MM, Dahlman JE, Pratt GW, Langer R, et al. Treating metastatic cancer with nanotechnology. Nat Rev Cancer. 2012;12(1):39–50. PubMed PMID: 22193407. Epub 2011/12/24. Eng.
21. Khullar O, Frangioni JV, Grinstaff M, Colson YL. Image-guided sentinel lymph node mapping and nanotechnology-based nodal treatment in lung cancer using invisible near-infrared fluorescent light. Semin Thorac Cardiovasc Surg. 2009;21(4):309–15. PubMed PMID: 20226343. Pubmed Central PMCID: 3109504. Epub 2009/01/01. Eng.
22. Benezra M, Penate-Medina O, Zanzonico PB, Schaer D, Ow H, Burns A, et al. Multimodal silica nanoparticles are effective cancer-targeted probes in a model of human melanoma. J Clin Invest. 2011;121(7):2768–80. PubMed PMID: 21670497. Pubmed Central PMCID: 3223837. Epub 2011/06/15. Eng.
23. Burns AA, Vider J, Ow H, Herz E, Penate-Medina O, Baumgart M, et al. Fluorescent silica nanoparticles with efficient urinary excretion for nanomedicine. Nano Lett. 2009;9(1):442–8. PubMed PMID: 19099455. Epub 2008/12/23. Eng.
24. Jokerst JV, Gambhir SS. Molecular imaging with theranostic nanoparticles. Acc Chem Res. 2011;44(10):1050–60. PubMed PMID: 21919457. Pubmed Central PMCID: 3196845. Epub 2011/09/17. Eng.
25. Misfeldt ML, Grimm DR. Sinclair miniature swine: an animal model of human melanoma. Vet Immunol Immunopathol. 1994;43(1–3):167–75. PubMed PMID: 7856049. Epub 1994/10/01. Eng.
26. Bradbury M. Clinical translation of an ultrasmall inorganic fluorescent hybrid nanoparticle probe. submitted.
27. Choi J, Burns AA, Williams RM, Zhou Z, Flesken-Nikitin A, Zipfel WR, et al. Core-shell silica nanoparticles as fluorescent labels for nanomedicine. J Biomed Opt. 2007;12(6):064007. PubMed PMID: 18163823. Epub 2008/01/01. Eng.
28. Kobayashi H, Koyama Y, Barrett T, Hama Y, Regino CA, Shin IS, et al. Multimodal nanoprobes for radionuclide and five-color near-infrared optical lymphatic imaging. ACS Nano. 2007;1(4):258–64. PubMed PMID: 19079788. Pubmed Central PMCID: 2600721. Epub 2008/12/17. Eng.
29. Ohnishi S, Lomnes SJ, Laurence RG, Gogbashian A, Mariani G, Frangioni JV. Organic alternatives to quantum dots for intraoperative near-infrared fluorescent sentinel lymph node mapping. Mol Imaging. 2005;4(3):172–81. PubMed PMID: 16194449. Epub 2005/10/01. Eng.
30. Choi CH, Zuckerman JE, Webster P, Davis ME. Targeting kidney mesangium by nanoparticles of defined size. Proc Natl Acad Sci U S A. 2011;108(16):6656–61. PubMed PMID: 21464325. Pubmed Central PMCID: 3080986. Epub 2011/04/06. Eng.
31. Maeda H, Wu J, Sawa T, Matsumura Y, Hori K. Tumor vascular permeability and the EPR effect in macromolecular therapeutics: a review. J Control Release. 2000;65(1–2):271–84. PubMed PMID: 10699287. Epub 2000/03/04. Eng.

32. Iyer AK, Khaled G, Fang J, Maeda H. Exploiting the enhanced permeability and retention effect for tumor targeting. Drug Discov Today. 2006;11(17–18):812–8. PubMed PMID: 16935749.
33. Sugahara KN, Teesalu T, Karmali PP, Kotamraju VR, Agemy L, Girard OM, et al. Tissue-penetrating delivery of compounds and nanoparticles into tumors. Cancer Cell. 2009;16(6):510–20. PubMed PMID: WOS:000272693700010. English.
34. Karmali PP, Kotamraju VR, Kastantin M, Black M, Missirlis D, Tirrell M, et al. Targeting of albumin-embedded paclitaxel nanoparticles to tumors. Nanomedicine. 2009;5(1):73–82. PubMed PMID: 18829396. Pubmed Central PMCID: 2824435. Epub 2008/10/03. Eng.
35. Ke S, Wen X, Gurfinkel M, Charnsangavej C, Wallace S, Sevick-Muraca EM, et al. Near-infrared optical imaging of epidermal growth factor receptor in breast cancer xenografts. Cancer Res. 2003;63(22):7870–5. PubMed PMID: 14633715. Epub 2003/11/25. Eng.
36. Moon WK, Lin Y, O'Loughlin T, Tang Y, Kim DE, Weissleder R, et al. Enhanced tumor detection using a folate receptor-targeted near-infrared fluorochrome conjugate. Bioconjug Chem. 2003;14(3):539–45. PubMed PMID: 12757377. Epub 2003/05/22. Eng.
37. Moghimi SM, Hunter AC, Murray JC. Long-circulating and target-specific nanoparticles: theory to practice. Pharmacol Rev. 2001;53(2):283–318. PubMed PMID: 11356986. Epub 2001/05/18. Eng.
38. Bradbury MS, Phillips E, Montero PH, Cheal SM, Stambuk H, Durack JC, et al. Clinically-translated silica nanoparticles as dual-modality cancer-targeted probes for image-guided surgery and interventions. Integr Biol-UK. 2013;5(1):74–86. PubMed PMID: WOS:000312391300008. English.
39. Oxenhandler RW, Adelstein EH, Haigh JP, Hook RR Jr, Clark WH Jr. Malignant melanoma in the Sinclair miniature swine: an autopsy study of 60 cases. Am J Pathol. 1979;96(3):707–20. PubMed PMID: 474716. Pubmed Central PMCID: 2042391. Epub 1979/09/01. Eng.
40. Millikan LE, Boylon JL, Hook RR, Manning PJ. Melanoma in Sinclair swine: a new animal model. J Invest Dermatol. 1974;62(1):20–30. PubMed PMID: 4809019. Epub 1974/01/01. Eng.

Image Processing Technologies for Motion Compensation

14

Claudio Vinegoni, Sungon Lee and Ralph Weissleder

Introduction

The impact of image processing in medical image analysis has increased in recent years concurrently with the development of novel imaging modalities and new user interfaces, facilitating both image analysis and maximizing the use of information present within the images.

One of the most important imaging processing technologies involves motion compensation. While images are assumed to contain information of a subject at one moment in time, measurements are, in general, severely hampered by the movement of the imaged organ. Specifically, physiological tissue motions give rise to strong artifacts, which vary in severity depending on the organ under investigation, the acquisition parameters (e.g., integration time and resolution), the imaging modality, and the ultimate imaging resolution, contributing in creating image distortion, blurring, and making image sequences highly unstable. Historically, the imaging techniques that have more extensively dealt with motion reduction methods are magnetic resonance imaging (MRI), particularly for high-resolution cardiac MRI, and X-ray computed tomography (X-CT). However, more recently, image processing approaches have been translated to other existing or newly developed imaging modalities.

In this chapter, we present several solutions that we and other groups have recently proposed for intravital laser scanning optical imaging, which could also be easily extended to widefield fluorescence imaging. Intravital microscopy is a relatively new imaging modality, which allows for investigating biological processes at the single cell level and in vivo due to its extended imaging depth, high resolution, and ease of implementation. Apart from its success in the biomedical field, intravital microscopy has also shown promise in the clinical settings, specifically for intraoperative imaging. Advancements in novel imaging systems in combination with the development of new targeted probes have provided a new platform and new capabilities to explore cell biology, and immunological response [1–3]. Unfortunately, motion artifacts have so far limited the full potential of optical microscopy for small animal and clinical imaging.

Respiration and cardiac activity are the major contributors to image artifacts; respiration is the most significant, affecting, in particular, the lungs and extending to all abdominal organs such as the liver, kidneys, pancreas, and spleen. Cardiac

C. Vinegoni (✉) · R. Weissleder
Center for Systems Biology, Massachusetts General Hospital, Harvard University, 185 Cambridge Street, Boston, MA 02114, USA
e-mail: cvinegoni@mgh.harvard.edu

R. Weissleder
e-mail: rweissleder@mgh.harvard.edu

S. Lee
Division of Electrical Engineering, Hanyang University, Ansan, 426-791 Republic of Korea

Y. Fong et al. (eds.), *Imaging and Visualization in The Modern Operating Room,*
DOI 10.1007/978-1-4939-2326-7_14,

activity also has a broad effect on many organs, and so far has prevented collecting information of the heart itself at the single cell level. Several other sources may contribute to tissue movement, such as peristalsis, muscle contraction, and organ drifting. Generally, these sources can be prevented, but apart from simple image drifting no compensation schemes can be adopted.

All physiological activities give rise to motion induced distortions within acquired images or sequences of images. These motion artifacts can be classified into two groups: in-frame and inter-frame motion distortions (Fig. 14.1). In-frame motion artifacts arise when the object of interest moves within a time scale of the order of the acquisition time. Inter-frame motion artifacts, instead, are due to motion events which occur between the acquisition of consecutive frames or scans and are not present, or at least are not noticeable, within a single acquired image (Fig. 14.2).

Various solutions for inter-frame and in-frame motion artifacts have been proposed, and the

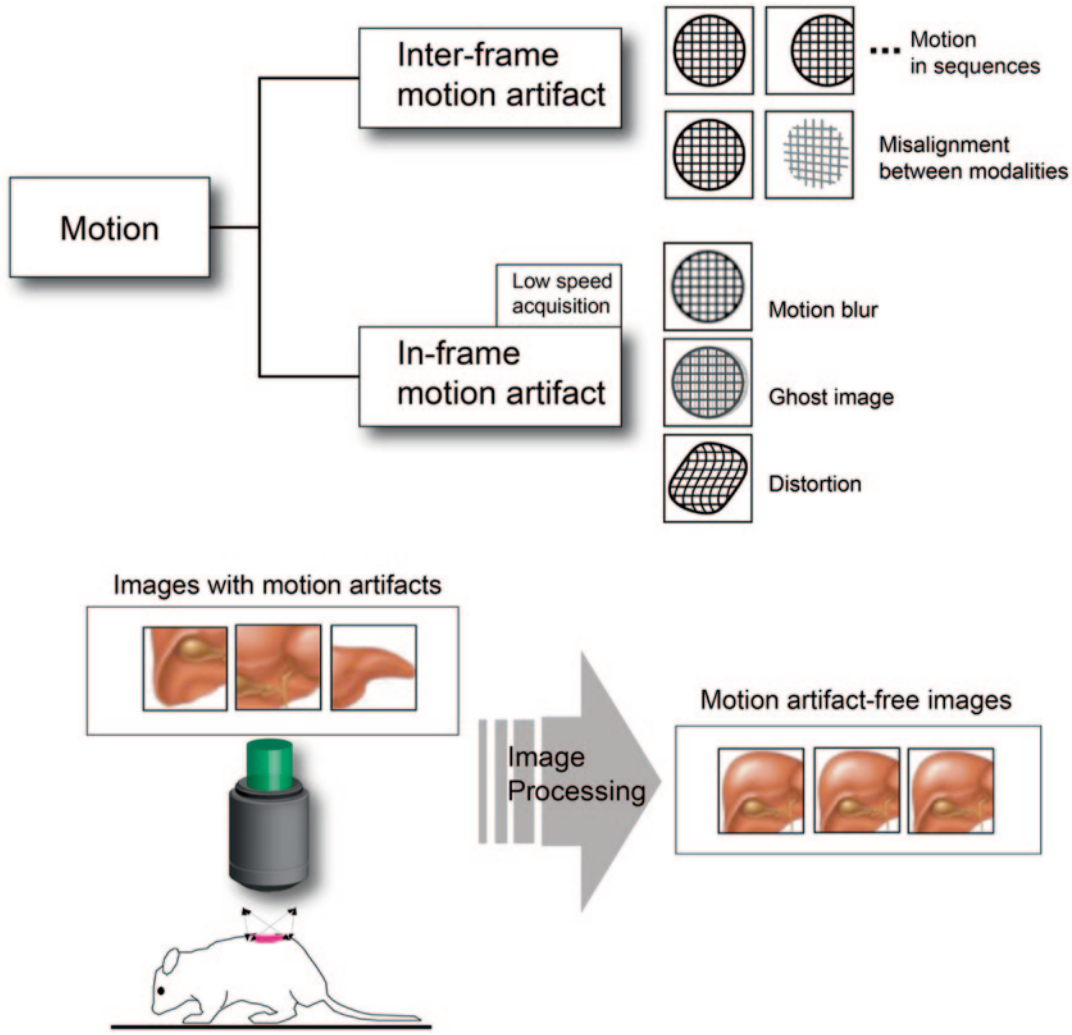

Fig. 14.1 Schematic showing different types of artifacts present during a typical image acquisition of an object in motion. Inter-frame and in-frame motion artifacts present different characteristics with the former affecting images over a long period of time (e.g., acquired sequences) and the latter giving rise to visible effects within single acquired images

literature is abundant with innumerable image processing algorithms [4–13]. We briefly discuss these solutions.

Inter-frame Motion Compensation

Inter-frame motion refers to motion caused by the imaging subject, with respect to the imaging device, and/or due to misalignments between different imaging modalities. The effect is typically evident over multiple image acquisition, such as time-lapse imaging sequences. In image sequences like video frame rate movies, inter-frame motion is, for the majority of cases, compensated by techniques known as "video stabilization," with the intent to remove unwanted artifacts due to relative movements, changes in the relative orientation of the imaging device and subject, or to the shaky motion of the acquisition apparatus (e.g., handheld charge-coupled device (CCD) for panoramic organ exploration). Historically, video stabilization has been developed to fix shaky videos by removing unwanted motion through image processing [6]. Recently, a similar idea has been successfully applied to in vivo microscopy where continual physiological movements severely impede microscopic observation of dynamic events in live tissues [7].

"Image registration" algorithms have been widely utilized as key technologies for aligning multiple images, acquired mainly from different modalities (e.g., MRI and CT or positron emission tomography, PET) into one coordinate system [8, 9], but they can also be applied to image sequences for inter-frame motion compensation. A typical application, as an example, arises when acquiring fluorescence contrast images in arteries by way of an imaging catheter and co-registering the signal with a simultaneously acquired angiogram [14]. Here the registration algorithm aligns multiple images from the different imaging techniques into one single coordinate system.

Both video stabilization and image registration are fundamentally based on the transformation motion models, which are historically classified as linear (global) or nonrigid (local) transformations. Linear transformations span from simple translation models to projective transformation models. Nonrigid transformations, instead, range from small regional variations describable with a small number of increased parameters to very dense displacement vector fields such as optical flow (Fig. 14.3). These algorithms can be utilized not only to align images but also to extend the imaged area by stitching separately acquired images. This is a typical case where motion (e.g., handheld reposition of the imaging device) is positively utilized to increase the field of view (Fig. 14.4) [10].

In-frame Motion Compensation

In-frame motion artifacts are present within single images and their origin can be ascribed to the relatively low-speed acquisition with respect to the imaged subject's motion. Common examples include image blurring in CCD acquired images, caused by the high-speed motion of the subject and the

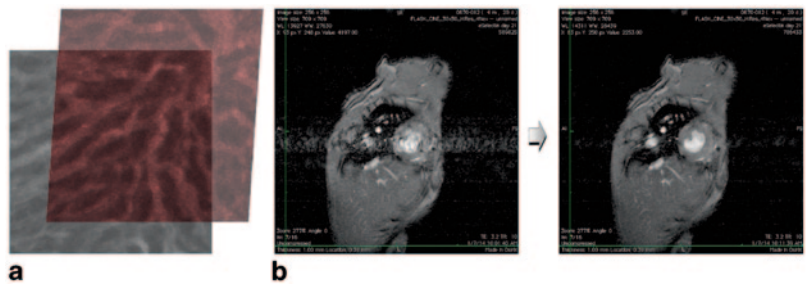

Fig. 14.2 Examples of motion compensation. **a** Inter-frame motion compensation: two microscopic images of mouse liver vessels are registered using an affine transformation model. **b** In-frame motion compensation: motion artifacts within an MRI image (*left*) are removed by motion-gated acquisition, leading to an artifact-free image (*right*)

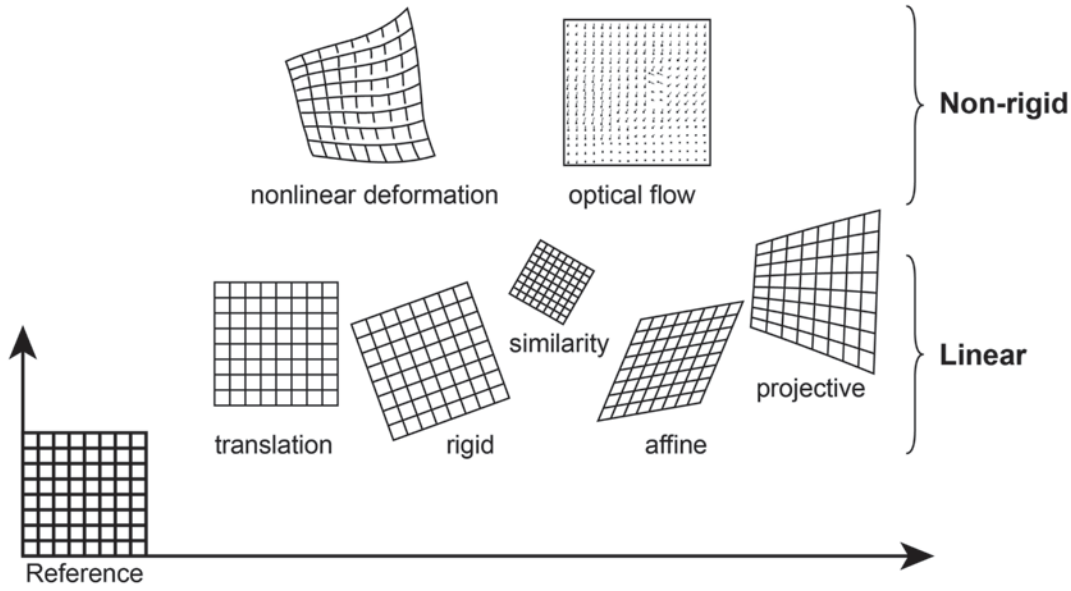

Fig. 14.3 Various transformation models, including both linear and nonrigid ones, which are commonly used for postprocessing acquired data. The final goal is to reduce image distortions induced by the imaged organ or the operator

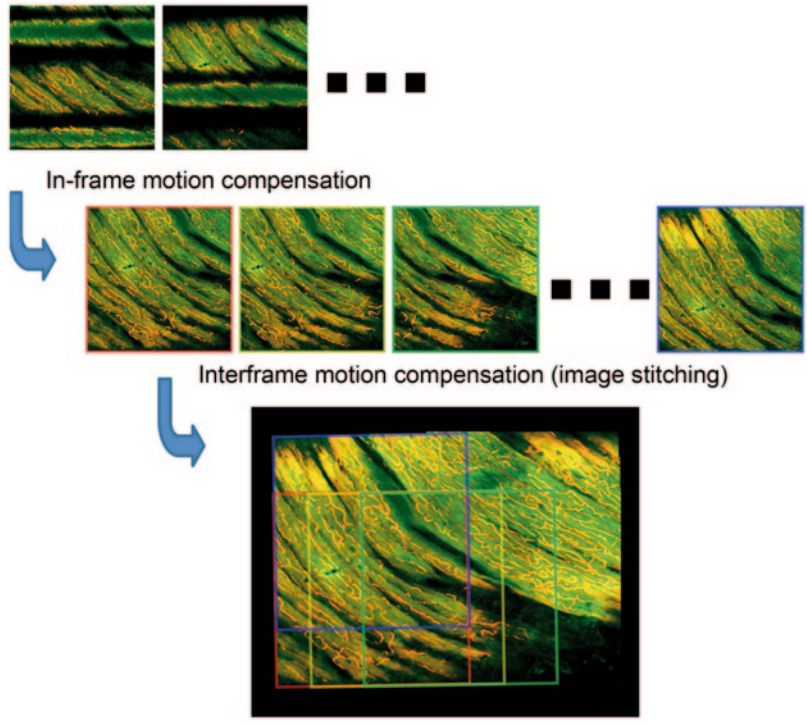

Fig. 14.4 Image mosaicking through in-frame and interframe motion compensation of a sequence of images obtained by laser scanning microscopy (LSM). During a first initial image processing phase, an automatic motion artifact removal algorithm [13] eliminates in-frame motion artifacts due to the heart beating. During a second phase, when the operator collects images over several adjacent areas of the heart, in-frame motion compensated images are combined together using a stitching algorithm, to give rise to a final panoramic image

relatively long exposure times (slow shutter speed) of the imaging devices. Ghost images in MRI are also well known to induce in-frame motion artifacts due to movement of subject and slow MRI scanning time. The effects can be mitigated by choosing a high-speed acquisition modality minimizing the motion during acquisition, leading to the elimination of the artifacts. For example, high shutter speed of a CCD can freeze a fast-moving object without motion blur in the resulting image. Although this simple high-speed approach can in principle reduce the motion artifacts, a reduced signal-to-noise ratio occurs as the absolute exposure time decreases depending on the speed increase.

Alternatively, slight motion blur artifacts can be removed from images through an image processing technology known as "motion deblurring," which needs no other images and information regarding the nature of the motion [11, 12]. Although these techniques are quite impressive in terms of visual appearance, in-frame motion compensation, in general, needs additional information such as motion parameters and multiple images in order to achieve a successful degree of motion compensation. To date, various motion reduction methods have been developed, particularly for high- resolution cardiac MRI, that speed up scanning acquisition times and/or involve the use of temporal or spatiotemporal redundancy [15–18]. Here the key principle underlying scan acceleration is based on the presence of quasi-periodic motion components, i.e., the predictable reproducibility of tissue position at certain time points during physiological (cardiac and respiratory) cycles, which allows for assisted motion-synchronized scanning [15]. A priori knowledge of the position, in combination with prospective triggering or retrospective gating acquisition schemes, can therefore enable fast-moving object imaging.

Acquisition Schemes for Motion Compensation in Laser Scanning microscopy

During LSM acquisition, an excitation laser scanning point moves along a predefined trajectory across a horizontal imaging plane. Due to the presence of physiological or operator induced motion components, the point along the described raster trajectory will not lie at the same depth within the imaged organ. Therefore, the acquired image is not representative of a single horizontal imaging plane across the sample but instead coincides with a curved surface with its profile modulated by both the speed of the motion and the microscope acquisition parameters (Fig. 14.5). The final image will then present in-frame artifacts such as distortion and blurring, the severity of which varies along a physiological cycle in relation to the instant speed (e.g., cardiac-induced motion will be minimal during the diastole, a cardiac phase with the heart at resting state).

Through the years, several acquisition schemes have been developed for cardiac and respiratory MRI with the intent to mitigate motion-induced artifacts. While the basic imaging principles of MRI and optical microscopy are different, the principles of image stabilization are adaptable to both techniques (Fig. 14.6) and we have recently successfully translated some of them to optical microscopy [19].

In cardiac MRI, "segmented cardiac-gated acquisition" has been widely and extensively used to correct for cardiac motion artifacts. Here, to acquire an MRI image at a specific time point during the cardiac cycle, only the data corresponding to a well-defined time window in the k-space are selected and gathered until the entire k-space is filled ("view per view" acquisition). Thanks to the quasi-periodicity and reproducibility of the cardiac motion, at least on the scale of the MRI resolution, a full k-space image can be reconstructed by collecting all segments acquired at different time points within a well-defined cardiac phase. This procedure can be done both in an active (prospective triggering) or passive mode (retrospective gating). In retrospective gating the electrocardiogram (ECG) signal is continuously measured during MRI acquisition. ECG-gating is then applied on all acquired images selecting the k-space lines corresponding to specific time intervals of the cardiac cycle. All segments are then postprocessed and combined to give rise to a final image representative of the organ at

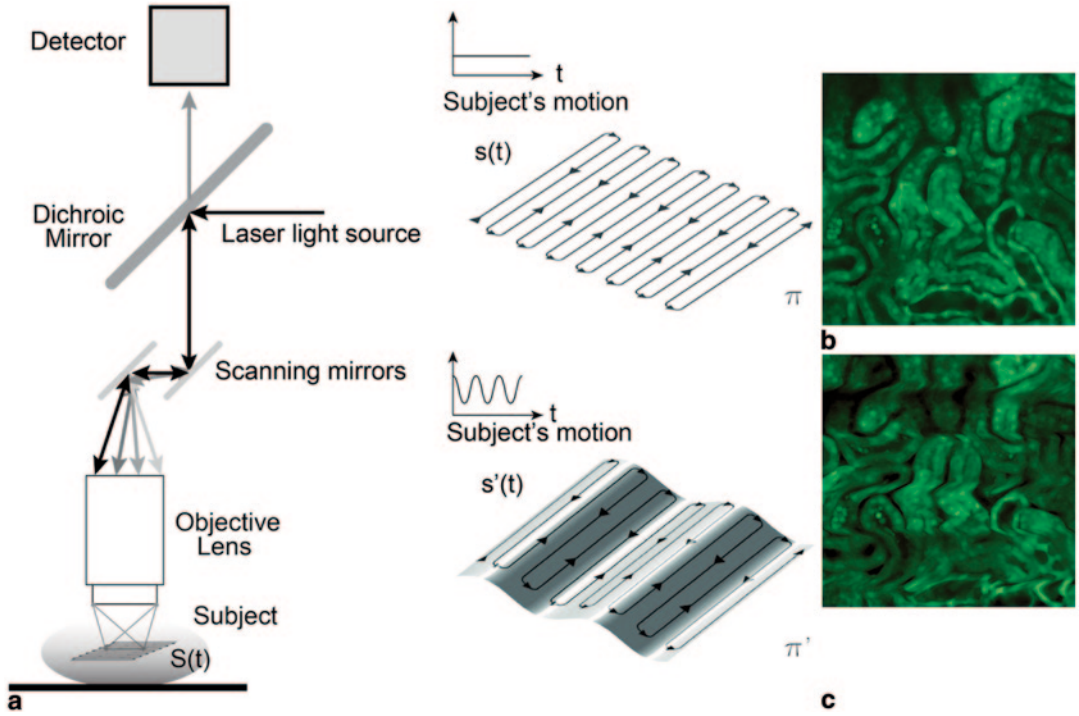

Fig. 14.5 **a** Scheme of principle for laser scanning confocal microscopy. Two galvanometer mirrors oscillating along orthogonal axes scan the excitation laser beam along a raster path. Light is focused onto the sample and the emission light is detected through a dichroic mirror. **b** When the subject is stationary, the raster scanning path lies on a horizontal imaging plane perpendicular to the imaging objective. **c** When the subject moves, the imaging plane in the organ's reference frame will appear as a curved surface modulated in time according to the motion periodicity [19]

a specific time of the physiological cycle. Prospective triggering, instead, requires acquisition directly initiated by the ECG signal. By varying the delay between a specific time point of the ECG and the acquisition, all k-space segments representative of a time point within the cardiac cycle are collected and a final artifact-free image is then reconstructed (Fig. 14.6).

Recently we have extended these imaging schemes specifically to LSM to image beating heart in mice (Fig. 14.7). Here, analogous to MRI, multiple images are acquired sequentially; by gating to specific time points in the ECG, views are grouped into segments to give rise to a final reconstructed image representative of a horizontal imaging plane free of any motion-induced artifact. While acquiring physiological parameters could facilitate image processing and artifact removal, other possibilities are available which do not require direct or indirect monitoring of the tissue under investigation. Recently, we have proposed several automatic artifact removal image processing algorithms which utilize correlation between individual image segments instead of using motion information in order to identify the data corresponding to the same specific cycle phase [13], combining them into a final "stabilized" image (Fig. 14.8).

Passive and Active Mechanical Stabilizers

Because LSM usually operates at higher resolutions than MRI, it is very important to reduce, as much as possible, the total displacement due to physiological motion, and to introduce high reproducibility in the motion in order to implement

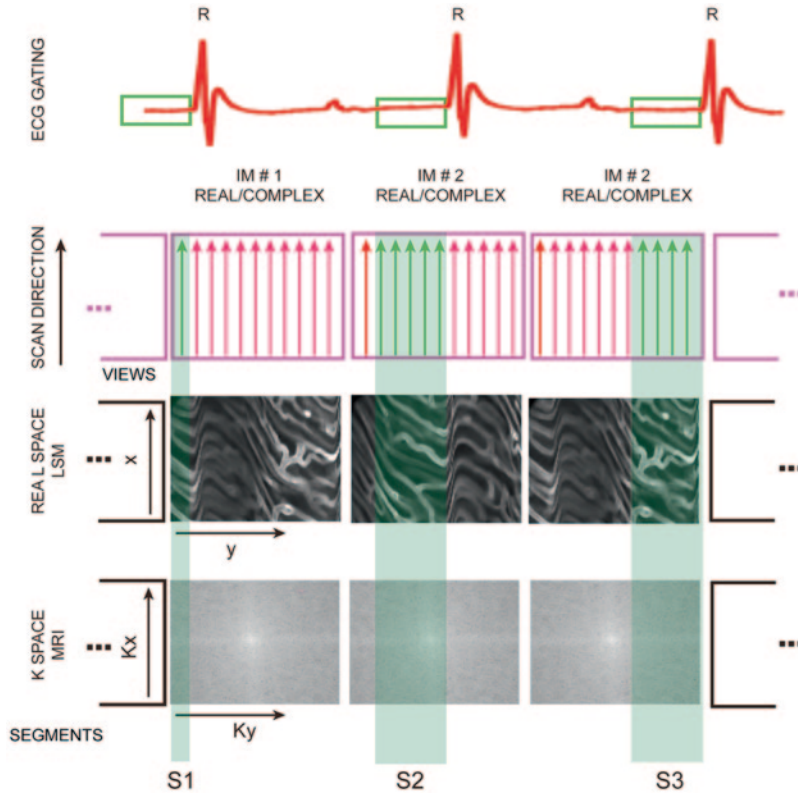

Fig. 14.6 Principle for sequential retrospective electrocardiogram (ECG)-gated imaging [19]. In MRI, a sequence of views is collected in the k-space by varying the phase-encoding gradient. Laser scanning microscopy (LSM) images are acquired pixel by pixel in the real space, with the excitation scanning laser beam moving along a predefined path. Groups of views are sequentially collected within a time-gated window corresponding to the end-diastole. The process is then repeated until the entire real space (LSM) or k-space (MRI) is filled. (Figure adapted from [19])

the reconstruction algorithms indicated above. Only under this assumption, segments belonging to the same specific phase of the cardiac cycle but collected at different point in times are equal and therefore can be patched together. In the absence of reproducibility the segments will be uncorrelated to each other, even if gating or triggering schemes are implemented.

One of the most obvious and easily implemented methods to attenuate motion-induced image artifacts consists of establishing physical immobilization, for example when imaging the skin of a patient during a routine dermatological check. When imaging inner organs, however, immobilization cannot always be achieved and mechanical restriction is commonly used to limit and confine tissue motion, for example by applying a gentle pressure. The limitation of this strategy is that it can negatively impact the physiological functions. Moreover, it will not completely suppress motion-induced artifacts and may fail to provide enough high-resolution images due to the random nature of the motion. For this reason, various mechanical stabilizers have been proposed and extensively used in small animal imaging (Figs. 14.9a, b) [20, 21], which could be translated with some degree of success into patients [22]. Although passive stabilizers are more commonly used, to further compensate residual motion components (Fig. 14.9b) gating algorithms or active tracking devices are highly recommended. Here, relative motion between the imaged organ and the imaging lens is completely removed by keeping their relative po-

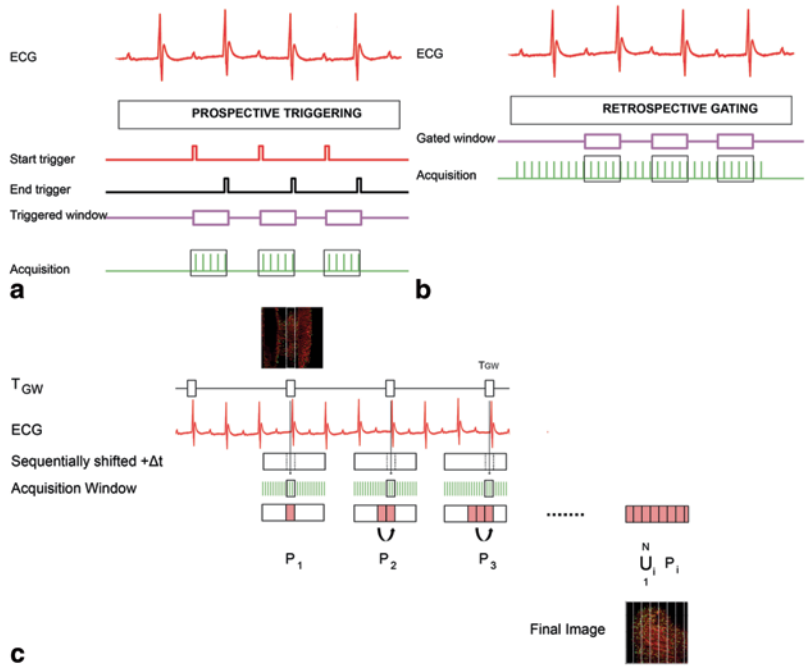

Fig. 14.7 **a** Prospective triggered acquisition scheme: images are acquired only during a specific triggered window, which is determined by the ECG. All acquired data are therefore used for image reconstruction. **b** Retrospective gated acquisition scheme: data for images are continuously acquired together with the ECG signal. Following this nonselective acquisition, only the data that were acquired during the time of a specific gated window, which is determined by ECG, are chosen for image reconstruction. **c** Simplified timing diagram and image reconstruction scheme for sequential retrospective cardiac-gated segmented microscopy. Segments from a continuous sequence of images are grouped together and a final image is reconstructed, which provides a true representation of the heart's morphology at the cardiac phase corresponding to a specific time-gated window [19]. (Figure adapted from [19])

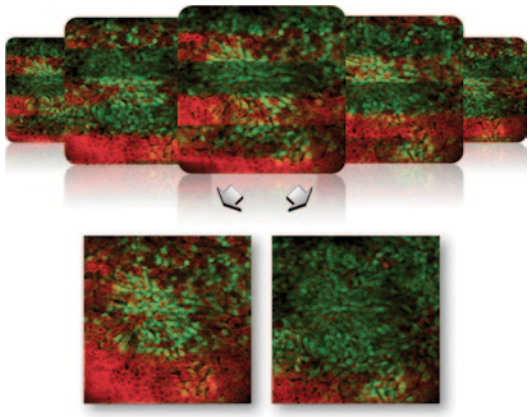

Fig. 14.8 Results of automatic artifact removal image processing [13]. The basic idea is to automatically identify within a sequence of images all artifact-free segments, combining them into a final "stabilized" image. Raw images (*upper part*) are in vivo microscopic images of a mouse liver. (Figure adapted from [13])

sition to each other constant over time. While in small animals this could be achieved sometimes by moving the subject, in human patients this strategy is not feasible and the imaging objective is typically tracking the moving organ. The objective lens is attached to a fast moving mechanism controlled with a feedback loop to track the tissue motion, while the organ's position is tracked with a high-speed imaging system. The relative position of both objective and tissue is therefore kept constant over time providing virtual, free of motion artifacts images. Recently, robotic systems have been developed based on this principle [23] that make use of visual information or contact-type displacement sensing. In the first solution, a vision based compensation system (Fig. 14.10a), a high-speed camera (955 fps) collects 2D images of the moving organ, which is preventively stabilized along the third dimension (vertical axis) by way of a compressive cover

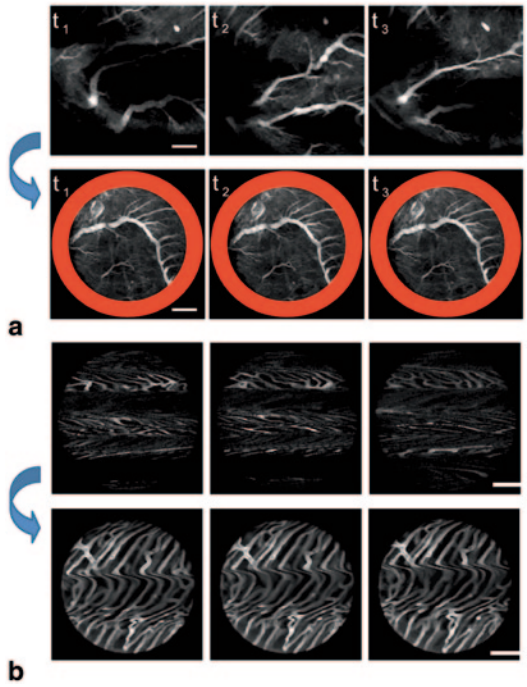

Fig. 14.9 Cardiac vasculature image sequence of a beating mouse heart at **a** low and **b** high resolution. Passive mechanical stabilization as proposed by [20, 21] were used to reduce image artifacts. At low resolution (**a**), motion artifacts look almost absent following mechanical stabilization. However, at high resolution (**b**), artifacts are still present, requiring further postprocessing. Scale bars: **a** 500 μm and **b** 50 μm. (Figure adapted from [13])

slip. A piezo-driven robotic closed arm with 2 degrees of freedom and consisting of a five-bar linkage with living hinges is then used to control the position of the imaging objective lens. Demonstrating optimal motion compensation for kidney imaging, the residual motion of this setup was less than 10 μm, while the maximum amplitude of the compensated motion was in excess of 150 μm. The second solution, instead, relies on motion compensation by contact-type displacement sensing (Fig. 14.10b). This solution is sometimes preferable over the first because of the reduced costs and the possibility to track motion in 3D. The signal from three strain gauges of a contact-type sensor consisting of three cantilever beam in direct contact with the imaged tissue is used to estimate the displacement and track tissue positions over time. Here a piezo-driven robotic closed arm with 3 degrees of freedom, one more than in the former configuration, is used.

Conclusion

Imaging technologies such as MRI, CT, and ultrasound have considerably improved over the course of the last two decades and novel image processing technologies for motion compensation have been proposed in part because of the implementation of implemented. Due to their portability and low cost integration, intraoperative optical imaging systems with different resolution scales are also increasingly used. While optical imaging techniques potentially offer the ability to acquire data at the single cellular level, physiological motion components have quite limited their application at the microscopic scale. Here we have presented different solutions that are currently available to suppress motion-induced image artifacts, which can be implemented for both wide field and laser scanning fluorescence optical microscopy. Translation into the clinical environment should be pretty straightforward and further facilitate the implementation of CCD and laser scanning based imaging technologies. Among the different applications, cardiovascular and tumor surgery would benefit the most by adoption of these methods. For example, intraoperative motion compensation in the beating heart could help detect differences between noncontracting necrotic myocardium and noncontracting viable but stunned or hibernated myocardium. These limitations are particularly problematic in the case of surgical revascularization of patients with severe myocardial dysfunction, where it may be impossible to ascertain which areas can or cannot be recovered to contraction by means of revascularization. Also, during typical cancer resections, tissue margins could be evaluated more accurately during the procedure itself without additional postoperative intervention.

Image processing technologies for motion compensation will also be enormously facilitated by the implementation of graphics processing units (GPU) for real-time processing acceleration, further allowing the adoption of these technologies to be seamless and immediate.

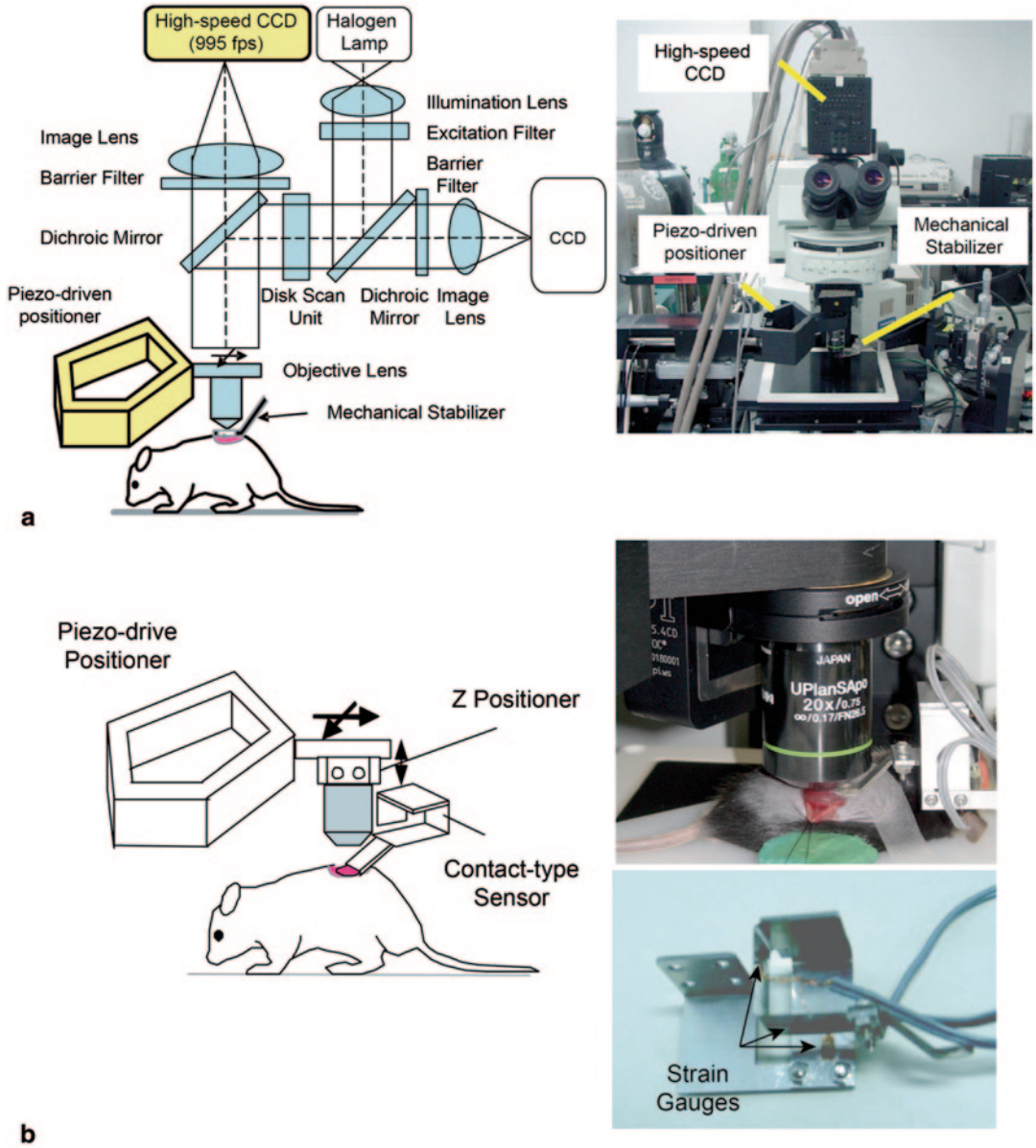

Fig. 14.10 Active motion compensations schemes [23]. **a** "Visual information"-based active motion compensation: a high-speed camera (955 fps) collects 2D images of the moving organ which is preventively stabilized along the third dimension (*vertical axis*) by way of a compressive cover slip. A piezo-driven robotic closed arm with 2° of freedom and consisting of a five-bar linkage with living hinges is then used to control the position of the imaging objective lens. **b** Contact-type sensing-based active motion compensation: The signal from three strain gauges of a contact-type sensor consisting of three cantilever beams in direct contact with the imaged tissue is used to estimate the displacement while a piezo-driven robotic closed arm with 3° of freedom moves the objective lens following the tissue position over time. (Figure adapted from [23])

References

1. Weigert R, Sramkova M, Parente L, Amornphimoltham P, Masedunskas A. Intravital microscopy: a novel tool to study cell biology in living animals. Histochem Cell Biol. 2010;133:481–91.
2. Pittet MJ, Weissleder R. Intravital imaging. Cell. 2011;147:983–91.
3. Bousso P, Moreau HD. Functional immunoimaging: the revolution continues. Nat Rev Immunol. 2012;12:858–64.
4. Stiller C, Konrad J. Estimating motion in image sequences. Signal Process Mag IEEE. 1999;16:70–91.
5. Szeliski R. Image alignment and stitching: a tutorial. Found Trends Comput Graph Vis. 2006;2:1–104.
6. Matsushita Y, Ofek E, Ge W, Tang X, Shum HY. Full-frame video stabilization with motion inpainting. IEEE Trans Pattern Anal Mach Intell. 2006;28:1150–63.
7. Soulet D, Paré A, Coste J, Lacroix S. Automated filtering of intrinsic movement artifacts during two-photon intravital microscopy. PLoS One. 2013;8:e53942.
8. Maintz JB, Viergever MA. A survey of medical image registration. Med Image Anal. 1998;2:1–36.
9. Crum WR, Hartkens T, Hill DL. Non-rigid image registration: theory and practice. Br J Radiol. 2004;77(2):S140–53.
10. Loewke KE, Camarillo DB, Piyawattanametha W, Mandella MJ, Contag CH, Thrun S, Salisbury JK. In vivo micro-image mosaicing. IEEE Trans Biomed Eng. 2011;58:159–71.
11. Shan Q, Jia J, Agarwala A. High-quality motion deblurring from a single image. ACM Trans Graph. 2008;27:1–10.
12. Cho S, Lee S. Fast motion deblurring. ACM Trans Graph. 2009;28:1–8.
13. Lee S, Vinegoni C, Sebas M, Weissleder R. Automated motion artifact removal for intravital microscopy, without a priori information. Sci Rep. 2014;4:4507.
14. Vinegoni C, Botnaru I, Aikawa E, Calfon MA, Iwamoto Y, Folco EJ, Ntziachristos V, Weissleder R, Libby P, Jaffer FA. Indocyanine green enables near-infrared fluorescence imaging of lipid-rich, inflamed atherosclerotic plaques. Sci Transl Med. 2011;3:84ra45.
15. Scott AD, Keegan J, Firmin DN. Motion in cardiovascular MR imaging. Radiology. 2009;250:331–51.
16. Tsao J, Kozerke S. MRI temporal acceleration techniques. J Magn Reson Imaging. 2012;36:543–60.
17. Atkinson DJ, Edelman RR. Cineangiography of the heart in a single breath hold with a segmented turboFLASH sequence. Radiology. 1991;178:357–60.
18. Finn JP, Edelman RR. Black-blood and segmented k-space magnetic resonance angiography. Magn Reson Imaging Clin N Am. 1993;1:349–57.
19. Vinegoni C, Lee S, Feruglio PF, Marzola P, Nahrendorf M, Weissleder R. Sequential average segmented microscopy for high signal-to-noise ratio motion-artifact-free in vivo heart imaging. Biomed Opt Express. 2013;4:2095–106.
20. Lee S, Vinegoni C, Feruglio PF, Fexon L, Gorbatov R, Pivoravov M, Sbarbati A, Nahrendorf M, Weissleder R. Real-time in vivo imaging of the beating mouse heart at microscopic resolution. Nat Commun. 2012;3:1054.
21. Vinegoni C, Lee S, Gorbatov R, Weissleder R. Motion compensation using a suctioning stabilizer for intravital microscopy. IntraVital. 2012;1:115–121.
22. Scott NA, Knight JL, Bidstrup BP, Wolfenden H, Linacre RN, Maddem GJ. Systematic review of beating heart surgery with the Octopus Tissue Stabilizer. Eur J Cardiothorac Surg. 2002; 21:804-17.
23. Lee S, Nakamura Y, Yamane K, Toujo T, Takahashi S, Tanikawa Y, Takahashi H. Image stabilization for in vivo microscopy by high-speed visual feedback control. IEEE Trans on Robot. 2008;24:45–54.
24. Lee S, Vinegoni C, Feruglio PF, Weissleder R. Improved intravital microscopy via synchronization of respiration and holder stabilization. J Biomed Opt. 2012;17:96018–1.

Part II
Current Clinical Applications

Near-Infrared Imaging with Fluorescent Tracers in Robotic Surgery

15

Pier Cristoforo Giulianotti, Despoina Daskalaki, Vivek Bindal and Kristin Patton

Introduction

From a surgeon's perspective, one of the most desired aspects of surgery is the ability to obtain the most information about the operative field. With the advent of minimally invasive surgery, the need for better visualization techniques has increased because of the reduced amount of direct feedback from tissues that the surgeon usually receives in open surgery. Near-infrared (NIR) imaging is one of such technologies which, combined with three-dimensional high-definition view, provides details in robotic surgery, which are otherwise not available to the surgeon.

NIR imaging refers to the use of the electromagnetic spectrum between 700 and 1000 nm, which is invisible to the human eye, along with fluorescent tracers to produce fluorescence. There are many advantages for using the NIR spectrum. It is invisible with the laparoscopic camera, so the appearance of the surgical field does not change unless the camera is activated to view the spectrum. It has a decent tissue penetration (up to 5 mm), it is nonionizing, and there is no unfavorable effect on the tissue. This technique provides for real-time guidance during a procedure, as image acquisition takes only a few milliseconds [1].

NIR imaging requires a contrast agent containing a molecule, called a fluorophore, that emits NIR fluorescent light after being excited by an NIR light source. Depending on the application, a targeting ligand is present that directs the fluorophore to the structure under study. Visualization of the tissue is based on the signal of the contrast agent in the region of interest relative to the background signal, known as the signal-to-background ratio (SBR). Indocyanine green (ICG) and methylene blue (MB) are the only NIR fluorophores that are registered with the Food and Drug Administration (FDA) and the European Medicines Agency (EMA) for clinical use [1].

When illuminated with NIR light, protein-bound ICG emits light that peaks at approximately 840 nm [2]. This fluorescence property of ICG was found in the 1970s, and the clinical application of real-time fluorescence imaging using ICG started in the early 1990s with fundus angiography in ophthalmology [3]. The application of ICG fluorescence imaging was extended to surgery as an intraoperative navigation tool of lymphatic flow, sentinel lymph node (SLN) mapping, determining blood flow during coronary artery bypass grafting, and identifying cerebral aneurysms for clip-

P. C. Giulianotti (✉) · D. Daskalaki · K. Patton
Department of Surgery, University of Illinois Hospital and Health Sciences System, 840 S. Wood Street, Room 435 E, Chicago, IL 60612, USA
e-mail: piercg@uic.edu

D. Daskalaki
e-mail: daskala@uic.edu

V. Bindal
Department of Surgery, Sir Ganga Ram Hospital, New Delhi, India

K. Patton
e-mail: kdpatton2@gmail.com

Y. Fong et al. (eds.), *Imaging and Visualization in The Modern Operating Room,*
DOI 10.1007/978-1-4939-2326-7_15, © Springer Science+Business Media New York 2015

ping [4–7]. ICG is safe to use, and complications following administration are rare [8, 9]. Circulating ICG is cleared rapidly by the liver and almost exclusively excreted into the bile. ICG is the most commonly used fluorophore in laparoscopic and robotic surgery. The Fluorescence Imaging Vision System was integrated into the DaVinci robotic platform in 2011. Since then, the role of near-infrared fluorescence (NIF)-ICG imaging has been rapidly expanding in all fields of robotic surgery. Up to date, there are various papers published in the scientific literature on the role of fluorescence in robotic surgery; however, the experience is still limited, because this technology is relatively new and some centers are only now starting to use this technique. The main surgical fields in which NIF-ICG is being used are general, urologic, gynecologic, and thoracic robotic surgery [10–15].

MB has been used for over 120 years for several medical applications. When diluted to levels that are almost undetectable to the human eye, MB becomes a fluorophore emitting at ≈700 nm [16]. This phenomenon is called "unquenching." At high dye concentration, fluorescence emission from MB is reabsorbed intermolecularly. When diluted, fluorescence emission becomes unquenched. MB is cleared equally by both the liver and kidney, permitting imaging of both the bile duct and the ureter.

Real-time cancer identification using fluorescence probes currently represents one of the most active research fields. Both ICG and MB are nonspecific NIR contrast agents. To permit targeted imaging, novel NIR fluorescent probes are being developed. These fluorophores can be conjugated to a tumor-specific ligand to target tumor cells. For instance, they can be conjugated to tumor-specific antibodies, nanobodies, small peptides, or they can be activated by enzymatic cleavage in order to become fluorescent [17].

In robotic surgery, NIR imaging provides the surgeon with many potential advantages in any given surgical procedure. It can aid in identifying a structure or lesion, which has to be resected (e.g., tumor tissue), or protected (e.g., bile ducts). It can help in dissection of blood vessels and lymph nodes, and it can identify the blood perfusion before performing an anastomosis. Researchers are currently working to enable targeted imaging, and it will change the way surgery is performed.

Clinical Applications of NIR Imaging in General Surgery

After intravenous injection of ICG, within 5–60 s, the first structures that are visualized are arteries, followed by veins. The visualization lasts a few seconds, but additional doses of ICG could be administered if necessary. The toxicity margin is very high; the maximal recommended dose in adults is 2 mg/kg [8, 9]. Subsequently, the organ and tissue microperfusion becomes evident, followed by the lymphatic and neural structures. After 45–60 min ICG accumulates in the liver and is secreted into the bile, and therefore can be used to assess the liver and bile ducts. The clinical applications of NIR imaging can be classified according to the visualization target and are summarized in Table 15.1.

Vascular Imaging

Identification of arteries and veins is one interesting application of ICG. Recognition of normal anatomy and/or identification of anatomical variations in real-time minimizes the risk of inadvertent damage to vascular structures. This is potentially a significant improvement, in a simple cholecystectomy (where vascular identification could decrease the risk of inadvertent damage of anomalous or accessory arteries), as well as in a complex case of hepatic or pancreatic resection (where identification and dissection of major vessels are a key step to the successful completion of the operation).

In urology, NIR-ICG has been recently used for super-selective arterial clamping in robotic partial nephrectomy (RPN). Borofsky et al. published their initial experience with 34 cases of zero-ischemia RPNs and reported that the imaging technique (often referred to as "firefly") facilitates super-selective arterial clamping, leading to improved functional outcomes [18].

Table 15.1 Clinical applications of near-infrared imaging in robotic surgery

Vascular imaging	
Anatomy of blood vessels	e.g., hepatic artery during hepatectomy, splenic artery, and vein during distal pancreatectomy
Organ and tissue perfusion	e.g., recognizing adequately perfused tissue during GI anastomosis, renal perfusion after transplant
Blood flow	e.g., after vascular anastomosis
Lymphatic channels	
Lymph node identification	e.g., SLN in endometrial cancer
Specialized tissue	
Nerve identification	e.g., phrenic nerve during thymectomy, inferior hypogastric plexus during pelvic dissection, recognition of parathyroids during thyroidectomy
Parathyroid identification	
Biliary imaging	
Fluorescent cholangiogram	e.g., extrahepatic biliary ducts during cholecystectomy and hepatectomy
Identification of lesions, based on their vascular and metabolic pattern	e.g., well- vs. poorly differentiated HCC, neuroendocrine lesions, angiomas

GI gastrointestinal, *SLN* sentinel lymph node, *HCC* Hepatocellular carcinoma

Organ and Tissue Perfusion

Evaluation of tissue perfusion is another important application of NIR imaging. Adequate ICG microperfusion assessment in colorectal and esophageal surgery allows real-time recognition of viable tissues (Fig. 15.1). Color demarcation is not always precise, and Doppler scanning requires specific probes that may present artifacts (poor contact/interphase). With fluorescence, the surgeon is able to revise the line of resection, if needed, and perform safer anastomoses. In the case of esophagectomy, the tubulization of the stomach could result in distal ischemia of the gastric conduit. Partial ischemia may lead to anastomotic leaks, which represent a severe complication. In robotic colorectal surgery, evaluation of the anastomotic perfusion is one of the commonest applications of ICG. In the last year the first experiences with NIR-ICG were published. Jafari et al. were the first to evaluate anastomotic tissue perfusion during robotic low anterior resections (RLAR) [19]. The authors conducted a retrospective case-control analysis to determine whether NIR-ICG could reduce the rates of anastomotic leak after RLAR. Since fluorescent imaging allows detection of low perfused areas otherwise invisible to the human eye, the authors stated that they frequently had to revise the point of bowel transection. They reported a 12% relative decrease of risk for anastomotic leak in the NIR-ICG group [19]. Other studies also confirmed the effectiveness of this technique in evaluating the bowel perfusion [20–22]. Hellan et al. reported a 40% rate of changing the point of bowel transection after fluorescent imaging [21]. Further studies are needed to determine whether this translates in a true reduction of anastomotic leaks, but these preliminary results look very promising. A prospective multicenter trial is in progress, in an effort to identify the real impact of NIR-ICG in changing the point of bowel transection during

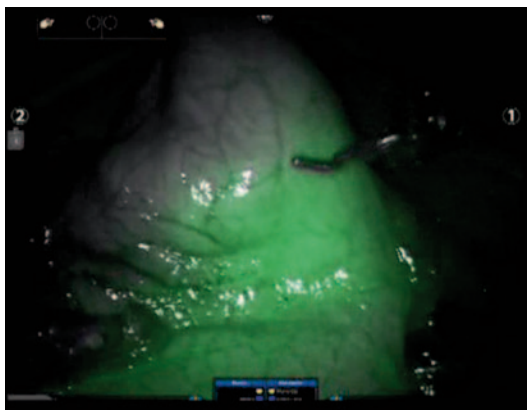

Fig. 15.1 Evaluation of gastric perfusion with NIR-ICG after robotic total esophagectomy

left-sided colorectal resections [11]. NIR imaging with ICG can also be used to evaluate blood flow and solid organ perfusion. An example of these applications could be found in robot-assisted renal transplant. After the completion of the vascular anastomosis, ICG can assess the blood flow through the anastomosed vessels and the perfusion of the transplanted kidney [23].

Biliary Imaging

Identification of biliary anatomy is probably one of the most important applications of ICG fluorescence in hepatobiliary surgery. Even in less complex surgical operations, such as cholecystectomy, NIR imaging could be helpful in decreasing the risk of biliary duct injury. Even though this is an uncommon complication, in most cases it is connected to misinterpretation of anatomy. ICG allows real-time visualization of the extrahepatic biliary ducts, offering a sort of continuous "non-radiographic" cholangiogram.

The first account of NIR-ICG during robotic cholecystectomy was published by our group at the University of Illinois at Chicago [24], in which we described how ICG fluorescence was able to identify during the procedure an aberrant biliary side branch from hepatic segment VI to the common hepatic duct (CHD). The side branch was successfully preserved, avoiding a postoperative biliary leak or bile duct occlusion. Other authors have published their experience since then, all confirming the usefulness of this technique [25, 26]. Buchs et al. first reported their results after 12 single-site robotic cholecystectomies with ICG fluorescence. The cystic duct (CD), common bile duct (CBD), and the CHD were successfully visualized prior to Calot's triangle dissection in 91.7, 50 and 33% of cases, respectively. After the dissection, the rates of visualization of the three structures were 100, 83.3 and 66.7% [25]. Spinoglio et al. published their results after 45 cases of robotic single-site cholecystectomies with NIF-ICG, with successful fluoresecent visualization of all three main biliary structures at a rate of 97% after dissection of Calot's triangle [26]. Recently, our group reported the results after 184 robotic cholecystectomies with ICG fluorescent cholangiography [10]. The overall visualization rates of the CD, CHD and CBD were 97.8, 94, and 96.1%, respectively. In our review, we included not only elective cases, but also patients with acute cholecystitis. Biliary visualization rates in complex situations, like acute cholecystitis and obese patients were independently analyzed. In the first group, the CD, CHD, and CBD were successfully identified in 91.6, 79.1, and 79.1% of cases, respectively, and in the second group, the rates were 97, 94 and 95%. NIR light has a penetration ability of 5–10 mm [27, 28], therefore inflammation and obesity are factors that could potentially hinder visualization of structures. Nevertheless, in our series, the success rate was high. It is noteworthy that no biliary duct injuries or allergic reactions to ICG occurred in any of the published series. NIR-ICG could improve outcomes of cholecystectomies, replacing x-ray cholangiograms, with no substantial increase in operative time and with minimal risk of adverse reaction to the dye.

NIR imaging is also a valuable tool in more complex procedures, such as hepatic resections and pancreaticoduodenectomies, especially during the dissection of the hepatic hilum. Identification of the vascular and biliary structures during these difficult procedures allows a more precise and accurate dissection, potentially decreasing the risk of intraoperative complications.

Lymph Node and Nerve Identification

NIR imaging provides the possibility of lymph node mapping and SLN identification. This application could be especially useful in oncologic surgery, allowing a selective and precise lymphadenectomy. In laparoscopic surgery, it is already being successfully used in cases of gastric and colorectal cancer [29, 30], and in robotic surgery, it is currently used for lymph node mapping and SLN detection in endometrial and cervical cancer. Rossi et al. first published their results of 20 patients receiving cervical injection of ICG [13]. The authors reported a success rate of 88% in the identification of SLN and concluded that this

type of imaging is a reliable method for SLN detection and lymph node mapping in early-stage endometrial and cervical cancer. The same authors recently reported that cervical ICG injection is more efficient than hysteroscopic endometrial injection in detecting SLN, with similar anatomic lymph node distribution [31]. In a study conducted by Holloway et al., they reviewed the detection rate of SLN in patients with endometrial cancer who underwent robotic staging, comparing the NIR-ICG with colorimetric imaging of isosulfan blue (ISB) [32]. Their results showed that NIR-ICG was more successful in detecting bilateral SLNs and lymph node metastasis, with 77 versus 97% detection rate of bilateral pelvic or aortic SLNs using ISB and ICG, respectively. When the two techniques were combined, the sensitivity and specificity of the technique were 90 and 100%, respectively.

Some authors, however, have reported some limitations of NIR-ICG in colorectal surgery, especially in cases of tattooed lesions and lymph node mapping [11]. There are descriptions of excessive or inadequate diffusion of the colorant around the tumor, spreading inside the abdominal cavity and leading to failed visualization of the lymph nodes, especially in patients who underwent neoadjuvant radiotherapy for rectal cancer [11].

Nerve identification is yet another interesting application of NIR imaging that will certainly expand in the future, especially once novel, more selective contrast agents become available. Identification of nerves and nerve plexuses could facilitate dissection, improving postoperative outcomes. Prostatectomy (prostatic nerves), colorectal surgery (inferior hypogastric plexus), thyroidectomy (identification of the recurrent laryngeal nerves), and thymectomy (phrenic nerve) are some of the best examples.

Wagner et al. published their experience with 10 patients that underwent unilateral right robotic thymectomy using NIF-ICG to identify the contralateral pericardiophrenic neurovascular bundle (PNB) [14]. They reported a success rate of 80% in visualizing the PNB, mainly from a left pleural view. No injuries occurred to the PNB. The authors believe that this technique could achieve maximal tissue resection and decrease the nerve injury rates.

Identification of Lesions

Difference in hemodynamic properties between normal and cancerous parenchyma, as well as differences in biliary excretion of ICG allow identification of lesions from the normal surrounding tissue. Hepatocellular carcinoma (HCC) is a good example of these properties. In fact, many study groups have demonstrated the different fluorescent patterns among well-differentiated HCC, poorly differentiated HCC, and colorectal metastases [33–35]. In well-differentiated HCCs the uptake of ICG is preserved, while the biliary excretion is impaired, so they appear as uniformly fluorescent lesions. Poorly differentiated HCCs and colorectal metastases, on the other hand, appear as hypofluorescent lesions surrounded by a fluorescent ring, due to biliary excretion disorders of the surrounding tissue that is being compressed by the tumor. In our overall experience, NIR-ICG has been useful in identifying HCCs (Fig. 15.2), hemangiomas (Fig. 15.3), pheochromocytomas (Fig. 15.4), and small neuroendocrine pancreatic tumors (Fig. 15.5).

Manny et al. published a series of three robotic partial adrenalectomies with NIR-ICG, confirming that this technique helps identifying the mass from the normal adrenal tissue, promoting parenchyma-sparing resections [36].

Other Applications in Robotic Surgery

Ureteral Stricture Identification

Recently, the indication for NIR-ICG has expanded to intraoperative localization of ureteral strictures. Lee et al. reported seven cases of robotic ureteroureterostomy for stricture [37]. ICG was administered intraureterally for delineation of the ureter, and an additional intraureteral dose was administered for distinction of healthy ureteral tissue from devitalized tissue, allowing for a safer repair. Upper urinary tract reconstruction

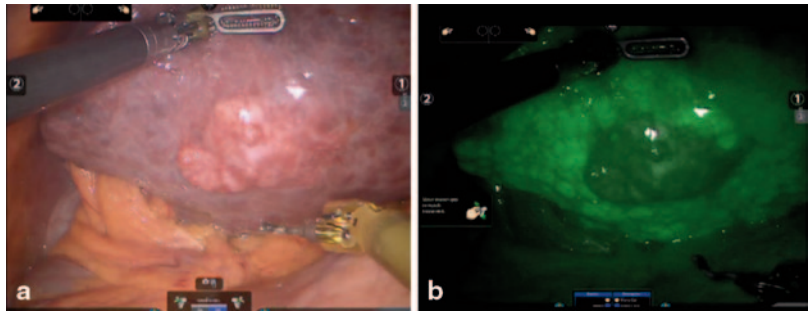

Fig. 15.2 HCC as it appears intraoperatively with normal light (**a**) and NIR-ICG (**b**)

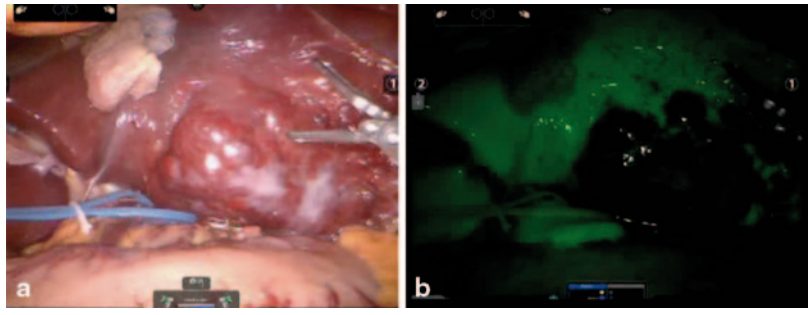

Fig. 15.3 Hepatic hemangioma as it appears intraoperatively, with normal light (**a**) and NIR-ICG (**b**)

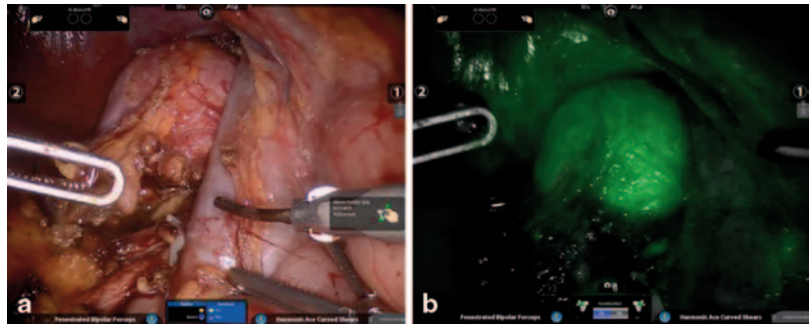

Fig. 15.4 Pheochromocytoma as it appears intraoperatively, with normal light (**a**) and NIR-ICG (**b**)

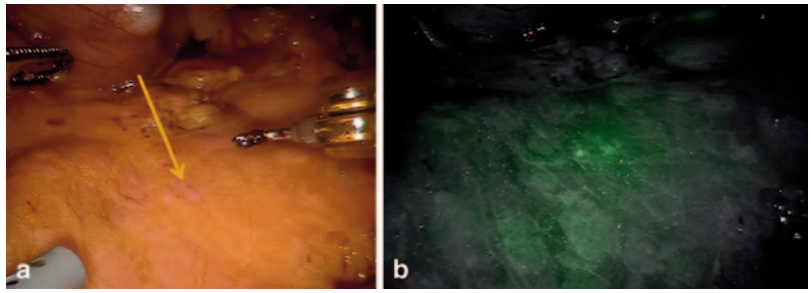

Fig. 15.5 Small pancreatic neuroendocrine tumor as it appears intraoperatively, with normal light (**a**) and NIR-ICG (**b**)

seems to be a promising new indication for NIR-ICG. In a separate study 40 patients underwent robotic pyeloplasty, ureteral implant, and ureteroureterostomy with ICG and demonstrated 100% radiological and symptomatic improvement after the procedure [12].

Segmentectomy in Early-Stage Lung Cancer

Pardolesi et al. recently described a novel technique for identification of intersegmental planes during robotic anatomic segmentectomy for small, early-stage lung cancer [15]. The ICG was injected intravenously after division of the bronchus, vein, and artery of the target segment. The result was a green coloration of the perfused parenchyma, with the target segment remaining uncolored. The authors reported an excellent demarcation of the segment to be removed, facilitating its transection.

ICG in Total Endoscopic Robot-Assisted Coronary Artery Bypass

A possible future application of NIR-ICG has been published by Hassan et al. [38]. They identified the internal mammary artery, delineated the coronary anatomy and evaluated the patency of the anastomoses during robotic coronary bypass, in a canine model.

Future Applications

New technologies will soon be available for improving NIR imaging [39]. Scientists are already working on new techniques to overcome the limit of low tissue penetration and improve the fluorescent signal [40, 41].

From a surgical standpoint, the most revolutionary future application will be in vivo, real-time cancer detection, and characterization. Specific targeting ligands and monoclonal antibodies conjugated to NIR fluorophores could provide real-time molecular diagnosis and detection of the tumor intraoperatively. Metildi et al. recently published a study where pancreatic tumors in orthotopic mice were labeled with fluorescent anti-carcinoembryonic antigen antibodies. Fluorescence-guided laparoscopic surgery was then performed and resulted in decreased local recurrence rate, decreased distant recurrence rate and longer median disease-free survival, when compared to the bright-light laparoscopic surgery [42, 43]. Future progress in NIR imaging is expected with better software to process images (subtraction and fusion images) and to make a quantitative evaluation of flow (speed) and pattern of perfusion (architecture).

Conclusions

NIF imaging with ICG is one of the latest innovations in surgery. This technique is safe, noninvasive, time-effective, and does not expose patients to radiation. Currently, the main applications of NIR-ICG in robotic general surgery are real-time visualization of the biliary anatomy and evaluation of anastomotic perfusion during gastro-intestinal (GI) and colorectal surgery. Even though there are only a few studies available in the literature, the results are encouraging. The future applications of this technology will hopefully allow real-time in vivo microscopy, which will be an invaluable asset in minimally invasive oncologic surgery. This is only the beginning of a new era for surgery. As technologic innovations will expand, so will the indications for NIR imaging. Further investigation and clinical trials are mandatory in order to establish the real value of NIR imaging and expand its indications.

References

1. Verbeek FP, van der Vorst JR, Schaafsma BE, Hutteman M, Bonsing BA, van Leeuwen FW, et al. Image-guided hepatopancreatobiliary surgery using near-infrared fluorescent light. J Hepatobiliary Pancreat Sci. 2012;19(6):626–37. Epub 2012/07/14.
2. Landsman ML, Kwant G, Mook GA, Zijlstra WG. Light-absorbing properties, stability, and spectral stabilization of indocyanine green. J Appl Physiol. 1976;40(4):575–83. Epub 1976/04/01.

3. Guyer DR, Puliafito CA, Mones JM, Friedman E, Chang W, Verdooner SR. Digital indocyanine-green angiography in chorioretinal disorders. Ophthalmology. 1992;99(2):287–91. Epub 1992/02/01.
4. Ogata F, Azuma R, Kikuchi M, Koshima I, Morimoto Y. Novel lymphography using indocyanine green dye for near-infrared fluorescence labeling. Ann Plast Surg. 2007;58(6):652–5. Epub 2007/05/25.
5. Kitai T, Inomoto T, Miwa M, Shikayama T. Fluorescence navigation with indocyanine green for detecting sentinel lymph nodes in breast cancer. Breast Cancer. 2005;12(3):211–5. Epub 2005/08/20.
6. Rubens FD, Ruel M, Fremes SE. A new and simplified method for coronary and graft imaging during CABG. Heart Surg Forum. 2002;5(2):141–4. Epub 2002/07/13.
7. Raabe A, Nakaji P, Beck J, Kim LJ, Hsu FP, Kamerman JD, et al. Prospective evaluation of surgical microscope-integrated intraoperative near-infrared indocyanine green videoangiography during aneurysm surgery. J Neurosurg. 2005;103(6):982–9. Epub 2005/12/31.
8. Marshall MV, Rasmussen JC, Tan IC, Aldrich MB, Adams KE, Wang X, et al. Near-infrared fluorescence imaging in humans with indocyanine green: a review and update. Open Surg Oncol J. 2010;2(2):12–25. Epub 2010/01/01.
9. Alford R, Simpson HM, Duberman J, Hill GC, Ogawa M, Regino C, et al. Toxicity of organic fluorophores used in molecular imaging: literature review. Mol Imaging. 2009;8(6):341–54. Epub 2009/12/17.
10. Daskalaki D, Fernandes E, Wang X, Bianco FM, Elli EF, Ayloo S, et al. Indocyanine green (ICG) fluorescent cholangiography during robotic cholecystectomy: results of 184 consecutive cases in a single institution. Surg Innov. 2014;21:615–21. Epub 2014/03/13.
11. Marano A, Priora F, Lenti LM, Ravazzoni F, Quarati R, Spinoglio G. Application of fluorescence in robotic general surgery: review of the literature and state of the art. World J Surg. 2013;37(12):2800–11. Epub 2013/05/07.
12. Bjurlin MA, Gan M, McClintock TR, Volpe A, Borofsky MS, Mottrie A, et al. Near-infrared fluorescence imaging: emerging applications in robotic upper urinary tract surgery. Eur Urol. 2014;65(4):793–801. Epub 2013/10/09.
13. Rossi EC, Ivanova A, Boggess JF. Robotically assisted fluorescence-guided lymph node mapping with ICG for gynecologic malignancies: a feasibility study. Gynecol Oncol. 2012;124(1):78–82. Epub 2011/10/15.
14. Wagner OJ, Louie BE, Vallieres E, Aye RW, Farivar AS. Near-infrared fluorescence imaging can help identify the contralateral phrenic nerve during robotic thymectomy. Ann Thorac Surg. 2012;94(2):622–5. Epub 2012/07/24.
15. Pardolesi A, Veronesi G, Solli P, Spaggiari L. Use of indocyanine green to facilitate intersegmental plane identification during robotic anatomic segmentectomy. J Thorac Cardiovasc Surg. 2014;148:737–8. Epub 2014/04/01.
16. Tanaka E, Chen FY, Flaumenhaft R, Graham GJ, Laurence RG, Frangioni JV. Real-time assessment of cardiac perfusion, coronary angiography, and acute intravascular thrombi using dual-channel near-infrared fluorescence imaging. J Thorac Cardiovasc Surg. 2009;138(1):133–40. Epub 2009/07/07.
17. Luo S, Zhang E, Su Y, Cheng T, Shi C. A review of NIR dyes in cancer targeting and imaging. Biomaterials. 2011;32(29):7127–38. Epub 2011/07/05.
18. Borofsky MS, Gill IS, Hemal AK, Marien TP, Jayaratna I, Krane LS, et al. Near-infrared fluorescence imaging to facilitate super-selective arterial clamping during zero-ischaemia robotic partial nephrectomy. BJU Int. 2013;111(4):604–10. Epub 2012/12/21.
19. Jafari MD, Lee KH, Halabi WJ, Mills SD, Carmichael JC, Stamos MJ, et al. The use of indocyanine green fluorescence to assess anastomotic perfusion during robotic assisted laparoscopic rectal surgery. Surg Endosc. 2013;27:3003–8. Epub 2013/02/14.
20. Bae SU, Baek SJ, Hur H, Baik SH, Kim NK, Min BS. Intraoperative near infrared fluorescence imaging in robotic low anterior resection: three case reports. Yonsei Med J. 2013;54(4):1066–9. Epub 2013/05/28.
21. Hellan M, Spinoglio G, Pigazzi A, Lagares-Garcia JA. The influence of fluorescence imaging on the location of bowel transection during robotic left-sided colorectal surgery. Surg Endosc. 2014;28(5):1695–702. Epub 2014/01/05.
22. Bianchi PP, Pigazzi A, Choi GS. Clinical robotic surgery association fifth worldwide congress, Washington DC, 3–5 October 2013: robotic colorectal surgery. Ecancermedicalscience. 2014;8:385. Epub 2014/02/01.
23. Tzvetanov I, Giulianotti PC, Bejarano-Pineda L, Jeon H, Garcia-Roca R, Bianco F, et al. Robotic-assisted kidney transplantation. Surg Clin N Am. 2013;93(6):1309–23. Epub 2013/11/12.
24. Calatayud D, Milone L, Elli EF, Giulianotti PC. ICG-fluorescence identification of a small aberrant biliary canaliculus during robotic cholecystectomy. Liver Int. 2012;32(4):602. Epub 2012/02/02.
25. Buchs NC, Hagen ME, Pugin F, Volonte F, Bucher P, Schiffer E, et al. Intra-operative fluorescent cholangiography using indocyanin green during robotic single site cholecystectomy. Int J Med Robot. 2012;8(4):436–40. Epub 2012/06/01.
26. Spinoglio G, Priora F, Bianchi PP, Lucido FS, Licciardello A, Maglione V, et al. Real-time near-infrared (NIR) fluorescent cholangiography in single-site robotic cholecystectomy (SSRC): a single-institutional prospective study. Surg Endosc. 2013;27(6):2156–62. Epub 2012/12/29.
27. Houston JP, Thompson AB, Gurfinkel M, Sevick-Muraca EM. Sensitivity and depth penetration of continuous wave versus frequency-domain photon migration near-infrared fluorescence contrast-enhanced imaging. Photochem Photobiol. 2003;77(4):420–30. Epub 2003/05/08.

28. Ishizawa T, Kaneko J, Inoue Y, Takemura N, Seyama Y, Aoki T, et al. Application of fluorescent cholangiography to single-incision laparoscopic cholecystectomy. Surg Endosc. 2011;25(8):2631–6. Epub 2011/03/23.
29. Kelder W, Nimura H, Takahashi N, Mitsumori N, van Dam GM, Yanaga K. Sentinel node mapping with indocyanine green (ICG) and infrared ray detection in early gastric cancer: an accurate method that enables a limited lymphadenectomy. Eur J Surg Oncol. 2010;36(6):552–8. Epub 2010/05/11.
30. Cahill RA, Anderson M, Wang LM, Lindsey I, Cunningham C, Mortensen NJ. Near-infrared (NIR) laparoscopy for intraoperative lymphatic road-mapping and sentinel node identification during definitive surgical resection of early-stage colorectal neoplasia. Surg Endosc. 2012;26(1):197–204. Epub 2011/08/20.
31. Rossi EC, Jackson A, Ivanova A, Boggess JF. Detection of sentinel nodes for endometrial cancer with robotic assisted fluorescence imaging: cervical versus hysteroscopic injection. Int J Gynecol Cancer. 2013;23(9):1704–11. Epub 2013/11/02.
32. Holloway RW, Bravo RA, Rakowski JA, James JA, Jeppson CN, Ingersoll SB, et al. Detection of sentinel lymph nodes in patients with endometrial cancer undergoing robotic-assisted staging: a comparison of colorimetric and fluorescence imaging. Gynecol Oncol. 2012;126(1):25–9. Epub 2012/04/18.
33. Ishizawa T, Bandai Y, Ijichi M, Kaneko J, Hasegawa K, Kokudo N. Fluorescent cholangiography illuminating the biliary tree during laparoscopic cholecystectomy. Br J Surg. 2010;97(9):1369–77. Epub 2010/07/14.
34. Ishizawa T, Fukushima N, Shibahara J, Masuda K, Tamura S, Aoki T, et al. Real-time identification of liver cancers by using indocyanine green fluorescent imaging. Cancer. 2009;115(11):2491–504. Epub 2009/03/28.
35. Kokudo N, Ishizawa T. Clinical application of fluorescence imaging of liver cancer using indocyanine green. Liver Cancer. 2012;1(1):15–21. Epub 2012/06/01.
36. Manny TB, Pompeo AS, Hemal AK. Robotic partial adrenalectomy using indocyanine green dye with near-infrared imaging: the initial clinical experience. Urology. 2013;82(3):738–42. Epub 2013/07/19.
37. Lee Z, Simhan J, Parker DC, Reilly C, Llukani E, Lee DI, et al. Novel use of indocyanine green for intraoperative, real-time localization of ureteral stenosis during robot-assisted ureteroureterostomy. Urology. 2013;82(3):729–33. Epub 2013/08/31.
38. Hassan M, Kerdok A, Engel A, Gersch K, Smith JM. Near infrared fluorescence imaging with ICG in TECAB surgery using the da Vinci Si surgical system in a canine model. J Card Surg. 2012;27(2):158–62. Epub 2012/03/01.
39. Schaafsma BE, Mieog JS, Hutteman M, van der Vorst JR, Kuppen PJ, Lowik CW, et al. The clinical use of indocyanine green as a near-infrared fluorescent contrast agent for image-guided oncologic surgery. J Surg Oncol. 2011;104(3):323–32. Epub 2011/04/16.
40. Gioux S, Mazhar A, Cuccia DJ, Durkin AJ, Tromberg BJ, Frangioni JV. Three-dimensional surface profile intensity correction for spatially modulated imaging. J Biomed Opt. 2009;14(3):034045. Epub 2009/07/02.
41. Themelis G, Yoo JS, Soh KS, Schulz R, Ntziachristos V. Real-time intraoperative fluorescence imaging system using light-absorption correction. J Biomed Opt. 2009;14(6):064012. Epub 2010/01/12.
42. Metildi CA, Kaushal S, Luiken GA, Hoffman RM, Bouvet M. Advantages of fluorescence-guided laparoscopic surgery of pancreatic cancer labeled with fluorescent anti-carcinoembryonic antigen antibodies in an orthotopic mouse model. J Am Coll Surg. 2014;219:132–41. Epub 2014/04/29.
43. Metildi CA, Kaushal S, Hardamon CR, Snyder CS, Pu M, Messer KS, et al. Fluorescence-guided surgery allows for more complete resection of pancreatic cancer, resulting in longer disease-free survival compared with standard surgery in orthotopic mouse models. J Am Coll Surg. 2012;215(1):126–35. Discussion 35–6. Epub 2012/05/29.

New Preoperative Images, Surgical Planning, and Navigation

16

Michael A. Scherer and David A. Geller

Introduction

Traditionally, two-dimensional (2D) computed tomography (CT) images and magnetic resonance images (MRI) have been used for surgical planning [1, 2]. Over the past two decades, the improvement in resolution of these imaging modalities has paved the way for increasingly advanced three-dimensional (3D) postprocessing techniques of anatomic structures. Provided with this 3D information, surgeons can now plan their procedure in great detail before entering the operating room. The natural extension of these preoperative surgical plans is an intraoperative navigation system that enables the surgeon to realize their surgical plan with precision. In the fields of neurosurgery, spinal surgery, and ENT surgery, for example, such planning and navigation systems have been used for over 20 years and are now widely viewed as standard-of-care technologies for certain procedures [3–7]. As these technologies mature, applications to soft-tissue organs have been investigated and used in the clinical setting [8–10]. Many approaches have been developed to perform intraoperative navigation, but all have the same goal in common: to improve surgical outcomes by increasing the amount of information available to the surgeon in the operation room (OR). This chapter aims to provide a summary of the state of the art for surgical planning and intraoperative navigation and to briefly discuss the advantages and drawbacks of such technologies.

D. A. Geller (✉)
University of Pittsburgh Medical Center, 3459 5th Avenue, MUH 7 South, Pittsburgh, PA 15213, USA
e-mail: gellerda@upmc.edu

M. A. Scherer
Analogic Corporation, 8 Centennial Drive, Peabody MA 01960, USA
e-mail: mscherer@analogic.com

Surgical Planning

Traditionally, surgeons have mentally reconstructed the organ and anatomic structures of interest from a 3D data set of 2D images prior to surgery. Surgeons have been required to train themselves to re-create the 3D surgical space from 2D images, a task which has varying degrees of difficulty depending on the imaging modality being used (and in all cases requires extensive training). In their simplest embodiment, 3D image reconstructions, now widely available on most commercially available radiologic workstations, reduce the mental processing required to plan a surgery.

The surgical planning process begins with a set of preoperative images, most commonly CT or MRI. Many different methods of 3D reconstruction are available, but the two primary categories used clinically are surface and volume rendering. A software program, usually installed on a high-performance PC with a dedicated graphics card, is used to perform the image processing required to generate the 3D reconstructions.

Y. Fong et al. (eds.), *Imaging and Visualization in The Modern Operating Room,*
DOI 10.1007/978-1-4939-2326-7_16,

Volume Renderings

Volume renderings are 3D projections of data sets that can generally be reconstructed automatically or semi-automatically once an image set is loaded. Volume renderings can be used to depict the 3D relationships of organs, vessels and bone, and has a wide variety of applications, from evaluation of abdominal aortic aneurysms to dental implants and staging of pancreatic cancer [11–14]. While more automated than surface renderings and useful from a diagnostic and visualization standpoint, volume renderings do not provide quantitative volumetric data. Volume renderings of the aortic vasculature and renal anatomy, for example, can be useful for diagnostic purposes but require additional postprocessing for volumetric data (Figs. 16.1, 16.2).

Surface Renderings

Surface renderings are generated by segmenting, or delineating, each anatomic structure of interest on each 2D image from the preoperative data set. Often, multiple data sets will be used for segmentation, taking advantage of the known changes in contrast between consecutive image acquisitions (e.g., arterial phase and venous phase hepatic scans).

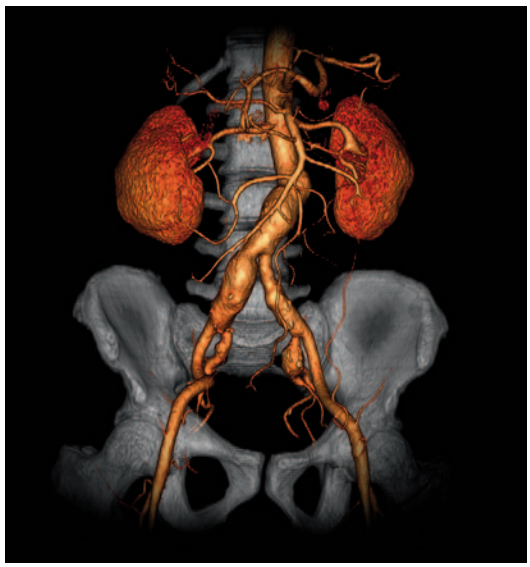

Fig. 16.1 Volume rendering of aortic vasculature and kidneys

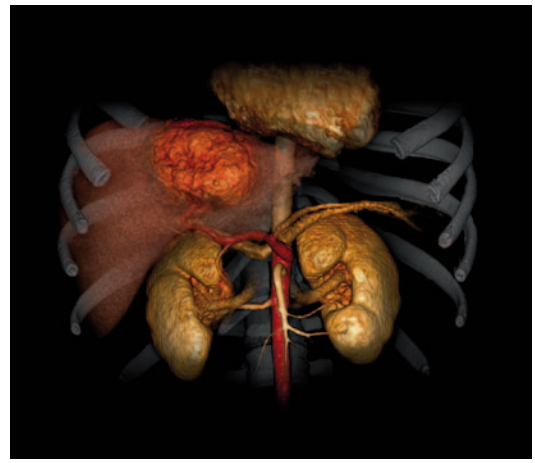

Fig. 16.2 Volume rendering of liver, liver tumor, kidneys, and heart, with ribcage in gray

Various approaches, ranging in their degree of automation, can be used to segment each anatomic structure. Most segmentation approaches use differences in pixel intensities of adjacent structures to separate one structure from another. Once these structures are segmented, 3D models of each can be displayed. For a hepatic resection, for example, the liver, tumors, hepatic and portal veins, and bile ducts may be segmented [15]. Advanced techniques, such as segmental risk analysis for hepatic surgery, can be used depending on the clinical application [16, 17]. For example, the territories of the liver as defined by portal venous inflow can be displayed (Fig. 16.3). Additionally, variant anatomy and tumors can be displayed in relation to one another (Fig. 16.4).

Resection Planning

Many commercially available surgical planning applications have resection planning capabilities that enable the surgeon to preoperatively define their surgical plan and assess the resulting volumetrics. For procedures where clinical outcomes have well-defined volumetric thresholds for success, such as hepatic resection or living donor liver transplantation (LDLT) this functionality

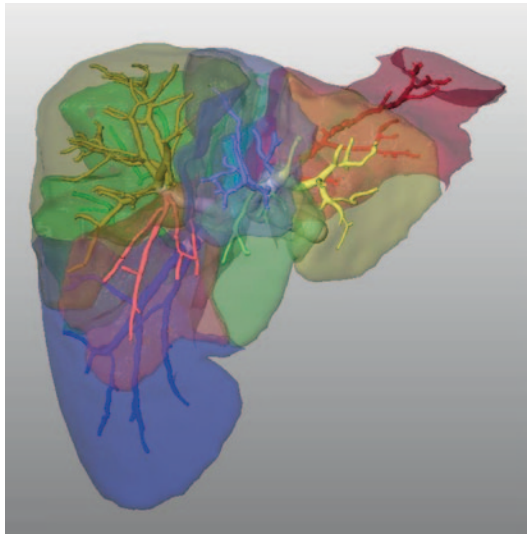

Fig. 16.3 Surface rendering of a liver and portal venous inflow, with segmental inflow territories identified by various colors

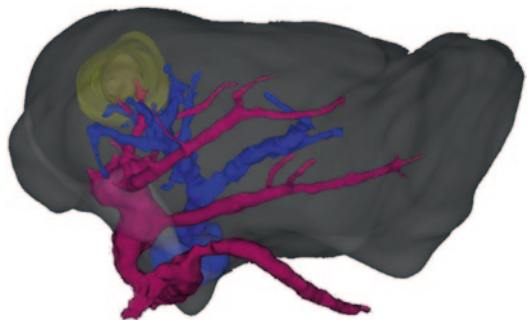

Fig. 16.4 Preoperative imaging of a liver, hepatic veins (*blue*), portal veins (*purple*), and tumor (*brown*)

can be used to accurately determine whether the patient has an adequate remnant prior to surgery (or in the case of LDLT, if the graft size is adequate), and if not, what modifications to the treatment plan need to be considered (Fig. 16.5). Another common application of volumetric analysis is assessment of portal vein embolization, where preembolization and postembolization liver remnant volumes are compared to assess hepatic sufficiency prior to surgical treatment.

Workflow

From a clinical workflow standpoint, many different models have been implemented. The primary challenge associated with segmentation is separating adjacent anatomic structures of interest. For example, in a portal venous phase abdominal CT scan, the abdominal wall is often composed of pixels with similar intensity values to those of the liver. In many instances, there is no physical separation between the liver and the abdominal wall, thus creating a challenge to separate the two structures. Nevertheless, image processing algorithms are steadily improving; a review of common approaches to segmentation is found below.

Thresholding Thresholding is a simple means to separate different classes of pixels based on a threshold value, set to a specific intensity. Multi-

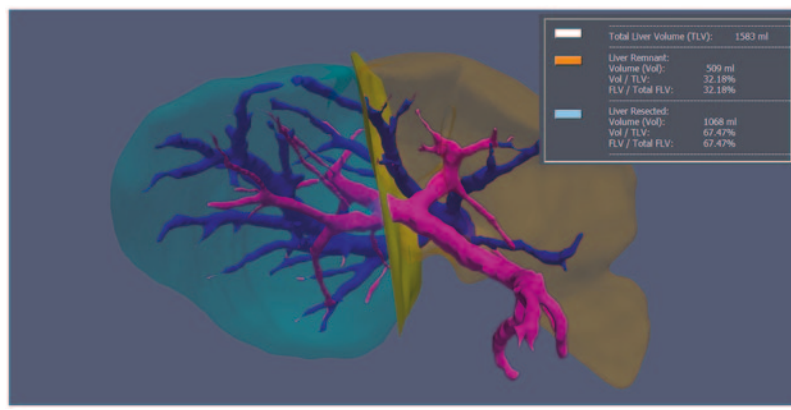

Fig. 16.5 *Right:* hemihepatectomy for a living donor liver procedure, with remnant and resected volumes in the *upper right hand corner*. Transection plane is displayed in *yellow*, portal veins in *purple*, hepatic veins in *blue*

ple thresholds can be used to include and exclude certain ranges of pixels [18].

Region-Growing Segmentation One implementation of the region-growing method involves placing initial seed contours on the organ of interest and then automatically propagating those contours to the edge of the structure [19, 20]. The propagation itself can be influenced by a number of pre-determined or adjustable factors, including pixel intensities.

Model-Based Segmentation This method utilizes an existing database of organ models as an initial framework for segmentation. This method can reduce the amount of time required for an initial estimate of organ segmentation but has accuracy limitations given the large variance in organ shapes and positions from patient to patient. This can also be referred to as statistical shape modeling or atlas-based segmentation [21].

Image Registration This method presupposes that an initial contour has been accurately defined and uses that contour's shape and/or pixel intensities within the defined area to automatically identify the remaining contours of the organ [22].

Most segmentation packages use a combination of these techniques or at least have some form of each available for use. As each technique is refined and optimized for a given application, image processing becomes more automated and less time-consuming. However, manual editing tools are still helpful to compensate for anatomic anomalies.

The clinical implementation and utilization of surgical planning software varies. Some commercially available workstations are installed on site and all processing and planning is performed by surgeons, radiology technicians, and radiologists [23–25]. Other planning services can be performed remotely per case, which entails the secure transfer of patient DICOM files, subsequent image processing, and the return of a detailed analysis to the hospital [26]. Still others exist as a hybrid between the aforementioned implementations, where a workstation is installed at the hospital for image transfer and processing, but that processing is performed remotely through server access [27].

Future Directions

Future areas of work include functional analysis of tissue, refined ablation modeling techniques, and increasingly automated methods of segmentation. While volumetric analysis provides useful quantitative information for surgical planning in certain scenarios, tissue viability is generally not taken into account in most software packages. If tissue function can be integrated into existing software, then clinicians will be able to make more informed decisions regarding the optimal course of therapy. Ablation modeling is still in its infancy and the parameters selected for ablative therapy are largely driven by ex vivo data provided by ablation device manufacturers. Aside from controllable device parameters such as wattage and ablation cycle time, tissue composition and blood flow from nearby vessels likely have an impact on the efficacy of ablative devices, and taking these patient-specific inputs into account will provide the surgeon with a better understanding of how to apply the ablation in the OR [28, 29]. Finally, automation of 3D postprocessing continues to improve, but there is still much work to be done for soft-tissue applications.

Intraoperative Navigation

Intraoperative navigation systems have been used in neurosurgery and ENT procedures for over 20 years [5]. These systems have been shown to improve patient outcomes, reduce morbidity, and decrease OR time [6, 7]. Surgical navigation systems consist of the following main components: a computer and display system to provide the information to the end user, a set of tracked devices used for spatial localization, and a localizing system to track these instruments in surgical space. There are two types of tracking systems commonly used in the OR: optical and electromagnetic (EM). Optical systems use infrared cameras to localize surgical instruments

by means of rigidly affixing a tracked body with reflective lenses to the instruments of interest (Fig. 16.6). Optical systems have the advantage of wireless tracking of surgical instruments but are subject to the inherent limitation of line of sight; that is, tracked instruments must be in direct, unblocked view from the localizing camera for tracking to occur. Additionally, optical instruments cannot account for needle flexure, which is common during needle-based interventions such as biopsies and radiofrequency or microwave ablation. Optical systems also require that each individual tracked instrument be characterized from other instruments through unique geometry constraints. Optical navigation systems are being used in both open and laparoscopic environments (Figs. 16.7, 16.8).

EM systems, on the other hand, are comprised of an EM field generator and submillimeter coils that can be integrated with the desired surgical instrument for accurate instrument tracking, even if the instruments are non-rigid, such as articulating laparoscopic ultrasound transducers and flexible ablation needles. However, EM localizers are susceptible to tracking error induced by metal artifacts in the surgical field. Additionally, EM systems introduce cables into the surgical field that can be unwieldy if not designed properly, and some existing systems have relatively small working volumes (i.e., the zone in which instruments can be reliably tracked). EM systems have been used successfully in the clinical setting for both prostate and lung procedures, where the working volume is less of an issue (Fig. 16.9).

One of the most important components of a navigation system is the degree to which it can accurately register preoperative image space to the intraoperative surgical space. Accuracy of navigation systems can be divided into three components: (1) inherent tracking error of the lo-

Fig. 16.7 The intraoperative setup consists of a double touch-screen user interface that displays both the 3D navigational as well as the ultrasound user interface. A stereo camera is placed above the patient to track instruments. Surgeons can interact with the system through the touch screens

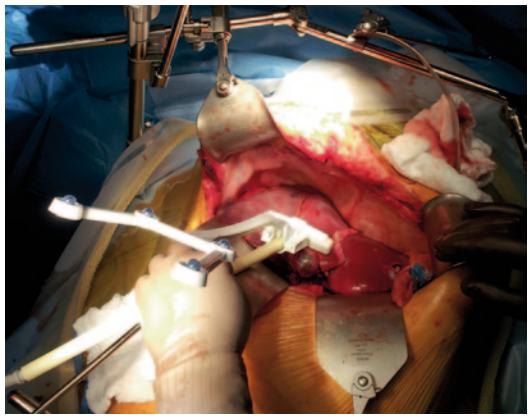

Fig. 16.6 An optical adapter for an ultrasound transducer is used to track the ultrasound device in surgical space after a registration has been performed. This allows direct comparison of real-time intraoperative ultrasound with preoperative 3D imaging

Fig. 16.8 The intraoperative setup for a laparoscopic navigation procedure, with the camera placed above the working area and the navigation system with integrated ultrasound available for display along with the endoscopic view

calizer system being used, (2) registration error, and (3) error induced by organ shift and deformation. Localizer system tracking error has been reduced as tracking systems are continuously refined. Errors associated with commonly used optical systems are on the order of 0.35 mm (root-mean-square (RMS) error) [30]. Registration error depends on a number of factors, including the registration approach used and the ability to accurately identify matching features from preoperative and intraoperative data sets. Error induced by organ shift and deformation is the largest contributor to overall navigation error and many approaches have been investigated to account for or mitigate this type of error. During a neurosurgical procedure, for example, even though the brain is confined by the skull, the brain can deform or shift due to swelling, retraction, and cerebrospinal-fluid drainage. Techniques to compensate for organ deformation are necessary if the navigation system is to be used throughout a procedure. One common technique to compensate for organ movement and deformation include updating the preoperative image set based on intraoperative image acquisition via CT, MRI, or ultrasound [31, 32]. Registration error feedback can be displayed to the surgeon either qualitatively or quantitatively, whether a surface-based approach or internal structures are used for registration (Fig. 16.10).

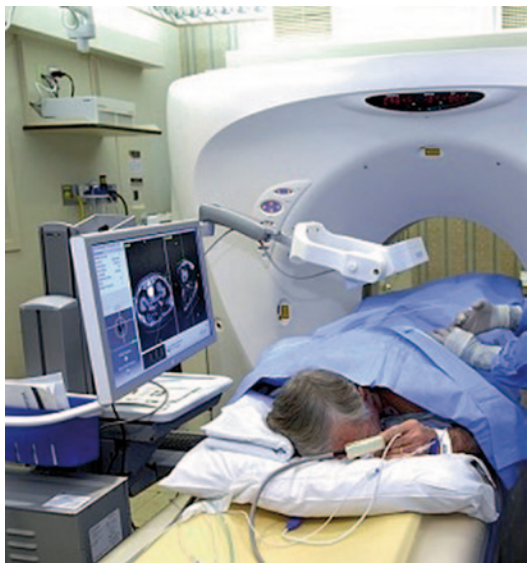

Fig. 16.9 An electromagnetic tracking system is used for a lung procedure

Workflow

Navigation systems must be designed such that they have minimal impact on the operating room environment and existing surgical workflow. A small hardware footprint, an intuitive user interface, and surgical instrument accessories that are easy to assemble are all necessary prerequisites for any navigation system to be successfully integrated into a clinical workflow. The workflow associated with navigation can be summarized as follows.

1. Transfer of preoperative data set to the navigation system. This can be performed via USB drive or network connection. Surgical planning can either be performed prior to the procedure via a separate software application, or on the navigation system itself.
2. Intraoperative hardware setup. The localizer system and display must be positioned properly. In the case of an optically based system, for example, the localizing camera must be positioned such that it can maintain proper line of sight to the tracked instruments in the surgical working area.
3. Instrument calibration. If necessary, surgical instruments such as resection or ablation devices can be calibrated. Precalibration of an

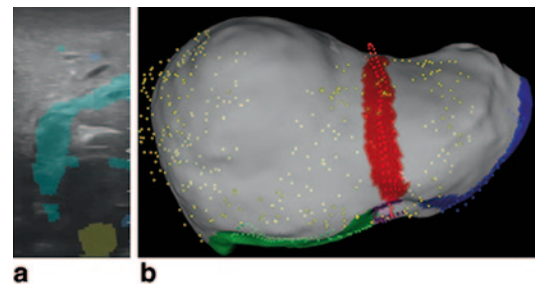

Fig. 16.10 2D augmentation of native sonography imagery with coregistered preoperative image data is used to confirm registration accuracy in **a**, whereas intraoperatively acquired surface data are used to confirm registration accuracy relative to preoperative 3D models in **b**

instrument can be performed prior to surgery if the tracked body can be reproducibly affixed to the instrument in the same position and orientation, i.e., there is a known relationship between the tracked device and the surgical instrument.

4. Registration. Tracked instruments are used to perform the registration necessary to map the preoperative images to the operating space.
5. Navigation. Once the registration has been performed and its accuracy accepted, tracked surgical instruments may be used to localize anatomic structures such as vessels or tumors. Navigation systems that support integration of ultrasound can display the ultrasound image relative to the preoperative images, enabling immediate comparison of anatomic structures from each modality [33–36]. Additionally, ablation needles, resection devices, and microscopes or endoscopes can be tracked in the surgical space [37, 38].

Applications

Surgical navigation has many different applications. In general, navigation is useful when preoperative imaging is already being used for planning purposes, since the combination of these images with instrument tracking provides real-time feedback during a surgical procedure.

Common applications in neurosurgery and spinal navigation include localization of small intracranial lesions, tumor resection, intracerebral biopsies, and pedicle screw placement, among others [4, 39]. More recently, applications for soft-tissue surgery have been developed, including those for the lungs, liver, and prostate [8, 40–42]. Soft-tissue navigation poses a challenge from a registration standpoint since the organ is usually mobilized during the surgical intervention and is more likely to be deformed throughout the procedure itself. Nevertheless, surgical navigation can play an important role in soft-tissue procedures, especially when currently available intraoperative imaging is not adequate to assess the extent of disease, such as in the case of disappearing liver metastases [43]. In these procedures, metastatic disease has been treated with chemotherapy such that the tumors are easily viewed on preoperative imaging but difficult or impossible to identify using intraoperative ultrasound [44]. Additionally, for laparoscopic procedures where manipulation, control and depth perception of the organ and surgical instruments is limited, navigation has even greater potential, enabling the surgeon to confirm their position [45].

Other approaches to surgical navigation include fluorescence imaging, which has been used clinically in hepatic and breast procedures [46, 47].

Future Directions

While there has been significant progress in the field of intraoperative navigation in recent years, much work is to be done to increase its clinical utility and prevalence. Integration of augmented reality (AR) platforms will address some of the workflow issues associated with current navigation systems, since an AR approach will provide direct feedback on the physical organ itself rather than indirectly via OR monitor. Further refinement of techniques to account for organ movement and deformation will also be necessary to improve precision required for continuous use of navigation throughout a procedure, particularly for soft-tissue organs such as the liver. As intraoperative imaging modalities such as CT and MRI become more prevalent in soft-tissue procedures, surgical navigation systems will benefit; there is already significant clinical experience with such systems for neurosurgery [48, 49]. Finally, integration with robotic technology will also be a major area of development, as the synergies between localization systems and robotic treatment platforms can potentially remove human error associated with needle placement [50, 51].

Conclusion

Imaging plays a crucial role in the diagnosis and treatment of many types of diseases. As diagnostic imaging, image postprocessing and intraoperative navigation technologies continue to improve, the operating room will more closely resemble the interventional suite, with an increasing amount of information available to aid the surgeon in the intraoperative decision-making process. Minimizing additional burden placed on existing intraoperative workflows will be critical to ensuring the successful integration of these technologies.

Acknowledgments The authors would like to thank representatives from Vital Images, Inc. and CAScination AG for assistance in preparing some of the figures in this chapter.

References

1. Gunvén P, Makuuchi M, Takayasu K, Moriyama N, Yamasaki S, Hasegawa H. Preoperative imaging of liver metastases. Comparison of angiography, CT scan, and ultrasonography. Ann Surg. 1985;202(5):573.
2. Vannier MW, Marsh JL, Warren JO, Editors. Three dimensional computer graphics for craniofacial surgical planning and evaluation. New York: ACM SIGGRAPH Computer Graphics, ACM; 1983.
3. Ewers R, Schicho K, Undt G, Wanschitz F, Truppe M, Seemann R, et al. Basic research and 12 years of clinical experience in computer-assisted navigation technology: a review. Int J Oral Maxillofac Surg. 2005;34(1):1–8.
4. Grunert P, Darabi K, Espinosa J, Filippi R. Computer-aided navigation in neurosurgery. Neurosurg Rev. 2003;26(2):73–99.
5. Orringer DA, Golby A, Jolesz F. Neuronavigation in the surgical management of brain tumors: current and future trends. Expert Rev Med Devices. 2012;9(5):491–500.
6. Maciunas RJ. Computer-assisted neurosurgery. Clin Neurosurg. 2006;53:267.
7. Weinberg JS, Lang FF, Sawaya R. Surgical management of brain metastases. Curr Oncol Rep. 2001;3(6):476–83.
8. Donati M, Basile F, Stavrou GA, Oldhafer KJ. Navigation systems in liver surgery: the new challenge for surgical research. J Laparoendosc Adv Surg Tech. 2013;23(4):372–5.
9. Galloway RL, Herrell SD, Miga MI. Image-guided abdominal surgery and therapy delivery. J Healthc Eng. 2012;3(2):203–28.
10. Sindram D, Simo KA, Swan RZ, Razzaque S, Niemeyer DJ, Seshadri RM, et al. Laparoscopic microwave ablation of human liver tumours using a novel three-dimensional magnetic guidance system. HPB. 2015;17(1):87-93.
11. Cavalcanti M, Rocha S, Vannier M. Craniofacial measurements based on 3D-CT volume rendering: implications for clinical applications. Dentomaxillofacial Radiology. 2004;33 (3):170-6.
12. Gao L, Heath DG, Kuszyk B, Fishman EK. Automatic liver segmentation technique for three-dimensional visualization of CT data. Radiology. 1996;201:359–64.
13. Xu H-X, Lu M-D, Zhou Y-Q, Zhang Q-P, Yin X-Y, Xie X-Y, et al. Three-dimensional gray scale volume rendering of the liver preliminary clinical experience. J Ultrasound Med. 2002;21(9):961–70.
14. Fishman EK, Ney DR, Heath DG, Corl FM, Horton KM, Johnson PT. Volume rendering versus maximum intensity projection in CT angiography: what works best, when, and why. Radiographics. 2006;26(3):905–22.
15. Simpson ALCL, Miga MI, Dumpuri P, Gonen M, Geller DA, Hemming AW, Stefansic JD., D'Angelica M, Jarnagin WR. Predicting post-operative liver volume: accuracy of dedicated liver planning software and assessment of early regeneration. J Am Coll Surg. 2014;219(2):199-207 [In Press].
16. Hansen C, Zidowitz S, Hindennach M, Schenk A, Hahn H, Peitgen H-O. Interactive determination of robust safety margins for oncologic liver surgery. Int J Comput Assist Radiol Surg. 2013;3:1–8.
17. Hansen C, Zidowitz S, Preim B, Stavrou G, Oldhafer K, Hahn H. Impact of model-based risk analysis for liver surgery planning. Int J Comput Assist Radiol Surg. 2013:1–8.
18. Pham DL, Xu C, Prince JL. Current methods in medical image segmentation 1. Ann Rev Biomed Eng. 2000;2(1):315–37.
19. Heimann T, Van Ginneken B, Styner MA, Arzhaeva Y, Aurich V, Bauer C, et al. Comparison and evaluation of methods for liver segmentation from CT datasets. IEEE Trans Med Imaging. 2009;28(8):1251–65.
20. Shang Q, Clements L, Galloway RL, Chapman WC, Dawant BM, Editors. Adaptive directional region growing segmentation of the hepatic vasculature. Medical imaging. Bellingham: International Society for Optics and Photonics; 2008.
21. Cabezas M, Oliver A, Lladó X, Freixenet J, Bach Cuadra M. A review of atlas-based segmentation for magnetic resonance brain images. Comput Methods Programs Biomed. 2011;104(3):e158–77.
22. Maintz J, Viergever MA. A survey of medical image registration. Med Image Anal. 1998;2(1):1–36.

23. DuBray BJ Jr, Levy RV, Balachandran P, Conzen KD, Upadhya GA, Anderson CD, et al. Novel three-dimensional imaging technique improves the accuracy of hepatic volumetric assessment. HPB. 2011;13(9):670–4.
24. Narita M, Oussoultzoglou E, Fuchshuber P, Pessaux P, Chenard M-P, Rosso E, et al. What is a safe future liver remnant size in patients undergoing major hepatectomy for colorectal liver metastases and treated by intensive preoperative chemotherapy? Ann Surg Oncol. 2012;19(8):2526–38.
25. Tong C, Xu X, Liu C, Zhang T, Qu K. Assessment of liver volume variation to evaluate liver function. Front Med. 2012;6(4):421–7.
26. Wald C, Bourquain H. Role of new three-dimensional image analysis techniques in planning of live donor liver transplantation, liver resection, and intervention. J Gastrointest Surg. 2006;10(2):161–5.
27. Mu X, Qian X, Tan Z, Lv L, Lu S, Hui N, et al. Successful adult-to-adult liver transplantation of an otherwise discarded partial liver allograft with a cavernous hemangioma: new strategy for expanding liver donor pool. Transpl Int. 2013;26(9):e79–80.
28. Butz T, Warfield SK, Tuncali K, Silverman SG, van Sonnenberg E, Jolesz FA, et al., Editors. Pre-and intra-operative planning and simulation of percutaneous tumor ablation. Medical image computing and computer-assisted intervention–MICCAI 2000. Berlin: Springer; 2000.
29. Chen C-C, Miga MI, Galloway RL. Optimizing electrode placement using finite-element models in radiofrequency ablation treatment planning. IEEE Trans Biomed Eng. 2009;56(2):237–45.
30. Wiles AD, Thompson DG, Frantz DD, Editors. Accuracy assessment and interpretation for optical tracking systems. Medical imaging 2004. Bellingham: International Society for Optics and Photonics; 2004.
31. Bucholz R, Yeh D, Trobaugh J, McDurmont L, Sturm C, Baumann C, et al. The correction of stereotactic inaccuracy caused by brain shift using an intraoperative ultrasound device. In: Troccaz J, Grimson E, Mösges R, editors. CVRMed-MRCAS'97. Berlin: Springer; 1997. pp. 459–66.
32. Nimsky C, Ganslandt O, Hastreiter P, Fahlbusch R. Intraoperative compensation for brain shift. Surg Neurol. 2001;56(6):357–64.
33. Bale R. Multimodality registration in daily clinical practice. Mathematical models for registration and applications to medical imaging. Berlin: Springer; 2006. pp. 165–83.
34. Galiano K, Obwegeser AA, Bale R, Harlander C, Schatzer R, Schocke M, et al. Ultrasound-guided and CT-navigation-assisted periradicular and facet joint injections in the lumbar and cervical spine: a new teaching tool to recognize the sonoanatomic pattern. Reg Anesth Pain Med. 2007;32(3):254–7.
35. Lindseth F, Kaspersen JH, Ommedal S, Langø T, Bang J, Hokland J, et al. Multimodal image fusion in ultrasound-based neuronavigation: improving overview and interpretation by integrating preoperative MRI with intraoperative 3D ultrasound. Comput Aided Surg. 2003;8(2):49–69.
36. Singh AK, Kruecker J, Xu S, Glossop N, Guion P, Ullman K, et al. Initial clinical experience with real-time transrectal ultrasonography-magnetic resonance imaging fusion-guided prostate biopsy. BJU Int. 2008;101(7):841–5.
37. Hassfeld S, Mühling J. Computer assisted oral and maxillofacial surgery—a review and an assessment of technology. Int J Oral Maxillofac Surg. 2001;30(1):2–13.
38. Hammill CW, Clements LW, Stefansic JD, Wolf RF, Hansen PD, Gerber DA. Evaluation of a minimally invasive image-guided surgery system for hepatic ablation procedures. Surg Innov. 2013;21(4):419–26:1553350613508019.
39. Laine T, Lund T, Ylikoski M, Lohikoski J, Schlenzka D. Accuracy of pedicle screw insertion with and without computer assistance: a randomised controlled clinical study in 100 consecutive patients. Eur Spine J. 2000;9(3):235–40.
40. Guo Y, Werahera PN, Narayanan R, Li L, Kumar D, Crawford ED, et al. Image registration accuracy of a 3-dimensional transrectal ultrasound–guided prostate biopsy system. J Ultrasound Med. 2009;28(11):1561–8.
41. Santos RS, Gupta A, Ebright MI, DeSimone M, Steiner G, Estrada M-J, et al. Electromagnetic navigation to aid radiofrequency ablation and biopsy of lung tumors. Ann Thorac Surg. 2010;89(1):265–8.
42. Peterhans M, Vom Berg A, Dagon B, Inderbitzin D, Baur C, Candinas D, et al. A navigation system for open liver surgery: design, workflow and first clinical applications. Int J Med Robot. 2011;7(1):7–16.
43. Kingham TP, Scherer MA, Neese BW, Clements LW, Stefansic JD, Jarnagin WR. Image-guided liver surgery: intraoperative projection of computed tomography images utilizing tracked ultrasound. HPB. 2012;14(9):594–603.
44. Bischof D, Clary B, Maithel S, Pawlik T. Surgical management of disappearing colorectal liver metastases. Br J Surg. 2013;100(11):1414–20.
45. Volonté F, Pugin F, Bucher P, Sugimoto M, Ratib O, Morel P. Augmented reality and image overlay navigation with OsiriX in laparoscopic and robotic surgery: not only a matter of fashion. J Hepatobiliary Pancreat Sci. 2011;18(4):506–9.
46. Aoki T, Yasuda D, Shimizu Y, Odaira M, Niiya T, Kusano T, et al. Image-guided liver mapping using fluorescence navigation system with indocyanine green for anatomical hepatic resection. World J Surg. 2008;32(8):1763–7.

47. Kitai T, Inomoto T, Miwa M, Shikayama T. Fluorescence navigation with indocyanine green for detecting sentinel lymph nodes in breast cancer. Breast Cancer. 2005;12(3):211–5.
48. Silbermann J, Riese F, Allam Y, Reichert T, Koeppert H, Gutberlet M. Computer tomography assessment of pedicle screw placement in lumbar and sacral spine: comparison between free-hand and O-arm based navigation techniques. Eur Spine J. 2011;20(6):875–81.
49. Tormenti MJ, Kostov DB, Gardner PA, Kanter AS, Spiro RM, Okonkwo DO. Intraoperative computed tomography image-guided navigation for posterior thoracolumbar spinal instrumentation in spinal deformity surgery. Neurosurg Focus. 2010;28(3):E11.
50. Abdullah BJJ, Yeong CH, Goh KL, Yoong BK, Ho GF, Yim CCW, et al. Robot-assisted radiofrequency ablation of primary and secondary liver tumours: early experience. Eur Radiol. 2014;24(1):79–85.
51. Patriciu A, Awad M, Solomon SB, Choti M, Mazilu D, Kavoussi L, et al. Robotic assisted radio-frequency ablation of liver tumors—randomized patient study. Med Image Comput Comput Assist Interv. 2005;8:526–33 (Springer).

New Generation Radiosurgery and Intraoperative Guidance

17

Segundo Jaime González and Vivian Strong

The use of radionuclides for intraoperative detection of cancer can be traced back to over half a century ago [1], when Harris et al. described the use of a gamma probe during a neck exploration of a patient with thyroid carcinoma, and successfully localized and resected residual thyroid tissue using iodine-131. Since then, the availability, reliability, and accuracy of these probes have significantly improved. Nonetheless, they still work as before, detecting particles that are released during the decay of an atom.

Nuclear Decay

The decay of an atomic nucleus occurs in a very predictable manner in some elements (i.e., carbon atoms) but in a rather unexpected fashion in others (i.e., unstable atoms). During this process, elements such as alpha, gamma, and beta particles are released from the nucleus, and each of these has unique characteristics. For instance, an alpha particle is the release of two protons and two neutrons from a decaying nucleus. This is considered a low-energy particle and can be stopped with a plain sheet of paper. On the other hand, beta and gamma particles have more energy and could readily pass a sheet of paper. However, beta rays can be stopped by human skin, but to stop gamma rays, several millimeters of lead could be required (Fig. 17.1). Beta and gamma particles represent readily detectable energy and both have significant potential for intraoperative use.

Beta Particles and Probes

A beta ray is a low-energy particle emitted from the nucleus of a decaying atom. These could be formed in one of two settings:

1. When a neutron is converted into two particles: a proton and a negatively charged particle (termed an electron)
2. When a proton is converted into two particles: a neutron and a positively charged particle (termed a positron)

In the case of proton decay, the resultant positron is denoted by a β^+ and in the case of a neutron, the resultant negatively charged energy (i.e., electron) is denoted by a β^-. Atoms that emit beta rays during their decay emit one of these two particles and beta probes can detect both, in a rather specific manner. Of note, these rays can travel up to several centimeters in air but in tissues they can only travel a few millimeters before annihilating. This is one of the main differences with gamma rays, which can travel significantly longer distances.

V. Strong (✉)
Surgery Department, Memorial Sloan-Kettering Cancer Center, 1275 York Avenue, New York, NY 10021, USA
e-mail: strong@mskcc.org

S. J. González
H. Lee Moffitt Cancer Center, FL, Tampa, USA

Y. Fong et al. (eds.), *Imaging and Visualization in The Modern Operating Room,*
DOI 10.1007/978-1-4939-2326-7_17,

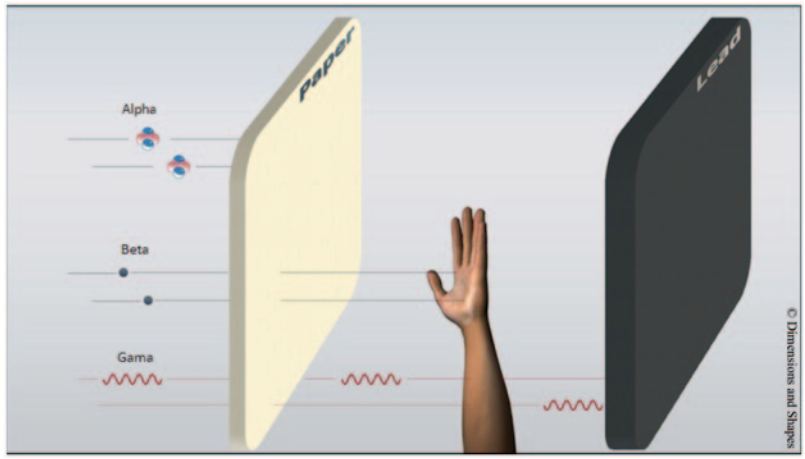

Fig. 17.1 Alpha, beta, and gamma rays. Gamma rays are the highest energy from these and require several feet of concrete or a few inches of lead to be stopped

Beta probes are devices designed to specifically detect beta rays. When used intraoperatively, the short distance traveled by beta rays allows a more accurate localization because beta probes are less affected by surrounding radiation [2–4]. This fact compares very favorably with the gamma probe (described below). Studies show a high sensitivity of the beta probe for beta rays and little influence of surrounding radiation (i.e., gamma rays). The variety of radioisotopes for clinical utility has increased significantly [5, 6], while many important innovations have been introduced and many others are on their way [7–9]. As an example, a beta probe composed of a phoswich detector was recently created that is able to differentiate between a positron and background scatter, and has an improved spatial resolution of 11 mm full width at half maximum (FWHM) [10].

F-18 is a positron-emitting atom that has been well tested for both imaging (i.e., fluorodeoxyglucose positron emission tomography, FDG PET, scan) and intraoperative utility. For intraoperative use, a beta probe (i.e., a PET probe) is required. Table 17.1 describes frequently used beta-emitting radioisotopes.

PET Probes

A PET probe is able to detect F-18 positrons (β^+ particles) and can be used to localize suspicious PET scan findings intraoperatively. The utility of this probe relies on the fact that the PET scan is a metabolic test, and tissues with high FDG uptake

Table 17.1 Radioisotopes emitting beta rays, relevant information, and their clinical applications

Beta ray	Half-life/energy	Notes	Applications
^{18}F	109.8 min	Beta rays only travel mm in tissue	Intraoperative localization utilizing the PET probe
^{131}I	8.02 days/606 keV	Contributor to Chernobyl nuclear disaster. In moderate doses increases risks of thyroid cancer, but not all large doses (therapeutic dose)	Gamma cameras, Graves' hyperthyroidism treatment of residual thyroid tissue (remnant ablation), metastatic thyroid cancer
^{32}P	14.3 days/1.7 MeV	Has multiple other uses besides medical ones	Brachytherapy

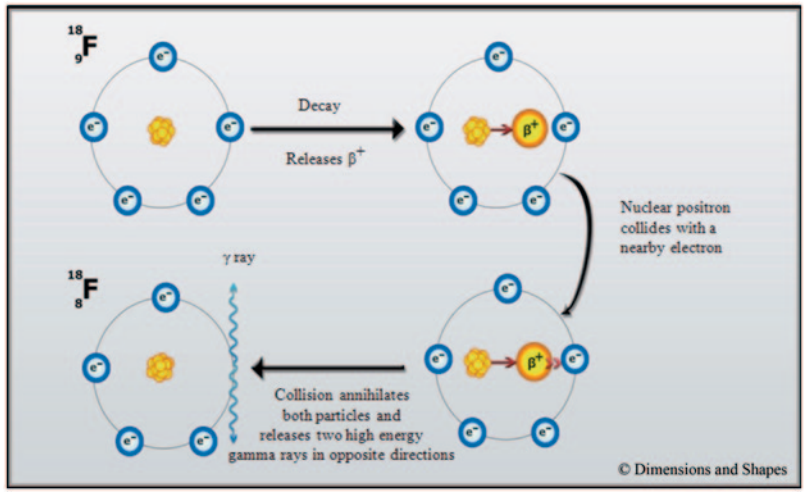

Fig. 17.2 Decay of ^{18}F-FDG. During this decay, a proton is transformed into a neutron and a positron, which is released from the nucleus. This then travels a short distance and is annihilated once it collides with an electron. The end result is that the nuclear mass remains the same, but the atom loses one electron during this reaction

may look and feel similar to normal surrounding tissue intraoperatively.

A preoperative injection of ^{18}F-fluorodeoxyglucose (^{18}F-FDG) is administered intravenously and the beta probe can intraoperatively locate areas with high FDG uptake. During the decay of ^{18}F-FDG, positrons (β^+) are emitted from the nucleus, then travel for a short distance and collide with a nearby electron, annihilating and creating a high-energy gamma ray during this reaction (Fig. 17.2).

PET probes are frequently used beta probes, because of the high glycolysis rate in cancer cells [11, 12]. The exact mechanism of this increased glucose use and FDG trapping is still being elucidated but a few explanations have been observed. First, glucose transporters are noted to be overexpressed in cancer cells (especially glucose transporter-1, Glut-1, and Glut-3); second, cancer cells have decreased levels of glucose phosphatase; and third, cancer cells have an increased activity of hexokinase [13]. All these events enhance the intraoperative trapping of FDG (Fig. 17.3).

The utility of PET probes has been well documented [6, 14, 15]. Limitations of PET probes include the size and the threshold of FDG uptake in solid tumors [16]. Preferential uptake of FDG by malignant lymph nodes has been noted [6] and allows for evaluation of regional lymph nodes to assist with staging and resection.

Recently, radiolabeled antibodies targeting cancer cells have been developed and combined with the FDG radioisotope, optimizing further intraoperative detection. Preliminary studies of this technology have shown promising results [17]. This may allow surgeons to detect specific target receptors, improving the precision of the intraoperative localization for malignant tissue.

Gamma Particles and Probes

Gamma particles are created from the annihilation of a positron emitted from the nucleus with a surrounding electron. In this collision, two high-energy gamma particles are formed and travel in the opposite direction for several centimeters (Fig. 17.2). Gamma rays can be detected by gamma cameras (Fig. 17.4).

Gamma probes are currently used in a variety of intraoperative procedures. Due to the high energy of the gamma rays and the long distance they travel, the gamma probe could easily be overwhelmed by surrounding radiation. To avoid this and optimize the detection of FDG uptake from only the tissue of interest, lead shielding and col-

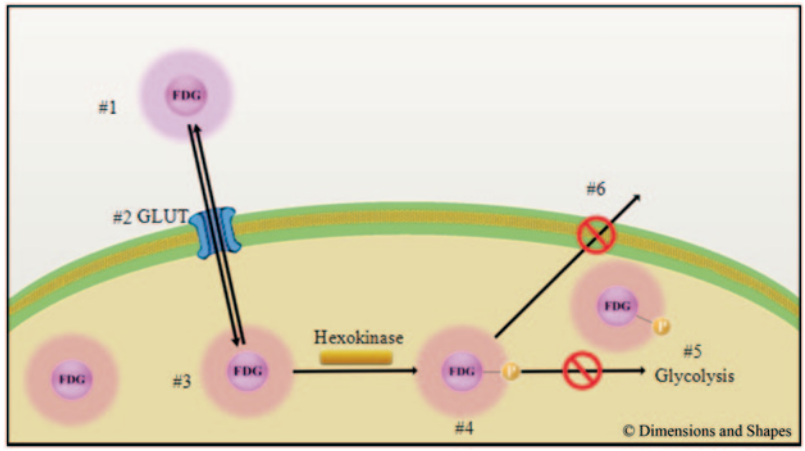

Fig. 17.3 ^{18}F-fluorodeoxyglucose (*FDG*) trapping in cancer cells. *FDG* is infused intravenously and reaches the cell surface (*#1*). Glucose transporters (*GLUTs*) located on the cell surface import it into the cell, just as another glucose molecule (*#2* and *#3*). Once inside, hexokinase phosphorylates *FDG* (*#4*). Because FDG-P is unable to undergo glycolysis (*#5*) or be exported from the cell (*#6*), it becomes trapped inside the cell

limation are required. As shown in Fig. 17.5, lead shielding covers the entire probe except at its tip, were collimation, designed to allow only rays from one direction to pass through. Continuous improvement has achieved a significant accuracy and impressive spatial resolution, and currently a resolution of less than 25 mm FWHM is desired for clinical applications (Fig. 17.6).

Gamma detection probes utilize either a scintillation or a semiconductor detector, both of which have different characteristics in terms of resolution, size, and costs (Table 17.2). These detectors contain a crystalline material that converts the radiation energy detected from the radionuclide into an electrical pulse, which is then analyzed. To create this electrical pulse, the scintillation units (Fig. 17.5) require two steps: radionuclide detection → light, magnified by a photomultiplier → electrical pulse; but the semiconductors can perform this in only one step: radionuclide detection → electrical pulse [18–21]. Each detector uses a different crystal to achieve an electrical pulse (Table 17.3). After production, the quality of the gamma probe is extensively evaluated. The most important characteristics that are tested are described in Table 17.4 [21–23].

The energy of gamma photons is expressed in kiloelectron volts (keV) and classified as low (0–150 keV), intermediate (150–400 keV), or high (over 400 keV) energy photons. Accurate selection of the radioisotope is of outmost importance for each particular clinical application. An energy level of at least 100 keV is required for proper imaging. In addition, the radioisotope should have a half-life of 2–3 weeks allowing the monoclonal antibodies to become physiologically integrated and provide accurate localization.

Besides the differences in energy levels and half-life, each radioisotope has an intrinsic accuracy based on the ability of the gamma probe to detect them [24, 25], and this should also be taken into consideration during the selection process. As a rule of thumb, gamma probes have better sensitivity for lower-energy rays (i.e., 99mTc, 125I) and radioisotopes with particularly high-energy levels (i.e., F-18) impose significant challenges for intraoperative detection [7, 26].

Sentinel Lymph-Node Biopsy with Gamma Probes

Gamma probes have been tested in many clinical situations, and are the standard of care technique for sentinel lymph-node biopsy. Some of the

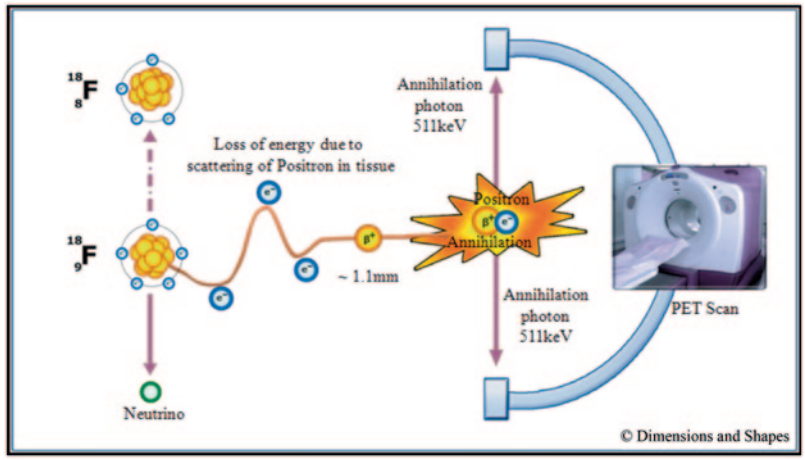

Fig. 17.4 During the decay of an F-FDG atom, a positron is expelled and annihilates with an electron creating a high-energy gamma particle that travels several centimeters. *PET* positron emission tomography

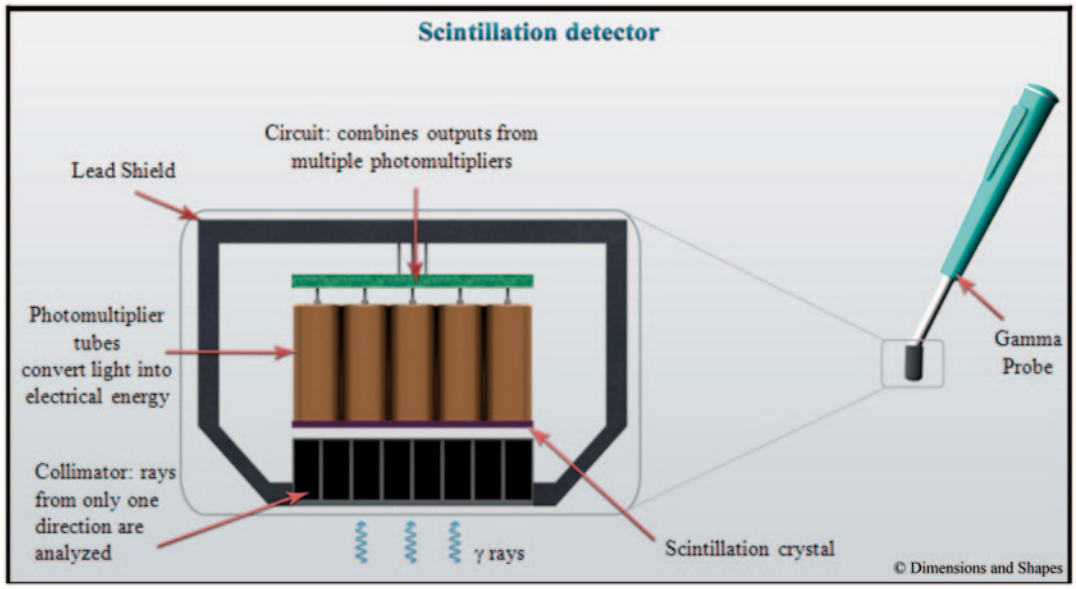

Fig. 17.5 Gamma probe construction. Lead shielding and collimation protect from surrounding radiation

most commonly used radionuclides for gamma detection are shown in Table 17.5.

Sentinel lymph-node biopsy (SLNB) using ^{99m}Tc is performed most commonly for breast cancer. In these cases, proper lymphatic staging could be done with this simple procedure allowing clinicians to reserve the more complex complete lymphadenectomy for patients with positive nodal disease. The procedure entails the local administration of a radiotracer, intraoperative localization with the gamma probe, and harvesting the lymph node with the highest count together with other nodes with counts of at least 10% of the hottest node. The accuracy of this procedure is dependent on two main elements, first the experience of the operator, with 20 SLNB procedures considered a threshold number to be able to master this technique [27, 28]. Second, the location of

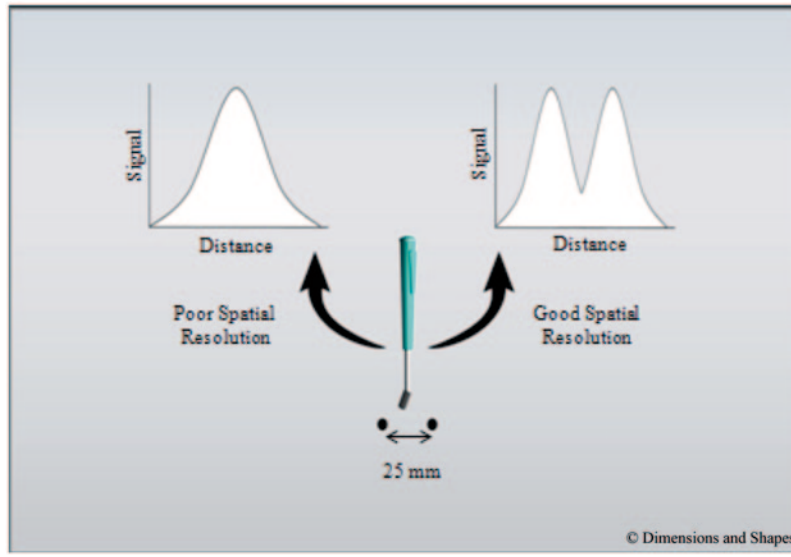

Fig. 17.6 Gamma probe spatial resolution. For acceptable clinical use, the probe should identify two independent areas of high uptake when those are as close as 25 mm in distance

Table 17.2 Gamma detectors: the two main detectors used for the construction of gamma probes and their characteristics

Detector type	Characteristics
Scintillation	High sensitivity but requires more lateral shielding
Semiconductor	High-energy resolution, less bulky, more expensive

Table 17.3 Examples of crystalline materials used for different detectors: scintillation and semiconductor detectors differ in their physical characteristics, and different materials are used to achieve optimal accuracy

Scintillation detectors	Thallium-activated cesium iodide (CsI[T1])
	Thallium-activated sodium iodide (NaI[T1])
	Bismuth germinate (GBO)
	Samarium-activated lutetium ortho-oxysilicate (LSO)
Semiconductors detectors	Cadmium zinc telluride (CdZnTe)
	Cadmium telluride (CdTe)
	Mercuric iodide (HgI2)

radiocolloid administration relative to the tumor or breast parenchyma can also impact accuracy. In a recent prospective trial at the Ohio State University, the accuracy of localization of an axillary sentinel lymph node was noted to be higher if the ^{99m}Tc sulfur colloid was administered intradermally (100%), compared to subareolar (95%) or intraparenchymal administration (90%) [29]. Furthermore, the number of required lymph nodes to harvest during this procedure has also been evaluated. Increasing the number of lymph nodes harvested to two or more decreases the false-negative rates from 14% (harvesting only one sentinel lymph node) to 5.4%. Interestingly, when six lymph nodes are harvested, the false-negative rate approaches 0% [30, 31]. Factors that negatively affect the accuracy of this procedure are history of prior chemotherapy, tumor burden within the lymphatics that could impede lymphoscintigraphy, and obesity [32, 33]. Breast cancer patients that are not candidates for SLNB include patients with palpable lymphadenopathy, multicentric tumors, prior breast surgery, history of breast radiation or advanced breast cancer [28, 34].

Other uses of the gamma probe for SLNB include the staging of patients with cutaneous

Table 17.4 Evaluation of gamma probes: during the extensive evaluation for accuracy, multiple characteristics are analyzed, some of which are described below

Characteristic description	Description
Sensitivity	Photons detected per photons emitted
Spatial selectivity	Total area at the tip of the probe able to detect photons
Energy resolution	Ability to detect a particular ray without being affected by other surrounding radiation with different energy levels
Quality of shielding	Improper shielding allows surrounding high-energy rays to be detected

Table 17.5 Radioisotopes emitting gamma rays, relevant information, and their clinical applications

Gamma emitting radioistopes	Half-life/energy	Notes	Applications
^{18}F	110 min/511 KeV gamma rays	Low-energy positrons (beta rays) only travel 2 mm before they annihilate, then emit a high-energy gamma ray	Used for gamma camera imaging
^{99m}Tc	6 h/140 KeV	Almost no beta ray emission; low cost; widely available	Used for both gamma camera imaging and intraoperative guidance
^{111}In	2.8 Days/35 KeV	Is concentrated in the RES, produces high background scatter for intraoperative guidance	Used for gamma camera imaging
^{125}I	60 Days/35 KeV	Energy too low for gamma camera imaging	Good for intraoperative guidance
^{131}I	8.02 days/364 KeV	Energy too high for routine intraoperative use. 10% of its radiation is gamma, and 90% is beta radiation	Intraoperative localization of recurrent thyroid malignancy

melanoma. For this, 1–3 ml of blue dye are administered subcutaneously around the malignancy as an adjunct to the ^{99m}Tc radiocolloid placed preoperatively. The utility of this procedure for cutaneous melanoma was first described by Morton et al. [35] and since then, this technique has been adapted as a standard staging procedure for patients at risk of lymphatic disease. The multiple other uses in or outside of clinical trials that have been performed with the gamma probe are extensive and out of the scope of this chapter but detailed reviews could be found elsewhere [26].

Evolution and the Future of Guidance

Besides using radioisotopes for intraoperative guidance, surgeons use other methods for localizing important structures. In fact the most commonly used and older type of guidance is simple landmark palpation. This allows surgeons to feel bony prominences, pulses as well as detect tumors or organs of interest. As an expansion of this method, multiple devices have been used, such as the nasogastric tube for localizing the esophagus, as well as biliary and ureteral stents to locate these structures during the dissection.

Both of these methods of guidance (radioisotope and palpation) have their advantages. Palpation guides the surgeon with direct tactile feedback, while radioisotopes guide with noise. As an analogy, imaging yourself in a room without light. Using tactile feedback, you can guide yourself through the room by feeling walls and furniture. Similarly, you can be trained to recognize a particular noise and approach or avoid the proximity of it depending on its nature. Combining both tactile and noise guidance, clearly improves guidance. However, when the light is turned on, visual guidance dominates and surrounding structures could be evaluated in an intuitive manner and other stimuli and perception becomes secondary. Unfortunately, surgeons can only see the superficial layer of exposed tissue, and are forced to rely on palpation and noise (or counts) to assess deeper structures. In a sense, we

are operating with closed eyes, and even though the ability for the human eyes to see through tissues is far from possible, it will certainly be the method that could turn the lights on in our surgical room and allow us to use our vision for guidance beyond the superficial tissue layers.

This notion is not new and attempts to integrate various visual feedbacks are under development. In fact, intraoperative probes have been created to display a visual interpretation of the radioisotope uptake. This is then displayed as an overlay image over the patient, in a real-time manner [36–39]. Furthermore, technologies that allow visualization of organs during procedures have also been developed. These permit surgeons to visualize internal structures in 3D throughout the procedure [40, 41]. Moreover, instruments with position tracking technology have been developed that can be tracked within the 3D anatomy of the patient [42]. The only drawback of this technology is that it uses preoperative rather than real-time imaging to guide surgery [43, 44]. Therefore, even though some specialties use these images as a guidance tool (i.e., orthopedics, dentistry, and neurosurgery), soft tissue surgery has a constant displacement of organs and cannot fully rely on preoperative images for intraoperative guidance.

A novel software algorithm was recently developed [45] that allows surgeons to visualize internal structures in 3D in real-time. This permits not only an accurate volumetric analysis of the region of interest, but also imports prior analysis from the radiologist that could be pertinent to the surgical procedure. This software integrates augmented reality, virtual reality, and position tracking technologies and allows the full synchronization of preoperative analysis to be visually available for surgeons during the procedure. And even though further studies are needed to standardize this and other upcoming technologies, it is fair to say that we may be approaching an era of turning "on" the light in our rooms.

References

1. Harris CC, Bigelow RR, Francis JE, Kelly GG, Bell P. A Csi(Ti)-crystal surgical scintillation probe. Nucleonics. 1956;14:102–8.
2. Imaging I. Beta Probes http://www.gammaprobe.com: Intramedical Imaging; 2013 [cited 2013]. http://www.gammaprobe.com/products/beta-probes/.
3. Raylman RR, Wahl RL. A fiber-optically coupled positron-sensitive surgical probe. J Nucl Med. 1994;35(5):909–13.
4. Strong VE, Galanis CJ, Riedl CC, Longo VA, Daghighian F, Humm JL, et al. Portable PET probes are a novel tool for intraoperative localization of tumor deposits. Ann Surg Innov Res. 2009;3:2.
5. Janicki C, Seuntjens J. Re-evaluation of the dose to the cyst wall in P-32 radiocolloid treatments of cystic brain tumors using the dose-point-kernel and Monte Carlo methods. Med Phys. 2003;30(9):2475–81.
6. González SJ, Wong J, González L, Brader P, Zakowski M, Gönen M, et al. Novel handheld PET probes provide intraoperative localization of PET-avid lymph nodes. Surg Endosc. 2011;25(10):3214–21.
7. Garcia-Parra R, Clinthorne N, Wang L, Picchio M, Piert M. Performance of beta- and high-energy gamma probes for the detection of cancer tissue in experimental surgical resection beds. Ann Nucl Med. 2011;25(7):486–93.
8. Tsuchimochi M, Sakahara H, Hayama K, Funaki M, Ohno R, Shirahata T, et al. A prototype small CdTe gamma camera for radioguided surgery and other imaging applications. Eur J Nucl Med Mol Imaging. 2003;30(12):1605–14.
9. Daghighian F, Mazziotta JC, Hoffman EJ, Shenderov P, Eshaghian B, Siegel S, et al. Intraoperative beta probe: a device for detecting tissue labeled with positron or electron emitting isotopes during surgery. Med Phys. 1994;21(1):153–7.
10. Yamamoto S, Matsumoto K, Sakamoto S, Tarutani K, Minato K, Senda M. An intra-operative positron probe with background rejection capability for FDG-guided surgery. Ann Nucl Med. 2005;19(1):23–8.
11. Gatenby RA, Gillies RJ. Why do cancers have high aerobic glycolysis? Nat Rev Cancer. 2004;4(11):891–9.
12. Gillies RJ, Gatenby RA. Adaptive landscapes and emergent phenotypes: why do cancers have high glycolysis? J Bioenerg Biomembr. 2007;39(3):251–7.
13. Buck AK, Reske SN. Cellular origin and molecular mechanisms of 18F-FDG uptake: is there a contribution of the endothelium? J Nucl Med. 2004;45(3):461–3.
14. Gulec SA. PET probe-guided surgery. J Surg Oncol. 2007;96(4):353–7.
15. Sun D, Bloomston M, Hinkle G, Al-Saif OH, Hall NC, Povoski SP, et al. Radioimmunoguided surgery (RIGS), PET/CT image-guided surgery, and fluorescence image-guided surgery: past, present, and future. J Surg Oncol. 2007;96(4):297–308.
16. González SJ, González L, Wong J, Brader P, Zakowski M, Gönen M, et al. An analysis of the utility

of handheld PET probes for the intraoperative localization of malignant tissue. J Gastrointest Surg. 2011;15(2):358–66.
17. Strong VE, Humm J, Russo P, Jungbluth A, Wong WD, Daghighian F, et al. A novel method to localize antibody-targeted cancer deposits intraoperatively using handheld PET beta and gamma probes. Surg Endosc. 2008;22(2):386–91.
18. Woolfenden JM, Barber HB. Radiation detector probes for tumor localization using tumor-seeking radioactive tracers. AJR Am J Roentgenol. 1989;153(1):35–9.
19. Bogalhas F, Charon Y, Duval MA, Lefebvre F, Palfi S, Pinot L, et al. Development of a positron probe for localization and excision of brain tumours during surgery. Phys Med Biol. 2009;54(14):4439–53.
20. Hoffman EJ, Tornai MP, Janecek M, Patt BE, Iwanczyk JS. Intraoperative probes and imaging probes. Eur J Nucl Med. 1999;26(8):913–35.
21. Zanzonico P, Heller S. The intraoperative gamma probe: basic principles and choices available. Semin Nucl Med. 2000;30(1):33–48.
22. Tiourina T, Arends B, Huysmans D, Rutten H, Lemaire B, Muller S. Evaluation of surgical gamma probes for radioguided sentinel node localisation. Eur J Nucl Med. 1998;25(9):1224–31.
23. Mariani G, Vaiano A, Nibale O, Rubello D. Is the "ideal" gamma-probe for intraoperative radioguided surgery conceivable? J Nucl Med. 2005;46(3):388–90.
24. Haigh PI, Glass EC, Essner R. Accuracy of gamma probes in localizing radioactivity: in-vitro assessment and clinical implications. Cancer Biother Radiopharm. 2000;15(6):561–9.
25. Corporation. N. Bluetooth® Gamma Detection Probe. Neoprobe Corporation. 2013.
26. Povoski SP, Neff RL, Mojzisik CM, O'Malley DM, Hinkle GH, Hall NC, et al. A comprehensive overview of radioguided surgery using gamma detection probe technology. World J Surg Oncol. 2009;7:11.
27. Hutchinson JR, Chagpar AB, Scoggins CR, Martin RC, Carlson DJ, Laidley AL, et al. Surgeon and community factors affecting breast cancer sentinel lymph node biopsy. Am J Surg. 2005;190(6):903–6.
28. Schwartz GF, Giuliano AE, Veronesi U, Committee CC. Proceedings of the consensus conference on the role of sentinel lymph node biopsy in carcinoma of the breast, April 19–22, 2001, Philadelphia, Pennsylvania. Cancer. 2002;94(10):2542–51.
29. Povoski SP, Olsen JO, Young DC, Clarke J, Burak WE, Walker MJ, et al. Prospective randomized clinical trial comparing intradermal, intraparenchymal, and subareolar injection routes for sentinel lymph node mapping and biopsy in breast cancer. Ann Surg Oncol. 2006;13(11):1412–21.
30. Martin RC, Chagpar A, Scoggins CR, Edwards MJ, Hagendoorn L, Stromberg AJ, et al. Clinicopathologic factors associated with false-negative sentinel lymph-node biopsy in breast cancer. Ann Surg. 2005;241(6):1005–12. Discussion 12–5.
31. Woznick A, Franco M, Bendick P, Benitez PR. Sentinel lymph node dissection for breast cancer: how many nodes are enough and which technique is optimal? Am J Surg. 2006;191(3):330–3.
32. Carmon M, Olsha O, Rivkin L, Spira RM, Golomb E. Intraoperative palpation for clinically suspicious axillary sentinel lymph nodes reduces the false-negative rate of sentinel lymph node biopsy in breast cancer. Breast J. 2006;12(3):199–201.
33. Noguchi M. Current controversies concerning sentinel lymph node biopsy for breast cancer. Breast Cancer Res Treat. 2004;84(3):261–71.
34. Tangoku A, Seike J, Nakano K, Nagao T, Honda J, Yoshida T, et al. Current status of sentinel lymph node navigation surgery in breast and gastrointestinal tract. J Med Invest. 2007;54(1–2):1–18.
35. Morton DL, Wen DR, Wong JH, Economou JS, Cagle LA, Storm FK, et al. Technical details of intraoperative lymphatic mapping for early stage melanoma. Arch Surg. 1992;127(4):392–9.
36. Chondrogiannis S, Ferretti A, Facci E, Marzola MC, Rampin L, Tadayyon S, et al. Intraoperative handheld imaging γ-camera for sentinel node detection in patients with breast cancer: feasibility evaluation and preliminary experience on 16 patients. Clin Nucl Med. 2013;38(3):e132–6.
37. Pauwels EK, Ribeiro MJ, Stoot JH, McCready VR, Bourguignon M, Mazière B. FDG accumulation and tumor biology. Nucl Med Biol. 1998;25(4):317–22.
38. Wendler T, Traub J, Ziegler SI, Navab N. Navigated three dimensional beta probe for optimal cancer resection. Med Image Comput Comput Assist Interv. 2006;9(Pt 1):561–9.
39. Singh B, Stack BC, Thacker S, Gaysinskiy V, Bartel T, Lowe V, et al. A hand-held beta imaging probe for FDG. Ann Nucl Med. 2013;27(3):203–8.
40. Matityahu A, Kahler D, Krettek C, Stöckle U, Grutzner PA, Messmer P, et al. 3D Navigation is more accurate than 2D navigation or conventional fluoroscopy for percutaneous sacroiliac screw fixation in the dysmorphic sacrum: a randomized multicenter study. J Orthop Trauma. 2014;28(12):707–10.
41. Hur JW, Kim JS, Cho DY, Shin JM, Lee JH, Lee SH. Video-assisted thoracoscopic surgery under O-Arm navigation system guidance for the treatment of thoracic disk herniations: surgical techniques and early clinical results. J Neurol Surg A Cent Eur Neurosurg. 2014;75(6):415–21.
42. Sobottka SB, Bredow J, Beuthien-Baumann B, Reiss G, Schackert G, Steinmeier R. Comparison of functional brain PET images and intraoperative brain-mapping data using image-guided surgery. Comput Aided Surg. 2002;7(6):317–25.
43. Wang J, Suenaga H, Hoshi K, Yang L, Kobayashi E, Sakuma I, et al. Augmented reality navigation with automatic marker-free image registration using 3-d image overlay for dental surgery. IEEE Trans Biomed Eng. 2014;61(4):1295–304.
44. Dixon BJ, Daly MJ, Chan H, Vescan A, Witterick IJ, Irish JC. Augmented real-time navigation with critical structure proximity alerts for endoscopic skull base surgery. Laryngoscope. 2014;124(4):853–9.
45. Gonzalez SJM, Yanhui Guo P, Lee CM MD, Morse D PhD, Drukteinis JM. Feasibility of augmented/virtual reality glasses for real-time, 3D intraoperative guidance. Presentation, 2014 H. Lee Moffitt cancer center and research institute scientific symposium.

Breast Lesion Localization

18

Nora M. Hansen

With the advent of routine screening mammography, the identification of nonpalpable lesions has increased, and surgeons have had to rely on techniques other than palpation-guided methods to identify these lesions during surgery. Nonpalpable breast cancers account for approximately one third of all diagnosed breast cancers [1]. The focus of this chapter is to review the localization techniques for breast lesions that can be used in the operating room (OR). Ultrasound localization will not be covered in this chapter since it is being covered in a separate chapter.

Image-guided localization is the most common technique used to localize nonpalpable breast lesions. Lesions can be localized using a variety of modalities such as mammography, ultrasound, hematoma-directed, magnetic resonance imaging (MRI), or radioactive seed localization (RSL). In many centers, a team approach is used which includes radiologists, nuclear medicine physicians, and surgeons. In some settings, surgeons have become accredited in both stereotactic and ultrasound techniques and perform the localization procedure themselves.

The majority of these localization techniques are performed outside the OR in the radiology suite, but it is imperative that the surgeon is familiar with these techniques, so they can effectively use the information in the OR for successful removal of the lesion. Ultrasound localization can be used in the OR by a surgeon who is experienced and preferably accredited in ultrasound.

N. M. Hansen (✉)
1Prentice Woman's Hospital, Northwestern Memorial Hospital, 250 East Superior Street, Suite 4-420, Chicago, IL 60611, USA
e-mail: nhansen@nmh.org

Needle Wire Localization

Improvements in imaging techniques and the increased use of these modalities have resulted in the increased detection on nonpalpable lesions requiring biopsy and eventual excision for final histopathologic diagnosis or treatment of a known breast malignancy [2]. Accurate localization of the lesion is required to ensure correct and adequate removal. Image localization techniques are performed by targeting clips that were placed during a biopsy using a variety of imaging modalities such as stereotactic biopsy, ultrasound-guided biopsy or MRI-guided biopsy, or mass or residual calcifications if no clip was placed. The most common method for preoperative localization has been wire localization performed with a hook wire and was introduced in the mid 1960s [3, 4]. Mammographic localization is usually performed using an upright mammographic attachment on a mammographic unit. Stereotaxy enables the exact position of the area of concern to be located. Other centers use a grid or holey plate that was used to calculate the position of the needle and subsequent wire placement in the X and Y planes. There are a variety of needles

Y. Fong et al. (eds.), *Imaging and Visualization in The Modern Operating Room,*
DOI 10.1007/978-1-4939-2326-7_18, © Springer Science+Business Media New York 2015

available but most use a stiffer, coaxial needle thru which the wire is placed. Some surgeons leave the needle in place while others prefer to have the needle removed (Figs. 18.1, 18.2). Once the lesion is removed, a specimen Xx-ray should be performed to ensure the lesion in question was removed (Fig. 18.3). Because the wire is placed thru the breast tissue there are several limitations.

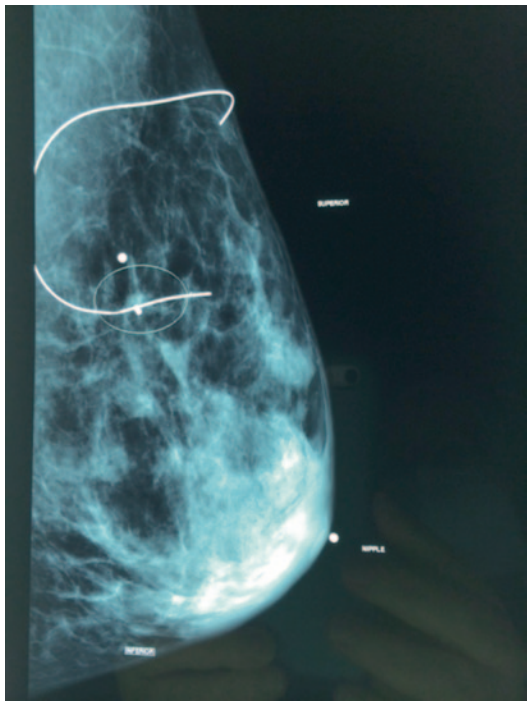

Fig. 18.1 Needle localization film—right lateral medial (LM) view

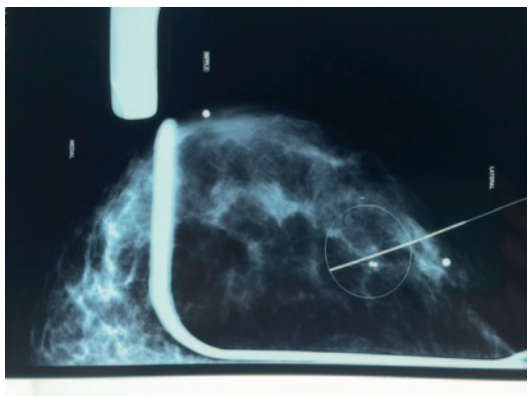

Fig. 18.2 Needle localization film—right craniocaudal (CC) view

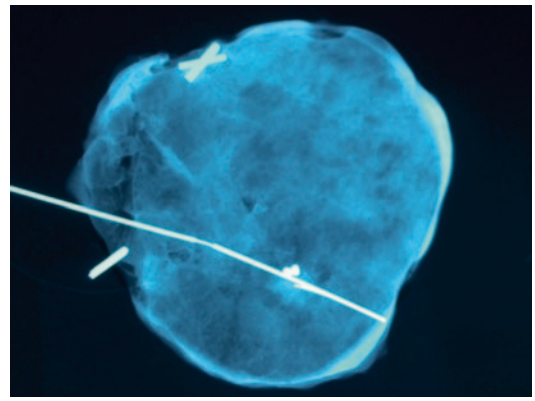

Fig. 18.3 Specimen X-ray—wire and clip visible in specimen

The wire can be inadvertently pulled, displaced, or transected prior to or during surgery limiting the accurate localization of the targeted lesion. The wire can migrate, kink, or fracture making it difficult to accurately identify the lesion. Often the entry point of the wire at the skin is not near the index lesion, and since the preferred method is to make the incision directly over the lesion in question, the wire may be difficult to locate within the breast (Fig. 18.4) [5, 6, 7]. Because the wire placement is done on the day of the surgery, scheduling needs to be coordinated with both the radiologist and the surgeon adding a level of complexity to the schedule. The wire placement can often be difficult for the patient and sometimes results in a vasovagal response. Due to these factors other localization methods have been developed.

Hematoma-Directed Localization

The majority of patients who require excision of a breast lesion have undergone a biopsy either with a fine needle aspiration or a core needle biopsy to determine whether or not the lesion in question needs to be removed. There are a variety of biopsy techniques that can be used but one of the most common biopsy techniques is the vacuum-assisted core biopsy. After this type of biopsy, there is a biopsy cavity which naturally fills with hematoma that can then be visualized on ultrasound. This technique was first described

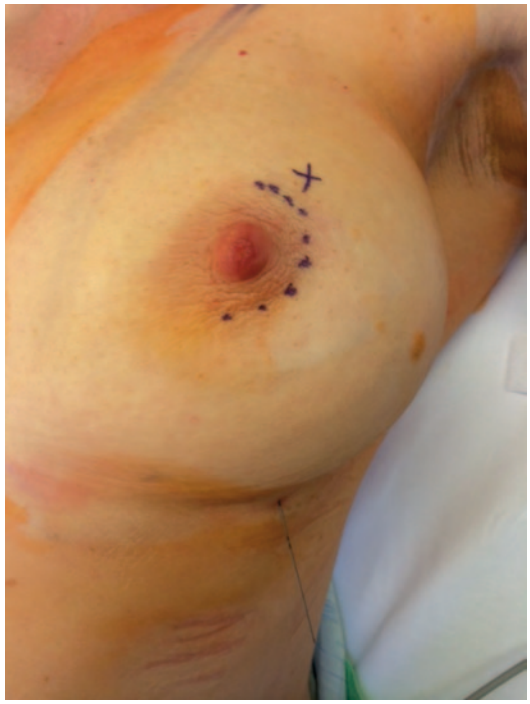

Fig. 18.4 Photograph after needle localization procedure in the operating room. Wire entry is at 6 o clock while lesion to be removed is marked with an X in superior lateral breast

in 2001 by the group at the University of Arkansas [8]. In this study, twenty patients with nonpalpable breast lesions detected on MRI had 2–5 ml of the patients own blood injected into the breast to target the nonpalpable lesion. Intraoperative ultrasound was then used to localize the hematoma and excise the lesion. This procedure was named the hematoma-directed ultrasound-guided (HUG) procedure. Ninety-five percent of the lesions were localized by hematoma injection, and all were identified at surgery and removed without complications. This group reported their 10-year experience with this technique in 2010 [9]. Rather than inject blood into the lesion itself, an ultrasound was used to determine if a hematoma was present after a percutaneous biopsy. If a hematoma was present, then the HUG approach was used. If a hematoma was not visualized, then the lesion was localized via a needle localization approach. Between 2000 and 2009, 455 patients underwent localization procedures, the majority (72%) of whom was localized using the HUG technique. The previous core biopsy site was removed in 100% of the HUG patients. Compared to the needle localized cohort, the HUG cohort had a lower complication rate (6 vs. 9%) as well as a statistically significant difference in margin positivity rate (24 vs. 47% p value 0.045). This technique relies on the naturally occurring hematoma after a core biopsy, and therefore there is no reliance on clips, needles, or any other device which makes it easier for the patients and perhaps more cost effective. Larrieux et al. [10] reported on 55 patients who underwent HUG and compared them to 55 patients who had a needle localization. They found that HUG is equivalent to NL with regard to volume of tissue excised, need for operative re-excision, and OR time. The time from biopsy to surgery was shorter in the HUG group allowing for more timely surgical care. There did appear to be a learning curve for the procedure with an initial longer operative time but this decreased over time. Other [11, 12] have validated this concept, but it is not a widely adopted technique. This may be due to several reasons including that there is a time frame that needs to be adhered to in order to see the hematoma and should be done within 5 weeks of the biopsy. On average the hematoma resorbs within 14 days, but Arentz et al. [9] noted that most hematomas are completely absorbed by 5 weeks [13]. The surgeon also needs to be experienced in ultrasound which may limit its widespread use.

Other Localization Agents

Indocyanine green fluorescence-guided occult lesion localization (IFOLL) uses an indocyanine green dye injected into the breast at the site of the abnormality within 1 h of surgery. Using the guidance of a near-infrared-sensitive camera, the indocyanine-derived flourscence is visualized and the lesion resected. This has been used in limited patients but is technically feasible and in two patients was successful with no complications and negative surgical margins [14].

Radio-Guided Occult Lesion Localization

Radio-guided occult lesion localization (ROLL) was developed as a new localization technique at the European Institute of Oncology, Milan, and described in 1997. The technique involves the infection of particles of colloidal human serum albumin labeled with radioactive technetium and injected directly into the lesion during mammography or ultrasonography. In the first 196 patients studied from 3/96 to 4/97 the technique was found to be satisfactory and reliable and since that time was routinely used as the localization technique [15]. ROLL was introduced in combination with sentinel node mapping in 2002 at the European Institute of Oncology as an alternative to wire localization. The technique was found to be superior to wire localization as it provided better centering of the lesion within the specimen and reduced the quantity of healthy tissue removed and provided the surgeon with a quick and simple means of locating and removing the lesion in the OR. In over 1000 patients, this technique has been shown to lead to fast and accurate removal of the lesion, reducing the invasiveness of the procedure as well as reducing the operative time [16]. There have been multiple reports to date on the ROLL technique which report similar results. Berdardi et al. reported that radiologist inexperience, lesion size $\leq$5 mm and location in central subareolar quadrant were most common risk factors for ROLL failure [17]. In a meta-analysis comparing ROLL to wire localization, accurate localization, periprocedural complications and reoperation rates were comparable between the two techniques; however, the risk of having positive resection margins was higher in the wire localization groups. The duration of the localization and surgical excision times were shorter for the ROLL group. Both the volume and weight of the excised breast lesions were similar between the groups [18]. It should be noted however that the injected tracer is not visible on radiographs and Tc99 is the same radiotracer used for sentinel node mapping which could create some confusion particularly for upper outer quadrant lesions.

Radioactive Seed Localization

Radioactive seed localization (RSL) is a recent alternative to wire localization and uses a fully implanted 4.5 mm 125 I encapsulated titanium seed that is visible both on mammography and ultrasound (Fig. 18.5). It has a long half life as compared to 99mTC, so it does not need to be performed on the day of surgery making scheduling less cumbersome. Seeds have a half life of 60 days so could be placed prior to neoadjuvant therapy in certain scenarios [19, 20]. It also has a different photopeak compared to 99mTC, so it can be performed together with a sentinel node biopsy procedure without interfering signals [21]. The radioactive seed(s) are placed into the breast lesion prior to surgery. It is preferable to have this done prior to the day of surgery so that the localization process does not interfere with the OR schedule. The seed(s) are placed via mammographic or ultrasound guidance (Fig. 18.6). A larger area can be bracketed with multiple seed placement. In the OR, a gamma probe is used to isolate the radioactive seed, and the surgical incision is made directly over the radioactive seed. A specimen radiograph is then obtained to confirm the removal of the lesion in question as well as the radioactive seed. Identification with a gamma probe allows the surgeon to more accurately resect the lesion (Fig. 18.7). Once the pathology specimen has been removed, it is placed in a

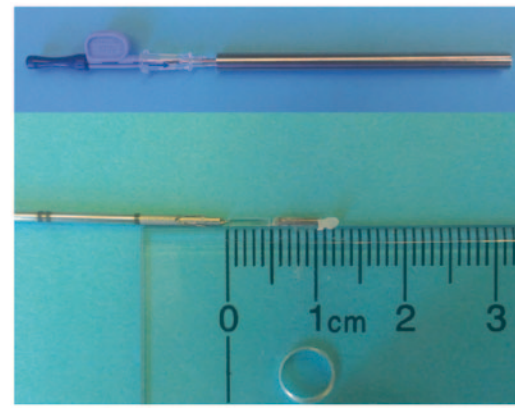

Fig. 18.5 RSL needle with stainless steel shielding in place

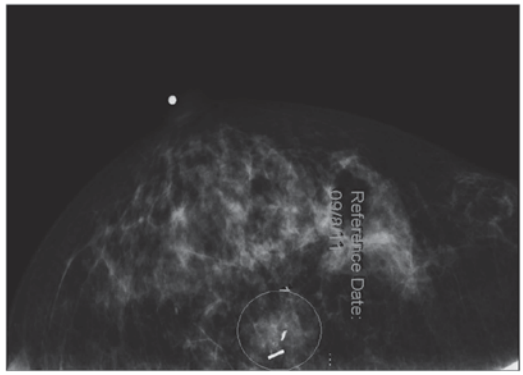

Fig. 18.6 Craniocaudal view of mammogram after RSL seed placement. Clip and seed in place

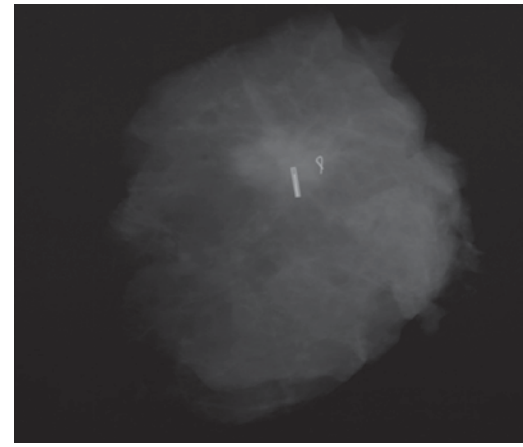

Fig. 18.7 Specimen radiograph confirming removal of clip and radioactive seed

specimen bag with the appropriate radioactive labels and sent to the pathology department (Fig. 18.8). There are a variety of gamma probes that can be used in this setting (Tables 18.1 and 18.2). There have been multiple studies performed which suggest that RSL leads to fewer positive margins and reoperation rates compared to NL and shorter operating times [21–24]. Other groups have demonstrated the success of RSL for high-risk lesions. Diego et al. analyzed 128 patients with high-risk lesions who were localized via RSL and compared them to 196 patients with high-risk lesions who were localized via WL. RSL was comparable to WL for high-risk lesions with similar OR times and upstage rates. The specimen volume was significantly decreased with RSL which may translate into a better cosmetic outcome [25]. The group at Memorial Sloan Kettering Cancer Center (MSKCC) switched their standard method of localizing nonpalpable breast lesions from wire localization to RSL in January of 2012. They have reported both their 6-month and 1-year experience using RSL. The majority of localizations were performed prior to the day of surgery (90%). In over 1100 patients, there was no difference in the rates of positive or close margins, and the specimen volume was not significantly increased. Initially there was a increase in operative time with RSL patients undergoing both lumpectomy and sentinel node biopsy most likely due to the need to adjust the gamma probe between the 125I and 99Tm [26, 27].

Fig. 18.8 Pathology specimen placed in bag and labeled with radioactive label for transport to pathology lab

It is imperative that when starting an RSL program all compliance issues regarding the radioactive seeds are in place. An RSL inventory log is useful to account for the receipt, administration, and ultimate retrieval of all radioactive seeds. At MSKCC, the pathology staff processed the specimen, and a trained pathology assistant used a gamma probe to identify the location of the radioactive seeds and then removed them placing them in a bag in a lead shielded storage container. It was important to do this prior to sectioning the specimen to avoid any injury or inadvertent cutting of the seeds [27]. RSL requires a

Table 18.1 Available gamma probes in the US

Company	Device control unit	Company website
RMD instruments	Navigator	rmdmedical.com
Devicor medical products, Inc.	Neoprobe	Mammotome.com
Care wise medical	C-trak	carewise.com
Intra medical imaging	Node seeker	gammaprobe.com

http://en.wikipedia.org/wiki/Gamma_probe

Table 18.2 Isotopes for clinical use with gamma probes

Tc99m-Technetium-99m
I125-Iodine125
I131-Iodine 131
I111-Indium 111
F18- Fluorine 18
Ga68-Gallium 68

http:/en.wikipedia.org/wiki/Gamma_probe

multidisciplinary team approach but if done correctly has several advantages over wire localization including real-time feedback about location of the lesion through intraoperative use of a gamma probe, increased OR efficiency by obviating the need for radiology on the day of surgery, ability to plan the surgical incisions without intervening wires, and improved patient satisfaction by avoiding the often painful wire placement [24, 28, 29].

Although there is a lot of evidence supporting the use of radio-guided localization and in several institutions, it has become the standard of care; the overall uptake of this technique has been slow. There have been several meta-analysis which have demonstrated the superiority of radio-guided localization compared to wire localization (WL) [30]. The question remains as to which technique ROLL versus RSL fits better into a specific practice. There are no real differences in clinical outcomes between the two techniques to suggest one technique is clinically superior to the other technique. Both techniques have been shown to adequately localize the abnormality and are competitively priced compared to WL [31]. The biggest difference between the two techniques is in the half life of the agent used in each technique. The ROLL technique must be done within 24 h of the radioactive injection while the RSL has a much longer half life allowing for more flexibility with scheduling and with patient selection. Each institution will need to determine which technique works best in their practice setting. Any localization technique requires a multidisciplinary team approach to make it a successful program.

Intraoperative Margin Analysis

Breast conservation has been an established surgical approach for early stage breast cancer for more than 30 years, and contemporary series report that 60–75% of women with early stage breast cancer are treated with breast conservation [1, 2]. The goal of breast conservation is to excise the tumor with a margin of normal tissue. This can be difficult for the surgeon to accomplish since it can be difficult to appreciate the microscopic extent of the tumor at the time of surgery. There is still great debate as to the optimal size of the negative margin; however, at least 20–25% of patients will require additional surgical intervention to obtain a negative margin which can increase the cost as well as patient anxiety [32]. Some studies have demonstrated a reduction in re-excision rates when additional tissue is routinely used from all six surfaces of the lumpectomy cavity [33, 34]; however, other groups have shown no advantage in obtaining negative margins by the removal of shave margins [35]. There have been several new techniques which have been designed to enhance the surgeons' ability to

identify a positive margin at the time of surgery. The MarginProbe (Dune Medical Devices Ltd., Caesarea, Israel) was developed to provide surgeons with real-time intraoperative assessment of lumpectomy margins. The device measures the local electrical properties of breast tissue. Schnabel et al. recently published a randomized prospective study of lumpectomy margin assessment using the MarginProbe in patients with nonpalpable malignancies. A total of 596 patients were enrolled. There was a reduction in needed re-excision procedures in the MarginProbe group 19.8% compared to 25.8% in the control group resulting in a 23% relative reduction [36].

Localization of nonpalpable breast lesions is an extremely important component to the successful management of patients with breast lesions. The more accurate the localization, the better the ability the surgeon has to completely remove the lesion. There are many techniques that can be used to localize these lesions, and it often requires a multidisciplinary team approach. Each surgeon needs to identify which localization techniques will work well in their clinical setting and work on ways to streamline the process and make it as efficient and effective as possible.

References

1. Lovrics PJ, Cornacchi SD, Farrokhyar F, Garnett A, Chen V, Franic, et al. The relationship between surgical factors and margin status after breast-conservation surgery for early stage breast cancer. Am J Surg. 2009;197(6):740–6.
2. Cady B, Stone MD, Schuler JG, Thakur R, Wanner MA, Lavin PT. The new era in breast cancer. Invasion, size and nodal involvement dramatically decreasing as a result of mammographic screening. Arch Surg. 1996;131:301–8.
3. Dodd GD, Fry K, Delany W. Preoperative localization of occult carcinoma of the breast. In: Nealton TP, editor. Management of the patient with cancer. Philadelphia: Saunders; 1965. pp. 88–113.
4. Frank HA, Hall FM, Steer ML. Preoperative localization of nonpalpable breast lesions demonstrated by mammography. N Engl J Med. 1976;295:259–60.
5. Davis PS, Wechsler RJ, Feig SA, March DE. Migration of breast biopsy localization wire. AJR Am J Roentgenol. 1988;150:787–88.
6. Homer MJ. Transection of the localization hooked wire during breast biopsy. AJR Am J Roentgenol. 1983;141:929–30.
7. Montrey JS, Levy JA, Brenner RJ. Wire fragments after needle localization. AJR Am J Roentgenol. 1996;167:1267–69.
8. Smith LF, Henry-Tillman R, Harms S, Hronas T, Mancino AT, Westbrook KC, et al. Hematoma–directed ultrasound-guided breast biopsy. Ann Surg. 2001;233(5):669–75.
9. Arentz C, Baxter K, Boneti C, Henry-Tillman R, Westbrook K, Korourian S, et al. Ten-year experience with hematoma-directed ultrasound-guided (HUG) breast lumpectomy. Ann Surg Oncol. 2010;17:S378–83.
10. Larrieux G, Cupp JA, Lian J, Scott-Conner CE, Weigel RJ. Effect of introducing hematoma ultrasound-guided lumpectomy in a surgical practice. J Am Coll Surg. 2012;215:237–43.
11. Inui H, Watatani M, Hashimoto Y, Hojo T, Hirai K, Yamato M, et al. Hematoma-directed and ultrasound-guided breast conserving surgery for non palpable breast cancer after mammotome biopsy. Surg Today. 2008;38(3):279–82.
12. Rahman RL, Crawford S, Larkin A, Quinlan R. Superiority of sonographic hematoma guided resection of mammogram only visible breast cancer: wire localization should be an exception-not a rule. Ann Surg Oncol. 2007;14(8):2228–32.
13. Liberman L, Hann LE, Dershaw DD, Morris EA, Abramson AF, Rosen PP. Mammographic findings after stereotactic 14-guage vacuum biopsy. Radiology 1997;203:343–7.
14. Aydogan F, Ozben V, Aytac E, Yilmaz H, Cercel A, Celik V. Excision of nonpalpable breast cancer with indocyanine green fluorescence-guided occult lesion localization (IFOLL). Breast Care (Basel). 2012;7(1):48–51.
15. Luini A, Zurrida S, Galimberti V, Paganelli G. Radioguided surgery of occult breast lesions. Eur J Cancer. 1998;34(1):204–5.
16. Paganelli G, Veronesi U. Innovation in early breast cancer surgery: radio-guided occult lesion localization and sentinel node biopsy. Nucl Med Commun. 2002;23(7):625–7.
17. Bernardi S, Bertozzi S, Londero AP, Gentile G, Giacomuzzi F, Carbone A. Incidence and risk factors of the intraoperative localization failure of nonpalpable breast lesions by radio-guided occult lesion localization: a retrospective analysis of 579 cases. World J Surg. 2012;36(8):1915–21.
18. Sajid MS, Parampalli U, Haider Z, Bonomi R. Comparison of radioguided occult lesion localization (ROLL) and wire localization for non-palpable breast cancers: a meta-analysis. J Surg Oncol. 2012;105(8):852–8.
19. Alderliesten T, Loo CE, Pengel KE, Rutgers EJ, Gilhuijs KG, Vrancken Peeters MJ. Radioactive seed localization of breast lesions: an adequate localization method without seed migration. Breast J. 2011;17:594–601.
20. Van Riet YE, Maaskant AJ, Creemers GJ, van Warmerdam LJ, Jansen FH, van de Velde CJ, et al.

Identification of residual breast tumour localization after neo-adjuvant chemotherapy using a radioactive 125 Iodine seed. Eur J Surg Oncol. 2010;36:164–9.
21. Gray RJ, Pockaj BA, Karstaedt PJ, Roarke MC. Radioactive seed localization of nonpalpable breast lesions is better than wire localization. Am J Surg. 2004;188:377–80.
22. Lovrics PJ, Cornacchi SD, Vora R, Goldsmith CH, Kahnamoui K. Systematic review of radioguided surgery for nonpalpable breast cancer. Eur J Surg Oncol. 2011a;37:388–97.
23. Lovrics PJ, Goldsmith CH, Hodgson N, McCready D, Gohla G, Boylan C, et al. A multicentered, randomized controlled trial comparing radioguided seed localization to standard wire localization for nonpalpable invasive and in situ breast carcinomas. Ann Surg Oncol. 2011b;18:3407–14.
24. McGhan LJ, McKeever SC, Pockaj BA, Wasif N, Giurescu ME, Walton HA, et al. Radioactive seed localization for nonpalpable breast lesions: review of 1000 consecutive procedures at a single institution. Ann Surg Oncol. 2011;18:3096–101.
25. Diego EJ, Soran A, McGuire KP, Costellic C, Johnson RR, Bonaventura M, et al. Localizing high-risk lesions for excisional breast biopsy: a comparison between radioactive seed localization and wire localization. Ann Surg Oncol. 2014;21(10):3268–72. doi:10.1245/s10434-014-3912-2.
26. Murphy JO, Moo TA, King T, Van Zee KJ, Villegas KA, Stempel M, et al. Radioactive seed localization compared to wire localization in breast-conserving surgery: initial 6-month experience. Ann Surg Oncol. 2013;20:4121–7.
27. Dauer LT, Thornton C, Miodownik D, Boylan D, Holahan B, King V, et al. Radioactive seed localization with 12I for nonpalpable lesions prior to breast lumpectomy and/or excisional biopsy: metholodogy, safety and experience of initial year. Health Phys. 2013;105(4):356–65.
28. Hughes JH, Mason MC, Gray RJ, McLaughlin SA, Degnim AC, Fulmer JT, et al. A multi-site validation trial of radioactive seed localization as an alternative to wire localization. Breast J. 2008;14(2):153–7.
29. Jakub JW, Gray RG, Degnim AC, Boughey JC, Gardner M, Cox CE. Current status of radioactive seed localization of non palpable breast lesions. Am J Surg. 2010;199(4):522–8.
30. Ahmed M, Douek M. ROLL versus RSL: toss of a coin? Breast Cancer Res Treat. 2013;140:213–7. 2–5.
31. Postma EL, Koffijberg H, Verkooijen HM, Witkamp AJ, van den Bosch MA, van Hillegersberg R. Cost-effectiveness of radioguided occult lesion localization (ROLL) versus wire-guided localization (WGL) in breast conserving surgery for non-palpable breast cancer: results from a randomized controlled multicenter trial. Ann Surg Oncol. 2013;20(7):2219–26.
32. Butler-Henderson K, Lee AH, Price RI, Waring K. Intraoperative assessment of margins in breast conserving therapy: a systemic review Breast. 2014;23(2):112–9.
33. Jacobson AF, Asad J, Boolbol Sk, Osborne MP, Boachie-Adjei K, Feldman SM. Do additional shaved margins at the time of lumpectomy eliminate the need for re-excision? Am J Surg. 2008;196:556–8.
34. Mook J, Klein R, Kobbermann A, Unzeitig A, Euhus D, Peng Y, et al. Volume of excision and cosmesis with routine cavity shave margins technique. Ann Surg Oncol. 2012;19:886–91.
35. Coopey SB, Buckley JM, Smith BL, Hughes KS, Gadd MA, Specht MC. Lumpectomy cavity shaved margins do not impact re-excision rates in breast cancer patients. Ann Surg Oncol. 2011;18(11):3036–40.
36. Schnabel F, Boolbol SK, Gittleman M, Karni T, Tafra L, Feldman S, et al. A randomized prospective study of lumpectomy margin assessment with use of margin probe in patients with nonpalpable breast malignancies. Ann Surg Oncol. 2014;21:1589–95.

Intraoperative Breast Imaging and Image-Guided Treatment Modalities

19

Arthur G. Lerner and Eric B. Whitacre

History

The status of breast lesion localization performed peri and intraoperatively by qualified breast and general surgeons has been heavily influenced by the sometimes contentious debate over which specialty—radiology or surgery—should be performing these and other image-guided breast procedures [1].

The debate began in the early 1990s, when surgeons expressed an interest in performing stereotactic breast biopsies. That interest gave birth to some legislative efforts to prevent surgeons from performing these procedures. The American Society of Breast Surgeons was actually started with the help of a grant that was to be used to counter proposed legislation in Texas that would have prevented surgeons from utilizing stereotactic technology. California also created an arduous pathway for surgeons to gain privileges and be credentialed in stereotactic breast biopsies.

Besides these legislative efforts, there were numerous reports of surgeons being denied privileges to perform these procedures in the centers and hospitals in which they worked. Eventually, third-party payers in a number of states began to withhold reimbursement for surgeons performing image-guided breast procedures.

Striving to ensure proper training for surgeons, the American Society of Breast Surgeons and the American College of Surgeons developed a series of didactic and hands-on courses that allowed surgeons to develop the imaging skills necessary to perform image-guided breast interventions.

In a separate attempt to prevent surgeons from utilizing the stereotactic technology, the FDA's National Mammography Quality Assessment and Advisory Committee debated developing regulation limiting stereotactic breast procedures to radiologists alone. The American Society of Breast Surgeons, the American College of Surgeons, the American Society of General Surgeons, and the Society of Surgical Oncology all testified before the Advisory Board effectively arguing that well-trained surgeons could safely and effectively perform stereotactic breast biopsies. One of the deciding factors in the Advisory Committee's decision to defer regulating stereotactic biopsies was that the American Society of Breast Surgeons had developed certification programs for surgeons in breast ultrasound and stereotactic breast biopsies as well as starting a database that in part recorded and reviewed image-guided procedures [2].

As more breast and general surgeons became certified in breast ultrasound, ultrasound-guided biopsies, and stereotactic breast biopsies, there was a natural evolution to employ these skills during

E. B. Whitacre (✉)
The Breast Cancer Center of Southern Arizona, 6288 East Grant Road, Tucson AZ 85712, USA
e-mail: ewhitacre@gmail.com

A. G. Lerner
Medical Tech Consultants, 10428 SW Lands End PL, Palm City FL 34990, USA
e-mail: aglerner@aol.com

Y. Fong et al. (eds.), *Imaging and Visualization in The Modern Operating Room,*
DOI 10.1007/978-1-4939-2326-7_19,

the peri and intraoperative periods to localize nonpalpable breast lesions scheduled for excision [3].

Part I: Intraoperative Breast Imaging

Intraoperative Ultrasound-Guided Wire and Nonwire Localizations

The ability to surgically manage nonpalpable breast abnormalities depends upon localizing the abnormality within the breast allowing the surgeon to excise the tissue in question without the advantage of being able to palpate the lesion. [4] Traditionally, the localization procedure was performed in a radiology suite using mammography to guide the insertion of one or more wires into the breast close to or within the targeted tissue (Fig. 19.1).

With the expansion of breast ultrasound into the operating room, nonpalpable sonographically visible nodular densities can be localized under ultrasound guidance by the surgeon as part of the operative procedure (Fig. 19.2).

Availability of echo visible tissue markers placed within the lesion at the time of an image-

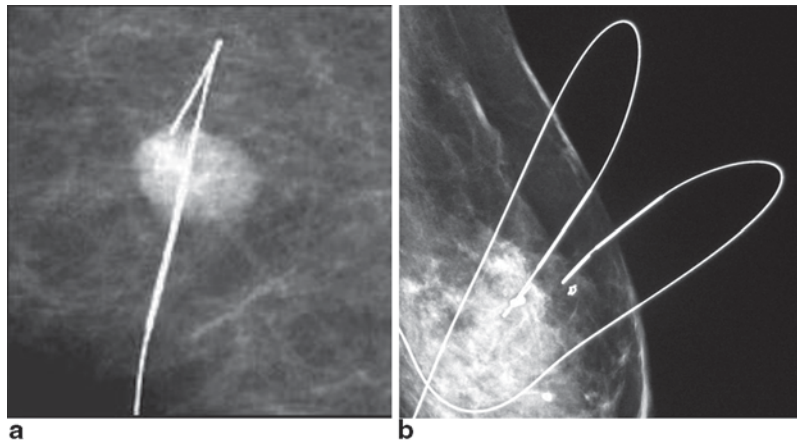

Fig. 19.1 Single-wire mammographic localization for a nonpalpable lesion prior to widespread use of routine preoperative needle biopsy. Today, most wire localizations are for lesions that have already undergone percutaneous needle biopsy with placement of biopsy markers

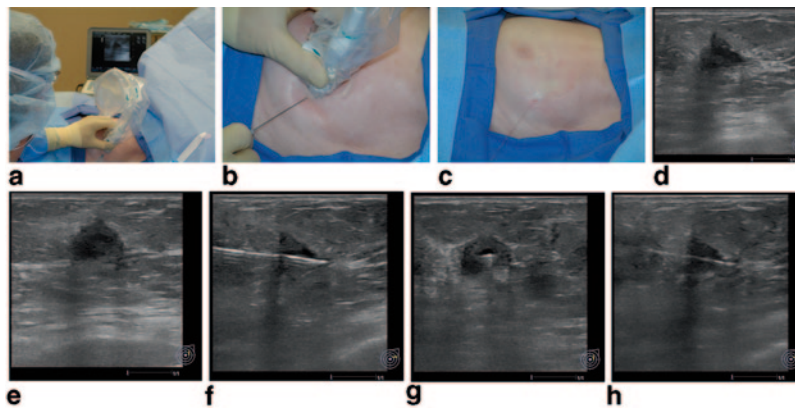

Fig. 19.2 Ultrasound-guided wire localization can be performed in the operating room with numerous advantages to the patient and the surgeon. These figures show the ultrasound localization procedure and corresponding images prior to lumpectomy. Note orthogonal views of the localization wire within the targeted lesion

guided procedure made it possible to utilize ultrasound as the imaging technology for the localization procedure [5]. No longer is it routinely necessary to localize clusters of abnormal calcifications by mammography. Placement of echogenic tissue markers at the time of stereotactic biopsy makes many of these areas amenable to intraoperative localization (Fig. 19.3).

More recently, a technique to insert radioactive seeds to localize nonpalpable breast lesions has been developed utilizing a 4.5×0.8 mm titanium seed labeled with I–125 [6]. The seed is placed percutaneously in a manner similar to placing a wire for localization, most commonly the day before surgery. Intraoperatively a gamma detector is used to guide the surgical procedure. The half-life of the seed is such that the seed can be placed up to 5 days before the procedure (Fig. 19.4).

Additional techniques have been described to provide targets for intraoperative localization, including localization of the post biopsy hematoma, and charcoal injected into the lesion or perilesional tissue [7, 8]. Enhancements to ultrasound units available in the operating room, including higher resolution probes with the addition of spatial compounding, also make it possible to localize traditional biopsy markers, not previously well seen on ultrasound.

For solid lesions visible on ultrasound, the need to place wires to guide the surgeon to a nonpalpable abnormality may be avoided by simply performing an ultrasound over the lesion using orthogonal views. If the lesion is centered on the ultrasound image in both projections and the transducer position on the skin is marked, the point at which the two projections cross each other, that point on the skin is directly above the abnormality. Using this technique often combined with ultrasound images obtained during the procedure itself, the ultrasound skilled surgeon can remove a solid nonpalpable abnormality without inserting wires (Fig. 19.5).

For surgeons skilled in breast ultrasound any of the described localization procedures can now move from the radiology suite to the operating room where the surgeon performs the localization. This creates numerous advantages for both the patient and the operating team. The surgeon, a familiar face to the patient, is now performing the procedure. This lessens patient anxiety and introduces the opportunity to use conscious sedation in combination with local anesthesia administered under ultrasound guidance—a technique not available in the radiology suite.

In addition, performing the localization in the operating room eliminates any potential scheduling difficulty in the radiology suite that could lead to a delay in the operating room schedule.

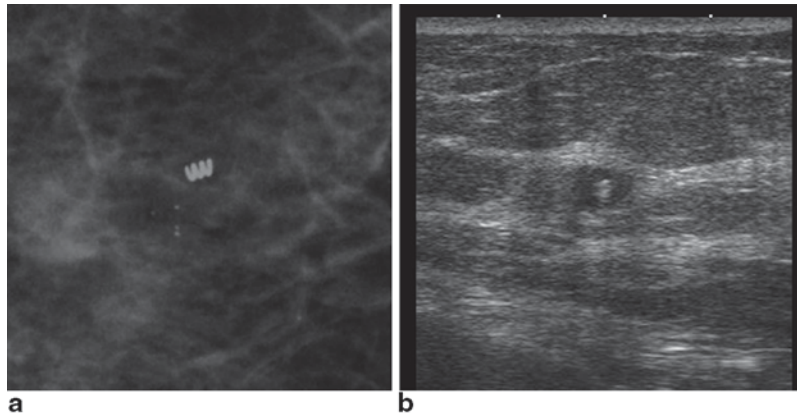

Fig. 19.3 An ultrasound visible (water-soluble polyethylene glycol-based hydrogel) biopsy marker as seen on mammogram and ultrasound

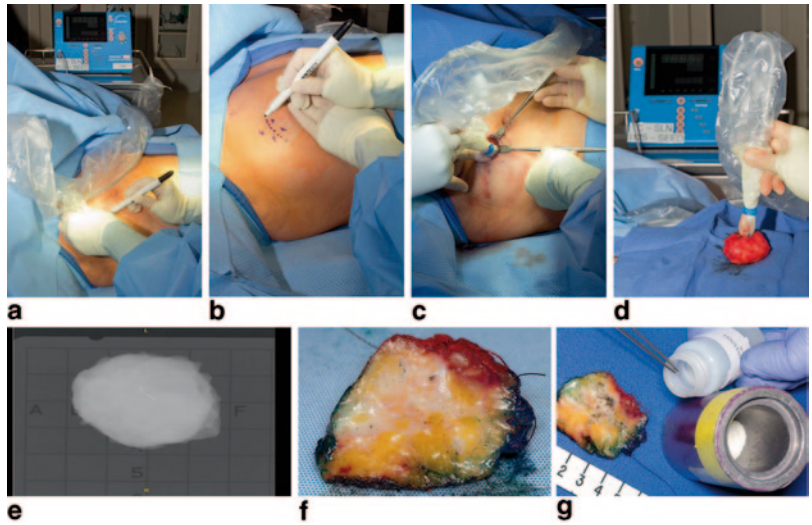

Fig. 19.4 A handheld gamma probe is first used to locate the I–125 radioactive seed previously inserted under image guidance. The probe is used continuously during the procedure to guide the dissection. X-ray of the specimen confirms the seed within the center of the lumpectomy specimen. Once the specimen has been inked for orientation, the seed is recovered. (Courtesy of Richard Gray, MD and Barbara Pockaj, MD)

Intraoperative X-ray of Imaged Localized Specimens

The challenges of managing nonpalpable breast imaging abnormalities include not only the need to employ some form of lesion localization, but also to document that the targeted abnormality has in fact been excised. This has been recognized since the 1980s [9].

The importance of documenting that the nonpalpable targeted lesion has been excised is clearly emphasized through the work of the American Society of Breast Surgeons, now resulting in the incorporation of this important confirmatory step into the Centers for Medicare and Medicaid Services Physician Quality Reporting System (PQRS) quality measures [10].

Initially, confirmation that the targeted abnormality was included in the resected specimen was performed using a specimen radiograph, interpreted by a radiologist in the radiology suite, who then communicated to the operating surgeon whether the targeted area was in the resected specimen. While this was effective, particularly if the specimen was X-rayed in two orthogonal views, it was time-consuming and resulted in delays in the surgical procedure.

As early as 1979, dedicated specimen imaging systems became clinically available. This resulted in higher definition imaging, and if the technology was located in the operating suite, decreased the time to confirm the adequacy of the excision [11, 12]. In addition, the recent improvements in the quality of the new dedicated imaging systems can be helpful in determining the need for directed margin excision. While this has not yet been documented in prospective studies, it proves very useful in the hands of a busy clinical surgeon [13] (Fig. 19.6).

Intraoperative Ultrasound as an Adjunct to Margin Assessment

The reduction and local recurrence rates when the resected malignant tumor does not approach the surgical margin of a lumpectomy have been well documented. As a result, surgeons strive to get free margins when performing breast-preserving procedures for invasive and noninvasive malignancies.

What constitutes an adequate surgical margin has been vigorously debated. Reviewing the

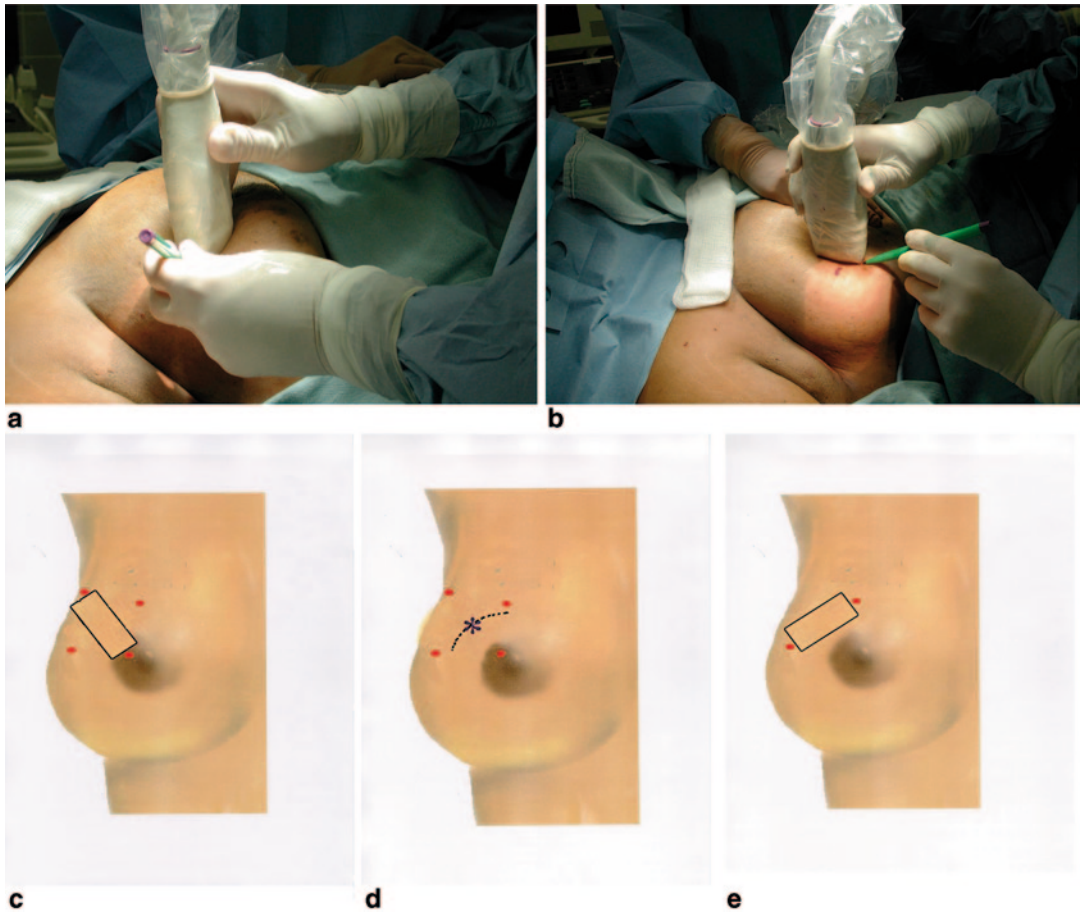

Fig. 19.5 Wire insertion may be avoided by simply performing ultrasound imaging using orthogonal views directly over the lesion. (Courtesy of Howard Snider, MD)

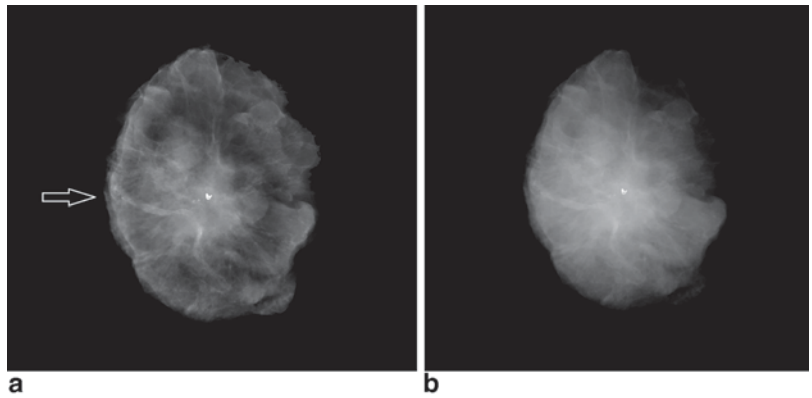

Fig. 19.6 Intraoperative specimen imaging using a high-quality digital unit shows stranding extending toward the medial margin of the specimen. Additional lumpectomy margins were excised at the time of surgery resulting in final negative margins. Compare detail relative to a standard-specimen X-ray

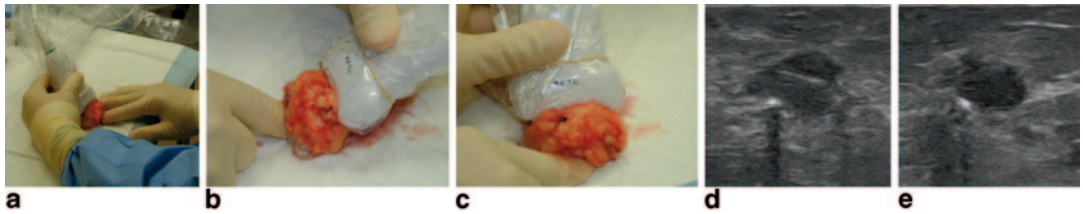

Fig. 19.7 Ex vivo scan of the lumpectomy specimen. Margins are individually imaged to assess for adequacy. Note location of the localization wire in the first view

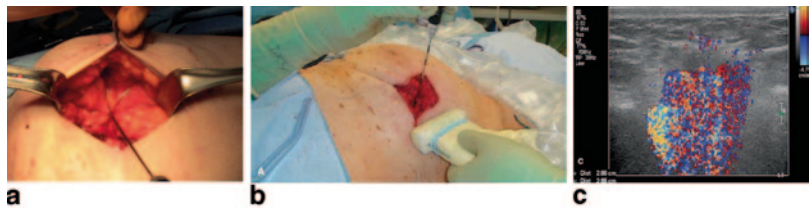

Fig. 19.8 Device placement into lumpectomy cavity under direct vision, with subsequent intraoperative ultrasound monitoring of the RF ablation of the lumpectomy margins (using power Doppler)

literature data suggesting that a larger negative margin reduces local recurrence rates is lacking [14, 15]. There is a growing consensus that returning to the National Surgical Adjuvant Breast and Bowel Project (NSABP) no ink on tumor is the standard that should now be applied for invasive cancer lumpectomies [16].

For lesions clearly visible on ultrasound, the ultrasound adept surgeon can use this technology to guide the resection and evaluate the gross adequacy of the margins about the resected abnormality [17]. When compared to traditional surgery guided strictly by palpation without imaging, use of intraoperative ultrasound contributes to better margin assessment, and reduces surgical re-excision for involved margins [18, 19].

Ex vivo orthogonal ultrasound images of the resected tissue provide the surgeon with a gross estimate of the tissue around the resected abnormality. In addition, the distance between the lesion and the skin or the chest wall can be evaluated with intraoperative scanning. Combined with other margin assessment techniques the number of patients having to return to the operating room as a result of involved margins can be reduced [20, 21] (Fig. 19.7).

Intraoperative ultrasound is also useful in monitoring intraoperative ablative procedures. Radiofrequency ablation of the lumpectomy cavity at the time of lumpectomy is still being pioneered. Percutaneous image-guided radio frequency (RF) ablation of small breast cancers was first reported in 1999 [22]. The technique utilizes real-time ultrasound for placement of the RF probe within the tumor. The RF energy causes molecules within the tumor to vibrate, creating surface friction when molecules move against one another. The heat generated by the surface friction is the energy that causes cell necrosis.

More recently, RF energy has been utilized post lumpectomy to treat margins and reduce local recurrence risk. Following placement of a probe under direct vision, intraoperative ultrasound is used to monitor intra cavity hyperthermia with RF energy, creating a 1 cm circumferential tumor-free zone. A multicenter trial is now underway to assess the long-term results of RF ablation of lumpectomy cavity margins [23] (Fig. 19.8).

Advantages of Intraoperative Ultrasound from the Patient Perspective

The anxiety and overall psychological stress that many women experience when faced with a surgical breast biopsy has been well documented

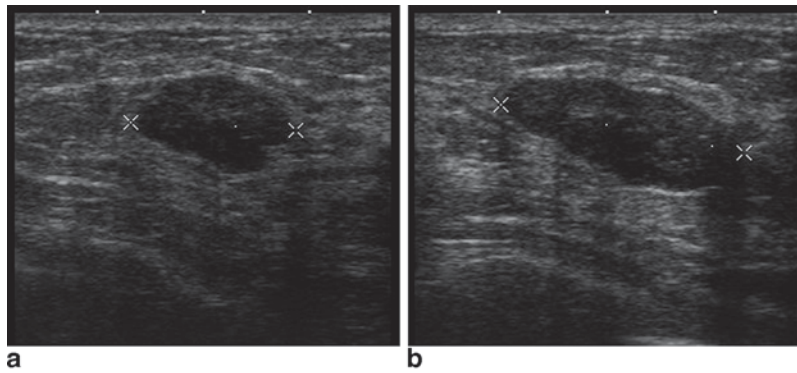

Fig. 19.9 Palpable fibroadenoma imaged in two orthogonal views

[24, 25, 26]. When preoperative needle localization is required for the procedure, anxiety levels may increase [27]. Seventy percent of women who undergo preoperative wire localization with mammography guidance experience moderate to severe pain. Approximately 7% experience vasovagal episodes [28].

Performing the localization procedure in the operating room immediately prior to surgery provides an opportunity to accomplish this procedure under conscious sedation with local anesthesia or, if the patient chooses, under general anesthesia. This approach may significantly lessen or eliminate the anxiety that accompanies the localization procedure.

An additional potential benefit for the patient of having the surgeon perform the localization is that the patient knows the surgeon, likely has great confidence in the surgeon, and this may well produce less concern and anxiety than having a similar procedure performed by someone unknown to the patient in an environment that eliminates the option of using conscious sedation as an adjunct to local anesthesia.

Part II: Image-Guided Breast Procedures—Extension into the Clinic

Development of new percutaneous and transcutaneous therapies of benign and malignant breast disease is one of the most important reasons for breast surgeons to develop expertise in image-guided procedures. Just as laparoscopic and robotic technology has transformed general surgery, minimally invasive image-guided breast procedures promise to radically change care of patients with breast disease.

Percutaneous Excision of Benign and High-Risk Lesions

The availability of large-bore vacuum-assisted devices has made it possible to remove all palpable and all image evidence of benign lesions. This is easily performed in the office setting under local anesthesia and offers multiple advantages for the patient: It avoids an incision, and the cost and discomfort of anesthesia and surgery. This technique has been shown to be successful for removal of fibroadenomas up to 3 cm in size with no residual palpable mass in 98% of patients at 6 months and very high patient satisfaction [29] (Fig. 19.9–19.11).

Additional experience supports use of these devices for percutaneous removal more complex entities such as benign papillomas, which had, until recently, routinely required surgical excision following simple Tru-cut needle biopsy with only partial removal of the lesion. A new generation of devices has been developed that permit percutaneous removal of intact tissue specimens comparable to excisional biopsies. These have been shown to be successful in accurate evaluation of high-risk pathology lesions (e.g., atypical ductal and lobular hyperplasia) with no signifi-

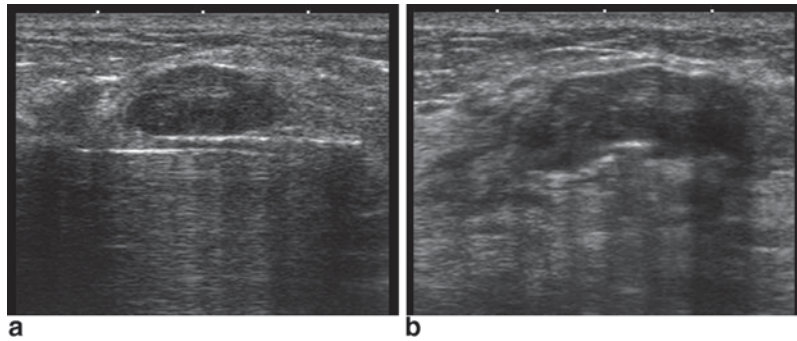

Fig. 19.10 Eight-gauge vacuum-assisted biopsy device positioned deep to the lesion in the same orthogonal views ensuring appropriate positioning

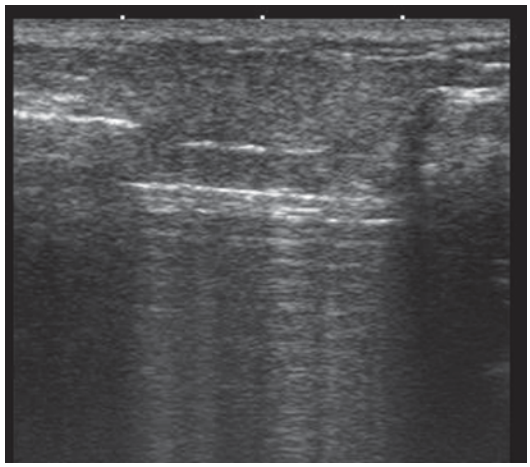

Fig. 19.11 Sonographic appearance following complete excision of imaged abnormality showing only the biopsy trough in the biopsy device (15 cores total from an eight-gauge biopsy device)

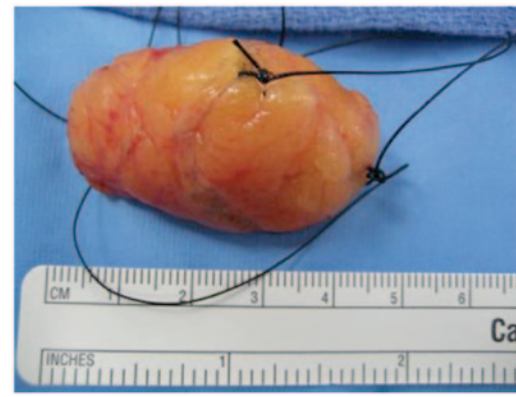

Fig. 19.12 Intact specimen from a percutaneous large-loop radio-frequency-assisted excision. (Courtesy of Richard Fine, MD)

cant upstaging to cancer as occurs with smaller, fragmented biopsy specimens [30] (Fig. 19.12).

Catheter Insertion for Accelerated Partial Breast Irradiation

While brachytherapy for post lumpectomy treatment of breast cancer has been available for many decades, the traditional "tube and button" technique is complex and difficult to perform. Accelerated partial breast irradiation (APBI) became widely available only with the development of indwelling catheters placed in the lumpectomy cavity. The first-generation catheters, which consisted of spherical balloons, were placed either in surgery or postoperatively using ultrasound guidance to position the catheter within the seroma cavity. Newer multicatheter devices allow for more tailored radiation dosing and mean that more patients are candidates for this technique.

While "spacers" have been developed to place within a lumpectomy cavity at the time of surgery, delayed placement of these newer devices under ultrasound guidance remains the preferred technique. This allows for the patient to recover without a foreign body in the lumpectomy while the final lumpectomy margins and sentinel node pathology are being processed. In addition, ultrasound assessment of the seroma cavity allows for

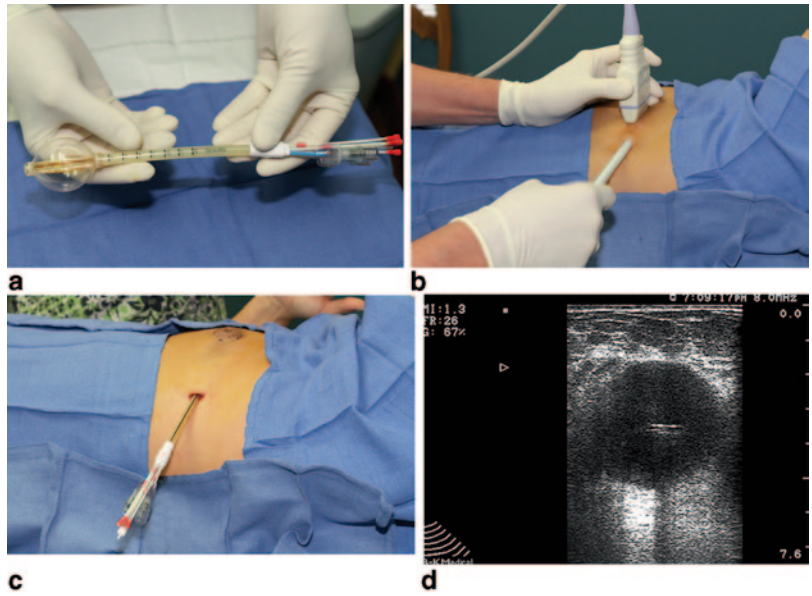

Fig. 19.13 Delayed insertion of a partial breast irradiation catheter performed in the clinic after post lumpectomy pathology showed negative margins and sentinel lymph nodes. (Courtesy of Victor Zannis, MD)

better assessment of the catheter size and direction of insertion, and permits a good initial assessment of skin spacing and conformance (Fig. 19.13).

Percutaneous and Transcutaneous Ablation Techniques

A variety of ablative technologies have been attempted for treatment of both benign and malignant breast disease. These include cryotherapy, interstitial laser therapy, radiofrequency ablation, high-intensity focused ultrasound (HIFU) and focused microwave thermotherapy. Of these, both cryoablation and laser ablation are FDA approved for the treatment of fibroadenomas and have specific current procedural terminology (CPT) procedure codes. Based on the results of published clinical experience and phase II clinical trials, several phase III clinical trials have been started to study their use in the treatment of breast cancer.

Cryoablation of Benign and Malignant Breast Tumors

Cryoablation of fibroadenomas performed in the clinic under ultrasound guidance is an established technique with well-documented efficacy in reducing the size of lesions up to 4 cm in diameter with high patient satisfaction [31, 32, 33]. A small handheld cryoprobe is inserted in the lesion under ultrasound guidance using local anesthesia, and a freeze-thaw cycle determined based on the tumor size is used for the ablation. Advantages of the technique include ready ultrasound visualization of the ice ball as it develops and minimal patient discomfort. Occasional patients will require excision of a persistent palpable mass.

Based on the clinical success with management of benign tumors, initial pilot and feasibility studies for the treatment of breast cancer showed complete ablation of 52–100% for tumors ranging from T1 to T3 in size. Results of a recent multiinstitutional phase 2 clinical trial

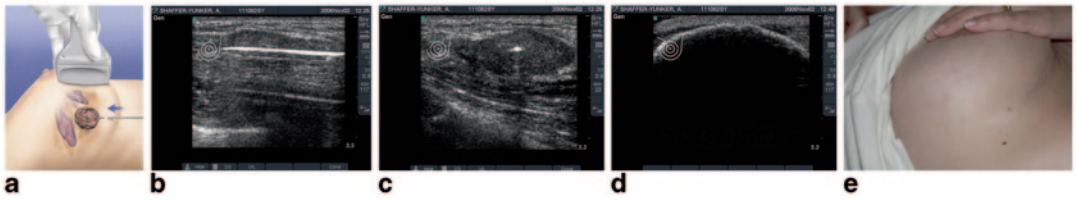

Fig. 19.14 Placement of a cryotherapy catheter and creation of an ice-ball that is easily visualized under continuous ultrasound monitoring. Cosmetic results, as with most percutaneous procedures, are excellent months following the procedure. (Courtesy of Deanna Attai, MD)

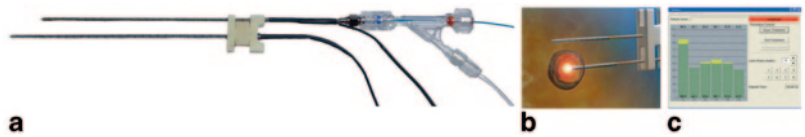

Fig. 19.15 Laser fiber and adjacent thermal probe with the artist's interpretation of the ablation procedure. The physician monitors temperature at the five thermistors; the procedure is complete when all five have reached 60 °C. (Courtesy of Novian Health Inc.)

demonstrated that for patients with tumors 1 cm or less, the ablation rate was 94 % [34]. Patient selection was important in determining the success of the procedure, which was less in patients with tumors > 1 cm or with significant ductal carcinoma in situ (DCIS). MRI following the procedure was essential in predicting the success of the procedure and will likely become a critical component in evaluating the success of cryoablation procedures in the future [35] (Fig. 19.14).

Two new phase III clinical trials have since been launched to further study the role of cryoablation for breast cancer, both utilizing ultrasound guidance for the procedure, and with imaginative titles that are appropriately suggestive of the intended effect: ICE-BREACCER [36] and FROST [37].

Laser Ablation of Benign and Malignant Breast Tumors

Interstitial laser ablation of breast lesions has paralleled the development of cryoablation, beginning first with successful demonstration of efficacy for fibroadenomas, followed by pilot series documenting success in ablation of breast cancer [38, 39].

Laser thermoablation can be performed under ultrasound, stereotactic or MRI guidance. Ultrasound guidance is the most convenient for both the patient and the physician, but other modalities may broaden applicability of the procedure. Once the lesion has been localized, a laser fiber is inserted percutaneously with an adjacent temperature probe and the lesion ablated (Fig. 19.15, 19.16).

Various laser fibers and protocols have been shown to successfully achieve cell death over the defined spherical volume—most involve heating the targeted area to 60 °C for several minutes. As with cryoablation, patient selection for the procedure is critical as only a defined volume of tissue is ablated. Post ablation imaging, especially MRI, is also critical in determining whether there is any viable tumor remaining, allowing those patients to undergo post ablation lumpectomy.

There is currently an international multiinstitutional single-arm phase III clinical trial evaluating the safety and efficacy of laser ablation in

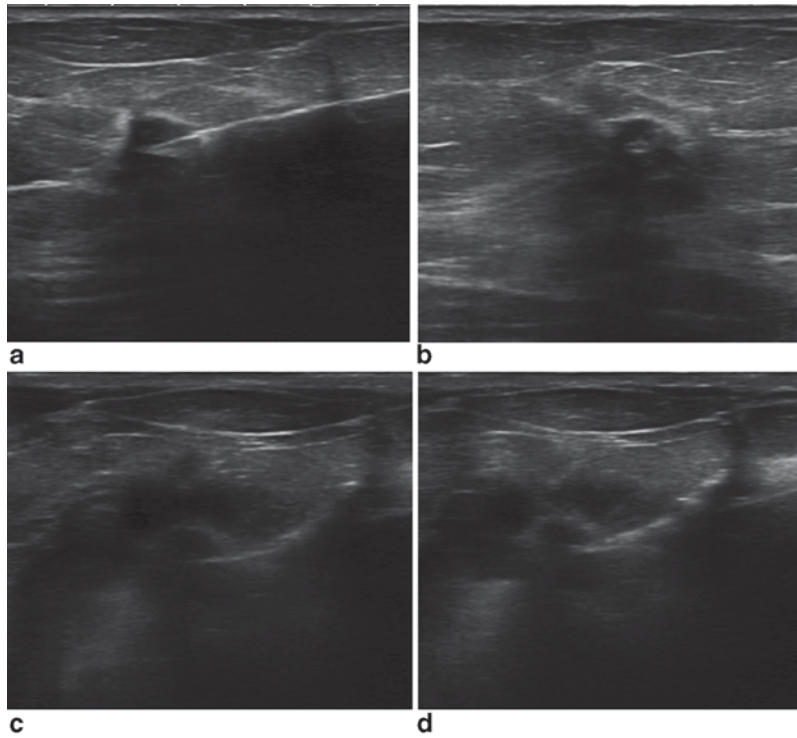

Fig. 19.16 Ultrasound-guided placement of a laser fiber into a small infiltrating ductal carcinoma, showing appropriate location of the laser tip in orthogonal views. Subsequent images show progressive ablation of the tumor and a rim of surrounding tissue. (Courtesy of Mike Shere, MD, Bristol, UK and Novian Health Inc.)

selected breast cancer patients with primary lesions up to 2 cm in diameter [40].

High-Frequency Ultrasound Transcutaneous Ablation

The percutaneous treatment of benign and malignant tumors using image-guided high-intensity focused ultrasound (HIFU) has been well documented [41]. The largest experience with this technique appears to be in treatment of uterine fibroids [42], although it has also been used to ablate liver lesions and prostate cancer. The percutaneous treatment of fibroadenomas of the breast has also been reported. This technology has also been applied to the percutaneous treatment of invasive breast cancer. MRI and ultrasonography are the imaging techniques utilized when percutaneously treating lesions with HIFU [43, 44].

Applying HIFU to the treatment of breast lesions has a potential advantage over other ablative technologies in that it is completely noninvasive with the energy being delivered percutaneously to ablate the chosen abnormality.

A unique technology that combines conventional ultrasound with HIFU in a module that allows the physician to plan control and monitor the ablation in real time has been developed [45]. A procedure performed under local anesthesia, with or without conscious sedation in the clinic, this technology has been successfully used in the treatment of fibroadenomas without lesion recurrences or regrowth followed out over two years (Figs. 19.17–19.19).

Summary

The remarkable advances in imaging technologies that has occurred over the past several decades has afforded the surgeon caring for breast patients a unique opportunity to utilize these imaging technologies in the operating room envi-

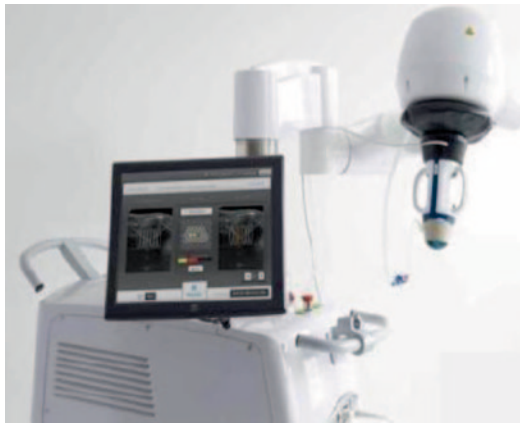

Fig. 19.17 Echopulse, a technology that combines B mode ultrasound with high-frequency ultrasound ablative technology. (Courtesy of Theraclion, Inc.)

ronment, and has allowed some surgical procedures to be moved to the clinic setting.

The transition from film-based imaging to digital imaging and the portability of many of the modern imaging technologies has given the surgical community a unique opportunity for hands-on participation in many of the diagnostic modalities previously available only in imaging centers. Many of these imaging technologies will become the cornerstone of new noninvasive or minimally invasive therapies for in situ and invasive breast cancers.

It is therefore imperative that surgeons caring for breast patients continue to develop the necessary skills to appropriately incorporate breast imaging technology into their practices.

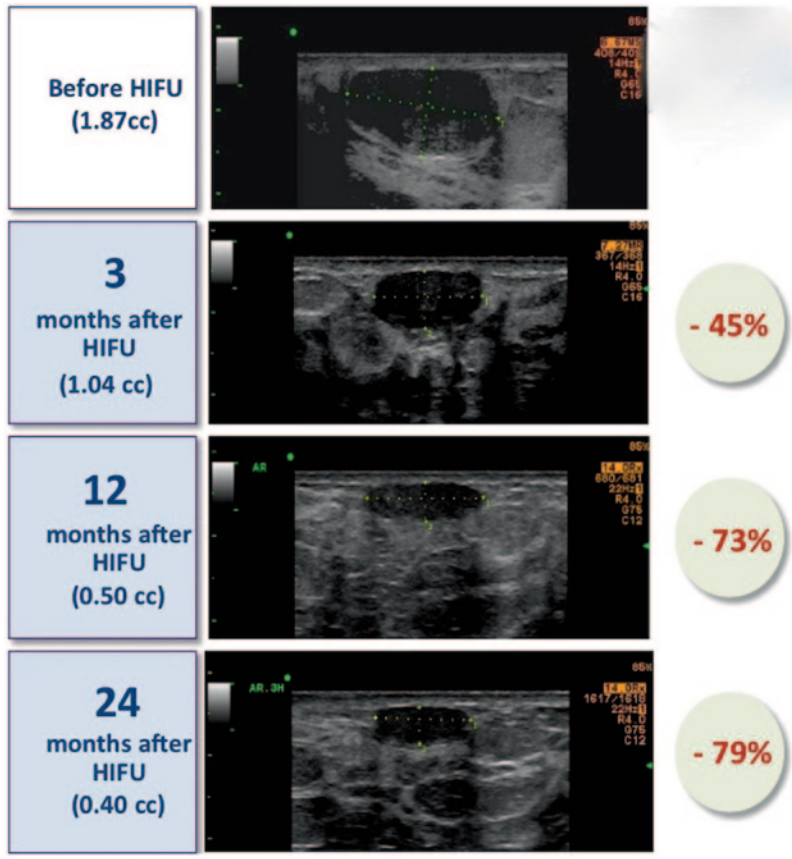

Fig. 19.18 High-frequency ablation of a biopsy-proven fibroadenoma with Echopulse demonstrating sequential reduction in volume during a 2-year followup. (Courtesy of Theraclion)

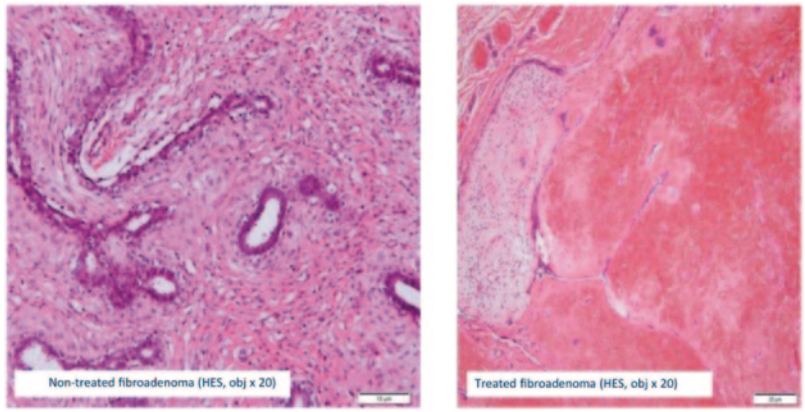

Fig. 19.19 Photomicrograph of a core needle biopsy of a fibroadenoma and the same fibroadenoma following high-frequency ultrasound-guided ablation utilizing Echopulse. (Courtesy of Theraclion)

References

1. Axis Imaging News, Nov. 4, 1999, http://www.axisimagingnews.com/1999/11/the-battle-over-the-breast/. Accessed February 1, 2015.
2. https://www.breastsurgeons.org/new_layout/programs/certification/index.php. Accessed 25 May 2014.
3. Fornage BD, Ross IM, Singletary SE, Paulus DD. Localization of impalpable breast masses: value of sonography in the operating room and scanning of excised specimens. Am J Roentgenol. 1994;163(3):569–73.
4. Burkholder HC, Witherspoon LE, Burns RP, Horn JS, Biderman MD. Breast surgery techniques: preoperative bracketing wire localizations by surgeons. Am Surg. 2007;73(6):574–8.
5. Klein RL, Mook JA, Euhus DM, Rao R, Wynn RT, Eastman AB, et al. Evaluation of a hydrogel based breast biopsy marker (HydroMARK®) as an alternative to wire and radioactive seed localizations for non-palpable breast lesions. J Surg Oncol. 2012;105(6):591–4.
6. Gray RJ, Pockaj BA. Breast surgery after radioactive seed localization. In: Bland KI, Klimberg VS. Breast surgery. New York: Walters Kluwer; 2011. pp 147–53.
7. Arentz C, Baxter K, Boneti C, Henry-Tillman R, Westbrook K, Korourian S, et al. Ten-year experience with hematoma-directed ultrasound-guided (HUG) breast lumpectomy. Ann Surg Oncol. 2010;17(Suppl 3):378–83.
8. Rose A, Collins JP, Neerhu P, Bishop CV, Mann GB. Carbon localization of impalpable breast lesions. Breast. 2003;12(4):264–9.
9. Letton AH, Mason EM. The treatment of nonpalpable carcinoma of the breast. Cancer. 1980;46(4 Suppl):980–2.
10. Imaging conformation of successful excision of image-localized breast lesion. Centers for Medicare and Medicaid Services, PQRS Quality measure #262. https://pqrspro.com/Image_Confirmation_of_Successful_Excision_of_Image-Localized_Breast_Lesion. Accessed 25 May 2014.
11. Kürzl R, Baltzer J, Lohe KJ. Intraoperative specimen radiography in mammographically suspect, non-palpable breast lesions. Experience with faxitron unit. Fortschr Med. 1979;97(38):1688–90.
12. Muttalib M, Tisdall M, Scawn R, et al. Intra-operative specimen analysis using faxitron microradiology for excision of mammographically suspicious, non-palpable breast lesions. Breast. 2004;13(4):307–15.
13. Author's personal experience (Eric Whitacre MD).
14. Revesz E, Khan SA. What are safe margins of resection for invasive and in situ breast cancer? Oncology (Williston Park). 2011;25(10):890–5.
15. Morrow M. Breast conservation and negative margins: how much is enough? Breast. 2009;18(Suppl 3):S84–6.
16. Houssami N, Morrow M. Margins in breast conservation: a clinician's perspective and what the literature tells us. J Surg Oncol. 2014;110(1):2–7.
17. de Paredes ES, Langer TG, Cousins J. Interventional breast procedures. Curr Probl Diagn Radiol. 1998;27(5):133–84.
18. Eggermann H, Ignatov T, Costa SD, Ignatov A. Accuracy of ultrasound-guided breast-conserving surgery in determination of adequate surgical margins. Breast Cancer Res Treat. 2014;145(1);129–36.
19. Eggermann H, Ignatov T, Beni A, Costa SD, Innatov A. Ultrasonography-guided breast-conserving surgery is superior to palpation-guided surgery for palpable breast cancer. Clin Breast Cancer. 2014;14(1):40–5.
20. Andarita FA, Nadler A, Zerhouni S, Escallon J. Perioperative measures to optimize margin clearance in breast conserving surgery. Surg Oncol. 2014 Jun;23(2):81-91.

21. Schnabel F, Boolbol S, Gittleman M, et al. A randomized study of lumpectomy margin assessment with use of margin probe in patients with nonpalpable breast malignancies. Ann Surg Oncol. 2014;21(5):1589–95.
22. Jeffrey SS, Birdwell RL, Ikeda DM, Daniel BL, Nowels KW, Dirbas FM et al. Radiofrequency ablation of breast cancer: first report of an emerging technology. Arch Surg 1999;134(100M):1064–68.
23. Klimberg VS, Ochoa D, Henry-Tillman R, Hardee M, Boneti C, Adkins LL, et al. Long-term results of phase II ablation after breast lumpectomy added to extend intraoperative margins (ABLATE l) trial. J Am Coll Surg. 2014;218(4):741–9.
24. Hughson AV, Cooper AF, McArdle CS, Smith DC. Psychosocial morbidity in patients awaiting breast biopsy. J Psychosom Res. 1988;32:173–80.
25. Northouse LL, Tocco KM, West P. Coping with a breast biopsy: how healthcare professionals can help women and their husbands. Oncol Nurs Forum. 1997;24 (3):473–80.
26. Northouse LL, Jeffs M, Cracchiolo-Caraway A, Lampman L, Dorris G. Emotional distress reported by women and husbands prior to a breast biopsy. Nurs Res. 1995;44:196–201. Erratum in: Nurs Res. 1995;44(6):382.
27. Vlymem JM. Benzodiazepine premedication: can it improve outcome in patients undergoing breast biopsy procedures? Anesthesiology. 1999;90(3):740–7.
28. Cancer Guide: http://cancerguide.org/jane_story.html. Created Sept 2012. Accessed 25 May 2014.
29. Fine RE, Whitworth PW, Kim JA, Harness JK, Boyd BA, Burak WE Jr. Low-risk palpable breast masses removed using a vacuum-assisted hand-held device. Am J Surg. 2003;186(4):362–7.
30. Whitworth PW, Simpson JF, Poller WR, Schonholz SM, Turner JF, Phillips RF, et al. Definitive diagnosis for high-risk breast lesions without open surgical excision: the intact percutaneous excision trial (IPET). Ann Surg Oncol. 2011;18(11):3047–52.
31. Hahn M, Pavlista D, Danes J, Klein R, Golatta M, Harcos A, et al. Ultrasound guided cryoablation of fibroadenomas. Ultraschall Med. 2013;34(1):64–8.
32. Littrup PJ, Freeman-Gibb L, Andea A, White M, Amerikia KC, Bouwman D, et al. Cryotherapy for breast fibroadenomas. Radiology. 2005;234(1):63–72.
33. Kaufman CS, Littrup PJ, Freeman-Gibb LA, et al. Office-based cryoablation of breast fibroadenomas with long term follow-up. Breast J. 2005;11(5):344–50.
34. ACOSOG-Z1072, http://www.cancer.gov/clinicaltrials/search/view?cdrid=600976&version=healthprofessional. Accessed 25 May 2014.
35. https://www.breastsurgeons.org/new_layout/annual_meeting2014/press_invite.php. Accessed 25 May 2014.
36. Cryotherapy for Breast Cancer Trial (ICE-BREACCER), http://clinicaltrials.gov/ct2/show/NCT01671943?term=cryotherapy+and+%22breast+cancer%22&rank=6. Accessed 25 May 2014.
37. Cryoablation of Small Breast Tumors in Early Stage Breast Cancer (FROST), http://clinicaltrials.gov/ct2/show/NCT01992250?term=cryotherapy+and+%22breast+cancer%22&rank=9. Accessed 25 May 2014.
38. Basu S, Ravi B, Kant R. Interstitial laser hyperthermia, a new method in the management of fibroadenoma of the breast: a pilot study. Lasers Surg Med. 1999;25(2):148–52.
39. Dowlatshahi K, Wadhwani S, Alvarado R, Valadez C, Dieschbourg J. Interstitial laser therapy of breast fibroadenomas with 6 and 8 year follow-up. Breast J. 2010;16(1):73–6.
40. A multicenter "Ablate and Resect" study of Novilase® interstitial laser therapy for the ablation of small breast cancers, http://clinicaltrials.gov/ct2/show/NCT01478438?term=novilase&rank=1. Accessed 25 May 2014.
41. Jenne JW, Preusser T, Günther M. High-intensity focused ultrasound: principles, therapy guidance, simulations and applications. Z Med Phys. 2012;22(4):311–22.
42. Cheung VY. Sonographically guided high-intensity focused ultrasound for the management of uterine fibroids. J Ultrasound Med. 2013;32(8):1353–8.
43. Merckel LG, Bartels LW, Köhler MD, et al. MR-guided high intensity focused ultrasound ablation of breast cancer with a dedicated breast platform. Cardiovasc Intervent Radiol. 2013;36(2):292–301.
44. Roubidoux MA, Yang W, Stafford RJ. Image-guided ablation in breast cancer treatment. Tech Vasc Inter Radiol. 2014;17(1):49–54.
45. "Echopulse" by Theraclion. http://www.theraclion.com/. Accessed 25 May 2014.

Sentinel Lymph Node Mapping: Current Practice and Future Developments

20

V. Suzanne Klimberg and Evan K. Tummel

Anatomy

Historically, lymph node groups are designated based on anatomical location. The axillary vein group is located superior and lateral to the axilla and runs along the axillary vein. However, these nodes may course lower below the vein as much as 3–4 cm, as an apron of nodes, or as a linear chain of nodes. It has always been taught that these lymph nodes receive most of the lymph draining from the upper extremity. The external mammary or anterior or pectoral groups are located at the border of the pectoralis minor muscle in association with the lateral thoracic vessels. These are the primary lymph nodes receiving lymph drainage from the breast. The scapular or posterior or subscapular group, located posteriorly in the axilla is closely associated with the subscapular vessels. These lymph nodes drain the posterior region of the neck and the posterior aspect of the shoulder region. Collectively, these nodes are termed level I nodes. The central group nodes, located posteriorly to the pectoralis minor group along with the interpectoral nodes of Rotter's nodes comprise the level II axillary nodes. The subclavicular or apical group, located medially to the pectoralis minor muscle and extending to the apex of the axilla, are considered level III nodes. These nodes receive lymph from all the other groups of axillary lymph nodes and become the lymphatics forming the thoracic duct on the left and on the right, the right lymphatic duct (Fig. 20.1). In addition to the axillary nodes, the breast lymph also drains into internal mammary nodes located retrosternal between the costal cartilages commonly to the second and third intercostal spaces approximately 2–3 cm lateral to the sternal margin.

Until recently, the lymphatic drainage of the arm was not considered when removing lymph nodes. The majority of draining lymphatics from the distal arm enter the axilla along the volar surface of the upper arm [1]. Axillary reverse mapping (ARM) maps the drainage of the arm as it traverses the axilla. Figure 20.2 demonstrates that this anatomy varies substantially from the traditional teaching, that the arm lymphatics course within a centimeter of the axillary vein (Fig. 20.2).

Indication for Staging Lymph Nodes and Development of SLNB

The current practice of staging the axilla varies widely, but for the clinically node-negative patient with invasive ductal cancer, should almost always include a sentinel lymph node biopsy (SLNB). The primary route of lymphatic drainage

V. Suzanne Klimberg (✉)
Winthrop P. Rockefeller Cancer Institute,
4301 W Markham, slot 725, Little Rock, AR 72212, USA
e-mail: klimbergsuzanne@uams.edu

E. K. Tummel
Department of Surgery, University of Arkansas | for Medical Sciences, Little Rock, AR, USA
e-mail: ETummel@gmail.com

Y. Fong et al. (eds.), *Imaging and Visualization in The Modern Operating Room,*
DOI 10.1007/978-1-4939-2326-7_20,

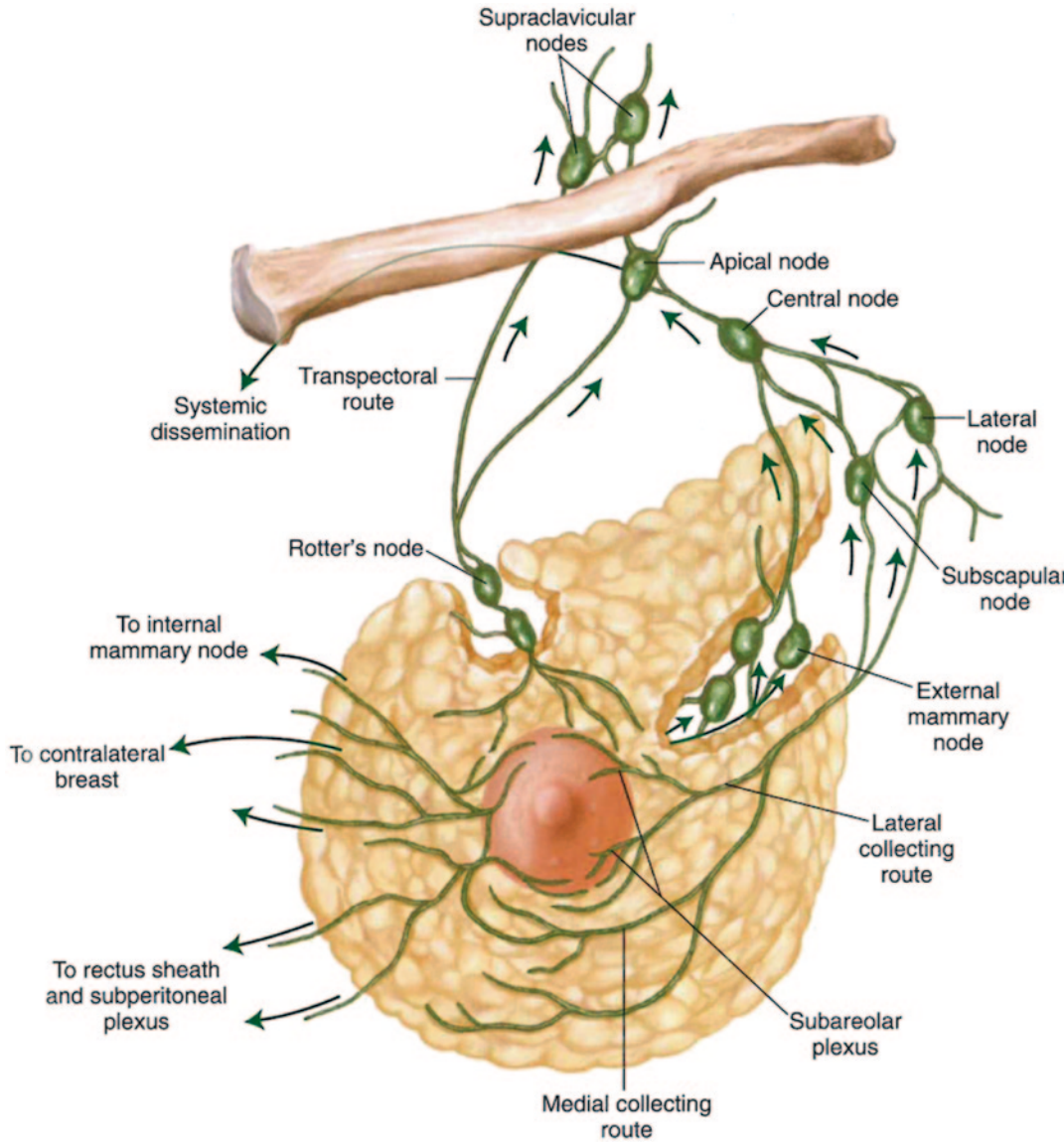

Fig. 20.1 Lymphatic drainage of the breast [33]

of the breast is through the axillary lymph nodes with more than 75 % of the lymph from the breast passing to the axillary lymph nodes [2]. Separate lymphatic drainage pathways for the breast and the upper extremity as well as the back can run side by side when crossing the axilla. It has also been demonstrated that the lymphatic drainage is highly variable between subjects. Only in a small percentage of cases (<5 %) the lymphatic drainage of the breast and the arm completely overlap [3]. SLNB should be considered in clinically node-negative patients T1–3 regardless of multicentricity who have not had previous axillary surgery. It may also be useful in patients with aggressive large (>2.5 cm) ductal carcinoma in situ [4]. Axillary status in breast cancer patients continues to serve as a major predictor of outcome while also influencing decisions for adjuvant therapy.

The potential sequele of axillary lymphadenectomy includes local sensory dysfunction, reduced shoulder mobility, and lymphedema. Ranging

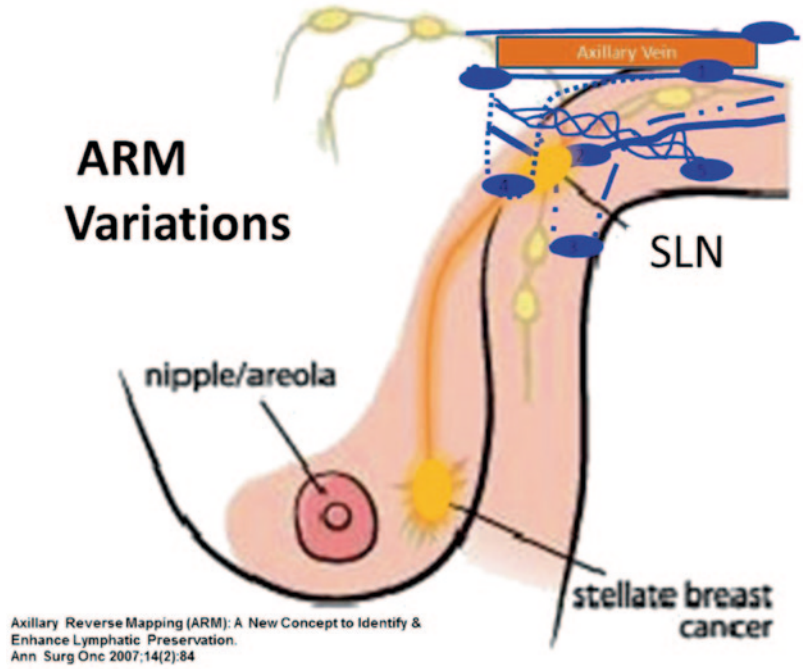

Fig. 20.2 Variations in the lymphatics draining the arm as they course through the axilla [31]

from 13 to 77 % after axillary lymph node dissection (ALND), lymphedema is the patient's most dreaded side effect of axillary surgery adversely affecting quality of life, job performance, and health-care costs. SLNB was designed to ameliorate the morbidity of ALND while still offering accurate staging of the patient. Despite the less invasive dissection, reported lymphedema rates for SLNB still range from 0 to 13 %, with larger studies reporting a range of 7–8 %.

Many different variations in mapping technique have been described. Type and number of agents, including dual versus single agents have been researched, as well as the site and timing of the material that is injected (i.e., injectate).

Agents

SLNB was originally described by Krag et al. with unfiltered 99m Technetium sulfur colloid (Tc99) [5, 6, 7] which has been validated in multiple studies and has become the gold standard with or without blue dye. Variations of Tc99 using filtered or unfiltered or as a nanocolloid in a human albumin base have also been used. Radioactive handling difficulties and potential radiation exposure have led to a plethora of ways to map lymph nodes without radioactivity.

Giuliano et al. first reported the use of isosulfan blue dye for mapping SLNB in breast cancer [8]. Since that time, other blue dyes used have included patent blue dye, which is the gold standard in the UK and Europe as opposed to its isomer isosulfan blue which is mainly used in the USA [9]. Increasingly, many countries have been using diluted methylene blue for SLNB as it is a cheaper alternative and more readily available although more caustic with higher reported local reactions and necrosis. Indigo carmine is also used primarily in Asia for SLNB with reportedly good localization rates [10]. The main drawbacks to blue dye are major allergic reactions, which occur with less than 1 % frequency but have resulted in death [11].

Recently, studies have used a Lymphoseek (technetium Tc99m tilmanocept) injection for subcutaneous, intradermal, subareolar, or peritumoral use. Lymphoseek with 0.5 mCi of radioactivity is given at least 15 min to within 15 h prior to SLNB [12]. In this small study, 13 centers contributed 148 patients given Lymphoseek and vital blue dye with a 99 % concordance rate.

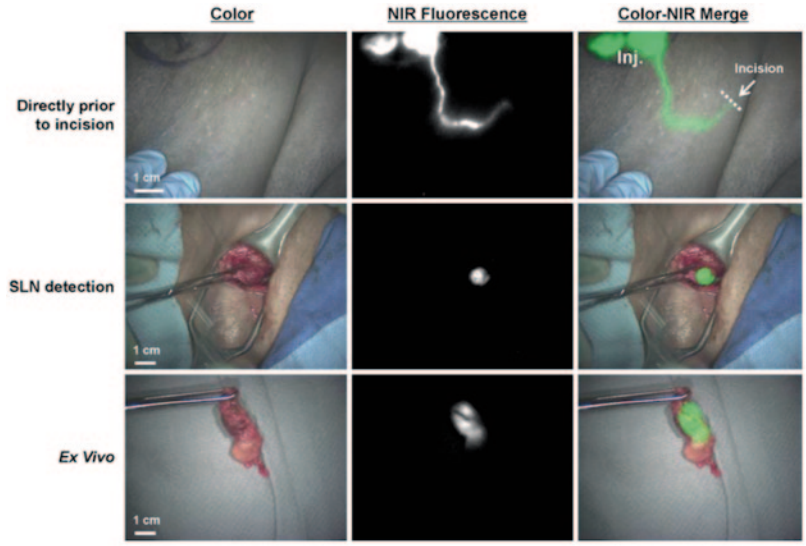

Fig. 20.3 Near-infrared (NIR) fluorescence-guided sentinel lymph node (SLN) mapping. The *top row* shows percutaneous NIR identification of afferent lymphatic channels flowing away from the injection site (*Inj.*). The planned incision site, based on the presumed location of the SLN, is shown as a *dashed line*. *Middle row:* real-time fluorescence identification of the SLN directly after incision. *Bottom row:* ex vivo image of the SLN. Scale bars 1 cm. Camera exposure times were 150 ms (*upper row*), 55 ms (*middle row*), and 50 ms (*bottom row*) [14]

Fluorescent dyes in particular isocyanogreen dye (ICG) have been used for SLNB, particularly in Asia. Until recently, ICG was used only experimentally when a handheld device (PDE®, Hamamatsu, Japan) to image near-infrared fluorescence attained Food and Drug Administration (FDA) approval and began to be marketed in the USA [13]. ICG mapping can be seen through the skin but tends to map to more nodes than other agents (Fig. 20.3) [14].

Recently, magnetic particles (superparamagnetic iron oxide, SPIO) have been used for sentinel lymph node (SLN) localization in the SentiMag study which compared SPIO to radioguided localization. This prospective multinational noninferiority study demonstrated a similar detection rate with the magnetic tracer (Sienna+®, Endomagnetics, Basel, Switzerland) and a handheld magnetometer, the SentiMag®. A similar average number of SLNs was detected and a higher per patient malignancy detection rate was found for the SPIO tracer [15]. The technique is straightforward and there is no associated radioactivity. SPIO is not FDA approved for SLNB in the USA.

As of yet the optimal size of particles and volume of injectate is not settled and will be the reason for further development of methods and tracers for SLN mapping.

Site and Timing of Injections

A plethora of studies have been generated describing various sites of injection including peritumoral, subareola, dermal, subdermal, and intratumoral [16]. Even the timing of injection has come under scrutiny with studies performing the injection of radioactive colloid anywhere from 30 min to 24 h preoperatively. Most recently, studies have described intraoperative injection of technetium, which can be performed dermally or in the subareolar complex with great success and accuracy and with the added advantage of being painless for the patient, avoiding vasovagal episodes and avoiding scheduling coordination issues with the operating room. In a study of 699 patients, intraoperative injection of Tc99 identified 98.6% of SLNs, 100% of intraoperative dermal injections (only used in six patients

with upper outer breast scars) and dual tracer with isosulfan blue dye in 94.8% [17].

Lymphoscintigraphy before SLNB is not uniformly performed and is of questionable value in mapping the breast [18]. Klauber-deMore et al. reviewed 13 studies in which lymphoscintigraphy was performed. The lymphoscintigram mapped to the internal mammary node (IMN) in 12.7% (0–35%) of patients. Eight of the studies report on IMN status and showed an18% IMN positivity (15/83 patient). In five studies that evaluated lymphoscintigraphy mapping, only 2 of 15 patients had positive IMN when the axilla was negative. In addition, techniques other than peritumoral injection map to these nodes even less [19, 20].

In cases where there is potential for significant drainage to the internal mammary vessels we recommend ultrasound (US) of the second and third intercostal spaces for visualization of suspicious internal mammary nodes.

When the breast fails to map additional injection of saline (20–40 cc) can be performed with massage to increase chances of mapping. When no SLN is found, ALND is performed [21].

Mapping of Multicentric Lesions

The drainage of the breast seems to be more important than the location of the tumor and thus localization of the SLN [22]. Within the EORTC 10981−22023 (AMAROS) trial the SLN was identified in 96% of patients with known multicentric tumors and 98% with unifocal tumors demonstrating an expected higher rate of positivity with multicentric disease (51%) compared to 28% in the unifocal group [23]. Importantly, the percentage of nonsentinel nodes were similar in each group, 40 and 39%, respectively.

Mapping After Neoadjuvant Chemotherapy

At this time, there is no consensus whether and when to perform a SLNB in patients receiving neoadjuvant chemotherapy. It has been shown that about 40% of known positive lymph nodes are converted to negative with chemotherapy and advocates of SLNB after chemotherapy point out that these patients could be spared an ALND. However, reported false negative SLNB rates after neoadjuvant chemotherapy are higher than those performed before systemic chemotherapy [24]. Dual mapping is recommended as the results of the ACOSOG Z1071 (Alliance) clinical trial study demonstrated improved sensitivity with radioactive and blue dye mapping [25].

Axillary Recurrence After a Negative SLNB

There have been seven randomized controlled trials demonstrating that patients with negative SLNs do not require ALND despite the known ~10% false negative rate. The rate of axillary recurrence is referred to as the clinical false negative rate. Van der Ploeg and colleagues performed a systematic review and meta-analysis of axillary recurrence in SLNB negative breast cancer patients [26]. In 48 studies encompassing 14,959 SLN negative breast cancer patients followed for a median of 34 months, 0.3% of patients had an axillary recurrence with the highest sensitivity rates and lowest recurrence rates seen with Tc99, superficial versus deep injections and the use of immunohistochemistry staining.

Completion ALND with Positive Nodes

In 2011, Giuliano et al. reported on the ACOSOG Z-0011 trial including patients with tumors smaller than 3 cm and a clinically node-negative axilla. Patients, who had one or two positive nodes at SLNB, were randomized to breast conservation therapy (BCT) with completion ALND or BCT with no further treatment of the axilla. The study did not accrue all its patients and may be underpowered. However, at 6.3 years median follow-up no statistically significant difference was found in regional recurrence or survival. Details of the radiation fields have not been reported, but by protocol axillary radiation was not

planned. Multiple small retrospective articles totaling 1035 patients with positive SLNB and no ALND report less than 2% axillary recurrence with 28–82-month follow-up [27]. In general, Europe has been less accepting of these data than the USA where many surgeons have stopped doing ALND under Z-0011 criteria.

Failure of Mapping

Technical factors including surgical experience and the 20–30 cases that it takes to become proficient in SLN mapping are the only ones that surgeons can predict and control. Dual versus single injection can aid the novice in locating SLNs. The inexperienced surgeon can validate his technique with a completion ALND. Palpation as well as intraoperative US of the axilla can help locate nodes that have low counts and are hard to find as well as nodes with high tumor burden that did not take up the radioactivity or blue dye or were just a technical miss (took up the dye but were not located by the surgeon) [28].

Factors that cause false negative SLNB and therefore not under control of the operator are tumor/patient factors including large size, upper outer location, older and obese patients, lobular or poorly differentiated ductal histology or partial to complete replacement of non-SLN with tumor and larger tumor size [29, 30].

Axillary Reverse Mapping

ARM has been described by Klimberg and colleagues as a technique to identify and separate the lymphatic drainage of the arm from that of the breast in an attempt to minimize unnecessary disruption of the arm lymphatics [31, 32, 33]. It is useful for ALND as well as SLNB, allowing visualization and protection of the arm lymphatics during lymphadenectomy, resulting in significantly reduced postoperative lymphedema while maintaining oncologic safety. It involves injection of blue dye in the upper inner volar surface of the arm simultaneously with breast lymphatic mapping. When performing SLNB, blue

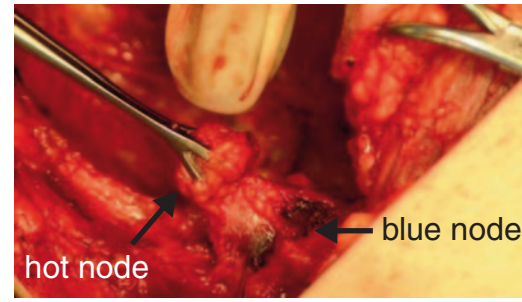

Fig. 20.4 Hot radioactive node in Babcock being dissected free from the blue nonradioactive arm node

lymphatics can be seen in ~30% of patients and during an ALND greater than 70% of the time. In ~10% of patients, the ARM node was separate but juxtaposed to the SLN and therefore potentially in harm's way if not distinguished by the blue dye (Fig. 20.4). When non-SLN blue nodes were resected, the positivity rate was low as were follow-up regional recurrence rates. Lymphedema for SLNB was less than 1% and ALND lymphedema rates were less than 6%, which compares favorably with national studies. When blue nodes are resected, the remaining lymphatics are reanastomosed end-to-end, which results in a very low lymphedema rate.

Boccardo and colleagues have developed what is called lymphatic microsurgical preventing healing approach the so-called LYMPHA procedure. This is basically performing a lympho-venous anastomosis after excision of the node rather than anastomosing end to end [34]. Lympho-venous anastomosis of the lower arm has also been used for moderately successful reversal of lymphedema.

No Surgical Staging

Recurrence scores from genomic assays on the primary tumor provide a quantitative estimate of the risk of distant recurrence and reveal the underlying tumor biology that traditional measures such as patient age, tumor size, and tumor grade, cannot provide. The recurrence score does not predict lymph node involvement. In fact lymph node involvement has been shown to be additive

to recurrence scores. Therefore, at this time, prognostic information is still gained by performing an SLNB or even an ALND.

Drawbacks of axillary irradiation without dissection are that pathologic node status is unknown, complexity of matching fields, risk of arm edema, and risk of brachial plexus injury. Recurrence appears to be the same; however, mixed reports indicate that the lymphedema rate might be higher at longer follow-up. Others argue that the omission of ALND would affect the choice of chemotherapy. Preliminary reports from the EORTC AMAROS trial found no difference in use or type of systemic therapy in patients randomized to ALND versus axillary radiation therapy (XRT) [35].

Future Developments

Percutaneous biopsy of SLN is common using US (Fig. 20.5) and avoids taking the patient with a clinically suspicious axilla to the operating room prior to neoadjuvant chemotherapy. However, occult metastases require excision of the lymph node for detection. Kim and colleagues have developed a method using ICG in a rat model and a novel handheld photoacoustic probe for image-guided needle biopsy (Fig. 20.6). Optical fibers are used to deliver pulsed laser light and direct photoacoustic image-guided insertion of a needle into lymph nodes identified by ICG. This highly sensitive method is being tested in the clinic and may provide less invasive staging of micrometastases [36].

Real-time MRI-navigated US may have a role in confirming positive nodes on MRI with much greater sensitivity than second-look US. Real-time US with supine MRI using a volume navigation technique increases the detection and biopsy of positive SLNs [37].

High-resolution, handheld cameras have been developed for nonpalpable breast localization plus SLNB or the so-called SNOLL technique (sentinel node and occult lesion localization) that is common in Europe and beginning to be adopted more widely in the USA [38]. These handheld gamma cameras enable intraoperative scintigraphy in real time.

The development of hybrid single-photon emission computed tomography/computed tomography (SPECT/CT) cameras can increase the precise anatomical localization of SLNB prior to surgery as opposed to scintigraphy. They also may be important in evaluating novel tracers [39].

Eleven quality indicators for the performance of SLNB have been identified based on a consensus of Quan and colleagues [40]. These include: pathologic evaluation protocol, pathologic reporting by AJCC guideline, protocol for injection of radiocolloid, proper identification of SLN, SLNB performance in eligible patients, SLNB concurrent with lumpectomy/mastectomy, completion of ALND for positive SLNB, SLNB performance in ineligible patients, axillary node positivity rate; number of nodes removed; axillary recurrence rate.

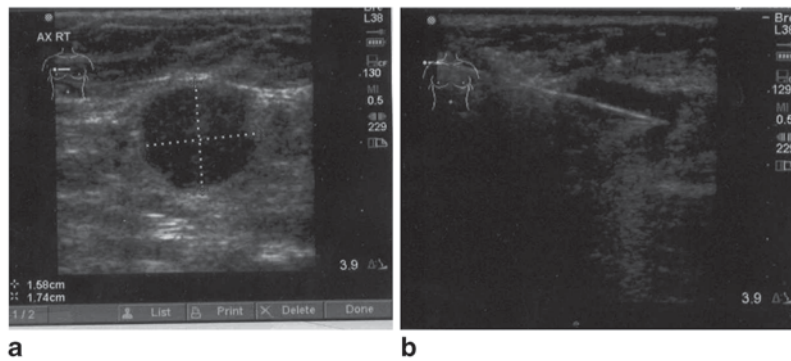

Fig. 20.5 **a** Ultrasound (US) demonstrating a positive node with rounded shape, hypoechoic, and without cortical structure. **b** US-guided needle biopsy to confirm nodal positivity

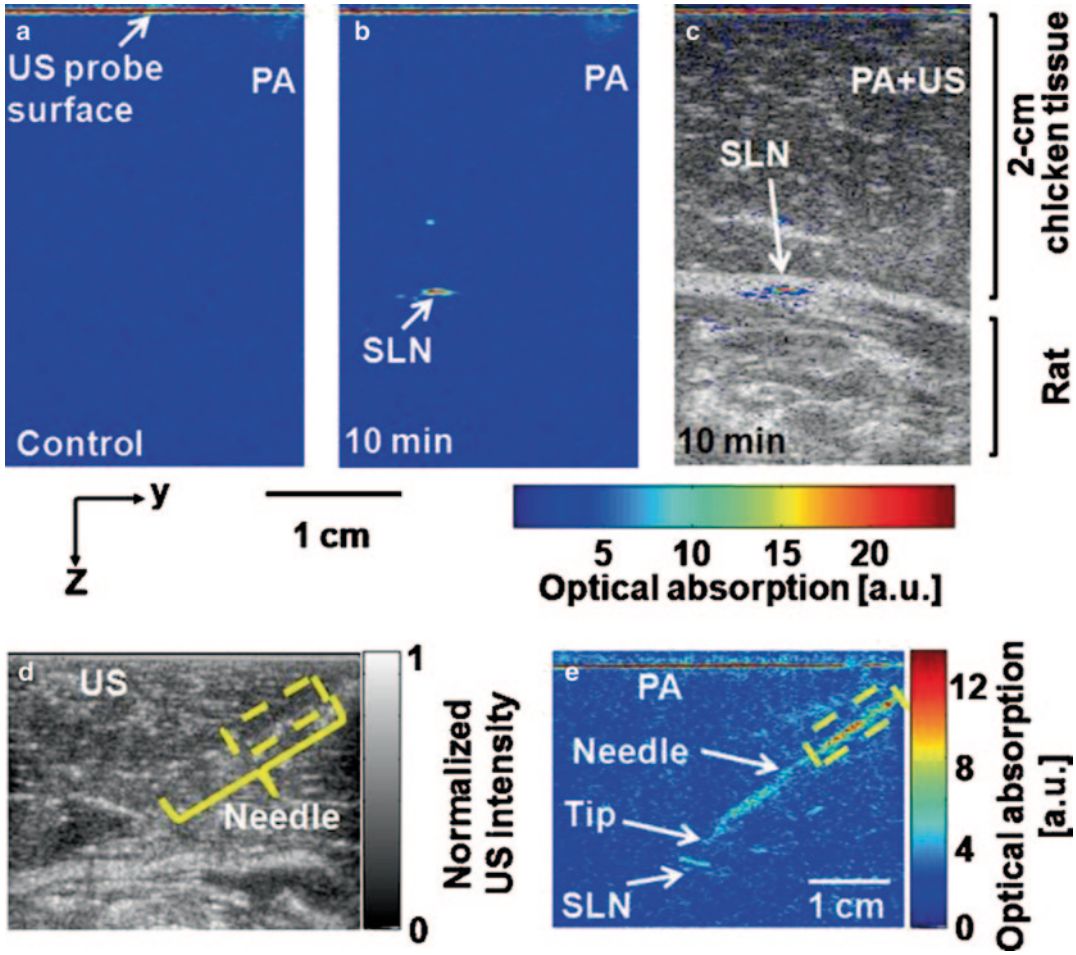

Fig. 20.6 Handheld array-based photoacoustic probe for guiding needle biopsy of SLN In vivo photoacoustic (*PA*) and ultrasound (*US*) B-scan imaging of an sentinel lymph node (*SLN*) dyed with indocyanine green (ICG) and guiding of a biopsy needle: **a** control PA image acquired before ICG injection, **b** PA image taken 10 min after ICG injection, **c** overlaid PA (pseudocolor) and US (*gray* scale) images, **d** US guidance of a biopsy needle, and **e** PA guidance of a biopsy needle. The image contrasts were calculated using the values within the regions of interest indicated by the *yellow dotted boxes* in **d** and **e**. (Color online only.) [36]

Summary

The literature will continue to be showered with various conjugates to Tc-99 and new dyes as well as new scanning devices in an effort to improve detection and accuracy of SLNB. At this time SLNB remains an important addition to hormonal and genomic information on tumors, however, as oncogenomics becomes more accurate SLNB may become obsolete.

References

1. Földi M. Remarks concerning the consensus document (CD) of the international society of lymphology The diagnosis and treatment of peripheral lymphedema. Lymphology. 2004;37(4):168–73.
2. Tanis PJ, Nieweg OE, Valdés Olmos RA, Kroon BB. Anatomy and physiology of lymphatic drainage of the breast from the perspective of sentinel node biopsy. J Am Coll Surg. 2001;192(3):399–409.
3. Boneti C, Korourian S, Bland K, et al. Axillary reverse mapping: mapping and preserving arm lymphatics may be important in preventing lymphedema during sentinel lymph node biopsy. J Am Coll Surg. 2008;206(5):1038–42.

4. Donker M, Straver ME, van Tienhoven G, van de Velde CJ, Mansel RE, Litière S, Werutsky G, Duez NJ, Orzalesi L, Bouma WH, van der Mijle H, Nieuwenhuijzen GA, Veltkamp SC, Helen Westenberg A, Rutgers EJ. Comparison of the sentinel node procedure between patients with multifocal and unifocal breast cancer in the EORTC 10981-22023 AMAROS trial: identification rate and nodal outcome. Eur J Cancer. 2013;49(9):2093–100.
5. Krag DN, Weaver DL, Alex JC, Fairbank JT. Surgical resection and radiolocalization of the sentinel lymph node in breast cancer using a gamma probe. Surg Oncol. 1993;2:335–9.
6. Krag D, Weaver D, Ashikaga T, et al. The sentinel node in breast cancer—a multicenter validation study. N Engl J Med. 1998;339:941–6.
7. Krag DN, Anderson SJ, Julian TB, et al. Sentinel-lymph-node resection compared with conventional axillary-lymph-node dissection in clinically node-negative patients with breast cancer: overall survival findings from the NSABP B-32 randomised phase 3 trial. Lancet Oncol. 2010;11(10):927–33.
8. Giuliano AE, Kirgan DM, Guenther JM, Morton DL. Lymphatic mapping and sentinel lymphadenectomy for breast cancer. Ann Surg. 1994;220:391–8.
9. Masannat Y, Shenoy H, Speirs V, et al. Properties and characteristics of the dyes injected to assist axillary sentinel node localization in breast surgery. Eur J Surg Oncol. 2006;32:381.
10. Aihara T, Takatsuka Y. Dye-guided sentinel node biopsy revisited; validation and observational study from a single institute. Breast Cancer. 2003;10:254.
11. Barthelmes L, Goyal A, Newcobe RG, McNeill F, Mansel RE. Adverse reactions to patent blue V dye—the NEW START and ALMANAC experience. Eur J Surg Oncol. 2010;36:399–403.
12. Wallace AM, Han LK, Povoski SP, et al. Comparative evaluation of [(99m)tc]tilmanocept for sentinel lymph node mapping in breast cancer patients: results of two phase 3 trials. Ann Surg Oncol. 2013;20(8):2590–9.
13. Sugie T, Sawada T, Tagaya N, Kinoshita T, Yamagami K, Suwa H, et al. Comparison of the indocyanine green fluorescence and blue dye methods in detection of sentinel lymph nodes in early-stage breast cancer. Ann Surg Oncol. 2013;20(7):2213–18.
14. Verbeek FP, Troyan SL, Mieog JS, Liefers GJ, Moffitt LA, Rosenberg M, et al. Near-infrared fluorescence sentinel lymph node mapping in breast cancer: a multicenter experience. Breast Cancer Res Treat. 2014;143:333–42.
15. Douek M, Klaase J, Monnypenny I, Garmo H, Kothari A, Zechmeister K, et al. The SentiMAG multicentre trial: sentinel node biopsy using a magnetic technique versus the standard technique. Eur Surg Oncol. 2013;39:S85–86
16. Klimberg VS. Axillary sentinel lymph node biopsy. In: Klimberg VS. Atlas of breast surgical techniques Saunders. 1st edn. Philadelphia: Elsevier; 2010. pp. 124–39.
17. Johnson CB, Boneti C, Korourian S, Adkins L, Klimberg VS. Intraoperative injection of subareolar or dermal radioisotope results in predictable identification of sentinel lymph nodes in breast cancer. Ann Surg. 2011;254(4):612–8.
18. Mathew MA, Saha AK, Saleem T, Saddozai N, Hutchinson IF, Nejim A. Pre-operative lymphoscintigraphy before sentinel lymph node biopsy for breast cancer. Breast. 2010;19:28–32.
19. Klauber-DeMore NL, Bevilacqua JL, Van Zee KJ, Borgen P, Cody HS 3rd. Comprehensive review of the management of internal mammary lymph node metastases in breast cancer. J Am Coll Surg. 2001;193(5):547–55.
20. Shimazu K, Tamaki Y, Taguchi T, Motomura K, Inaji H, Koyama H, Kasugai T, Wada A, Noguchi S. Lymphoscintigraphic visualization of internal mammary nodes with subtumoral injection of radiocolloid in patients with breast cancer. Ann Surg. 2003;237(3):390–8.
21. Chagpar AB, Martin RC, Scoggins CR, Carlson DJ, Laidley AL, El-Eid SE, et al. Factors of predicting failure to identify a sentinel lymph node in breast cancer. Surgery. 2005;138:56–63.
22. Layeeque R, Henry-Tillman R, Korourian S, et al. Subareolar sentinel node biopsy for multiple breast cancers. Am J Surg. 2003;186:730–5.
23. Donker M, Straver ME, van Tienhoven G, van de Velde CJ, Mansel RE, Litière S, et al. Comparison of the sentinel node procedure between patients with multifocal and unifocal breast cancer in the EORTC 10981–22023 AMAROS trial: identification rate and nodal outcome. Eur J Cancer. 2013;49(9):2093–100.
24. Kuehn T, Bauerfeind I, Fehm T, et al Sentinel-lymph-node biopsy in patients with breast cancer before and after neoadjuvant chemotherapy (SENTINA): a prospective, multicenter cohort study. Lancet Oncol. 2013;14(7):609–18.
25. Boughey JC, Suman VJ, Mittendorf EA, et al. Sentinel lymph node surgery after neoadjuvant chemotherapy in patients with node-positive breast cancer: the ACOSOG Z1071 (Alliance) clinical trial. JAMA. 2013;310(14):1455–61.
26. Van der Ploeg IM, Nieweg OE, van Rijk MC, Valdes Olmos RA, Kroon BB. Axillary recurrence after a tumour-negative sentinel node biopsy in breast cancer patients: a systematic review and meta-analysis of the literature. Eur Surg Oncol. 2008;34:1277–84.
27. Cyr A, Gao F, Gillanders WE, et al. Disease recurrence in sentinel node-positive breast cancer patients forgoing axillary lymph node dissection. Ann Surg Oncol. 2012;19:3185–91.
28. Chagpar AB, Martin RC, Scoggins CR, Carlson DJ, Laidley AL, El-Eid SE, et al. Factors of predicting failure to identify a sentinel lymph node in breast cancer. Surgery. 2005;138:56–63
29. Krag D, Weaver D, Ashikaga T, et al. The sentinel node in breast cancer—a multicenter validation study. NEJM. 1998;339(14):941–6.

30. Wei S, Bleiweiss IJ, Nagi C, Jaffer S. Characteristics of breast carcinoma cases with false-negative sentinel lymph nodes. Clin Breast Cancer. 2014;S1526–8209(13):00314–5.
31. Thompson M, Korourian S, Henry-Tillman R, Adkins L, Mumford S, Westbrook KC, Klimberg VS. Axillary reverse mapping (ARM): a new concept to identify and enhance lymphatic preservation. Ann Surg Oncol. 2007;14(6):1890–5.
32. Boneti C, Korourian S, Bland K, et al. Axillary reverse mapping (ARM): mapping and preserving arm lymphatics may be important in preventing lymphedema during sentinel lymph node biopsy. J Am Coll Surg. 2008;206:1038–42.
33. Klimberg VS. Axillary sentinel lymph node biopsy. In: Bland KI, Klimberg VS, editors. Mastery techniques in general surgery: breast surgery. 1st edn. New York: Lippincott; 2011. pp. 155–69.
34. Boccardo F, Casabona F, Decian F, Friedman D, Murelli F, Puglisi M, et al. Lymphatic microsurgical preventing healing approach (LYMPHA) for primary surgical prevention of breast cancer-related lymphedema: over 4 years follow-up. Microsurgery. 2014. doi:10.1002/micr.22254.
35. Straver ME, Meijnen P, van Tienhoven G, van de Velde CJ, Mansel RE, Bogaerts J, et al. Role of axillary clearance after a tumor-positive sentinel node in the administration of adjuvant therapy in early breast cancer. J Clin Oncol. 2010;28(5):731–7.
36. Kim CL, Erpelding TN, Maslov K, Jankovic L, Akers WJ, Song L, et al. Handheld array-based photoacoustic probe for guiding needle biopsy of sentinel lymph nodes. J Biomed Opt. 2010;15(4):046010.
37. Pons EP, Azcón FM, Casas MC, Meca SM, Espona JL. Real-time MRI navigated US: role in diagnosis and guided biopsy of incidental breast lesions and axillary lymph nodes detected on breast MRI but not on second look US. Eur J Radiol. 2014;83(6):942–50.
38. Lombardi A, Nigri G, Scopinaro F, Maggi S, Mattei M, Bonifacino A, et al. High-resolution, handheld camera use for occult breast lesion localization plus sentinel node biopsy (SNOLL): a single-institution experience with 186 patients. Surgeon. 2013;S1479–666X(13):00125–X.
39. Gnanasegaran G, Ballinger JR. Molecular imaging agents for SPECT (and SPECT/CT). Eur J Nucl Med Mol Imaging. 2014;41(Suppl 1):S26–35.
40. Quan ML, Wells Bj, McCready D, et al. Beyond the false negative rate: development of quality indicators for sentinel lymph node biopsy in breast cancer. Ann Surg Oncol. 2010;17:579–91.

Narrow Band Cystoscopy

21

Harry W. Herr

Introduction

Bladder tumors are common neoplasms that arise from the bladder mucosa. Bladder tumors also frequently recur, making them prevalent epithelial neoplasms. There are 75,000 new cases of bladder cancer diagnosed each year in the USA and over 500,000 men and women are currently living with the disease. Early detection and timely follow-up care are important because of the high rate of bladder cancer recurrence, and because some tumors may progress to life-threatening bladder wall invasion.

Successful treatment of both primary and recurrent bladder tumors depends on detection, tumor type, tumor extent (stage), and complete local destruction. Each of these critical components comprising diagnosis, treatment and follow-up surveillance is facilitated by endoscopic evaluation, or cystoscopy. Diagnosis including tumor type and stage is made by cystoscopy, and local control is achieved by cystoscopy-guided biopsy and transurethral resection (TUR). Standard cystoscopy uses conventional white light (WL), which is composed of an equal mixture of primary color wavelengths comprising the visible spectrum.

H. W. Herr (✉)
Department of Urology, Memorial Sloan-Kettering Cancer Center, 1275 York Avenue, New York, NY 10021, USA
e-mail: herrh@mskcc.org

Modern cystoscopy began with invention of the first practical cystoscope by Max Nitze in 1877 [1], and has since evolved from wire filaments and incandescent bulbs to fiberoptics, rod lens systems and digital chip cameras. Each technical innovation aimed to bring brighter WL illumination within the bladder, permitting improved recognition of a multitude of maladies, including urothelial tumors. The modern cystoscope is equipped with a charged-coupled device (CCD) or chip placed at the tip of a flexible or rigid instrument. The digital chip collects images in high definition and transmits them to be displayed on a video screen. High quality WL images are created to produce a uniformly sharp and focused magnified picture of the bladder interior and mucosal abnormalities.

In order to detect, diagnose, and remove bladder tumors, they must be visualized by cystoscopy. Most bladder neoplasms are papillary or nodular and are easy to see using white light cystoscopy. However, lateral margins may be obscure, because tumor cells spread out from the base and blend in with normal appearing surrounding bladder mucosa. Papillary tumors may also be small, subtle, hidden in bladder folds, multiple, or occur in clusters resembling normal bladder mucosa that may be overlooked. Nonpapillary neoplasms appear as flat, poorly defined, red patches disguised among normal urothelium, and are commonly overlooked or mistaken for benign inflammatory lesions. Because white light imaging (WLI) cystoscopy sometimes fails to detect

Y. Fong et al. (eds.), *Imaging and Visualization in The Modern Operating Room,*
DOI 10.1007/978-1-4939-2326-7_21, © Springer Science+Business Media New York 2015

all bladder tumors, biopsy and tumor resection may be incomplete, contributing to early and possibly invasive tumor recurrences.

The frequency of "missed lesions" found in random or selected-site biopsies of "normal-appearing" mucosa in bladder tumor patients varies from 8 to 41% [2], and a repeat second biopsy after an initial TUR finds persistent tumors in 14–76% of patients [3]. Additional tumors are found at the same sites in 44–86% of patients and distant sites within the bladder in 14–56%. Because residual tumors are missed by WLI cystoscopy, a new generation of optical methods designed to enhance cystoscopic visualization was developed [4]. These include narrow band imaging (NBI), fluorescence cystoscopy, optical coherence tomography, and confocal endomicroscopy. Only the first two methods have been introduced into clinical practice. The latter are promising new investigational technology. We have had NBI capability available for flexible digital cystoscopy and transurethral tumor resection since 2006, and the author uses both WLI and narrow band cystoscopy to diagnose, evaluate, and treat bladder tumors. This chapter provides a comprehensive review, including visual examples, of NBI cystoscopy.

Narrow Band Cystoscopy

NBI is a novel optical image technology that improves the visibility of blood vessels and bladder mucosa in order to enhance tissue contrast between cancerous and normal bladder epithelium. This makes it an excellent tool for diagnosing bladder cancers during cystoscopy. Urothelial neoplasms are hypervascular owing to microvessel density. NBI exploits angiogenic features of bladder tumors by filtering WL into two discrete bands of light, one blue at 415 nm and one green at 540 nm. Both bands are absorbed by hemoglobin. The shorter wavelength in NBI is 415 nm light, which penetrates only the superficial layers of the mucosa. This is absorbed by superficial capillary vessels and appears brownish on the video image. The second NBI wavelength is 540 nm light, which penetrates deeper into the bladder wall. It is absorbed by blood vessels located deeper in the submucosal layer, and appears green on imaging. Narrow band blue light vividly displays surface mucosal capillaries (brown), which defines capillary dense cancerous lesions within the mucosa. Green light highlights vessels in the submucosa that helps to identify fronds of papillary tumors and to determine submucosal invasion of papillary and solid neoplasms. Bladder tumors are identified by the concentration of brown and green images that contrasts with pink to white normal mucosa.

Figure 21.1 shows the NBI filter technology. The urologist can change the optical filter and switch back and forth between WL and narrow band mode by simply pushing a button on the digital flexible cystoscope or camera head attached to the resectoscope. There is no additional cost to patients over standard cystoscopy. NBI cystoscopy is safe and poses no risks to patients. In contrast to fluorescence cystoscopy, there is no need for intravesical dye or time constraints performing procedures owing to photo-bleaching associated with long dye dwell times, postoperative monitoring, or potential local side effects. NBI may be used on or off anytime during the procedure. Figure 21.2 shows an example of a flexible digital cystoscope and resectoscope camera head equipped with NBI capability, including built-in light-source unit, video processor, and HD TV monitor. Imaging equipment is light, mobile, and ideal for use in inpatient and outpatient operating rooms, procedure rooms, and clinics.

Figure 21.3 shows cystoscopic appearance of normal bladder mucosa by WLI cystoscopy and NBI cystoscopy. NBI highlights delicate network of superficial mucosal capillaries (brown) and the more prominent blood vessels (green) coursing through the submucosa. NBI improves visualization of tumors by enhancing the contrast between well-vascularized lesions and the surrounding pale-yellow or white normal mucosa.

Papillary tumors appear dark green or brownish green on NBI cystoscopy. Figure 21.4 shows a papillary tumor that is distinct from adjacent normal white mucosa. Individual fronds are clearly seen owing to enhanced visualization of submucosal vessels in fibrovascular stalks (dense green) covered by overlying epithelium (pale green).

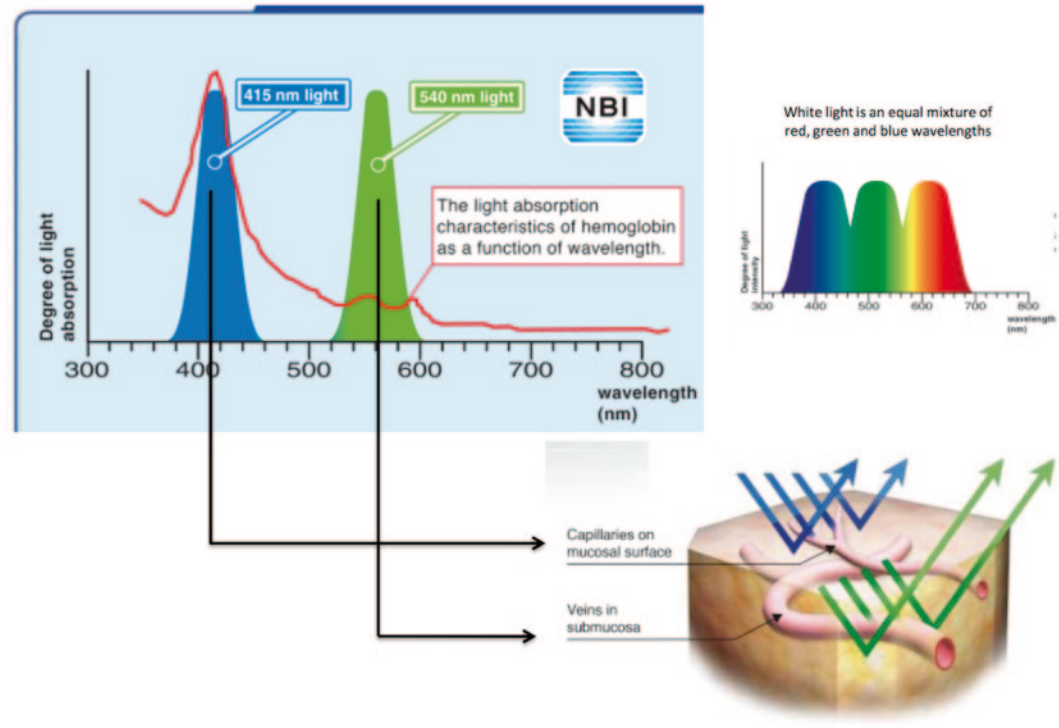

Fig. 21.1 Narrow band imaging filter technology. Light source and video processor are used to deliver high-definition light through the cystoscope. (Provided by Olympus)

Fig. 21.2 Cystoscopy video imaging system, including flexible digital cystoscope, light source unit, video processor, video screen, camera head to attach to eye-piece on resectoscope, equipped for both white light and narrow band imaging. (Provided by Olympus)

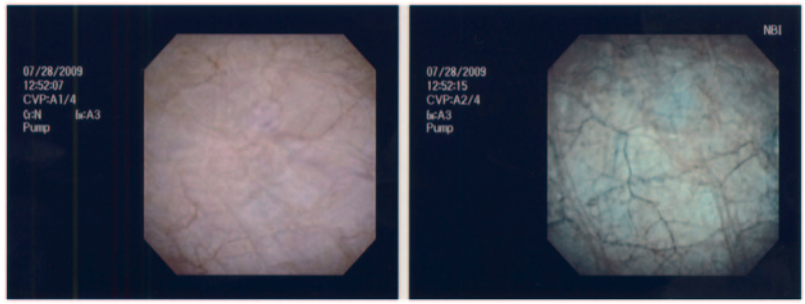

Fig. 21.3 Normal bladder. WLI cystoscopy (*left*) and NBI (*right*). Mucosa is bland on WLI cystoscopy; NBI shows *prominent green* submucosal vessels and *faint brown* superficial capillaries, but no evidence of concentrated enhancement (neovascularity)

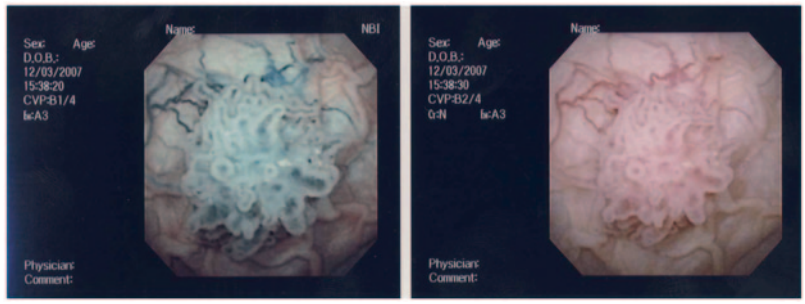

Fig. 21.4 Papillary tumor (low-grade) on NBI cystoscopy (*left*) and WLI cystoscopy (*right*)

The greenish cast also identifies this tumor as a low-risk (low grade) papillary neoplasm. In contrast, Fig. 21.5 shows a similar papillary tumor on WLI cystoscopy that has dense dark brown capillary fronds on NBI cystoscopy, identifying it as likely a high-risk (high-grade) tumor. Subtle or "missed" lesions on WLI cystoscopy can also be detected by NBI. Figure 21.6 shows a cluster of papillary tumors seen on NBI cystoscopy that were undetected on WLI cystoscopy.

Carcinoma in situ (CIS) is a high-grade preinvasive bladder cancer that appears as a flat or slightly raised, poorly outlined erythematous red patch. Undetected and unsuccessfully treated, CIS becomes an invasive, life-threatening cancer. Owing to superficial capillary-dense neovascularity, CIS appears dark brown on NBI cystoscopy. Figure 21.7 shows innocuous-appearing mucosa on WLI cystoscopy, but NBI cystoscopy shows mucosal brown lesion characteristic of CIS. Figure 21.8 shows an example of hyperemic mucosa on WLI cystoscopy and brown patches on NBI cystoscopy corresponding to biopsy of CIS. The underlying submucosal vessels highlighted green are normal in appearance and distribution, indicating noninvasive tumor. Figure 21.9 on WLI cystoscopy shows mild erythema of the mucosa, but brown patches on NBI cystoscopy indicate biopsy-confirmed CIS. Figures 21.10 and 21.11 illustrate examples of CIS that appeared to be more extensive on NBI than WLI cystoscopy, features that aid complete endoscopic destruction. Figure 21.12 shows bland normal-appearing mucosa on WLI cystoscopy that is in fact replaced by CIS seen on NBI cystoscopy. The contrast between papillary and flat morphologic types of bladder cancer is best illustrated in mixed lesions. Figure 21.13 shows visible low-grade papillary tumors (green) surrounded by patches of poorly defined CIS (brown).

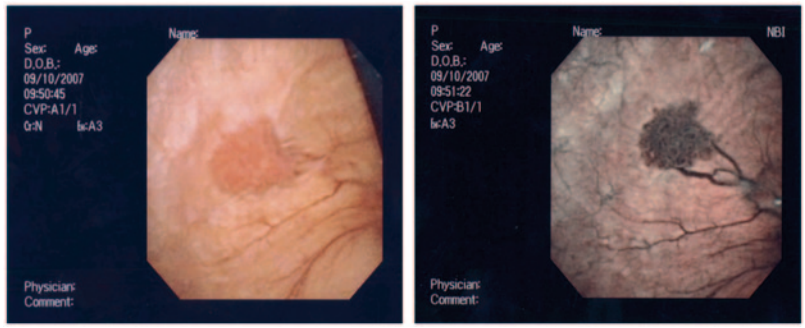

Fig. 21.5 Papillary tumor (high-grade) on WLI cystoscopy (*left*) and NBI cystoscopy (*right*)

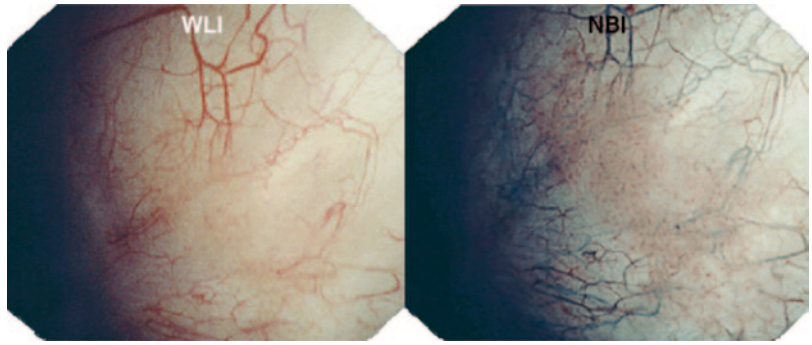

Fig. 21.6 Negative *WLI* cystoscopy (*left*); *NBI* cystoscopy (*right*) shows cluster of papillary tumors. (Courtesy of Dr. Stephen Jones, Cleveland Clinic, Cleveland, Ohio)

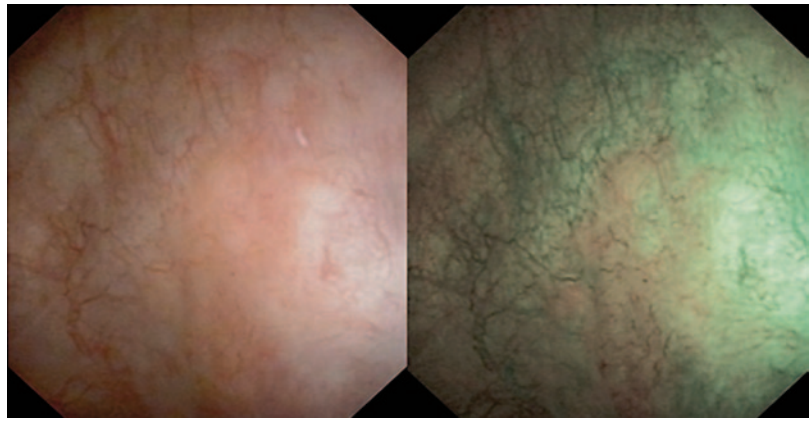

Fig. 21.7 Normal WLI cystoscopy (*left*); NBI cystoscopy (*right*) shows carcinoma in situ (*brown patch*)

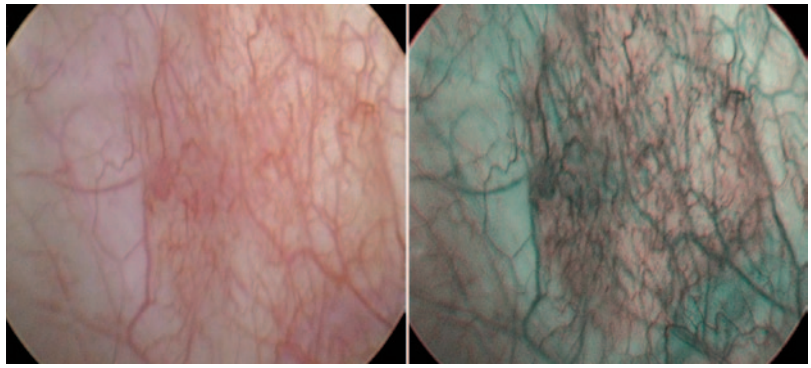

Fig. 21.8 Hyperemic bladder mucosa on WLI cystoscopy (*left*); NBI (*right*) reveals carcinoma in situ. (Courtesy of Dr. E. Cauberg, Academic Medical Center, Amsterdam, Netherlands)

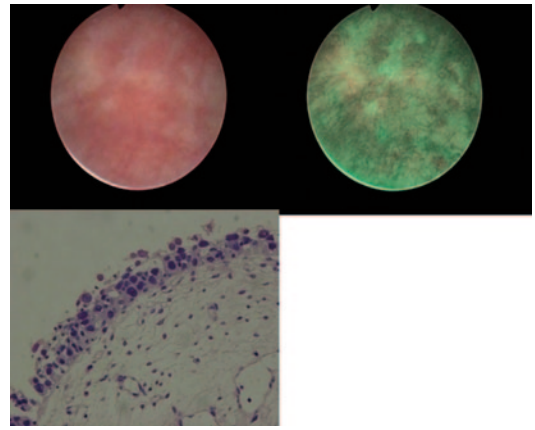

Fig. 21.9 White light cystoscopy (*left*) shows mild erythema. NBI cystoscopy (*right*) shows *brown patches* scattered among normal *green background,* typical of carcinoma in situ (below). (Courtesy of Dr. K. Tatsugami, Kyushu University, Fukuoka, Japan)

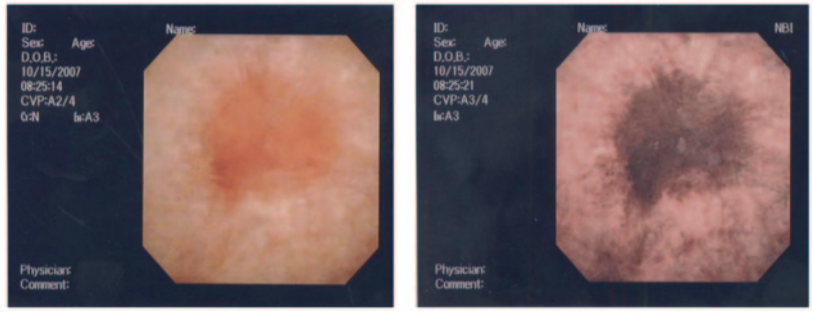

Fig. 21.10 Carcinoma in situ of bladder (CIS) visualized on WLI cystoscopy (*left*), and NBI cystoscopy (*right*). The *patchy brown areas* surrounding the dominant lesion on NBI cystoscopy, not detected on WLI cystoscopy, showed biopsy-proved carcinoma in situ. Index lesion measured 1 cm (WLI), but CIS extended another 1–2 cm (NBI)

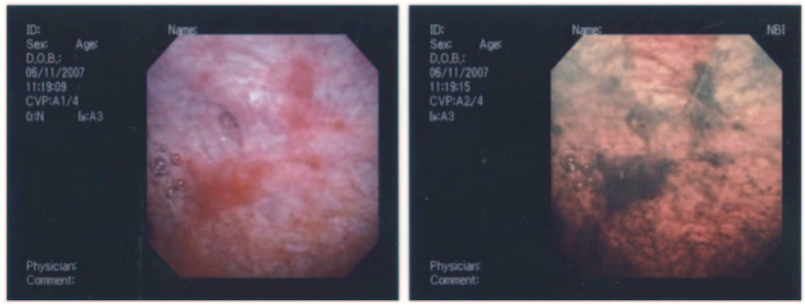

Fig. 21.11 Carcinoma in situ visualized on WLI (*left*) appears more extensive by NBI (*brown-black lesions*) cystoscopy (*right*). Wide resection around NBI visible lesions confirmed diffuse carcinoma in situ

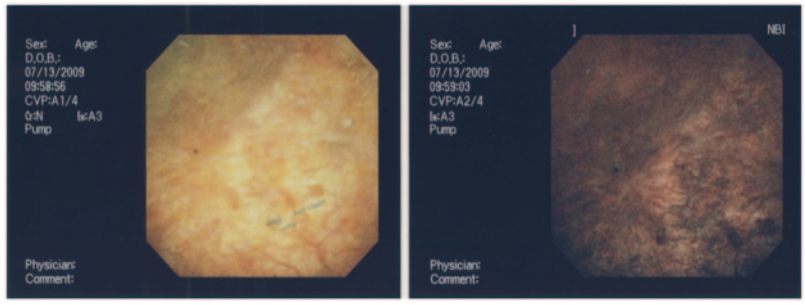

Fig. 21.12 WLI cystoscopy (*left*) shows unremarkable mucosa, that on NBI cystoscopy (*right*) is replaced by carcinoma in situ (*brown patches*)

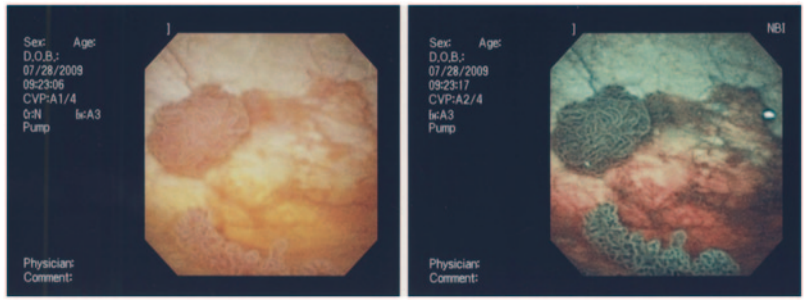

Fig. 21.13 Papillary tumors on WLI cystoscopy (*left*) appear *dark green* on NBI cystoscopy (*right*), but surrounding *brown lesions* indicate associated carcinoma in situ

NBI Detection of Bladder Tumors

NBI cystoscopy detects more tumors than WLI cystoscopy. Table 21.1 shows results of individual studies [5–13]. WLI cystoscopy identifies 57–84 % of all papillary tumors and 50–68 % of CIS, compared to 78–97 % and 90–100 %, respectively, with NBI cystoscopy. The studies show superior sensitivity and negative predictive value (> 90 %) for NBI over WLI cystoscopy, making NBI cystoscopy useful for identifying abnormal lesions and for excluding a diagnosis of bladder tumor. Additional biopsies of suspicious lesions detected only with NBI, some of which show no cancer, have not resulted in increased complications. Negative tumor margins of suspicious lesions identified by NBI also confirms complete tumor resection.

We recently updated our results in 538 patients undergoing surveillance cystoscopy for recurrent bladder tumors [6]. Of 151 patients (28 %) with recurrences, 89 % were found with both WLI and NBI.

In 11 % of patients, recurrent tumors were detected only by NBI cystoscopy. Other series have also reported more tumors found on NBI over WLI cystoscopy in 27–41 % of cases. Zheng et al. performed a metaanalysis of eight studies including 1022 patients and found NBI cystoscopy consistently improved detection of bladder tumors, including CIS, compared with WLI cystoscopy [14]. Li et al. also conducted a meta-analysis in 1040 patients having 1476 tumors detected by biopsy [15]. A total of 17% of patients had tumors detected only by NBI and 24 % had more tumors found by NBI than WLI cystoscopy. NBI provides a clearer view of papillary lesions and better defines the extent and margins of papillary and CIS lesions from surrounding normal-appearing epithelium. Figure 21.14 shows how NBI cystoscopy facilitates TUR or fulguration with negative mucosal margins.

NBI is usually used as an add-on procedure to WLI cystoscopy, raising a question of whether observer bias favors enhanced tumor detection after a “first-look” cystoscopy, because the same urologist usually performs NBI after first observing

Table 21.1 Detection of bladder tumors by white light imaging (WLI) and narrow band imaging (NBI) cystoscopy

Series	No. patient	Cystoscopy	Sensitivity	Specificity	PPV	NPV
Bryan [5]	29	WLI	82 %	79 %	70 %	81 %
		NBI	96 %	85 %	61 %	92 %
Herr and Donat [6]	427	WLI	87 %	85 %	66 %	96 %
		NBI	100 %	82 %	63 %	100 %
Cauberg [7]	95	WLI	79 %	75 %	–	–
		NBI	95 %	69 %	–	–
Tatsugami [8]	104	WLI	57 %	86 %	69 %	79 %
		NBI	93 %	71 %	63 %	95 %
Shen [9]	78	WLI	77 %	82 %	–	79 %
		NBI	92 %	73 %	–	87 %
Xiaodong [10]	64	WLI	79 %	76 %	–	–
		NBI	97 %	68 %		
Geavlete [11]	95	WLI	84 %	–	–	–
		NBI	95 %	–	–	–
Zhu [12]	12	WLI	50 %	91 %	–	–
		NBI	78 %	80 %	–	–
Chen [13]	179	WLI	79 %	81 %	–	–
		NBI	97 %	79 %	–	–

PPV positive predictive value, *NPV* negative predictive value

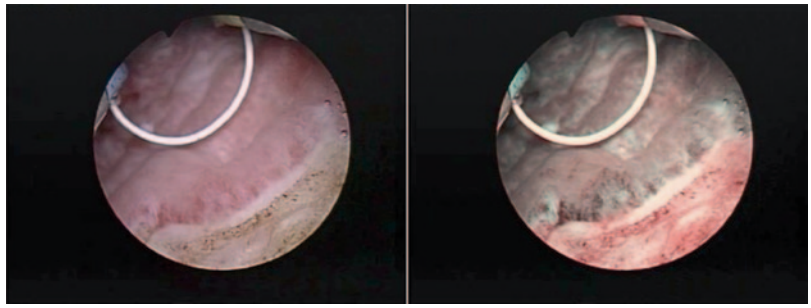

Fig. 21.14 TUR using WLI cystoscopy shows bland margin of resection (*left*) and no obvious tumor. NBI cystoscopy (*right*) clearly shows tumor at margin of resection (*brown* mucosa) representing CIS on wider TUR. (Courtesy of Dr. B Geavlete, Bucharest, Romania)

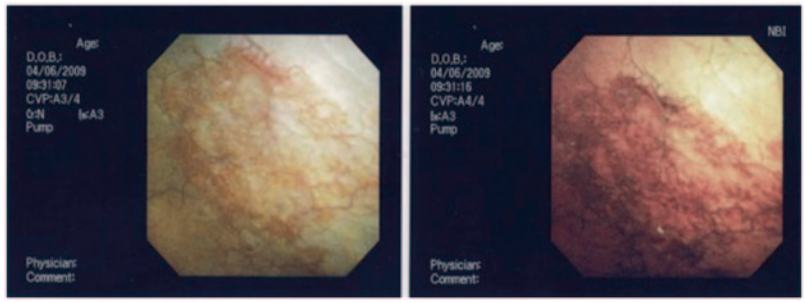

Fig. 21.15 WLI cystoscopy (*left*) shows *faint red* mucosa after BCG that appears benign. NBI (*right*) shows capillary-dense *brown* lesions typical of carcinoma in situ

the bladder with WLI cystoscopy and spends more time examining the bladder. Cauberg et al. studied 45 patients in which NBI cystoscopy was performed by a second surgeon who was blinded to the results of the initial WLI cystoscopy; additional tumors were found in 24%, including one patient with CIS detected only by NBI [16]. In order to address observer bias a randomized trial, in which the bladder was inspected first by WLI, then NBI, or vice versa, confirmed that a "second look" did not compromise the superiority of NBI over WLI flexible cystoscopy to detect papillary and CIS lesions [9]. The issue is not, however, whether one modality is better than the other, but that narrow band plus WLI cystoscopy detects more bladder tumors, at no increased risk or cost to patients, than standard WLI cystoscopy alone.

NBI Evaluation of Response to Intravesical Therapy

Intravesical bacille Calmette-Guerin (BCG) immunotherapy or chemotherapy is used to prevent tumor recurrences and to treat residual CIS after complete resection of visible tumors. The response to intravesical therapy is determined 3 months after treatment by cystoscopy, biopsy, or TUR as necessary. BCG and chemotherapy cause an intense inflammatory reaction or chemical cystitis, which resembles CIS on WLI cystoscopy. The mucosa appears diffusely red, friable, and edematous, individual lesions are poorly defined, and vision is sometimes poor. We evaluated 61 patients 3 months after BCG by NBI cystoscopy [17]. All had red lesions suggesting BCG inflammation or CIS on WLI cystoscopy. Of 22 patients having residual tumor, NBI correctly identified 21 as having CIS. Figure 21.15 shows a benign-appearing bland lesion after BCG that

under NBI has capillary-dense mucosa indicating CIS. Of 30 patients who had negative NBI cystoscopy, only one had persistent focal disease. Figure 21.16 shows a red lesion at cystoscopy after BCG therapy, which could be residual cancer or BCG-inflammation. NBI cystoscopy shows enhanced submucosal vessels (dense green) but unremarkable overlying mucosa (green) resembling normal mucosa. This is consistent with acute inflammation (confirmed by biopsy). We defer the 3-month biopsy in BCG-treated patients who have negative urine cytology and benign-appearing lesions observed on NBI cystoscopy. Inflammatory lesions present a challenge for both WLI and NBI cystoscopy and more study is needed in differentiating benign from malignant disease, especially after intravesical radiation or chemotherapy that damages the bladder, and in patients with chronic bacterial infections or interstitial cystitis.

Therapeutic Impact of NBI-assisted TUR

Although the therapeutic impact of NBI cystoscopy in the management of patients with bladder tumors has not been proved, it seems logical that better visualization of tumors would translate in improved tumor staging, better local control, and fewer tumor recurrences. Naselli et al. found NBI-assisted biopsies detected more tumors in 13% of 47 patients missed during a WLI-assisted second TUR [18], suggesting that NBI cystoscopy facilitates more complete tumor resections. The same authors also proved the feasibility and safety of performing TUR entirely by means of NBI[19]. Cauberg et al. reported that among 158 patients, tumors recurred in 30% after WLI-assisted TUR compared to 15% with NBI-assisted TUR [20], and we found fewer tumor recurrences in 126 patients who had recurrent low-grade papillary tumors treated by outpatient biopsy and fulguration using flexible NBI versus WLI cystoscopy [21]. We have a prospective trial ongoing to determine if NBI-TUR of new bladder tumors can prolong the 2-year recurrence-free interval over WLI-TUR, and a multicenter international, randomized study has been launched to investigate whether NBI-assisted TUR reduces the frequency of tumor recurrences compared to WLI-assisted TUR [22]. Although prospective studies are required to determine whether visual advantages of NBI can translate into real therapeutic benefit for individual patients, current evidence suggests NBI improves the overall quality of diagnostic cystoscopy and transurethral surgery.

NBI Cystoscopy Learning Curve

Two papers have addressed new user's experience with NBI cystoscopy. We evaluated 50 patients subjected to WLI and NBI cystoscopy for recurrent bladder tumors. Each patient was independently viewed by three experienced urologists,

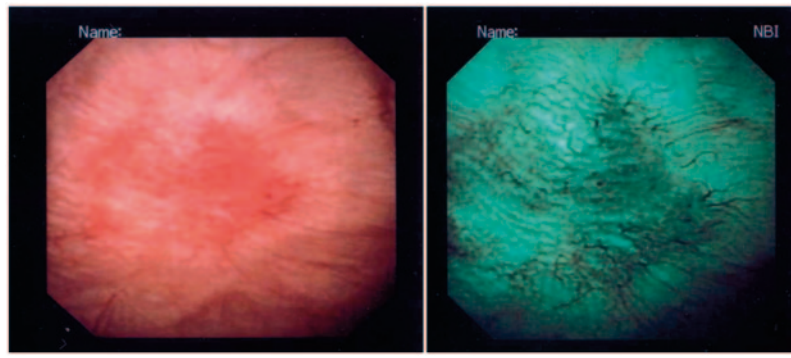

Fig. 21.16 WLI cystoscopy (*left*) shows *red, granular* lesions after BCG. NBI (*right*) shows dominant submucosa vessels (*dense green*) consistent with inflammation, and normal overlying mucosa (*green*)

and one novice (fellow in training), assessing the presence or absence of tumor. We found no significant differences among urologists adapting to NBI cystoscopy to visualize lesions or in determining final pathology [23]. Bryan et al. also found no difference between new users and experienced users in detecting more tumors using NBI technology over WLI cystoscopy [24].

Interpretation of NBI Cystoscopy

The first principle of endoscopy is that it is still subjective. No visual modality is perfect, nor can it substitute for a surgeon's quality and experience. However, NBI cystoscopy appears to improve visibility of bladder lesions over standard WLI cystoscopy in the hands of both experienced and novice urologists. Normal bladder mucosa and vasculature are easy to identify. Predominately green lesions are most likely either benign inflammation (cystitis) or low-grade papillary tumors that usually pose little risk to patients. Predominately brown lesions are more often than not cancers, either flat CIS or high-grade papillary carcinoma.

Indeterminate lesions can pose problems. I use a simplified scheme where if a lesion is more green than brown, it is usually a benign or low-grade tumor, whereas a lesion that is more brown than green probably represents a high-grade tumors. Figure 21.17 shows two indeterminate pink lesions that are green against a green background on NBI cystoscopy, proved to be benign inflammation. Figure 21.18 shows flat red lesions on WLI cystoscopy, which is characteristic of both inflammation and carcinoma. Brownish appearance on NBI cystoscopy against the green background favors malignant bladder neoplasm.

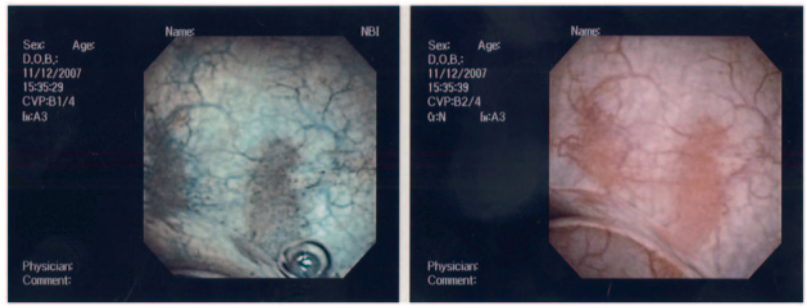

Fig. 21.17 Indeterminate bladder lesion on WLI cystoscopy (*right*) that is benign (*cystitis*) on NBI cystoscopy (*left*)

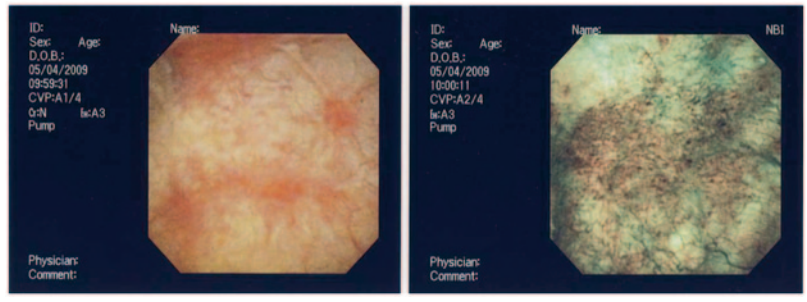

Fig. 21.18 *Focal red* areas on WLI cystoscopy (*left*). NBI cystoscopy (*right*) shows *brown* lesions against *green* background indicating carcinoma in situ

Conclusions and the Future

NBI cystoscopy has become integrated into clinical practice to evaluate and manage bladder tumors. However, many questions remain, such as Does NBI cystoscopy detect more significant tumors and results in better outcomes? Can NBI reliably predict histopathologic diagnosis? Are false positive findings a problem that may pose risks to patients because of unnecessary biopsies, especially after intravesical therapy? Is observer bias significantly distorting results in favor of NBI over WLI cystoscopy? Is NBI cost-effective? And lastly, since optical imaging is inherently subjective, the quality of the surgeon must be considered when interpreting reported results. Like other new optical methods, such as fluorescence cystoscopy, optical coherence tomography, and confocal endomicroscopy, NBI will likely be used mostly as a supplement to conventional WLI cystoscopy [25]. More research is needed to define how NBI and other imaging modalities can best be implemented in the management of bladder cancer. However, growing experience shows that NBI cystoscopy is an effective method to identify abnormal bladder lesions, including dangerous cancers and their extent, and may provide higher diagnostic precision than standard WLI cystoscopy.

The next evolution of NBI cystoscopy will be identification of CIS by computer software and highlighted on the monitor during bladder inspection. Further, enhanced detection by NBI may improve the outcome of other emerging technologies such as confocal endomicroscopy or optical coherence tomography, which may allow real-time in vivo histologic diagnosis of cancer and local invasiveness.

References

1. Herr HW. Max Nitze, the cystoscope and urology. J Urol. 2006;176:1313–16.
2. Herr HW, Al-Ahmadie H, Dalbagni G, et al. Bladder cancer in cystoscopically normal-appearing mucosa: a case of mistaken identity? BJUI. 2010;106:1499–1501.
3. Vianello A, Costantini E, Del Zingaro M, et al. Repeated white light transurethral resection of bladder cancers: systematic review and meta-analysis. J Endourol. 2011;25:1703–12.
4. Liu J-J, Droller MJ, Liao JC. New optical imaging technologies for bladder cancer: considerations and perspectives. J Urol. 2012;188:361–8.
5. Bryan RT, Billingham LI, Wallace DMA. Narrow-band imaging flexible cystoscopy in the detection of recurrent urothelial cancer of the bladder. BJUI. 2007;101:702–6.
6. Herr HW, Donat SM. A comparison of white-light cystoscopy and narrow-band imaging cystoscopy to detect bladder tumor recurrences. BJUI. 2008;102:1111–14.
7. Cauberg EC, Kloen S, Visser M. Narrow band imaging cystoscopy improves detection of non-muscle-invasive bladder cancer. Urology. 2010;76:658–63.
8. Tatsugami K, Kuroiwa K, Kamoto T. Evaluation of narrow-band imaging as a complementary method for the detection of bladder cancer. J Endourol. 2010;24:1807–11.
9. Shen YL, Zhu YP, Ye DW, et al. Narrow-band imaging flexible cystoscopy in the detection of primary non-muscle invasive bladder cancer: a 'second look' matters. Int Urol Nephrol. 2012;44:451–7.
10. Xiaodong S, Zhangqun Y, Shixin B, et al. Application of narrow band imaging in the early diagnosis and recurrent monitoring of bladder cancer. J Contemp Urol Reprod Oncol. 2009;6:325–7.
11. Geavlete B, Jecu M, Multescu R, et al. Narrow-band imaging cystoscopy in non-muscle-invasive bladder cancer: a prospective comparison to the standard approach. Ther Adv Urol. 2012;4:211–7.
12. Zhu YP, Shen YJ, Ye DW, et al. Narrow-band imaging flexible cystoscopy in the detection of clinically unconfirmed positive urine cytology. Urol Int. 2012;88:84–7.
13. Chen G, Wang B, Hongzhao L, et al. Applying narrow-band imaging in complement with white-light imaging cystoscopy in the detection of urothelial carcinoma of the bladder. Urol Oncol. 2013;31:475–79.
14. Zheng C, Lv Y, Zhong Q, et al. Narrow band imaging diagnosis of bladder cancer: systematic review and meta-analysis. BJUI. 2012;110:E680–7.
15. Li K, Lin T, Fan X, et al. Diagnosis of narrow-band imaging in non-muscle-invasive bladder cancer: a systematic review and meta-analysis. Int J Urol. 2013;20:602–9.
16. Cauberg ECC, de la Rosette J, de Reijke TM. How to improve the effectiveness of transurethral resection in nonmuscle invasive bladder cancer? Curr Opin Urol. 2009;19:504–10.
17. Herr HW. Narrow-band imaging cystoscopy to evaluate the response to BCG therapy: preliminary results. BJUI. 2010;105:314–6.
18. Naselli A, Introini, C, Bertolotto F, et al. Narrow band imaging for detecting residual/recurrenct cancerous tissue during second transurethral resection of newly diagnosed non-muscle-invasive high-grade bladder cancer. BJUI. 2009;105:208–11.
19. Naselli A, Introini C, Bertolotto F, et al. Feasibility of transurethral resection of bladder lesion performed entirely by means of narrow-band imaging. J Endourol. 2010;24:1131–4.

20. Cauberg EC, Mamoulakis C, de la Rosette J, et al. Narrow band imaging-assisted transurethral resection for non-muscle invasive bladder cancer significantly reduces residual tumor rate. World J Urol. 2011;29(4):503–9.
21. Herr HW, Donat SM. Reduced bladder tumor recurrence rate associated with narrow-band imaging surveillance cystoscopy. BJUI. 2011;107:396–8.
22. de la Rosette J, Gravas S. A multi-center, randomized international study to compare the impact of narrow band imaging versus white light cystoscopy in the recurrence of bladder cancer. J Endourol. 2010;24:660–1.
23. Herr H, Donat M, Dalbagni G, Taylor J. Narrow-band imaging cystoscopy to evaluate bladder tumors-individual surgeon variability. BJUI. 2010;106:53–5.
24. Bryan RT, Shat ZH, Collins SI, et al. Narrow-band imaging flexible cystoscopy: a new user's experience. J Endourol. 2010;24:1339–43.
25. Cauberg EC, deBruin DM, Faber DJ, et al. A new generation of optical diagnostics for bladder cancer: technology, diagnostic accuracy, and future applications. Eur Urol. 2009;56:287–96.

Fluorescence Imaging of Human Bile and Biliary Anatomy

22

Takeaki Ishizawa and Norihiro Kokudo

Human Bile Fluorescence Imaging Using Indocyanine Green

Fluorescence imaging using indocyanine green (ICG) was first used as an intraoperative navigation tool for coronary arteriography during cardiac bypass surgery at the beginning of the twenty-first century [1, 2]. Protein-bound ICG emits fluorescence that peaks at approximately 840 nm when exposed to light excitation at 750–810 nm [3, 4]. Because human bile also contains proteins such as albumin and lipoproteins that bind with ICG [5], we hypothesized that fluorescent images of the biliary tract could be obtained following injection of ICG [6]. We confirmed that fluorescence cholangiography could be performed using intravenous ICG injection because ICG was excreted into bile and acted as a fluorescence source [7].

A diluted ICG solution (approximately 0.025 mg/mL) should be used for injection of ICG in the biliary tract [6]. If the ICG concentration is too high, the fluorescence intensity will diminish, because of absorption of near-infrared light by ICG [8]. To obtain clear cholangiograms by this technique, it is also important to aspirate a small amount of bile into the syringe before injecting to promote ICG protein-binding in the syringe (Fig. 22.1a) [6, 9]. Using ICG diluted with radiographic contrast, conventional radiographic cholangiography can be performed easily and immediately following fluorescence cholangiography, when evaluating both the extrahepatic biliary system and the intrahepatic bile duct anatomy (Fig. 22.1b, c, d).

Alternatively, fluorescence cholangiography can be performed using ICG (Fig. 22.2) intravenously, usually 2.5 mg diluted with a 1 mL solution [7, 10]. Although biliary excretion of ICG begins within minutes after the intravenous injection, ICG should be administered at least 15 min before the imaging to obtain better contrast between the fluorescing bile ducts and nonfluorescing surrounding organs (fluorescence of ICG in the extrahepatic bile ducts continues up to 6 h after injection) [10–12]. Intravenous injection of ICG has potential advantages over conventional radiographic cholangiography in saving time and avoiding bile duct injury associated with catheterization to inject contrast materials. Fluorescence cholangiography has recently gained attention as a novel navigation tool that provides a roadmap of the extrahepatic ducts to reach the critical view of safety [13] in laparoscopic cholecystectomy, which can reduce the need for intraoperative radiographic cholangiography [12, 14].

N. Kokudo (✉)
Hepato-Biliary-Pancreatic Surgery Division, Department of Surgery, Graduate School of Medicine, University of Tokyo, 731 Hongo Bunkuo-ku, Tokyo 113-8655, Japan
e-mail: kokudo-2su@h.u.tokyo.ac.jp

T. Ishizawa
Department of Gastroenterological Surgery, Cancer Institute Hospital, Japanese Foundation for Cancer Research, Tokyo, Japan

Y. Fong et al. (eds.), *Imaging and Visualization in The Modern Operating Room,*
DOI 10.1007/978-1-4939-2326-7_22, © Springer Science+Business Media New York 2015

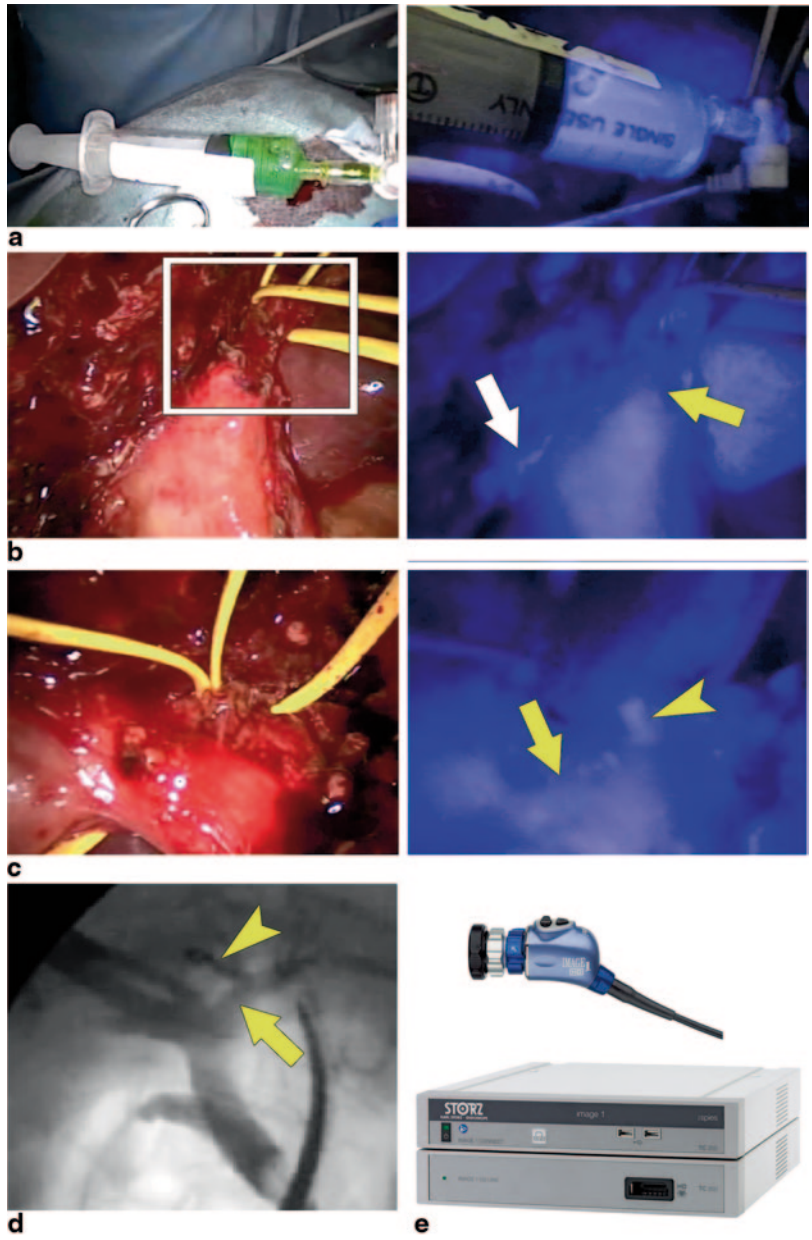

Fig. 22.1 Fluorescence cholangiography by intrabiliary injection of ICG. **a** A small amount of bile is aspirated into a syringe prior to injection of ICG diluted with radiographic contrast material (ICG 0.025 mg/mL) into the bile ducts. **b** Fluorescence imaging (*right*) identifies confluence of the right (*white arrow*) and left (*yellow arrow*) hepatic duct. **c** Magnified view of the framed area in **b**. In addition to the left hepatic duct (*yellow arrow*), the hepatic duct from the Spiegel lobe to be preserved (*yellow arrowhead*) is visualized on fluorescence images (*right*). **d** Conventional radiographic cholangiography following fluorescence cholangiography delineates the anatomy of the intra- as well as extrahepatic bile ducts including the left hepatic duct (*yellow arrow*) and the hepatic duct from the Spiegel lobe (*yellow arrowhead*). **e** All of these fluorescence images were obtained with the D-Light P laparoscopic imaging system (KARL STORZ GmbH & Co. KG, Tuttlingen, Germany). This image shows a subsequent model of this system (SPIES^{TM} Camera System, KARL STORZ)

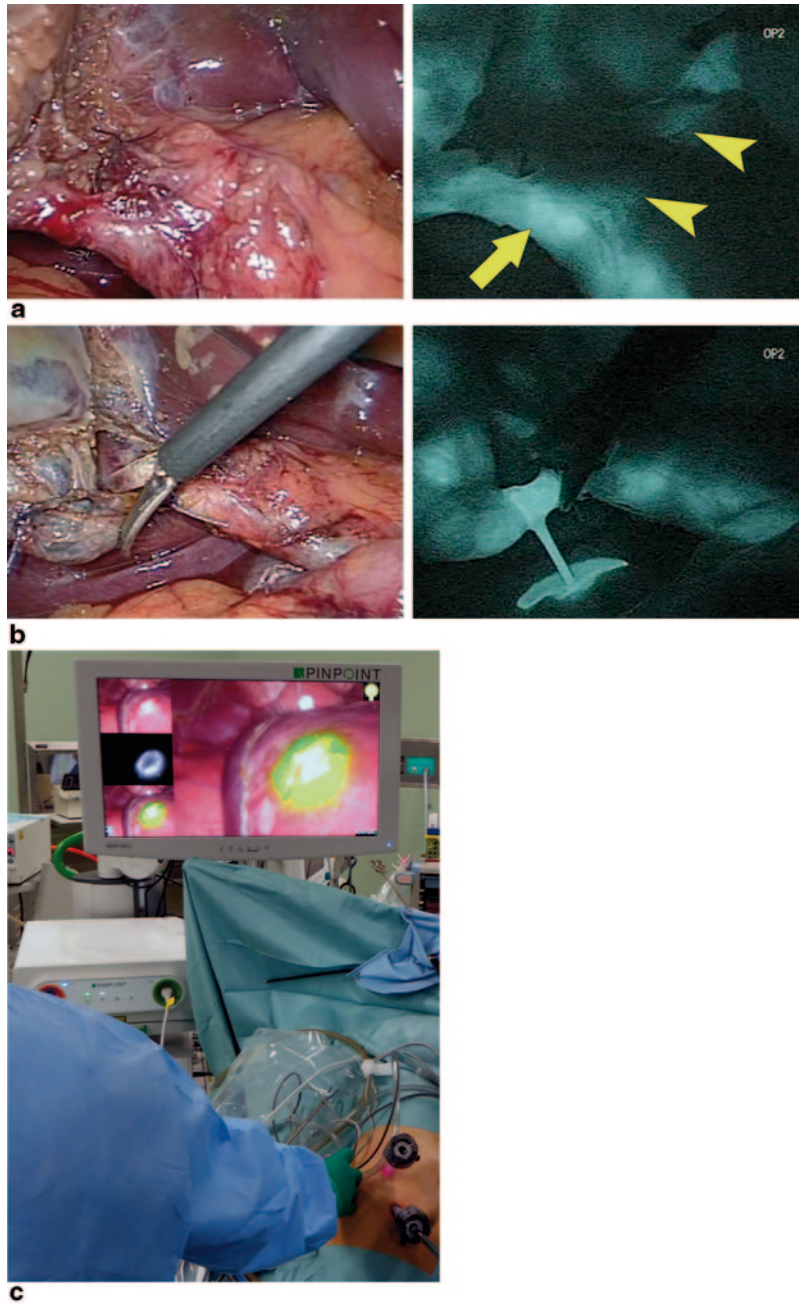

Fig. 22.2 Fluorescence cholangiography by intravenous injection of ICG. **a** Fluorescence imaging following preoperative intravenous injection of ICG (2.5 mg) delineates the cystic duct (*yellow arrow*) and the common hepatic duct (*yellow arrowheads*) during dissection of Calot's triangle in laparoscopic cholecystectomy. **b** Fluorescing bile leaking from the cut stump of the cystic duct. **c** ICG fluorescence imaging of metastatic liver cancer with the PINPOINT® endoscopic fluorescence imaging system (Novadaq Technologies Inc., Toronto, Canada)

Fluorescence Imaging Systems for Open Surgery

Fluorescence images of the bile ducts can easily be obtained during open hepatobiliary surgeries using commercially available fluorescence imaging systems. The SPY® system (Novadaq Technologies Inc., Toronto, Canada) was the first near-infrared imaging system and was launched in Canadian and European markets in 2002 and then approved by the Food and Drug Administration (FDA) in 2005. However, this system was designed and used mainly for coronary arteriography during cardiac bypass surgery and has been rarely applied to intraoperative cholangiography [2]. Alternatively, the PDE® system (Hamamatsu Photonics, Hamamatsu, Japan) has been used in Japan for the identification of sentinel lymph nodes during breast surgery since 2005 [15]. It was first used to visualize the bile ducts in 2008 [6, 8]. Recently, this system has become commercially available in the USA and Europe at a cost of approximately US$48,000 (Fig. 22.3a). The HyperEye Medical System (Mizuho Ikakogyo Co., Ltd. Tokyo, Japan) [16] is another fluorescence imaging system for open surgery available in Japan that enables simultaneous near-infrared and visible light full-color images of ICG fluorescence from the bile ducts (Fig. 22.3b) [9]. In 2011, Hutteman and colleagues reported the results of ICG fluorescence imaging of the bile duct using the Mini-Fluorescence-Assisted Resection and Exploration (Mini-FLARE^{TM}) near-infrared imaging system (Fragioni laboratory, Brookline, MA, USA) [17]. Recently, several European medical equipment manufacturers have developed near-infrared imaging devices for open surgery, such as Fluobeam® Imaging System (Fluoptics, Grenoble, France) (Fig. 22.3c) [17]

Fig. 22.3 Fluorescence imaging systems for open surgery. **a** The portable camera head, control units, and TV monitor of PDE®. **b** Structure of the HyperEye Medical System Handy (Mizuho Ikakogyo Co., Ltd., Tokyo, Japan). **c** Intraoperative fluorescence imaging with Fluobeam® Imaging System (Fluoptics, Grenoble, France). The *arrowhead* shows a portable camera head, which can be covered with a sterile drape and used by the operating surgeon. Imaging data is transmitted from a control unit to a laptop PC (*arrow*)

and the Artemis Handheld System (Quest Medical Imaging, Middenmeer, The Netherlands).

All of these near-infrared imaging systems consist of a camera unit (fixed or portable) with light-emitting diodes and a control unit. Some are also equipped with software to control the light source, adjust camera sensitivity, and evaluate the fluorescence intensity, which is useful for intraoperative assessment of portal uptake function [18]. Fluorescence imaging of the bile ducts can be obtained with these imaging systems simply by setting a camera imaging head above the operative field and turning off the surgical lights (ceiling lights can usually be kept on during observation) [6].

Laparoscopic and Robotic Fluorescence Imaging Systems

The first clinical application of laparoscopic optical imaging using ICG was for sentinel node navigation during gastric surgery, reported in 2004 [19]. Although the authors' technique was not based on ICG fluorescence but instead on the amount of infrared light absorbed by the ICG that accumulated in the nodes, development of this imaging technique led to a subsequent prototype (Olympus Medical Systems, Tokyo, Japan), enabling visualization of ICG florescence in real time during laparoscopic surgery (Fig. 22.2a, b) [20–22]. Another prototype laparoscopic imaging system (Hamamatsu Photonics and Shinko Optical, Tokyo, Japan), which was originally developed to visualize sentinel lymph nodes during resection of gastric cancer [23] and to evaluate the placental vascular network in the treatment of twin-twin transfusion syndrome [24], has also been used for fluorescence cholangiography [7, 10]. ICG fluorescence imaging using these prototype imaging systems is clinically useful for visualizing the extrahepatic bile ducts and can be used to identify hepatic segments [21] and the location of hepatic malignancies [22] during laparoscopic hepatobiliary surgeries. However, standard-definition color images must be improved to next-generation quality to meet the needs of more complicated procedures.

In 2011, a fluorescence imaging system for robotic surgery (FIREFLY, Novadaq Technologies Inc.) was launched in the USA [25, 26], followed by the company's latest PINPOINT® endoscopic fluorescence imaging system [27, 28], which enables the superimposition of fluorescence images on full-color images with high-definition quality (Fig. 22.2c). Alternatively, another high-definition laparoscopic fluorescence imaging system (D-Light P System, KARL STORZ GmbH & Co. KG, Tuttlingen, Germany) became commercially available in Europe in 2012 and then in the USA and Japan in 2013. Although simultaneous visualization of ICG fluorescence images and background color images is not available in this system, fluorescence images can be changed quickly from the full-color images using a foot switch (Fig. 22.1) [13, 29].

Future Perspectives in Fluorescence Cholangiography

Intraoperative fluorescence cholangiography has the potential to enhance the safety of hepatobiliary surgery. However, the feasibility and quality of the fluorescence images require improvement for this technique to become a widely used intraoperative navigation tool benefitting both surgeons and patients. Some authors have developed novel non-ICG-dependent fluorescence probes optimized for visualization of the bile ducts [30]. New generation near-infrared imaging systems also continue to be developed and evaluated [31, 32]. Among these, a wearable display for the fluorescence images similar to a "google glass" system [33] may enable surgeons to confirm fluorescence images without moving their visual focus from the TV monitor to the surgical field, enhancing the feasibility of fluorescence imaging especially during open surgery (Fig. 22.4). Finally, it is important to note that the administration of ICG for cholangiography has not yet been approved. Although the safety of ICG has been established for clinical use for more than 50 years, further accumulation of clinical experience and subsequent large multicenter trials are needed to prove the efficacy of fluorescence cholangiography using ICG.

Fig. 22.4 Simulation of intraoperative fluorescence imaging in the near future. Future intraoperative imaging systems may enable the superimposition of fluorescence images on full-color images with information obtained by other pre- and intraoperative imaging modalities. Surgeons can obtain all the necessary information through a wearable display in real time during open as well as laparoscopic surgery. In this picture, the operating surgeon wears a head-mount display (Sony Corporation, Tokyo, Japan) for three-dimensional laparoscopic imaging

Acknowledgments The authors would like to thank Drs. Yosuke Inoue, Junichi Arita, Yu Takahashi, and Akio Saiura for their support and guidance on the use of fluorescence imaging at the Cancer Institute Hospital.

References

1. Rubens FD, Ruel M, Fremes SE. A new and simplified method for coronary and graft imaging during CABG. Heart Surg Forum. 2002;5:141–4.
2. Reuthebuch O, Haussler A, Genoni M, et al. Novadaq SPY: intraoperative quality assessment in off-pump coronary artery bypass grafting. Chest. 2004;125:418–24.
3. Landsman ML, Kwant G, Mook GA, et al. Light-absorbing properties, stability, and spectral stabilization of indocyanine green. J Appl Physiol. 1976;40:575–83.
4. Mordon S, Devoisselle JM, Soulie-Begu S, et al. Indocyanine green: physicochemical factors affecting its fluorescence in vivo. Microvasc Res. 1998;55:146–52.
5. Mullock BM, Shaw LJ, Fitzharris B, et al. Sources of proteins in human bile. Gut. 1985;26:500–9.
6. Ishizawa T, Tamura S, Masuda K, et al. Intraoperative fluorescent cholangiography using indocyanine green: a biliary road map for safe surgery. J Am Coll Surg. 2008;208:e1–4.
7. Ishizawa T, Bandai Y, Kokudo N. Fluorescent cholangiography using indocyanine green for laparoscopic cholecystectomy: an initial experience. Arch Surg. 2009;144:381–2.
8. Mitsuhashi N, Kimura F, Shimizu H, et al. Usefulness of intraoperative fluorescence imaging to evaluate local anatomy in hepatobiliary surgery. J Hepatobiliary Pancreat Surg. 2008;15:508–14.
9. Kawaguchi Y, Ishizawa T, Masuda K, et al. Hepatobiliary surgery guided by a novel fluorescent imaging technique for visualizing hepatic arteries, bile ducts, and liver cancers on color images. J Am Coll Surg. 2011;212:e33–9.
10. Ishizawa T, Bandai Y, Ijichi M, et al. Fluorescent cholangiography illuminating the biliary tree during laparoscopic cholecystectomy. Br J Surg. 2010;97:1369–77.
11. Cherrick GR, Stein SW, Leevy CM, et al. Indocyanine green: observations on its physical properties, plasma decay, and hepatic extraction. J Clin Invest. 1960;39:592–600.
12. Verbeek FP, Schaafsma BE, Tummers QR, et al. Optimization of near-infrared fluorescence cholangiography for open and laparoscopic surgery. Surg Endosc 2014;28(4):1076–82.
13. Strasberg SM, Hertl M, Soper NJ. An analysis of the problem of biliary injury during laparoscopic cholecystectomy. J Am Coll Surg. 1995;180:101–25.
14. Dip FD, Asbun D, Rosales-Velderrain A, et al. Cost analysis and effectiveness comparing the routine use of intraoperative fluorescent cholangiography with fluoroscopic cholangiogram in patients undergoing laparoscopic cholecystectomy. Surg Endosc. 2014;28(6):1838–43.
15. Kitai T, Inomoto T, Miwa M, et al. Fluorescence navigation with indocyanine green for detecting sentinel lymph nodes in breast cancer. Breast Cancer. 2005;12:211–5.
16. Handa T, Katare RG, Nishimori H, et al. New device for intraoperative graft assessment: HyperEye charge-coupled device camera system. Gen Thorac Cardiovasc Surg. 2010;58:68–77.
17. Hutteman M, van der Vorst JR, Mieog JS, et al. Near-infrared fluorescence imaging in patients undergoing pancreaticoduodenectomy. Eur Surg Res. 2011;47:90–7.
18. Kawaguchi Y, Ishizawa T, Miyata Y, et al. Portal uptake function in veno-occlusive regions evaluated by real-time fluorescent imaging using indocyanine green. J Hepatol. 2013;58:247–53.
19. Nimura H, Narimiya N, Mitsumori N, et al. Infrared ray electronic endoscopy combined with indocyanine green injection for detection of sentinel nodes of patients with gastric cancer. Br J Surg. 2004;91:575–9.
20. Tagaya N, Shimoda M, Kato M, et al. Intraoperative exploration of biliary anatomy using fluorescence imaging of indocyanine green in experimental and clinical cholecystectomies. J Hepatobiliary Pancreat Sci. 2010;17:595–600.
21. Ishizawa T, Zuker NB, Kokudo N, et al. Positive and negative staining of hepatic segments by use of fluorescent imaging techniques during laparoscopic hepatectomy. Arch Surg. 2012;147:393–4.

22. Kudo H, Ishizawa T, Tani K, et al. Visualization of subcapsular hepatic malignancy by indocyanine-green fluorescence imaging during laparoscopic hepatectomy. Surg Endosc. 2014;28(8):2504–8.
23. Kusano M, Tajima Y, Yamazaki K, et al. Sentinel node mapping guided by indocyanine green fluorescence imaging: a new method for sentinel node navigation surgery in gastrointestinal cancer. Dig Surg. 2008;25:103–8.
24. Harada K, Miwa M, Fukuyo T, et al. ICG fluorescence endoscope for visualization of the placental vascular network. Minim Invasive Ther Allied Technol. 2009;18:1–5.
25. Buchs NC, Hagen ME, Pugin F, et al. Intra-operative fluorescent cholangiography using indocyanin green during robotic single site cholecystectomy. Int J Med Robot. 2012;8:436–40.
26. Spinoglio G, Priora F, Bianchi PP, et al. Real-time near-infrared (NIR) fluorescent cholangiography in single-site robotic cholecystectomy (SSRC): a single-institutional prospective study. Surg Endosc. 2013;27:2156–62.
27. Sherwinter DA. Identification of anomolous biliary anatomy using near-infrared cholangiography. J Gastrointest Surg. 2012;16:1814–5.
28. Ris F, Hompes R, Cunningham C, et al. Near-infrared (NIR) perfusion angiography in minimally invasive colorectal surgery. Surg Endosc. 2014;28(7):2221–6.
29. Schols RM, Bouvy ND, Masclee AA, et al. Fluorescence cholangiography during laparoscopic cholecystectomy: a feasibility study on early biliary tract delineation. Surg Endosc. 2013;27:1530–6.
30. Figueiredo JL, Siegel C, Nahrendorf M, et al. Intraoperative near-infrared fluorescent cholangiography (NIRFC) in mouse models of bile duct injury. World J Surg. 2010;34:336–43.
31. Venugopal V, Park M, Ashitate Y, et al. Design and characterization of an optimized simultaneous color and near-infrared fluorescence rigid endoscopic imaging system. J Biomed Opt. 2013;18:126018.
32. Gioux S, Coutard JG, Berger M, et al. FluoSTIC: miniaturized fluorescence image-guided surgery system. J Biomed Opt. 2012;17:106014.
33. Liu Y, Zhao YM, Akers W, et al. First in-human intraoperative imaging of HCC using the fluorescence goggle system and transarterial delivery of near-infrared fluorescent imaging agent: a pilot study. Transl Res. 2013;162:324–31.

PET-Guided Interventions from Diagnosis to Treatment

23

Mikhail Silk, François Cornelis and Stephen Solomon

Section 1: Basics of PET

Positron emission tomography (PET) is based on the physics of radionuclides that undergo β^+ decay. The commonly used radionuclides for PET imaging and their respective half-lives are listed in Table 23.1.

As the radioisotope undergoes positron β^+ emission, it emits a positron, an antiparticle of the electron with opposite charge. The emitted positron travels in tissue for a short distance (less than 1 mm), and interacts with an electron. Both electron and positron are annihilated, and produce a pair of gamma 511 keV photons moving in opposite directions (Fig. 23.1). Only paired photons arriving at 180° in nanoseconds of each other are counted and eventually reformatted into an image. When photons do not happen in these temporal "pairs" they are ignored.

Radionuclides used for PET imaging are incorporated either into compounds normally used by the body such as glucose, water or ammonia or into molecules that bind to receptors or other sites of drug action. The radionuclide Fluorine 18, specifically in the glucose analog ^{18}F-fluoro-2-deoxy-glucose (FDG), has revolutionized medical management for cancer patients [1]. Based on the Warburg effect (i.e., increased rate of anaerobic glycolysis seen in cancer) tumor cells take up a higher percentage of FDG compared to normal cells [1, 2] (Table 23.2). Once metabolized by the cell, the FDG becomes trapped (Fig. 23.2) and the higher concentration of FDG is visualized as a "hot-spot" on PET imaging.

PET/CT

PET imaging, while excellent to detect the presence of tumor cells, does not give information of anatomic location. For this reason, PET scans are increasingly combined with computed tomography (CT) or magnetic resonance imaging (MRI) scans, for coregistration of anatomic and metabolic information [3, 4]. PET and CT fusion is accurate for the brain. However, fusion of independent CT and PET scans is more difficult at other anatomical sites. Differences between scans in patient positioning (arm position, supine vs. prone, etc.) result in non-linear organ displacement making accurate anatomical fusion challenging [5].

In 2000 [6], the first hybrid CT-PET system was described which was able to reduce the errors commonly encountered with image fusion. Since the two scans can be performed in immediate sequence during the same session, with the patient not changing position, the two sets of images are more-precisely registered. Areas of abnormality on the PET imaging can be better

M. Silk (✉) · F. Cornelis · S. Solomon
Department of Radiology, Memorial Sloan-Kettering Cancer Center, 1275 York Avenue, New York, NY 10021, USA
e-mail: solomons@mskcc.org

Y. Fong et al. (eds.), *Imaging and Visualization in The Modern Operating Room,*
DOI 10.1007/978-1-4939-2326-7_23, © Springer Science+Business Media New York 2015

Table 23.1 Half-life of Various Positron Emitting Isotopes

Radionuclide	Half-life
Fluorine 18	110 min
Carbon 11	20 min
Nitrogen 13	10 min
Oxygen 15	122 s
Rubidium 82	75 s

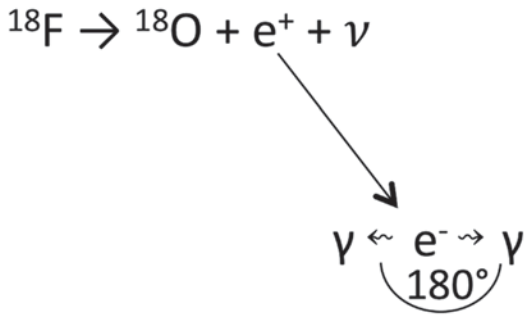

Fig. 23.1 Decay products of ^{18}F (e^+ = positron, υ = neutrino) and resulting annihilation with an electron (e^-). Resultant photons (γ) travel 180° from each other

Table 23.2 Relative FDG-PET uptake by tumors

Tumor origin	High-to-moderate	Variable	Low
Lung	x		
Colorectal	x		
Esophageal	x		
Stomach	x		
Head and neck	x		
Cervical	x		
Ovarian	x		
Breast	x		
Melanoma	x		
Lymphoma	x	x	
Thyroid		x	
Testicular		x	
Hepatocellular		x	
Renal		x	
Bladder		x	
Sarcoma		x	
Neuroendocrine		x	
Prostate			x

correlated with anatomy on the CT images. In addition to aiding in anatomic localization, the combination with CT aids in the correction of the attenuation of tissues and improves the results of such explorations. FDG PET/CT is able to create more accurate images displaying the anatomic location of metabolic activity [3, 4].

Section 2: PET/CT-Guided Biopsy

FDG PET images can detect malignancy before the tumor is large enough to be observed on conventional cross sectional imaging. However, some FDG avid findings are false-positive for cancer, which has led to both overstaging and under-treatment of patients [7–9] (Table 23.3). FDG PET/CT guided biopsies can aid in managing cancer patients to both diagnose cancer early and avoid incorrect tumor staging due to false-positive FDG avid findings.

In vitro and in vivo studies have demonstrated FDG uptake is directly correlated with the number of viable tumor cells [10–14]. In tumors with extensive necrosis or fibrosis FDG PET/CT-guided biopsy is more likely to improve the diagnosis of cancer. An additional advantage of FDG PET/CT guidance is in the follow up of surgically or radiation-treated tumors. Posttreatment anatomic changes may make conventional cross sectional imaging difficult to interpret. Avid findings on PET/CT facilitate active targeting in these situations.

Common PET/CT-Related Artifacts

The CT portion of PET/CT is captured in seconds, the PET component can take a few minutes and this can lead to significant misregistration. Areas in the lungs or organs affected by respiratory movement require patient cooperation [15] or anesthesia for breath control to reduce artifact from diaphragmatic movements (Fig. 23.3). Patients with metallic objects (i.e., metal stents, surgical clips, etc.) can have false positive findings due to attenuation correction. X-ray energy is attenuated more by metallic objects than PET energy. This leads to overestimation of the attenuation for PET activity and results in artifactual increased FDG activity.

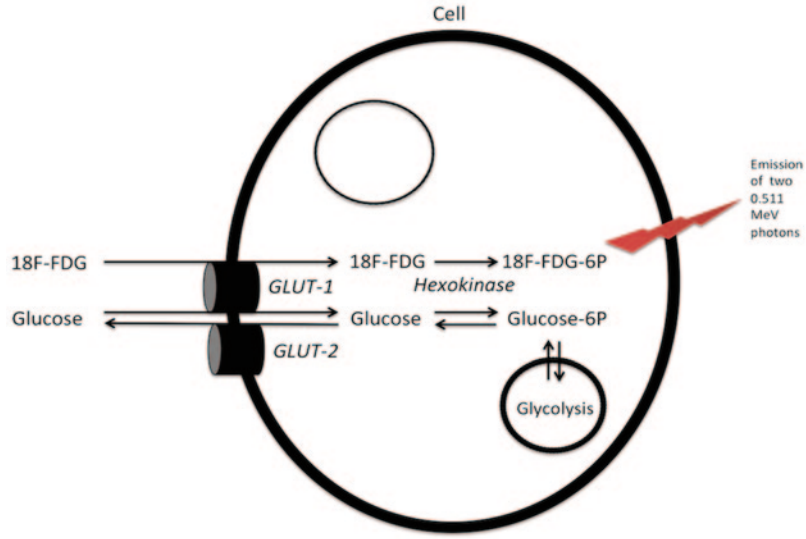

Fig. 23.2 Uptake of ^{18}F-fluoro-2-deoxy-glucose (*FDG*) is by the glucose transporter (*GLUT*)-1 transport protein [3]. ^{18}F-FDG is later phosphorylated by hexokinase where it becomes trapped within the cell

Table 23.3 Common Areas of Physiologic Uptake of FDG. (Adapted from Kobayashi et al. 2012)

Abnormal uptake	Cause	Typical location
Brown adipose tissue	Increased glycolytic metabolism	Neck, supraclavicular area, shoulder, axilla
Thymus	Physiologic, rebound hyperplasia (i.e. following chemotherapy)	Retrosternal
Myocardium	Fasting myocardium shifts to a glycolytic metabolism	Mediastinum (confused with lymph nodes or pulmonary masses)
Bone marrow	Granulocyte colony stimulating factor (GCSF) or chemotherapy induced	Variable
Spleen	Physiologic to extrasplenic infection, GCSF therapy, extramedullary hematopoiesis	Diffuse uptake in spleen
Skeletal muscle	Heavy use/active contraction, insulin injection, recent surgery	Variable

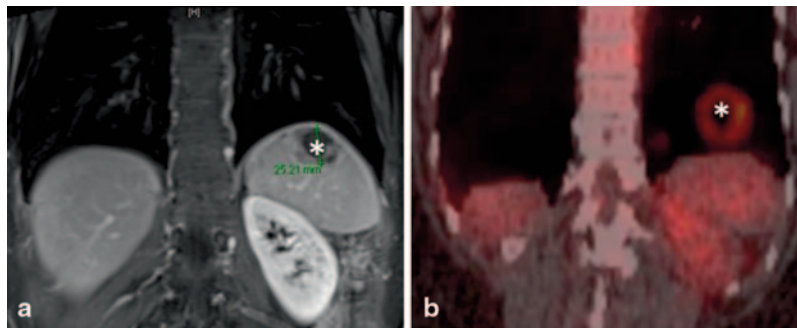

Fig. 23.3 PET/CT misregistration due to diaphragmatic movement. CT image (**a**) and PET/CT fused image (**b**) demonstrating artifact from respiratory motion. The tumor (*asterisk*) appears to be supradiaphragmatic in PET/CT fusion due to a change in anesthesia vent settings during the procedure

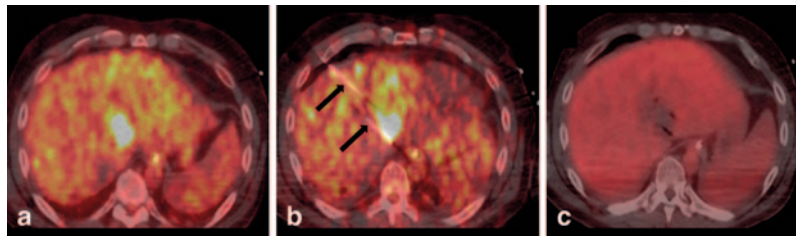

Fig. 23.4 Images during split dose PET-guided ablation. Localizing PET/CT after administration of 4 mCi of FDG demonstrating avid tumor in liver (**a**). Post insertion of Irreversible Electroporation (IRE) electrodes (**b**, *black arrows*). Post ablation PET/CT while patient is still on the procedure table after administration of an 8 mCi dose shows loss of uptake in the ablated area

Section 3: PET/CT-Guided Ablation and Surgery

PET/CT-Guided Ablation

Ablative technologies (e.g., radiofrequency, microwave, cryoablation, etc.) are well-established methods in treating tumors especially in patients who are not ideal candidates for surgical resection. PET/CT-guided ablations can help to ensure initial needle placement [16, 17] and new techniques are being developed to evaluate residual viable tissue during the procedure [18].

A diagnostic PET/CT scan is typically obtained before the PET/CT-guided procedure day. The prior diagnostic PET/CT scan confirms the avidity of the area being targeted, aids in planning, and subsequently permits a lower FDG dose during the procedure day since only a localizing PET scan is required. Additionally, localizing PET scans have shorter acquisition times (30 s–2 min compared to the typical 5 min for a diagnostic PET scan [15]) facilitating repetitive use during a procedure. Patients are instructed in a similar fashion when optimizing a diagnostic PET/CT scan to avoid caffeine and strenuous exercise as well as avoid excessive sugar intake.

Breath-hold during localizing PET/CT imaging is helpful to minimize misregistration and distortion of small tumors in areas subject to respiratory motion [19, 20]. CT-fluoro or ultrasound can be used to guide needle placement and periodic fusion with the localizing PET scan can help guide needle trajectory. Ablative modalities do not dissipate radioactivity [16, 21], however residual FDG avidity combined with a postprocedure CT can help in the assessment of ablative margins and can aid in confirmation of treatment efficacy.

A new method for real-time assessment of margins involves splitting the dose of FDG administered [22]. A standard dose of 12 mCi (444 MBq) is divided into a localizing dose 4 mCi (148 MBq) and a treatment efficacy dose of 8 mCi (296 MBq). By the time, the ablation has concluded the majority of the localizing dose decays away. The second FDG dose, by the time the postablation PET is acquired, is close to seven times the activity of the original dose. The PET acquisition is dominated by the second dose such that residual activity of the first dose is not registered by the PET scanner (Fig. 23.4).

A major technical concern regarding ablations is the inability to measure the margin of the ablation. Current surrogates for margin assessments (CT measurement of ablation defect in relation to original tumor size [23], identification of viable tissue adherent to ablation probe [24, 25]) are limited. False negative findings commonly occur due to vascular injury or procedural edema prohibiting contrast enhancement [26]. The benefit of the split-dose technique is the ability to confirm that an ablation was at least an "A1 ablation" similar to an R1 resection. The treatment efficacy dose does not guarantee 100% tumor cell death, but lack of avidity on post ablation scans represent the reduction in viable cancer volume below the threshold for FDG PET/CT detection.

PET/CT-Guided Surgery

A major challenge facing surgeons is the correlation of preoperative PET scans with intraoperative findings. Hand-held PET gamma cameras which detect 511 keV photons [27] and novel probes able to detect beta emissions [28] have had promising results. Similar to PET-guided percutaneous ablations a diagnostic PET is obtained before the date of surgery to confirm avidity of the area in question and aid in procedure planning. On the operation date 5–15 mCi of FDG are injected and physical activity should be kept to a minimum for 60 min post injection. Surgical exploration is scheduled 2–4 h after administration of FDG. The gamma camera is used to evaluate areas with abnormal uptake visualized on pre-op PET scans. A target to background ratio (TBR) of 1.5:1 [29] differentiates tumor tissue from normal adjacent tissues and areas with high TBR should be investigated.

TBR is affected by physiologic uptake and accumulation. Areas around the brain, heart, kidneys, and bladder can be challenging to assess accurately. Background radiation from physiologic uptake tends to decrease over time compared to tumor activity, which remains stable for a longer period. Planning the time required between injection and surgical exploration is particularly important when investigating these challenging areas.

Radiation Dose for PET-Guided Procedures

Safety studies of radiation dose from intra-operative [30, 31] and percutaneous [32] PET-guided procedures have demonstrated no significant difference in radiation exposure compared to fluoroscopically guided procedures if proper techniques are followed. In PET, the source of radiation (511 keV) is significantly higher than that of CT (140 keV). Personal protective devices such as lead shielding, aprons, and glasses are ineffective against PET radiation [33]. However, proper techniques similar to CT-guided procedures; such as limiting exposure time and increasing distance from patient when feasible, were shown to reduce overall radiation dose during PET/CT procedures [32]. In addition, since a majority of FDG is excreted in the urine [34], patients should void before being prepped for the procedure.

Section 4: Monitoring Treatment Response After PET-Guided Procedures

Postoperative PET monitoring can detect residual disease months before findings are definitive on contrast enhanced CT imaging [35–38]. Local control rates for ablative techniques with newer technologies (i.e., MWA) may be as high as 88–96 % [39–41], and detection of local recurrence at an earlier time may allow for repeat curative therapy. The resolution of PET activity has a negative predictive value of 96–100 % [35, 42]. The ideal time interval for repeat PET/CT imaging is controversial since inflammatory changes are likely to be present after any intervention and foci of increased FDG uptake do not always represent residual disease.

Lung tissue is especially prone to having increased uptake not related to local recurrence following treatment [37, 42, 43]. At 3 months, the diagnostic accuracy of a PET/CT scan following RFA ablation of a lung tumor was 66 % (sensitivity 91 %, specificity 63 %, positive predictive value (PPV) 23 %, and negative predictive value (NPV) 98 %) [42]. Some FDG uptake patterns are more indicative of treatment failure (Fig. 23.5). Focal uptake (Fig. 23.5b) or a rim with a focus at the site of the original lesion (Fig. 23.5f) is more likely to represent recurrent disease [37]. A negative 3-month PET/CT is useful in ruling out residual disease but positive findings need to be confirmed by biopsy before subsequent treatment is indicated.

PET/CT following local liver treatment is accurate even with short duration follow up and offers earlier detection of recurrence over contrast enhanced CT or MRI imaging [44–46]. Similar to lung tissue, a negative PET/CT has a NPV of 96–100 %, but unlike the lungs, a positive PET/CT is more indicative of residual disease with

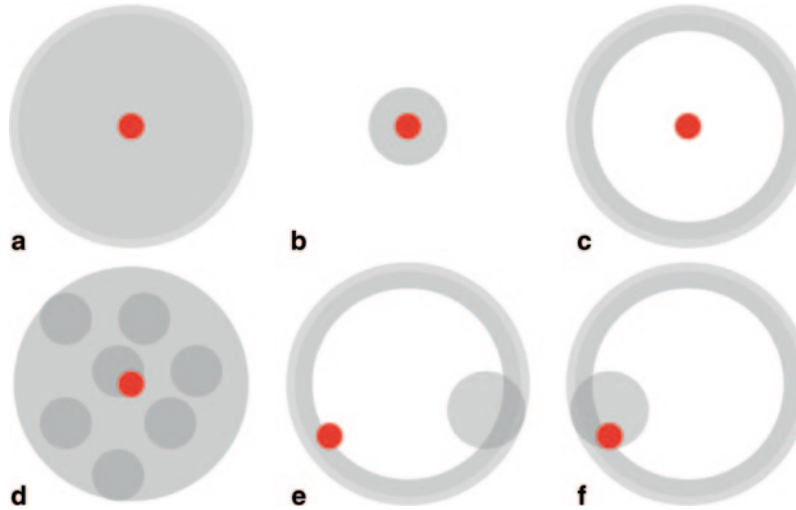

Fig. 23.5 Patterns of uptake on posttreatment FDG PET/CT. Diffuse (**a**), focal (**b**), rim (**c**), heterogeneous (**d**), rim with focus different than original lesion (**e**), rim with focus in site of original lesion (**f**). The *red dot* represents the location of the primary disease. (Adapted from [37])

a PPV of 80–97% [35, 47–50]. Nonspecific rim enhancement (Fig. 23.5c) can be observed within 5 months [38] and should not prompt intervention without histological confirmation. A 3-month PET/CT is useful in ruling out residual disease and positive findings, with the exception of non-focal rim enhancement, should be considered highly suspicious for local recurrence.

The clinical usefulness of PET/CT in the posttreatment of other areas of the body is promising. In follow up of patients with treated breast cancer PET/CT is reported to have a diagnostic accuracy of 91% (sensitivity 91%, specificity 92%, PPV 95%, and NPV 88%) [51, 52]. PET/CT's role is currently being investigated for the treatment response of soft tissue tumors, but preliminary reports are promising in its ability to differentiate between pathologic and benign findings [53, 54].

Conclusion

PET/CT has revolutionized the standard of care for cancer patients. Whereas the role of PET/CT in cancer staging is well established, integrating metabolic imaging into procedures is a new and rapidly expanding field. PET guidance during procedures allows for identification and targeting of tumors previously impossible to identify with conventional modalities. New PET techniques facilitate an immediate assessment of therapeutic margins allowing for repeat intervention while patients are still on the operating table. PET/CT use in posttreatment follow up can identify local recurrence at a shorter time point when a repeat intervention is still possible.

References

1. Juweid ME, Cheson BD. Positron-emission tomography and assessment of cancer therapy. N Engl J Med. 2006;354(5):496–507.
2. Rigo P, Paulus P, Kaschten BJ, Hustinx R, Bury T, Jerusalem G, et al. Oncological applications of positron emission tomography with fluorine-18 fluorodeoxyglucose. Eur J Nucl Med Mol Imaging. 1996;23(12):1641–74.
3. Kong G, Jackson C, Koh DM, Lewington V, Sharma B, Brown G, et al. The use of 18F-FDG PET/CT in colorectal liver metastases—comparison with CT and liver MRI. Eur J Nucl Med Mol Imaging. 2008;35(7):1323–9.
4. Perry C, Herishanu Y, Metzer U, Bairey O, Ruchlemer R, Trejo L, et al. Diagnostic accuracy of PET/CT in patients with extranodal marginal zone MALT lymphoma. Eur J Haematol. 2007;79(3):205–9.
5. Grgic A, Nestle U, Schaefer-Schuler A, Kremp S, Ballek E, Fleckenstein J, et al. Nonrigid versus rigid registration of thoracic 18F-FDG PET and CT in patients with lung cancer: an intraindividual

comparison of different breathing maneuvers. J Nucl Med. 2009;50(12):1921–6.
6. Beyer T, Townsend DW, Brun T, Kinahan PE, Charron M, Roddy R, et al. A combined PET/CT scanner for clinical oncology. J Nucl Med. 2000;41(8):1369–79.
7. Lardinois D, Weder W, Roudas M, von Schulthess GK, Tutic M, Moch H, et al. Etiology of solitary extrapulmonary positron emission tomography and computed tomography findings in patients with lung cancer. J Clin Oncol. 2005;23(28):6846–53.
8. Metser U, Even-Sapir E. Increased (18)F-fluorodeoxyglucose uptake in benign, nonphysiologic lesions found on whole-body positron emission tomography/computed tomography (PET/CT): accumulated data from four years of experience with PET/CT. Semin Nucl Med. 2007;37(3):206–22.
9. Cerci JJ, Pereira Neto CC, Krauzer C, Sakamoto DG, Vitola JV. The impact of coaxial core biopsy guided by FDG PET/CT in oncological patients. Eur J Nucl Med Mol Imaging. 2013;40(1):98–103.
10. Higashi K, Clavo AC, Wahl RL. In vitro assessment of 2-fluoro-2-deoxy-D-glucose, L-methionine and thymidine as agents to monitor the early response of a human adenocarcinoma cell line to radiotherapy. J Nucl Med. 1993;34(5):773–9.
11. Kubota R, Kubota K, Yamada S, Tada M, Ido T, Tamahashi N. Active and passive mechanisms of [fluorine-18] fluorodeoxyglucose uptake by proliferating and prenecrotic cancer cells in vivo: a microautoradiographic study. J Nucl Med. 1994;35(6):1067–75.
12. Minn H, Clavo AC, Grenman R, Wahl RL. In vitro comparison of cell proliferation kinetics and uptake of tritiated fluorodeoxyglucose and L-methionine in squamous-cell carcinoma of the head and neck. J Nucl Med. 1995;36(2):252–8.
13. Minn H, Joensuu H, Ahonen A, Klemi P. Fluorodeoxyglucose imaging: a method to assess the proliferative activity of human cancer in vivo. Comparison with DNA flow cytometry in head and neck tumors. Cancer. 1988;61(9):1776–81.
14. Slosman DO, Pittet N, Donath A, Polla BS. Fluorodeoxyglucose cell incorporation as an index of cell proliferation: evaluation of accuracy in cell culture. Eur J Nucl Med. 1993;20(11):1084–8.
15. Shyn PB, Tatli S, Sainani NI, Morrison PR, Habbab F, Catalano P, et al. Minimizing image misregistration during PET/CT–guided percutaneous interventions with monitored breath-hold PET and CT acquisitions. J Vasc Interv Radiol. 2011;22(9):1287–92.
16. Schoellnast H, Larson SM, Nehmeh SA, Carrasquillo JA, Thornton RH, Solomon SB. Radiofrequency ablation of non-small-cell carcinoma of the lung under real-time FDG PET CT guidance. Cardiovasc Intervent Radiol. 2011;34(Suppl. 2):S182–5.
17. Sainani NI, Shyn PB, Tatli S, Morrison PR, Tuncali K, Silverman SG. PET/CT-guided radiofrequency and cryoablation: is tumor fluorine-18 fluorodeoxyglucose activity dissipated by thermal ablation? J Vasc Interv Radiol. 2011;22(3):354–60.
18. Ryan ER, Sofocleous CT, Schöder H, Carrasquillo JA, Nehmeh S, Larson SM, et al. Split-dose technique for FDG PET/CT-guided percutaneous ablation: a method to facilitate lesion targeting and to provide immediate assessment of treatment effectiveness. Radiology. 2013;268(1):288–95.
19. Shyn PB, Tatli S, Sainani NI, Morrison PR, Habbab F, Catalano P, et al. Minimizing image misregistration during PET/CT-guided percutaneous interventions with monitored breath-hold PET and CT acquisitions. J Vasc Interv Radiol. 2011;22(9):1287–92.
20. Soret M, Bacharach SL, Buvat I. Partial-volume effect in PET tumor imaging. J Nucl Med. 2007;48(6):932–45.
21. Sainani NI, Shyn PB, Tatli S, Morrison PR, Tuncali K, Silverman SG. PET/CT-guided radiofrequency and cryoablation: is tumor fluorine-18 fluorodeoxyglucose activity dissipated by thermal ablation? J Vasc Interv Radiol. 2011;22(3):354–60.
22. Ryan ER, Sofocleous CT, Schoder H, Carrasquillo JA, Nehmeh S, Larson SM, et al. Split-dose technique for FDG PET/CT-guided percutaneous ablation: a method to facilitate lesion targeting and to provide immediate assessment of treatment effectiveness. Radiology. 2013;268(1):288–95.
23. Wang X, Sofocleous CT, Erinjeri JP, Petre EN, Gonen M, Do KG, et al. Margin size is an independent predictor of local tumor progression after ablation of colon cancer liver metastases. Cardiovasc Intervent Radiol. 2013;36(1):166–75.
24. Sofocleous CT, Nascimento RG, Petrovic LM, Klimstra DS, Gonen M, Brown KT, et al. Histopathologic and immunohistochemical features of tissue adherent to multitined electrodes after RF ablation of liver malignancies can help predict local tumor progression: initial results. Radiology. 2008;249(1):364–74.
25. Sofocleous CT, Garg S, Petrovic LM, Gonen M, Petre EN, Klimstra DS, et al. Ki-67 is a prognostic biomarker of survival after radiofrequency ablation of liver malignancies. Ann Surg Oncol. 2012;19(13):4262–9.
26. Weight CJ, Kaouk JH, Hegarty NJ, Remer EM, O'Malley CM, Lane BR, et al. Correlation of radiographic imaging and histopathology following cryoablation and radio frequency ablation for renal tumors. J Urol. 2008;179(4):1277–81. Discussion 81–3.
27. Gulec SA. PET probe-guided surgery. J Surg Oncol. 2007;96(4):353–7.
28. González SJ, González L, Wong J, Brader P, Zakowski M, Gönen M, et al. An analysis of the utility of handheld PET probes for the intraoperative localization of malignant tissue. J Gastrointest Surg. 2011;15(2):358–66.
29. Gulec SA, Daghighian F, Essner R. PET-probe: evaluation of technical performance and clinical utility of a handheld high-energy gamma probe in oncologic surgery. Ann Surg Oncol. 2006;13:525–9.

30. Andersen PA, Chakera AH, Klausen TL, Binderup T, Grossjohann HS, Friis E, et al. Radiation exposure to surgical staff during F-18-FDG-guided cancer surgery. Eur J Nucl Med Mol Imaging. 2008;35(3):624–9.
31. Povoski SP, Sarikaya I, White WC, Marsh SG, Hall NC, Hinkle GH, et al. Comprehensive evaluation of occupational radiation exposure to intraoperative and perioperative personnel from 18F-FDG radioguided surgical procedures. Eur J Nucl Med Mol Imaging. 2008;35(11):2026–34.
32. Ryan ER, Thornton R, Sofocleous CT, Erinjeri JP, Hsu M, Quinn B, et al. PET/CT-guided interventions: personnel radiation dose. Cardiovasc Intervent Radiol. 2013;36(4):1063–7.
33. Ahmed S, Zimmer A, McDonald N, Spies S. The effectiveness of lead aprons in reducing radiation exposures from specific radionuclides. J Nucl Med. 2007;48(MeetingAbstracts_2):470P.
34. Moran JK, Lee HB, Blaufox MD. Optimization of urinary FDG excretion during PET imaging. J Nucl Med. 1999;40(8):1352–7.
35. Langenhoff BS, Oyen WJ, Jager GJ, Strijk SP, Wobbes T, Corstens FH, et al. Efficacy of fluorine-18-deoxyglucose positron emission tomography in detecting tumor recurrence after local ablative therapy for liver metastases: a prospective study. J Clin Oncol. 2002;20(22):4453–8.
36. Anderson GS, Brinkmann F, Soulen MC, Alavi A, Zhuang H. FDG positron emission tomography in the surveillance of hepatic tumors treated with radiofrequency ablation. Clin Nucl Med. 2003;28(3):192–7.
37. Singnurkar A, Solomon SB, Gonen M, Larson SM, Schoder H. 18F-FDG PET/CT for the prediction and detection of local recurrence after radiofrequency ablation of malignant lung lesions. J Nucl Med. 2010;51(12):1833–40.
38. Nielsen K, van Tilborg AA, Scheffer HJ, Meijerink MR, de Lange-de Klerk ES, Meijer S, et al. PET-CT after radiofrequency ablation of colorectal liver metastases: suggestions for timing and image interpretation. Eur J Radiol. 2013;82(12):2169–75.
39. Huang S, Yu J, Liang P, Yu X, Cheng Z, Han Z, et al. Percutaneous microwave ablation for hepatocellular carcinoma adjacent to large vessels: a long-term follow-up. Eur J Radiol. 2014;83(3):552–8.
40. Groeschl RT, Pilgrim CHC, Hanna EM, Simo KA, Swan RZ, Sindram D, et al. Microwave ablation for hepatic malignancies: a multiinstitutional analysis. Ann Surg. 2013;259(6):1195–200.
41. Little MW, Chung D, Boardman P, Gleeson FV, Anderson EM. Microwave ablation of pulmonary malignancies using a novel high-energy antenna system. CardioVasc Intervent Radiol. 2013;36(2):460–5.
42. Bonichon F, Palussiere J, Godbert Y, Pulido M, Descat E, Devillers A, et al. Diagnostic accuracy of 18F-FDG PET/CT for assessing response to radiofrequency ablation treatment in lung metastases: a multicentre prospective study. Eur J Nucl Med Mol Imaging. 2013;40(12):1817–27.
43. Yoo DC, Dupuy DE, Hillman SL, Fernando HC, Rilling WS, Shepard JA, et al. Radiofrequency ablation of medically inoperable stage IA non-small cell lung cancer: are early posttreatment PET findings predictive of treatment outcome? AJR Am J Roentgenol. 2011;197(2):334–40.
44. Chen W, Zhuang H, Cheng G, Torigian DA, Alavi A. Comparison of FDG-PET, MRI and CT for post radiofrequency ablation evaluation of hepatic tumors. Ann Nucl Med. 2013;27(1):58–64.
45. Sahin DA, Agcaoglu O, Chretien C, Siperstein A, Berber E. The utility of PET/CT in the management of patients with colorectal liver metastases undergoing laparascopic radiofrequency thermal ablation. Ann Surg Oncol. 2012;19(3):850–5.
46. Kuehl H, Antoch G, Stergar H, Veit-Haibach P, Rosenbaum-Krumme S, Vogt F, et al. Comparison of FDG-PET, PET/CT and MRI for follow-up of colorectal liver metastases treated with radiofrequency ablation: initial results. Eur J Radiol. 2008;67(2):362–71.
47. Denecke T, Steffen I, Hildebrandt B, Ruhl R, Streitparth F, Lehmkuhl L, et al. Assessment of local control after laser-induced thermotherapy of liver metastases from colorectal cancer: contribution of FDG-PET in patients with clinical suspicion of progressive disease. Acta Radiol (Stockholm, Sweden: 1987). 2007;48(8):821–30.
48. Veit P, Antoch G, Stergar H, Bockisch A, Forsting M, Kuehl H. Detection of residual tumor after radiofrequency ablation of liver metastasis with dual-modality PET/CT: initial results. Eur Radiol. 2006;16(1):80–7.
49. Joosten J, Jager G, Oyen W, Wobbes T, Ruers T. Cryosurgery and radiofrequency ablation for unresectable colorectal liver metastases. Eur J Surg Oncol. 2005;31(10):1152–9.
50. Donckier V, Van Laethem JL, Goldman S, Van Gansbeke D, Feron P, Ickx B, et al. [F-18] fluorodeoxyglucose positron emission tomography as a tool for early recognition of incomplete tumor destruction after radiofrequency ablation for liver metastases. J Surg Oncol. 2003;84(4):215–23.
51. Emad-Eldin S, Abdelaziz O, Harth M, Hussein M, Nour-Eldin NE, Vogl TJ. The clinical utility of FDG-PET/CT in follow up and restaging of breast cancer patients. Egypt J Radiol Nucl Med. 2013;44(4):937–43.
52. Kurata A, Murata Y, Kubota K, Osanai T, Shibuya H. Multiple 18F-FDG, PET-CT for postoperative monitoring of breast cancer patients. Acta Radiol. 2009;50(9):979–83.
53. Leal AL, Etchebehere M, Santos AO, Kalaf G, Pacheco EB, Amstalden EM, et al. Evaluation of soft-tissue lesions with 18F-FDG PET/CT: initial results of a prospective trial. Nucl Med Commun. 2014;35(3):252–9.
54. Hoshi M, Oebisu N, Takada J, Ieguchi M, Wakasa K, Nakamura H. Role of FDG-PET/CT for monitoring soft tissue tumors. Oncol Lett. 2014;7(4):1243–8.

Index

Y. Fong et al. (eds.), *Imaging and Visualization in The Modern Operating Room,*
DOI 10.1007/978-1-4939-2326-7, © Springer Science+Business Media New York 2015